



Chair of Mining Engineering and Mineral Economics

Doctoral Thesis

Dynamic crack patterns, crack interactions, and resulting blast fragmentation - Experimental investigation on blast-induced fines and underlying mechanisms in small-scale blasting of mortar and granite cylinders

Ivan Kukolj, Mast.inz.saobr., Mast.inz.rud.

January 2021

**Dynamic crack patterns, crack interactions, and resulting
blast fragmentation**

Experimental investigation on blast-induced fines and
underlying mechanisms in small-scale blasting
of mortar and granite cylinders

Dissertation

by Ivan Kukolj

Submitted to the
Chair of Mining Engineering and Mineral Economics

in fulfilment of the requirements of the degree of

Doktor der montanistischen Wissenschaften

at

Montanuniversitaet Leoben

Declaration of Authorship



MONTANUNIVERSITÄT LEOBEN
www.unileoben.ac.at

EIDESSTÄTLICHE ERKLÄRUNG

I declare on oath that I wrote this thesis independently, did not use other than the specified sources and aids, and did not otherwise use any unauthorized aids.

I declare that I have read, understood, and complied with the guidelines of the senate of the Montanuniversität Leoben for "Good Scientific Practice".

Furthermore, I declare that the electronic and printed version of the submitted thesis are identical, both, formally and with regard to content.

Datum 13.01.2021

A handwritten signature in blue ink, appearing to read 'Ivan Kukolj', written over a horizontal line.

Signature Author
Ivan Kukolj

Dedication

To my dear family

Acknowledgements

This work was financed by the Austrian Science Fund (FWF): project P27594-N29 and Montanuniversitaet Leoben (MUL), and carried out at the Chair of Mining Engineering and Mineral Economics.

I would like to thank Prof Dr. Finn Ouchterlony for being my supervisor and mentor, for helping me broaden my horizons and face my flaws and ignorance.

I would like to thank Prof Dr. Peter Moser for granting me this amazing opportunity to work and study at MUL and learn from some of the best researchers in their field of science.

I would like to thank Gerold Wölfler, Dr. Bernd Oberdorfer (Österreichisches Gießerei Institut, MUL), Prof Dr. Christian Weiss, Dr. Jan Lubensky (Chair of Process Technology and Environmental Protection, MUL), Prof Dr. Heinrich Mali (Chair of Geology and Economic Geology, MUL), Prof Dr. Andreas Böhm (Chair of Mineral Processing, MUL), and Prof Dr. Thomas Antretter (Chair of Mechanics, MUL), for their substantial contribution to the project and my thesis, and overall professional experience.

I am also grateful to Dr. Alexander Tscharf, Dr. Phillipp Hartlieb, Thomas Seidl, Dr. Peter Schimek, Dr. Radoslava Ivanova, and all my colleagues at the Chair of Mining Engineering and Mineral Economics, MUL, for their kind and invaluable support during all these years.

I would also like to thank Dr. Armin Iravani, my project colleague during this dissertation, for our four years of cooperation.

This dissertation has changed my life in a way I had considered impossible before I arrived in Austria. Thank you all who have taken part in this once-in-a-lifetime experience of mine.

Thank you, Montanuniversitaet!

Glück auf!

Abstract

Industrial raw-mineral exploitation in most cases relies on rock fragmentation. In common mining and quarrying practice, the initial fragmentation is carried out by blasting due to its economic advantages.

Blast-induced fines in rock negatively affect multiple aspects of raw-mineral sustainability. The Austrian Science Fund (FWF) sponsored project P27594-N29 to investigate the cause of the fines by studying blast fragmentation through small-scale blast tests and numerical simulations. This thesis covers the experimental part of the project.

Various theoretical models have been developed to describe blast fragmentation and the generation of the blast fines, focussing on crushing-shearing, usually around the blast hole, and/or dynamic branching-merging of running cracks as the main underlying mechanisms. However, published studies do not cover any experimental investigation on the link between blast-induced crack development and final crack patterns with the resulting fragmentation in rock.

As the blast-driven fracturing leads to the final fragmentation, this thesis focuses on the corresponding mechanisms during the development and in the final states of blast-induced crack patterns and the resulting fragmentation, considering the two main mechanisms.

The blast tests were carried out by blasting confined mortar and granite cylinders with detonating cord with 6, 12, and 20 g/m of PETN. The blast-driven dynamic cracking at the frontal end face of the cylinder, opposite to the initiation point, was filmed with a high-speed camera. The post-mortem external crack patterns were captured with digital photography. The internal crack patterns and fracture surfaces were obtained with computer tomography (CT), optical microscopy, and scanning-electron microscopy (SEM). The crack patterns were used to identify the mechanisms and count topological features (i.e., crack tips and crack intersections). The blasted cylinders were screened by sieving and laser-diffraction spectroscopy to measure the blast fragmentation. The fragmentation results were correlated with the quantified mechanisms from the crack patterns and with identified microscopic mechanisms.

The crack development at the frontal end face occurs in three fracture phases: 1) initial crack emerging and propagation, 2) increasingly complex branching and merging of running cracks, and 3) spalling and inrush (spillage) of the blast fumes. The topological branching/merging features are highly correlated with the used specific charge (q) and the resulting blast-induced fines. Branching/merging indicators in the high-speed images (HSI) increase with time, usually following a bilinear function with a kink point in the second fracture phase. The crack patterns become more uniform along the axis of the blasted cylinders with the increase of q .

The blast loading forms a crushed zone only around the blast hole. This zone includes a compaction zone in the mortar cylinders. The thickness of the crushed zone does not directly depend on the material of the blasted cylinder, though rather on the loading and the boundary conditions. The micrographs show that the crushed zone is not only formed by crushing-shearing, as the reviewed literature suggests, though also by microscopic variations of crack branching-merging.

All observed mechanisms are related to the main mechanisms in both blasted materials. Furthermore, they represent variations of these main mechanisms at different size scales, affected by the loading conditions and the micro-structure of the blasted material. An s - $n(s)$ description of the fragmentation data shows that the main mechanisms dominate in different fragment-size ranges, which is not directly affected by q or by the blasted material.

Zusammenfassung

Die industrielle Gewinnung von Rohstoffen beruht in den meisten Fällen auf der Zerkleinerung von Gestein. In der gängigen Bergbau- und Abbaupraxis wird die Erstzerkleinerung aufgrund der wirtschaftlichen Vorteile meist durch Sprengen durchgeführt.

Die sprengungsinduzierten Feianteile im Gestein wirkt sich auf mehrere Aspekte der rohstofflichen Nachhaltigkeit negativ aus. Der österreichische Wissenschaftsfonds (FWF) unterstützte Projekt P27594-N29 zur Untersuchung der Ursache der Feianteile durch die Untersuchung der Sprengzerkleinerung mittels kleinmaßstäblicher Sprengversuche und numerischer Simulationen. Die vorliegende Arbeit deckt den experimentellen Teil dieses Projekts ab.

Verschiedene theoretische Modelle beschreiben die Sprengzerkleinerung und den Feianteil. Der Schwerpunkt liegt dabei auf der Quetsch-Scherung, um das Sprengloch herum, und/oder auf der dynamischen Verzweigung/Verschmelzung von Rissen als die wichtigsten zugrundeliegenden Mechanismen. Die veröffentlichten Studien umfassen jedoch keine experimentellen Untersuchungen über den Zusammenhang zwischen den sprengungsinduzierten Rissbildern mit der daraus resultierenden Zerkleinerung im Gestein. Diese Arbeit konzentriert sich auf die entsprechenden Mechanismen bei der Entstehung und im Endzustand von sprengungsinduzierten Rissbildern und der daraus resultierenden Zerkleinerung unter dem Fokus der beiden Hauptmechanismen.

Die Sprengversuche wurden durch Sprengung von eingeschlossenen Mörtel- und Granitzylindern mit Sprengschnüren (6, 12 und 20 g/m PETN) durchgeführt. Die durch die Sprengung hervorgerufene dynamische Rissbildung an der Stirnfläche des Zylinders wurde mit einer Hochgeschwindigkeitskamera gefilmt. Die postmortalen äußeren Rissbilder wurden mit Digitalfotografie erfasst. Die inneren Rissbilder und Bruchflächen wurden mit Computertomografie (CT), optischer Mikroskopie und Rasterelektronenmikroskopie (REM) erfasst. Die erfassten Rissbilder wurden verwendet, um die Mechanismen zu identifizieren und topologische Merkmale (d.h. Risspitzen und Risskreuzungen) zu zählen. Die gesprengten Zylinder wurden durch Sieben und Laserbeugungsspektroskopie untersucht.

Die Ergebnisse der Zerkleinerung wurden mit den quantifizierten Mechanismen aus den Rissbildern und den identifizierten mikroskopischen Mechanismen korreliert. Die Rissentwicklung an der Stirnfläche erfolgt in drei Bruchphasen: 1) initiale Rissentstehung und -ausbreitung, 2) zunehmend komplexere Verzweigung und Verschmelzung von Rissen und 3) Abplatzen und Einströmen der Sprengdämpfe. Die topologischen Verzweigungs-/Verschmelzungsmerkmale sind hoch korreliert mit der verwendeten spezifischen Sprengladung (q) und den daraus resultierenden Feinanteilen.

Die Verzweigung-/Verschmelzung in den Hochgeschwindigkeitsaufnahmen (HSI) nehmen mit der Zeit zu und folgen in der Regel einer bilinearen Funktion. Die CT Rissbilder werden mit der Zunahme von q gleichmäßiger.

Die Sprengladung bildet nur um das Sprengloch herum eine Quetschzone, mit einer Verdichtungszone in den Mörtelzylindern. Die Dicke der Quetschzone hängt von der Belastung und den Randbedingungen ab. Die Quetschzone wird nicht nur durch Quetsch-Scherung gebildet, wie die rezensierte Literatur vermuten lässt, sondern auch durch mikroskopische Variationen der Rissverzweigung und -verschmelzung.

Alle beobachteten Mechanismen sind mit den Hauptmechanismen in beiden gesprengten Materialien verwandt. Außerdem stellen sie Variationen dieser Hauptmechanismen auf verschiedenen Größenskalen dar, die von den Belastungsbedingungen und der Mikrostruktur des gesprengten Materials beeinflusst werden. Eine s - $n(s)$ -Beschreibung der Zerkleinerungsdaten zeigt, dass die Hauptmechanismen in verschiedenen Fragmentgrößenbereichen dominieren, was nicht direkt von q oder vom gesprengten Material beeinflusst wird.

Table of Contents

Declaration of Authorship	III
Dedication	IV
Acknowledgements	V
Abstract	VI
Zusammenfassung	VIII
List of symbols and abbreviations	1
1 Introduction	2
1.1 Objectives	3
1.2 Scientific contribution	4
1.3 Thesis structure and research scope	5
1.4 List of papers and contributions of the author related to this thesis	6
2 Literature review	7
2.1 Single-hole blasting and fragmentation	8
2.2 Mechanisms that cause blast fines	14
3 Experimental method and materials	30
3.1 Blast tests	31
3.1.1 Blast cylinders and damping material	31
3.1.2 Explosive charge and stemming	38
3.1.3 Blast chamber	41
3.1.4 Conducted blast tests	44
4 Measurements and analyses	45
4.1 Fracture patterns	45
4.1.1 High-speed images (HSI)	45
4.1.2 Post-mortem images (PMI) of surface cracks	47
4.1.3 Computer-tomography (CT) measurements	50
4.1.4 Fracture tracing	51
4.1.5 Fracture-pattern topology	52
4.1.6 Fracture abundance	60
4.1.7 In-plane (2D) fragmentation	61
4.1.8 Main radial cracks	64
4.1.9 Crack-propagation speed	65
4.1.10 Macro-mechanisms	65

4.1.11	Measurement uncertainty of the crack patterns.....	70
4.2	Blast-hole expansion, cylinder swelling, and deformation zones	72
4.2.1	Estimates of blasted-off material, total blast-hole fines, and crack-generated fines	79
4.3	Fracture-surface analysis	80
4.4	Investigation in micro- and meso-scale.....	86
4.4.1	Thin sections	87
4.4.2	Small fragments	91
4.4.3	Micro- and meso-mechanisms	92
4.5	Blast-fragmentation analysis.....	97
4.5.1	Manual and mechanical sieving	97
4.5.2	Laser-diffraction granulometry.....	101
4.5.3	Screening data and fragment-size distribution (FSD).....	103
4.5.4	Simplified $n(s)$ model.....	105
4.5.5	Specific surface area of the fines (Blaine and Permeran measurements) and blast-energy register (BER).....	108
4.6	Statistical data processing and analysis	113
5	Results	114
5.1	Fracture phases in HSI	115
5.2	Number of main radial cracks (N)	119
5.3	Topological features	121
5.3.1	Absolute node counts and their proportions	121
5.3.2	Ternary diagrams of the node-count proportions.....	127
5.3.3	Average number of connections per line (C_L) and per branch (C_B)	132
5.3.4	Node-connectivity probabilities (p_l and p_c).....	135
5.3.5	Fracture abundance - areal frequency (p_{20}) and fracture intensity (p_{21}) ..	139
5.4	In-plane (2D) fragmentation	144
5.5	Crack-propagation speed	152
5.6	Macro-mechanisms	155
5.7	Blast-hole expansion, deformation zones, and radial swelling.....	160
5.7.1	Blast-hole expansion and cylinder swelling	160
5.7.2	Deformation zones	162
5.8	Micro- and meso-mechanisms.....	167
5.8.1	Mortar thin sections	168
5.8.2	Granite thin sections.....	180
5.8.3	Small fragments	188

5.9	Blast-induced fracture surfaces	193
5.9.1	Height maps and surface-roughness images	193
5.9.2	Fracture-surface roughness	198
5.10	Blast fragmentation.....	201
5.10.1	Screening results and fragment-size distributions (FSDs).....	201
5.10.2	Blast fines.....	207
5.10.3	Specific surface area of the fines and blast-energy register (BER)	211
5.10.4	Resulting “s-n(s)” curves	215
5.11	Correlation analysis	217
5.11.1	Summary of the correlation results.....	223
5.12	Summary of results.....	225
5.12.1	Traced fracture patterns, topological features, and derived results	225
5.12.2	Identified mechanisms and deformation zones	229
5.12.3	Blast fragmentation	232
6	Discussion.....	234
6.1	Traced fracture patterns	234
6.2	Topological features	239
6.3	Crack-propagation speed	243
6.4	Observed mechanisms	244
6.5	Blast-hole expansion, mantle swelling, and deformation zones.....	246
6.6	Fracture-surface roughness.....	248
6.7	The fragment-size distribution (FSD) curves	249
6.8	Blast fines	251
6.9	Specific surface area and blast-energy register (BER)	252
6.10	Resulting “s-n(s)” curves.....	255
7	Summary and conclusions	257
8	Future work	262
9	Bibliography	264
10	List of Figures.....	277
11	List of Tables.....	297
Appendix 1	Sample production	311
	Datasheets of materials used for sample production	318
Appendix 2	Material properties (procedure and result data).....	319
	Density	319
	Uniaxial compressive strength (UCS) tests	325

Indirect uniaxial tensile strength (Brazilian UTS - BTS) tests	327
Ultrasound tests	328
Wedge splitting test (WST).....	332
Preliminary deformation	337
Average grain size and average pore size (mortar)	351
Appendix 3 Blast-test set-up	356
Test site	356
Conducted blast tests.....	358
Blast cylinders and the damping layer.....	360
Charge coupling and stemming.....	362
Technical drawings and model details of the blast chamber	364
Appendix 4 High-speed-imaging (HSI) equipment and configuration	373
Appendix 5 CT scanning and pre-processing.....	375
Appendix 6 Image sets (HSI, PMI, PMM, CTt, CTnp)	376
Appendix 7 MATLAB® scripts for processing the crack patterns	377
Appendix 8 Crack-pattern analysis – result-data sets	378
Sets from HSI and PMI	378
Crack-propagation data sets	393
Sets from CTt.....	394
Sets from CTnp.....	399
Appendix 9 Additional results of the topological analysis	401
Crack-line count (N_L) and branch count (N_B).....	401
Branch-connectivity probabilities (p_{II} , p_{IC} , and p_{CC})	405
Fracture abundance – dimensionless fracture intensity (p_{22})	408
Appendix 10 Results of statistical analyses	412
Number of main radial cracks (N).....	412
Absolute node counts (N_i , J_{int} , N_{TB}).....	413
Average number of connections per line (C_L) and per branch (C_B).....	427
Node-connectivity probabilities (p_I and p_C).....	430
Fracture abundance (p_{20} , p_{21} , and p_{22}).....	438
In-plane (2D) fragmentation	444
Fracture-surface roughness	449
Regression lines of the s-n(s) data.....	451
Appendix 11 Blast-fragmentation measurement (additional details)	458
Manual and mechanical sieving	458

Laser-diffraction granulometry.....	459
Datasheets of (measuring) balance scales	462
Appendix 12 Statistical methods	463
Student's two-sample t-test.....	463
Single-factor (One-way) ANOVA and the F-test.....	464
Two-factor (Two-way) ANOVA with replication and the F-test	467
Comparison of slopes of two linear-regression lines	471
Comparison of multiple regression lines	472
One-way analysis of covariance (ANCOVA).....	474
Appendix 13 Result data – Macro-mechanism event logs	475
Blast test 22.2 (mortar, 6 g/m).....	475
Blast test 23.2 (mortar, 6 g/m).....	475
Blast test 20 (mortar, 12 g/m).....	476
Blast test 21 (mortar, 12 g/m).....	476
Blast test 22.1 (mortar, 20 g/m).....	477
Blast test 23.1 (mortar, 20 g/m).....	477
Blast test 26.1 (granite, 6 g/m)	478
Blast test 27 (granite, 6 g/m)	478
Blast test 24 (granite, 12 g/m)	479
Blast test 25 (granite, 12 g/m)	479
Blast test 26.2 (granite, 20 g/m)	479
Appendix 14 Blast-hole expansion- raw measurement data of the normalized blast-hole radius	480
Appendix 15 Selected sets of the uCT sections.....	487
Appendix 16 Selected micrographs of thin sections and small fragments	488
Appendix 17 Blast-induced fracture surfaces (raw results)	489
Appendix 18 Screening data, FSDs, and curve-fitting results	490
Sieving data	490
Merged screening data (laser-diffraction granulometry and sieving).....	496
Data on specific surface areas and blast-energy register (BER).....	503
Fitting results – Swebrec 3p	515
Fitting results – Swebrec 5p	520
Resulting “s-n(s)” curves and raw fitting data	524
Appendix 19 Blaine and Permeran tests (raw data).....	534
Appendix 20 Correlation analysis (raw data tables)	535

List of symbols and abbreviations

ΔA_f [cm ²]	Area of a fragment-size fraction	branching-merging	branching-merging
$(m_{n+1} - m_n)$ [g]	Mass of a fragment-size fraction (n+1 n)	bt, ms	Mica (biotite or muscovite) (in the granite)
$\bar{r}_{bh,a}$ [mm]	The radius of a circle with the same area as A_{bh} , i.e., average position of ablated blast hole	c [-]	The factor of grain-size-correction strength
$\bar{r}_{m,a}$ [mm]	The radius of a circle with the same area as A_m , i.e., average position of the mantle	C ₁ [mm]	The lengths of radial cracks in the CZM
\emptyset_h [mm]	Initial blast-hole (borehole) diameter	C _{1, C₂, C₃} [-]	Constants used in the simplified n(s) model
\dot{p} [MPa/ μ s]	The loading rate of the blast	Calc.	Calculated
$0_{m,pi}$	In-line merging	C _B [-]	The average number of connections per crack branch
2D	Two-dimensional	cc	Cleavage cracking (meso/micro-mechanism)
3D	Three-dimensional	C-C	Full connectivity (i.e., connected on both ends) of a crack line or a crack branch
A_{bh} [mm ²]	The area circumscribed inside ablated blast-hole after the blast	CDF	Cumulative distribution function
A_f [cm ²]	Total fragmented area	cem	cement matrix (in the mortar)
a-lt _s	Side crack arrest	CGF	Crack-generated fines
a_m [cm ² /g]	Mass-specific area (for a fragment-size fraction)	C _L [-]	The average number of connections per crack line
A_m [mm ²]	The area circumscribed by outer lasso curve around the mantle after blast	C _p [m/s]	P-wave speed
$a_{m,tot}$ [cm ² /g]	Total mass-specific area of a blasted cylinder	CPL	Cross-polarized light (optical transmitted-light microscopy)
ANCOVA	Statistical analysis of covariance	C _R [m/s]	Rayleigh-wave speed
ANOVA	Statistical analysis of variance	Crack, crack wake, crack flanks, crack tip, process zone - see Figure 65	
a_s [cm ⁻¹]	Volume-specific area	C _s [m/s]	S-wave speed
Ave	Average value (arithmetic mean)	CT	Computer tomography
b [-]	Undulation parameter (factor)	CTnp	Non-planar computer-tomography cross-sections
BER	Blast-energy register	CTnp	Non-planar CT sections
BH	Blast hole	CTt	Transverse CT sections
branching/merging	Branching and/or merging	CZI	Crushing zone index
		CZM	Crushed-zone model

D	Physical dimension	I-I	No-connectivity (i.e., not connected on either end) of a crack line or a crack branch
D_{cent} [-]	The scatter of data points in a CT-ternary diagrams	I-nodes	End nodes (tips) of the cracks
d_g [-]	Average grain size	Interp.	Interpretation
$d-l_{t,s}$	Side crack deflection	IQR	Interquartile ranges
d_p [-]	Average pore size in the mortar	IZR	Impulszentrum für Rohstoffe
E [Pa]	Young's modulus	J_{int} [-]	Sum of the joining nodes (X, Y, and R)
E_c [J/g]	Specific energy consumption	K [MN·m ^{-3/2}]	Stress-intensity factor
E_{dyn} [Pa]	Dynamic Young's modulus	kfs	Potassium (K) feldspar (in the granite)
em	Cracking due to elastic mismatch (meso/micro-mechanism)	K_{Ic} [MN·m ^{-3/2}]	Critical stress-intensity factor
E_{PETN} [J/g]	Specific explosive energy for PETN	l_c [g/m]	Linear charge concentration of PETN cord
ER	Energy Register	L_C [mm]	The characteristic length, the arithmetic mean of the crack-line lengths
EU	European Union	l_{ch} [mm]	Charge length
F	The ratio of two scaled sums of squares reflecting different sources of variability	LLDPE	Linear low-density polyethylene
f_A [-]	Particle-shape factor	$l_{t,s}$	Crack extension
F_C [-]	Fines-correction factor in the CZM	$l_{t,si}$	Discontinuous (interrupted) crack extension
fc	Flaw-induced cracking (meso/micro-mechanism)	LTU	Luleå University of Technology
F_{crit}	The inverse of the F-probability distribution (right-tailed)	m_{CGF}^+ [%]	Maximum estimate of m_{CGF}
FSD	Fragment-size distribution	$m_{-0.04\text{ mm}}$ [g]	Sieved mass passing 0.04-mm sieve
FWF	The Austrian Science Fund	$m_{-0.1\text{ mm}}$ [g]	Sieved mass passing 0.1-mm sieve
G_{dyn} [GPa]	Dynamic shear modulus	$m_{-0.25\text{ mm}}$ [g]	Sieved mass passing 0.25-mm sieve
G_f [N/m]	Specific fracture energy	$m_{-0.5\text{ mm}}$ [g]	Sieved mass passing 0.5-mm sieve
$g_r(v)$ [-]	The grain-size-correction factor	$m_{-1\text{ mm}}$ [g]	Sieved mass passing 1-mm sieve
HSI	High-speed image(s)	mc	Micro-fault-induced cracking (meso/micro-mechanism)
ic	Impingement/impact cracking (meso/micro-mechanism)	m_{CGF}^- [%]	Minimum estimate of m_{CGF}
I-C	Semi-connectivity (i.e., connected on only one end) of a crack line or a crack branch	m_{CGF} [g]	Mass of the crack-generated fines (CGF)
IG	Intergranular fracturing		

m_{CGF_cyl} [%]	Mass proportion of the crack-generated fines (CGF) relative to M_{cyl}	ÖGI	The Austrian Foundry Research Institute
m_{CGF_sieve} [%]	Mass proportion of the crack-generated fines (CGF) relative to m_{sieve}	p	Pore in the cement matrix (in the mortar)
M_{cyl} [g]	Initial mass of a blast cylinder	$P(x)$ [%]	Mass-passing probability as a function of the mesh size
m_{sieve} [g]	Total mass of sieved material	p_{20} [mm ⁻²]	Areal fracture frequency (fracture abundance)
m_{sieve_f} [g]	Mass of additionally sieved larger fragments	p_{21} [mm ⁻¹]	Fracture intensity (fracture abundance)
m_{tot_fines} [g]	Total mass of fines smaller than 1 mm	p_{22} [-]	Dimensionless fracture intensity (fracture abundance)
MUL	Montanuniversitaet Leoben	P_B [%]	Relative proportion of the boundary intersections
N [-]	The number of main radial cracks (fractures), initiated at a single blast hole	p_C [-]	The probability of any branch end being a connected node
n [-]	The number of radial cracks in the CZM	p_{CC} [-]	The probability of the C-C branch type
$n(s)$ [-]	Number of fragments of size s	p_{cl}	Partial cleavage and lamellar steps (micro-mechanisms transitioning between IG and TG)
$n(v)$ [-]	The number of fragments/kg as a function of volume v of the fragments	PF [g/t]	Powder factor
N_B [-]	The number of crack branches	p_g	Plagioclase (in the granite)
$n_b(s)$ [-]	The number of major fragments of size s	p_h [MPa]	The peak pressure level in the blast hole
NBC	Natural breakage characteristics	P_l [%]	Relative proportion of I-nodes
$n_{bm}(s)$ [-]	The number of branching-merging fragments of size s	p_l [-]	The probability of any branch end being an isolated node
$n_{crush}(s)$ [-]	The number of crushing-induced fragments of size s	p_{lC} [-]	The probability of the I-C branch type
N_l [-]	The number of I-nodes	p_{ll} [-]	The probability of the I-I branch type
N_L [-]	The number of crack lines	P_l [-]	Relative mass passing at x_l
N_R [-]	The number of R-nodes	pm	Cracking due to plastic mismatch (meso/micro-mechanism)
N_{TB} [-]	The number of the boundary intersections	PMI	Post-mortem image(s) of the frontal end face
N_X [-]	The number of X-nodes	PMM	Post-mortem image(s) of the cylinder mantle
N_Y [-]	The number of Y-nodes		
\emptyset [mm]	Diameter		

PPL	Plane-polarized light (optical transmitted-light microscopy)	s [-]	The number of (DEM) particles forming a fragment
P _R [%]	Relative proportion of R-nodes	SEM	Scanning-electron microscopy
P _u [%]	Relative mass passing at of x_u	SHPB	Split-Hopkinson-Pressure Bar
p-value	Probability evidence of the null hypothesis in statistical data analysis	Sign. diff.	Significantly different
P _X [%]	Relative proportion of X-nodes	s_n [-]	Local slope (GGs exponent)
P _Y [%]	Relative proportion of Y-nodes	Std	Standard deviation
q [kg/m ³]	Specific charge	Std. error	Standard error
Q [kg]	Quantity of explosive charge	STL	Stereolithography, a file format for mesh models
qtz	Quartz	T _B	Boundary intersections T _B (i.e., T _H +T _M)
R	Correlation coefficient	T _{b,sp}	Secondary T-branching
R _{BER} [cm ² /J]	Rittinger coefficient for BER	TCM	Two-component model
r_{bh} [mm]	Borehole radius	TG	Transgranular fracturing
$r_{blast,ob}$ [mm]	The outer limit of blasted-off zone before blasting	T _H	Intersections with the blast-hole wall
r_o [mm]	Initial blast-hole radius in the CZM	T _M	Intersections with the (outer) mantle of the cylinder
r_c [mm]	The radius of the crushed zone in the CZM	T _{m,sp}	Secondary T-merging
rc	Refracturing (meso/micro-mechanism)	UCS [MPa]	Uniaxial compressive strength
R _{ch} [mm]	Charge diameter	uCT	Micro-level computer tomography
$r_{comp,ia}$ [mm]	Inner limit of the compacted zone <u>a</u> fter blasting	UTS [MPa]	Uniaxial tensile strength
$r_{comp,ib}$ [mm]	Inner limit of the compacted zone <u>b</u> efore blasting	v [mm ³]	Volume of the fragments
$r_{comp,o}$ [mm]	The <u>o</u> uter limit of the <u>o</u> ur compacted zone after blasting	V _b [m ³]	Volume of the cracks in the CZM
$r_{crush,i}$ [mm]	Inner limit of the <u>crushed</u> zone after blasting	V _c [m ³]	Volume of the crushed material in the CZM
$r_{crush,o}$ [mm]	The <u>o</u> uter limit of the <u>crushed</u> zone after blasting	VOD [m/s]	Velocity of explosive detonation
r_{cyl} [mm]	Blast-cylinder radius	V _t [m ³]	Total volume being blasted in the CZM
R-nodes	Nodes of other (i.e., not I-, X-, Y-, or boundary) intersections	V _{uncorr} [-]	The volume scale of the Poisson process of statistical fragmentation
ROI	Region of interest	x [mm]	(Screening-)mesh size
RQ	Research question	x_{30} [mm]	Fragment size at P = 30%
		x_{50} [mm]	Median fragment size
		x_{80} [mm]	Fragment size at P = 30%

x_a [mm]	Surface-equivalent fragment size	δr_{bh} [mm]	The average blast-hole expansion
x_l [mm]	The lower limit of fragment-size class	$\Delta r_{blast,b}$ [mm]	The thickness of the blasted-off zone before blasting
x_{max} [mm]	Maximum fragment size	$\Delta r_{comp,a}$ [mm]	Thickness of the <u>compacted</u> zone <u>after</u> blasting
x_{min} [μ m]	Minimum fragment size	$\Delta r_{comp,b}$ [mm]	Thickness of the zone to be <u>compacted</u>
X-nodes	Cross intersections	$\Delta r_{crush,non-c}$ [mm]	Thickness of the <u>non-compacted</u> part of the <u>crushed</u> zone
$Y_{b,pa}$	Primary side Y-branching	$\Delta r_{crush,tot}$ [mm]	Thickness of the whole <u>crushed</u> zone <u>after</u> blasting
$Y_{b,ps}$	Primary in-line Y-branching	δr_m [mm]	The average expansion or swelling of the mantle
$Y_{b,sa}$	Secondary side Y-branching	$\Delta V_{blast,b}$ [mm ³]	Original volume of the <u>blasted-off</u> layer
$Y_{m,ps}$	Primary in-line Y-merging	$\Delta V_{comp,b}$ [mm ³]	Original volume of the <u>compaction</u> zone
$Y_{m,sa}$	Side Y-merging	θ [°]	The angle between the VOD vector and the Mach-cone front
Y-nodes	Branching/merging intersections	λ [mm]	The maximum penetration of the crack branches away from their parent cracks
α [-]	The degree of branching-merging in the simplified n(s) model	μ [-]	Poisson ratio
β [-]	The degree of crushing/grinding in the simplified n(s) model	μ_{dyn} [-]	Dynamic Poisson ratio
β_r [-]	The factor of the relative importance of the two processes (crushing and branching-merging)	ρ, ρ_b [g/cm ³]	Material (bulk) density
$\Delta m_{bh,i}$ [g]	The mass of the blast-hole-wall fines passing i-mm sieve (i = 1, 0.5, 0.25, 0.1, or 0.04)	ρ_c [g/cm ³]	Calculation density for a_m
ΔM_{blast} [g]	Estimated mass of the blasted-off material	ρ_g	Grain-level density
ΔM_{comp} [g]	Estimated mass of the compacted material		
ΔM_{loss} [g]	Material loss recorded during the sieving		

1 Introduction

Commercial blasting in the raw-minerals industry produces a considerable amount of waste fines. Downstream mechanical comminution by crushing and milling continues the process chain and further produces waste fines. Current market demands for raw minerals demand production increase, which in return exerts feasibility and sustainability issues.

Blasting is a highly dynamic process and the crack growth that defines breakage is considered a major source of fines (Ouchterlony & Moser, 2013). Such crack-generated fines (CGF) are produced by different kinds of industrial comminution of mineral raw materials. Fines are inherently related to the amount of energy required in fragmentation. Most of the fracture area created resides in the fines and this area determines the energy consumed (Steiner, 1991). Therefore, blast-generated fines negatively affect cost and revenue, environment and health protection, and sustainability, related to the extraction of raw minerals (Ouchterlony & Moser, 2013; Sanchidrián, 2018; Ouchterlony et al., 2018).

Improved understanding of the mechanisms causing CGF could improve the technologies applied in industrial blasting and mechanical comminution. By manipulating these mechanisms and influencing conditions, the resulting CGF could be suppressed at the source, rather than dealing with them afterwards.

Many researchers used small-scale blast tests to investigate the effects of blast loading in rock and mortar samples on the resulting fragmentation and crack patterns (Wilson & Holloway, 1987; Moser et al., 2000; Moser, 2003; Reichholf, 2003; Grasedieck, 2006; D. Johansson, 2011; Ivanova, 2015; Schimek, 2015). Although these post-blast observations may infer that the branching-merging mechanism causes most fines in rock and rock-like materials, further experimental evidence considering this mechanism is still required.

This thesis covers the experimental part of the three-year FWF project P27594-N29: “Fines generated by dynamic crack propagation, as in blasting of rock and rock-like materials” (2015–2018) (Iravani et al., 2018b, 2018a; Kukolj et al., 2018a, 2018b, 2019; Iravani, 2020) investigated if the branching-merging mechanism (Ouchterlony & Moser, 2013) is a major source of blast fines.

This thesis covers conducted small-scale blast experiments on cylindrical samples, and follow-up investigations of blast-induced dynamic crack propagation and fragmentation (i.e., fines generation) in rock and mortar material.

1.1 Objectives

The main objective of this thesis is to identify and quantify main mechanisms of dynamic blast-driven crack development in mortar and granite, and determine their relationship with the resulting blast fragmentation and fines. This objective requires the following research questions (RQ) to be answered:

- RQ1: What mechanisms can be identified in the development and in the final states of blast-induced cracks and fractures?
- RQ2: How can these mechanisms be identified and measured/quantified?
- RQ3: Which of these mechanisms are related to the generic mechanism of crack-tip branching-merging and how?
- RQ4: How do these mechanisms affect the blast fragmentation and the generation of blast fines?

Therefore, the following tasks were carried out:

- 1) observe potential physical mechanisms that cause blast-generated fines and quantify their relevant features resulting from small-scale blast tests;
- 2) determine the importance of the blast-induced branching/merging for crack generated fines (CGF);
- 3) measure the quantities and fragment-size distributions (FSDs) of blast fines;
- 4) correlate these mechanisms and features (i.e., patterns that indicate the mechanisms) with measured quantities of fines;
- 5) compare the measured FSDs with those of existing models based either on the mechanism of crack branching/merging or other mechanisms;
- 6) provide a scientific explanation of how and in what proportions these fine particles are generated.

1.2 Scientific contribution

Various theoretical models were developed to describe the generation of the blast fines and the underlying mechanisms (Djordjevic, 1999; Thornton et al., 2002; Esen et al., 2003; Åström et al., 2004a, 2004b; Onederra et al., 2004; Åström, 2006; Kekäläinen et al., 2007; Iravani, 2020).

Ouchterlony & Moser (2013) indicated the importance of understanding how crack-generated fines (CGF) are produced. They proposed the mechanism of branching-merging of a dynamically propagating crack tip as the dominating source of CGF. These models were tested through numerical investigations, simulations (e.g., Iravani, 2020), and experimental blast tests (e.g., Reichholf, 2003; Svahn, 2003; Moser, 2005; Grasedieck, 2006). However, published studies do not cover any experimental investigation on the link between blast-induced crack/fracture development and final crack patterns in rock with the resulting fragmentation. Therefore, these models still lack valid experimental proof and scientific explanation considering the sources of CGF and, hence, blast fines in general.

This thesis provides the following scientific contributions:

- The development of a working test set-up for small-scale blast tests on cylindrical rock and mortar specimens. The set-up includes a confinement with a transparent window that suppresses end-face spalling and allows a direct study of the dynamic and mainly radial cracking of the test cylinder.
- Visualization and analysis of the internal crack systems in blast-fractured specimens (preserved with the confinement) for load levels spanning from near limit load to almost complete fragmentation.
- Visualization and analysis of fracture surfaces of blast-generated fragments (from the blasted cylinders).
- Identification of microscopic blast-induced cracks, fractures, and other features in the blasted cylinders, considering blasting conditions and material structure.
- A topological description of crack systems independent of the geometry and development of a MatLab script to objectively quantify and compare them.
- Correlation of identified mechanisms and observed fracture features with resulting blast fragmentation of mortar and granite and test of main theoretical models that describe the generation of blast fines and CGF.

1.3 Thesis structure and research scope

Table 1 shows the structure of this thesis based on the objectives and aims of the underlying FWF project.

Table 1: Overview of the thesis structure and corresponding research tasks.

Research tasks	Thesis section
Provide an overview of the most important literature sources relevant to the main research topic of the thesis.	2
Develop a blast-test set-up with high-speed filming and conduct the small-scale blast tests.	3
Upon the blast tests, investigate the internal blast-induced crack patterns in the cylinders with computer tomography (CT).	4.1
Trace the crack patterns in the high-speed images (HSI) and the CT scans and classify relevant features of captured crack development as macro-mechanisms.	
Quantify these macro-mechanisms in the conducted blast tests.	
Measure geometrical and structural deformations in the blasted cylinders.	4.2
Analyse the blast-induced fracture surfaces of larger fragments from the blasted cylinders.	4.3
Investigate the internal blast-induced cracks and fractures with microscopy.	4.4
Measure fragment-size distributions (FSDs) of blasted cylinders and the quantities of blast fines.	4.5
Process the resulting data.	4.6
Present and analyse the results.	5
Compare the results with those of other relevant studies and discuss the findings.	6
Summarize the thesis findings and answer the research questions.	7
Provide crucial points for future research based on the applied methodology and the findings.	8

1.4 List of papers and contributions of the author related to this thesis

- Iravani, A., Kukolj, I., Ouchterlony, F., Antretter, T., & Åström, J. A. (2018b). Modelling blast fragmentation of cylinders of mortar and rock. In H. Schunnesson & D. Johansson (Eds.), *12th International Symposium on Rock Fragmentation by Blasting* (pp. 597–610). Luleå Univ. of Technology. ISBN: 978-91-7790-134-1
- Iravani, A., Ouchterlony, F., Kukolj, I., & Åström, J. A. (2020). Generation of fine fragments during dynamic propagation of pressurized cracks. *Physical Review E*, *101*(2), 23002. <https://doi.org/10.1103/PhysRevE.101.023002>
- Kukolj, I., Iravani, A., Ouchterlony, F., Weiss, C., & Lubensky, J. (2018a). Filming blast fragmentation of rock and mortar cylinders. In Schunnesson, H.; Johansson, D. (Eds.), *Rock Fragmentation by Blasting, Proceedings of 12th International Symposium on Rock Fragmentation by Blasting* (pp. 483–494). Luleå University of Technology, Luleå. ISBN: 978-91-7790-134-1
- Kukolj, I., Iravani, A., & Ouchterlony, F. (2018b). Using Small-scale Blast Tests and Numerical Modelling to Trace the Origin of Fines Generated in Blasting. *BHM Berg- Und Hüttenmännische Monatshefte*, *163*(10), 427–436. <https://doi.org/10.1007/s00501-018-0778-9>
- Kukolj, I., Oberdorfer, B., & Ouchterlony, F. (2019). Internal Fractures After Blasting Confined Rock and Mortar Cylinders. *BHM Berg- Und Hüttenmännische Monatshefte*, *164*(10), 422–430. <https://doi.org/10.1007/s00501-019-00899-6>

2 Literature review

In this research, fines are a size fraction of fragmented rock or rock-like material below a specified limit. This limit is usually determined considering the economic feasibility of the fragmented material as a product or considering its impact on the environment and health.

Generally, fines are considered unavoidable in raw-mineral extraction and processing. In common mining, most of the fines are caused by blasting, crushing, and milling (Ouchterlony & Moser, 2013). Further fines generation is expected from material handling and transportation before crushing.

As energy consumption is directly correlated to the quantity of fines, their excessive production/generation is primarily considered as a waste of energy (Böhm et al., 2004). Furthermore, as the requirements regarding worker health and environmental footprint are rapidly becoming stricter, the feasibility of rock blasting is questioned in many commercial applications (Moser, 2003, 2005).

This has inspired much scientific effort to improve the understanding of fines generation by comminution in mining and quarrying.

The EU project “Less Fines” (Moser, 2003, 2005) investigated these aspects concerning the sustainability of natural resources since fines are often an unsellable liability or waste. The health aspects of mineral fines were studied in the EU Horizon 2020 project “Sustainable Low Impact Mining, SLIM” (Sanchidrián, 2018; Ouchterlony et al., 2018).

2.1 Single-hole blasting and fragmentation

The blasting process starts with an explosive detonation in the blast hole. This event exerts shock impact onto the blast-hole wall and subsequently stress waves that propagate through the surrounding material. These stress waves are of two types – P (primary longitudinal compressive waves) and S (transverse and lateral shear waves). The P wave causes displacement in its propagation direction. The waves propagate with the P wave at the front and the S waves are lagging.

Affected particles along the wave path in the radial direction can experience compression or tension. The wave front firstly induces compression of particles it reaches. The compression can induce a crushing of the material near the blast-hole wall (the crushed zone). The compressive wave is followed by a tensile tail. The P-wave speed C_p [m/s] in a linearly elastic material is given by (Z.-X. Zhang, 2016):

$$C_p = \left[\frac{E_{dyn} \cdot (1 - \mu_{dyn})}{\rho \cdot (1 + \mu_{dyn})(1 - 2\mu_{dyn})} \right]^{0.5} \quad \text{Equation 1}$$

where E_{dyn} [Pa] is the dynamic Young's modulus, ρ [kg/m³] is the material density, and μ_{dyn} [-] is the dynamic Poisson ratio of the blasted material.

The tensile tail can cause fracturing at the blast-hole wall and, consequently, the development of a shear wave (Fourney, 2015). The shear waves displace particles perpendicularly to their propagation path (plane), i.e., the shear waves have two components – horizontal shear waves (SH) and vertical shear waves (SV). The S-wave speed C_s [m/s] in a linearly elastic material is given by (Z.-X. Zhang, 2016):

$$C_s = \left[\frac{E_{dyn}}{2\rho \cdot (1 + \mu_{dyn})} \right]^{0.5} \quad \text{Equation 2}$$

As the stress waves propagate, their fronts (i.e., their conical propagation around and along the blast hole) can be of different shapes considering the velocity of detonation VOD [m/s], the sound-wave velocities through the blasted material (C_p and C_s), and the wave interaction with boundaries of the blasted material (i.e., specimen). When VOD is higher than C_p , the wave front forms a Mach cone (Figure 1) with angle:

$$\theta = \sin^{-1}(C_p/VOD) \quad \text{Equation 3}$$

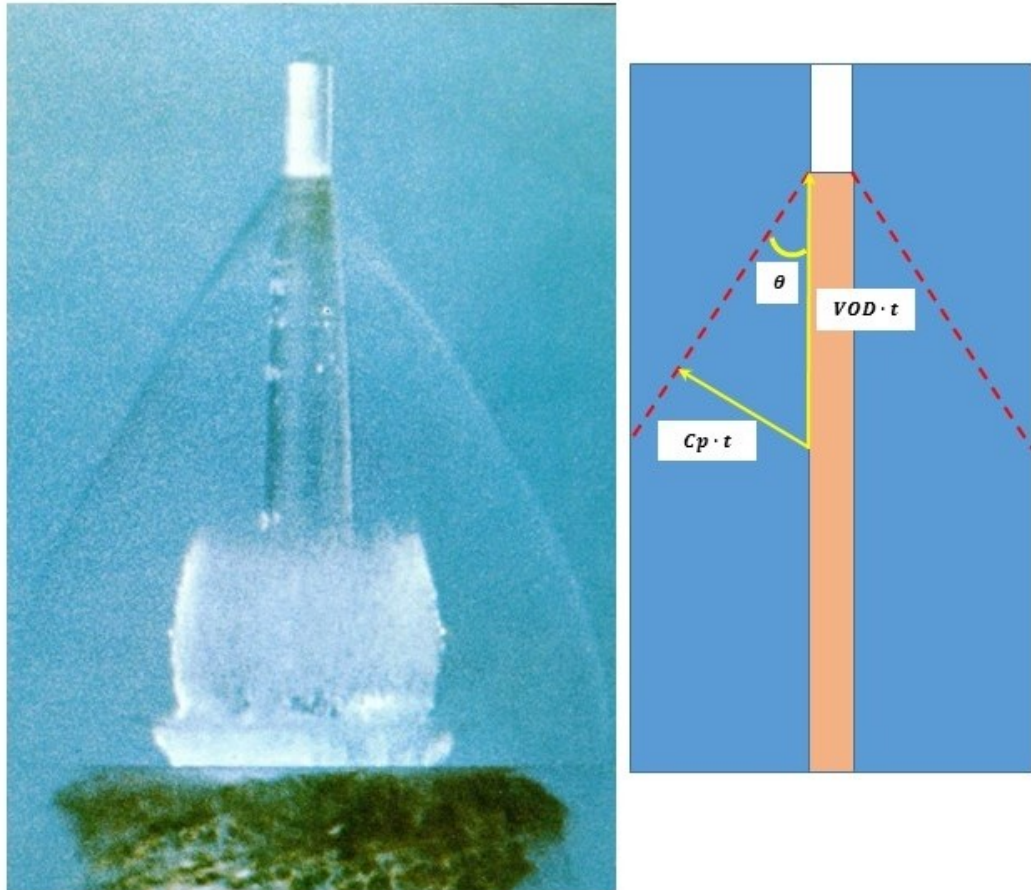


Figure 1: Blast-driven stress-wave front and induced crack propagation. The high-speed image captured supersonic explosive detonation and resulting deformation in a PMMA sample (C. H. Johansson & Persson, 1970).

When the outgoing compressive-stress wave from the blast hole reaches a material boundary or discontinuity, its further propagation and reflection are determined by the acoustic-impedances of the materials at the boundary interface. Equal material properties (matched acoustic impedances) at the interface result in the absence of wave reflection. In the case of a blast sample confined by a different material (i.e., with different acoustic impedance), the compressive wave partly reflects into the sample (reflected wave) and partly continues to propagate farther away from the cylinder (transmitted wave). If the acoustic impedance of the surrounding material is smaller than that of the sample, the reflected wave is tensile. If the reflected tensile wave exceeds the dynamic tensile strength of the cylinder, spall cracks appear close to the boundary (Rossmannith & Uenishi, 2005, 2006). Fourney (2015) discussed how the blast-induced stress waves and their interaction with each other and the boundaries of the blasted material affect the crack propagation.

Enough blast energy induces fracturing and further fragmentation in rock and rock-like material. Such an event usually results in zones (Figure 2) of material failure and structural disturbance (Kutter & Fairhurst, 1971; Fournery, 1993; Jaeger et al., 2007).

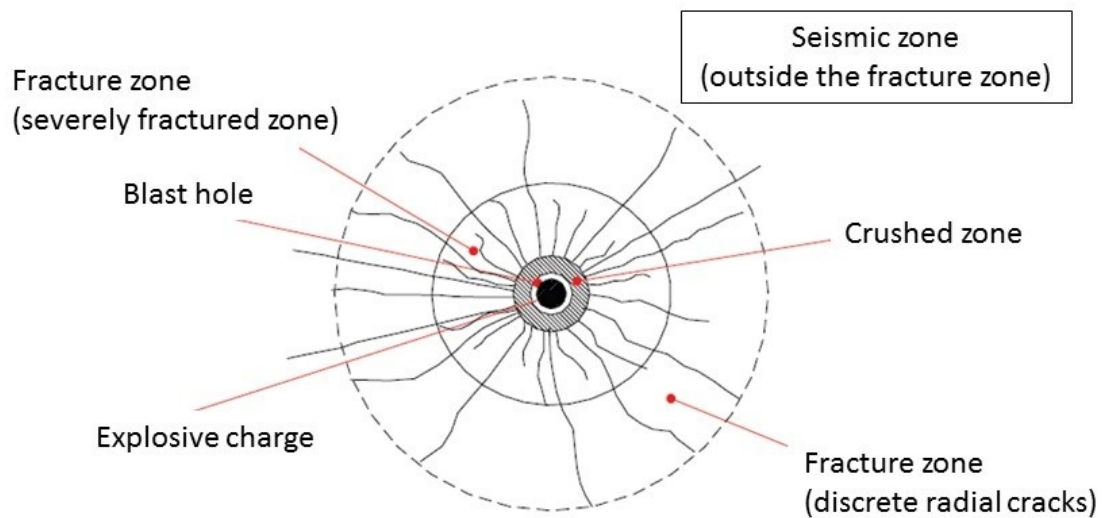


Figure 2: Conceptual sketch of deformation zones around a blast hole, modified figure from Whittaker et al. (1992) and Saiang & Nordlund (2009).

These zones are radially distributed in a sequence around the blast charge:

1. crushed zone,
2. fracture zone
 - a. severely fractured zone and
 - b. discrete radial cracks farther out, and
3. seismic zone.

These zones are defined by the degree of fracturing and dominating mechanisms that cause material failure.

Upon the explosive detonation, high shock-impact is exerted on the blast-hole wall. Following, crushing of the material around the blast hole can be generated by the intensive blast-induced crushing-shear stresses. The crushing propagates radially until the maximum shear stress decreases below a critical level. The thickness of the crushed zone increases with the quantity of explosive charge (Q) and with better coupling between the explosive charge and the blast-hole wall (Z.-X. Zhang, 2016). The blast-hole expansion (i.e., enlargement) is affected by (Z.-X. Zhang, 2016):

- the used explosive charge (i.e., its type, distribution, and coupling),
- boundary conditions of the blasted material, and
- and properties of the blasted material.

As after some distance the tangential stress becomes tensile, tensile radial cracking occurs under high enough loading. The stress-wave propagation in the radial direction can form a fracture zone by developing the tensile cracks outside the crushed zone. The tensile stress opens existing cracks in and further propagates them. Generally, these cracks will further propagate radially if this loading provides enough crack-driving force, i.e., when the stress-intensity factor (K), at the edges of flaws and existing cracks, exceeds the (local) fracture toughness of the material, i.e., the critical stress-intensity factor (K_{Ic}) (Atkinson, 1987a). Analogously, the cracks initiated near the blast hole will propagate radially outwards.

The number of radial cracks decreases farther from the crushed zone in the radial direction primarily due to the load decay (i.e., stress-field weakening). Furthermore, as propagating cracks reduce the stress level near their flanks, less strain energy is provided for further extension of smaller nearby cracks. Ouchterlony (1974) showed that a system of radially propagating cracks cannot sustain all initiated cracks to propagate all the way. Dominant cracks emerge from the dense radial crack pattern around the blast hole and propagate at the expense of the smaller ones.

The propagating (radial) cracks initiated at the crushed zone are slower than the stress waves. Their theoretical peak propagation velocity can theoretically be as high as of the Rayleigh wave, C_R (i.e., about $0.9C_s$). However, the maximum crack-propagation velocity was rarely measured above even $0.5C_R$. In most cases, a crack tip splits (branches) at a K that corresponds to a much lower velocity (Atkinson, 1987b).

Fourney (2015) conducted blast tests with Homalite 100, *a transparent plastic material*, and concluded that *“individual cracks were measured with velocities in the borehole region of 25 000 in/s (635 m/s). This velocity is slightly greater than $\frac{1}{2}C_R$ and over 40 per cent higher than velocities corresponding to a K for successful branching. These high velocities occurred in the borehole region due to the interference of the stress fields from neighbouring cracks inhibiting branching.”*

High-speed filming was often used to capture such dynamic crack development (Wilson & Holloway, 1987; Q. Zhang, 2014; Chi et al., 2019). The obtained high-speed images (HSI) were then used to estimate the crack-propagation speed (i.e., sampled velocity). Wilson and Holloway (1987) blasted 2-3 g of PETN in concrete samples and measured the propagation speed of radial cracks to range from 1000 m/s, near the borehole, to 200 m/s, farther out. Johansson & Ouchterlony (2013) observed rough fracture surfaces

of blasted magnetite-mortar specimens and estimated the crack propagation speed to be about 200 m/s. Similarly, Schimek et al. (2015) estimated the speed in magnetite mortar to be about 260 m/s.

Ouchterlony (1974) showed that for partial loading of radial cracks, the system of static radial cracks reaches a decreasing K field after propagation over less than half of the borehole radius. Thus, blast-hole cracks “*reach a maximum K while part of the dense radial crack pattern and higher than normal crack velocities can be expected*” (Fourney, 2015). As the dominant cracks radially propagate away from the blast hole, the influence of neighbouring shorter cracks decreases, and crack branching becomes more probable.

As soon as cracks, induced by the stress waves, start to propagate, blast fumes partly flow into them and contribute to their further extension before venting out. Brinkmann (1987) and Olsson et al. (2002) confirmed this effect of the blast fumes on the crack development by observing rock blocks blasted with and without liners around the explosive charge. The additional pressurization of the cracks exerted by the blast fumes may increase the probability of crack branching. However, the blast fumes cannot be the only cause for this mechanism (Fourney, 2015).

Banadaki (2011) studied blast-induced fractures in cylinders and cubes of Laurentian and Barre granite. These samples were blasted unconfined and with a single blast hole. He used detonating (PETN) cords of different linear charge concentration (l_c) to only induce fracturing without fragmentation (i.e., falling apart) of the samples. This corresponds to blasting with a subcritical charge quantity. The resulting crack density was defined as the total length of the traced cracks in each zone (i.e., concentric radial bands) divided by the corresponding surface area of the zone. Sanderson & Nixon (2015) defined this measure in 2D images of crack patterns as fracture intensity (p_{21}). Banadaki’s (2011) results showed that the average density of the cracks longer than 2.5 mm in the innermost layer is larger than in the other two layers.

D. Johansson (2008) and Chi (2018) conducted small-scale blast tests, focussing on the influence of the sample confinement, and indicated that both blast-induced crack patterns and fragmentation are drastically affected by the boundary conditions.

Generally, in single-hole blasting, a larger specific (blast) charge (q [kg/m^3]) and a better radial charge coupling (for a constant charge diameter) in an unconfined (free) sample deliver smaller blast fragments of a more uniform distribution. A critical quantity of

charge corresponds to the limit value below which fragmentation does not occur (e.g., as in Banadaki's (2011) blast tests).

The critical charge quantity just barely breaks a sample apart in a few larger (major) fragments and some very fine material, showing a multimodal distribution or a combined discrete and continuous distribution for the same quantity of charge (D. Johansson, 2008; D. Johansson & Ouchterlony, 2011; Iravani et al., 2018a; Iravani, 2020). Such fragmentation is referred to as “dust and boulders” (D. Johansson & Ouchterlony, 2013). Stronger confinement around the sample further increases the critical charge quantity.

Sanchidrián et al. (2009, 2012, 2013, 2014) compared different distribution functions to a large set of sieving data using different error-weighting functions and logarithmic error descriptions. They showed and confirmed the benefits of using the Swebrec functions for describing Fragment-size distributions (FSDs) of blasted rock and rock-like material. Considering the “dust and boulders” phenomenon, these functions were successfully used to describe the fines tail, i.e., size fraction below the lower limit of the major fragments (i.e., boulders) (Ouchterlony, 2005, 2010; Ouchterlony & Moser, 2013).

Steiner (1991) introduced the concepts of Natural Breakage Characteristics (NBC) and Energy Register (ER). These concepts describe the correlation between material properties and the fracture area, generated with mechanical comminution. The ER concept states that an energy-optimal-comminution sequence results in a plot of mass-specific area a_m [cm^2/g] against specific-energy consumption [J/g] with a linear correlation between different degrees of comminution (Böhm et al., 2004). Here, NBC implies a vertical parallel uplift of the sieving curves in a log-log diagram (Figure 3).

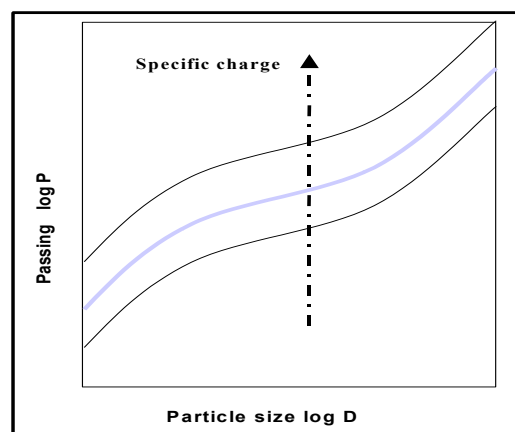


Figure 3: Parallel shifting of sieving curves in NBC concept (Moser et al., 2003a).

Moser et al. (2000) followed up on the NBC studies by blasting small-scale cylindrical and cubic blocks. Their blast tests, undertaken with different quantities of specific charge, resulted in FSDs with such parallel uplift in the range 0–5 mm. Ouchterlony & Moser (2006) indicated that the NBC is consistent in sieving curves of different types of blast fragmentation roughly up to 20-mm fragment size. However, this relation in the ultra-fines region still lacks experimental proof (Ouchterlony & Moser, 2013).

2.2 Mechanisms that cause blast fines

In rock blasting, the upper size limit of fines is often set to 1 mm for small-scale comminution (Djordjevic, 1999, 2002; Reichholf, 2003; Michaux, 2006; Ouchterlony & Moser, 2013). Ouchterlony & Moser (2013) pointed out that the upper size limit of 1 mm *“has no direct physical background unless it could be related to the grain size.”*

The fines smaller than the average grain size are often referred to as “ultra-fines” (Scott et al., 1998; Djordjevic, 2002). These fines are considered to originate mostly from *“grain liberation from the rock matrix”* (Djordjevic, 2002; Michaux & Djordjevic, 2005). This liberation is assumed to be related to transgranular and intergranular fracturing driven by shearing failure or dynamic crack propagation. Fines caused by crack growth, due to rock breakage or fragmentation, are referred to as crack generated fines (CGF) (Ouchterlony & Moser, 2013).

Some blast-fragmentation theories postulate that blast-induced fines originate mainly from an annular crushed zone around a blast hole. The original crushed-zone model (CZM) used a set of calculation formulas to define two non-overlapping Rosin-Rammler components for the coarse material (≥ 1 mm) and the fine material (< 1 mm), from the crushed zone (Thornton et al., 2002).

Esen et al. (2003) focused on calculation methods to determine the extent of the crushed zone, resulting in their formula for the radius of the crushed zone r_c [mm]:

$$r_c = 0.812 \cdot r_o \cdot CZI^{0.219} \quad \text{Equation 4}$$

$$CZI = \frac{(P_b)^3}{(K) \cdot \sigma_c^2}$$

where:

r_c - the extent of the crushed zone (i.e., of the outer bound of the blasted-off material around the blast hole) in the CZM model [mm],

r_o – initial radius of the blast hole [mm],

CZI - the crushing zone index, a dimensionless index that identifies the crushing potential of a charged blast hole,

P_b – blast-hole pressure [Pa], calculated using the non-ideal detonation theory,

K – rock stiffness [Pa], and

σ_c – uniaxial compressive strength (UCS) [Pa].

They (Esen et al., 2003) further assumed that the material in the crushed zone is homogenous and isotropic, defining K as:

$$K = \frac{E_{dyn}}{1 + \mu_{dyn}} \quad \text{Equation 5}$$

where:

E_{dyn} – dynamic Young's modulus [Pa] and

μ_{dyn} – dynamic Poisson ratio [-]

The original CZM model presumes that the size of blast fragments is inversely proportional to the distance to a blast hole. This notion was further carried with the two-component model (TCM) through a more complicated link between the blast-hole distance and the fragment size (Djordjevic, 1999). With a further focus on the blast-induced fines, Djordjevic (2002) criticized the TCM as it “*frequently underestimates the amount of fines found after blasting.*” He observed that much fines can be generated even in blasts that leave visible blast-hole halves. He pointed at “*the shear failure along the in-situ joints and along blast-induced cracks*” as “*the only remaining significant source of fines*” and introduced a related correction factor for the TCM. In-flight collisions and digging were also mentioned as sources of fines.

Onederra et al. (2004) further developed the CZM model. They stated that: “the estimation of the volume of crushed and/or sheared rock material follows simple geometric calculations given by (i) the radius of crushing r_c and thus the volume of a (hollow) cylinder of crushed rock; (ii) the distribution of n major radial cracks, which are assumed to be evenly distributed around a blast-hole, planar and also continuous along the length of the explosive charge. These two components define the total volume of a ‘star’-shaped crushed region (i.e., $V_c + V_b$) (Figure 4).”

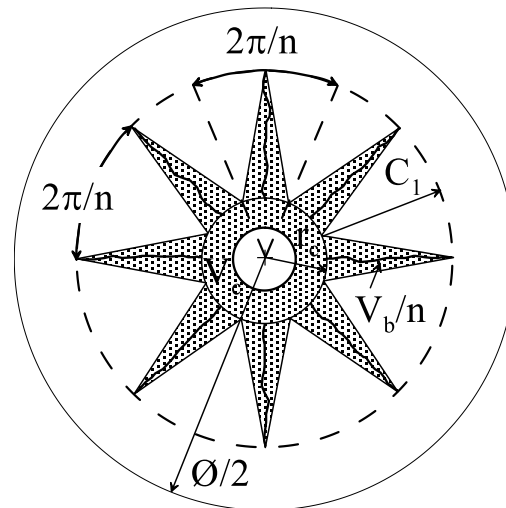


Figure 4: Volume of crushed material around 2D blast-hole (Ouchterlony & Moser, 2013) in CZM (Onederra et al., 2004).

They also stated that “...the source of fines from overall breakage is directly proportional to a volume of crushed material bounded by major blast-induced (radial) fractures.” The formula for the quantity of -1-mm fines (f_c) (Equation 6) comprises V_c [m^3], V_b [m^3], the total volume being blasted (V_t [m^3]), and a fines-correction factor (F_r [-]).

$$f_c = \left(\frac{V_c + V_b}{V_t} \right) \cdot 100 + F_r \quad \text{Equation 6}$$

The number of radial cracks is estimated to lie in the range of $n = 2-43$ (Onederra et al., 2004). The lengths of the radial cracks C_1 [mm] are calculated in a similar way as for r_c :

$$C_1 = r_o \left(\frac{T_s}{P_{eq}} \right)^{\frac{1}{\emptyset}} - r_c \quad \text{Equation 7}$$

$$P_{eq} = P_b \left(\frac{r_c}{r_o} \right)^{\emptyset}$$

where:

T_s – static tensile strength of rock being blasted [Pa],

r_o – (initial) blast-hole radius [m],

r_c – radius of crushing [m],

\emptyset – the pressure-decay factor, and

P_{eq} – the equilibrium pressure [Pa].

Onederra et al. (2004) further provided results on total crack lengths (C_1+r_c). Ouchterlony & Moser (2013) pointed out that these lengths “*do not suffice to explain the complete fragmentation of the blast volume,*” since they are smaller than half of the distances between the blast holes.

The CZM concept of a central crushed zone around the blast-hole as a major source of -1-mm blast fines is still generally accepted in blasting practice, though it lacks solid experimental support (Ouchterlony & Moser, 2013).

Onederra et al. (2004) further noted that “*in full-scale blasting operations, the crushed zone around a blast hole is not the only significant source of fines, and that in most cases, the contribution of breakage can be expected to be significant.*” Ouchterlony & Moser (2013) agreed with these aspects of the model, although pointing out some issues:

- “*Focusing on a crusher product overestimates the amount of fines created by blasting;*
- *The Rosin-Rammler function is an improper choice for the FSD in the fines region* (Ouchterlony, 2005, 2009);

- *A 2D digital image-based method like Split Online is for many reasons an unreliable method to measure the amount of sub-1-mm fines (Ouchterlony et al., 2007);*
- *The quasi-rotational symmetry of the blast-induced cracks defining the breakage zone could only be valid until the reflected wave from the bench face arrives and destroys this initial field symmetry;*
- *There is no direct evidence that the fine material from the radial crack arms of the breakage zone is generated by crushing or even partly by crushing.”*

A different view than the CZM has been developed in the laboratories of Monatanuniversitaet (MUL) and Luleå University of Technology (LTU), focussing on the CGF (Ouchterlony & Moser, 2013). Miklautsch (2002) blasted Ø120-mm mortar cylinders with PETN. These cylinders, when blasted in steel confinement, showed only a crushed zone of about Ø10 mm and a compaction zone of Ø20 mm, without any star-shaped cracking. The quantity of -1-mm fines he measured was 1.0–1.2%. This quantity rose to 3% by including the volume of the compacted zone. His free-cylinder shots (unconfined) resulted in about 13% of -1-mm fines.

Furthermore, cautious or careful contour blasting with enough decoupling of the explosive charge from the blast-hole wall results in many of major fragments (i.e., “boulders”) with surfaces including intact sections of the blast-hole wall. Such cases show that, despite an almost non-existent crushed zone and without fragment collisions, much fines are still generated.

This is a clear indication that *“it is still possible that the macroscopic crack propagation process itself is a strong source of fine material.”* (Ouchterlony & Moser, 2013)

Reichholf (2003) shot free cylinders and cubes made of rocks, mortar, and concrete. He glued the blasted specimens back together and indicated that blast fragments from around the blast hole were too fine to be put back together. He associated this missing material to -1-mm fines. This was investigated by Svahn (2003).

Svahn (2003) blasted Ø300×600-mm mortar cylinders with concentric differently coloured radial layers around a charge column (Figure 5).

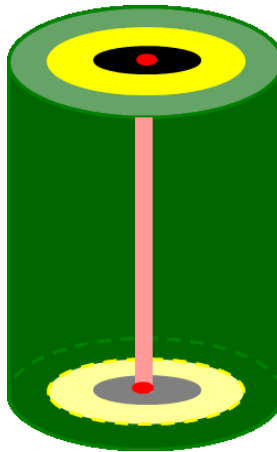


Figure 5: Conceptual sketch (Ouchterlony & Moser, 2013) of the layered mortar cylinder used in the blast tests (Svahn, 2003).

Figure 6 shows the FSDs for the black core and outer two layers (yellow + green) as absolute average mass passing each mesh size x instead of the usual normalized values $P(x)$ in [%].

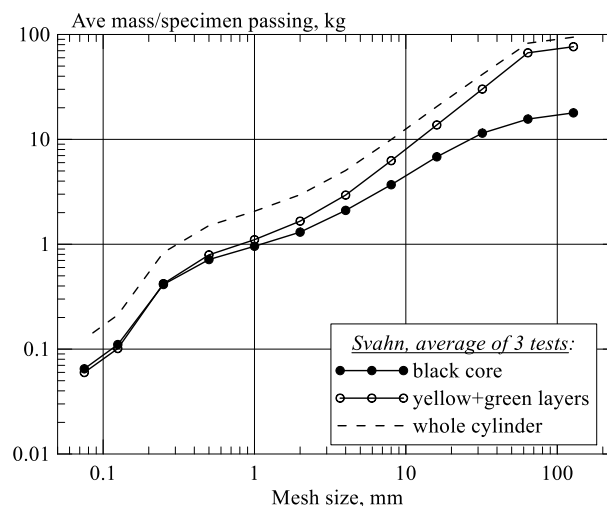


Figure 6: Sieving FSDs for each coloured layer in Svahn's (2003) blast cylinders. (Ouchterlony & Moser, 2013)

The FSD for the Ø120-mm black core contains the whole range of fragment sizes, showing the same general character as the FSD of the outer layers. These results show no tendency either for the core material to consist only of fines or for the outer layers to contain no fines. The black core even contains less -1-mm material in absolute terms than the outer layers. There was no crushing inside the yellow and green layers. Therefore, crack propagation must be the main source of the fine fragments in these layers. Joint in-fill or shearing has not contributed, although the in-flight collisions may have.

Because the black layer was not completely crushed and blasted off, the lower curve in Figure 6 is an absolute upper limit to the contribution by a crushed zone around the blast hole. Ouchterlony & Moser (2013) observed that, *“in most of these blast shots, most of the -1-mm material must have come from outside the central core.”*

Ouchterlony & Moser (2013) observed that *“due to their rotational symmetry, the cylindrical specimens (Figure 5) were ideal for testing the model of Onederra et al. (2004):*

- *Firstly, the expected blast-induced fracturing of such a cylinder is irregular since the cracks are not evenly distributed around the blast-hole, not planar, and not continuous along the length of the explosive charge (Moser et al., 2003b).*
- *Secondly, an analysis of the top $2\pi/n$ sector in Figure 4, assures that the absolute amount of -1-mm material will always decrease with each successive layer of material (outer $\varnothing = 120, 200, \text{ and } 300 \text{ mm}$ for black, yellow, and green layers in Figure 6).”*

They further used Svahn’s (2003) findings to show that *“the real amount of fine material from the green layer is twice that of the yellow layer instead of less than half of it, as the model predicts.”* This was done to indicate that, by following the CZM of Onederra et al. (2004), *“we are forced to conclude that more -1-mm fine material is produced by other mechanisms than crushing in the joint free green layer.”* (Ouchterlony & Moser, 2013)

However, Michaux (2006) rather considered that the fine material from the green layer *“... could be generated along the surface of the major radial cracks with a mechanism of shear failure.”* Here, he was referring to the concept of *“compressive shear failure along the surfaces of new fractures on the larger fragments”* as a major mechanism causing the fines generation (Djordjevic, 1999; Esen et al., 2003).

Iravani's (2020) blast simulations confirmed Svahn's findings (see also Kukolj et al., 2018a, 2018b) by showing spatial origins of blast-induced fines (-1 mm) in cylindrical specimens (Figure 7).

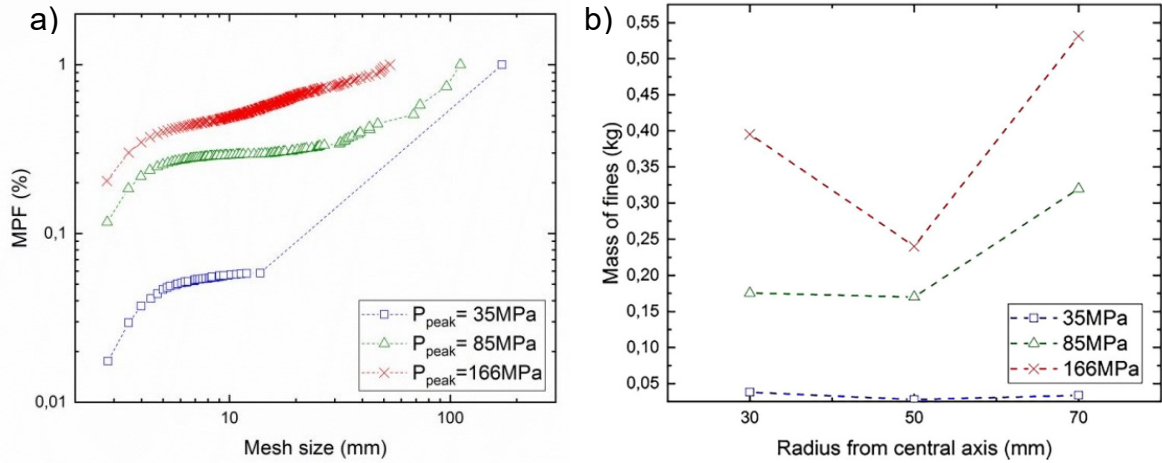


Figure 7: Results from simulated blast fragmentation by Kukolj et al. (2018a):
a) FSD curves of modelled cylinders; b) mass of fine particles concerning the radius from the blast hole and peak blast-hole pressure.

Ouchterlony & Moser (2013) stated that “*the CZM extension is on the right track by associating the radial crack growth with the creation of fines but most probably wrong in associating the growth with crushing, i.e., compressive or shear failure. The radial crack growth itself is caused by tangential tensile stresses.*”

They further explained that dynamic tensile stresses due to blast-wave reflections from free faces induced secondary cracking that could also generate fine material, resulting in more fines in the green layer.

Åström (2006) investigated statistical models of brittle fragmentation. Concerning blast fragmentation of brittle materials, he indicated that “*instability of fast propagating crack plays a fundamental role for the FSD in the small fragment regime.*” Furthermore, he explained that “*unstable cracks leave behind a trace of small fragments along their propagation paths.*” He explained that these small fragments follow a “*universal power-law FSD which has its origin in an inherently scale-invariant branching-merging process.*” With a finite penetration depth of branching cracks and a Poisson process of activated cracks, he concluded that “*the resulting FSDs seem to explain a wide class of numerical and experimental results.*”

Åström et al. (2004a) further developed this model, adding a grain-size correction. Their model yields the FSD with Equation 8 (Åström, 2006). Here, n denotes the number of fragments/kg as a function of volume of the fragments v [mm³] and D denotes the physical dimension.

$$n(v) \propto \left\{ (1 - \beta_r) v^{(2D-1)/D} \cdot e^{[-(2/\lambda)^D \cdot v]} + \beta_r \cdot e^{[-(v^{1/D+\lambda})^D / v_{uncorr}]} \right\} [1 + c \cdot g_r(l)] \quad \text{Equation 8}$$

$$g_r(l) = e^{\{-(\log_2(l) - \sigma)^2 / w\}} \text{ and } l = v^{1/D}$$

The first term describes the branching-merging mechanism, and λ [m] is the maximum penetration of the crack branches away from their parent cracks. Kekäläinen et al. (2007) developed a similar theoretical model to describe crack branching-merging. The second term describes the Poisson process, and v_{uncorr} [mm³] is the volume scale of this process. The factor β_r [-] describes the relative importance of the two processes. The grain-size correction function $g_r(v)$ [-] is log-normal with the two additional parameters σ and w , with $\sigma \approx 3$ and $w \approx 10$ as default values. The factor c [-], in Equation 8, is the strength of the grain-size correction, used as a curve-fitting parameter.

Åström et al. (2004a) fitted sieving curves from full-scale and model scale blasting in Bårarp gneiss (Moser et al., 2003b) to Equation 8, with $D = 3$. Considering the resulting fitting curves, Ouchterlony & Moser (2013) pointed out that “*the almost straight line in the resulting curves implies that the branching-merging term in Equation 8a dominates and that the exponential cut-offs are insignificant.*” With a primary interest in the description of fines, they further explained that $cg_r(v)$ in Equation 8a gives a limited contribution to $n(v)$ in the region of the grain size. They indicated this range as a “bump,” which starts at about 2 mm³ and proceeds down to 0.001 mm³, corresponding to the mesh size of 63–75 μm , where dry sieving ceases to provide meaningful results due to the measurement error. They indicated the importance of lowering the lower size limit of the screening below the traditional size to allow for the detection of the “bump” in the FSD for crack generated fines (CGF).

Ouchterlony & Moser (2013) used a data set from Grimshaw (1958) that ranges down to 2 μm to investigate this principle. They concluded that most of Grimshaw’s (1958) sieving curves, covering 12 Darley Dale sandstone samples, showed the “bump” related the grain size between 0.05–5 mm, just as Equation 8 had predicted.

By setting $\beta_r = 0$ and $D = 3$, the v -factor exponent $-(2D-1)/D$ becomes $-5/3 \approx -1.67$. Then, letting $\lambda \rightarrow \infty$ removes the exponential cut-off (Åström et al., 2004b). Figure 8a shows a fit with a free exponent to Grimshaw's (1958) mass passing data after conversion to $n(x; v \propto x^3) \propto P'(x)/3px^5$ (Ouchterlony & Moser, 2013). Here, the free exponent becomes -5.42 , yielding the v -exponent of $-5.42/3 = -1.81$, which almost matches the value -1.67 predicted by the theory.

Ouchterlony & Moser (2013) used this branching-merging term for a closed-form integration to calculate a $P(x)$ function with the grain-size correction, provided by an error function. They concluded that the “5-parameter Swebrec function fits the bump reasonably well but fails to display the slope flattening below.” They further related this flattening to the possibility that blasted-rock muck piles contain much more ultra-fine material than assumed and consequently much more energy dissipates in the generation of the associated fragment areas (Ouchterlony et al., 2003; Sanchidrián & López, 2003).

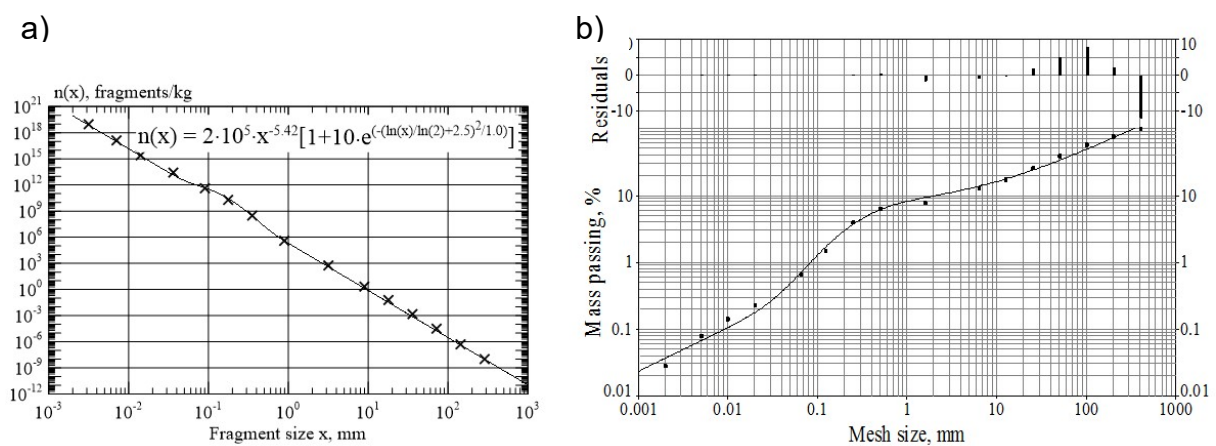


Figure 8: FSD curve for Darley Dale sandstone shot B (Grimshaw, 1958): a) $n(x)$ data; b) curve fit to the corresponding $P(x)$ function. Note the “bump” in the region 0.1-5 mm. (Ouchterlony & Moser, 2013)

Michaux (2006) carried out a similar research, though rather focusing on the area of blast-generated fragments. He conducted blast tests on confined mortar (grout) and rock samples. The resulting fragments were sieved down to $38 \mu\text{m}$. Each fragment larger than 6.3 mm was manually measured (x , y , and z). The smaller fragments, 6.3 mm down to $38 \mu\text{m}$, were measured using image processing. Next, he composed data sets covering density, average fragment volume and mass, surface area, and fragment count for each size fraction of the sieved material.

The obtained data were plotted (Michaux, 2006, 2009) in different ways against mesh (fragment) size, e.g., as inverted energy register curves, as cumulative fragment-mass passing $P(x)$, as the surface area generated per unit mass $A(x)$ (m^2/kg), as cumulative number of fragments retained on each sieve size fraction $N(x)$.

The x - $A(x)$ data sets were plotted in a log-lin scale. Here, the fragment size x [m] was expressed as the arithmetic mean of the lower and the upper limits of the size fractions (bins). The resulting curves are polylines with three different slopes. He identified two kinks connecting these regions at $100 \mu\text{m}$ and 1 mm (Figure 9a).

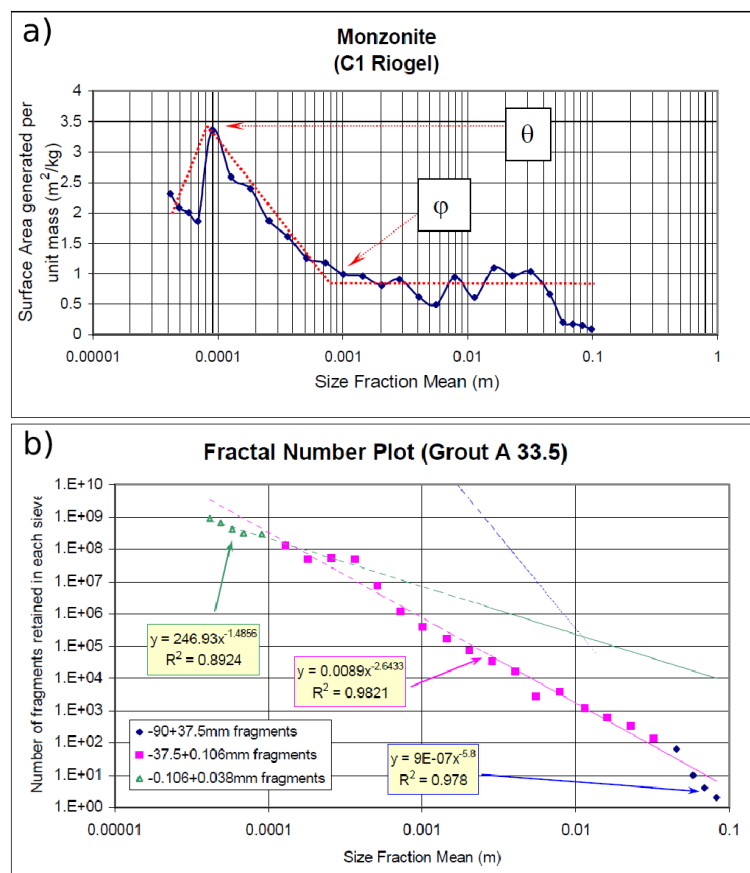


Figure 9: Selected plots of x - $A(x)$ and x - $N(x)$ with fixed indicated size ranges (Michaux, 2006):
a) The plot of x - $A(x)$ in a log-lin scale for monzonite with three regions of different curve slope;
b) The plot of x - $N(x)$ in a log-log scale for grout with three regions with different curve slopes.

The x - $N(x)$ data sets were plotted in a log-log scale (Michaux, 2009). In these plots, three fixed regions were defined of $38 \mu\text{m} \leq x < 0.106 \text{ mm}$, $0.106 \text{ mm} \leq x < 37.5 \text{ mm}$ and $x \geq 37.5 \text{ mm}$ (Figure 9b). Michaux (2006) postulated that the identified regions of x - $A(x)$ and x - $N(x)$ curves indicate different fragmentation mechanisms. In both types of the data plots, the slopes of each region varied considering the material and the test type.

Iravani et al. (2018a) followed up on these studies using numerical blast simulations and results from small-scale blast tests. They assessed and compared the results of the simulations and experimental blast tests in terms of “s-n(s)” FSDs (Åström, 2006; Kekäläinen et al., 2007). Here, s and n(s) express the number of (DEM) particles forming a fragment and the number of fragments of size s, respectively.

Based on the measured slopes of the “s-n(s)” curves, Iravani et al. (2018a) indicated two crucial fragmentation mechanisms:

- unstable tensile-crack propagation with branching-merging and
- compressive-impact crushing or crushing-shearing fracturing.

They used these mechanisms to describe fragmentation results with “*a universal mass-passing-fraction function.*” They concluded that “*the key to resolving the fines and energy problem thus lies in minimizing crushing while inducing enough tensile load to reach the breakage threshold.*”

Iravani (2020) showed that the slope of the resulting “s-n(s)” curves, or their specified ranges, can be used to determine the dominating mechanisms for the corresponding fragment-size range. Furthermore, the curve-slope transitions (offsets) often indicate transition point between the fragment-size ranges. The position of these offsets mostly depends on the properties and internal structure of the blasted material. By fitting the s-n(s) model to the screening data covered in this thesis and from several other experimental small-scale blast tests (Grimshaw, 1958; D. Johansson, 2011), Iravani (2020) identified the following fragment-size ranges produced by small-scale blast fragmentation (Figure 10):

1. boulders (major fragments),
2. intermediate fragments, and
3. fines.

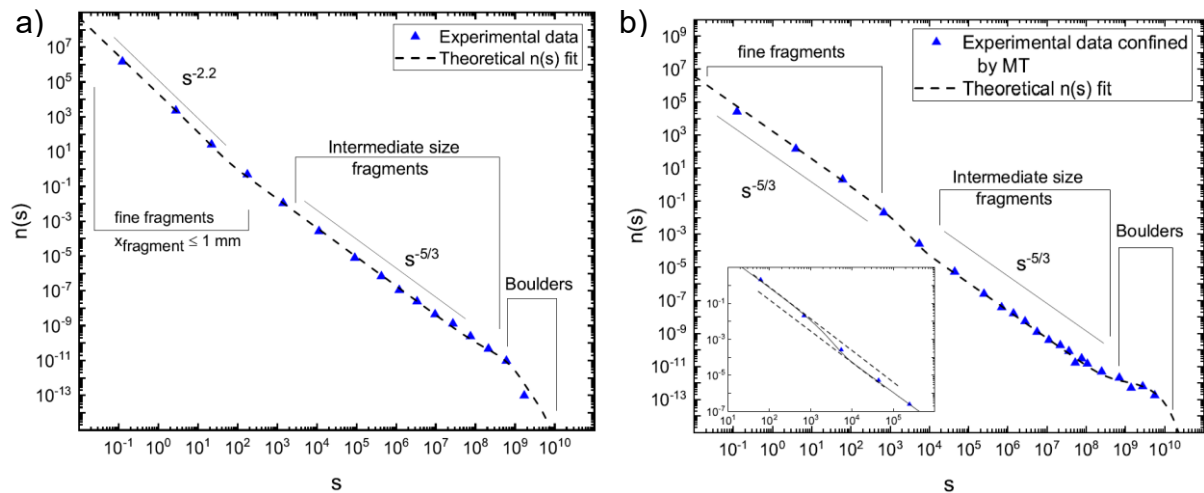


Figure 10: An s - $n(s)$ curves fitted to different sieving data with identified fragment-size ranges (Iravani, 2020): a) from D. Johansson (2008), b) from data covered in this thesis.

Iravani (2020) found that the slope (i.e., power-law exponent) in the s - $n(s)$ curves was either $-5/3$ (rounded to -1.67), expected for the branching-merging mechanism, or of a higher absolute value, indicating an increasing contribution of crushing-shearing. With these implications, he showed that “*there is a universal branching-merging mechanism operating during tensile crack growth.*” He concluded: “*the blast-induced fine-fragments of a brittle material like rock or mortar are formed not only by crushing-shearing but also due to branching-merging at the tips of dynamically propagating cracks or some similar mechanism. The active fine-fragments generating mechanism depends on the external stress level surrounding the propagating crack.*”

They further clarified that, while only tensile fracturing caused fragments larger than fines, it also produced some fines. In many cases where the s - $n(s)$ slope was smaller than 1.67 , the crack branching-merging was identified as the main fines-generating mechanism.

Fracture surfaces of blasted rock and rock-like materials contain traces of dynamic crack propagation and, hence, information on CGF. Z.-X. Zhang et al. (2000) showed on dynamically loaded fracture surfaces of Short-Rod specimens that side branches become more frequent with increasing loading rate. Nukala et al. (2008) related the anomalous roughness (i.e., undulation in the fracture profiles) in 2D fracture simulations to crack branching and coalescence of micro-cracks. Morel et al. (2002) used statistical models to investigate the fracture-surface roughness of quasi-brittle materials (e.g., concrete and rock).

They related the R-curve (crack-growth-resistance curve) behaviour to the fracture-surface roughness. Nasser et al. (2010) studied the correlation between fracture toughness and fracture roughness of granite samples with pronounced fracture-toughness anisotropy. They indicated a clear link between fracture-surface roughness and fracture toughness along the three petrographic symmetry planes for each investigated rock type.

Ouchterlony & Moser (2013) pointed out that *“it is highly probable that the roughness in dynamic fracture carries information about the branching-merging process but this post-mortem information might be interpretable in several ways.”*

Q. Zhang (2014) studied impact-generated fracture surfaces in rock specimens (sandstone, gabbro, coarse-grained marble, and fine-grained marble) with Split-Hopkinson-Pressure-Bar (SHPB) tests. The tests used a loading rate ranging from quasi-static to dynamic at different striking speeds. He measured roughness and captured micrographs with scanning-electron microscopy (SEM) of these surfaces. The results of this study showed a clear link between fracture-surface roughness and observed microscopic failure mechanisms (referred to as ‘modes’). In the micrographs, he classified main failure mechanisms as:

- intergranular fracturing (IG),
- transgranular fracturing (TG), and
- mechanisms transitioning between IG and TG (e.g., partial cleavage with lamellar steps), further defined based on the configuration and orientation of intra-crystalline lamellae (i.e., ‘twinning’) of the affected grains.

Based on the nature of related crack propagation, these mechanisms are probably caused by micro-level branching/merging of crack tips.

Figure 11 shows a model of these mechanisms presented in a hexagonal-crystal system, as proposed by Q. Zhang (2014).

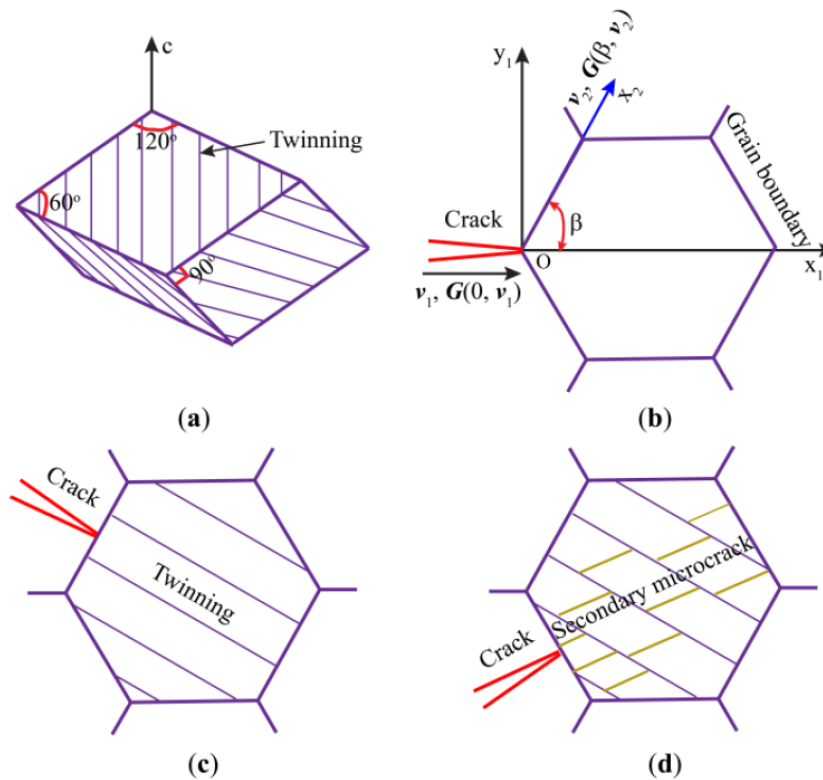


Figure 11: Micro-mechanical model: a) Hexagonal crystal system of the dolomite in the marble; b) schematic diagram showing the microscopic model of intergranular and transgranular fractures; c) formation of secondary micro-cracks nearly parallel to the twinning (i.e., cleavage); d) formation of secondary micro-cracks almost normal to the twinning (i.e., lamellar steps). (Q. Zhang, 2014)

Figure 12 and Figure 13 (Q. Zhang, 2014) show typical examples of these mechanisms in SEM micrographs.

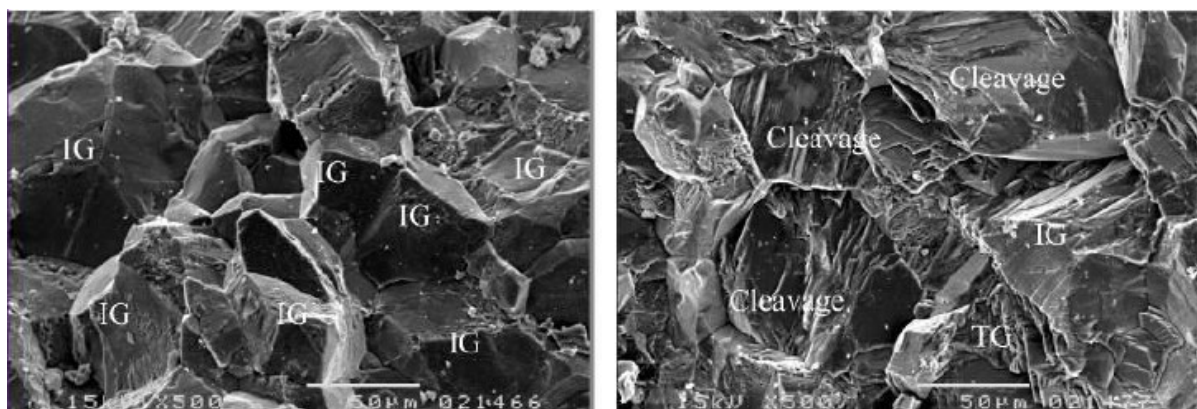


Figure 12: Identified dynamic-fracture mechanisms in fine-grained marble. (Q. Zhang, 2014)

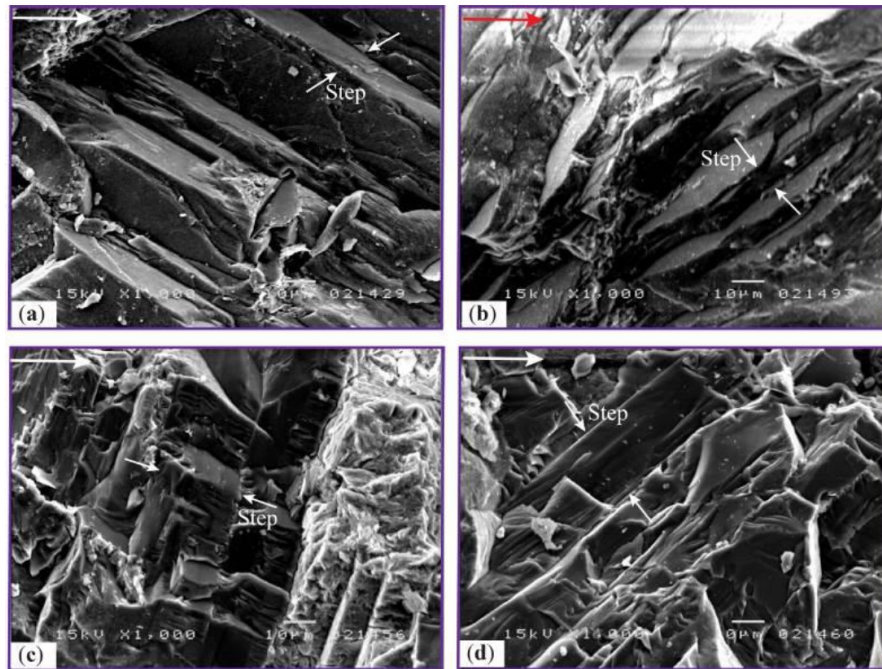


Figure 13: Cleavages and lamellar steps in: a), b) sandstone and c), d) gabbro. (Q. Zhang, 2014)

Q. Zhang (2014) concluded that:

- Quasi-static loading typically generates fracture surfaces with dominating IG fractures (Figure 14a) with a few TG fractures;
- Dynamic loading at a striking speed of 2.8 m/s (Figure 14b) generates mostly TG fractures, still with a considerable number of IG fractures;
- With further increase of the impact speed (or loading rate), TG fractures were increasingly prevailing over IG fractures (Figure 14c), and the resulting fracture surfaces were smoother.

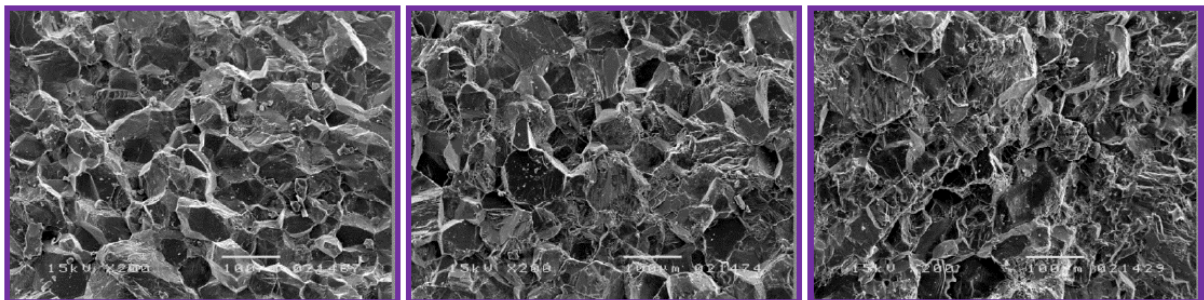


Figure 14: Captured SEM micrographs of fracture surfaces, generated at different loading rates (increasing from left to right), in marble specimens. (Q. Zhang, 2014)

In this thesis, the expression “branching-merging” indicates the mechanism of crack-tip branching followed up by merging. However, the expression “branching/merging” indicates a mechanism that could be interpreted as branching, merging, or a combination of the two.

3 Experimental method and materials

This thesis covers small-scale blast tests on rock and mortar specimens of measured material properties, capturing dynamic blast-driven crack development, and analysing the resulting post-mortem fracture systems and blast fragmentation (Figure 15).

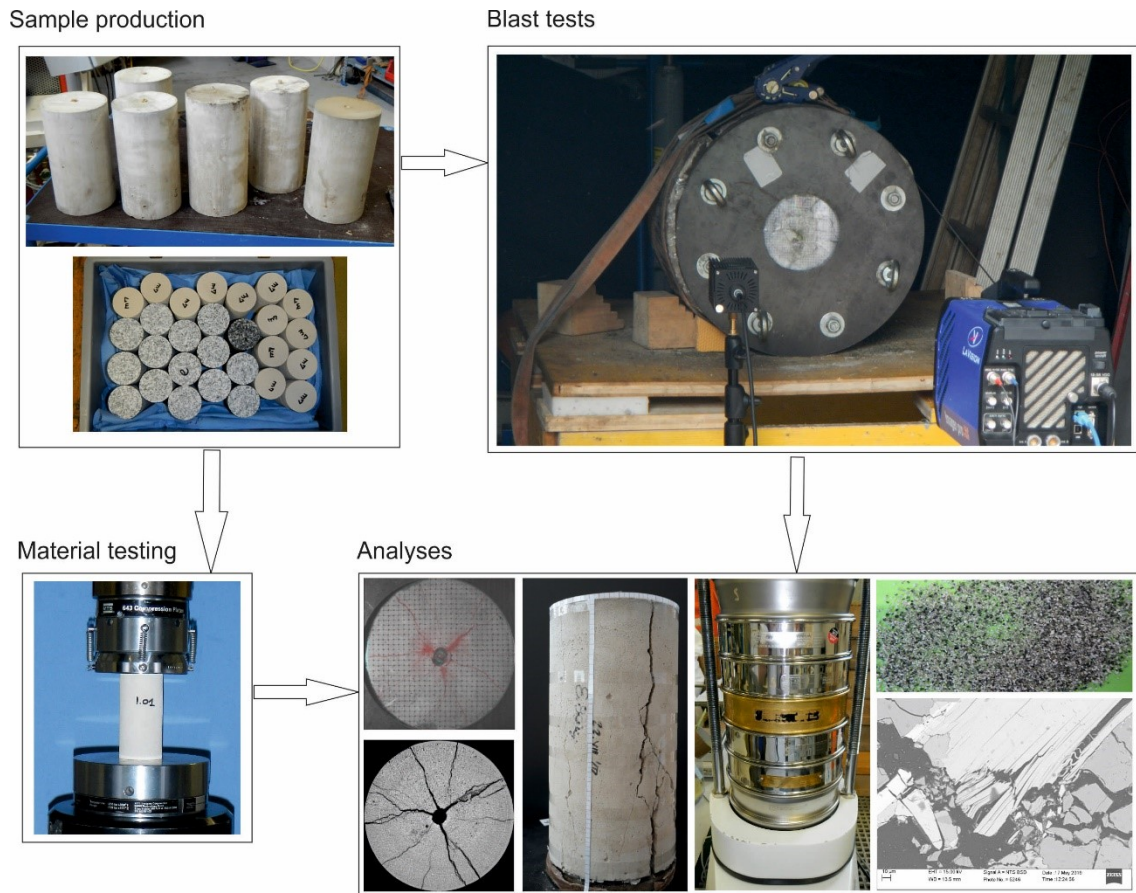


Figure 15: Symbolic workflow of the experimental method.

3.1 Blast tests

The blast-test procedure included blast loading of a hollow thick-walled granite or mortar cylinder inside a confinement. The resulting dynamic cracking was filmed at the frontal end face of the cylinder utilizing high-speed filming (see Appendix 4). Figure 16 shows the blast-test set-up.

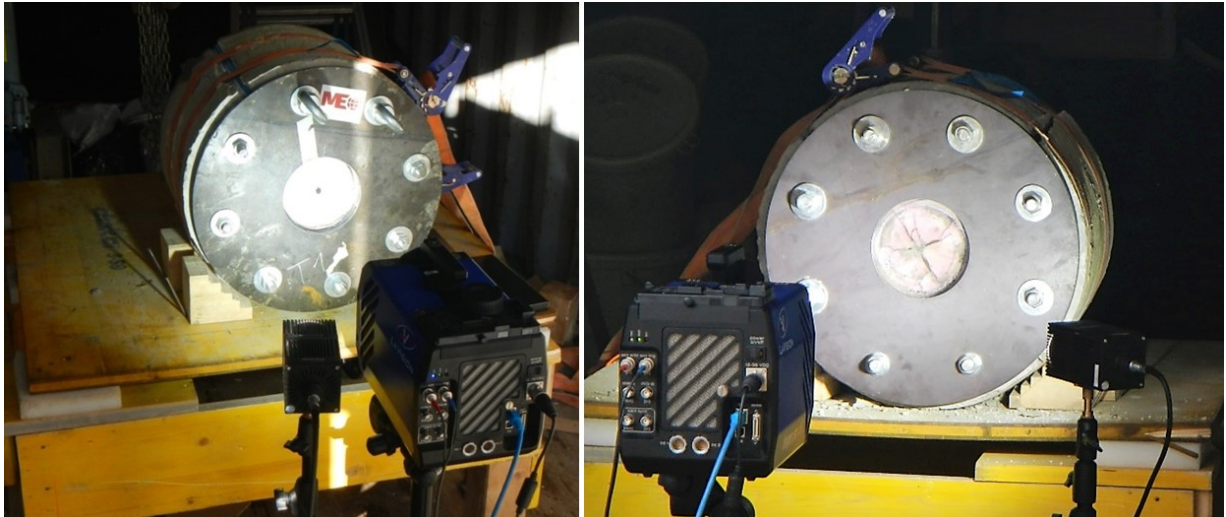


Figure 16: Experimental set-up for the blast-tests, showing the frontal end face.

The high-speed images (HSI) were used to detect: a) crack initiation, b) direction of crack propagation, c) crack arrest, and d) to some extent the branching and/or merging of cracks at crack intersections.

3.1.1 Blast cylinders and damping material

The blast specimens (Figure 17) were cylindrical to provide initial radial symmetry. This symmetry, however, is lost as soon as blast fracturing occurs (Ouchterlony & Moser, 2013). The preliminary test phase (i.e., before blast test 20) used only $\text{Ø}140 \times 280$ -mm mortar cylinders. Starting with blast test 20, the testing used larger cylinders of mortar and granite (Neuhauser granodiorite, Poschacher Naturalsteinwerke GmbH, Austria), all $\text{Ø}150 \times 300$ mm in size. Here, the size of the blast cylinders was changed to fit the available core-drilling equipment in the laboratory (IZR, MUL).



Figure 17: Blast cylinders before blasting.

Shorter cylinders were also blasted as a part of the pre-testing phase and additional investigations. In some cases, radial notches were cut in the borehole at the cylinder frontal end face. The purpose was to fix an otherwise undetermined crack-initiation point and allow the filming to capture the event in a smaller region of interest (ROI) and, hence, at a higher resolution.

The production of most mortar cylinders followed the recipe in Table 2. The intention was to use the same material as had been used by Schimek (2015) and Ivanova (2015). Other recipes were also tried in the preliminary test phase (see Appendix 1). The granite blast cylinders were core-drilled. Each mortar batch and granite block provided six blast cylinders. A total of 40 cylinders (15 of the granite and 25 of the mortar) were blasted.

Table 2: Ingredients of the mortar mixture.

Ingredient	Manufacturer	Proportion [%]
Quartz sand ME (0.1–0.3 mm)	Quarzwirke Österreich GmbH	59.06
Portland cement CEM I 42.5N	Schwenk GmbH	24.84
Tap water (Leoben)	-	15.78
Plasticizer (Mischöl XF)	Murexin GmbH	0.07
Defoamer (Estrilan K)	Avenarius Agro GmbH	0.24

The blast cylinders had a central axial borehole with a 10-mm diameter. The boreholes in the granite cylinders were drilled with water-cooling. In the mortar cylinders, a rod was fixed at the borehole position during the casting procedure and pulled out later before the mortar had hardened. A plastic pipe was used as the cylinder mould (Figure 18).



Figure 18: Casting moulds for the mortar blast cylinders.

The granite blast cylinders were produced by core drilling with water-cooling in the same direction from 500×500×450-mm blocks to maximize experimental repeatability (Figure 19).



Figure 19: Original granite block and final granite blast cylinders.

Next, each blast cylinder was processed by transverse cutting and milling with water-cooled diamond tools to make the end faces parallel and smooth (± 0.1 mm). Finally, a thin layer of white paint followed by a square-grid mesh (pencil-drawn lines with permanent marker dots at the intersection points) was applied onto the frontal end face of the cylinder, the area where the crack propagation was later filmed (Figure 20).

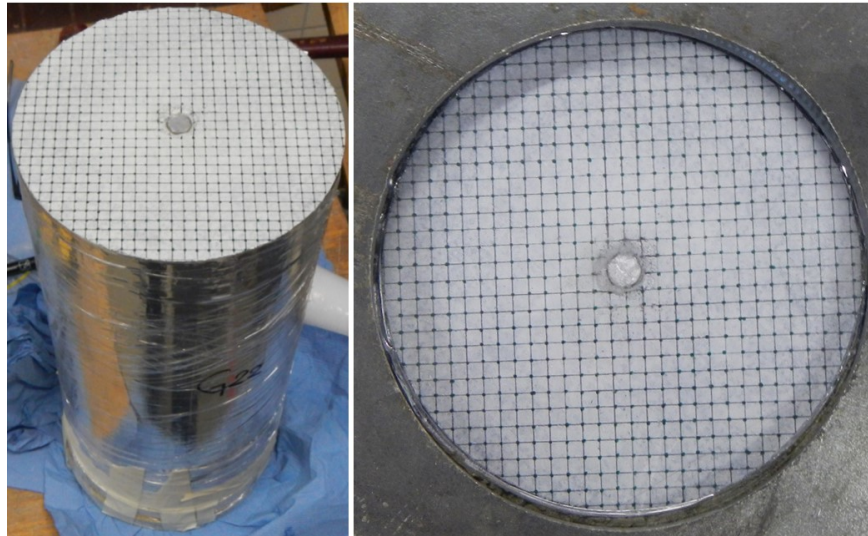


Figure 20: Blast cylinder ready for the blasting test.

Mortar samples for material testing were made from the batch used in the final test phase. In addition to blast cylinders, mortar batch 7 included a block (350×350×150 mm) that was core-drilled after more than 28 days of curing. The granite material-test samples were core-drilled from the same granite blocks (blocks 1 and 2) and in the same direction as the granite blast cylinders. The sample cores were further transversely cut and processed to provide final samples – cylinders (Ø50×100 mm and Ø50×25 mm) and cubes (Ø100×100×75 mm).

A blasted cylinder contains blast-induced crack patterns and incipient fragmentation if the fragments are prevented from breaking apart during the process. To achieve this, the cylinder was radially wrapped by two layers of aluminium tape (Tesa® 56223) and a layer of linear low-density polyethylene (LLDPE) foil (Figure 21).

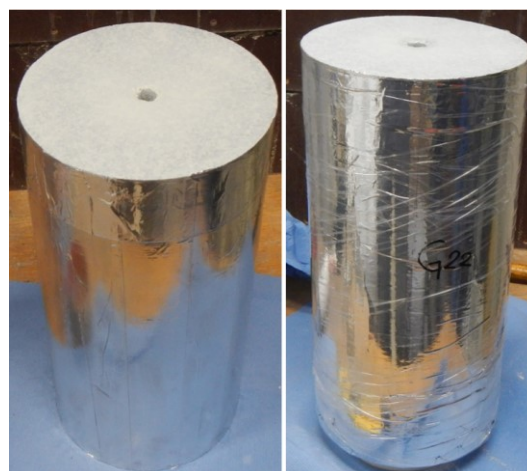


Figure 21: Blast-cylinder mantle wrapped in layers of aluminium tape and LLDPE foil.

As shown in Figure 22, the cylinder (1) is also radially confined by a 25-mm-thick damping layer (2) inside a four-segment blast chamber (3) (see also Sun (2013)). Another purpose of the foils around the cylinder is to prevent water from the freshly poured cementitious damping material (2) to penetrate the cylinder and affect its material properties.

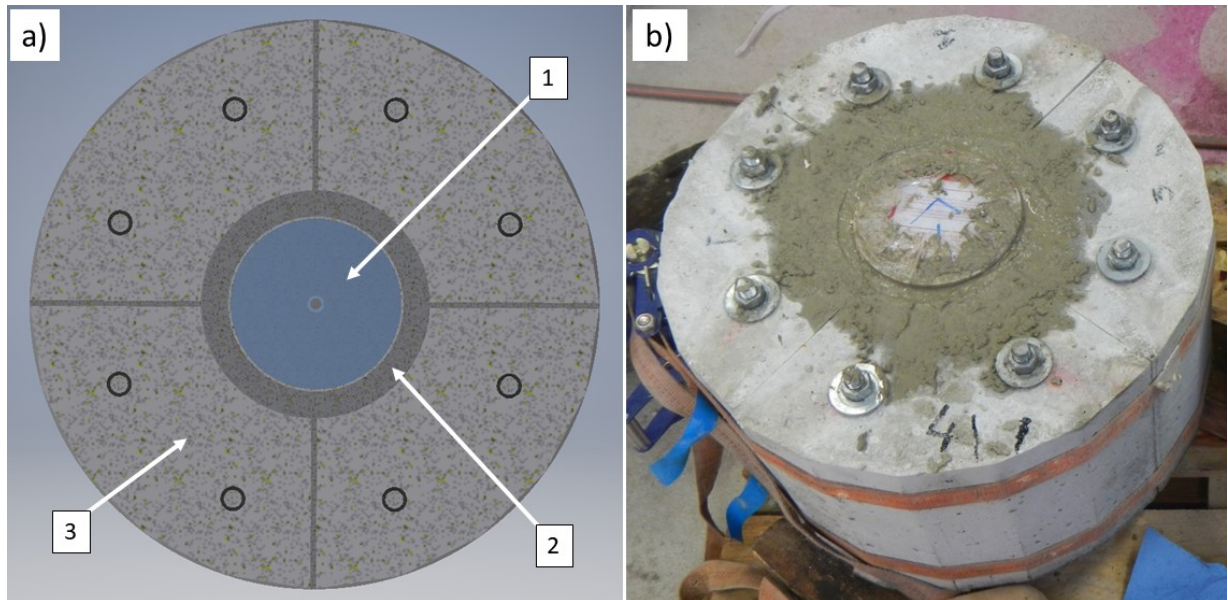


Figure 22: Blast-chamber segments with the damping layer and the cylinder inside.
a) transverse cross-section: 1 – blast cylinder wrapped in aluminium and LLDPE foil;
2 – damping layer; 3 – chamber segments; b) fresh damping material between the cylinder and the segments.

D. Johansson (2010; 2011) investigated how radial confinement affects the fragmentation of mortar cylinders, showing the importance of the material properties of the damping layer. The damping layer affects the acoustic-impedance matching of propagating stress waves at the radial cylinder boundary and reduces the reflected tensile waves (Rossmannith & Uenishi, 2005). Furthermore, this configuration reduces the transmitted compressive waves and, thus, protects the chamber segments. The set-up used different materials for the damping layer during the project. The final set-up used a commercial concrete mixture (Trockenbeton 20, Baunit) with added 5-mm-long fiberglass threads of about 0.13% of the mass of the damping layer. The fiberglass was added to hold the blasted cylinder in place when disassembling the chamber after the blasting. As the damping material was in a water-saturated and partly-cured state when blasted, only its density and dynamic material properties were measured.

Table 3 shows a summary of the measured material properties. Appendix 2 contains the descriptions of the testing procedures with detailed results.

Table 3: Measured material properties.

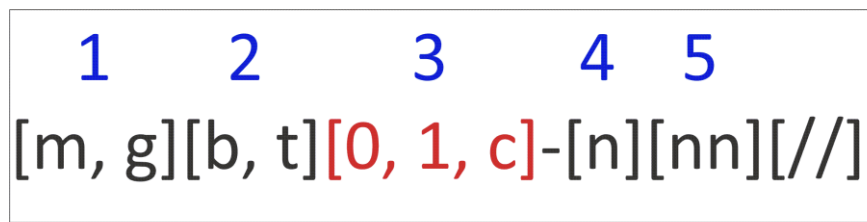
Property	Granite			Mortar			Damping material		
	Ave	Std	Data count	Ave	Std	Data count	Ave	Std	Data count
Compressive strength UCS [MPa]	171.50	9.00	10	27.70	1.10	8	-	-	-
Brazilian tensile strength UTS [MPa]	10.85	1.52	7	2.90	0.49	15	-	-	-
Bulk density ρ_b [g/cm ³]	2.75	0.03	30	1.66	0.01	28	2.19	0.01	4
Grain-level density ρ_g [g/cm ³]	2.68	0.04	4	2.38	0.02	4	-	-	-
Porosity [%]	0.5	-	-	30	-	-	Water-saturated		
**Ave. grain size d_g [mm]	0.42	0.08	1468	0.14	0.04	589	-	-	-
**Ave. pore size d_p [mm]	-	-	-	0.62	0.22	149727	-	-	-
Young's modulus E [GPa]	65.30	0.83	5	12.20	0.31	8	-	-	-
*Dynamic Young's modulus E_{dyn} [GPa]	64.08	-	-	15.38	-	-	2.27	-	-
Poisson ratio μ [-]	0.24	0.02	5	0.23	0.05	8	-	-	-
*Dynamic Poisson ratio μ_{dyn} [-]	0.11	-	-	0.09	-	-	0.19	-	-
P-wave velocity C_p [m/s]	4892	92	13	3069	62	8	1098	258	3
S-wave velocity C_s [m/s]	3242	80	13	2065	40	8	641	110	3
*Dynamic shear modulus G_{dyn} [GPa]	28.90	-	15	7.08	-	8	0.95	-	-
Specific fracture energy G_r [N/m] (WST)	67.22	6.19	4	234.08	10.23	3	-	-	-

* Values derived from the measurements of the P- and S-wave velocities (see Appendix 2).

** Values were obtained from microscopic measurements (see Section 4.4 and Appendix 2).

The blast cylinders and samples for testing material properties were marked to show the sample material ('m' – mortar or 'g' – granite), test type ('b' – blast cylinders or 't' – samples for testing material properties), sample size/shape ('0' – shorter cylinders, '1' – longer cylinders, 'c' – cubical samples; used only for material-testing samples), sample batch number (for mortar: 1–7, for granite: 1, 2), and sample number. The stacks of multiple shorter blast cylinders were marked with '/' at the end. In this case, the batch number and the sample number indicate only the cylinder (piece) at the frontal end face, i.e., the one that was filmed.

Figure 23 depicts the sample-marking nomenclature.



1. Sample material: m - mortar, g - granite;
2. test type: b - blast test, t - material-properties test;
3. sample size/shape of material-testing samples:
0 - Ø50×25 mm , 1 - Ø50×100 mm; c - 100×100×75 mm
4. batch number (single digit),
5. sample number (single or double digit).

Example:

mb-71 - Mortar blast cylinder, batch 7, sample 1;
 gt0-211 - Granite material-testing sample,
 Ø50×25 mm in size, batch 2, sample 11;
 mb-42// - Axially stacked cylinders, batch 4, sample 2.

Figure 23: Nomenclature for blast cylinders and material-test samples. Note that the marking in position 3 (marked red) applies only to material-test samples.

Blasted material and the linear charge concentration are often referred to together with a corresponding blast-test number in a shorter form (Figure 24).

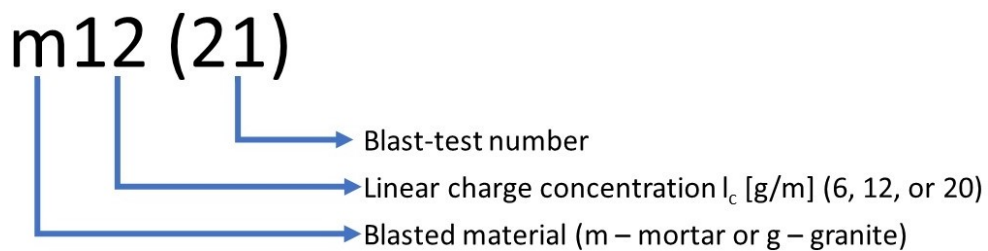


Figure 24: Shorter notation for "blast configuration" (blasted material, linear charge concentration, and blast test).

Further details on the samples are provided in Appendix 1 and Appendix 2.

3.1.2 Explosive charge and stemming

The blast loading was achieved by detonating a fully-decoupled PETN (Pentaerythritol tetra nitrate) cord (Maxam, 2019), with linear charge concentration (I_c [g/m]) of 6, 12, or 20 g/m, inside the through-going central borehole of the cylinder. The velocity of detonation (VOD) varies only slightly for the selected linear charge densities (Schimek, 2015; Maxam, 2019). Therefore, the PETN cord provides repeatable blast-loading conditions. Table 4 shows the important cord parameters.

Table 4: Properties of PETN cords (Maxam™) used for the blast tests.

Product	I_c [g/m]	Charge diameter R_{ch} [mm]	PVC-skin thickness [mm]	Cord diameter [mm]	PETN density [g/cm ³]		VOD [m/s]	
		Measured		Calc.	Calc.	Maxam	Maxam	Schimek (2015)
Sipecord	6	4.30±0.02	0.30–0.40	4.7	0.59	**1.4	7100	*7220±100
Riocord	12	5.30±0.02	0.30–0.54	5.9	0.77		7300±200	
Riocord	20	5.60±0.02	0.30–0.56	6.2	1.09			

* Measured on a 5-g/m detonation cord.

** Averaged value without indicated deviation (Maxam, 2019).

As the borehole diameter ($2r_{bh}$ [mm]) was the same in all blast tests (10 mm), the data from Table 4 were used to calculate the coupling ratio as:

$$\text{Coupling ratio} = \frac{R_{ch}}{2 \cdot r_{bh}} = \frac{R_{ch}}{10} \quad \text{Equation 9}$$

Table 5 shows the calculated coupling ratio.

Table 5: Calculated coupling ratio.

I_c [g/m]	Charge diameter R_{ch} [mm]	Coupling ratio [-]
6	4.3	0.43
12	5.3	0.53
20	5.6	0.56

The PETN cord was initiated utilizing a shock-tube system (NONEL™). The hand-triggered initiation starts in a blasting machine (Exel™ Start DS2) and the initiation pulse propagates through the shock tube at about 2,000 m/s and reaches a detonator (Detinel™ MS N-7 or N-6), which is coupled™ to the cord end-on-end. The detonation propagates inside the PETN cord in the cylinder towards the frontal end face that is being filmed.

A stemming plug was positioned at the frontal end face to 25–30-mm depth in the borehole. The plug reduced the amount of blast fumes that leaked out and obscured the crack development in the frontal end face. The best working plug configuration (Figure 25) comprises two aluminium cylinders of $\text{Ø}10 \times 10$ mm in size and an expanding silicone-coupling layer (PolyMax, UHU) in between.

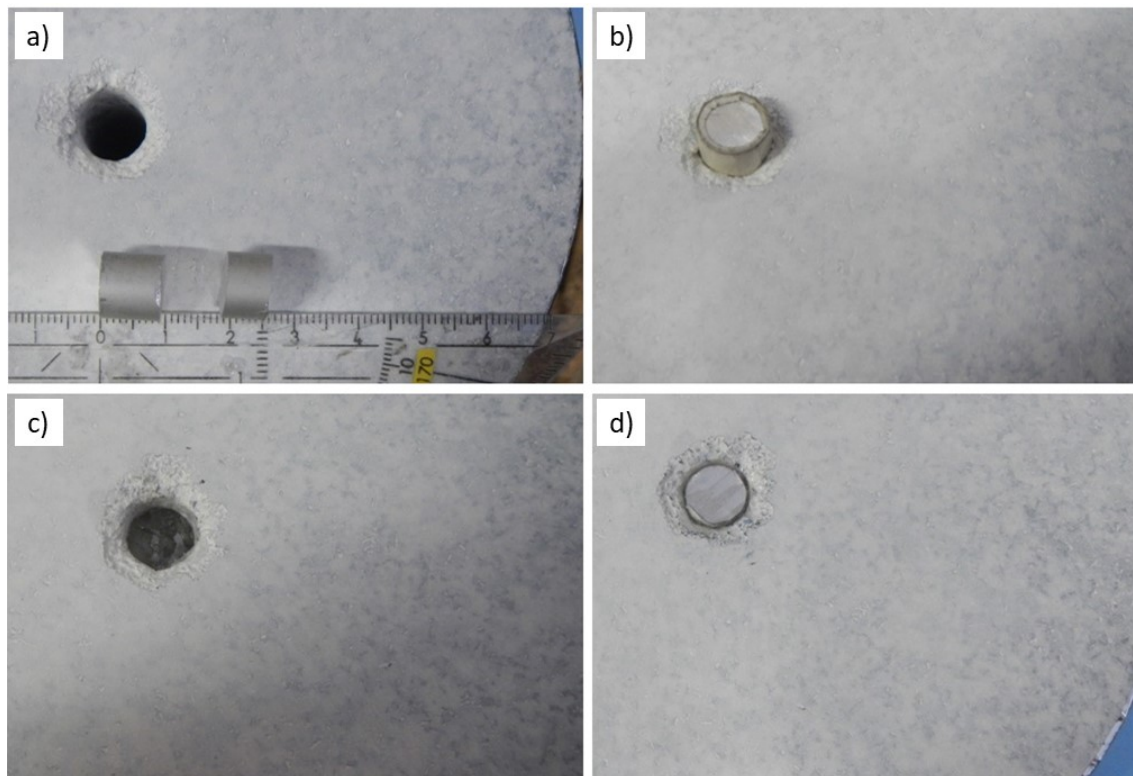


Figure 25: Plug configuration and positioning: a) aluminium plug parts; b) positioning of the shorter plug part, wrapped in masking tape, in the borehole; c) added layer of silicone on top of the shorter part; d) final placement of the longer part in the borehole.

The detonation creates a flash (i.e., high-intensity light pulse). The CMOS imaging sensor in the HSI camera (see Appendix 4) can be damaged if directly exposed to such a light source (Janesick, 2004; Tarasov et al., 2007; Zellner et al., 2016). Without a proper cover, the flash also obscures the early crack development at the frontal end face (Figure 26). Therefore, the plug protects the camera from the flash and allows early crack development at the frontal end face to be filmed.

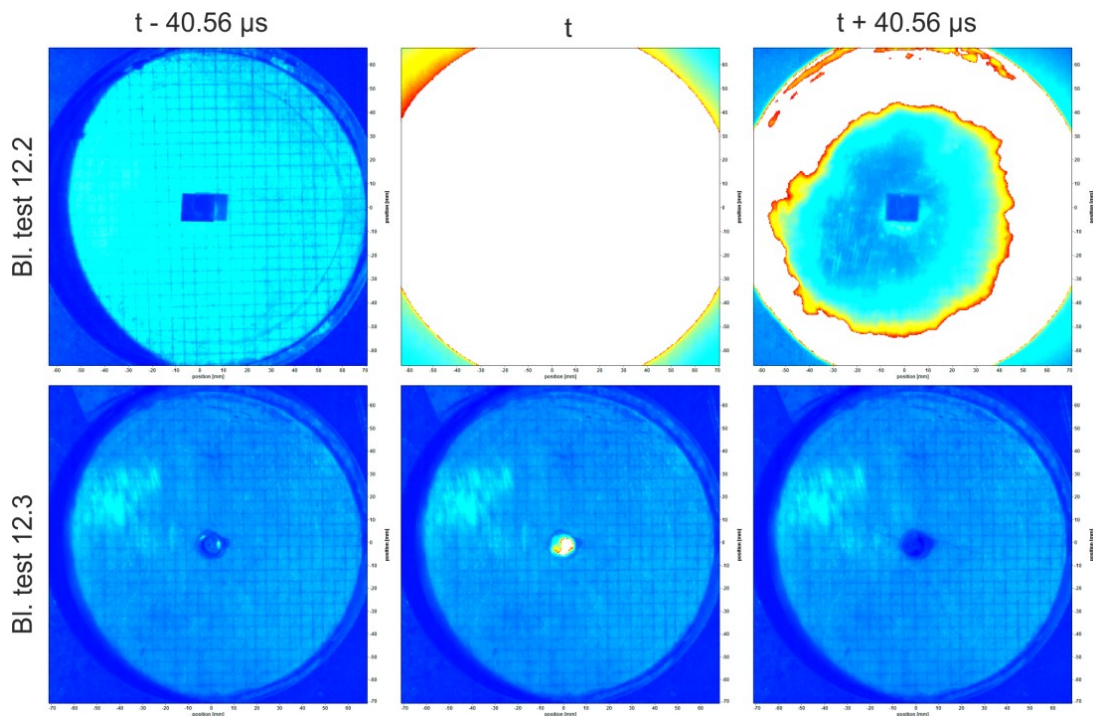


Figure 26: Comparison of two plug configurations and resulting filming (two sets of sequential frames capturing the blast detonation): Blast test 12.3 (bottom row) included the final plug configuration and blast test 12.2 (top row) included a shorter wooden dowel as the plug.

3.1.3 Blast chamber

The blast chamber (Figure 27) with its four concrete segments (4) was held together axially by a frontal- (1) and a rear-end (9) steel plate connected by eight axial through-going threaded steel rods. A thin layer of casing oil provided coupling between the damping layer (5) and the segments. The segments were designed to move about 5 mm outward radially under the influence of the blast. The radial motion was also limited by the use of safety straps around the segments (see Figure 16).

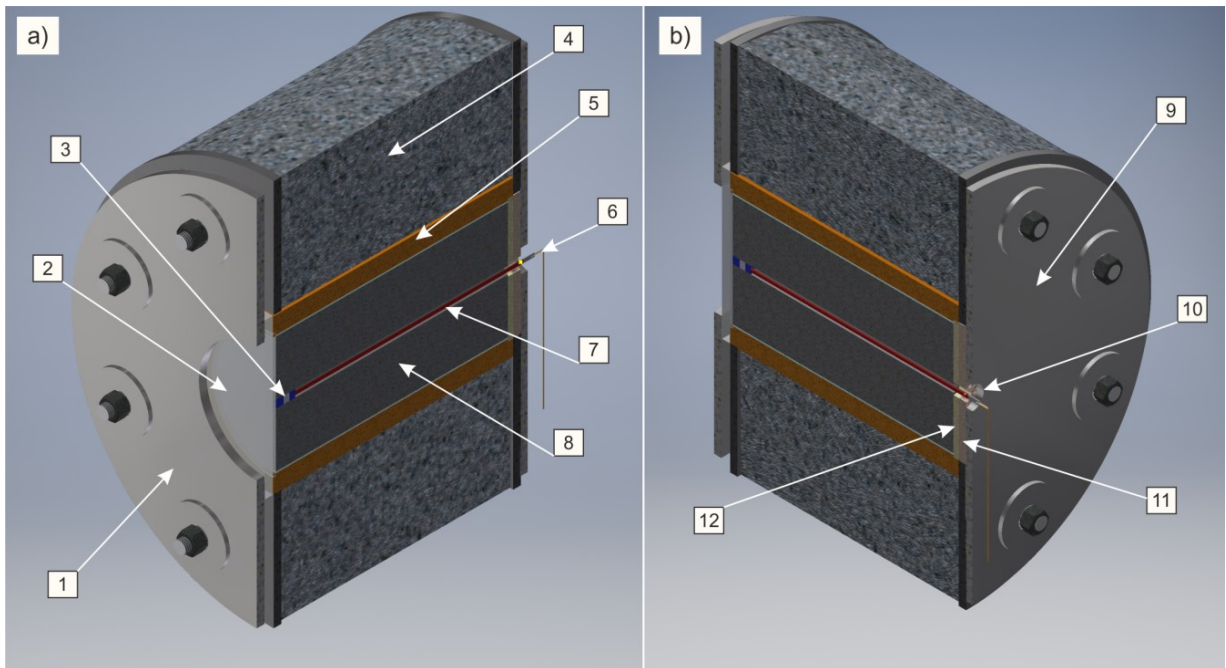


Figure 27: Axial half-cross sections of the prepared blast chamber: a) frontal view; b) rear view (1 – Frontal end face, steel plate; 2 – Protective window; 3 – Borehole with stem plug; 4 – Chamber segment; 5 –Damping layer; 6 – Shock tube and detonator; 7 – PETN cord; 8 – Blast cylinder Detonator; 9 – Rear-end face, steel plate; 10 – Detonator opening; 11 – Wooden disk; 12 – Rubber disc).

The radial compressive waves propagating outwards towards the segments are reflected at the outer boundary of the chamber to return as tensile waves with a higher radial velocity. The ensuing relative movement opens a temporary radial gap between the chamber segments and the damping layer (Figure 28). This reduces both the wave transmission from the segments back into the cylinder and the propagation of radial cracks from the cylinder into the segments. This effect creates a form of “momentum trap” (Sun, 2013; Isakov et al., 2014; Xia & Yao, 2015).

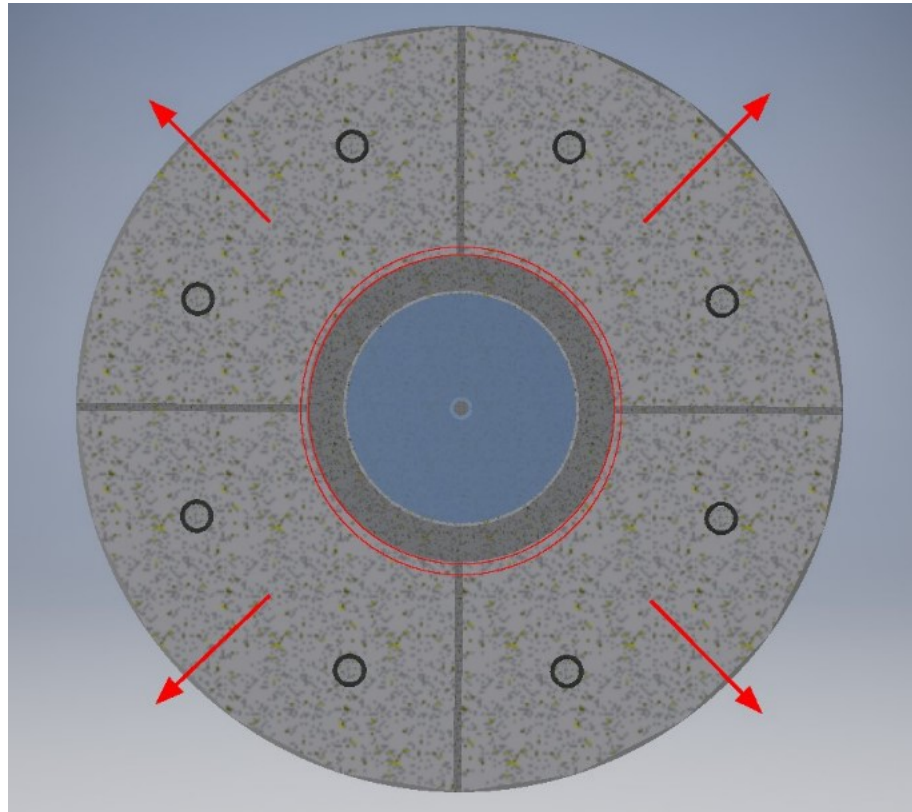


Figure 28: Cross-section of the blast chamber with the radial blast-induced movement of the segments. The arrows indicate the movement direction; the red circles indicate the resulting gap.

The rear steel plate included a central $\text{\O}30\text{-mm}$ opening (7) aligned with the cylinder borehole for inserting the PETN cord. The steel plates included openings for inserting the rods. The gaps around the rods in the openings were filled with silicone (a commercial product for general sealing purposes) to prevent blast-induced damage to the rods.

The gaps around the rods were introduced to simplify the chamber preparation and cylinder extraction, to prevent damage to the segments, and to make the radial movement more even in the axial direction.

The frontal steel plate had a central window opening of $\text{\O}150\text{ mm}$ in diameter (see Figure 27). A protective 14-mm-thick Polycarbonate window (2) was fitted between the end face of the cylinder and the frontal steel plate. The window was evenly pressed onto the end face by tightening the nuts on the rods to 30-Nm torque.

The window reduces the spalling of the frontal end face and blast-throw from it, in most cases. Thus, the dynamic cracking process could be safely filmed by the camera at the frontal end of the chamber. The rear end face of the cylinder was covered with a $\text{\O}160\times 5\text{-mm}$ rubber disc, made of blast-mat material, and a $\text{\O}160\times 10\text{-mm}$ wooden disc,

both with a central $\text{\O}10\text{-mm}$ borehole. The disks were firmly pressed between the cylinder and the rear steel plate. They reduce the amount of material ejected through the detonator opening during the blasting.

The prepared blast chamber was placed horizontally on a support table and secured with four wooden wedges and safety straps (Figure 29). Technical drawings of the blast chamber are provided in Appendix 3.

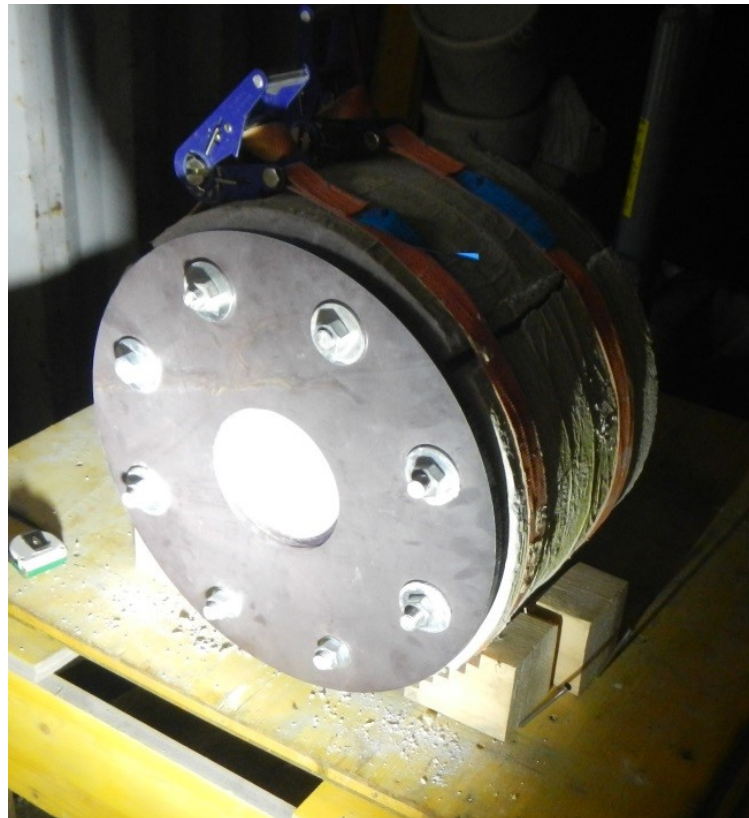


Figure 29: Blast chamber just before a blast test.

3.1.4 Conducted blast tests

The blast tests were marked starting with the blast-test sequence number. Some blast tests were conducted on the same day and, therefore, share this number, followed by a full stop and an appended number (e.g., '.1'). Table 6 shows an overview of the most important conducted blast tests. Appendix 3 includes more details on the blast tests.

Table 6: Short overview of the blast tests in the final test phase.

Blast test	I_c [g/m]	Blast cylinder	Cylinder size [mm]	M_{cyl} [g]	Cylinder density [g/cm ³]	q [kg/m ³]	I_{ch} [mm]	Plug length [mm]
20	12	mb-72	Ø152×292	8800	1.68	0.610	267	25
21	12	mb-75	Ø152×291	8980	1.72	0.614	268	23
22.1	20	mb-74	Ø152×303	9380	1.72	1.020	278	25
22.2	6	mb-71	Ø151×299	8940	1.67	0.307	274	25
23.1	20	mb-76	Ø151×296	9020	1.72	1.028	271	25
23.2	6	mb-73	Ø151×298	8920	1.67	0.307	273	25
24	12	gb-26	Ø149×306	14040	2.66	0.640	281	25
25	12	gb-22	Ø149×302	13820	2.64	0.634	277	25
26.1	6	gb-21	Ø149×302	13880	2.65	0.321	280	22
26.2	20	gb-24	Ø149×303	13820	2.63	1.069	281	22
27	6	gb-25	Ø149×297	14420	2.80	0.320	275	22
28.1	12	gb-23	Ø149×317	13840	2.52	0.644	295	22

Notation:
 I_c – linear charge concentration of PETN cord [g/m];
 M_{cyl} – initial mass of a blast cylinder;
 q – specific charge [kg/m³];
 I_{ch} – charge length [mm].

The difference in material density of some blasted cylinders (Table 6) and corresponding material-test samples (Table 3) is discussed in Appendix 2.

4 Measurements and analyses

The post-blast measurements and analyses cover:

- crack-pattern measurements and analyses;
- investigation on deformation zones (around the blast hole, near the cylinder mantle, at the wakes of larger blast-induced cracks/fractures);
- microscopic investigations;
- fracture-surface analysis of blast fragments;
- blast-fragmentation analysis.

4.1 Fracture patterns

The crack patterns result from the blast-induced fracturing (i.e., crack initiation, propagation, and interaction). These compositions of crack paths and intersections (crack branches and nodes in 2D) facilitate interpretations as to what mechanisms caused them.

4.1.1 High-speed images (HSI)

The initial image in an HSI sequence is the one where a slight plug movement or dimmed detonation flash around the plug is first noticed. Next, the blast-hole wall and all observable cracks at the frontal end face are traced in each image starting with the initial image.

Following the detonation resulting shock waves initiate and drive primary cracking around the borehole in the cylinder. Then the blast fumes from the blast hole partially penetrate and extend already generated cracks (Brinkmann, 1987; Olsson et al., 2002). At this point, the initial cracks usually branch and merge in a complex manner, forming new crack families and intersections, leading to the final fragmentation.

The whole image sequence consists of three blast-fracturing phases (Figure 30). The first phase begins just before the initial image and covers initial crack initiation, coalescence, and propagation. The second phase starts when the first crack branching/merging occurs at the end face. This moment is based on observable crack development and it is, therefore, highly influenced by the filming configuration and arrangement (i.e., the obtainable level of detail relates to the spatial resolution and the temporal resolution).

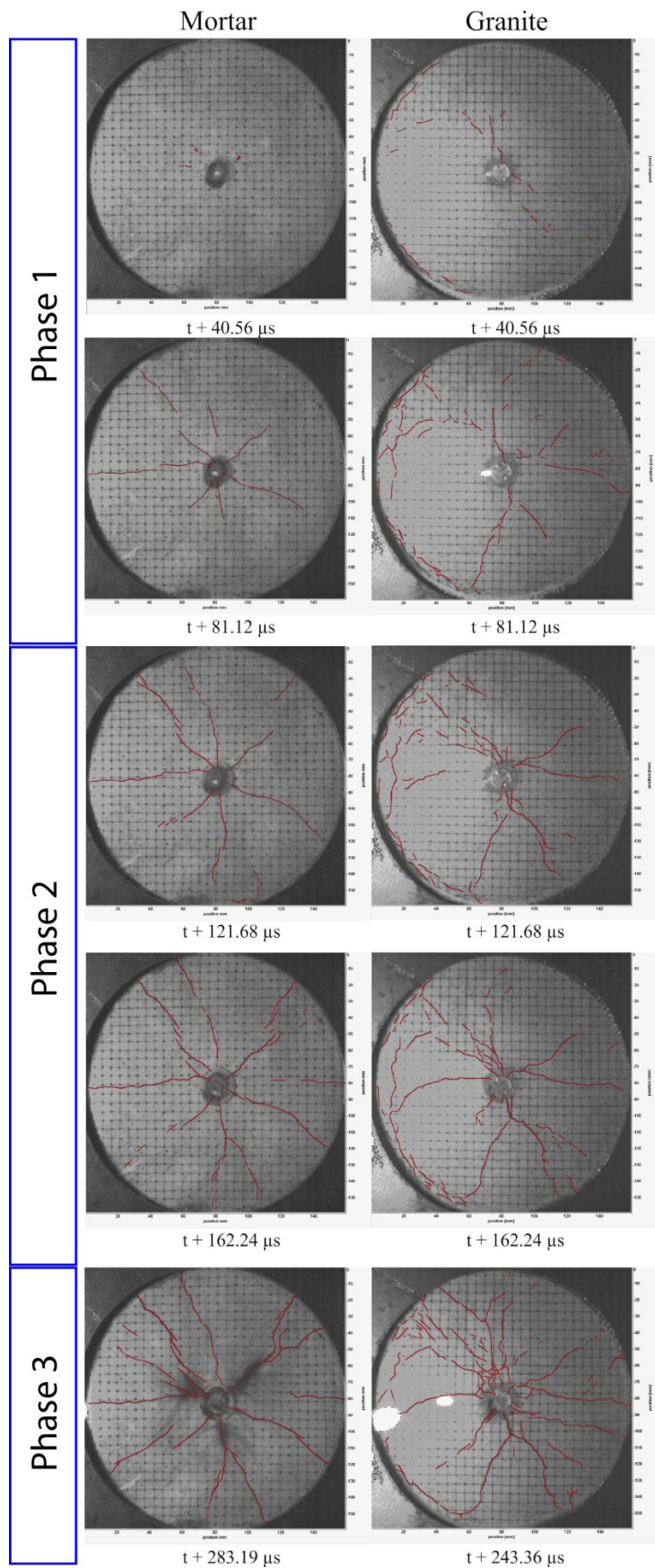


Figure 30: Blast-fracturing phases at the filmed end face of the cylinder. Selected HSI of tests m12(21) (left column) and g12(25) (right column). The notes (t) refer to the time elapsed from the detonation.

The crack pattern in the HSI grows image by image. The tracing is carried out until end-face spalling and/or fumes intrusion either obscures the cracks or distorts their imaging. However, minor fumes spillage is acceptable (Figure 31). This point in the image sequence defines the beginning of the third blast-fracturing phase. The analysis does not cover the third phase.

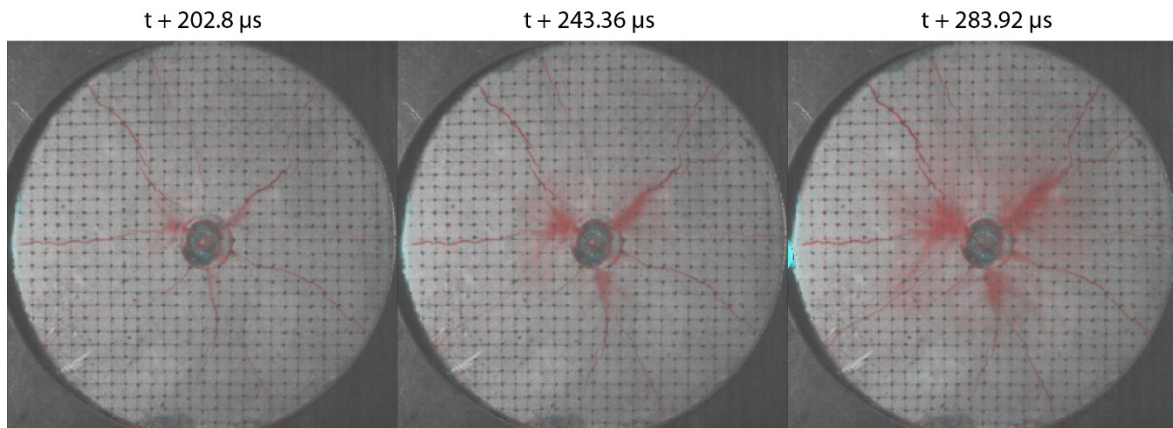


Figure 31: Selected HSI from m12(21). The three images show how a minor spill of the fumes escalates to massive inrush (283.92 μs). The inrush indicates the beginning of the third phase.

4.1.2 Post-mortem images (PMI) of surface cracks

After being extracted from the blast chamber the cylinders were carefully cleaned from damping material debris and protective tapes and foils. Then the mantle and the end faces of the broken but not yet disjoined cylinders were photographed (Figure 32).



Figure 32: Removal of protective foils from blast cylinder mb-72, m12(20).

The end faces were photographed before positioning the cylinder on a turning table. The images of the frontal end faces were captured with a resolution of 2675×2591 px. The table (Figure 33) is automatically driven by a programmed stepper motor secured below the table surface and turns in 200 angular steps per whole rotation (i.e., with 1.8° per step).

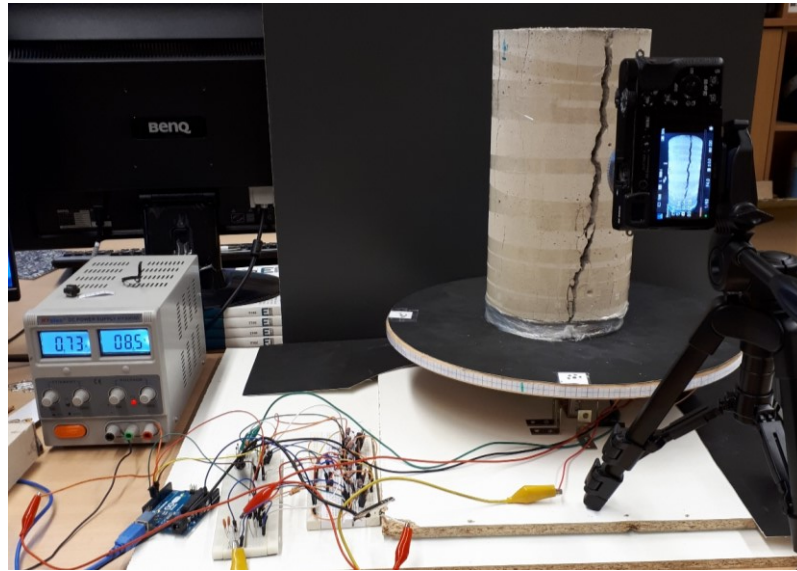


Figure 33: Photogrammetry set-up – the turning table, the programmed stepper-motor drive, and the digital camera.

A programmed digital camera (Sony Alpha 5000) captured mantle images of a rotating cylinder synchronous to the rotation steps. This generated an image set that is used to construct a 3D model of the mantle in a photogrammetry program – Agisoft Photoscan (Agisoft, 2019).

The 3D model is then 'unwrapped' around its central axis in CloudCompare (CloudCompare [GPL Software], 2019) and exported as a 2D crack-pattern map of the mantle (Figure 34).

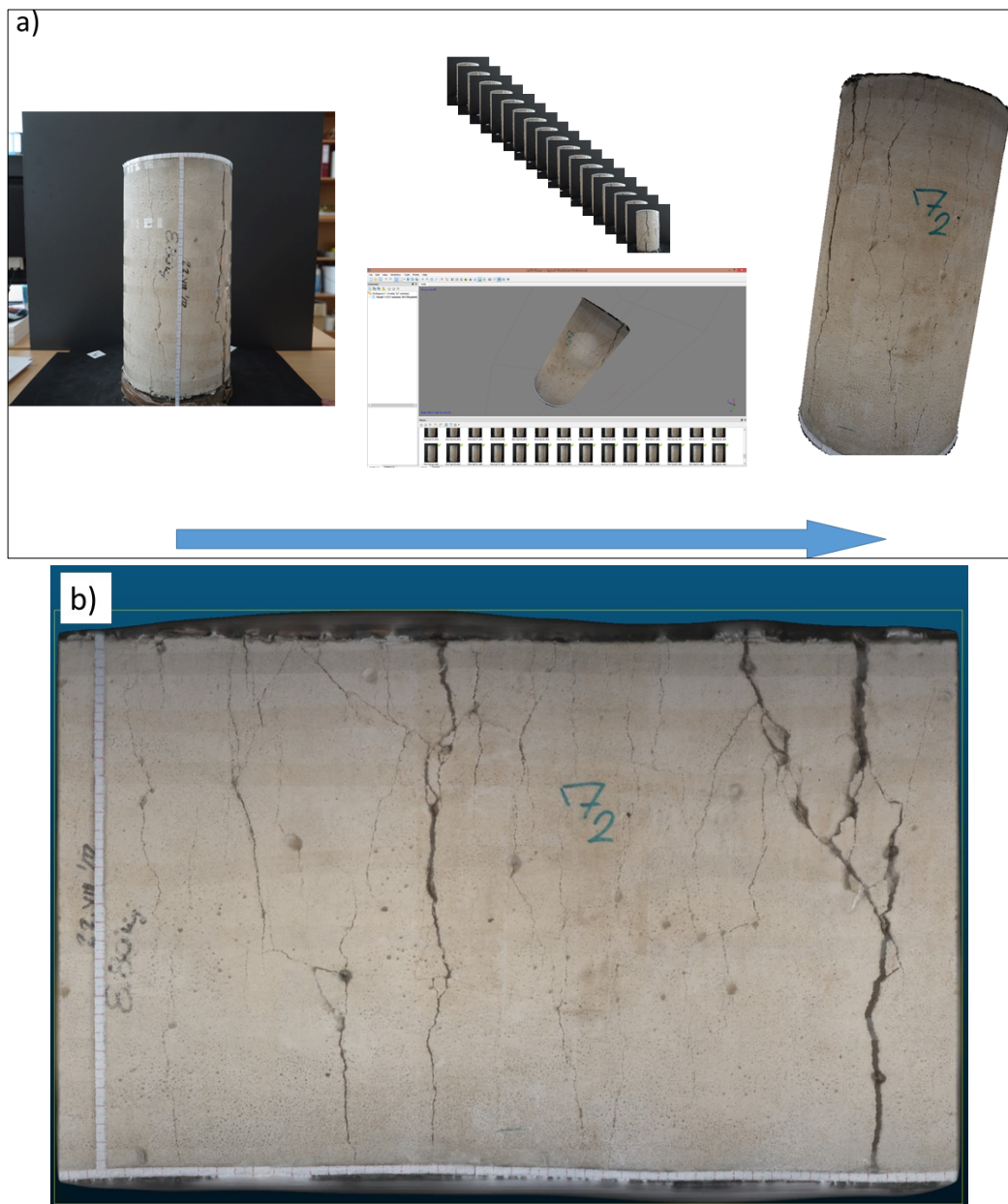


Figure 34: Principle of the photogrammetry procedure: a) process workflow; b) resulting image of blast cylinder mb-72, m12(20).

4.1.3 Computer-tomography (CT) measurements

The CT investigations took place at the Austrian Foundry Research Institute (ÖGI), Leoben. Figure 35 shows the CT procedure.

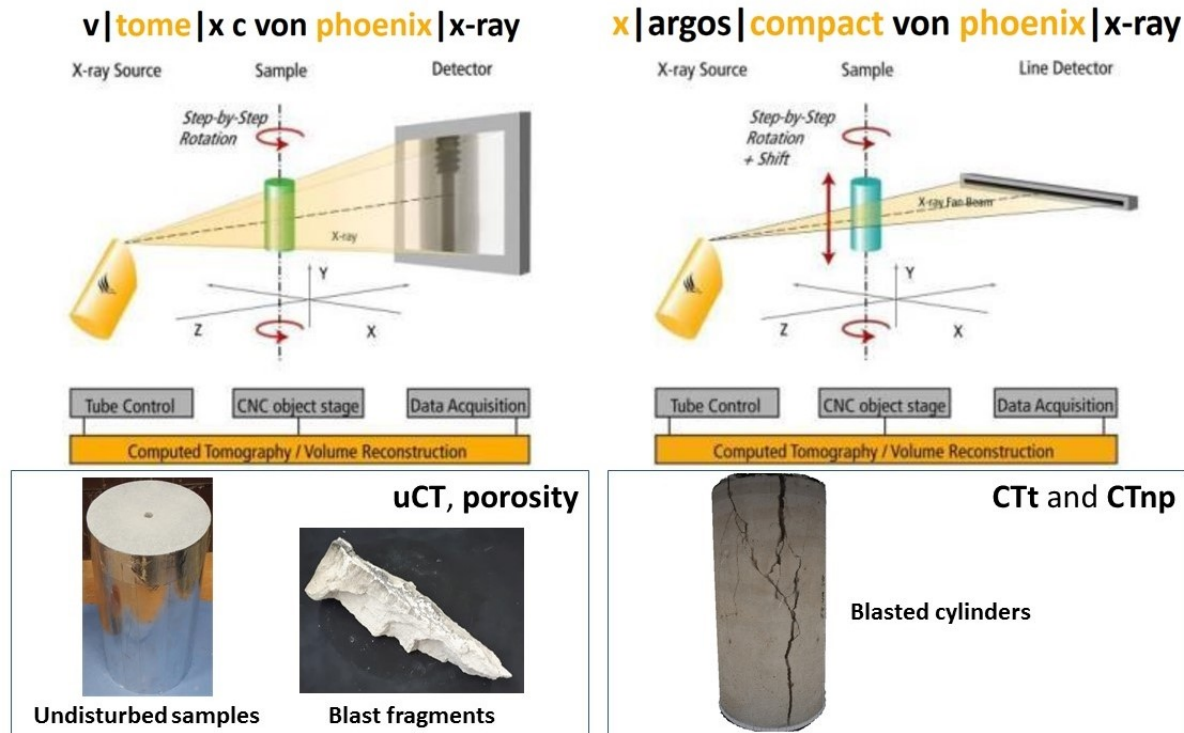


Figure 35: Principle of the CT procedure

The CT covered:

- whole blasted cylinders
- selected larger fragments of blasted cylinders, and
- undisturbed samples of both materials.

The scanning of whole blasted cylinders was carried out with a voxel size of 130 μm in the radial direction and 3 mm in the axial direction. The scanning of the fragments and undisturbed samples was carried out at a higher resolution (uCT) with a voxel size of 60-120 μm .

The scans of blasted cylinders were used to produce transverse (CTt) and non-planar (unfolded tubular) sections (CTnp) and to investigate the arrangement of the interior crack patterns and evaluate their axial persistence (Figure 36).

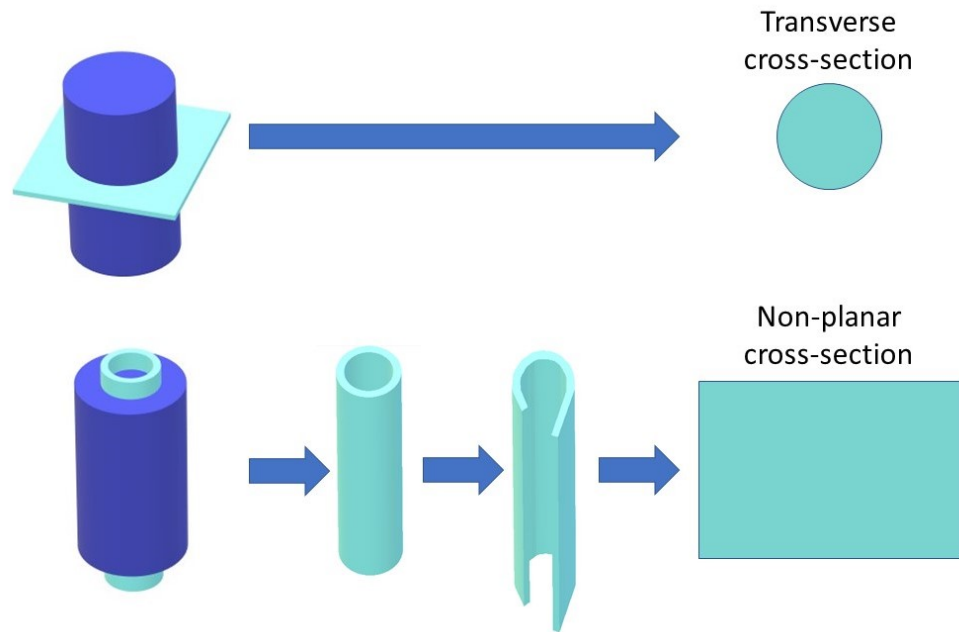


Figure 36: Definitions of the cylinder cross-sections - transverse and non-planar.

The CT sections of the interior fracture surfaces were converted to a closed triangular mesh, providing STL (Stereolithography) objects of the blasted cylinders. Similarly, the high-resolution CT images resulted in 3D models of the fragments, exposing their inner structure and blast-generated fracture surfaces for further analysis in more detail. More details on the CT procedure are provided in Appendix 5.

4.1.4 Fracture tracing

Visible cracks in the HSI, the PMI, and CT images were traced manually in GIMP 2.10.2 (Chastain & Pfaffman, 2006). An original image is placed on a layer above the background layer, which is filled black. The resolution of the image is then increased by interpolation to allow easier manual tracing of the crack in the following steps:

1. the image is scaled based on the length references measured at the end face or provided with the filming configuration;
2. a transparent layer for crack tracing is created above the other layers;
3. the original image is then edited by increasing the image contrast and brightness;
4. with the tracing layer activated, the cracks in the original image, the blast-hole contour, and the mantle contour are traced with a red, green, and blue brush, respectively (Figure 37). The selected brush size depends on the width of the crack being traced;

5. the tracing layer is exported as a bitmap image (.bmp). Further on, the crack traces are analysed as topological crack patterns.

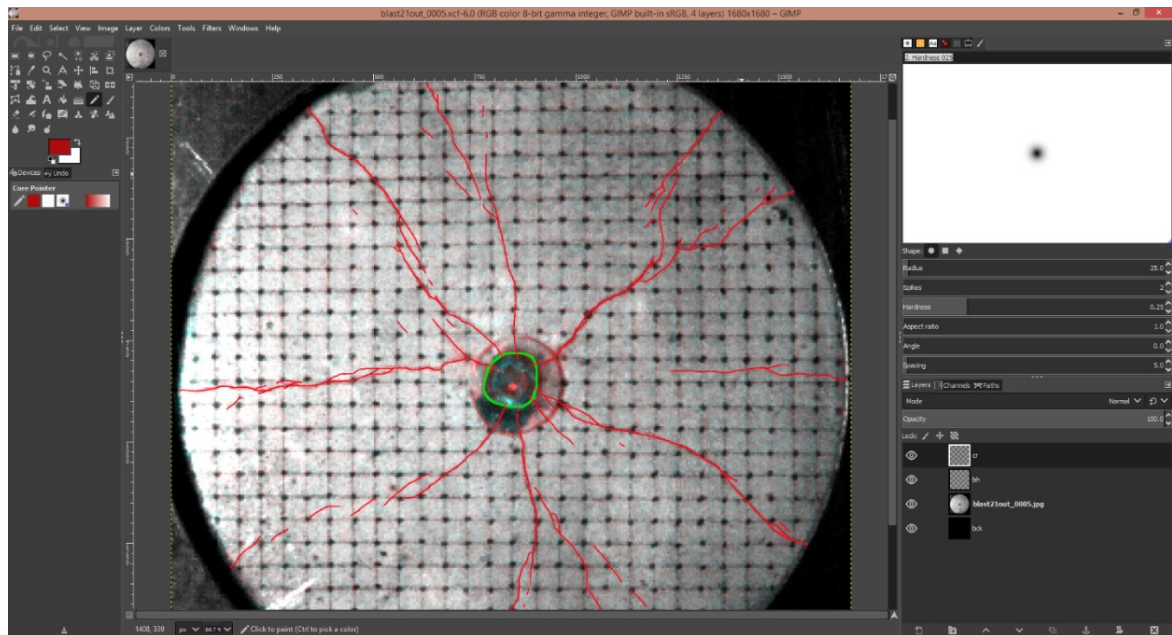


Figure 37: Tracing process in GIMP. Original image and different trace types (i.e., cracks, the blast hole, and the mantle) are traced with different colours.

The traces were further measured and analysed in ImageJ (Ferreira & Rasband, 2012) and with a MATLAB[®] script (Appendix 7) considering the fracture paths, topological features, in-plane (2D) fragmentation, and crack-propagation speed.

4.1.5 Fracture-pattern topology

Comparison of the fracture patterns (ideally) requires a method that prevents errors due to scaling mismatch and image distortion. Such methods disregard the information on crack length and width, rather focusing on the configuration of line segments, intersections, and tips in fracture patterns.

The topological analysis used here is based on the work of Sanderson & Nixon (2015) and Sanderson et al. (Sanderson et al., 2019). This analysis (Figure 38) converts the traced fracture patterns into scale-invariant networks of line segments (e.g., crack branches) and nodes (i.e., crack intersections and crack tips).

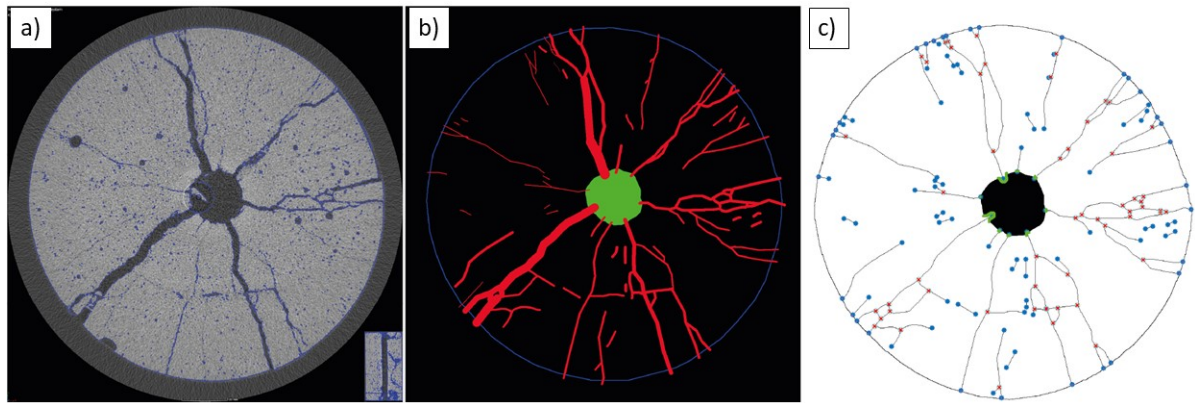


Figure 38: Principle of the topological analysis: a) Original fracture-pattern image (HSI, CT section, or PMI); b) Trace image with fracture paths coloured red; c) Resulting topological image with fracture lines (thinned fracture paths) and different topological nodes (tips and intersections).

This analysis was adapted to the description of the fracture patterns in the blasted cylinders. Its original purpose was to describe fracture networks for oil extraction. It allows calculation of the probability of fluid passage through the fracture networks. Although such calculation is not important for the tasks of this thesis, the connectivity measure was used to assess the level of fracturing and fragmentation in the material.

The original patterns (see Figure 38b) consist of fracture paths and their intersections. Here, the paths are consistent end-to-end fracture traces. The fracture-pattern images are converted into topological images by “thinning” the fracture traces (see Figure 38b and c). The resulting patterns are composed of one-pixel-thick median lines (fracture or crack lines) and intersections of the traced fractures. These patterns are then converted to topological networks of nodes, branches, and lines (Figure 39).

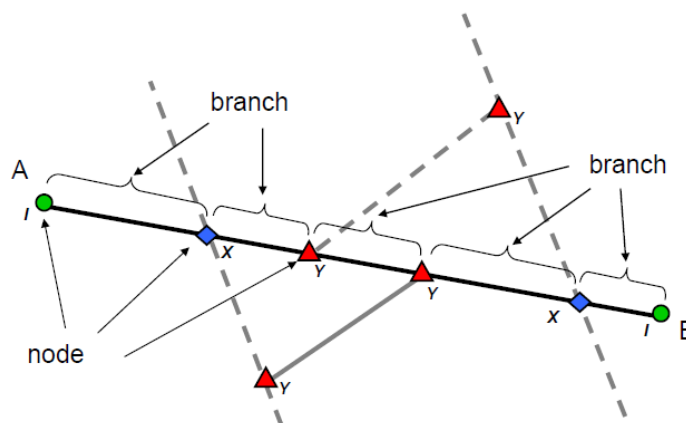


Figure 39: Fracture path (A-B) with intersecting fracture lines (dashed lines), showing topological nodes and branches: I-nodes (circles), Y-nodes (triangles), and X-nodes (diamonds). (Sanderson & Nixon, 2015)

The (fracture or crack) lines consist of an end-to-end (i.e., tip-to-tip) sequence of (crack) branches. Here, branches are line segments with nodes on each end.

These topological features (nodes, branches, and lines) are then counted and used to quantitatively describe and compare the fracture patterns in the HSI, PMI, PMM, and the CT sections. Furthermore, this allows a description of crack branching/merging in the blasted cylinders and its further correlation to resulting blast fragmentation.

The topological features were compared considering either axial position (transverse CT sections, CTt), radial position (non-planar CT sections, CTnp; post-mortem “unfolded” mantle images, PMM), or time that lapsed from the blast detonation (HSI and PMI).

The fracture patterns were analysed as systems of connected nodes (Figure 40). Manzocchi (2002) and Sanderson & Nixon (2015) defined three types of topological nodes - isolated tips (I-nodes), crossing fractures (X-nodes), and abutments or splays (Y-nodes or T-nodes). The marking resembles the shape of the features.

The nodes in the fracture patterns of the blasted cylinders are distinguished as:

- end nodes (tips) of the cracks (I),
- intersections with the blast-hole wall (T_H), intersections with the (outer) mantle of the cylinder (T_M),
- cross intersections (X), branching/merging intersections (Y), and other (complex) intersections (R, stands for ‘rest’).

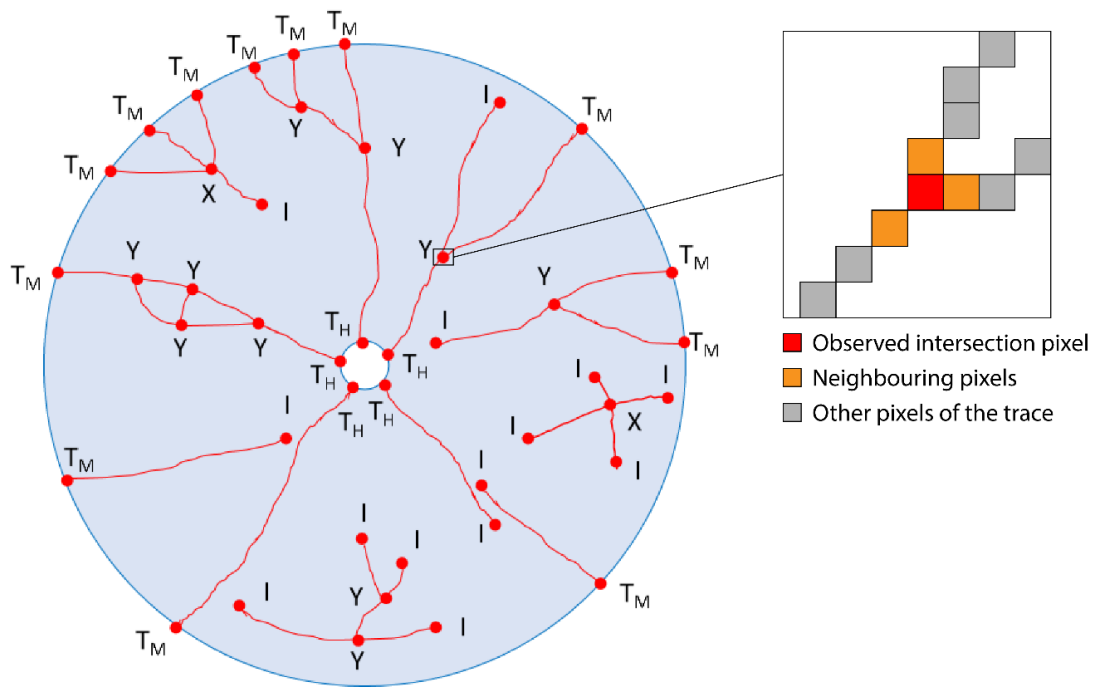


Figure 40: Conceptual sketch of the topological nodes and marking.

They are detected using a MATLAB[®] script (Appendix 7) by counting the number of branches connected to the node being measured. The branches are related to the neighbouring pixels around the node pixel. Therefore, a node could have up to 8 branches, although this number rarely exceeds four (Manzocchi, 2002; Sanderson & Nixon, 2015; Sanderson et al., 2019).

To account for this issue, R-nodes are defined to have more than four neighbouring pixels, though they are below treated like X-nodes. The nodes were counted and their count denoted – N_I for I-nodes, N_Y for Y-nodes, N_X for X- and R-nodes, and N_{TB} for the boundary intersections T_B (i.e., T_H+T_M). Here, Y-, X-, and R-nodes are considered as joining nodes and their sum count is written as J_{int} .

The original analysis (Manzocchi, 2002; Sanderson & Nixon, 2015) plots proportions of I-, X-, and Y-nodes in the ternary diagram (Figure 41). For the blasted cylinders, these (I-Y-X) diagrams would not make sense since N_X in most processed images is very low compared to N_I and N_Y .

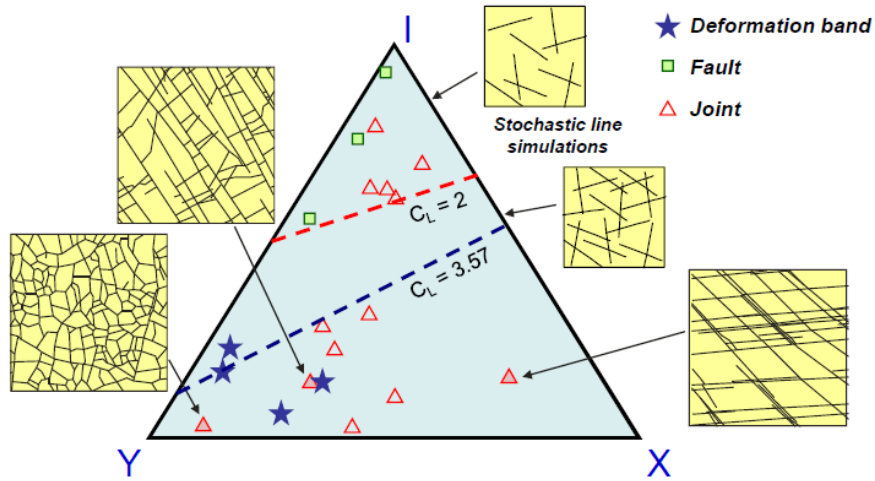


Figure 41: Ternary diagram of node-type (I, Y, and X) proportions for different fracture patterns. (Sanderson & Nixon, 2015)

The node-type proportions (P_I , P_Y , P_X , P_R , and P_B) are relative values of the node count (i.e., $\frac{\text{Count of a particular node type}}{\text{Total node count}}$ [%]). The proportions were plotted in ternary diagrams with I (P_I), T_B (P_B), and J_{int} ($P_Y+P_X+P_R$) as axes coordinates (Figure 42).

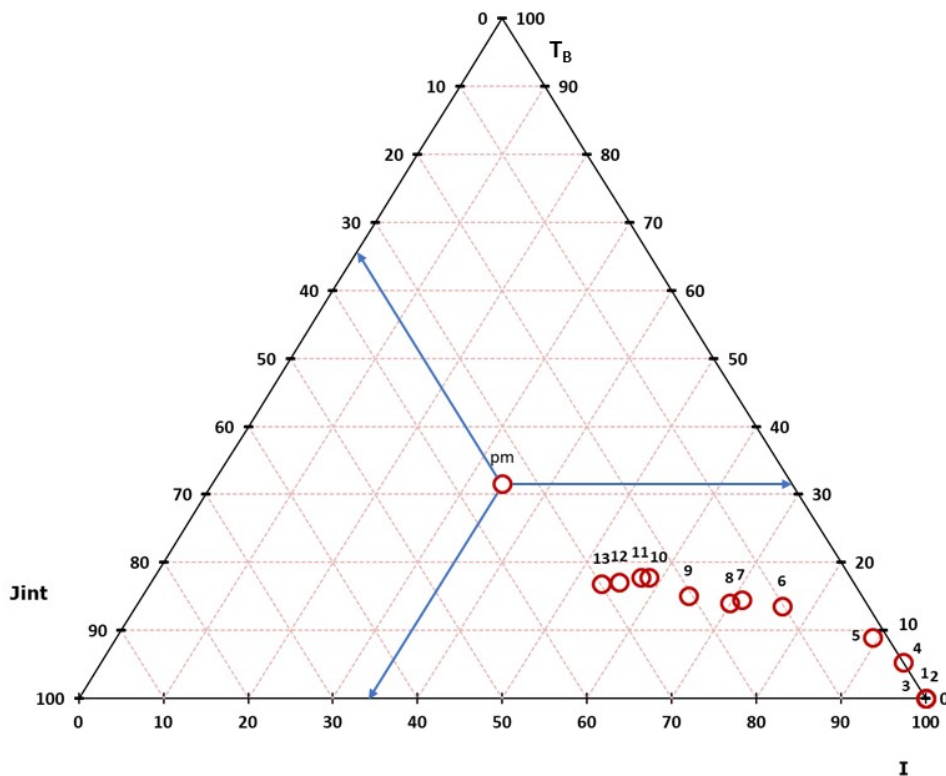


Figure 42: Example of the ternary diagram used for plotting proportions of the topological nodes. It covers a sequence of HSI, marked in sequence numbers, and the corresponding PMI (pm). The blue arrows indicate the values for plotting point 'pm.'

These (I-T_B-J_{int}) diagrams are used to analyse the fracture-pattern development considering crack branching/merging and in-plane fragmentation. Figure 42 shows an example of the development that starts with only single isolated cracks. Then, they coalesce, extend, and branch, with some of them reaching the boundaries.

The scatter of data points in CT-ternary diagrams (i.e., for the CT_t and for the CT_{np}) was measured as the distance (D_{cent} [-]) from the geometrical centre (centroid, 'C') of the data cluster (swarm of points) and its data points (Figure 43). This distance is expressed in the units of the graph. This measure indicates the topological-feature persistence along the cylinder axis, and it could also be used to evaluate if two crack patterns are significantly different or not by quantifying the overlap of the corresponding swarms.

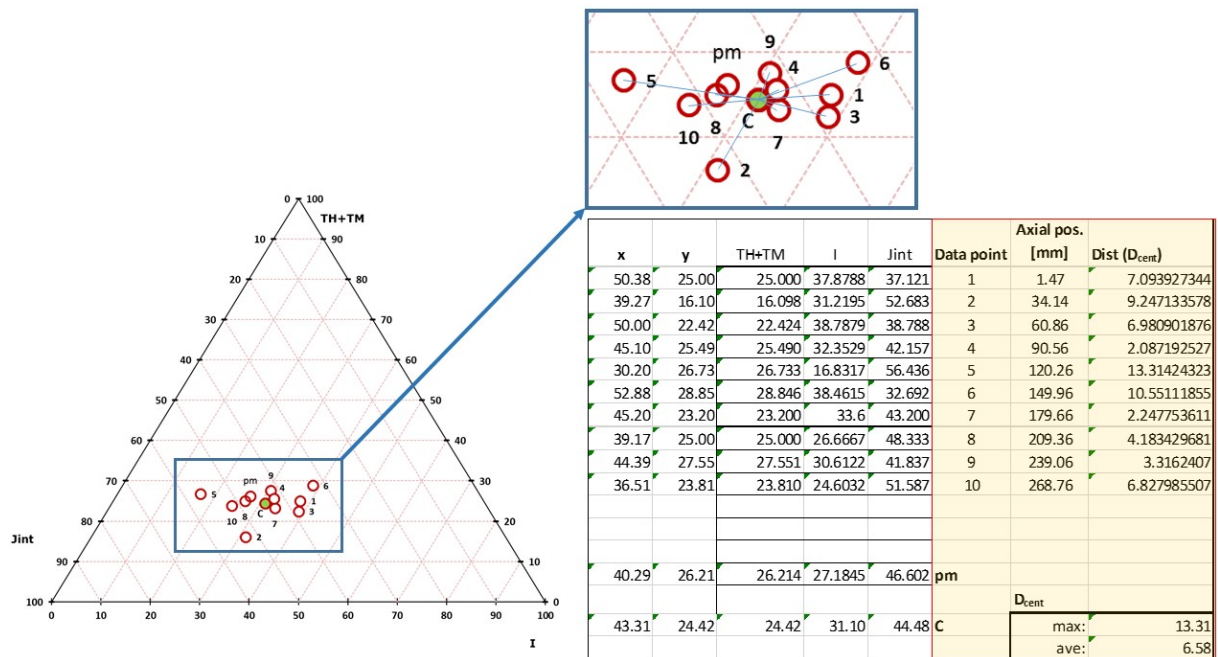


Figure 43: Determination of the data scatter (D_{cent}) in the CT ternary diagrams.

Since I-, Y-, and T_B-nodes are considered as the tip of a single line, the number of crack lines (N_L [-]) is written as:

$$N_L = 1/2 (N_I + N_Y + N_{T_B}) \quad \text{Equation 10}$$

Branches include two nodes. Here, each I-node belongs to one branch, each Y- and T_B-node - three branches, and each X- and R-node - four branches. The number of branches (N_B [-]) is written as:

$$N_B = 1/2 (N_I + 3N_Y + 3N_{TB} + 4N_X + 4N_R)$$

Equation 11

Sanderson & Nixon (2015) further evaluated connectivity in the node plots considering the ratio of the number of branches to lines (N_B/N_L [-]) and the average number of connections per line (C_L) (Figure 41 and Figure 44).

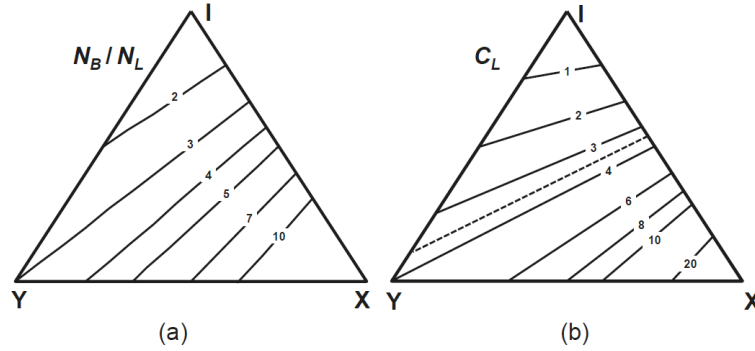


Figure 44: Ternary diagrams of node proportions with the comparative parameters: a) ratio of the number of branches to lines (N_B/N_L); b) the average number of connections per line (C_L). (Sanderson & Nixon, 2015)

The ratio N_B/N_L can be written as:

$$\frac{N_B}{N_L} = \frac{(N_I + 3N_Y + 3N_{TB} + 4N_X + 4N_R)}{(N_I + N_Y + N_{TB})}$$

Equation 12

Given that an intersection must be an X- or Y-node and each provides a connection of two lines, C_L [-] can be written as (Sanderson & Nixon, 2015):

$$C_L = \frac{2(N_Y + N_{TB} + N_X + N_R)}{N_L}$$

Equation 13

They also defined the average number of connections per branch (C_B [-]), a dimensionless number in the range 0–2, as:

$$C_B = \frac{3N_Y + 3N_{TB} + 4N_X + 4N_R}{N_B + N_{TB}}$$

Equation 14

These parameters (N_L , N_B , N_B/N_L , C_L , and C_B) were calculated for the fracture patterns in the HSI, PMI, and CTt.

Sanderson & Nixon (2015) prefer working with branches over fracture paths to assure result repeatability. They categorized branches considering their apparent connectivity (Figure 45). They mapped many C_B data points corresponding to different crack/fracture patterns and pointed out the relationship between this parameter and the ternary plots

that describe crack/branch connectivity or crack/branch type (I, X, and Y). This parameter ranges from 0, indicating only isolated I-I branches or only I-nodes in crack pattern, to 2, indicating only fully connected C-C braches or only X and Y nodes in crack pattern.

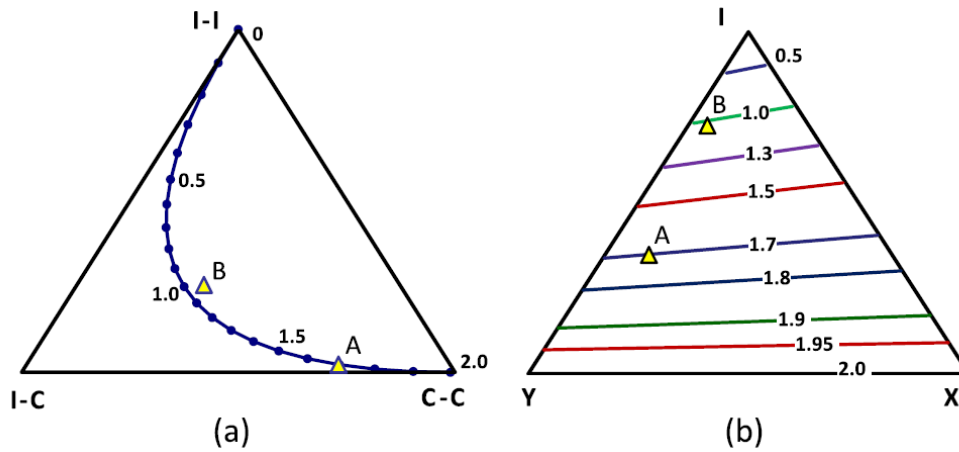


Figure 45: Proportions of fracture branches plotted in a ternary diagram (Sanderson & Nixon, 2015): a) “proportions of different branch types with numbers 0 to 2.0 indicating connections per branch (C_B);” b) values of C_B on the original triangular plot.

Connecting branches (C-C) are linked to other branches at their both ends, semi-connecting branches (I-C) are linked at only one end, and non-connecting branches (I-I) are isolated, i.e., not linked at either end. They count the branches similarly as the nodes and plot their (type) proportions in another ternary diagram, with C-C, I-C, and I-I as axes.

They used the node counts to calculate the probability of any branch end being an isolated (p_I [-]) or connected (p_C [-]) node and the probability of each branch type (i.e., p_{II} [-] for I-I, p_{IC} [-] for I-C, and p_{CC} [-] for C-C). For the blasted cylinders, these were calculated as:

$$\begin{aligned}
 p_I &= \frac{N_I}{N_I + 3N_Y + 3N_{TB} + 4N_X + 4N_R} && \text{Equation 15} \\
 p_C &= \frac{3N_Y + 3N_{TB} + 4N_X + 4N_R}{N_I + 3N_Y + 3N_{TB} + 4N_X + 4N_R} \\
 p_{II} &= p_I^2, && p_{IC} = p_I \cdot p_C, && p_{CC} = p_C^2
 \end{aligned}$$

These probabilities were calculated for the fracture patterns in the HSI, PMI, and CTt.

4.1.6 Fracture abundance

Sanderson & Nixon (2015) defined three measures of fracture (crack) abundance in 2D images – areal fracture frequency (p_{20}), fracture intensity (p_{21}), and dimensionless fracture intensity (p_{22}):

$$p_{20} = \frac{N_L}{A} [mm^{-2}] \quad \text{Equation 16}$$

$$p_{21} = \frac{\sum L}{A} [mm^{-1}] \quad \text{Equation 17}$$

$$p_{22} = \frac{N_L \cdot L_C^2}{A} = p_{21} \cdot L_C [-] \quad \text{Equation 18}$$

Areal fracture frequency (p_{20}) was calculated as the ratio of the number of calculated fracture (crack) lines and the cross-section area (A [mm^2]) in the images.

Fracture intensity (p_{21}) was calculated by dividing total fracture-line length ($\sum L$ [mm]) by the cross-section area in the images.

Dimensionless fracture intensity (p_{22}) was calculated by multiplying fracture intensity by the characteristic length (L_C [mm]), which is calculated as the arithmetic mean of the fracture-line lengths.

These parameters were calculated for the fracture patterns in HSI, PMI, and CTt.

4.1.7 In-plane (2D) fragmentation

The 2D fragmentation (Figure 46) considers the fracture patterns in the traced images (HSI, PMI, or CT).

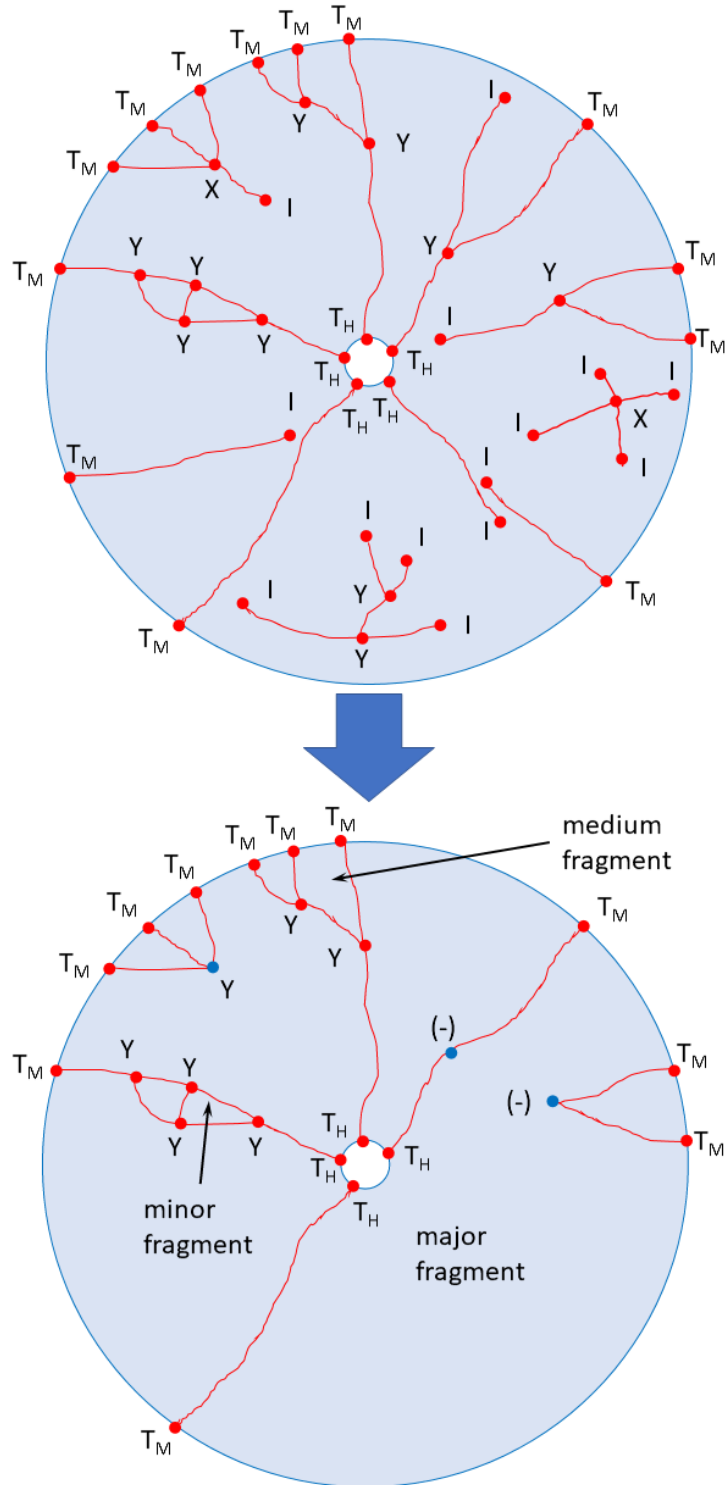


Figure 46: In-plane (2D) fragmentation - definition and preparation for counting of 2D fragments. The fragment patterns are obtained by deleting non-connected and semi-connected branches.

Note the relation between the number of major 2D fragments and the number of connected fracture lines in the images. Here, 2D fragments are defined as enclosed contours consisting of traced fracture paths, blast-hole segments, and mantle segments. These fragments were counted and measured (sized). The counting was done on the topological images and the sizing was done directly on the trace images.

Counted fragments were categorized considering their connectivity with the cylinder boundaries as – major (connected with both the blast-hole wall and the mantle), medium (connected with either the blast-hole wall or the mantle), and minor (interior fragments).

Fragment size (Figure 47) was calculated using a MATLAB® script (Appendix 7) as the minor axis of the ellipse that has the same normalized second central moments as the region (i.e., 2D fragment being measured).

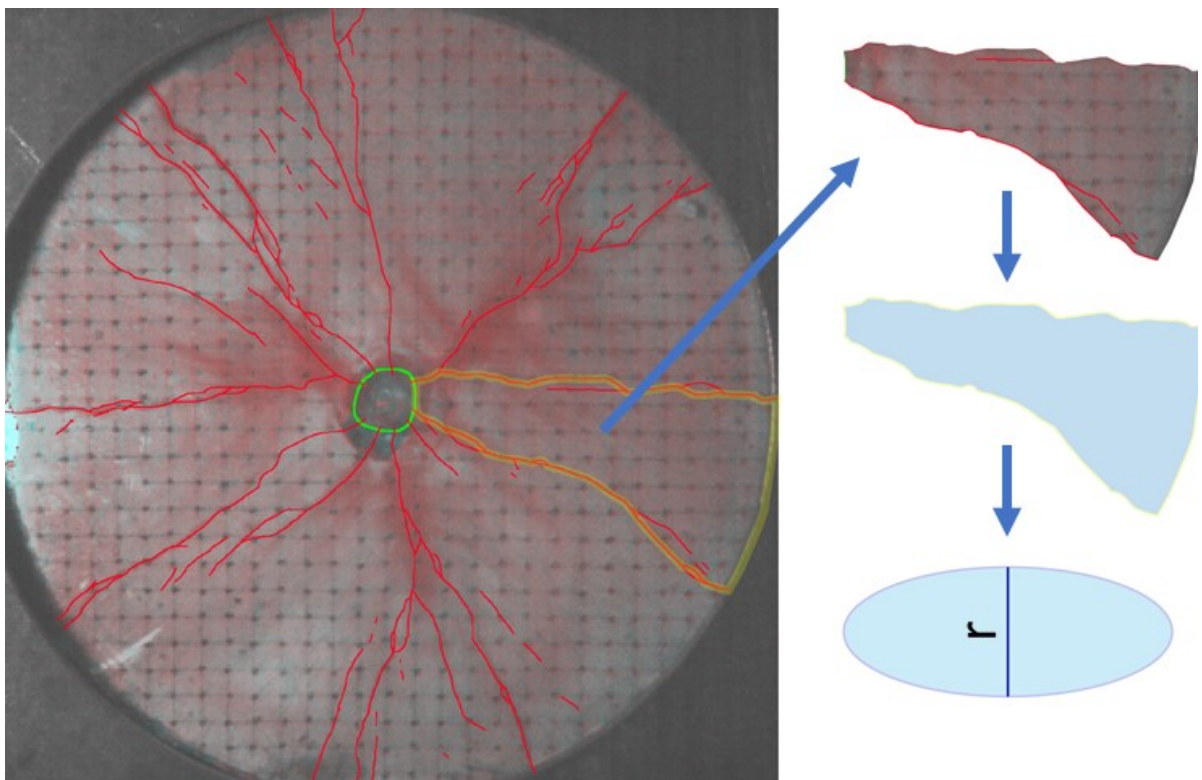


Figure 47: Determination of 2D-fragment size.

The 2D-fragment counts and their proportions were also presented and analysed in ternary diagrams (Figure 48) for the HSI and the CTt, similar to those described in Section 4.1.5.

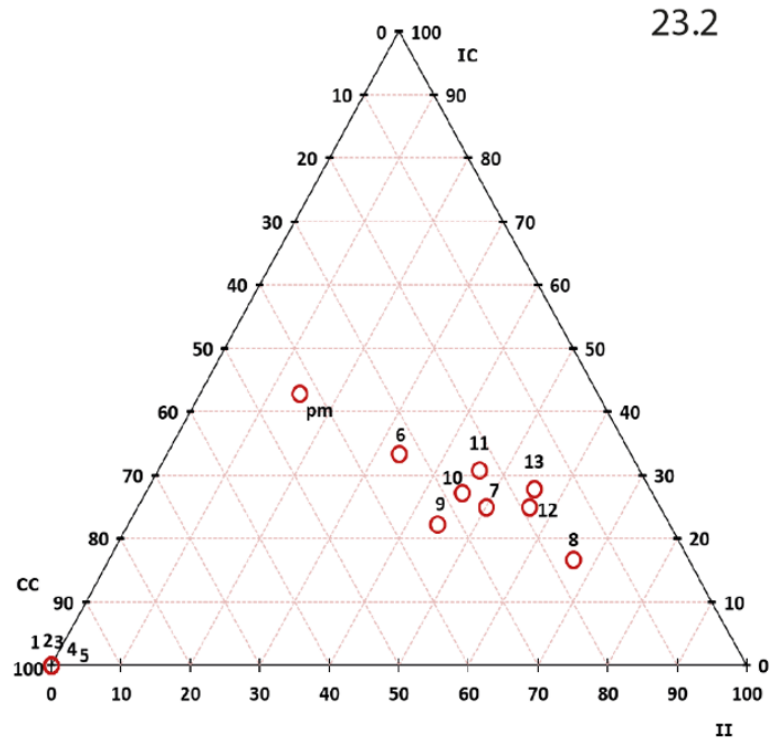


Figure 48: Example a ternary diagram used to describe in-plane (2D) fragmentation in HSI. It covers a sequence of HSI, marked in sequence numbers, and the corresponding PMI (pm). The number in the upper-right corner denotes the reference blast-test number.

The diagram axes represent the 2D-fragment connectivity categories – ‘II’ for minor (interior, not connected to either the blast hole or the mantle), ‘IC’ for medium (semi-connected, connected to the blast hole or the mantle), and ‘CC’ for major (connected, connected to the blast hole and the mantle) 2D fragments.

The data scatter (D_{cent} [-]) was also measured in the ternary diagrams of the 2D-fragment proportions in the CTt.

4.1.8 Main radial cracks

Primary connected paths in the fracture patterns of the blasted cylinders can be considered as main radial cracks, N (Grady & Kipp, 1987). The main radial cracks were obtained from HSI, PMI, and CTt images as the number of major (CC) 2D fragments. Grady & Kipp (1987) developed a model for estimating the number of radial cracks (fractures), initiated at a single blast hole, per unit length:

$$N = \pi \cdot \phi_h \left(\frac{\dot{p}}{6 \cdot C_p \cdot K_{Ic}} \right)^{2/3}, \quad \text{Equation 19}$$

where ϕ_h [m] is the initial blast-hole (borehole) diameter, C_p [m/s] is the P-wave velocity in the blasted material, \dot{p} [MPa/ μ s] is the loading rate of the blast, and K_{Ic} [MN \cdot m $^{-3/2}$] is the critical (dynamic) stress-intensity factor of the blasted material.

Ouchterlony (1997) adjusted this equation to better fit available parameters in common blasting practice:

$$N = \frac{\pi}{3^{2/3}} \left(\frac{p_h \cdot \sqrt{\phi_h}}{K_{Ic}} \right)^{2/3}, \quad \text{Equation 20}$$

where p_h [MPa] is the peak pressure level in the blast hole.

Figure 49 shows an approximation of the blast-hole pressure level (Iravani et al., 2018b).

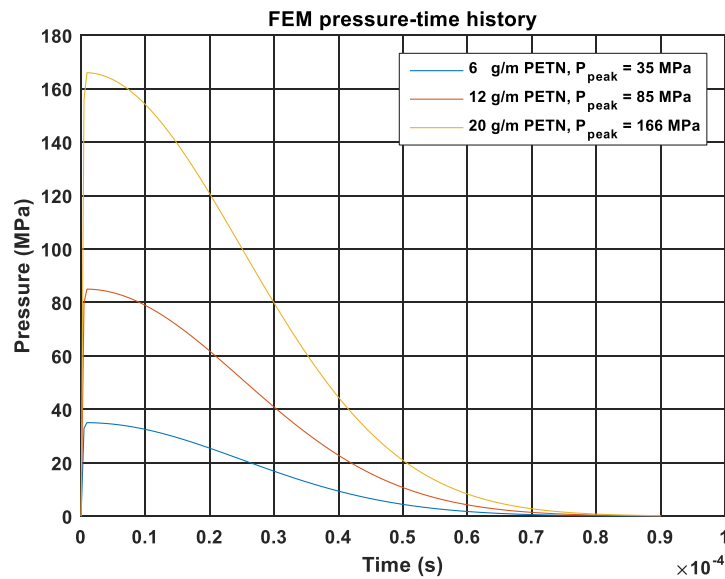


Figure 49: Estimated blast-hole pressure levels concerning elapsed time and the linear charge concentration. (Iravani et al., 2018b)

Here, the loading rate can be calculated for the initial (raising) part of the curve as the peak pressure level divided by $1 \mu\text{s}$ (initial pressure-rise time). Therefore, the loading rate (\dot{p}) and the peak pressure level in the blast hole (p_h) can be roughly approximated to 35, 85, and 166 [MPa/ μs , MPa] for the PETN linear charge concentrations of 6, 12, and 20 g/m, respectively (Iravani et al., 2018b).

Equation 19 and Equation 20 were used to estimate K_{Ic} based on the fracture-patterns in the post-mortem images (i.e., CTt and PMI or final traceable HSI).

4.1.9 Crack-propagation speed

The image-by-image crack-pattern traces were used to calculate the apparent crack-propagation speed by dividing the crack extension by the inter-frame time.

The results covering data for each image from the HSI sets were then presented in box-and-whisker plots and their average values per HSI set (C_{ave}) were statistically compared.

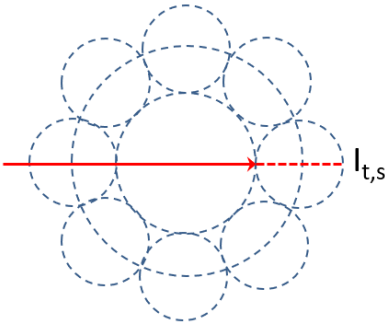
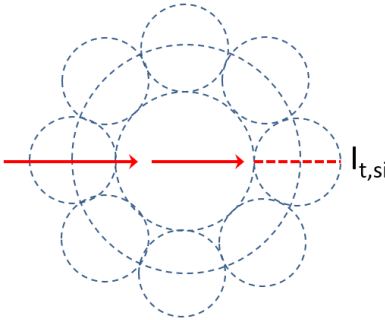
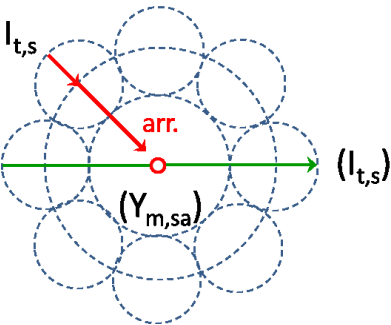
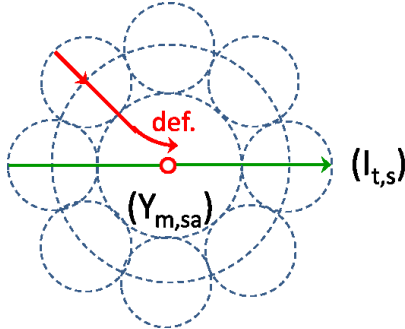
4.1.10 Macro-mechanisms

Table 7, Table 8, Table 9, and Table 10 show interpreted macroscopic crack-propagation and crack-interaction features. These mechanisms are marked with two numbers, of which the first one denotes the mechanism type (1- crack-propagation paths, 2 – crack branching, 3 – crack merging, or 4 – crack branching-merging) and the second one the sequence number of the corresponding mechanism within the type category. The mechanisms are also provided with letter notation (e.g., $l_{t,s}$) to provide a shorter description of the mechanisms.

Note that although these mechanisms and those covered in Section 4.4.3 are fracture features (i.e., elements of fracture patterns), in many cases they can only be identified considering a local (surrounding) fracture pattern. For example, an X-branching/merging is an intersection point, though it is identified considering its four branches.

Blenkinsop (2007) referred to similar remnant features as traces of “micro-faults.” A record of these macro-mechanisms for the HSI is defined here as an event log. The resulting event logs refer to the mechanisms by noting their respective number, as defined in Table 7, Table 8, Table 9, and Table 10.

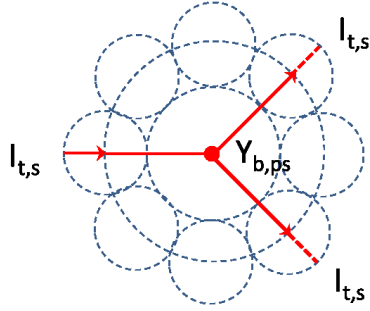
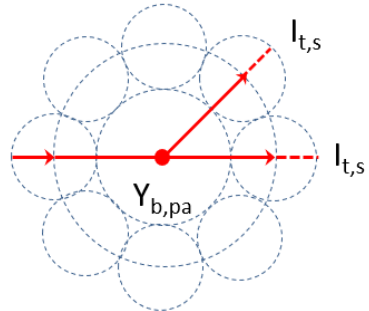
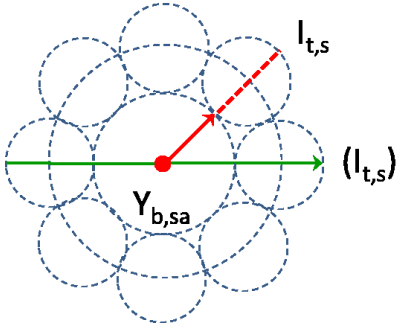
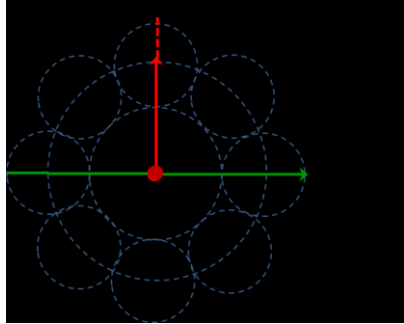
Table 7: Macro-mechanisms (Crack-propagation paths).

1 Crack-propagation paths	
<p>1.1 Crack extension ($l_{t,s}$)</p> 	<p>1.2 Discontinuous crack extension ($l_{t,si}$)</p> 
<p>1.3 Side crack arrest ($a-l_{t,s} \rightarrow Y_{m,sa}$)</p> 	<p>1.4 Side crack deflection ($d-l_{t,sk} \rightarrow Y_{m,sa}$)</p> 

The mechanisms in Table 7 have the following meaning:

- Crack extension (**1.1**): A crack tip (I-node) propagates along a (straight) path;
- Discontinuous crack extension (**1.2**): A crack tip (I-node) propagates along a (straight) discontinuous path;
- Side crack arrest (**1.3**): A propagating acute-angled crack seemingly arrests before it reaches the flank of another crack it, forming an I-node but no Y-node;
- Side crack deflection (**1.4**): A propagating acute-angled crack seemingly deflects before it reaches the flank of another crack it, forming an I-node but no Y-node.

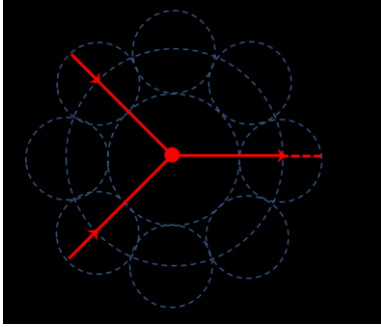
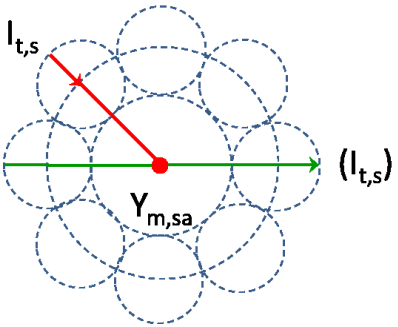
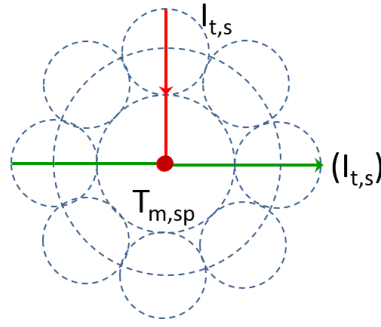
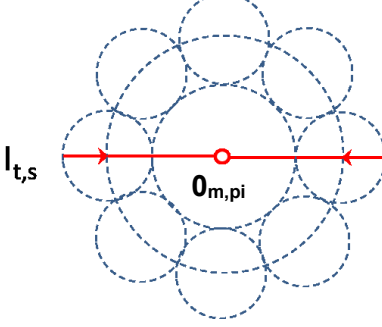
Table 8: Macro-mechanisms (Crack interactions - Branching).

2 Crack interactions - Branching	
<p>2.1 Primary in-line Y-branching ($l_{t,s} \rightarrow Y_{b,ps}$)</p> 	<p>2.2 Primary side Y-branching ($l_{t,s} \rightarrow Y_{b,pa}$)</p> 
<p>2.3 Secondary side Y-branching ($l_{t,s} \rightarrow Y_{b,sa}$)</p> 	<p>2.4 Secondary T-branching ($l_{t,s} \rightarrow T_{b,sp}$)</p> 

The mechanisms in Table 8 have the following meaning:

- Primary in-line Y-branching (**2.1**): The tip of a propagating crack branches into two symmetric cracks. Here, a primary (almost) symmetric branching creates a diverging Y-node;
- Primary side Y-branching (**2.2**): An asymmetric side branch is initiated at an acute angle at or directly behind the tip of a propagating crack. Here, a primary asymmetric branching creates a diverging Y-node;
- Secondary side Y-branching (**2.3**): An acute-angled side branch is initiated on the flank of a crack (i.e., well behind the tip). Here, a secondary asymmetric branching creates a diverging Y-node;
- Secondary T-branching (**2.4**): A right-angled side branch is initiated on the flank of a crack, i.e. well behind the tip, forming a T-node. A T-node is treated like a Y-node in the topological analysis.

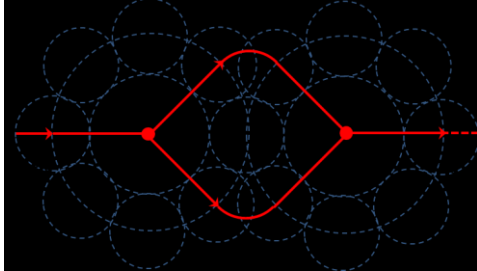
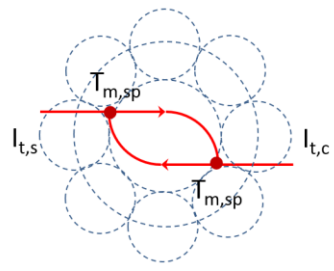
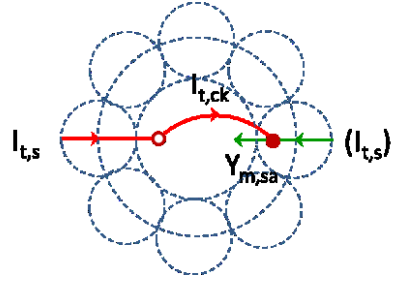
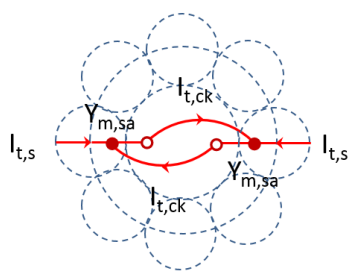
Table 9: Macro-mechanisms (Crack interactions - Merging).

3 Crack interactions - Merging	
<p>3.1 Primary in-line Y-merging ($2l_{t,s} \rightarrow Y_{m,ps}$)</p> 	<p>3.2 Side Y-merging ($l_{t,s} \rightarrow Y_{m,sa}$)</p> 
<p>3.3 Secondary T-merging ($l_{t,s} \rightarrow T_{m,sp}$ OR $l_{t,c} \rightarrow T_{m,sp}$)</p> 	<p>3.4 In-line merging ($l_{t,s} \rightarrow 0_{m,pi} \leftarrow l_{t,s}$)</p> 

The mechanisms in Table 9 have the following meaning:

- Primary in-line Y-merging (**3.1**): Two propagating cracks merge into one symmetric branch. Here, a primary (almost) symmetric merging forms a Y-node;
- Side Y-merging (**3.2**): A propagating acute-angled crack reaches the flank of another crack and merges with it. Here, a secondary or delayed asymmetric merging creates a converging Y-node;
- Secondary T-merging (**3.3**): A propagating right-angled crack reaches the flank of another crack and merges with it. Here, a secondary perpendicular merging forms a T-node;
- In-line merging (**3.4**): Two cracks propagating in opposite directions run into each other, annihilating the tips and forming a kink if the cracks aren't aligned or seemingly leaving no node if the cracks are aligned.

Table 10: Macro-mechanisms (Crack interactions - Branching-merging).

4 Crack interactions – Branching-merging	
<p>4.1 In-line 2Y-branching-merging $(I_{t,s} \rightarrow Y_{b,ps} + Y_{m,ps} \rightarrow I_{t,s})$</p> 	<p>4.2 Double en-passant merging $(I_{t,c} \rightarrow T_{m,sp} + T_{m,sp} \leftarrow I_{t,c})$</p> 
<p>4.3 En-passant tip deflection and merging $(I_{t,s} \rightarrow I_{t,ck} \rightarrow Y_{m,sa})$</p> 	<p>4.4 Double en-passant tip deflection and merging $(I_{t,s} \rightarrow I_{t,ck} \rightarrow Y_{m,sa} + Y_{m,sa} \leftarrow I_{t,ck} \leftarrow I_{t,s})$</p> 

The mechanisms in Table 10 have the following meaning:

- In-line 2Y-branching-merging (4.1): A propagating crack splits into two branches that subsequently merge again, forming a pair of Y-nodes ($Y_b + Y_m = 2Y$) and leaving a disconnected island;
- Double en-passant merging (4.2): Two cracks propagating at an offset and in parallel but opposite directions, run into each other, each tip reaching the flank of the other crack at right angles, merging and forming a pair of T-nodes ($T_m + T_m$), leaving a disconnected 'island';
- En-passant tip deflection and merging (4.3): Two cracks propagating in opposite directions run into each other, one tip reaching the flank of the other crack at acute angles, merging, forming a Y-node (Y_m) and leaving an I-node at a partly connected branch;
- Double en-passant tip deflection and merging (4.4): Two aligned cracks propagating in opposite directions run into each other, each tip reaching the flank of the other crack at acute angles, merging and forming a pair of Y-nodes ($Y_m + Y_m$), leaving a disconnected island.

4.1.11 Measurement uncertainty of the crack patterns

The interpretations based on the crack patterns are relatively uncertain due to the temporal and spatial sampling of the filming and resolution of the PMI and sections.

The spatial resolution limits the precision of crack-extension measurements. The temporal resolution introduces an uncertainty of the crack development between the exposure times of HSI. The only way of determining whether a crack tip has extended is by comparing its position with that in the neighbouring frames in the sequence. This introduces a problem of determining how the crack tip extended. Figure 50 shows how the same observed extension could result from different potential mechanisms and, thus, indicate different crack-propagation speed.

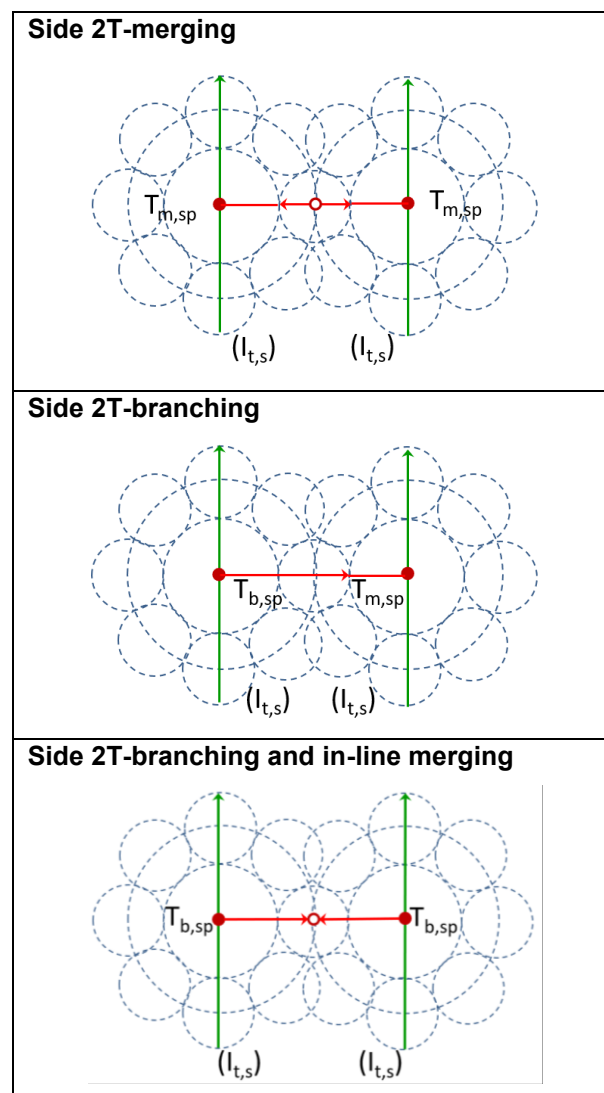


Figure 50: Examples of difficulties in determining influencing mechanisms based on observed crack patterns in HSI

The pattern in Figure 50 has the following different interpretations:

- A crack initiated between two subparallel cracks reaches these cracks at right angles and merges with them, forming two T-nodes ($T_m + T_m = H$).
- A T-branch is initiated on a flank of a crack and reaches the flank of an adjacent subparallel crack (at right angles), forming two T-nodes ($T_b + T_m = H$).
- Two T-branches are initiated on a flank of two adjacent subparallel cracks and reach each other's tip in between the cracks (at right angles), forming two T-nodes and an in-line merging ($T_b + T_b = H$).

It is often not clear whether crack intersections result from branching, merging, or both. It is also often difficult to determine if there were two side-branched-out cracks that merged or if there was a third (smaller) crack, in-between the two cracks, which propagated in both directions and made T-merging with the two cracks (Dalmas et al., 2013).

Furthermore, the tracing is more difficult due to the fumes, dust, light flickering, and filming noise, as they might lead to false crack detection. Therefore, the crack-propagation speed measurements provide only averaged inter-frame values measured during the first two blast-fracture phases.

4.2 Blast-hole expansion, cylinder swelling, and deformation zones

The detonation in the blast cylinders is sufficient to induce both the (mostly radial) tensile fracturing and the crushing-shear crushing around the blast hole (Figure 51).

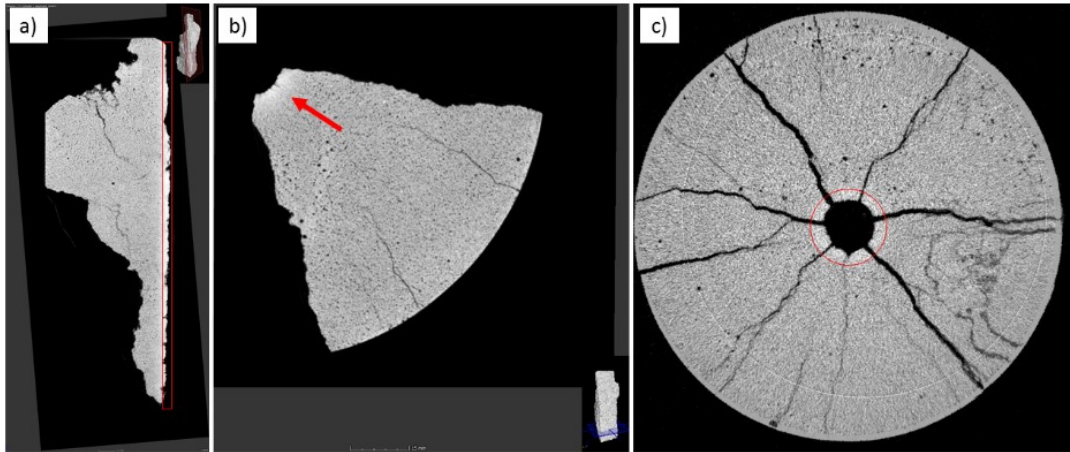


Figure 51: Example of the deformation zones in the mortar (CT sections): a) longitudinal (side) section of a fragment (m12(20)); b) transverse section of a fragment (m12(20)); c) transverse section of a blasted cylinder (m12(21)). The compaction zone and the crushed zone appear lighter in the images due to the higher material density.

During the formation of the crushed zone, some of its material is blasted-off, leaving an expanded (ablated) blast hole. A compacted zone can be formed by further radial compression of the crushed material around the blast hole. This material compaction also contributes somewhat to the blast-hole expansion due to the respective decrease of material volume. This zone was found only in the blasted mortar cylinders (see Section 5.7). Therefore, the blast-hole expansion has three components:

- an annulus of material removed (blasted off) from the blast-hole wall, and
- an annular volume increase (of the blast hole) in the mortar introduced by compacting material in which the pores have been annihilated by a crushing-shearing displacement, and
- the radial rigid-body movement.

Outside these zones, there is still a large, annular crushed zone. This zone, for simplicity, is assumed to have the same density and shape as before blasting. Given the common underlying mechanisms (i.e., compression-shearing), the original (true) crushed zone consists of (in the radially ascending order):

- the blasted-off layer,
- the compacted zone (in the mortar), and
- the rest of the crushed zone.

Figure 51 shows the compacted zone around the blast hole in transverse CT sections (CTt) of a blasted cylinder and a blast fragment.

A fracture zone is created further out from the crushed zone in the radial direction. Although blast-induced cracks and fractures are also found in the crushed zone, the underlying mechanisms are different. The development of the crushed zone is mostly governed by crushing and shearing failure, whereas tensile failure is the leading fracture mechanism in the fracture zone.

The development of blast-induced cracks radially expands the cylinder by increasing the volume of its inner voids. The extent of the radial expansion (i.e., swelling) (δr_m in Figure 52) depends on the blast loading, material properties of the cylinder, and the boundary conditions (D. Johansson & Ouchterlony, 2011).

Many of the largest (major) blast fragments have roughly pie- or wedge-shaped (sector-formed) transverse cross-sections (Figure 51b). The CTt of whole blasted cylinders (Figure 51c) consist mainly of such fragment sections separated by open radial cracks.

In these simplified wedge-shaped fragment sections, the annulus of the material outside the crushed zone, which has not failed, is also assumed to have preserved its original shape and density. In a simplified model of such the wedge-shaped fragment sections (Figure 52), the limits of these deformation zones become circular arcs.

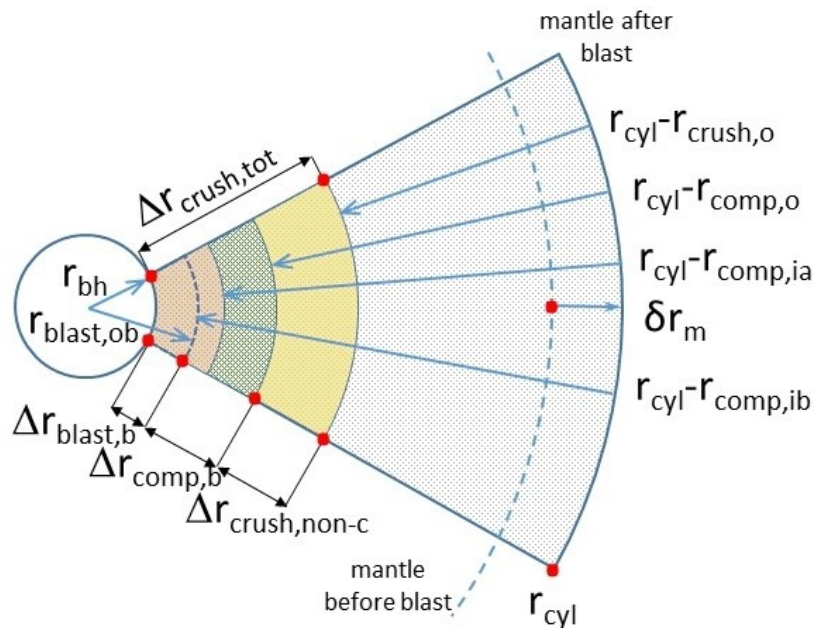


Figure 52: Wedge-shaped fragment section with deformation zones.

Table 11 shows the terminology used to describe this model.

Table 11: Terminology of symbols in Figure 52, related to a single fragment or fragment assembly. The subscript letters after comma denote: o - outer, i - inner, b - before, and a - after.

r_{bh} [mm]	<u>b</u> ore <u>h</u> ole radius (known, i.e., measured before-hand).
r_{cyl} [mm]	blast- <u>cyl</u> inder radius (known).
$r_{crush,o}$ [mm]	the <u>o</u> uter limit of the <u>crush</u> ed zone after blasting.
$\Delta r_{crush,tot} = r_{crush,o} - r_{bh}$ [mm]	the thickness of the whole <u>crush</u> ed zone after blasting (computable).
$r_{crush,i}$ [mm]	<u>i</u> nnner limit of the <u>crush</u> ed zone after blasting (measurable).
$\Delta r_{crush,non-c} = r_{crush,o} - r_{crush,i}$ [mm]	the thickness of the <u>non-c</u> ompacted part of the crushed zone (measurable).
$r_{comp,o} = r_{crush,i}$ [mm]	the <u>o</u> uter limit of the compacted zone after blasting.
$r_{comp,ia}$ [mm]	the <u>i</u> nnner limit of the compacted zone <u>a</u> fter blasting (measurable).
$\Delta r_{comp,a} = r_{comp,o} - r_{comp,ia}$ [mm]	the thickness of the compacted zone <u>a</u> fter blasting (measurable).
$r_{comp,ib}$ [mm]	the <u>i</u> nnner limit of the compacted zone <u>b</u> efore blasting (measurable).
$\Delta r_{comp,b}$ [mm]	the thickness of the zone to be <u>comp</u> acted (<u>b</u> efore the blasting) (computable from the density change).
$r_{blast,ob} = r_{comp,ib}$ [mm]	the <u>o</u> uter limit of <u>blast</u> -ed-off zone before blasting (computable).
$\Delta r_{blast,b} = r_{blast,ob} - r_{cyl}$ [mm]	the thickness of the <u>blast</u> -ed-off zone before blasting (computable).
A_m [mm ²]	the area circumscribed by outer lasso curve around the <u>m</u> antle after the blast, see Figure 53.
A_{bh} [mm ²]	the area circumscribed inside ablated <u>blast-h</u> ole after the blast
$\bar{r}_{m,a}$ [mm]	the radius of a circle with the same area as A_m , i.e., average position of the <u>m</u> antle.
$\bar{r}_{bh,a}$ [mm]	the radius of a circle with the same area as A_{bh} , i.e., average position of the ablated <u>blast h</u> ole.
δr_m [mm]	the average expansion or swelling of the <u>m</u> antle.
δr_{bh} [mm]	the average <u>blast-h</u> ole expansion.
$\Delta V_{blast,b}$ [mm ³]	the original volume of the <u>blast</u> -ed-off layer
$\Delta V_{comp,b}$ [mm ³]	original volume of the <u>comp</u> action zone

Here,

- r always denotes a radial distance from the centre of the borehole, before or after blasting,
- Δr_{nn} denotes a difference in radial position between two zone limits at a given point in time, before or after blasting, and
- δr_{nn} denotes a change in given radial position caused by the blast.

Table 11 and Figure 52 imply that:

$$\Delta r_{crush,tot} = \Delta r_{blast,b} + \Delta r_{comp,b} + \Delta r_{crush,non-c} \quad \text{Equation 21}$$

In Equation 21, all terms are measurable or calculable before-hand, except $\Delta r_{blast,b}$. This quantity can, thus, be computed by rearranging the terms:

$$\Delta r_{blast,b} = \Delta r_{crush,tot} - (\Delta r_{comp,b} + \Delta r_{crush,non-c}) \quad \text{Equation 22}$$

To compute $\Delta r_{comp,b}$, it is assumed that the compaction does not alter the mass involved. With the material density before the blasting of ρ_b [g/cm³] (bulk density) and a higher density after blasting ρ_g [g/cm³] (grain-level density), since annihilating the pores decreases the volume, and a charge length of l_{ch} [mm], the conserved mass over this length is:

$$\rho_b \cdot l_{ch} \cdot \pi(r_{comp,o}^2 - r_{comp,ib}^2) = \rho_g \cdot l_{ch} \cdot \pi(r_{comp,o}^2 - r_{comp,ia}^2) \quad \text{Equation 23}$$

This yields:

$$r_{comp,ib} = r_{comp,ia} \sqrt{1 - (\rho_g / \rho_b - 1) (r_{comp,o}^2 / r_{comp,ia}^2 - 1)} < r_{comp,ia} \quad \text{Equation 24}$$

and

$$\Delta r_{comp,b} = r_{comp,o} - r_{comp,ib} \quad \text{Equation 25}$$

The same computations can be repeated for each wedge-shaped fragment section in the CTt. However, a more practical alternative is to calculate an average for whole CTt. The contours of the blast hole and the mantle were traced in the CTt images. The tracing was done with the “lasso/blow” tool (Ferreira & Rasband, 2012) in ImageJ (Figure 53).

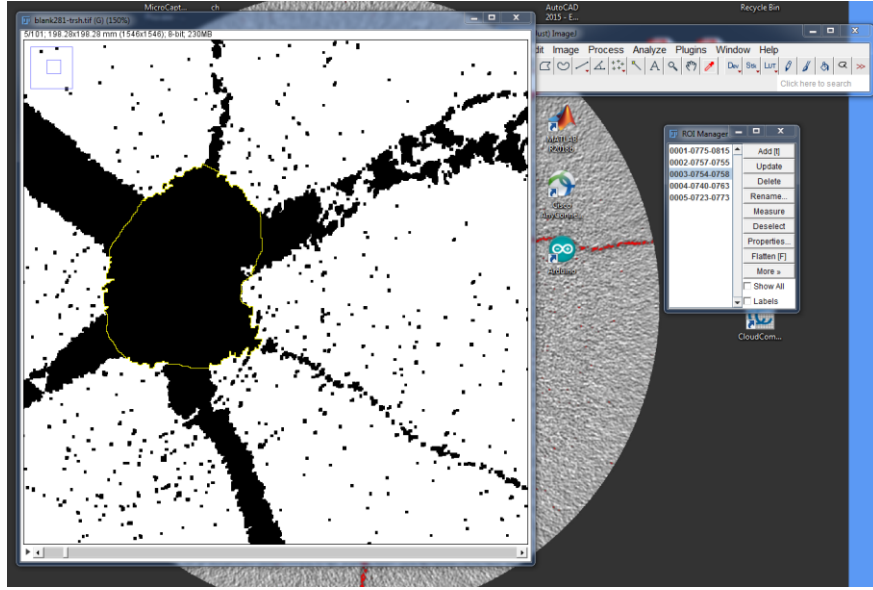


Figure 53: Application of the “lasso/blow” tool in ImageJ to trace the blast-hole wall in the binary image of a CTt section. The resulting yellow contour was used to calculate the area of the blast hole.

The closed contours, segmented with the lasso/blow tool, were then analysed in ImageJ to calculate the circumscribed areas, A_m for the mantle and A_{bh} for the blast-hole contour, respectively. The contours are not circular, as the crushing/compaction processes and the rigid body expansion of the fragments are not ideally radially symmetrical. Therefore, the calculated areas were used to define the average circular radii:

$$\bar{r}_{m,a} = \sqrt{A_m/\pi} \text{ [mm]} \text{ and } \bar{r}_{bh,a} = \sqrt{A_{bh}/\pi} \text{ [mm]} \quad \text{Equation 26}$$

Therefore, the average values of expansion or swelling of the mantle and blast-hole contours are:

$$\delta r_m = \bar{r}_{m,a} - r_{cyl} \text{ and } \delta r_{bh} = \bar{r}_{bh,a} - r_{bh} > \delta r_m \quad \text{Equation 27}$$

Here, δr_m [mm] denotes a rigid body expansion and δr_{bh} [mm] the same expansion plus the thickness of the blasted-off zone and of the compaction movement:

$$\delta r_{bh} - \delta r_m = \Delta r_{blast,b} + \Delta r_{comp,b} - \Delta r_{comp,a} \quad \text{Equation 28}$$

The deformation zones, the blast-hole expansion, and the swelling were measured in the CTt, uCT sections of the blast fragments (Figure 51), and the SEM thin sections.

The compacted-zone thickness ($\Delta r_{comp,a}$ [mm]) was measured by applying a grey-level threshold, tracing the outer contour of the zone, and calculating the difference between the equivalent-circle radii of its bounding contours in CTt images or by direct measurement in uCT sections in ImageJ (Figure 54).

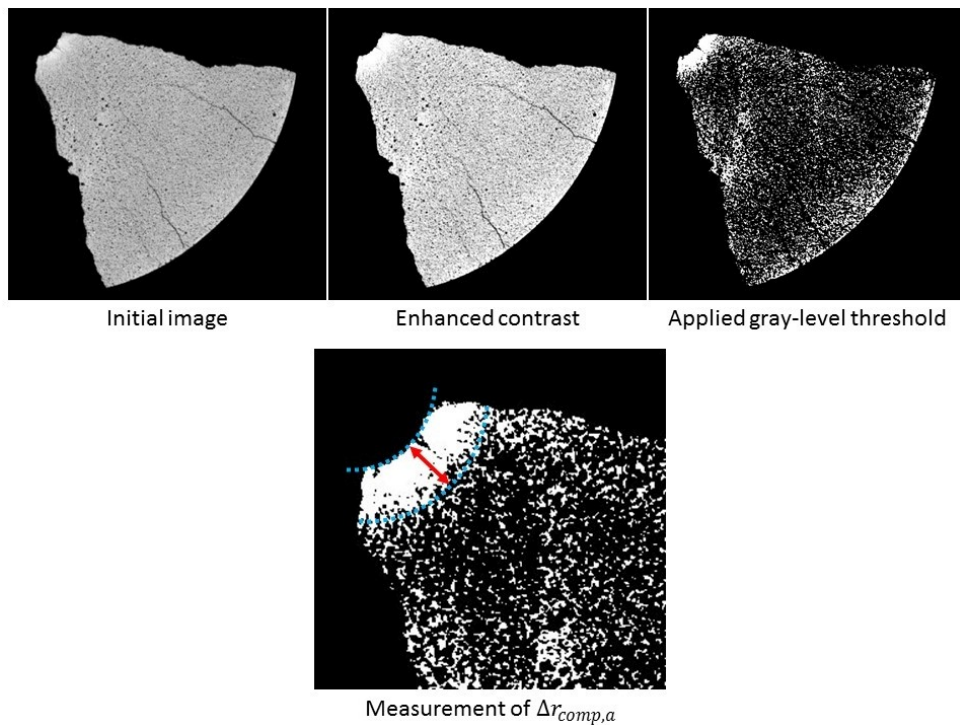


Figure 54: Measurement of the compacted zone ($\Delta r_{comp,a}$) in a uCT image from m12(20).

As the blasted cylinder from blast test 26.2 (granite, 20 g/m) had collapsed when dismantling the blast chamber, blast-hole expansion was estimated by measuring a larger blast fragment in the uCT images. This was done by fitting a circle to the blast-hole contour of the fragment in ImageJ (Figure 55).

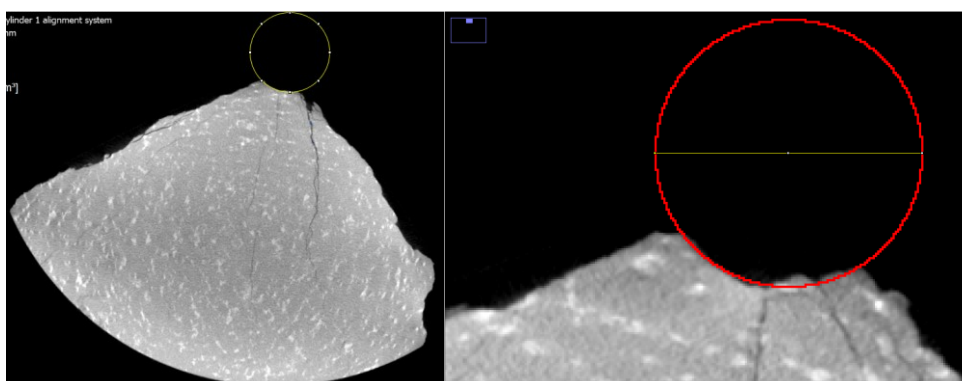


Figure 55: Transverse section of the uCT scan from g20(26.2) with a best-fitted circle to the blast-hole contour.

This procedure was done on 14 transverse uCT sections in a sequence with about 3-mm equidistance, located near the axial middle of the fragment.

Here, the (normalized) radius of this fitted circle ($r_{bh,norm}$ [mm]) corresponds to $\bar{r}_{bh,a} - \delta r_m$ from the measurements on the blasted cylinders. This is because $r_{bh,norm}$, unlike $\bar{r}_{bh,a}$, does not include the radial rigid-body displacement ($\delta r_m = 0$ mm) (Figure 56).

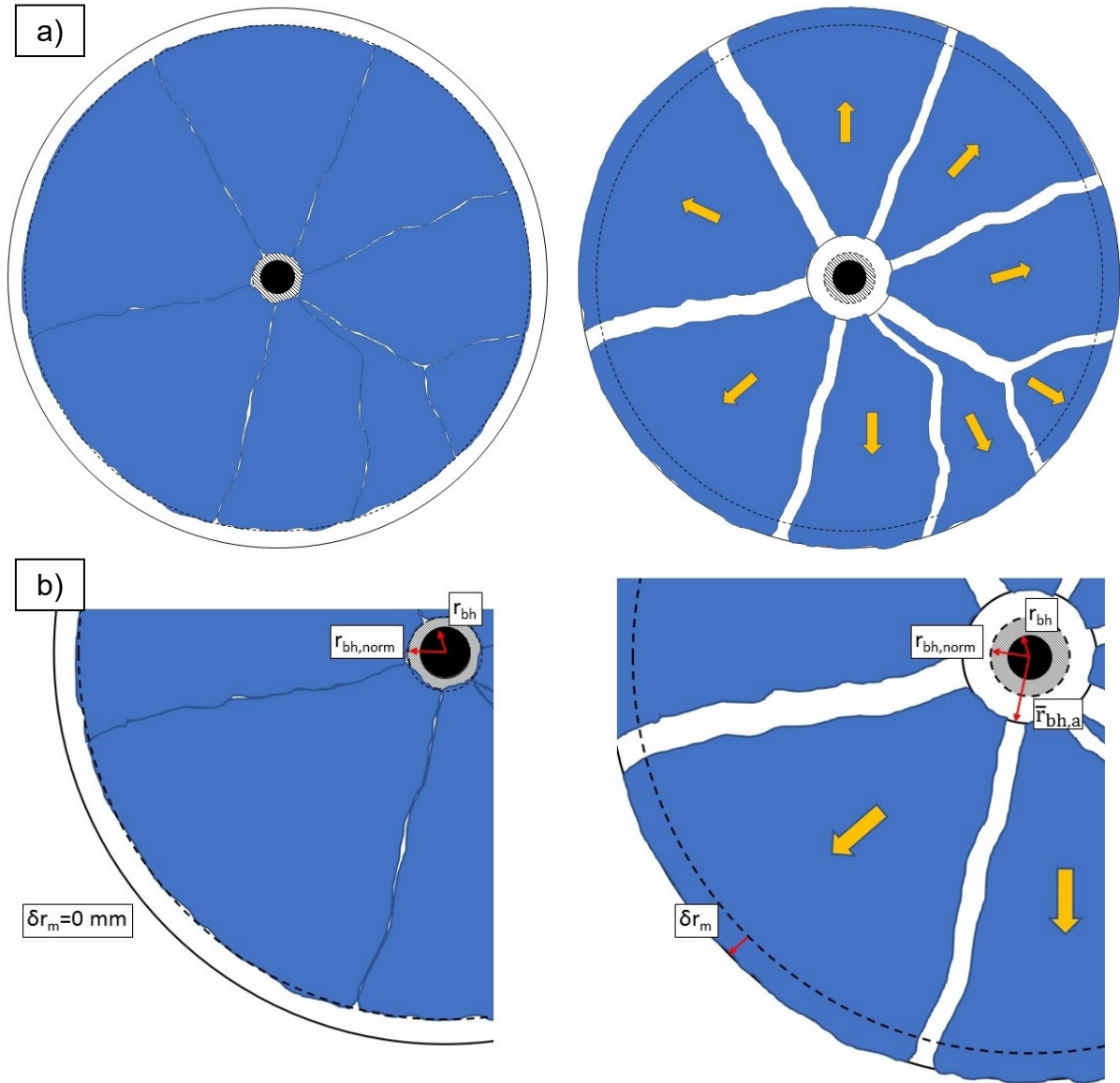


Figure 56: Difference between the measured average radii in the CTt of blasted cylinders and that of a single fragment: a) cross-section of a fragmented cylinder and the same cross-section with radially displaced fragments; b) enlarged sections from a), with notation.

Therefore,

$$r_{bh,norm} = \bar{r}_{bh,a} - \delta r_m \quad \text{Equation 29}$$

From Equation 28 and Equation 29, it can be written:

$$r_{bh,norm} - r_{bh} = \Delta r_{blast,b} + \Delta r_{comp,b} - \Delta r_{comp,a} \quad \text{Equation 30}$$

The deformation zones in the thin sections were observed by “stitching” the micrograph images in a sequence starting at the blast-hole wall. The borders of the deformation zones were determined considering the observed features in the images:

- The outer boundary of the compaction zone in the mortar was marked (measured) where the air pores in the cement matrix did not appear deformed (i.e., squashed) any more (e.g., see Figure 124).
- The outer boundary of the crushed zone was marked (measured) where the density of the micro-cracks (suddenly) decreased in the radial direction (e.g., see Figure 127).

4.2.1 Estimates of blasted-off material, total blast-hole fines, and crack-generated fines

According to Figure 52 and Table 11, the original volumes of the blasted-off layer ($\Delta V_{blast,b}$ [mm³]) and of the compaction zone ($\Delta V_{comp,b}$ [mm³]) can be calculated as:

$$\Delta V_{blast,b} = l_{ch} \cdot \pi (r_{comp,ib}^2 - r_{bh}^2) \quad \text{Equation 31}$$

$$\Delta V_{comp,b} = l_{ch} \cdot \pi (r_{comp,o}^2 - r_{comp,ib}^2) \quad \text{Equation 32}$$

The calculated $\Delta V_{blast,b}$ values were multiplied by the average bulk density (ρ_b) (see Table 3) to estimate the mass of blasted-off material (ΔM_{blast} [g]):

$$\Delta M_{blast} = \frac{\Delta V_{blast,b} \cdot \rho_b}{1000} \quad \text{Equation 33}$$

The quantity $\Delta V_{comp,b}$ was multiplied by the average grain-level density (ρ_g) (see Table 3) to estimate the mass of the compacted material (ΔM_{comp}):

$$\Delta M_{comp} = \frac{\Delta V_{comp,b} \cdot \rho_g}{1000} \quad \text{Equation 34}$$

The total mass of fines smaller than 1 mm (m_{tot_fines} [g]) was calculated as a sum of the sieved mass passing the 1-mm sieve ($m_{-1\text{ mm}}$ [g]) and the estimated mass of blasted-off material (ΔM_{blast}):

$$m_{tot_fines} = m_{-1\text{ mm}} + \Delta M_{blast} \quad \text{Equation 35}$$

Note here that m_{tot_fines} is exaggerated, as both ΔM_{blast} and ΔM_{comp} are assumed to contain only particles (fines) smaller than 1 mm. The mass of crack-generated fines (CGF) was calculated as:

$$m_{CGF} [g] = m_{-1\text{ mm}} - \Delta m_{bh,-1\text{ mm}} \quad \text{Equation 36}$$

$$m_{CGF_cyl} [\%] = \frac{m_{CGF}}{M_{cyl}} \cdot 100$$

$$m_{CGF_sieve} [\%] = \frac{m_{CGF}}{m_{sieve}} \cdot 100$$

where $\Delta m_{bh,-1\text{ mm}} [g]$ denotes the measured mass of the blast-hole-wall fines smaller than 1 mm (see Section 4.5.1). The mass proportions of CGF were also expressed as maximum (m_{CGF}^+) and minimum mass estimates (m_{CGF}^-) in [%]:

$$m_{CGF}^+ = \frac{m_{CGF}}{m_{sieve-1\text{ mm}}} \quad \text{Equation 37}$$

$$m_{CGF}^- = \frac{m_{CGF}}{m_{tot_fines}} \quad \text{Equation 38}$$

4.3 Fracture-surface analysis

Blast-generated fracture surfaces were analysed in the 3D models provided by the high-resolution CT of larger fragments from m6(22.2), m12(20), m20(22.1), g6(27), g12(25), and g20(26.2). Each scanned larger fragment has two main fracture surfaces generated mostly by the main radial cracks. These fracture surfaces (Figure 57) are oriented mostly along the blast hole and include at least a part of the blast hole and the cylinder mantle. These two fracture surfaces were declared as 'left' and 'right' considering the direction of the detonation and blast-hole position. Out of each fragment-scan model, these two fracture surfaces were further cropped and analysed.

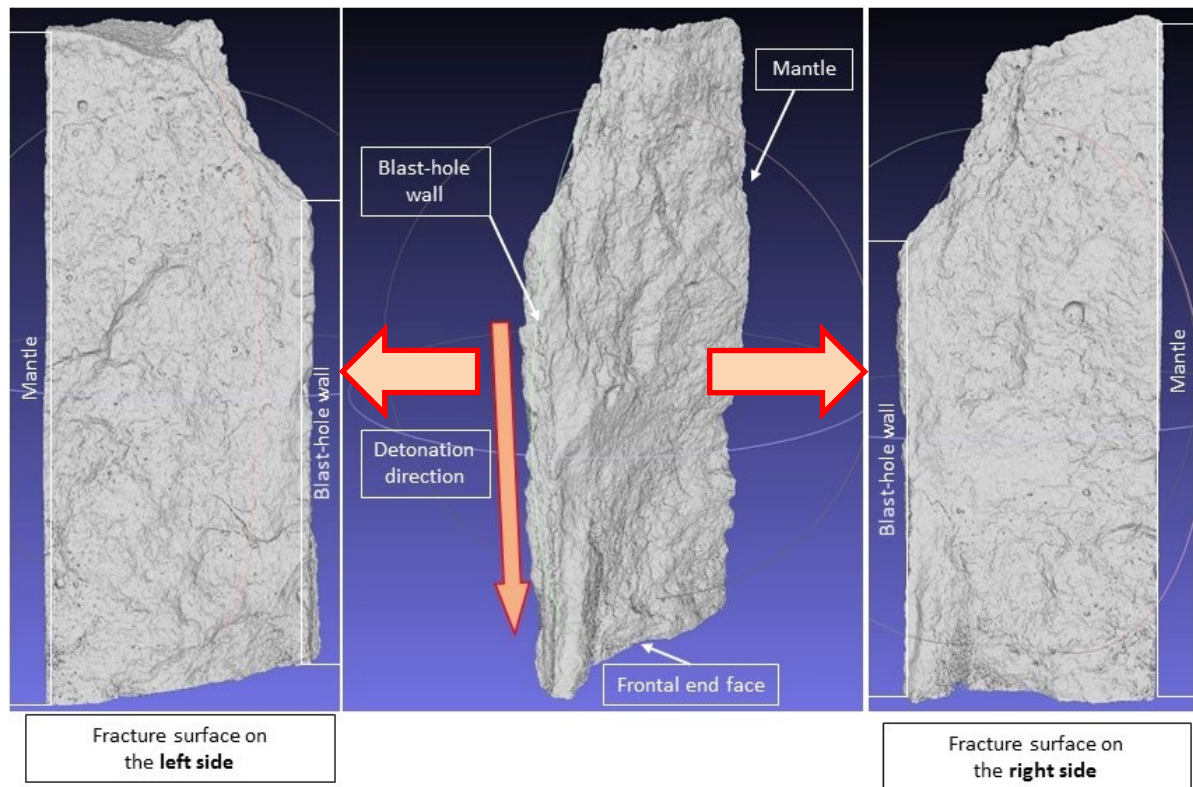


Figure 57: Example of the analysed fracture surfaces (side images) of a larger fragment, m20(22.1).

The analysis covered the measurement and mapping of:

- distance to the surface mean plane (height maps), and
- fracture-surface roughness (map images and data evaluation).

The procedure is as follows:

- the 3D mesh models (including texture maps) are split into data sets for each fracture surface in MeshLab (Cignoni et al., 2008) (Figure 58). Each fracture surface is exported as a separate STL mesh model without compression and information reduction;

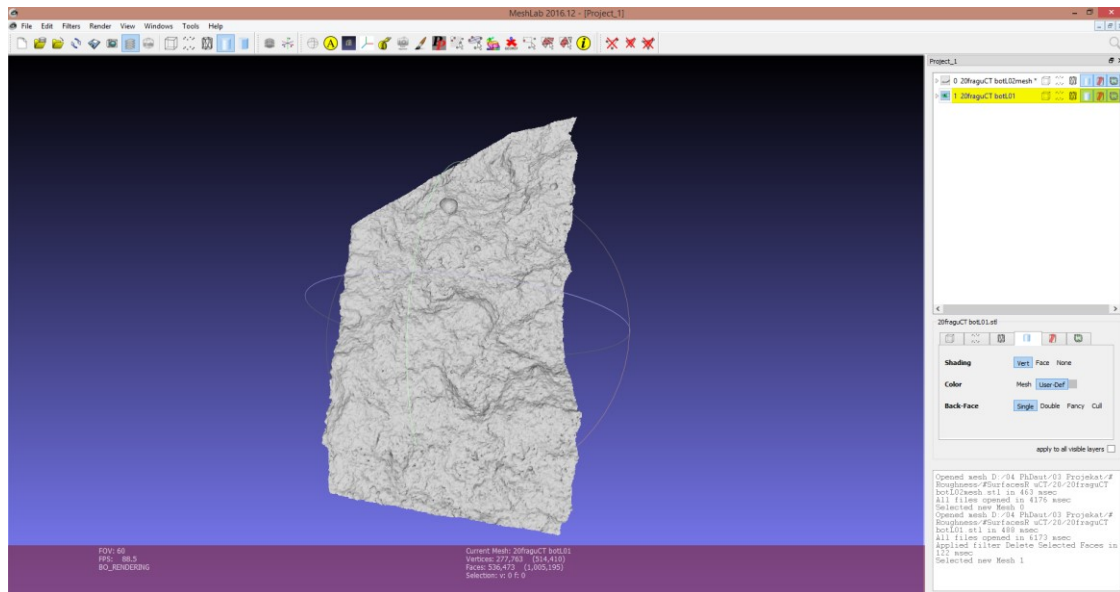


Figure 58: Processing of fracture-surface models in MeshLab.

- the fracture-surface mesh models are imported in CloudCompare (*CloudCompare [GPL Software], 2019*). They are marked concerning their original position in the corresponding blast cylinder (left or right);
- the models are further sampled into point clouds with about 10^6 points per data set;
- a best-fitted plane is generated through the point cloud for each analysed fracture surface;
- the plane is then used to obtain the position and orientation matrix of the point cloud;
- the matrix is inverted to generate a transformation matrix;
- the point cloud is repositioned in the X-Y plane of the coordinate system by applying the transformation matrix (Figure 59);
- the point cloud is then translated along the Z-axis with the lowest data point at 0.

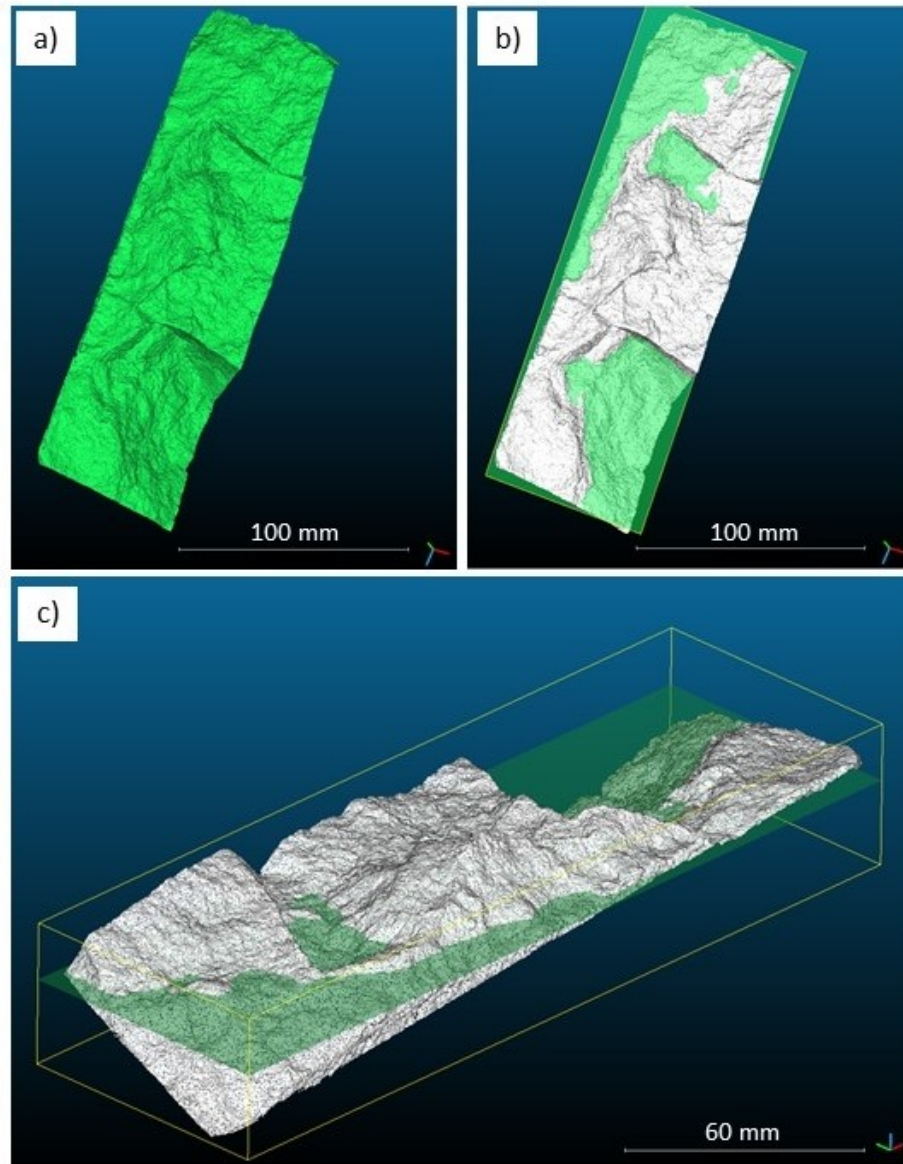


Figure 59: Process of sampling and model transformation in CloudCompare: a) initial imported mesh model of a fracture surface; b) the model is sampled into a point cloud (data points are coloured white), which is then used for fitting a plane; c) the position parameters of the plane are used to transform (i.e., reposition) the point cloud into the X-Y plane.

In this way, height maps could be generated as the Z-coordinate values of the points indicate their height in the coordinate system. The colour-coded height maps were further used to identify topographic features of the fracture surfaces (Figure 60).

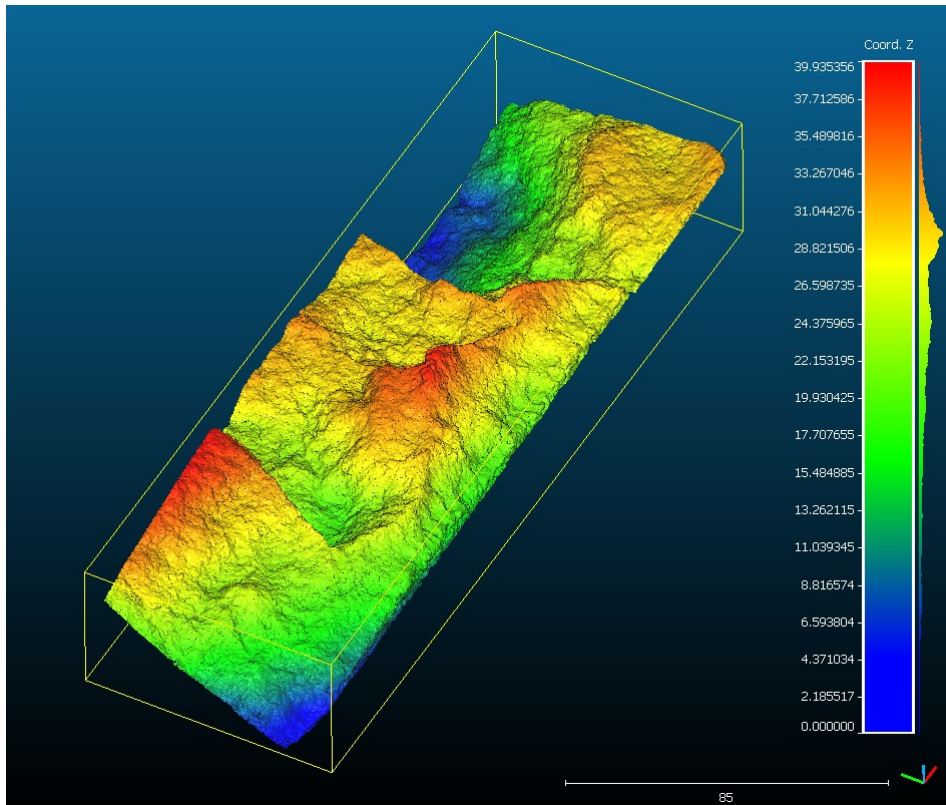


Figure 60: Height map obtained by analysing Z-axis values of the data points. The results are presented as colour-coded maps with a histogram bar. The provided scale is in [mm].

Surface roughness is firstly measured in CloudCompare by using provided tools (i.e., *Tools > Other > Roughness*) with the kernel size of 1, 3, and 5 mm. Here, kernel size determines the neighbourhood size, i.e., it is related to the radius of a sphere that encloses neighbourhood points around a measured point. Such kernel sizes were chosen considering the CT-scanning level of detail and expected size of the topographic features (e.g., ridges, valleys, and striations). This analysis assigns a set of result data to each evaluated point.

This roughness measure is also referred to as “*point surface roughness*” (Sampaleanu, 2017). It is considered analogous to the asperity amplitude used in “*Joint Roughness Coefficient*” estimates, whilst the kernel size is equivalent to the profile length or joint length (Barton & Choubey, 1977; Barton, 1982).

Surface roughness is calculated for each point, where the 'roughness' value is equal to the absolute distance between this point and the best-fitting (least squares) plane computed for its nearest (kernel-defined) neighbours.

Figure 61 shows how surface roughness is determined in CloudCompare.

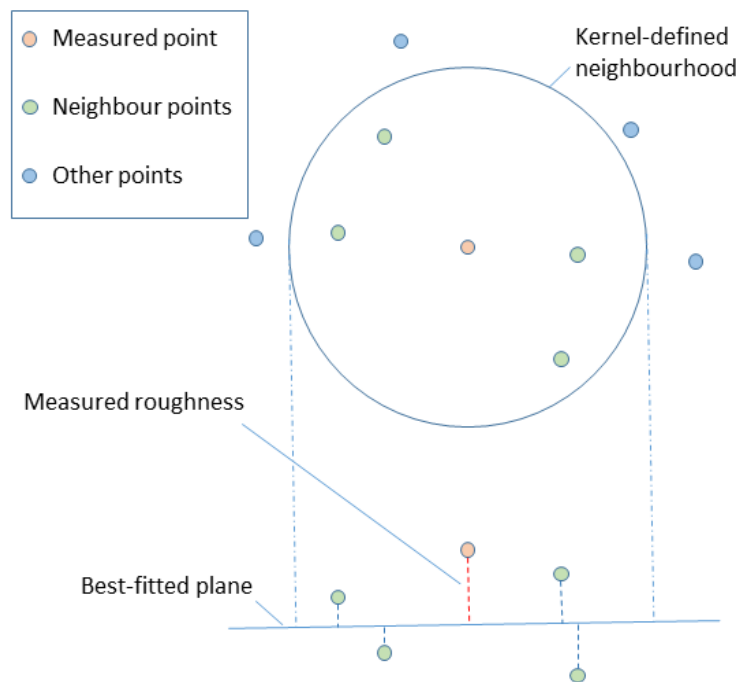


Figure 61: Principle of local-roughness measurement on point cloud in CloudCompare.

The roughness values are provided in [mm] since the data-point coordinates are measured (scaled) in [mm]. Finally, all result data on surface roughness were exported, statistically analysed, and compared. Figure 62 shows an example of the colour-coded results of surface-roughness measurements.

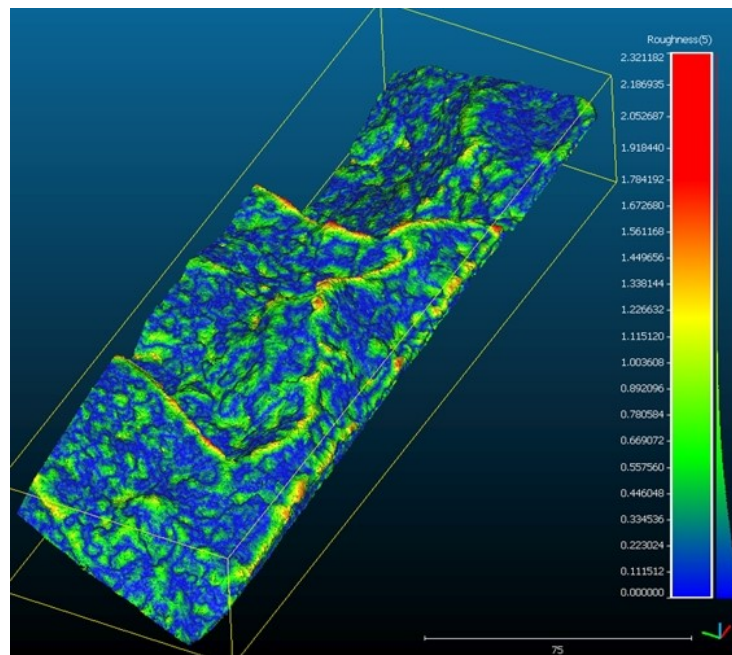


Figure 62: Example of a colour-coded image of local surface roughness with a kernel of 5 mm. The provided scale is in [mm]. Note the green-to-red ridges and blue valleys.

4.4 Investigation in micro- and meso-scale

The observation and analyses at the grain-size level are denoted with the prefix 'meso-' and those below that level with 'micro-' (e.g., micro-mechanisms).

Microscopic observations were used to analyse:

- structural changes due to blast-induced fracture mechanisms in thin sections and at fracture surfaces of smaller blast fragments,
- deformation zones at/with a higher level of detail,
- chemical content to identify minerals affected by fracture mechanisms,
- fines shape and chemical content, and
- the effects of blasting on the material structure of the cylinders.

The microscopic analyses were carried out with optical microscopy (Olympus BX60) and SEM (Evo MA 10) at the Chair of Geology and Economic Geology, MUL (Figure 63).

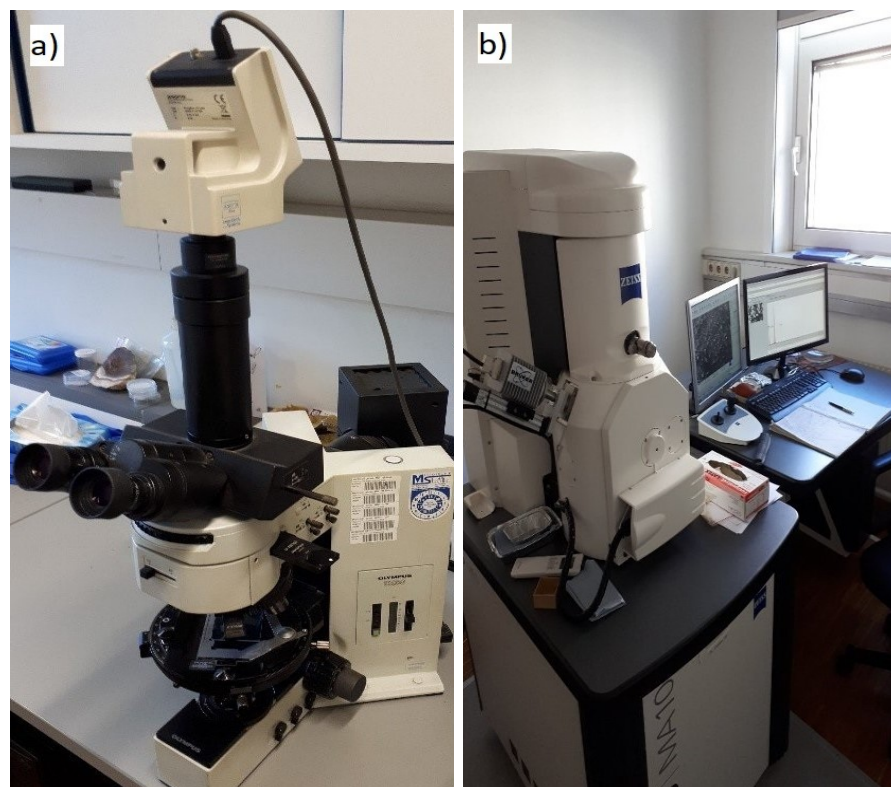


Figure 63: Microscopy equipment: a) optical light-reflection microscope Olympus BX60, b) SEM system Evo MA 10.

The optical microscopy provided transmitted-light micrographs with:

- plane-polarized light (PPL) and
- cross-polarized light (CPL).

4.4.1 Thin sections

The thin sections were produced at the Chair of Mineralogy (MUL). Some larger blast fragments were impregnated with epoxy resin and cut in transverse slices, oriented with reference to the corresponding original blast cylinder (Figure 64).

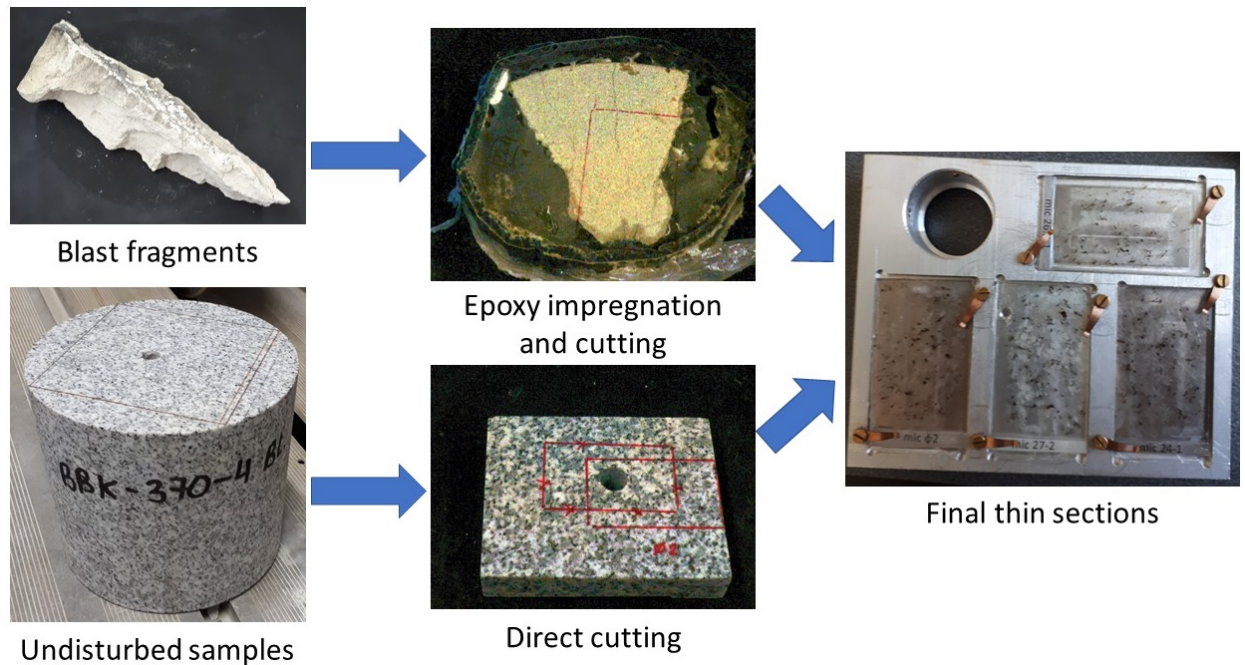


Figure 64: Principle of the thin-section production.

The slices were further processed to provide thin sections (24×46 mm, about 30 μm thick) for microscopic analyses. The thin sections cover:

- the blast-hole wall and the deformation zones (see Section 4.2),
- larger radial cracks and crack intersections,
- the near-mantle region, and
- the intermediate region.

Figure 65 shows the terminology used for the observed cracks in the thin sections.

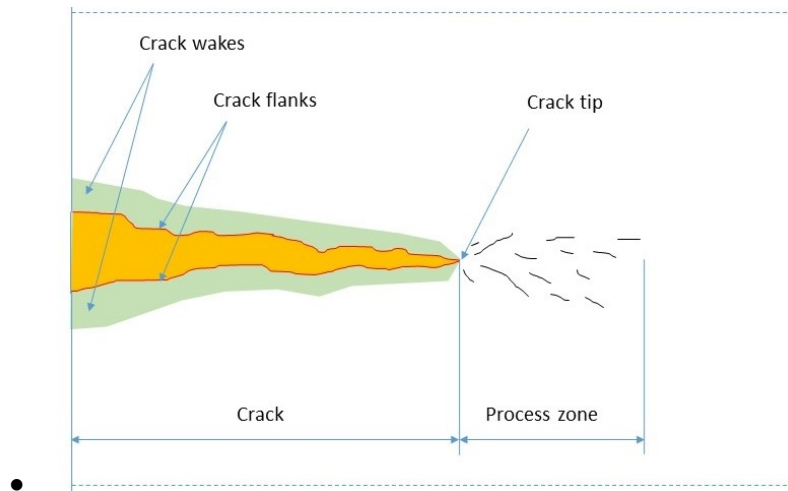


Figure 65: Terminology used for observed cracks/fractures in the thin sections.

The thin sections were cut out in the transverse plane of the corresponding blast cylinder. The thin sections were observed and analysed with optical microscopy and SEM. Selected parts of the thin sections were also scanned with the SEM to determine their chemical content.

Thin sections were also made from undisturbed (non-blasted) cylinders to investigate the pre-blasted material structure (e.g., mineral content) and determine the average apparent grain size.

The average apparent mineral/grain size of the mortar and granite was measured using a modified “average grain-intercept” method (ASTM standard E122 2004). The corresponding results are provided in Section “Average grain size and average pore size (mortar)” in Appendix 2. This method quantifies the grain- or crystal-size for a given material (d [mm]) by drawing a set of randomly positioned line segments on the micrograph, counting the number of times each line segment intersects a grain boundary, and dividing the line length (l [mm]) by the number of intercepts (n [-]):

$$d = \frac{l}{n} \quad \text{Equation 39}$$

This method is primarily intended for investigating materials with closely-packed grains (e.g., granitic rock), but not materials with a multiphase structure (e.g., mortar and concrete). For mortar, the line length (l) is calculated as a sum of only the line sections intersecting the examined grains. This means that the parts of the line crossing over the cement matrix are excluded from the analysis (Figure 66).

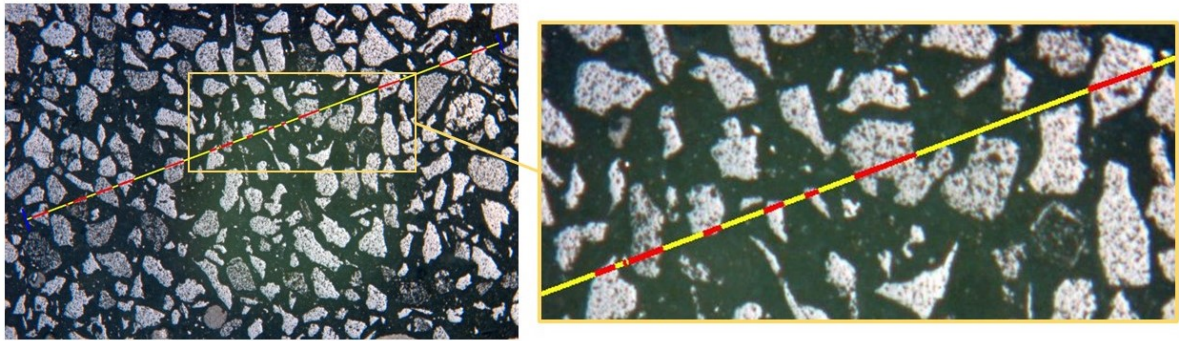


Figure 66: Measurement of the average grain size (“Average-grain intercept” method) in mortar micrographs. Only red segments (intersections with the grains) of the whole scan line are considered.

The average grain size was also measured with morphological segmentation and feature analysis of the micrographs (thin-section images) in ImageJ. This was done by enhancing the image contrast, converting the image to greyscale, histogram adjustment and applying a grey-level threshold, image masking based on edge detection, and using the “particle analysis” routine. Figure 67 shows the process of “particle analysis” in ImageJ.

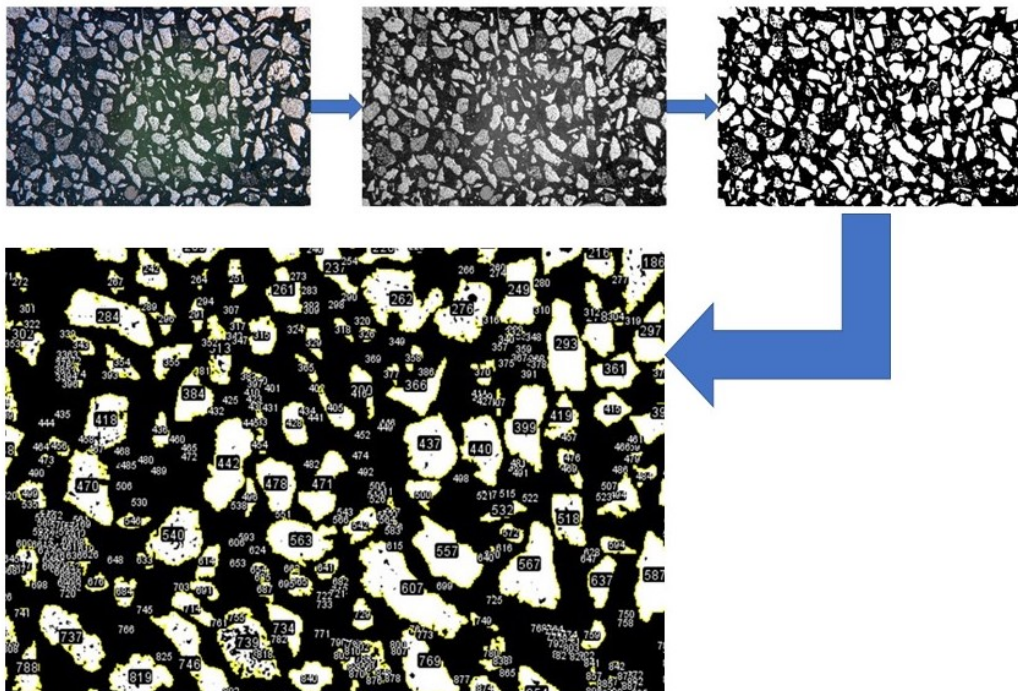


Figure 67: Application of the “particle analysis” on a mortar optical micrograph in ImageJ. The mortar pores were detected and filtered out considering their shape circularity.

The “average grain-intercept” method requires a minimum of 200 minerals along the scan line per thin section (Reichholf, 2003). The same can be done with “particle analysis.” However, this number is often higher (i.e., 300) to account for the projection

error (Mali, 2019). This error is due to the difference between the projected grain size in the thin-section plane and the real grain size and the structural anisotropy of the analysed material (Figure 68).

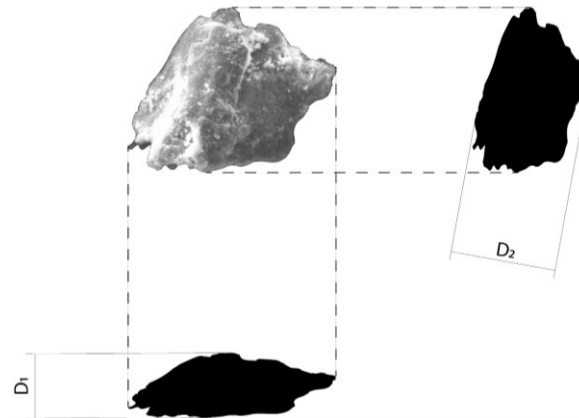


Figure 68: Illustration of uncertainty issues of grain-size measurement due to grain-figure projection. Note the difference between diameters D2 and D1.

The thin sections that covered the near-blast-hole region also show the deformation zones, described in Section 4.5, in greater detail. Here, it was possible to observe transitions between the deformation zones.

The thin sections also covered the fracturing zone and the near-mantle zone to investigate possible blast-induced fracture mechanisms and how they differ concerning the deformation zone they belong. At this level of detail, the macro-mechanism patterns (see Section 4.1.10) became inapplicable due to the unknown sequencing of the fracture development and increased complexity of fracture patterns (Figure 69).

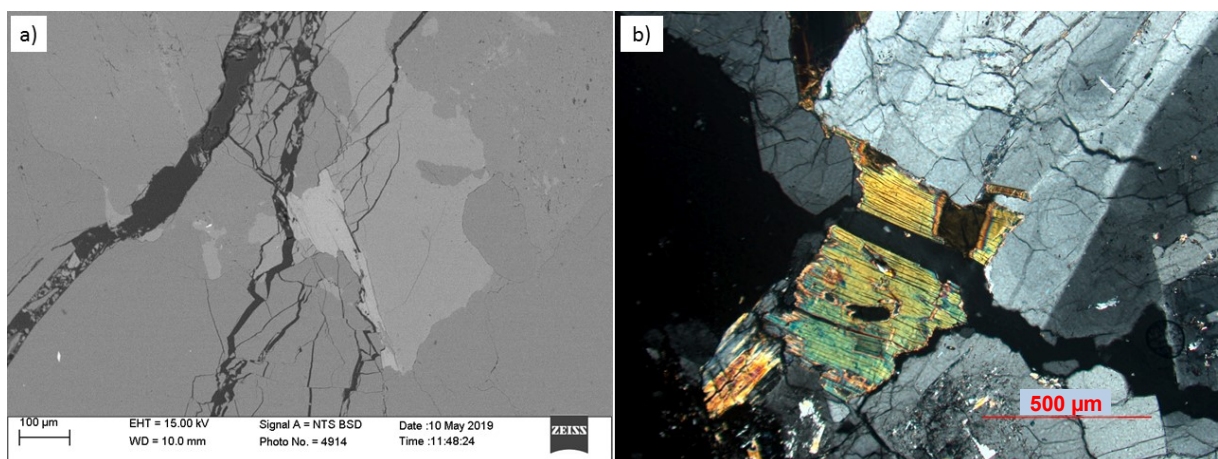


Figure 69: Example thin-section micrographs of complex fracture patterns at the meso/micro-level from blast test 26.2 (granite, 20 g/m): a) SEM image; b) CPL optical microscopy.

4.4.2 Small fragments

Some smaller blast fragments were cleaned from loose fines and dust and carbon-coated for further fracture-surface analysis with the SEM. These fragments were extracted from the intermediate region inside the cylinder, i.e., they did not include cylinder boundaries – the blast hole, the mantle, or the end faces (Figure 70).

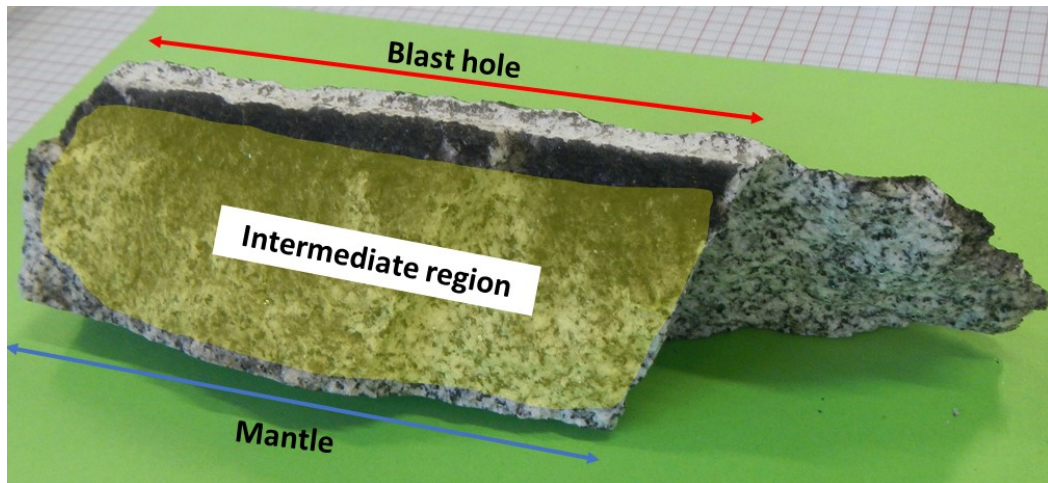


Figure 70: Spatial origin(s) of the small blast fragments (shown on a larger fragment).

Their size was chosen to fit the sample holder, to about 30×30×10 mm (Figure 71).



Figure 71: Small blast fragments prepared for SEM.

4.4.3 Micro- and meso-mechanisms

The observed thin sections and fracture surfaces show fractographic features that can indicate probable underlying mechanisms. As the CT scanning of larger fragments was at high resolution (uCT, Section 4.1.3), the resulting cross-sections were also used for analysing meso-cracks and related mechanisms at the meso-scale.

The main failure mechanisms observed in the micrographs are defined here as proposed by Q. Zhang (2014):

- intergranular fracturing (IG),
- transgranular fracturing (TG), and
- mechanisms transitioning between IG and TG - partial cleavage and lamellar steps (pcl).

Blenkinsop (2007) summarized basic deformation mechanisms in rock and minerals considering the genesis of the material. Table 12 shows such deformation mechanisms that were identified in the micrographs of the blasted cylinders.

Table 12: Micro- and meso-mechanisms of deformation in minerals and rock.

Mechanism	Characteristic features	Fracture type	Abbreviation
Impingement	Impact contacts between grains.	Intergranular	ic
Flaw-induced cracking	Joined to a flaw (including grain boundaries).	Intergranular and transgranular	fc
Refracture	Cement fracture	Intergranular and transgranular	rc
Cleavage	Micro-cracks in sets parallel to cleavage planes.	Intragranular	cc
Elastic mismatch	Localized at contacts of different grains.	Intergranular and transgranular	em
Plastic mismatch	Intracrystalline plastic deformation.	Intragranular	pm
Micro-fault-induced cracking	Adjacent to micro-faults, wedge-shaped towards micro-fault.	Intergranular and transgranular	mc

These mechanisms were used to describe blast-related mechanisms of the features in the micrographs and indicate the genesis mechanisms that may have affected them. The mechanisms, indicated in the micrographs, are referred to using abbreviations, as defined in Table 12. The micrographs of undisturbed samples were used to improve this investigation by indicating pre-blast deformation features.

Impingement micro-cracks connect contact points of adjacent grains and lead to intragranular fracturing (Figure 72).

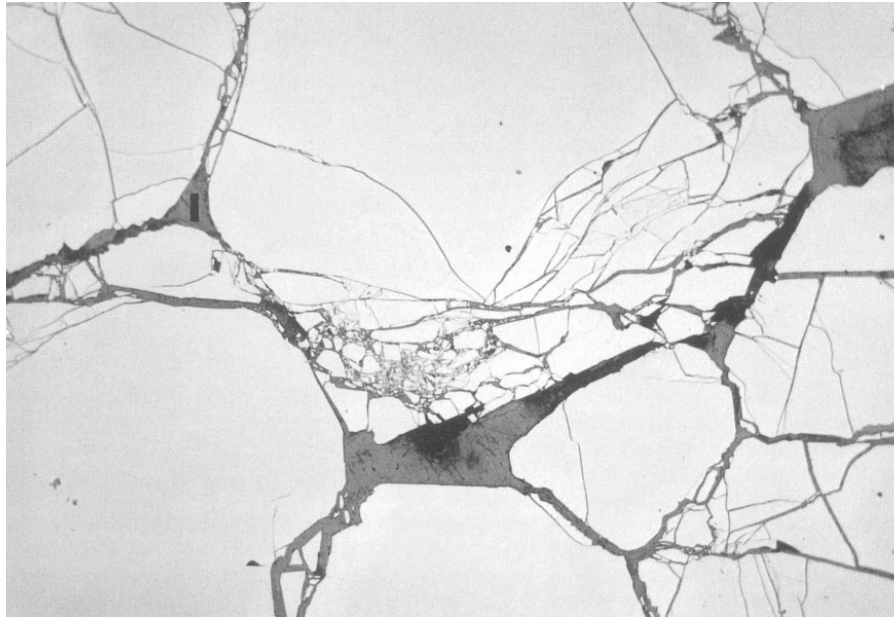


Figure 72: Impingement micro-cracks. An example SEM micrograph (Blenkinsop, 2007).

These micro-cracks may form different patterns (Gallagher et al., 1974) depending on the boundary loads, packing arrangement, size, sorting, and grain shape (Figure 73).

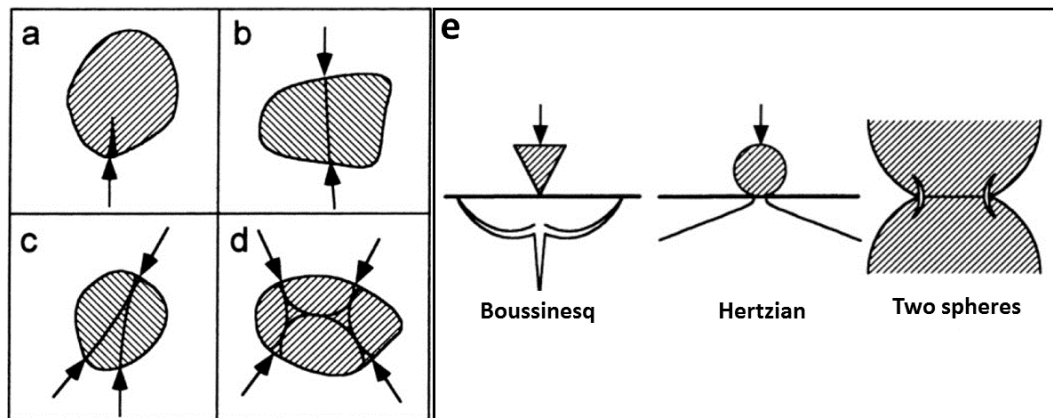


Figure 73: Conceptual sketches of: a) to d) basic impingement-crack patterns; e) basic failure modes for their further description (Blenkinsop, 2007).

For describing them, Blenkinsop (2007) suggests simplified models of in-plane stress-induced failure: by a pointed object (Boussinesq configuration), spherical object (Hertzian configuration), or by as an interaction of spherical objects. Furthermore, he points out the importance of intragranular flaws, the configuration of simultaneous contacts, and material properties of the interacting grains in the generation of different impingement-crack patterns.

Flaw-induced micro-cracks (Figure 74) originate from flaws such as other micro-cracks, pores, dislocated cleavage planes, flat elongated grains (e.g., mica), and grain boundaries. The flaws act as stress-concentration points and lead to complex, mostly tensile, failure and development of these cracks. For describing them, Blenkinsop (2007) recommended an analytical solution of Horii & Nemat-Nasser (1985) for flaw-induced crack propagation.

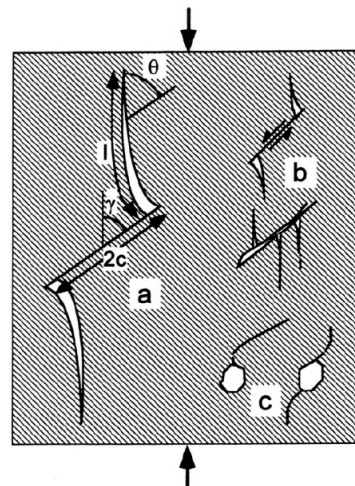


Figure 74: Conceptual sketch of flaw-induced micro-cracks (Blenkinsop, 2007): a) principle of the analytical solution of Horii and Nemat-Nasser (1985). The flaw length is $2c$ at angle γ to load direction (arrows), and the micro-crack length is l at angle θ to the flaw; b) examples of flaw-induced micro-cracks; c) examples of interaction between micro-cracks and pores.

Blenkinsop (2007) described the refracturing mechanism (Figure 75a) as micro-fracturing of pre-existing flaws, including the opening of grain boundaries (e.g., repetitive micro-fracturing in cement). Unlike flaw-induced fracturing, refracturing is a repetitive process that takes place strictly in micro-scale (i.e., below the average grain size).

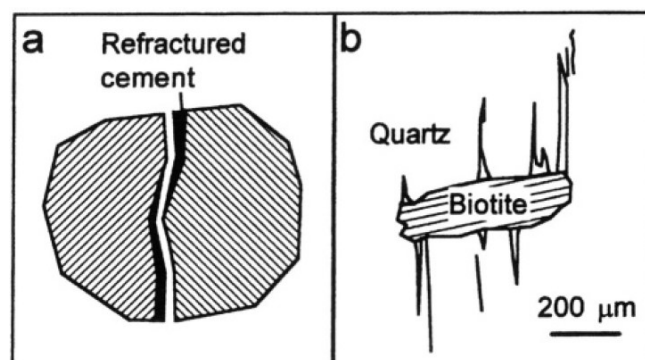


Figure 75: Conceptual sketches (Tapponnier & Brace, 1976) of: a) refractured micro-crack, fractured cement on both fracture flanks; b) elastic-mismatch micro-cracks at the contact between mica and quartz.

Cleavage micro-cracks are formed concerning the internal structure (i.e., cleavage planes) of mineral grains. Micro-cracks in biotite are affected by the basal (001) cleavage. In feldspars, cleavage planes (001), (010), and (110) strongly influence the generation of these micro-cracks. In crystal quartz, the fracture toughness is lowest along the rhombohedral planes, followed by the basal plane. Accordingly, micro-crack development is most probable along these planes.

Elastic-mismatch micro-cracks (Figure 75b) are often observed in contact regions of quartz and feldspar grains with mica grains (Tapponnier & Brace, 1976; Wong & Biegel, 1985; Hippertt, 1994). They are caused by the difference in elastic strain across the contact boundaries and recognized by the intragranular micro-cracks around contacts between grains of different minerals. However, resulting features are like those from thermally-induced micro-cracks.

Plastic-mismatch micro-cracks (Figure 76) may be initiated by the strain incompatibility between the area of plastic deformation and the adjacent undeformed area.

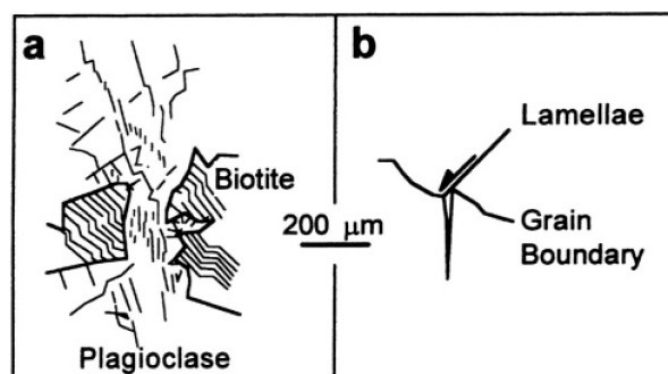


Figure 76: Conceptual sketches of elastic-mismatch micro-cracks: a) intensive micro-cracking in plagioclase between kinked biotite grains; b) a micro-crack initiated at the end of a lamella displaces a grain boundary. (Blenkinsop, 2007)

“Plastic-mismatch micro-cracking is the main cause of semi-brittle behaviour. It can be recognized by the close association between intragranular micro-cracks and areas or individual micro-structures of intracrystalline plasticity, such as sub-grains, kink bands, deformation lamellae or twins.” (Blenkinsop, 2007)

Blenkinsop (2007) defined “micro-faults” as *“shear micro-fractures that contain grain fragments formed by cataclasis.”* Furthermore, he described micro-fault-induced micro-cracks (i.e., “microscopic feather fractures”) as *“intragranular micro-cracks initiated at the micro-faults, characteristically wedge-shaped, and opening towards the fault plane”* (Figure 77).

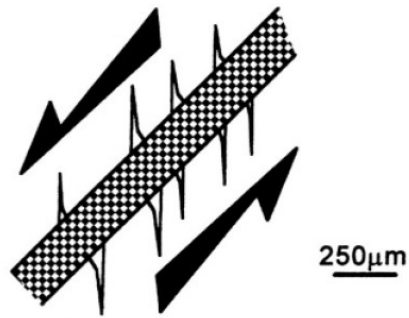


Figure 77: Conceptual sketch of micro-fault-induced micro-cracks. (Blenkinsop, 2007)

Micro-cracks can result from stresses due to differential thermal expansion or contraction between adjacent minerals. Such micro-cracks may form in grains of one mineral surrounded by another during heating or cooling. Elastic-mismatch micro-cracks are also probable if the thermal change is accompanied by pressure changes. *“Thermally-induced micro-cracking in granite is seen as intragranular micro-cracks concentrated in quartz surrounded by feldspar.”* (Blenkinsop, 2007)

4.5 Blast-fragmentation analysis

The fragmentation analysis was carried out in the laboratory of the Chair of Mineral Processing (IZR, MUL). The analysis process covered:

- manual and mechanical sieving,
- screening by laser-diffraction granulometry, and
- measurement of the specific surface area of the sieved blast fines.

The word “screening” is also used in this thesis as a more general term, covering both sieving and laser-diffraction granulometry.

4.5.1 Manual and mechanical sieving

Figure 78 shows an overview of the sieving procedure.

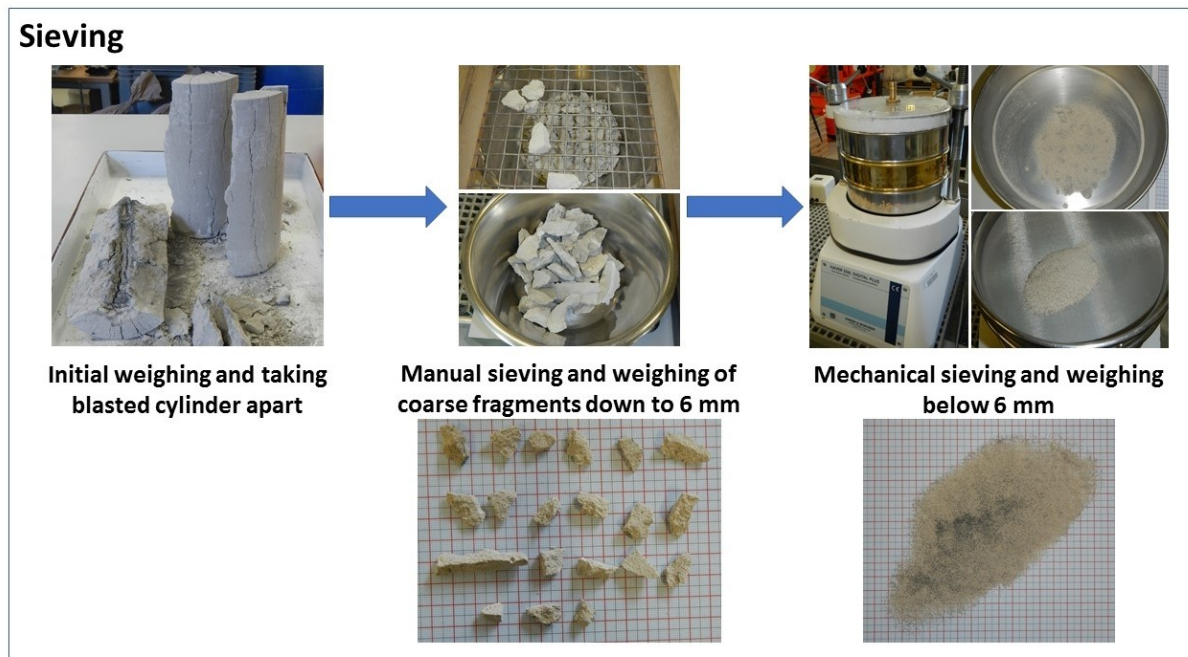


Figure 78: Overview of the sieving procedure.

Manual sieving of the larger fragments was followed up by mechanical sieving of smaller fragments and fine material.

A blasted cylinder was firstly weighed on a measuring scale KERN DS65K0.5. Next, it was put on an analysis plate or tray to prevent loss of material (Figure 79). The cylinder was then carefully broken apart, its larger fragments aligned one next to another, and the rest of the fragmented material spread on the plate. All fragments that included the blast-hole wall were identified.

For blast tests 23.2, 21, 23.1, 26.1, and 28.1, fine material from the blast-hole wall was then brushed off and sieved separately as blast-hole-wall fines.

Next, the larger fragments were manually sieved. The coarse sieving covered sizes – 125, 100, 80, 60, 50, 40, 31.5, 25, 20, 18, 16, 14, 12.5, 10, and 8 mm. Then, all fragment classes were weighed on a measuring scale, with a KERN DS 65K0.5 down to 50-mm sieve size and with a Mettler Toledo XA1502S for the smaller sizes. Datasheets of the measuring scales are provided in Appendix 11.



Figure 79: Blasted cylinder taken apart and prepared for sieving (g12(25)).

Finally, the rest of the material was sieved without prior splitting with a mechanical sieve shaker HAVER EML Digital Plus (Figure 80) for size classes – 6.3, 5, 4, 3.15, 2, 1, 0.5, 0.25, 0.1, and 0.04 mm. This was done in two steps for 6.3–2 mm and then for 1–0.04 mm. The total mass of the sieved material was marked as m_{sieve} [g].

The blast-hole-wall fines were only mechanically sieved with 2–0.04-mm sieves. The mass of the blast-hole-wall fines passing 1-mm sieve was marked as $\Delta m_{\text{bh},-1 \text{ mm}}$ [g]. Measurement data for the blast-hole-wall material was added to the rest sieving data considering the respective size classes.

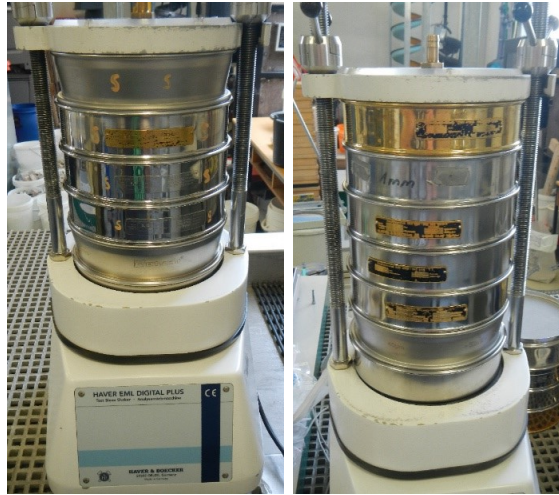


Figure 80: Mechanical sieve shaker HAVER EML Digital Plus (laboratory of the Chair of Mineral Processing, IZR, MUL).

Material losses were recorded during the sieving as the difference between the initial mass of blast cylinder (M_{cyl} [g]) and m_{sieve} :

$$\Delta M_{loss} = M_{cyl} - m_{sieve} \quad \text{Equation 40}$$

The resulting measurement data were plotted as cumulative relative mass passing against the sieve size in [mm] in a log-log scale with m_{sieve} as the reference.

$$P(x) = \frac{m_i}{m_{sieve}} \cdot 100[\%] \quad \text{Equation 41}$$

where i corresponds to a respective sieve class or mesh size (e.g., “-1 mm”).

The same was done separately for the blast-hole-wall fines below 1-mm sieve size with an additional plot of these fines relative to the total sieved mass of the corresponding size class:

$$P(x) = \frac{\Delta m_{bh,i}}{m_{sieve}} \cdot 100[\%] \quad \text{Equation 42}$$

$$P(x) = \frac{\Delta m_{bh,i}}{m_i} \cdot 100[\%] \quad \text{Equation 43}$$

More details on the sieving procedure are provided in Appendix 11.

The blasted cylinder from m20(22.1) had to be additionally sieved, as its two largest fragments (100|80 and 80|63 mm), although fractured, had still been seemingly whole. All larger fragments from the sieved blasted cylinders were inspected for potentially through-going interlocked cracks with uCT (Figure 81).

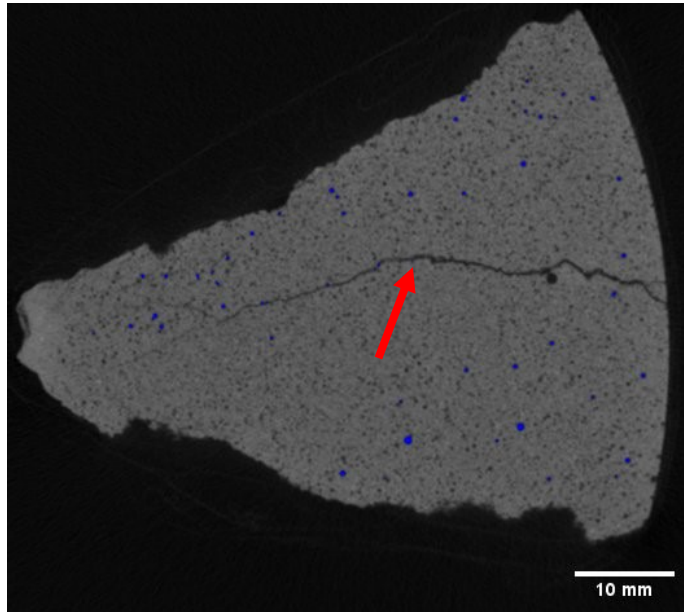


Figure 81: A potential through-going interlocked crack in a larger fragment from m6(22.2).

All fragments with potentially through-going interlocked cracks were then subjected to light prying. This additional fragmentation consisted of placing the blade of a pocket knife up to 5 mm deep in a surface opening of a larger (potentially through-going) crack and manually rotating the blade along its long axis. If such a crack could not be opened by light prying, the procedure was stopped. The aim was just to liberate already generated, though interlocked, smaller fragments.

After the second sieving, the resulting data were added to the initial sieving data (blast test 22.1) for each size class.

4.5.2 Laser-diffraction granulometry

Figure 82 shows an overview of the laser-diffraction granulometry.

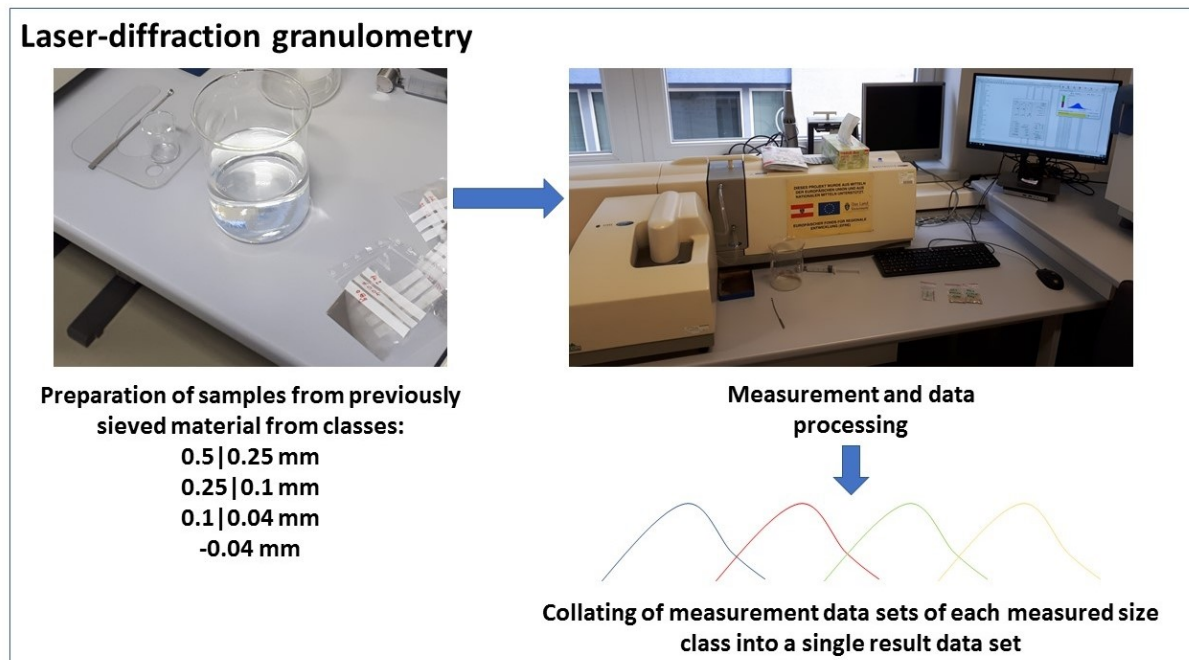


Figure 82: Overview of the laser-diffraction granulometry.

The four smallest size classes from the mechanical sieving (i.e., 0.5|0.25 mm, 0.25|0.1 mm, 0.1|0.04 mm, and -0.04 mm) were further analysed over the range 0.02–2000 μm with particle-size analyser Malvern Mastersizer 2000 equipped with Malvern Hydro 2000G (Instruments Malvern Ltd, 2007) for wet sample preparation (Malvern, 1999). The aim was to also measure the FSDs in the ultra-fines region. This analysis used the “Fraunhofer method” to measure the grain-size distribution concerning particle volume of approximated particle spheres. This analysis produces a percentile volume-passing distribution.

Samples from each of the four size classes were analysed separately. Therefore, the whole result-data set for a single blasted cylinder covers four sub-sets related to the analysed sieved classes. Figure 83 shows an example of the results (of a sub-set) provided by the control software.

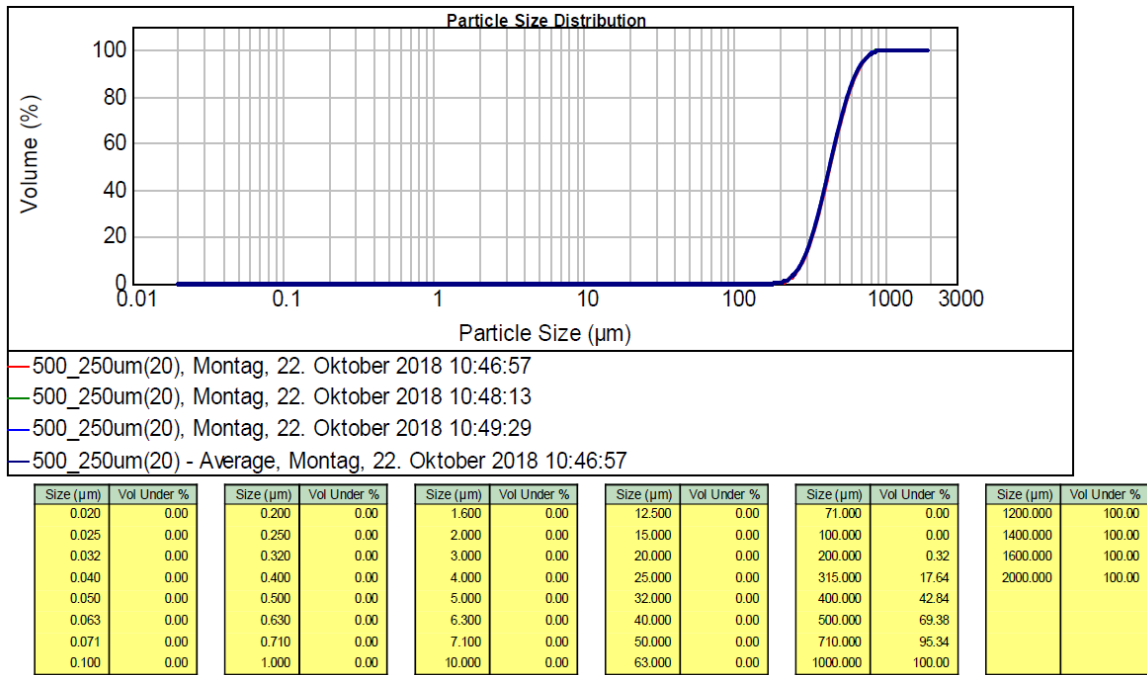


Figure 83: Example of results obtained by the laser-diffraction granulometry for a single size class (e.g., 0.5|0.25 mm).

As the results from the manual/mechanical sieving are provided concerning mass passing, the laser-diffraction result data must be converted before collating them and merging them with the sieving results. The volume-passing distribution can be considered the same as mass-passing distribution, assuming the grain-level density is the same for all sieve classes. Some error in the horizontal axis of the result curves was expected due to the (initially) assumed grain shape as perfect spheres and the equal grain-level density in all size classes. The four mass-passing data sub-sets from each analysed blasted cylinder were collated together (i.e., redistributed into the new size classes) and merged with the sieving results (i.e., appended to the corresponding coarser sieving-data bin), forming sets of merged screening data (see Appendix 11).

4.5.3 Screening data and fragment-size distribution (FSD)

The sieving data and the merged screening data (i.e., collated data from sieving and laser-diffraction granulometry per blasted cylinder) were further used for statistical analysis and comparison of blast fragmentation.

The screening result data were plotted in log-log plots, where the x-axis indicates the (screening) mesh size (x) in [mm] and the y-axis the cumulative mass passing (P) in [%]. Figure 84 shows an example of a log-log plot of the screening data.

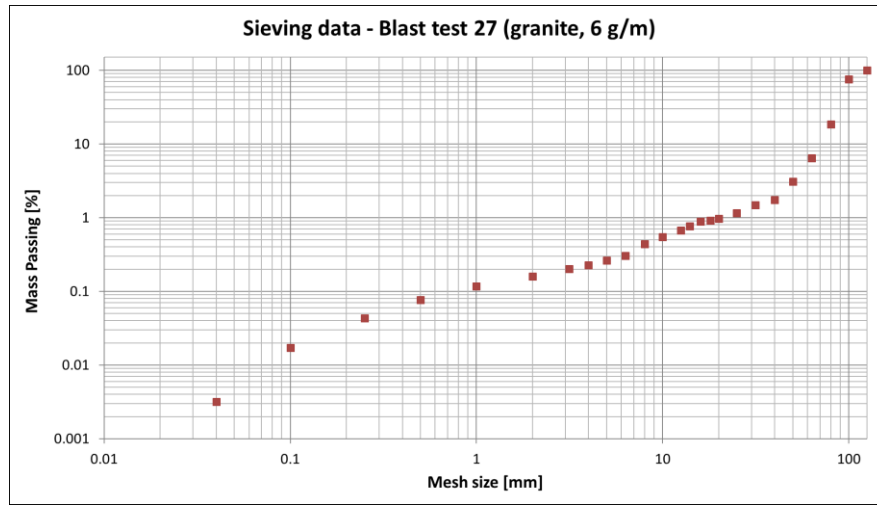


Figure 84: Example log-log plot of screening data. Sieving data for blast test 27 (granite, 6 g/m).

The specific fragment sizes (x -values) for desired percentiles were calculated with a linear interpolation between the two fragment sizes next to the cumulative mass passing at 30%, 50%, and 80%. For example, x_{50} [mm] in linear space (lin-lin) is:

$$x_{50} = x_l + \frac{x_u - x_l}{P_u - P_l} \cdot (P_{50} - P_l) \quad \text{Equation 44}$$

where:

x_l [mm] – the lower limit of fragment-size class, spanning x_{50} ,

x_u [mm] – the upper limit of (same) fragment-size class,

P_l [%]– relative mass passing at x_l , and

P_u [%]– relative mass passing at of x_u .

These values were also calculated in logarithmic space (log-log). For example,

$$x_{50} = EXP \left\{ \ln(x_l) + [\ln(x_u) - \ln(x_l)] \cdot \frac{\ln(P_{50}) - \ln(P_l)}{\ln(P_u) - \ln(P_l)} \right\} \quad \text{Equation 45}$$

In addition to the percentile fragment sizes, Reichholf (2003), Schimek (2015), and Ivanova (2015) used the ratio x_{80}/x_{30} to describe their sieving curves. In this way, by assuming their sieving curves were linear in the fragment-size range 80–30 mm in log-log space, they described their sieving curves with this generalized curve-slope parameter. This ratio was also calculated and compared here.

The sieving data sets were fitted to the “Swebrec 3p” function and the sets of merged screening data to the “Swebrec 5p” function (Ouchterlony, 2005). The fitting to both Swebrec functions was carried out with the recommended $1/\sqrt{x}$ weighting (Ouchterlony, 2005). These functions were chosen for the FSD analysis as they had been proven to be most suitable for such applications (Sanchidrián et al., 2009, 2012, 2013, 2014). The original Swebrec 3p function (Equation 46) includes three parameters: the median fragment size (x_{50} [mm]), the maximum fragment size (x_{max} [mm]) and an undulation parameter (b [-]).

$$P(x) = \left[1 + \left(\frac{\ln\left(\frac{x_{max}}{x}\right)}{\ln\left(\frac{x_{max}}{x_{50}}\right)} \right)^b \right]^{-1} \quad \text{Equation 46}$$

The Swebrec 5p function (Equation 47) includes two additional parameters (a and c) for describing the (ultra-)fines tail. This extension of the original Swebrec 3p function reflects the frequent bimodal nature of FSDs obtained by blasting rock and rock-like material.

$$P(x) = \left[1 + a \cdot \left(\frac{\ln\left(\frac{x_{max}}{x}\right)}{\ln\left(\frac{x_{max}}{x_{50}}\right)} \right)^b + (1 - a) \cdot \left(\frac{\frac{x_{max}}{x} - 1}{\frac{x_{max}}{x_{50}} - 1} \right)^c \right]^{-1} \quad \text{Equation 47}$$

4.5.4 Simplified $n(s)$ model

This section covers the recent development of the $n(s)$ model and its implementation to produce s - $n(s)$ curves (Iravani et al., 2018a; Iravani, 2020). Here, s denotes the number of (DEM) particles forming a blast-generated fragment and $n(s)$ the number of blast-generated fragments of size s .

When being blasted, a cylinder expands radially, inducing tangential tension and tensile cracks. Near the blast hole, fragments are broken by continual shear deformation forming the crushed zone (Åström & Timonen, 2012). The tensile cracking and the crushing/grinding are considered as the main underlying mechanisms in the blast fragmentation.

Propagating (dynamic) tensile cracks easily become unstable, branch, and further merge, forming fragments. This inherently universal process leads to a characteristic “ s - $n(s)$ ” FSD (Åström, 2006; Kekäläinen et al., 2007). The number of branching-merging fragments $n_{bm}(s)$ of size s in an interval ds can be written as (Åström, 2006; Iravani et al., 2018a):

$$n_{bm}(s)ds = C_2 \cdot s^{-\alpha} \cdot e^{-s/c_3} ds \quad \text{Equation 48}$$
$$\alpha = (2D - 1)/D$$

where C_2 and C_3 are constants and D is the physical (geometry) dimension of the fragmented body (1, 2, or 3).

The power-law part of the “ s - $n(s)$ ” FSD results from branching-merging cracks, whilst the exponential part denotes a cut-off at the outer fracture-zone boundary, where fragmentation energy has been locally depleted.

Although the crushing/grinding induces some tensile fractures, it is essentially dense crushing-shear failure (i.e., material fracturing). This mechanism is typically a part of the fragmentation process following initial material fracturing. Presence of this mechanism alters the shape of the “ s - $n(s)$ ” FSD. Openings of initial tensile cracks are eventually filled with smaller fragments. Further compressive shearing of the tensile-crack flanks crushes the smaller fragments and continuously decreases their size by further grinding and compaction. Such grinding and compaction can be considered as a hierarchical process in which “ever-smaller fragments are broken to fill pore space that opens in continuous shear deformation” (Åström & Timonen, 2012).

Such a process has a power-law “s-n(s)” FSD $n_{\text{crush}}(s)ds = C_1s^{-\beta}ds$, where C_1 is a constant and β indicates the degree of crushing/grinding, being $\beta \sim 1.8-3.5$, when $D = 3$ (Åström, 2006; Iravani et al., 2018a). Dimensionless size s denotes the number of grains composing a fragment (Iravani et al., 2018a).

The lower limit of β is defined as $\beta > \alpha$, while the upper one of 3.5 has been determined in the practical application rather than theoretically. A value of $\beta \approx 3.5$ indicates a very high degree of grinding. For low blasting loads, the fragments formed by branching and merging in the fracture zone make just a small fraction of the total mass of a blasted cylinder. Large (major) fragments remain between the formed main radial fractures. Iravani et al. (2018a) used the term “boulder(s)” for such fragments, referring to the coarsest size range of blast-generated fragments.

When blasted with small blast charge (low load), the mass fraction of these major fragments usually dominates the FSD. By increasing the load, the mass fraction of the major fragments decreases and eventually vanishes. Therefore, this is considered as a Poisson process with an exponential FSD for the major fragments (Grady & Kipp, 1987).

With $n(s)$ describing the number-density of fragments with s number of grains, an “s-n(s)” FSD, as the number of fragments in a size-interval ds , can be written as (Iravani et al., 2018a):

$$n(s)ds = C_1 \cdot s^{-\beta} ds + C_s \cdot s^{-\alpha} \cdot e^{-s/c_3} ds + n_b(s)ds \quad \text{Equation 49}$$

Here, β and α are curve slopes for respective fragment-size ranges, C_3 determines the typical size of the major fragments, $n_b(s) \sim \exp(-s/s_b)$ is the FSD part for the major-fragment range, and s_b is the characteristic size of a major fragment, affected by the number of induced tensile cracks. Occasionally a large-size cut-off to the crushing power law also occurs. This cut-off can be approximated by multiplying that first term on the right-hand side in Equation 49 by another exponential function.

The transformation from the screening data (x - $P(x)$) obtained within this dissertation was carried out according to the instructions of (Iravani et al., 2020), described as follows. Let x_{min} denote the smallest mesh size. Then, s and $n(s)$ are calculated as:

$$s = \left(\frac{x}{x_{min}} \right)^3 \quad \text{Equation 50}$$

$$n(s) = C \frac{d(P(x))}{s \cdot ds/dx} = C \frac{x_{min}^3 \cdot d(P(x))}{3x^2 \cdot s(x)} \quad \text{Equation 51}$$

$$C = \frac{M_0 \cdot x_{min}^3}{3m_{grain}}$$

where:

C - the prefactor that “shifts” the s - $n(s)$ curve along the y -axis in a log-log plot without changing its shape,

M_0 – the total (screened) mass of fragmented material, and

x_{grain} – the grain size of the material.

Here, the value of the prefactor C was taken as 1. The difference quotient for two successive mesh sizes $x(i+1)$ and $x(i)$ was used to calculate the derivative of $P(x)$:

$$d(P(x(j))) \cong \frac{P(x(i+1)) - P(x(i))}{x(i+1) - x(i)} \quad \text{Equation 52}$$

with $x(j)$ as the geometric mean (Equation 53), defining mid points of all size bins except the first one.

$$x(j) = \sqrt{x(i+1) \cdot x(i)} \quad \text{Equation 53}$$

$$j = 2, 3, \dots, n - 1$$

Equation 50 further defines the corresponding s values (Equation 54) and Equation 51 and Equation 52 the corresponding $n(s(j))$ values.

$$s(j) = \left(\frac{x(j)}{x_{min}} \right)^3 \quad \text{Equation 54}$$

Finally, the obtained s - $n(s)$ data were used to calculate the corresponding regression lines (least squares method without weighting) in log-log space to obtain the slope (exponent) parameters α and β for the fragment-size ranges that were determined by analysing the FSDs (see Section 4.5.3).

4.5.5 Specific surface area of the fines (Blaine and Permeran measurements) and blast-energy register (BER)

The analysis followed the same procedure as described by Böhm et al. (2004) and was used for similar purposes by Reichholf (2003) and Niiranen (2015). The specific surface area is described as the mass-specific (a_m [cm²/g]) or the volume-specific (a_s [cm⁻¹]) area of fragmented material.

The specific surface area is the total particle surface of fragmented material divided by its mass or volume. The specific surface area is determined with the upper and the lower particle-size limits of a particle size distribution determined by screening. The specific surface area of the finest particles is determined with the Carman-Kozeny equation of the gas flow through a granular-particle bed.

Here, the specific surface of a particle set was measured based on its permeability by using the Blaine's apparatus (constant volume) (DIN 66126–2:2015) and the Permeran apparatus (by Outokumpu) (constant pressure). Both methods were used to determine the specific surface area for the two finest fractions of the sieved material (0.1|0.04 mm and -0.04 mm) at the laboratory of the Chair of Mineral Processing (IZR, MUL). More details on the application of these methods are provided in the work of Niiranen (2015).

Application of the Blaine's apparatus is limited to measurement range of the volume-specific surface area (a_s) of around 3,000 cm⁻¹ to 12,000 cm⁻¹, due to the permeation of the particle collective with air at room temperature and normal pressure. When $a_s > 12,000$ cm⁻¹, the pores (between the particles) cannot be considered large compared to the mean free path of the gas molecules. For such values, the Carman-Kozeny equation is no longer valid (Teipel & Winter, 2011; Niiranen, 2015).

The estimation of the particle-shape factor (f_A) (Steiner, 1991; Böhm et al., 2004) starts by determining the local slopes (GGs exponents) s_n of the sieving curves (Figure 85).

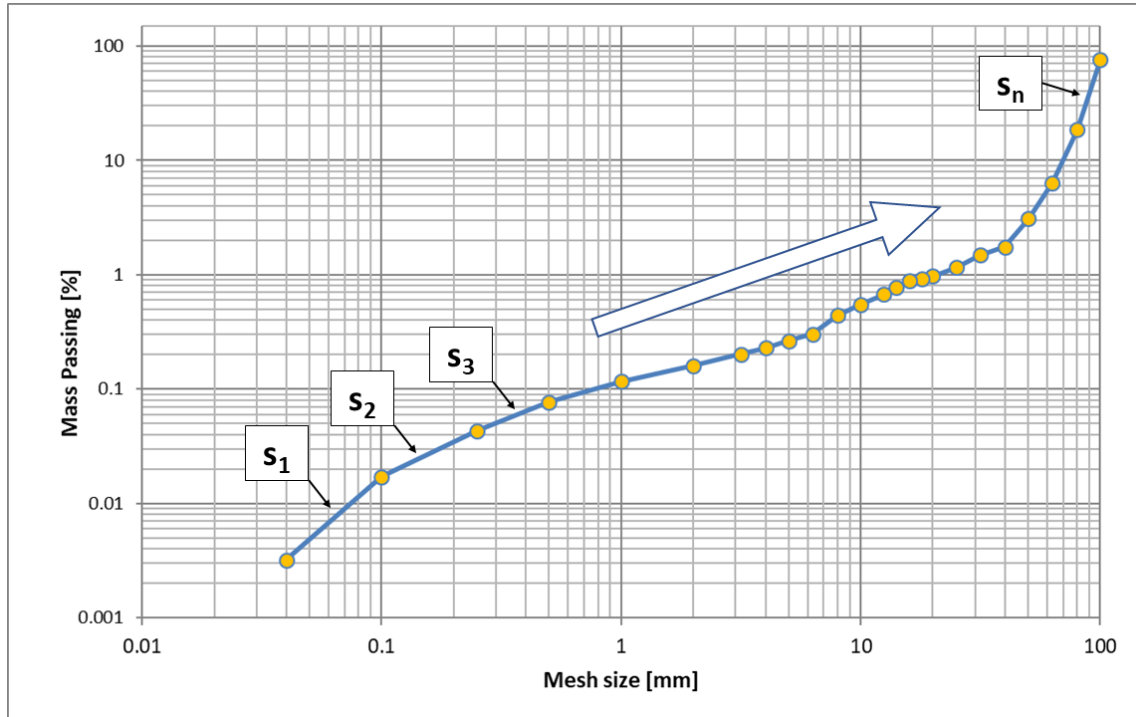


Figure 85: Definition of local (GGs) slopes (s_n) in the sieving curves.

These slopes (s_n [-]) were calculated for the considered size classes as (Schuhmann, 1940; Reichholf, 2003):

$$s_n = \frac{\ln\left(\frac{P_n}{P_{n+1}}\right)}{\ln\left(\frac{x_n}{x_{n+1}}\right)} \quad \text{Equation 55}$$

where:

n - the sequential number of GGS slope between the (sieving) fragment-size classes, starting from the smallest one (i.e., s_1 for size class 0.1|0.04 mm)

x_n [mm] – the lower limit of fragment-size class,

x_{n+1} [mm] – the upper limit of fragment-size class,

P_n [%] – relative mass passing at x_n , and

P_{n+1} [%] – relative mass passing at x_{n+1} .

Note here that if a sieving-data set includes empty size bins (i.e., no material was retained for certain fragment-size fractions), the respective slope is calculated for the first non-empty neighbouring bins (Figure 86).

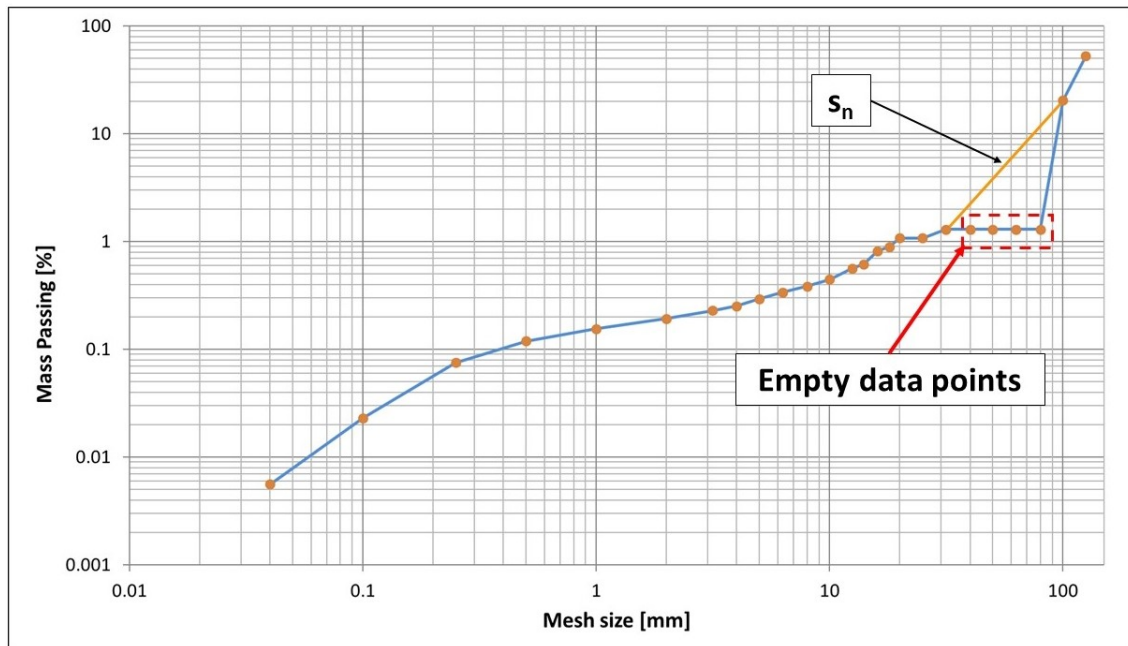


Figure 86: Local (GGS) slope (s_n) over a range of empty data points.

The surface-equivalent fragment size (x_a [mm]) is calculated as (Böhm et al., 2004):

$$x_a = \left(\frac{1}{s_n} - 1 \right) \cdot \left[\frac{P_{n+1} - P_n}{\left(\frac{P_n}{x_n} \right) - \left(\frac{P_{n+1}}{x_{n+1}} \right)} \right] \quad \text{Equation 56}$$

Multiplying x_a with the particle-surface area a_s (for the size class 100|40 μm) yields the particle-shape factor (f_A [-]) of the particle-size classes (Böhm et al., 2004):

$$f_A = \frac{a_s \cdot x_a}{10} \quad \text{Equation 57}$$

The blast-energy register (BER) was obtained based on the following procedure (Moser et al., 2000, 2003a; Reichholf, 2003; Böhm et al., 2004; Moser, 2005):

- Measure the volume-specific surface a_s for the size class 100|40 μm .
- Calculate f_A from a_s and the surface-equivalent fragment size x_a (Equation 57).
- Assume f_A is constant for all fragment-size classes (Böhm et al., 2004).
- The specific surface a_s of the remaining classes is calculated from their surface equivalent particle size (x_a) and the shape factor (f_A) (Equation 57).
- The mass-specific surface (a_m) of the remaining classes is calculated by dividing the a_s value of the respective class by the density (ρ_c) (Equation 58). This (calculation) density is chosen as the grain-level density (ρ_g) or the material (bulk) density (ρ_b), depending on the considered size class and the average grain size of the material (d_g). Here, ρ_c for the size classes larger than the original grain size of the blasted material is the material (bulk) density, and for those classes smaller than the grain size it is the grain-level density (ρ_g) (see Table 13). However, as the measured ρ_b is unexpectedly higher than ρ_g for the granite (see Table 3 and Appendix 2), ρ_g was chosen for ρ_c for the whole size range of fragmented granite material.

$$a_m = \frac{a_s}{\rho_c} \quad \text{Equation 58}$$

Table 13: Determination of the material density used in the BER calculations (i.e., the calculation density).

Material	Grain-level density ρ_g [g/cm ³]	Bulk density ρ_b [g/cm ³]	Average grain size d_g [mm]	Calculation density ρ_c [g/cm ³]	Size class [mm]
Mortar	2.38	1.66	0.14	1.66	$\geq 0.5 0.25$
				2.38	$< 0.5 0.25$
Granite	2.68	2.75	0.42	2.68	$\geq 1 0.5$
					$< 1 0.5$

- “The sum of the specific surface of all the size classes weighted by mass represents the total specific surface of the comminution product” (Böhm et al., 2004). Therefore, the total mass-specific area (a_{m_tot} [cm²/g]) is calculated by dividing the total fragmented area (A_f [cm²]) by the total sieved mass (m_{sieve}) (Equation 59). Here, A_f is the sum of the fractions of the fragmented area (ΔA_f [cm²]). Here, ΔA_f is calculated by multiplying a_m by the

mass fraction of the respective size class $(m_{n+1} - m_n)$ [g] (Equation 60), where $n + 1$ and n denote the upper and the lower size limit, respectively. Note here that $(m_{n+1} - m_n)$ was calculated from the corresponding percentile mass fraction concerning the total sieved mass, not the original mass of the cylinder.

$$a_{m_tot} = \frac{A_f}{m_{sieve}} \quad \text{Equation 59}$$

$$A_f = \sum_k (\Delta A_f)_k \mid k - \text{size class}$$

$$\Delta A_f = (m_{n+1} - m_n)[g] \cdot a_m \quad \text{Equation 60}$$

$$(m_n - m_{n-1})[g] = \frac{(m_{n+1} - m_n)[\%]}{100} \cdot m_{sieve}[g]$$

- The Blast-energy register (BER) (Moser et al., 2000, 2003a; Reichholf, 2003; Moser, 2005) is obtained by plotting a_{m_tot} against the specific energy consumption (E_c [J/g]), which is calculated by multiplying the powder factor (PF [g/t]) by the specific explosive energy for PETN (E_{PETN} [J/g]), given as 4168 J/g (López, 2002; Moser et al., 2003a; Reichholf, 2003) (Equation 61). Here, the powder factor (PF) was calculated as the ratio of the specific charge (q [kg/m³]) and the initial mass of the regarded cylinder (M_{cyl} [g]). The slope exponent of the plotted data (i.e., linear regression lines fitted to the data by non-weighted least-squares fitting) represents the Rittinger coefficient for BER (R_{BER} [cm²/J]). These regression lines, obtained for each blasted material, have a fixed starting point at the origin (0,0) of the coordinate system.

$$E_c = PF \cdot E_{PETN} \quad \text{Equation 61}$$

$$PF = \frac{q}{M_{cyl}} \cdot 10^6$$

4.6 Statistical data processing and analysis

The result data in this study were statistically evaluated and compared considering means (average) values of respective samples and/or linear-regression slopes and intercepts.

The means of sampled data were evaluated and compared with the following methods:

- Student's two-sample t-test,
- One-way analysis of variance (ANOVA) and the F-test, and
- Two-way analysis of variance (ANOVA) with replication and the F-test.

The slopes and intercepts of the linear-regression lines, drawn through sampled result data, were evaluated and compared with the following methods:

- Student's t-test for comparison of two linear-regression lines,
- multiple linear regression with dummy variables for comparison of multiple regression lines, and
- simplified One-way analysis of covariance (ANCOVA).

These statistical methods are described in Appendix 12. Finally, selected results were subjected to correlation analysis. All these statistical methods were implemented in MS Excel (Napier-Munn, 2014; Zaiantz, 2020a, 2020b).

5 Results

This section presents results of the measurements and analyses (see Section 4) conducted on obtained crack patterns, CT scans and micrographs, and fragmented material of the blasted cylinders. The results indicate and show different mechanisms and factors influencing the blast-induced fines in the small-scale blast test.

The results are presented considering the following inputs:

- high-speed images (HSI),
- post-mortem images of the frontal end face of the cylinders (PMI),
- “unfolded” post-mortem images of the cylinder mantle (PMM),
- transverse CT sections (CTt),
- non-planar CT sections (CTnp),
- micro-CT scans (uCT),
- optical and SEM micrographs,
- data obtained with fragmentation measurements and analyses,
- the material of blasted cylinder (blasted material), and
- linear charge concentration I_c [g/m].

The results were compared either directly (i.e., by indicating similarities or differences in figures or features) or through statistical evaluation (see Section 4.6).

5.1 Fracture phases in HSI

Although the resulting crack patterns differ from one blast cylinder to another, the high-speed images (HSI, see Section 4.1.1) from both mortar and granite shots show similar development of crack patterns, both with time and with increasing charge (Figure 87). More information on the whole image sets and crack traces is provided in Appendix 6.

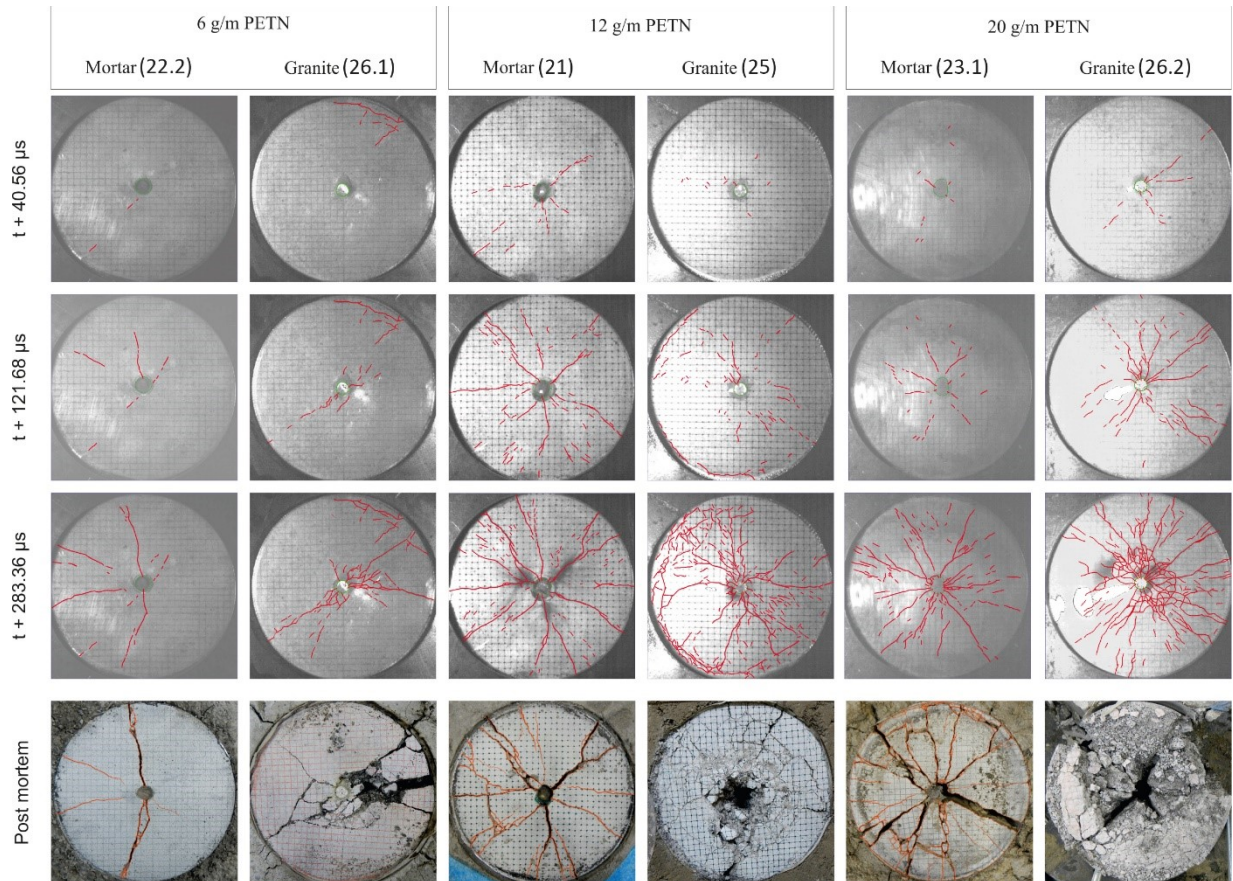


Figure 87: Images of crack-pattern development captured with the high-speed camera and PMI of the frontal end face. The cracks were traced in red (HSI) and orange (PMI) colour. The numbers in the brackets mark corresponding blast tests.

Table 14 shows the distribution of the fracture phases in the HSI concerning elapsed time from the detonation. The phase cells are marked with sequence numbers (e.g., '1' for fracture phase 1) and colours considering corresponding phases (green – phase 1, yellow – phase 2, and red – phase 3).

Following the plug-movement in the initial frame, initial cracks emerge and propagate at the end face. These cracks may firstly appear at the borehole, at the mantle, or somewhere in between.

Table 14: Fracture-phase distribution in the captured blast shots (HSI).

Material	mortar		granite		mortar		granite		mortar		granite	
	22.2	23.2	26.1	27	20	21	24	25	22.1	23.1	26.2	
I_c [g/m]	6				12				20			
Elapsed time [μ s]	40.56	1	1	1	1	1	1	1	1	1	1	1
	81.12	1	1	1	1	1	1	1	1	1	1	1
	121.68	1	1	1	1	1	2	2	1	1	1	2
	162.24	1	1	1	1	1	2	2	2	2	1	2
	202.80	1	1	1	2	1	2	2	2	2	1	2
	243.36	1	1	1	2	2	2	2	2	2	2	2
	283.92	2	2	1	2	2	2	3	2	2	2	3
	324.48	2	2	2	2	2	3	3	3	3	2	3
	365.04	2	2	2	2	2	3	3	3	3	2	3
	405.60	2	2	2	2	3	3	3	3	3	2	3
	446.16	3	3	2	2	3	3	3	3	3	3	3
	486.72	3	3	3	3	3	3	3	3	3	3	3
	527.28	3	3	3	3	3	3	3	3	3	3	3

The initial cracks are mainly radial in the mortar, whereas in the granite there are also many tangential cracks even at this stage (Figure 88), usually near the mantle (i.e., the outer rim of the frontal end face).

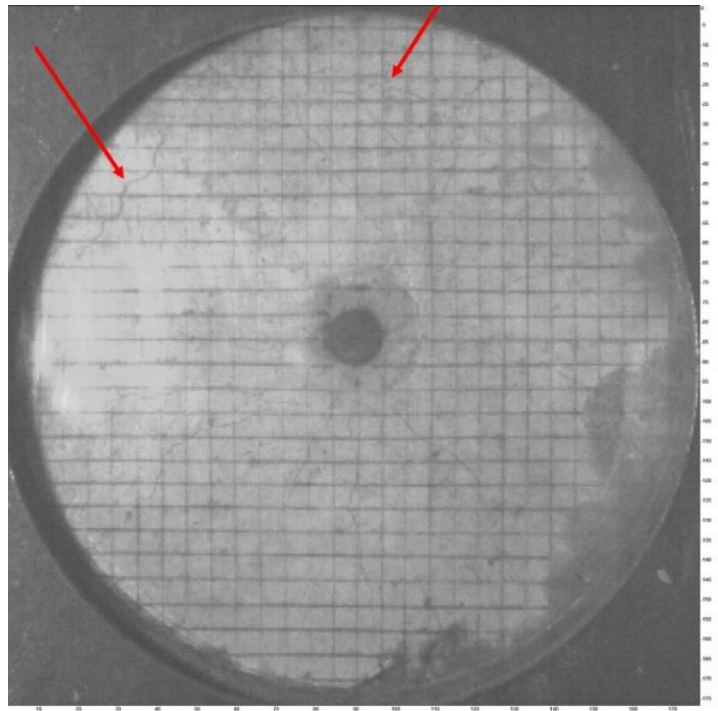


Figure 88: Tangential cracks in the first phase at at $t+121.68 \mu$ s (g12(24)).

In the second phase, the propagation includes multiple branching/merging at the frontal end face. As the initial cracks extend and open sufficiently, blast fumes rush out from them (see Figure 87). At the start of the third phase, most of the initial cracks have reached the borehole wall and the mantle. In this phase, the fumes are often associated with additional fragmentation at the frontal end face, e.g., by loosening and further breaking fragments near the crack edges. Furthermore, the blast fumes rush out in front of the end face carrying smaller fragments and partially obscure further crack development. During the whole event, earlier visible short cracks may close and stay undetected during the rest of the filming period (Figure 89).

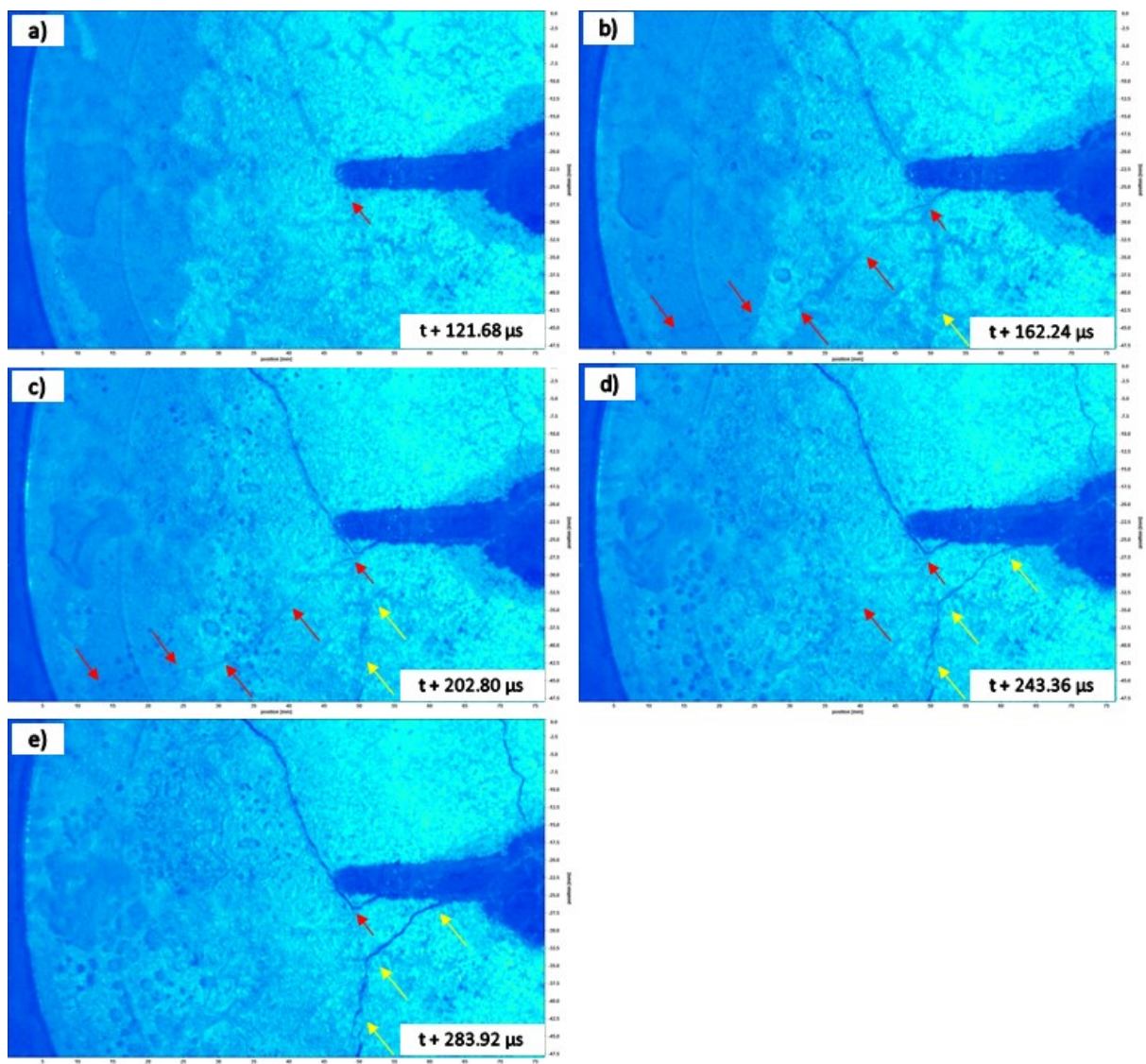


Figure 89: Example of crack closure. A crack marked with red arrows firstly propagates (a to c) and then closes when another crack (marked with yellow arrow) propagates nearby (d and e). Selected HSI (m12(9)).

The filming results indicate only a minor (if any) influence of the linear charge concentration on the duration of the phases.

The third-phase images of the granite shots show an axial movement of the end face starting near the blast hole and spreading out radially (Figure 90).

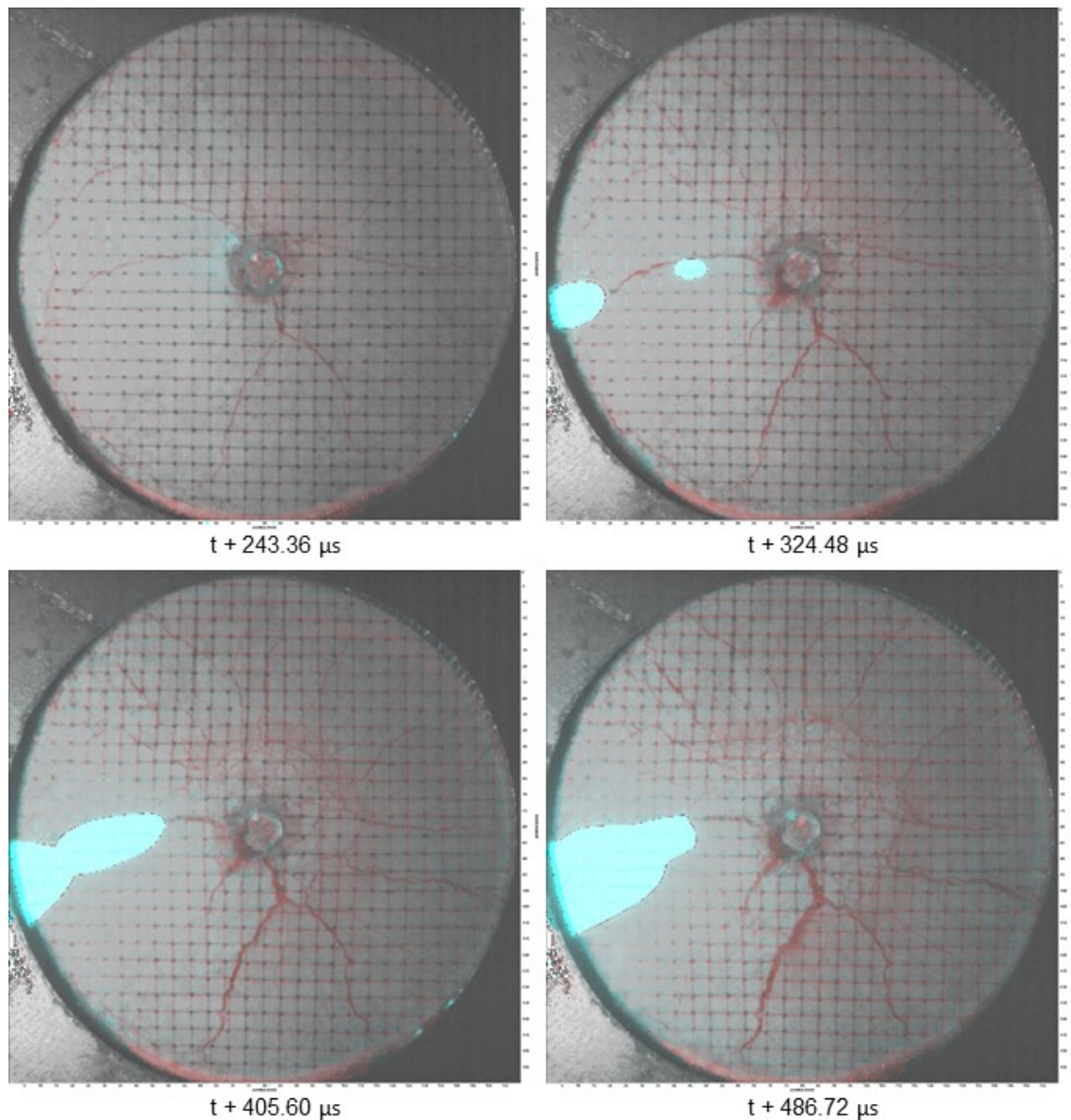


Figure 90: Effect of the “radial spall wave” at the frontal end face in the granite (g12(25)) and bending of the protective window (note the light reflection on the left side in the images).

This is most probably a result of earlier end-face spalling. The movement is strong enough to bend the protective window outwards causing a mirror image of the light source to appear and move at the window surface. Less intensive bending of the window may also be caused by the plug movement and by the fumes.

5.2 Number of main radial cracks (N)

Table 15 shows a summary of counted primary connecting paths (i.e., main radial cracks, N [-]) (see Section 4.1.8) in the post-mortem images of the frontal end face (PMI), last traced high-speed image (HSI) per cylinder, and transverse CT sections (CTt). Here, the provided values for CTt are average counts per image set. This summary also includes the corresponding critical stress-intensity factor (K_{Ic} [MPa/m^{0.5}]), calculated with Equation 19 (Grady & Kipp, 1987) and Equation 20 (Ouchterlony, 1997). The K_{F-s} (static) (Equation 72) and K_{F-d} (dynamic) (Equation 73) parameters are calculated values of K_{Ic} based on the WST (see Appendix 2).

Table 15: Summary of counted main radial cracks with estimated stress-intensity factor. The values marked red indicate spalling, where “sp” stands for “unknown due to spalling.”

Material	Blast test	I_c [g/m]	PMI	HSI	CTt (Ave)	K_{Ic} [MPa/m ^{0.5}]		WST	
						Grady & Kipp	Ouchterlony	K_{F-s}	K_{F-d}
Mortar	23.1	20	9	11	5.3	4.11	2.53	1.74	1.91
	22.1		5	5	-	4.48	2.76		
	20	12	4	4	-	3.21	1.97		
	21		6	7	5.7	1.89	1.16		
	22.2	6	2	2	-	3.74	2.30		
	23.2		3	3	2.9	2.14	1.32		
Granite	26.2	20	sp	8	-	1.39	1.36	2.16	2.09
	24	12	sp	sp	-	-	-		
	25		sp	10	-	0.51	0.50		
	28.1				5.4	2.05	1.26		
	27	6	8	5	-	0.59	0.58		
	26.1		5	4	3.8	0.89	0.87		

The spalling mentioned in Table 15 is related to the beginning of the third fracture phase (see Section 5.1). After this point in time, the crack patterns at the frontal end face are no longer representative of the internal ones.

Figure 91 shows a summary of N in the CTt.

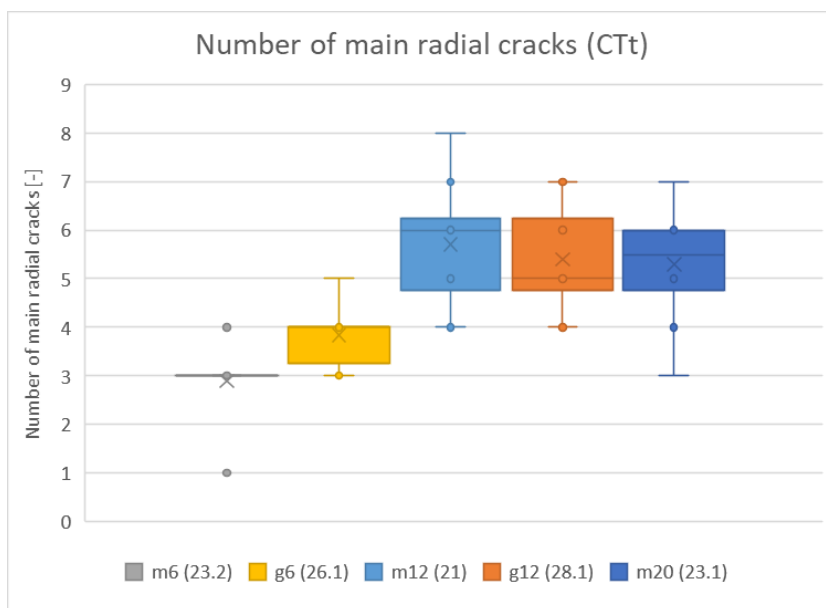


Figure 91: Main-radial-crack count relative to blast material and linear charge concentration in CTt.

Table 16 shows an overview of the mean values of N in the CTt.

Table 16: Average values (means) of N in CTt.

Variable	Ave	Std	Data count
m6(23.2)	2.90	0.70	10
g6(26.1)	3.83	0.55	12
m12(21)	5.70	1.19	10
g12(28.1)	5.40	1.02	10
m20(23.1)	5.30	1.10	10

The number of the main radial cracks increases when increasing the linear charge concentration from 6 g/m to 12 g/m in both materials. This number does not significantly change when further increasing the concentration to 20 g/m in the mortar. The blasted material does not significantly influence these results (see Table 99, Table 100, and Table 101).

5.3 Topological features

This section provides an overview of counted topological nodes, branches, and lines (see Section 4.1.5) and calculated fracture abundance (see Section 4.1.6) in the traced high-speed images (HSI), post-mortem images of the frontal end face (PMI), transverse CT sections (CTt), non-planar CT sections (CTnp), and “unfolded” post-mortem images of the cylinder mantle (PMM). Proportions of the node counts considering their type were used to generate ternary diagrams (I - T_b - J_{int}). Raw result-data sets are provided in Appendix 8 and the related results not covered this section are provided in Appendix 9.

The results are provided with summaries of statistical data evaluations and comparisons (see Section 4.6). Further details on the statistical results are provided in Appendix 10.

5.3.1 Absolute node counts and their proportions

Figure 92 and Figure 93 show absolute node counts (N_I , J_{int} , and N_{T_b}) [-] and their proportions [-] in the HSI.

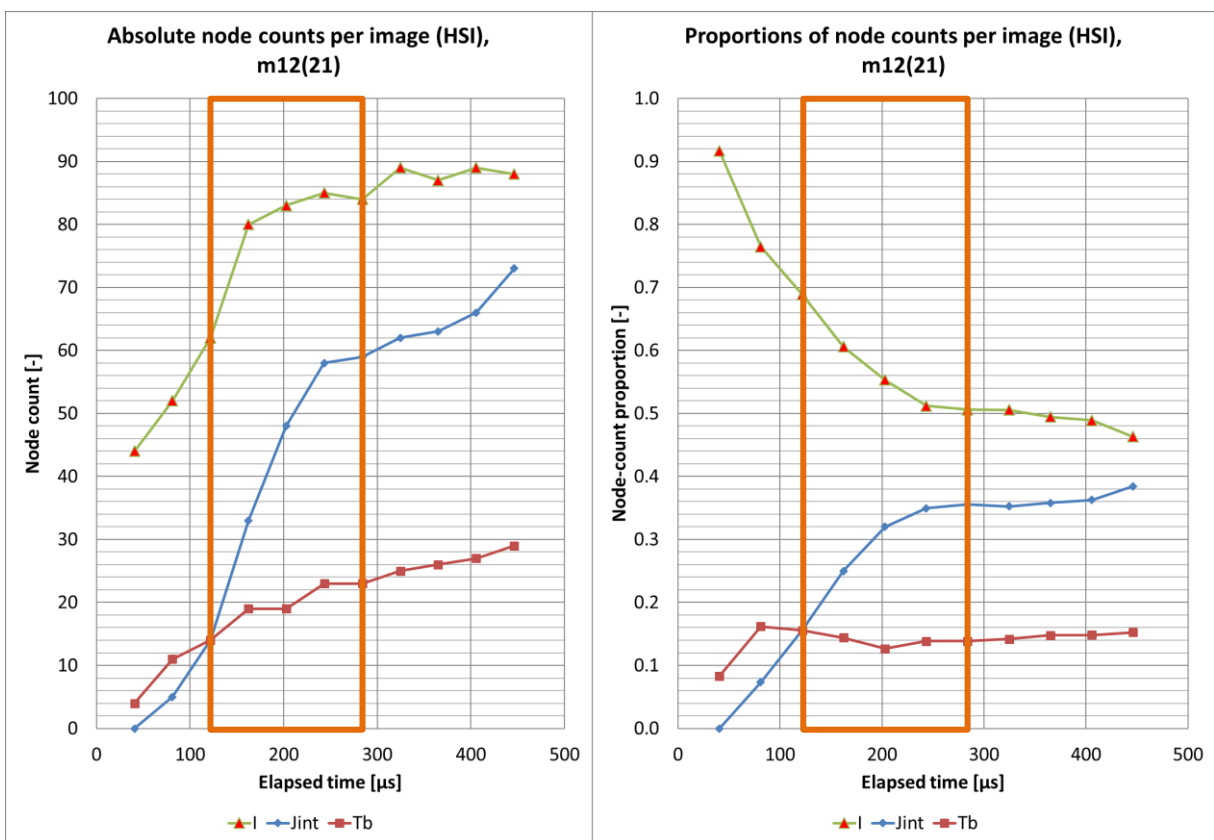


Figure 92: Node counts from the high-speed images (HSI) concerning elapsed time from the detonation in the mortar (m12(21)). The orange box marks the second fracture phase.

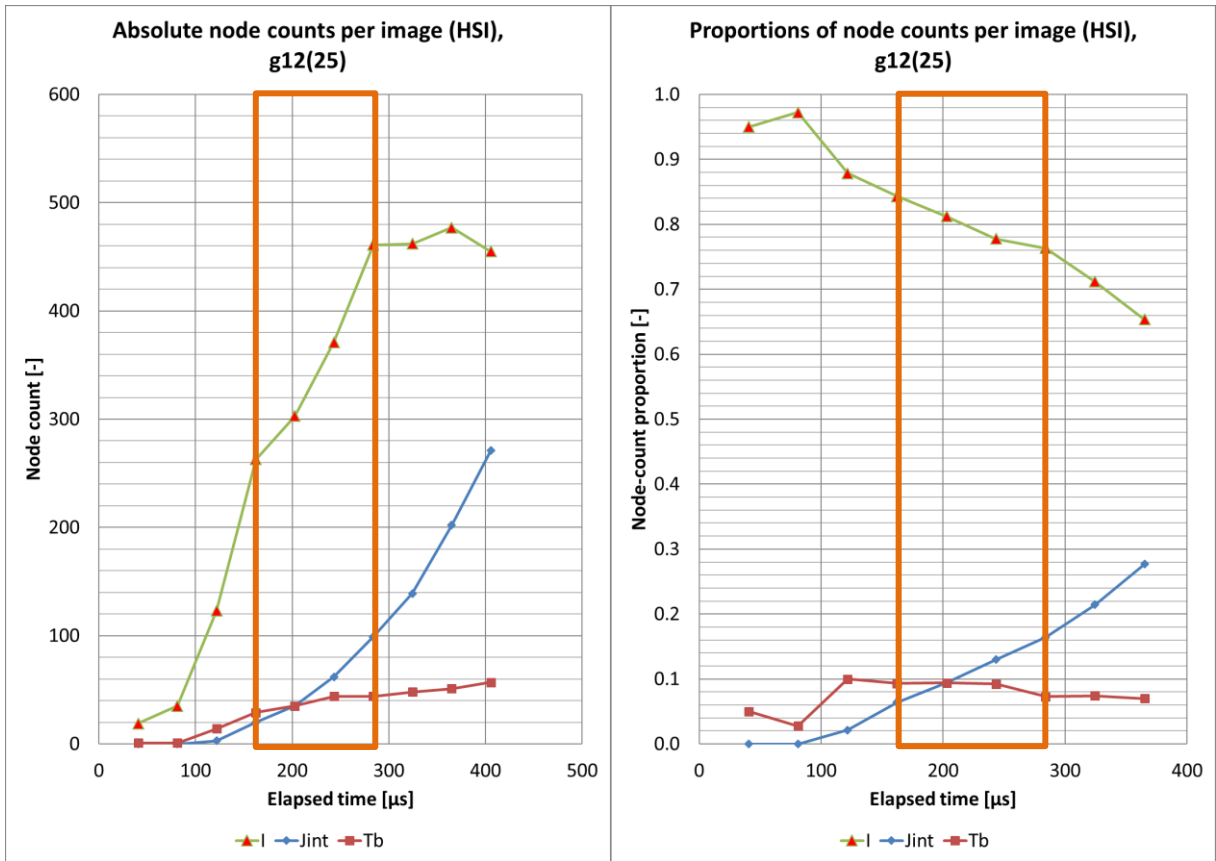


Figure 93: Node counts from the high-speed images (HSI) concerning elapsed time from the detonation in the granite (g12(24)). The orange box marks the second fracture phase.

The absolute node count increases with the elapsed time and often levels out. The proportions of the I-nodes develop differently than those of the intersection nodes (T_b and J_{int}).

The regression-line slopes of the absolute values of N_I , J_{int} , and N_{TB} in the HSI (see Table 102, Table 103, and Table 104) are statistically different to each other considering the blasted materials and the linear charge concentration (l_c) (see Table 108, Table 109, and Table 110). In general, the slopes of the fitted linear-regression lines steepen with increasing linear charge concentration, and they are steeper in the granite than in the mortar. Exceptions to this observation are for N_I (in the granite) and J_{int} , as their slopes decrease when further increasing the linear charge concentration from 12 to 20 g/m.

An I-node is converted to a joining node when the crack tip meets another crack or a boundary. The J_{int} -node proportion, in most cases, increases and levels out with time, opposite to the I-node proportion. This levelling-out (i.e., change in the curve slope) usually occurs during the transition between the first two fracture phases (see Section

5.1). The T_b -node proportions either increase at a relatively low rate or remain about the same over time.

The absolute node counts and their proportions for the CTt do not show a clear trend of development along the cylinder axis (Figure 94 and Figure 95). They are better described as a relatively large scatter around an average.

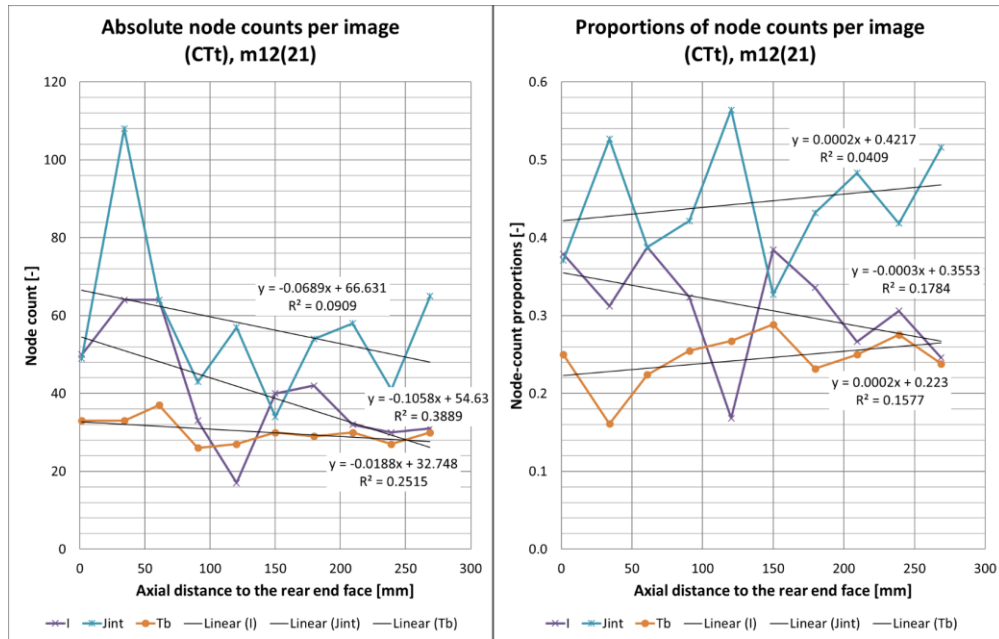


Figure 94: Node counts and their proportions from the CTt relative to the axial position in the mortar (m12(21)).

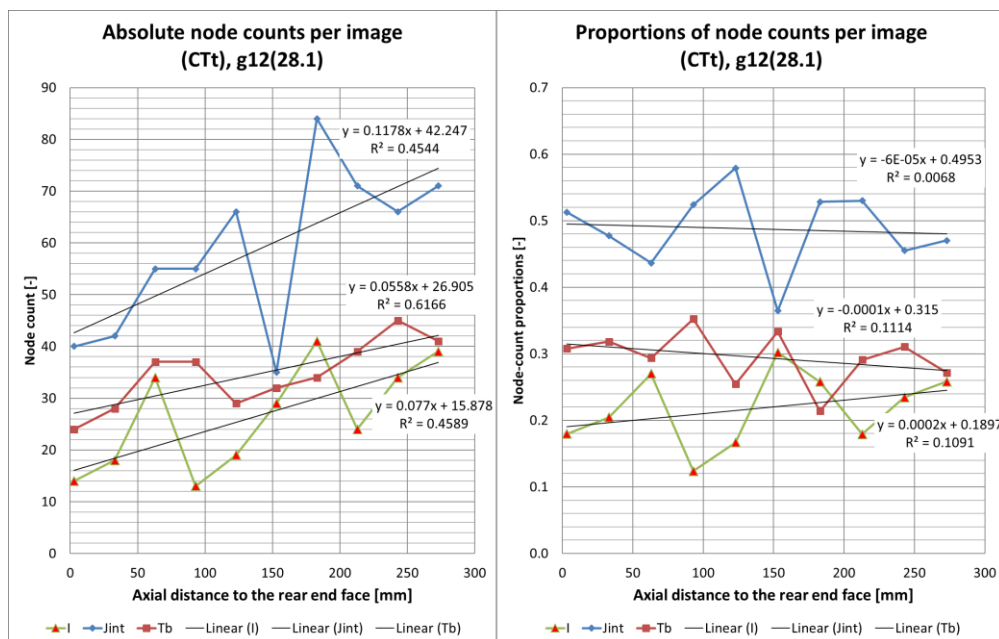


Figure 95: Node counts and their proportions from the CTt relative to the axial position in the granite (g12(28.1)).

Table 17 shows an overview of the mean values of N_I , J_{int} , and N_{TB} in the CTt.

Table 17: Average values (means) of N_I , J_{int} , and N_{TB} in CTt.

Variable		Ave	Std	Data count
N_I	m6(23.2)	16.6	10.24	10
	g6(26.1)	4.3	2.36	10
	m12(21)	40.3	15.20	10
	g12(28.1)	26.5	10.32	10
	m20(23.1)	46.8	12.37	10
J_{int}	m6(23.2)	26.0	28.92	10
	g6(26.1)	11.8	4.39	10
	m12(21)	57.3	20.46	10
	g12(28.1)	58.5	15.87	10
	m20(23.1)	57.4	14.52	10
N_{TB}	m6(23.2)	13.7	3.89	10
	g6(26.1)	11.8	2.66	10
	m12(21)	30.2	3.36	10
	g12(28.1)	34.6	6.45	10
	m20(23.1)	32.4	3.69	10

The mean values of N_I in the CTt are about the same for the 12-g/m shots and 20-g/m shots in the mortar (see Table 111).

The mean value of N_I increases with increasing linear charge concentration from 6 to 12 g/m. However, it is about the same in the two blasted materials for the 6- and for the 12-g/m shots (see Table 112).

The mean values of J_{int} in the CTt are about the same for the 12-g/m shots in both materials and 20-g/m shot in the mortar (see Table 113 and Table 115).

The mean values of J_{int} and of N_{TB} increase with increasing linear charge concentration from 6 to 12 g/m. However, they are about the same in the two blasted materials for the 6- and for the 12-g/m shots (see Table 114 and Table 116).

Figure 96 and Figure 97 show the node counts and their proportions from the CTnp. The node counts and their proportions in the mortar show curves of a similar shape.

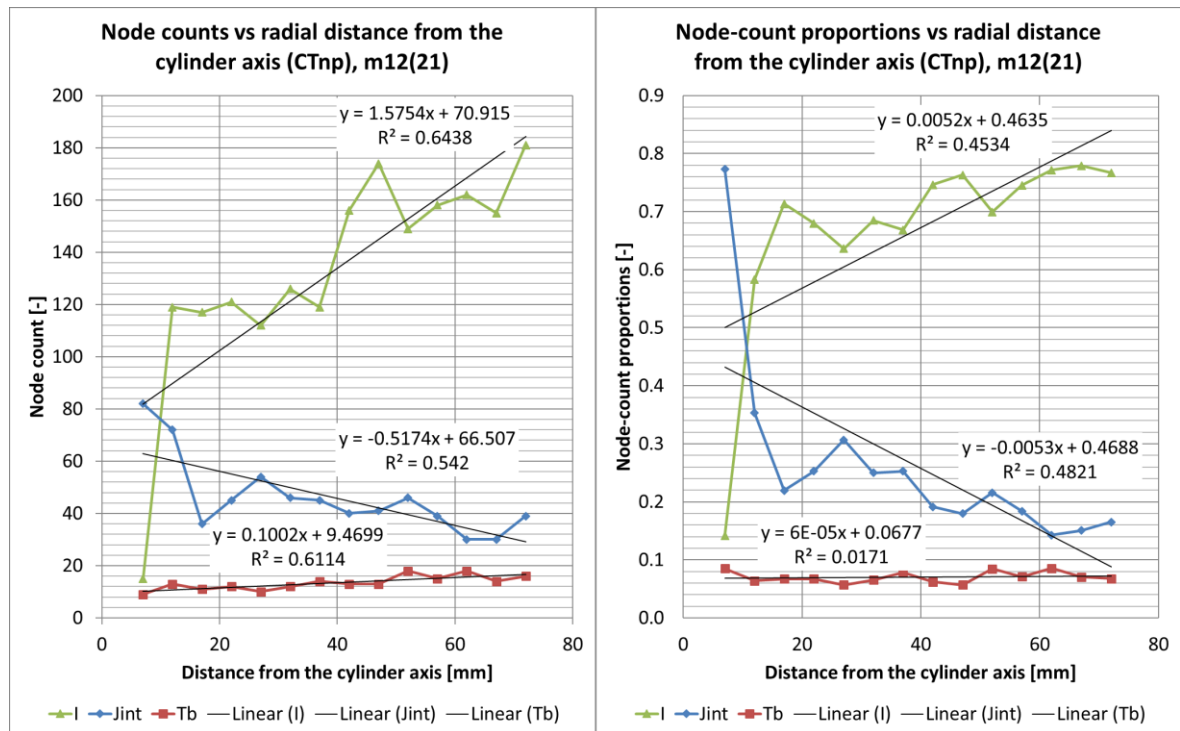


Figure 96: Node counts and their proportions from the CTnp concerning the radial position in the mortar (m12(21)).

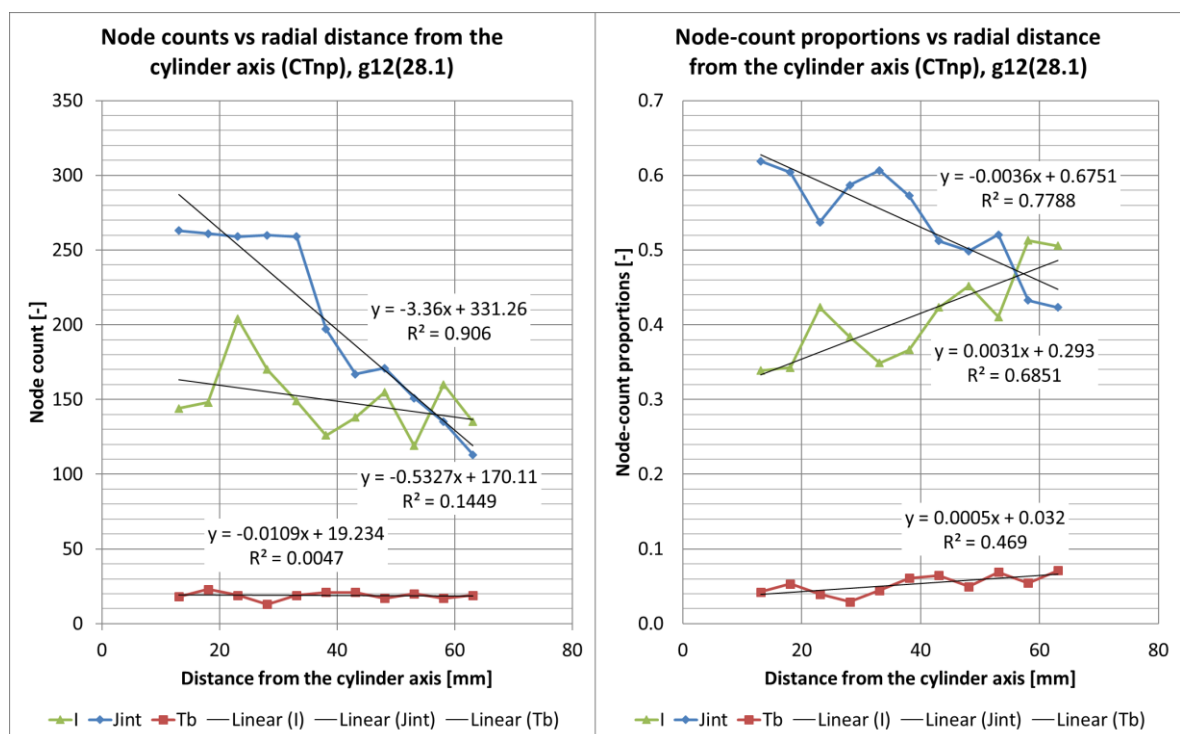


Figure 97: Node counts and their proportions from the CTnp concerning the radial position in the granite (g12(28.1)).

The number of crack tip nodes (I-nodes) steadily increases with distance from the blast hole and seemingly levels out in the mortar CTnp. The number of internal intersections (J_{int} -nodes) steadily decreases with distance from the blast hole. The number of boundary intersections (T_b -nodes), where the boundaries are the cylinder end faces, stays about the same. In the granite, the counts of the I-nodes and the J_{int} -nodes in the CTnp drop with increasing distance from the blast hole, while the number of T_b -nodes stays about the same. The I-node proportion increases, though and that of the J_{int} -nodes decreases, with increasing distance, and the proportion of the T_b -nodes stays about the same.

The statistical evaluations and comparisons of the N_I results, of the J_{int} results, and of the N_{TB} results, for the CTnp (see Table 121, Table 122, and Table 123) show no significant difference in the slopes of the regression lines (see Table 117) considering the linear charge concentration (l_c). The same applies to the intercepts of the linear-regression lines for the 12- and 20-g/m shots. Both the slopes and the intercepts increase with increasing linear charge concentration from 6 to 12 g/m. The absolute values of the slopes and of the intercepts of N_I and J_{int} are larger for the granite than for the mortar. However, the slopes of N_I for the two blasted materials have mutually opposing trends.

5.3.2 Ternary diagrams of the node-count proportions

The ternary diagrams in Figure 98 show summarized node-count proportions from the HSI, PMI, CTt, and CTnp images.

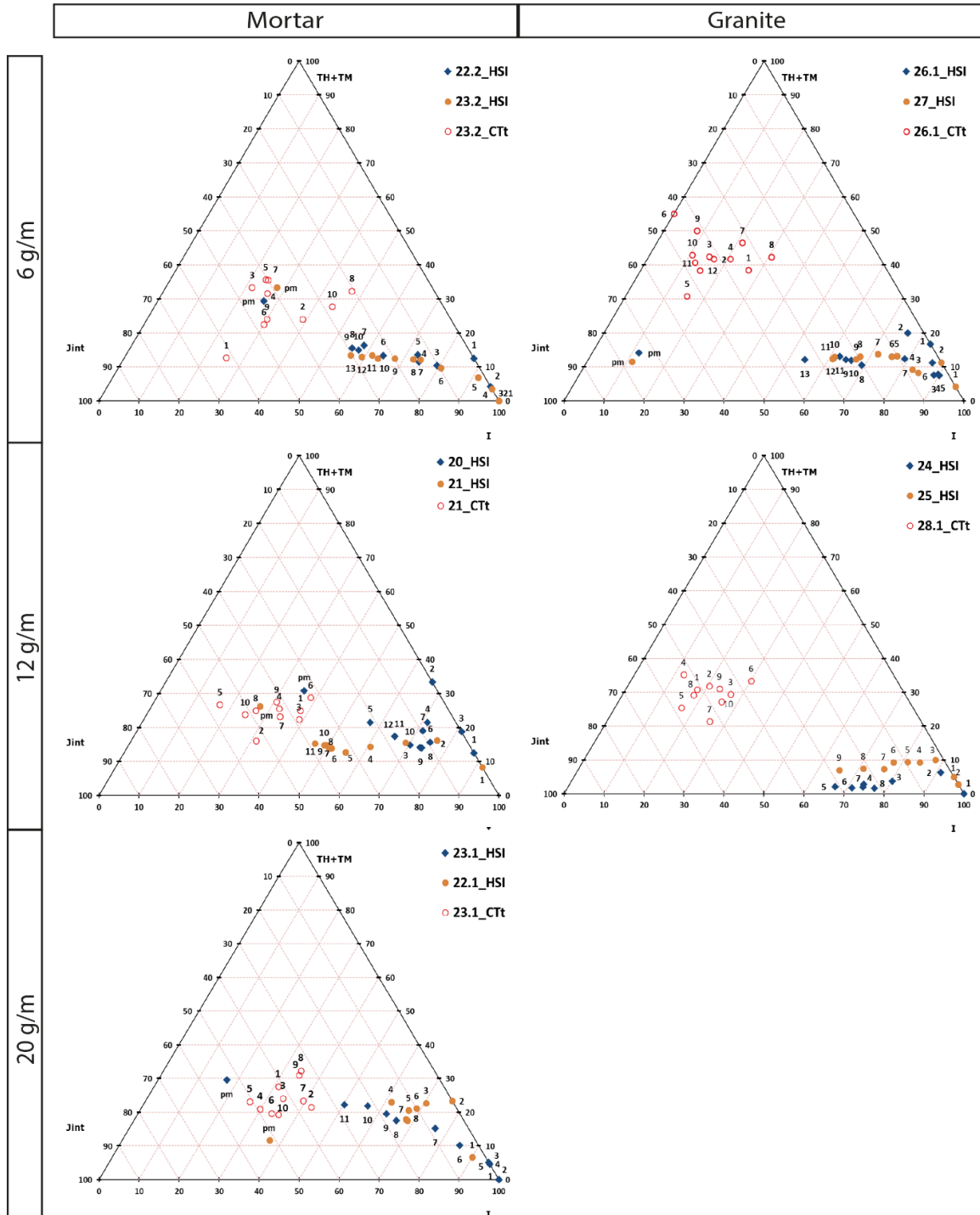


Figure 98: Node-count proportions (set of ternary diagrams). Red and orange points represent the HSI with numbers indicating their time sequence with time steps of 40.56 μ s and 'pm' representing the PMI. Blue points indicate the CTt with numbers indicating the sequence in their axial position starting from the rear end face.

Figure 99 shows the results from the CTt in more detail.

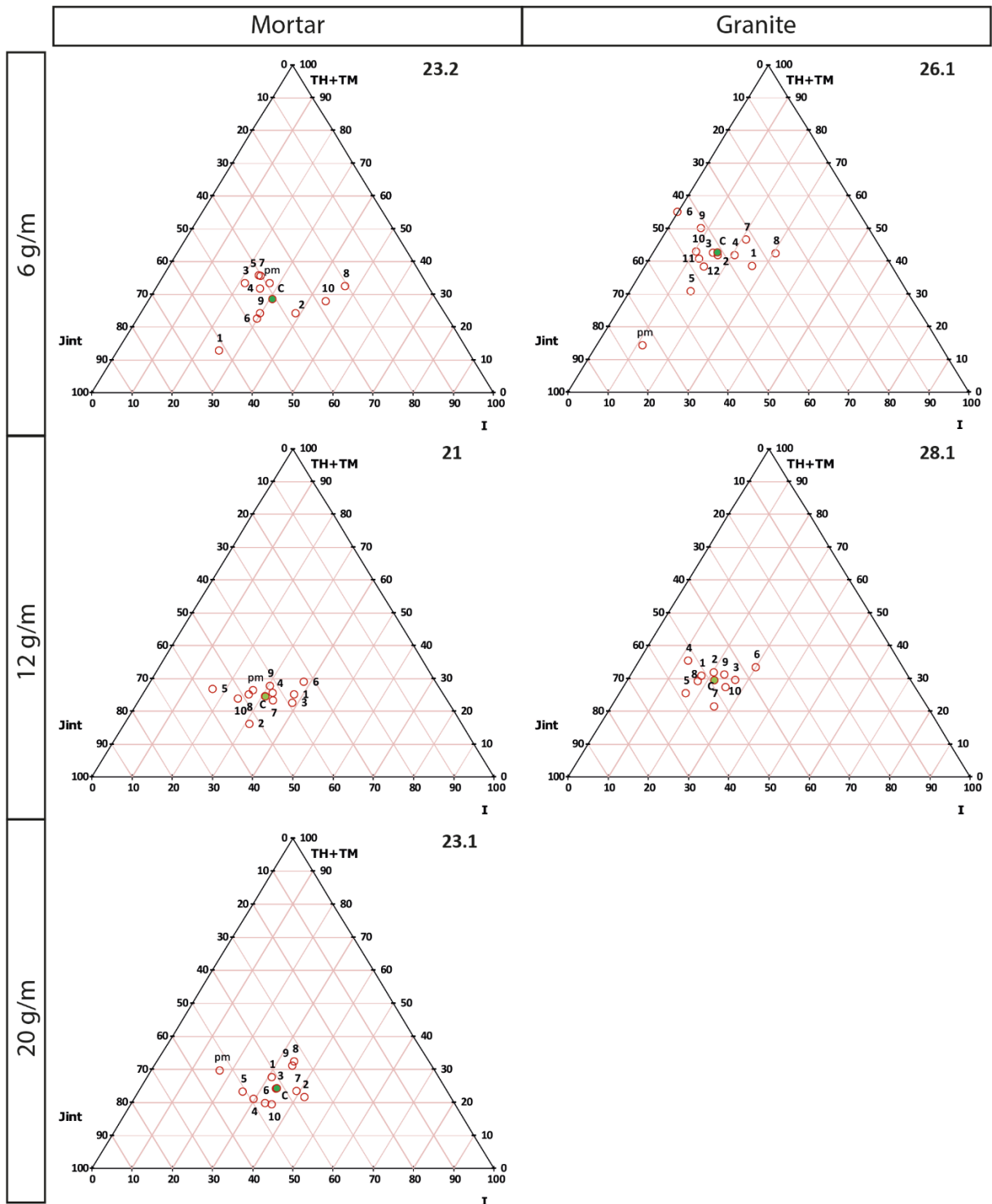


Figure 99: Node-count proportions (set of ternary diagrams) from transverse CT sections. The data points are marked with numbers that indicate the sequence in the axial position of the sections starting from the rear end face. Point 'pm' represents the PMI and point 'C' the geometrical centre of the data points marked with numbers.

The axes in the ternary diagrams show the proportion of isolated nodes (I [%]), internal joining nodes (J_{int} [%]) and boundary joining nodes ($T_B = T_H + T_M$ [%]), the sum of which is 100%. The I -nodes correspond to crack tips, the J_{int} -nodes (Y , X , or R -type) to, e.g., branching-merging events and the T_B -nodes to cracks that have connected with either blast hole or mantle.

The node groups from the CTt of both materials (red circles in Figure 98 and Figure 99) scatter less with increasing linear charge concentration. The data points for the HSI follow the same development pattern within a sequence. They start near the lower right corner of the diagram ($I \approx 100\%$ and $J_{int} \approx T_B \approx 0\%$) and progress towards the centre (I , J_{int} , and $T_B \approx 50\%$), as the proportion of I -nodes steadily decreases.

In 6- and 12-g/m mortar shots, the node proportions of the PMI lie inside the clusters of the CT data that show the variations of the internal crack patterns. However, this is not the case for the 20-g/m granite and mortar shots due to the end-face spalling, which is more pronounced in the granite.

Table 18 shows a summary of the data scatter in the ternary diagrams (D_{cent} [-]) of the CTt (see Figure 43).

Table 18: Measured scatter of the node counts in the CTt.

Material	Blast test	I_c [g/m]	Centroid point			D_{cent}		
			T_b	I	J_{int}	Max	Ave	Std
Mortar	23.1	20	24.3	34.0	41.7	9.1	5.9	2.51
	21	12	24.4	31.1	44.5	13.3	6.6	3.52
	23.2	6	28.5	30.9	40.7	20.6	10.0	5.26
Granite	28.1	12	29.5	21.8	48.8	11.1	5.8	2.84
	26.1	6	42.5	16.1	41.3	15.9	7.7	4.77

The statistical results of D_{cent} are not significantly different (Table 19).

Table 19: Statistical evaluation of average D_{cent} in CTt with One-way ANOVA ($\alpha = 0.05$).

Variable	Ave	Std	Data count	F	F_{crit}	p-value	Sign. diff.
m20(23.1)	5.91	2.51	10	2.00	2.57	0.11	No
m12(21)	6.58	3.52	10				
m6(23.2)	10.07	5.26	10				
g12(28.1)	5.77	2.84	10				
g6(26.1)	7.69	4.77	12				

The calculated values of D_{cent} in the CTt show that the scatter increases with smaller linear charge concentration and that the scatter is larger in the mortar than in the granite.

Figure 100 shows the topological results from the CTnp and the PMM.

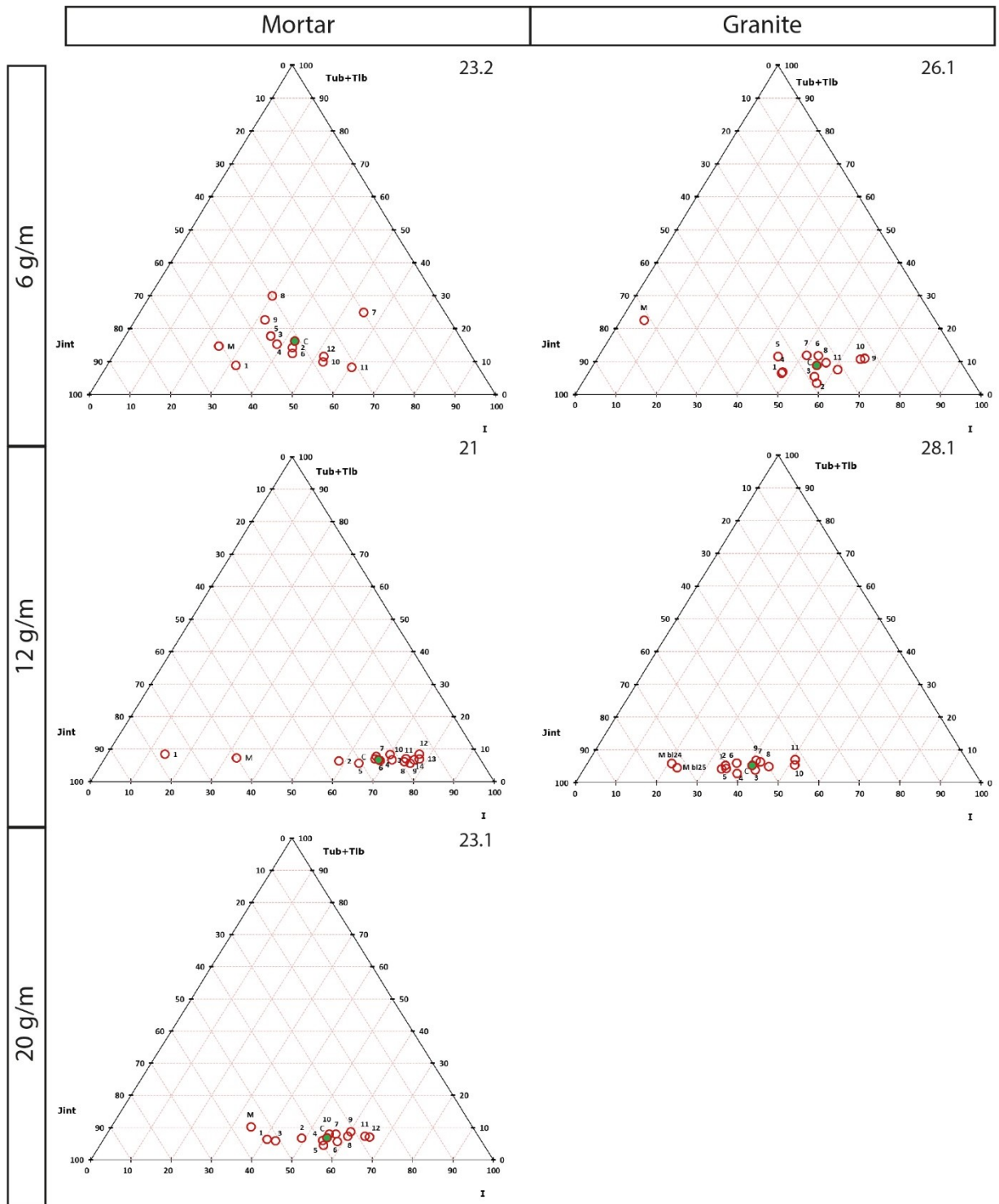


Figure 100: Node-count proportions (set of ternary diagrams) from CTnp. The data points are marked with numbers that indicate the sequence in the radial position of the sections starting from the cylinder axis. Point 'M' represents the PMM and point 'C' the geometrical centre of the data points marked with numbers.

The resulting points are mostly concentrated near the bottom line, between the lower right corner and the central vertical line of the diagram. The average D_{cent} seemingly decreases with increasing linear charge concentration (Table 20), similarly as for the CTt (see Table 18).

Table 20: Measured scatter of the topological results D_{cent} for the CTnp.

Material	Blast test	Charge [g/m]	Centroid point			D_{cent}		
			Tb	I	Jint	Max	Ave	Std
Mortar	23.1	20	6.9	55.3	37.9	19.3	7.3	4.45
	21	12	7.0	67.0	26.0	52.1	9.4	12.34
	23.2	6	16.2	42.5	41.3	19.1	9.7	5.37
Granite	28.1	12	5.3	41.0	53.8	10.7	5.5	3.06
	26.1	6	8.8	55.2	36.0	11.9	6.7	3.29

However, the statistical analysis of D_{cent} in CTnp indicates no significant difference (Table 21).

Table 21: Statistical evaluation of average D_{cent} in CTnp with One-way ANOVA ($\alpha = 0.05$).

Variable	Ave	Std	Data count	F	F_{crit}	p-value	Sign. diff.
m20(23.1)	7.32	4.45	12	0.79	2.54	0.54	No
m12(21)	9.41	12.34	14				
m6(23.2)	9.71	5.37	12				
g12(28.1)	5.46	3.06	11				
g6(26.1)	6.72	3.29	11				

5.3.3 Average number of connections per line (C_L) and per branch (C_B)

Figure 101 shows an example of how the average number of connections per line (C_L [-]) and per branch (C_B [-]) change with time in the HSI (see Section 4.1.5).

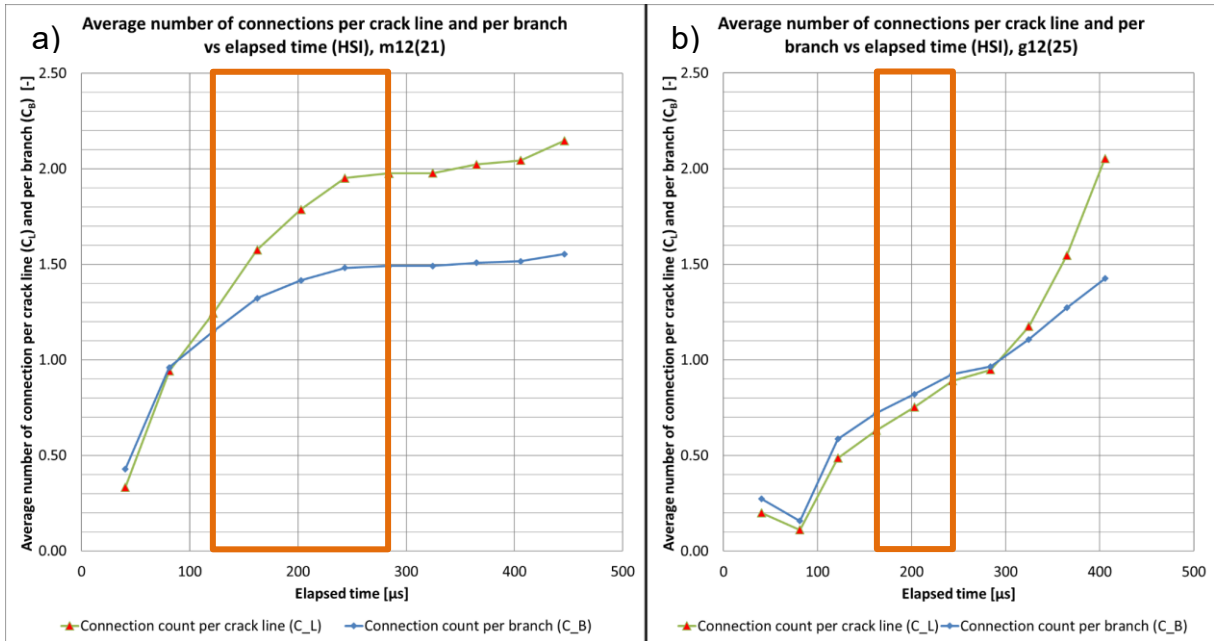


Figure 101: Average number of connections per line (C_L) and per branch (C_B) concerning time elapsed from the detonation (HSI): a) m12(21); b) g12(25). The orange box marks the second fracture phase.

In all HSI, the C_L and C_B curves have (about) the same initial values and firstly increase at about the same rate (like N_L and N_B , see Appendix 9). Then, C_L continues to increase at a higher rate. In some cases (for m6(22.2), m12(20), m12(21), m20(22.1), and g12(24)), at least one of the curves levels out in the second fracture phase (Figure 101a).

Figure 102 shows the measured values of C_L and C_B in the CTt. These plots indicate that the result data scatter less (i.e., the respective interquartile ranges (IQR) are narrower) with increasing linear charge concentration.

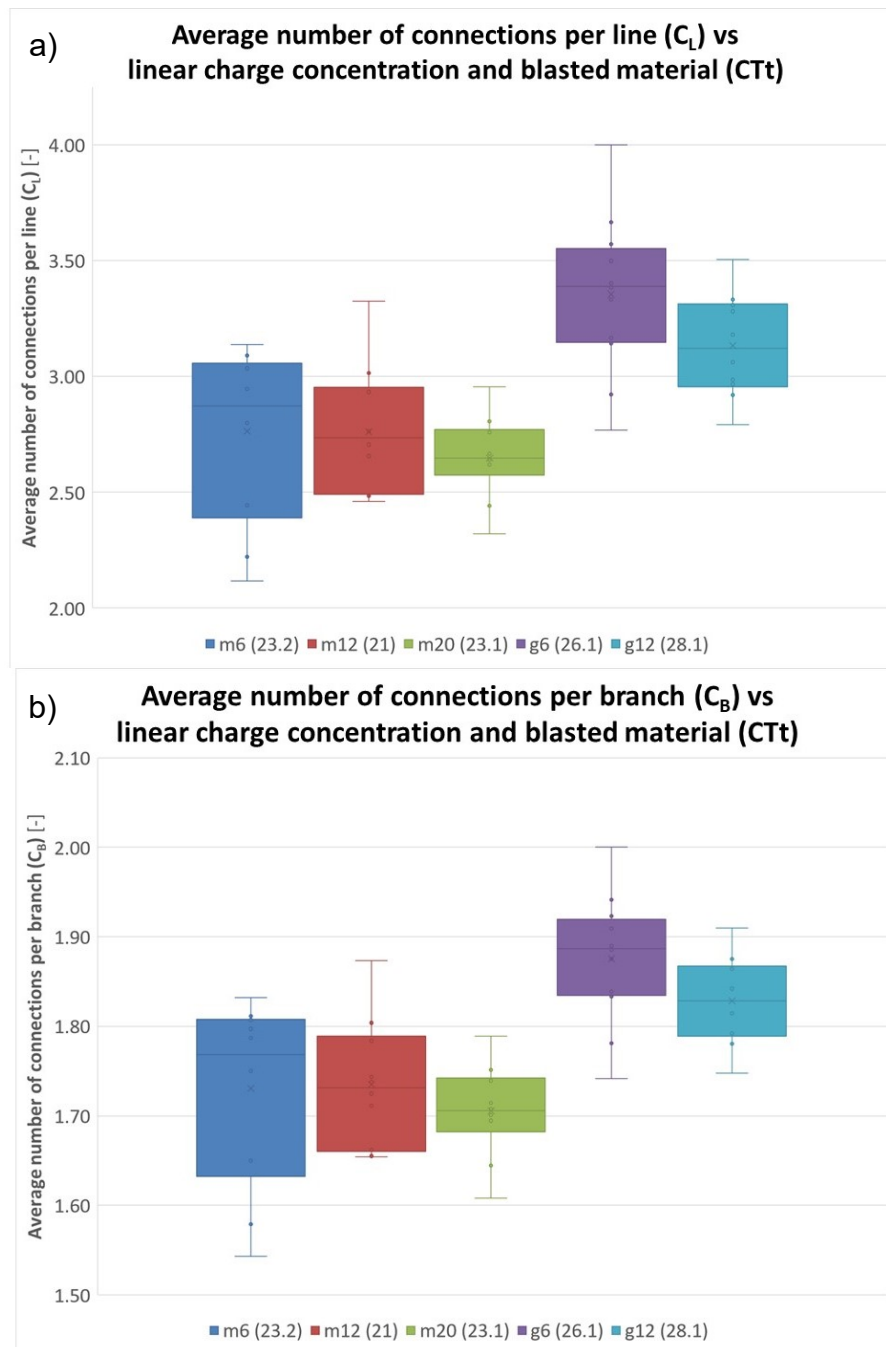


Figure 102: Summary of the average number of connections:
a) per line (C_L) in the CTt; b) per branch (C_B) in the CTt.

The C_L and C_B are larger in the granite than in the mortar and that they do not change significantly by changing the linear charge concentration (see Table 124, Table 125, and Table 127).

Table 22 shows a summary of C_L and C_B in CTt (average values) and PMI (or the last traced HSI before the spalling).

Table 22: Summary of C_B and C_L in CTt and PMI (or the last traced HSI).

Material	I_c [g/m]	Blast test	C_B	C_L	Source
Mortar	6	22.2	1.79	2.94	PMI
		23.2	1.77	2.89	PMI
			1.73	2.76	CTt
	12	20	1.69	2.63	PMI
		21	1.78	2.94	PMI
			1.74	2.76	CTt
	20	22.1	1.69	2.89	PMI
		23.1	1.87	3.45	PMI
			1.71	2.65	CTt
Granite	6	26.1	1.92	4.02	PMI
			1.88	3.35	CTt
		27	1.93	5.90	PMI
	12	24	1.03	1.05	HSI (324.48 μ s)
		25	1.43	2.05	HSI (405.6 μ s)
		28.1	1.83	3.13	CTt
	20	26.2	1.47	1.96	HSI (243.36 μ s)

5.3.4 Node-connectivity probabilities (p_l and p_c)

Figure 103 shows an example of how node-connectivity probabilities (see Section 4.1.5) develop with time in the HSI.

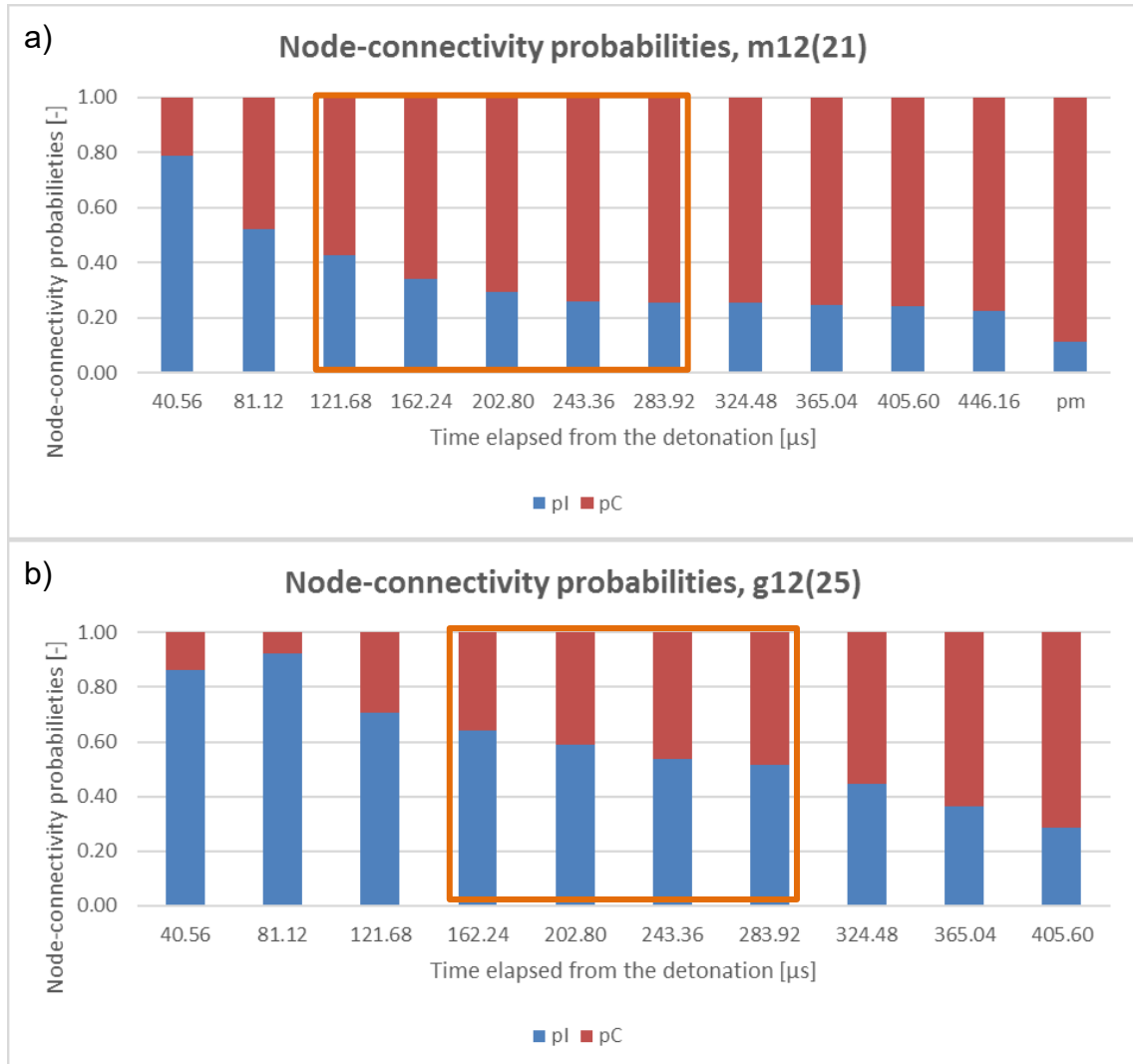


Figure 103: Development of node-connectivity probabilities (p_l and p_c) in the HSI: a) m12(21); b) g12(25). The orange box marks the second fracture phase.

The probability of a node being connected (p_c) increases with time. This increase often follows a non-linear trend (Figure 104). However, like for C_L and C_B and N_L and N_B (see Section 5.3.3 and Appendix 9), this trend could be bilinear with the curve gradient changing between the first two fracture phases (see Section 5.1).

The slopes of the linear-regression lines of both p_l and p_c do not significantly differ considering the blasted material (see Table 131). The slopes for p_l decrease, whilst for p_c they increase, with increasing linear charge concentration (see Table 130 and Table 172).

Figure 104 also shows a linear-regression fit in the time range of the second fracture phase.

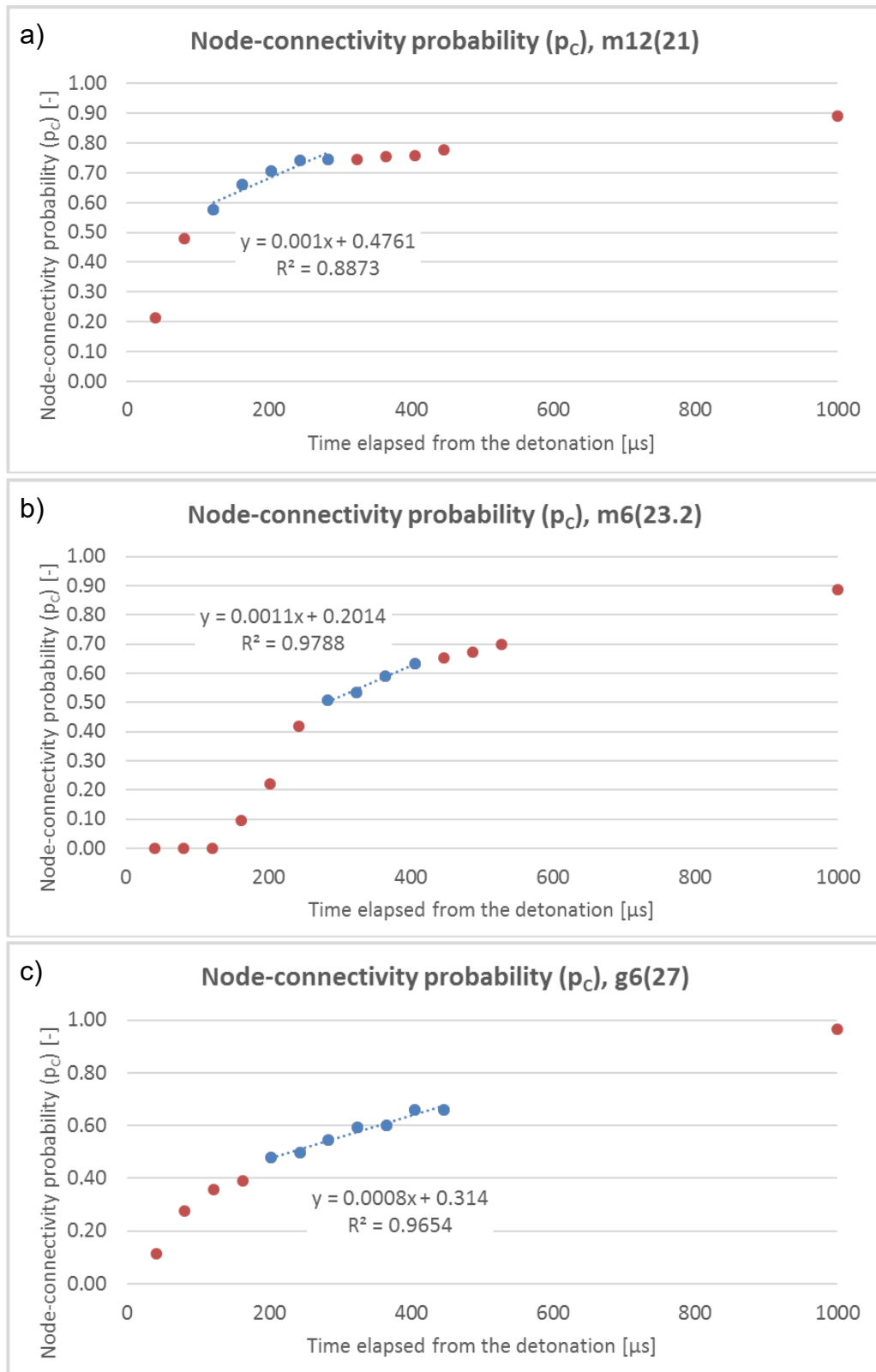


Figure 104: Development of node-connectivity probability (p_c) in the HSI: a) m12(21); b) m6(23.2); c) g6(27). The data points of the second fracture phase are marked blue.

Table 23 shows a summary of the estimated curve slopes of p_c in the second fracture phase.

Table 23: Summary of the estimated p_c slopes in the second fracture phase of the HSI.

Blast test	I_c [g/m]	Slope	Std. error	Data	R^2
22.2	6	4.52E-05	1.51E-04	4	0.0430
23.2		1.06E-03	1.10E-04	4	0.9788
20	12	1.00E-04	2.43E-04	4	0.0780
21		1.04E-03	2.13E-04	5	0.8873
22.1	20	-5.31E-04	2.68E-04	5	0.6621
23.1		2.17E-03	3.35E-04	5	0.9336
26.1	6	5.27E-04	2.20E-04	4	0.7415
27		8.08E-04	6.84E-05	7	0.9654
24	12	1.45E-03	6.39E-04	4	0.7197
25		1.03E-03	1.31E-04	4	0.9690
26.2	20	2.73E-03	3.75E-04	4	0.9637

The linear-regression slopes for p_i and for p_c , in the second fracture phase (see Section 5.1), do not significantly differ to each other, both considering the blasted material and the linear charge concentration (see Table 136).

Table 24 shows a summary of p_i and p_c in the CTt (average values) and PMI (or the last traced HSI before the spalling).

Table 24: Summary of p_i and p_c in CTt and PMI (or the last traced HSI).

Material	I_c [g/m]	Blast test	p_i	p_c	Source
Mortar	6	22.2	0.107	0.893	PMI
		23.2	0.114	0.886	PMI
			0.135	0.865	CTt
	12	20	0.156	0.844	PMI
		21	0.110	0.890	PMI
			0.132	0.868	CTt
	20	22.1	0.154	0.846	PMI
		23.1	0.064	0.936	PMI
			0.147	0.853	CTt
Granite	6	26.1	0.041	0.959	PMI
			0.062	0.938	CTt
		27	0.035	0.965	PMI
	12	24	0.487	0.513	HSI (324.48 μ s)
		25	0.287	0.713	HSI (405.6 μ s)
		28.1	0.086	0.914	CTt
		20	26.2	0.264	0.736

The plots of the node-connectivity probability p_c in the CTt (Figure 105) show relations between the average values like those for C_L and C_B in Figure 102.

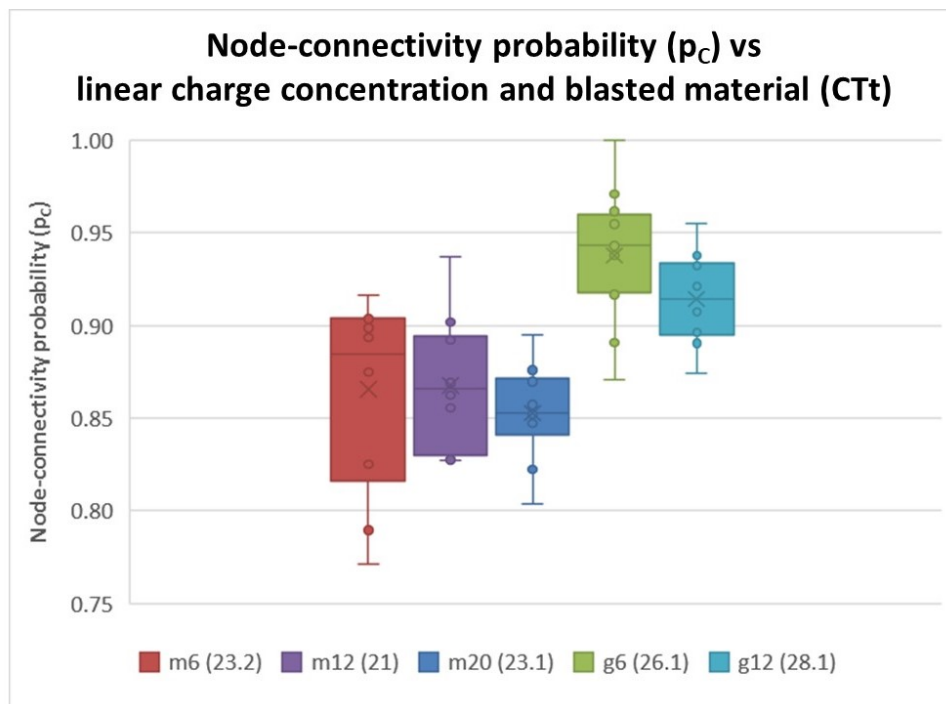


Figure 105: Summary of the node-connectivity probability (p_c) in the CTt.

The probability p_c is higher in the granite than in the mortar. The scatter (IQR) of the result data decreases with increasing linear charge concentration. The average value of p_c does not significantly change with increasing linear charge concentration (see also Table 140).

5.3.5 Fracture abundance - areal frequency (p_{20}) and fracture intensity (p_{21})

Areal frequency p_{20} and fracture intensity p_{21} (see Section 4.1.6) were calculated based on the trace images of HSI, PMI, and CTt. Results on dimensionless fracture intensity p_{22} are provided in Appendix 9.

These values increase over time in the HSI and then, in most cases, drop in the PMI and the CTt (Figure 106 and Figure 107).

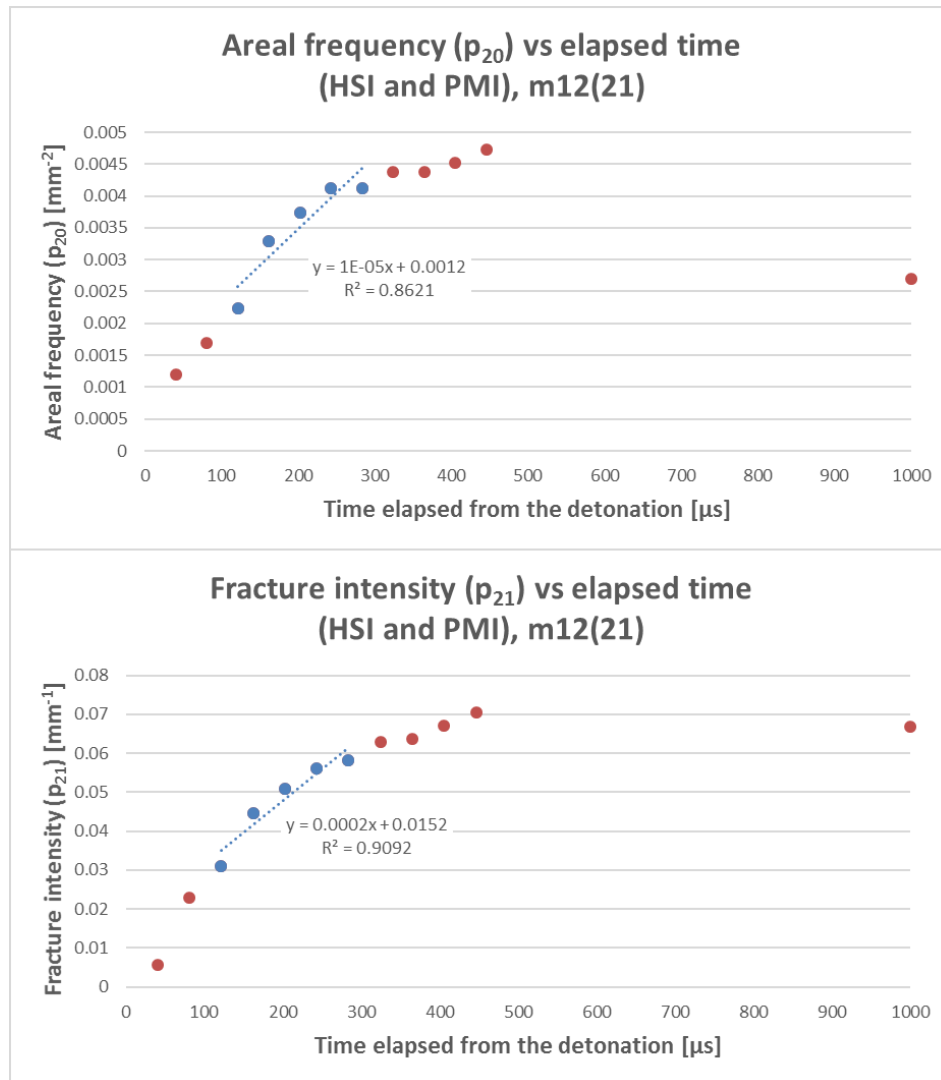
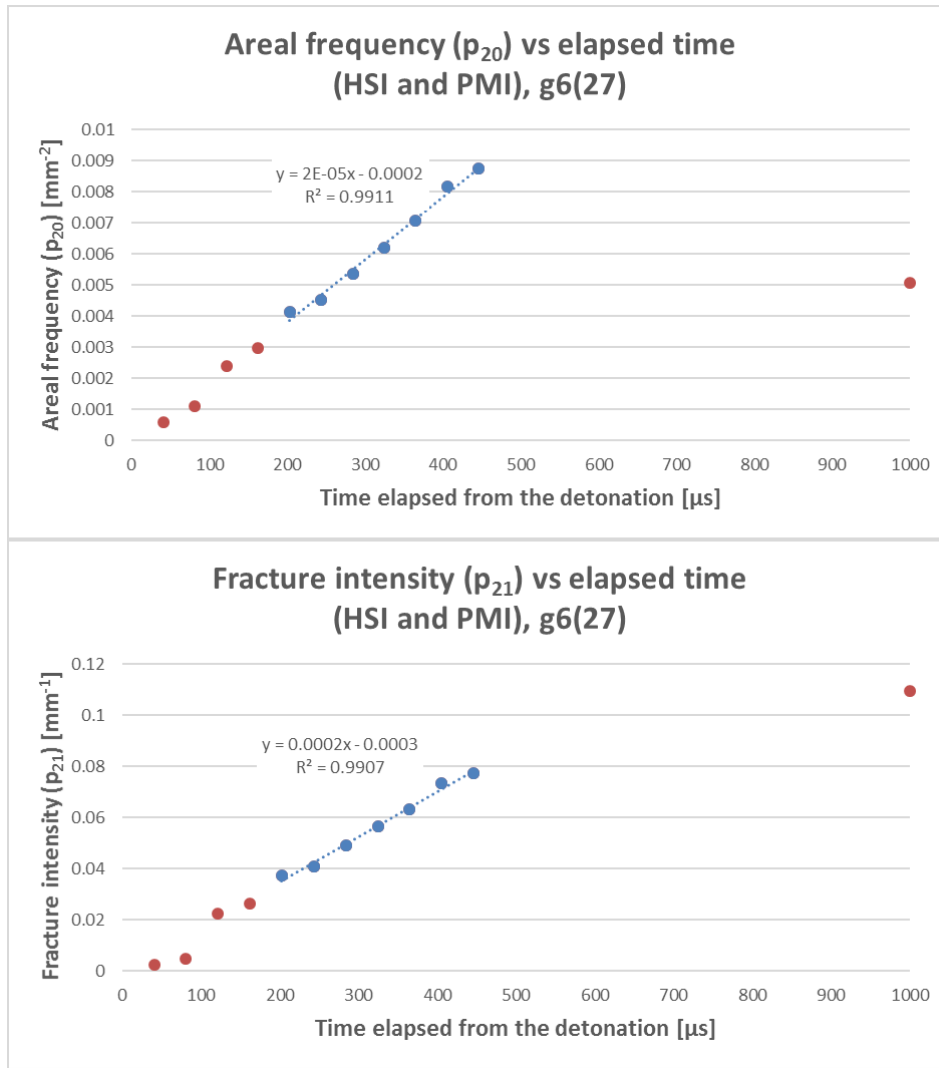


Figure 106: Fracture abundance (p_{20} and p_{21}) in HSI and PMI (m12(21)). The data points of the second fracture phase are marked blue.



**Figure 107: Fracture abundance (p_{20} and p_{21}) in HSI and PMI (g6(27)).
The data points of the second fracture phase are marked blue.**

The trend of the value increase in the HSI is bilinear in most cases, similarly as for p_i and p_c (see Section 5.3.4). The bilinear trend of these curves reflects a kink (i.e., change in the gradient) between the first two fracture phases (see also Appendix 9). The occasional value jumps and drops in the graphs (see also Figure 242) can be attributed to a possible measurement/detection error given the relatively coarse spatial and temporal resolutions of the HSI.

Table 25 shows a summary of the estimated curve slopes of p_{20} and p_{21} in the second fracture phase.

Table 25: Summary of estimated fracture abundance (p_{20} and p_{21}) regression-line slopes in the second fracture phase of the HSI.

Material	I_c [g/m]	Blast test	Data	p_{20}		p_{21}	
				Slope	R^2	Slope	R^2
Mortar	6	22.2	4	7.4E-07	0.900	8.3E-06	0.979
		23.2	4	5.4E-06	0.750	1.1E-04	0.999
	12	20	4	8.1E-06	0.993	1.0E-04	0.999
		21	5	1.1E-05	0.862	1.6E-04	0.909
	20	22.1	5	1.2E-05	0.998	1.4E-04	0.990
		23.1	5	1.2E-05	0.960	3.1E-04	0.982
Granite	6	26.1	4	1.2E-05	0.984	1.3E-04	0.997
		27	7	2.0E-05	0.991	1.8E-04	0.991
	12	24	4	9.8E-05	0.966	4.9E-04	0.977
		25	4	6.0E-05	0.977	4.3E-04	0.988
	20	26.2	2	5.4E-05		7.0E-04	

The statistical evaluation of the linear-regression slopes of the p_{20} and p_{21} data (Table 145) indicates that the slopes are significantly different from each other, both considering the blasted material and the linear charge concentration. On average, the slopes become steeper with increasing linear charge concentration, and they are steeper in the granite than in the mortar.

Table 26 shows a summary of the fracture-abundance results in CTt (average values) and PMI (or the last traced HSI before the spalling).

Table 26: Summary of the fracture-abundance (p_{20} and p_{21}) results.

Material	I_c [g/m]	Blast test	p_{20} [mm ⁻²]	p_{21} [mm ⁻¹]	Source
Mortar	6	22.2	0.0009	0.023	PMI
			0.0012	0.019	HSI (405.60 μ s)
		23.2	0.0009	0.024	PMI
			0.0028	0.033	HSI (527.28 μ s)
			0.0016	0.032	CTt
		12	20	0.0011	0.028
	0.0017			0.029	HSI (486.72 μ s)
	21		0.0027	0.067	PMI
			0.0047	0.070	HSI (446.16 μ s)
			0.0033	0.067	CTt
			0.0033	0.067	CTt
	20	22.1	0.0076	0.078	PMI
			0.0030	0.045	HSI (324.48 μ s)
		23.1	0.0054	0.101	PMI
			0.0052	0.089	HSI (446.16 μ s)
0.0036			0.074	CTt	
0.0036			0.074	CTt	
Granite	6	26.1	0.0045	0.065	PMI
			0.0058	0.058	HSI (527.28 μ s)
			0.0008	0.022	CTt
		27	0.0051	0.109	PMI
			0.0088	0.077	HSI (446.16 μ s)
			0.0088	0.077	HSI (446.16 μ s)
	12	24	0.0279	0.136	HSI (324.48 μ s)
		25	0.0159	0.147	HSI (405.60 μ s)
		28.1	0.0030	0.065	CTt
	20	26.2	0.0078	0.087	HSI (243.36 μ s)

These fracture-abundance parameters in the CTt increase with the linear charge concentration (Figure 108). Parameters p_{20} and p_{21} are lower in the granite than in the mortar for 6 g/m and about the same for the linear charge concentration of 12 and 20 g/m in both blasted materials (see also Table 147, Table 148, and Table 150).. Parameter p_{22} is independent of the linear charge concentration.

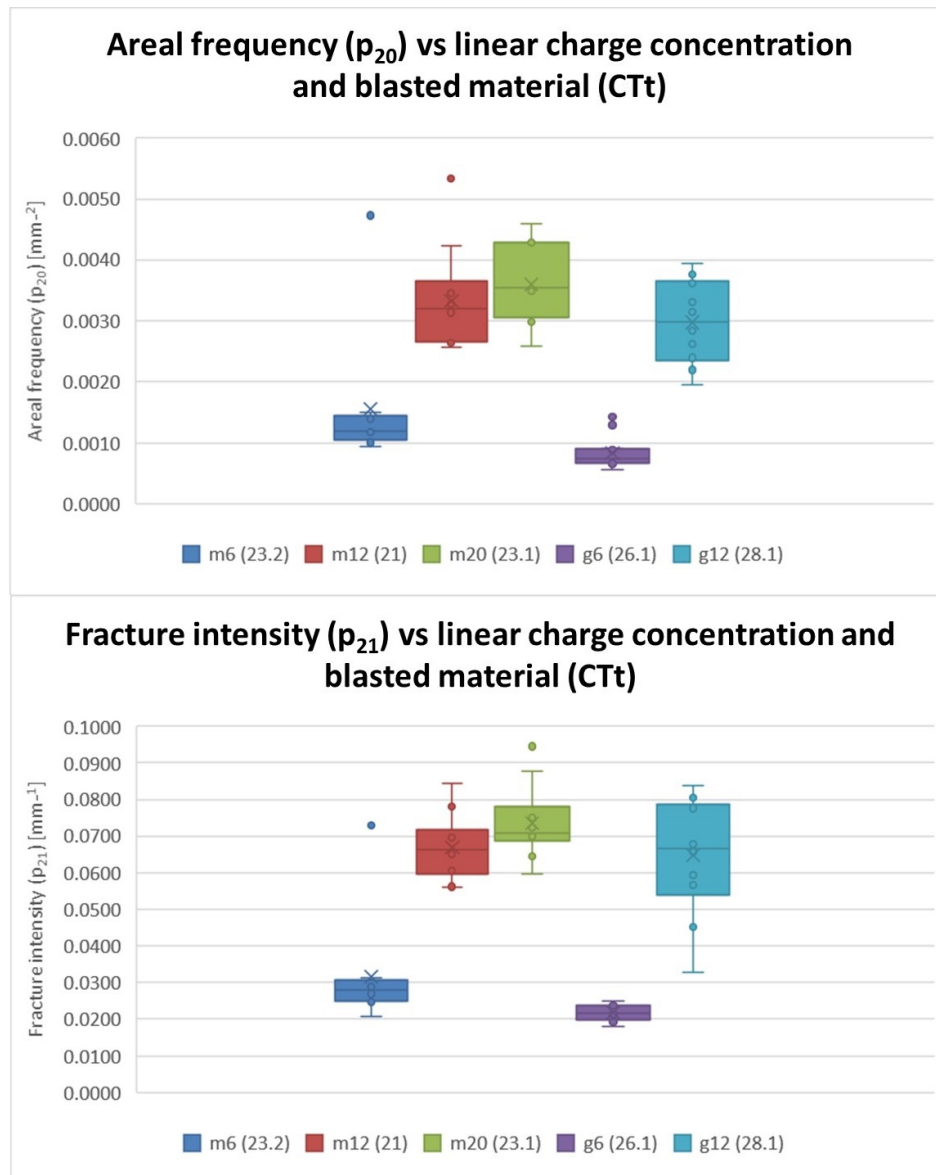


Figure 108: Summary of the calculated fracture abundance parameters (p_{20} and p_{21}) in the CTt.

5.4 In-plane (2D) fragmentation

The traced crack patterns were also used to analyse in-plane (2D) fragmentation (see Section 4.1.7) in the HSI, CTt, CTnp, and the PMI (where possible).

Figure 109 shows an example of fragment-count development over time in HSI. In most cases, the 2D-fragment count linearly increases with elapsed time.

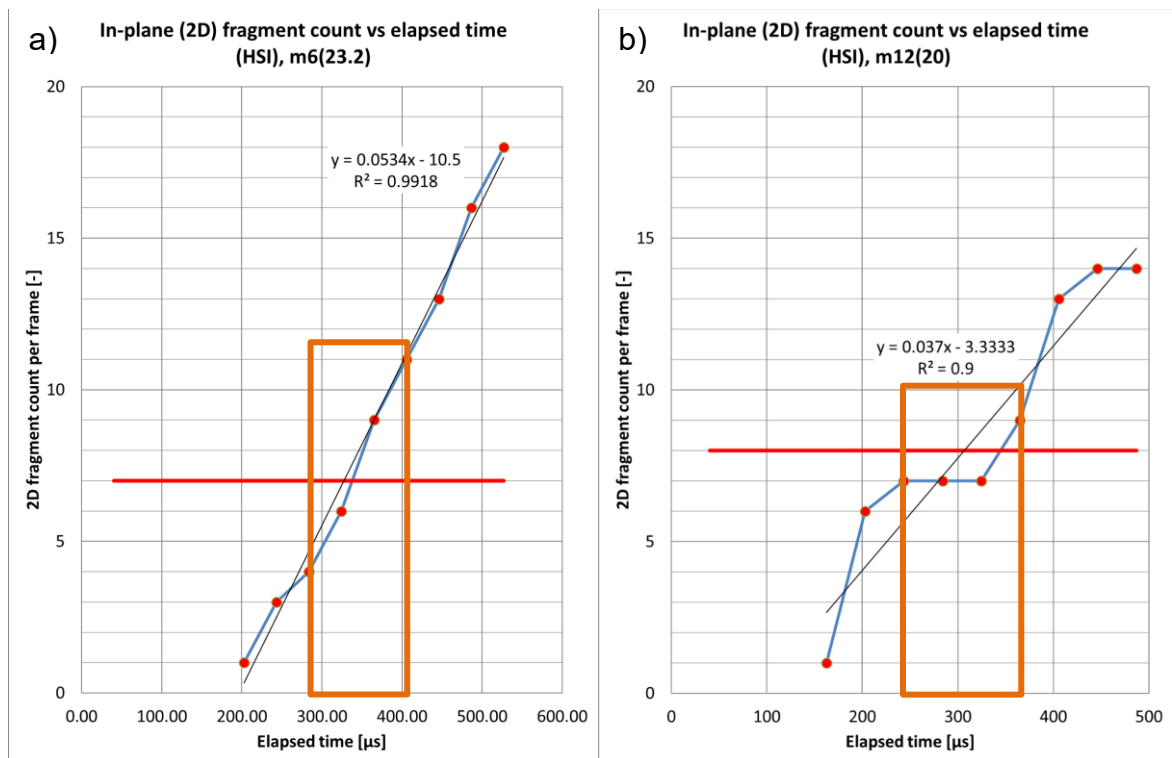


Figure 109: Total in-plane (2D) fragment count in the HSI: a) m6(23.2); b) m12(20). The red horizontal line shows the count value in the corresponding PMI. The orange box marks the second fracture phase.

In some cases (for m12(21), g6(26.1), and g12(25)), this curve shows a non-linear trend with an elapsed time (Figure 110). This non-linear trend could again be considered linear with a kink (i.e., change in the gradient) between the first two fracture phases (see Section 5.1).

These results also show occasional mismatching of HSI crack patterns with those in the PMI (see also Appendix 9). This is the case for m12(20), m12(21), and m6(23.2). Here, the fragment count exceeds that in the corresponding PMI.

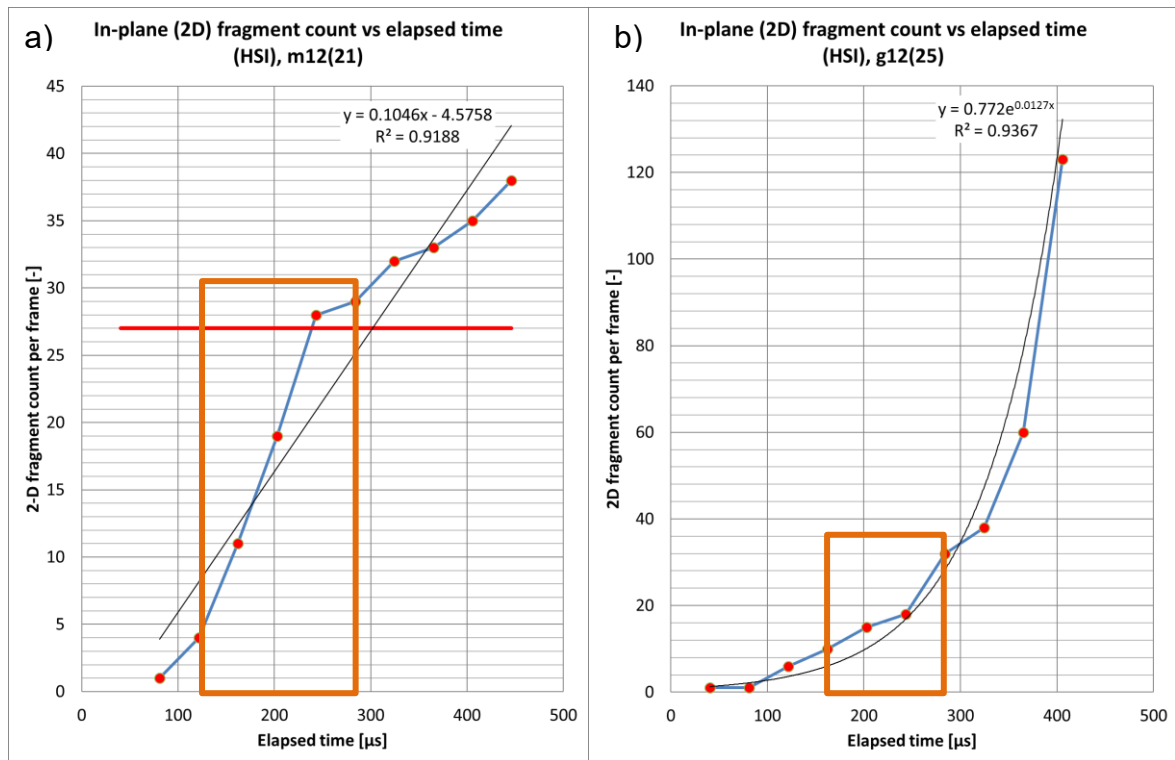


Figure 110: Total in-plane (2D) fragment count in the HSI: a) m12(21); b) g12(25). The red horizontal line shows the count value in the corresponding PMI. The orange box marks the second fracture phase.

The linear-regression lines fitted to these data are mostly significantly different to each other (see Table 151, Table 152, Table 153, and Table 154). The slopes of the linear-regression lines of the complete data sets (Table 27) indicate that, on average, the slope (gradient) increases with increasing linear charge concentration and that it is larger in the granite than in the mortar. However, even for the same linear charge concentration and blasted material, some lines are significantly different to each other.

Table 27: Summary of the slopes of the linear-regression lines for 2D-fragment count in HSI with 95%-confidence limits.

Variable	Slope	lower	upper
m6(22.2)	0.014	-0.244	0.271
m6(23.2)	0.053	-0.204	0.311
m12(20)	0.037	-0.221	0.295
m12(21)	0.105	-0.151	0.360
m20(22.1)	0.038	-0.230	0.306
m20(23.1)	0.147	-0.121	0.415
g6(26.1)	0.081	-0.170	0.332
g6(27)	0.112	-0.143	0.367
g12(24)	0.660	0.392	0.929
g12(25)	0.297	0.039	0.555
g20(26.2)	0.323	0.199	0.447

Such cases are even more pronounced when observing just the data from the second fracture phase in the HSI (Table 28).

Table 28: Summary of the slopes of the linear-regression lines for 2D-fragment count for the second fracture phase in HSI with 95%-confidence limits.

Variable	Slope	<i>lower</i>	<i>upper</i>
m6(22.2)	0.007	-0.174	0.189
m6(23.2)	0.059	-0.123	0.241
m12(20)	0.015	-0.167	0.197
m12(21)	0.165	-0.002	0.333
m20(22.1)	0.039	-0.142	0.221
m20(23.1)	0.153	-0.015	0.320
g6(26.1)	0.086	-0.096	0.268
g6(27)	0.158	0.001	0.315
g12(24)	0.782	0.600	0.963
g12(25)	0.170	-0.012	0.352
g20(26.2)	0.414	0.339	0.490

Figure 111 shows the total 2D-fragment count in the CTt.

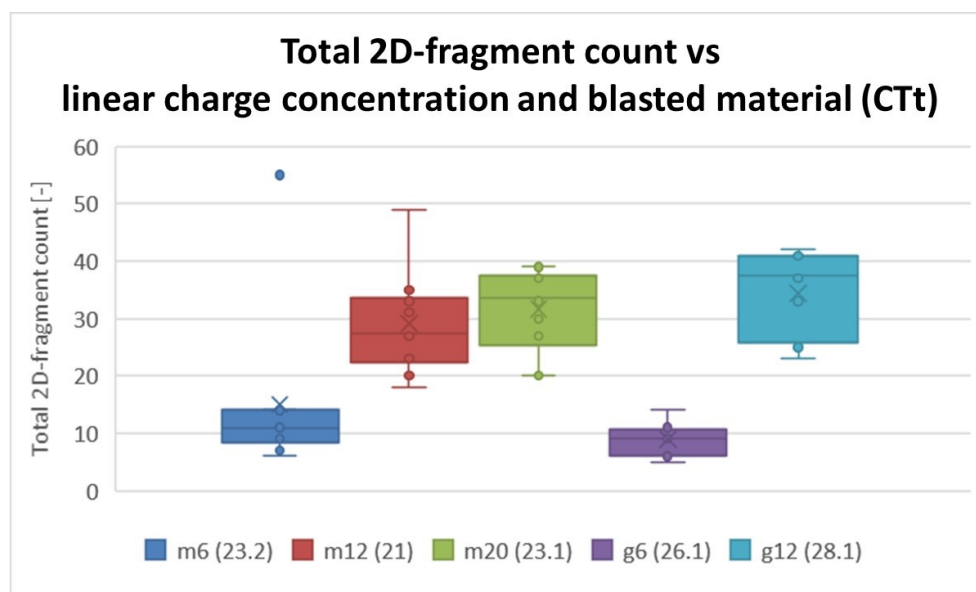


Figure 111: Summary of the total 2D-fragment count in CTt.

The scatter (IQR) of the result data increases with increasing linear charge concentration. It is about the same in both blasted materials. The total 2D-fragment count increases by increasing the linear charge concentration from 6 g/m to 12 g/m, though it stays about the same with a further increase to 20 g/m (see Table 155, Table 156, and Table 157).

The CTnp images show that the total 2D-fragment count stays about the same except near the blast hole (Figure 112).

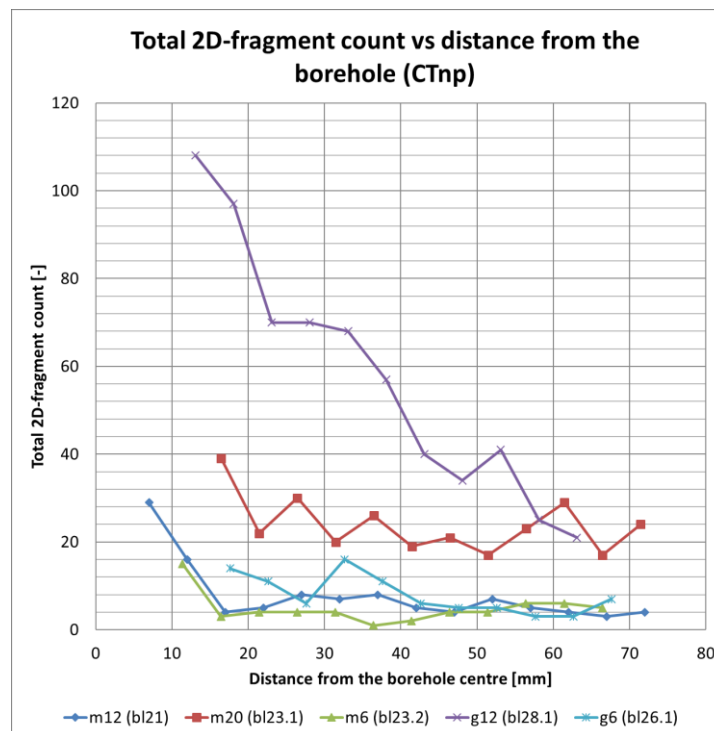


Figure 112: Total 2D-fragment count concerning radial distance from the cylinder axis in CTnp.

The only exception to this is from g12(28.1). Here, the count seems to linearly drop with the radial distance from the blast hole (i.e., from the centre of the initial borehole or the axis of the blast cylinder).

The 2D-fragment count is not affected by the linear charge concentration and it is larger in the granite than in the mortar (see Table 158).

Figure 113 and Figure 114 show ternary diagrams of 2D-fragment proportions (see Section 4.1.7) in the HSI and the PMI in the mortar and in the granite, respectively.

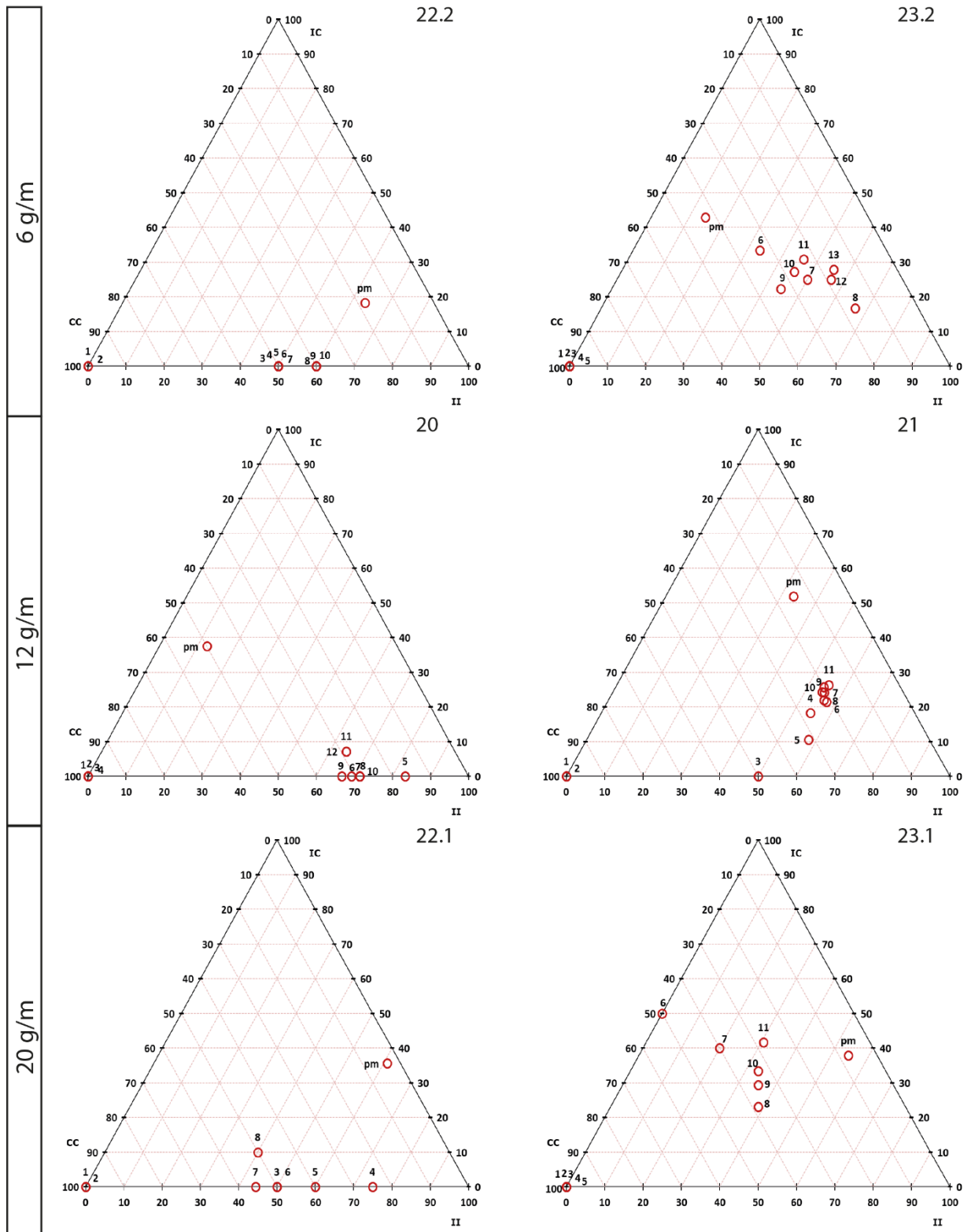


Figure 113: In-plane 2D-fragment proportions (set of ternary diagrams) of the HSI and the PMI in the mortar. Orange circles represent the HSI with numbers indicating their time sequence with time steps of 40.56 μ s and 'pm' representing the PMI.

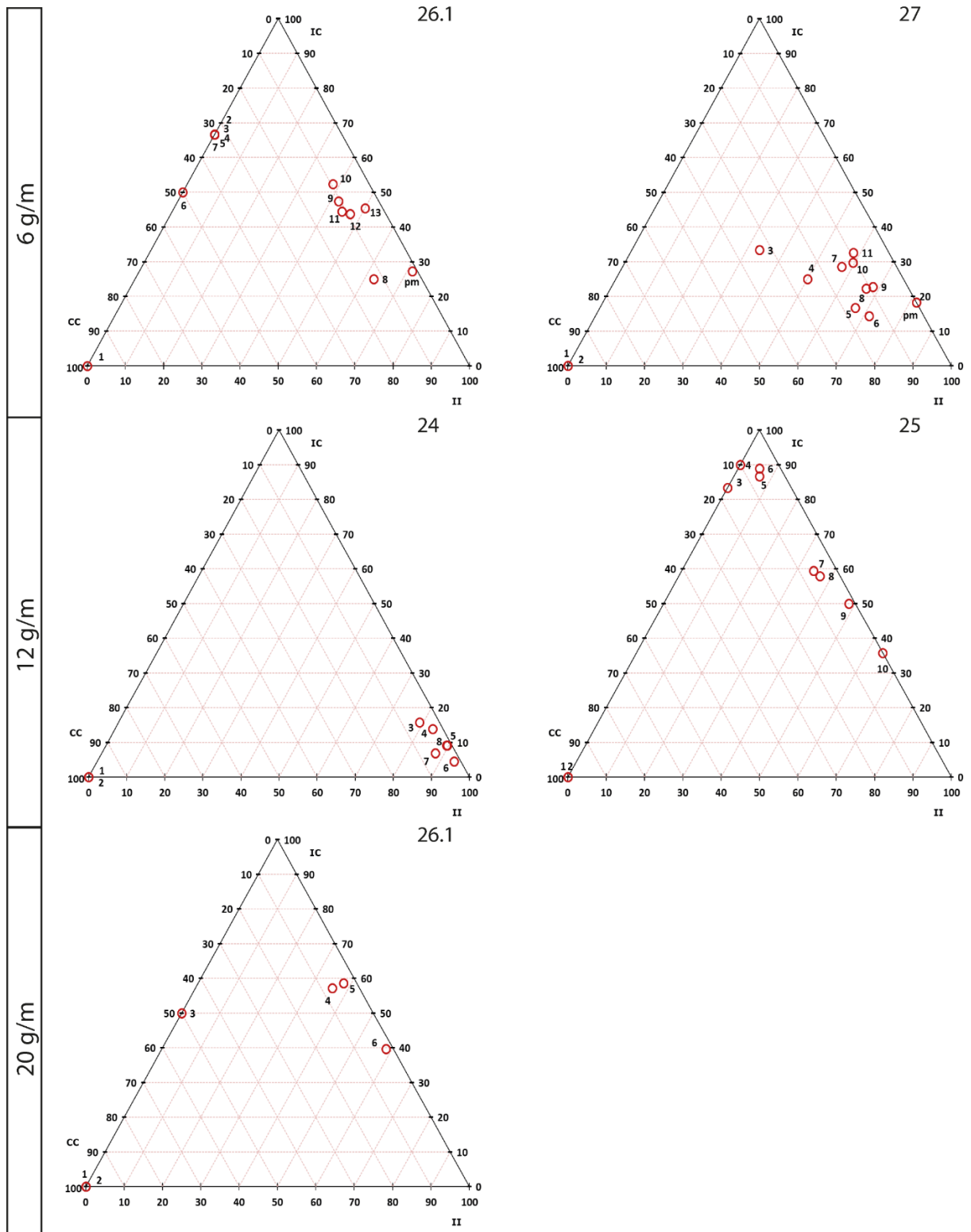


Figure 114: In-plane 2D-fragment proportions (set of ternary diagrams) of the HSI and the PMI in the granite. Orange circles represent the HSI with numbers indicating their time sequence with time steps of 40.56 μ s and 'pm' representing the PMI.

The HSI start with a single major 2D fragment (100% CC). Then, the proportion of isolated (II) and semi-connected (IC) fragments increase. In the mortar, this development usually leads towards the centre of the ternary diagram. This development

in the granite usually leads toward the right side of the diagram (>70% II). Figure 115 shows ternary diagrams of 2D-fragment proportions in the CTt.

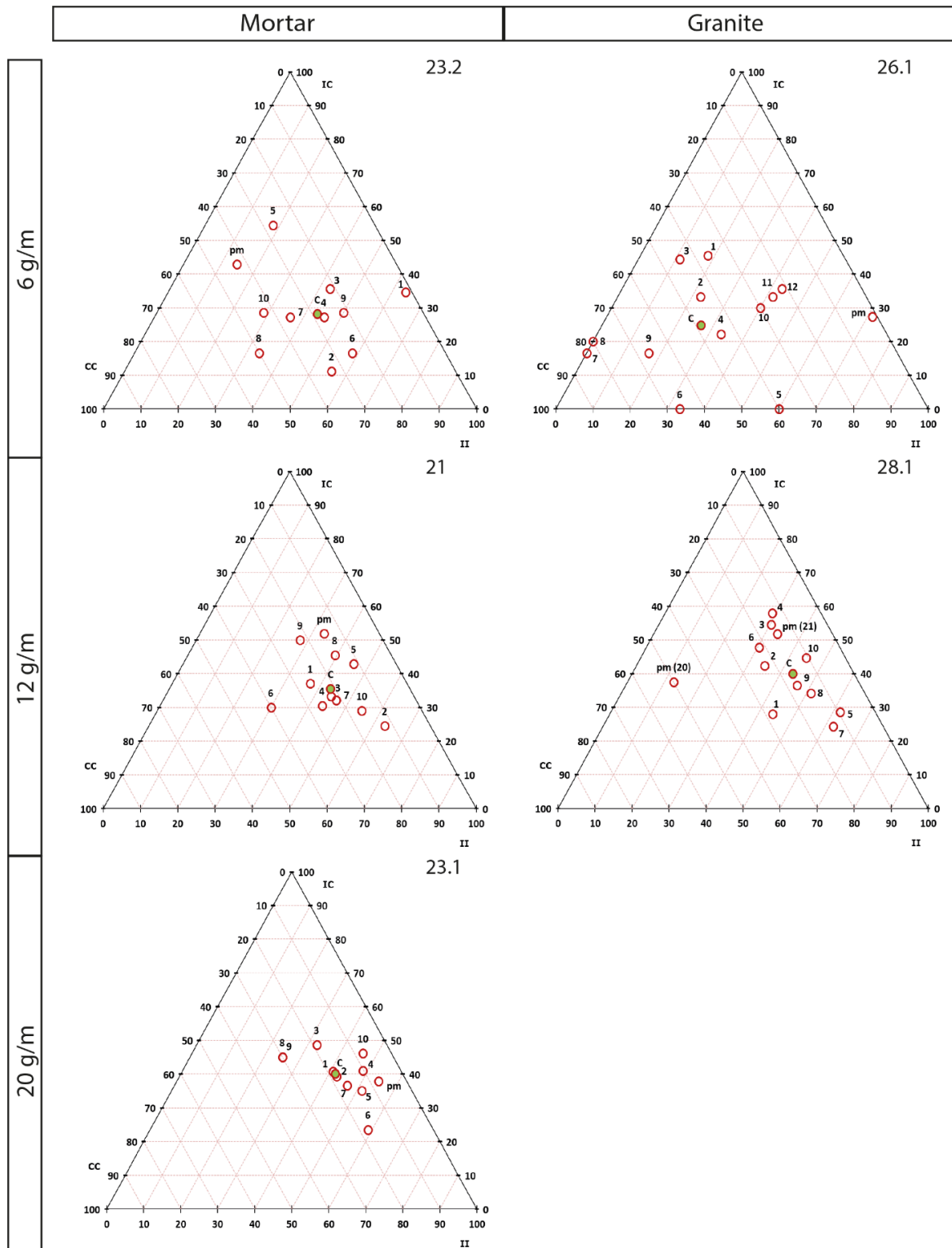


Figure 115: In-plane 2D-fragment proportions (set of ternary diagrams) from CTt. The data points are marked with numbers that indicate the sequence in the axial position of the sections starting from the rear end face. Point 'pm' represents the post-mortem state at the frontal end face and point 'C' the geometrical centre of the data points marked with numbers.

Table 29 shows a summary of the data scatter in the ternary diagrams (D_{cent}) of the 2D-fragment proportions in the CTt.

Table 29: Measured scatter of the 2D-fragment proportions in the CTt.

Material	Blast test	I_c [g/m]	Centroid point			D_{cent}		
			Tb	I	Jint	Max	Ave	Std
Mortar	23.1	20	40	42	18	18.78	9.11	5.70
	21	12	35	43	21	18.22	9.90	5.48
	23.2	6	28	43	29	28.97	14.41	8.02
Granite	28.1	12	40	43	17	19.01	12.10	5.28
	26.1	6	25	27	49	32.50	20.81	8.01

The statistical results of D_{cent} show significant difference only considering those from blast test 26.1 (Table 30).

Table 30: Statistical evaluation of measured scatter D_{cent} of the 2D-fragment proportions in CTt with One-way ANOVA ($\alpha = 0.05$).

Variable	Ave	Std	Data count	F	F_{crit}	p-value	Sign. diff.
m6(23.2)	14.41	8.02	10	1.47	2.87	0.24	No
m12(21)	9.90	5.48	10				
m20(23.1)	9.11	5.70	10				
g12(28.1)	12.10	5.28	10				
m6(23.2)	14.41	8.02	10	5.52	2.57	0.001	Yes
m12(21)	9.90	5.48	10				
m20(23.1)	9.11	5.70	10				
g12(28.1)	12.10	5.28	10				
g6(26.1)	20.81	8.01	12				

The scatter increases by decreasing the blast charge and it is larger in the granite than in the mortar.

5.5 Crack-propagation speed

Figure 116 shows selected results of measured crack-propagation speed (see Section 4.1.9) per frame in HSI.

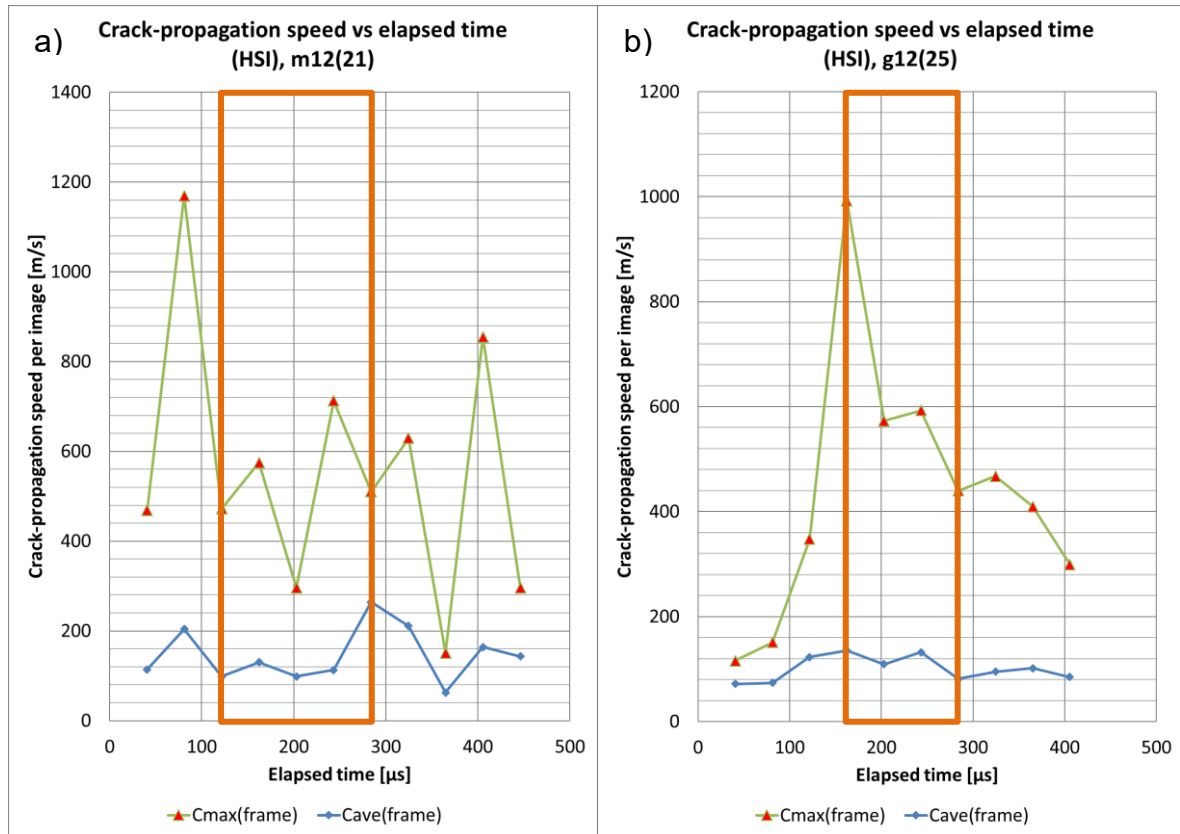


Figure 116: Maximum crack-propagation speed per frame (HSI): a) m12(21); b) g12(25). The graphs show maximum (C_{max}) and average (C_{ave}) values. The orange box marks the second fracture phase.

The plots of maximum crack-propagation speed per frame throughout a whole filming sequence often show local peaks that could be related to the fracturing phases and the occurring crack branching/merging (Kukolj et al., 2018a). The second fracture phase (see Section 5.1) covers the increase of the crack branching/merging until the end-face spalling in the third fracture phase. This increase leads to more crack extensions per traced image and, hence, a potential change in the C_{max} and C_{ave} curves. However, such peaks could also be related to the relatively coarse temporal resolution of the HSI.

Figure 117 shows an overview of the average values of the measured crack-propagation speed per blasted cylinder.

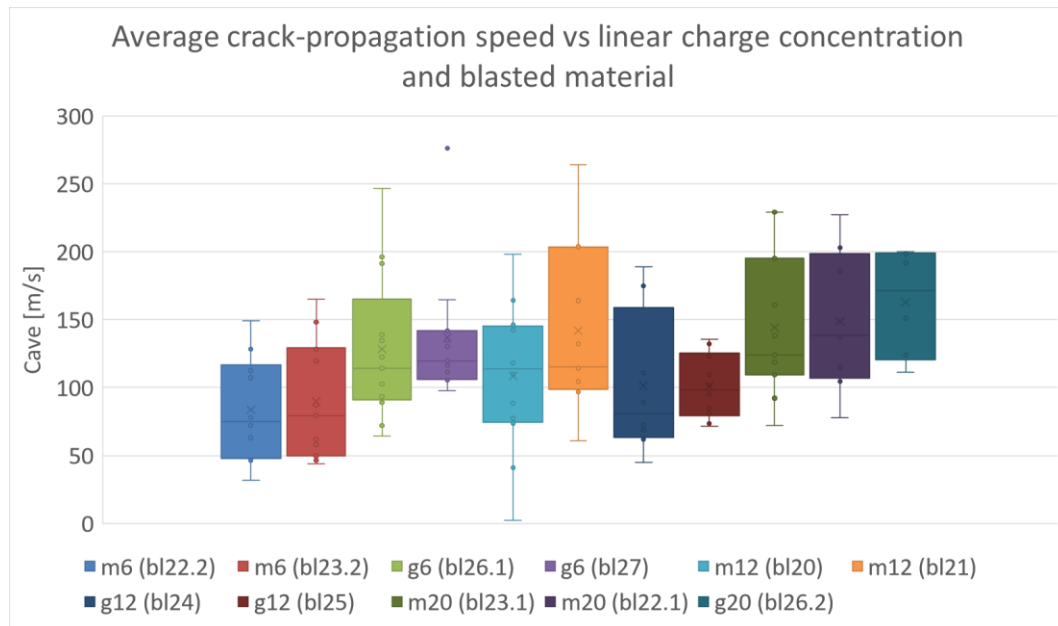


Figure 117: Summary of measured average crack-propagation speed (CTt).

Table 31 shows an overview of obtained average crack-propagation speed in the HSI.

Table 31: Overview of calculated average crack-propagation speed.

Variable	Ave	Std	Data count
22.2(m6)	83.6	38.9	10
23.2(m6)	89.8	43.0	13
20(m12)	108.7	55.1	12
21(m12)	141.8	60.5	11
23.1(m20)	144.4	53.0	11
22.1(m20)	148.7	51.8	8
26.1(g6)	128.3	53.4	13
27(g6)	136.6	50.1	11
24(g12)	101.4	53.3	8
25(g12)	100.8	23.6	10
26.2(g20)	162.8	39.5	6

The average crack-propagation speed does not significantly differ considering the blasted material (Table 33). The crack-propagation speed increases with increasing linear charge concentration up to 12 g/m in the mortar. All other measured values are about the same in both blasted materials (Table 32 and Table 33).

Table 32: Statistical evaluation of average crack-propagation speed in HSI with One-way ANOVA ($\alpha = 0.05$).

Variable	Ave	Std	Data count	F	F _{crit}	p-value	Sign. diff.
22.2(m6)	83.6	38.9	10	0.13	4.33	0.73	No
23.2(m6)	89.8	43.0	13				
20(m12)	108.7	55.1	12	1.65	2.06	0.12	No
21(m12)	141.8	60.5	11				
23.1(m20)	144.4	53.0	11				
22.1(m20)	148.7	51.8	8				
26.1(g6)	128.3	53.4	13				
27(g6)	136.6	50.1	11				
24(g12)	101.4	53.3	8				
25(g12)	100.8	23.6	10				
26.2(g20)	162.8	39.5	6				
All data							

Table 33: Statistical evaluation of average crack-propagation speed in HSI with Two-way ANOVA ($\alpha = 0.05$).

	SS	df	MS	F	p-value	Sign. diff.
Material	3612.7	1	3612.7	1.536	2.18E-01	No
I_c [g/m]	28625.8	2	14312.9	6.087	3.14E-03	Yes
Between groups	25508.1	2	12754.0	5.424	5.70E-03	Yes
Within groups	251591.3	107	2351.3			
Total	310911.0	112	2776.0			

5.6 Macro-mechanisms

Observed macro-mechanisms (see Table 7, Table 8, Table 9, and Table 10) were noted for each set of HSI that covers the whole frontal end face of blast cylinder. Figure 118 shows an example of observed HSI.

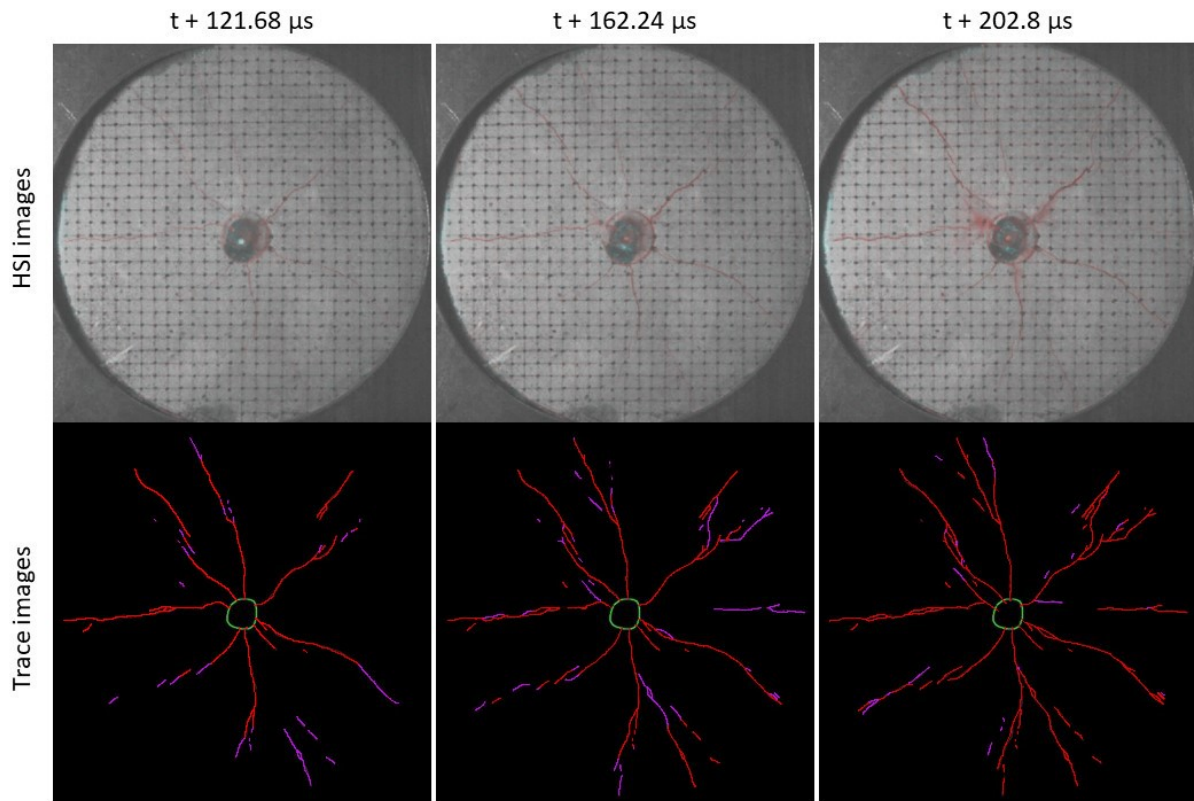


Figure 118: Excerpt from the HSI set (m12 (21)) of HSI images with fractures marked red and the corresponding trace images (green – blast-hole wall, red – cracks from the previous image, and violet – new cracks, extensions).

The sets consist of HSI with increased contrast and fractures in red colour and trace images with fractures from the previous image marked red and new fractures (extensions) marked purple. Figure 119 shows a trace image with extensions in a higher resolution.

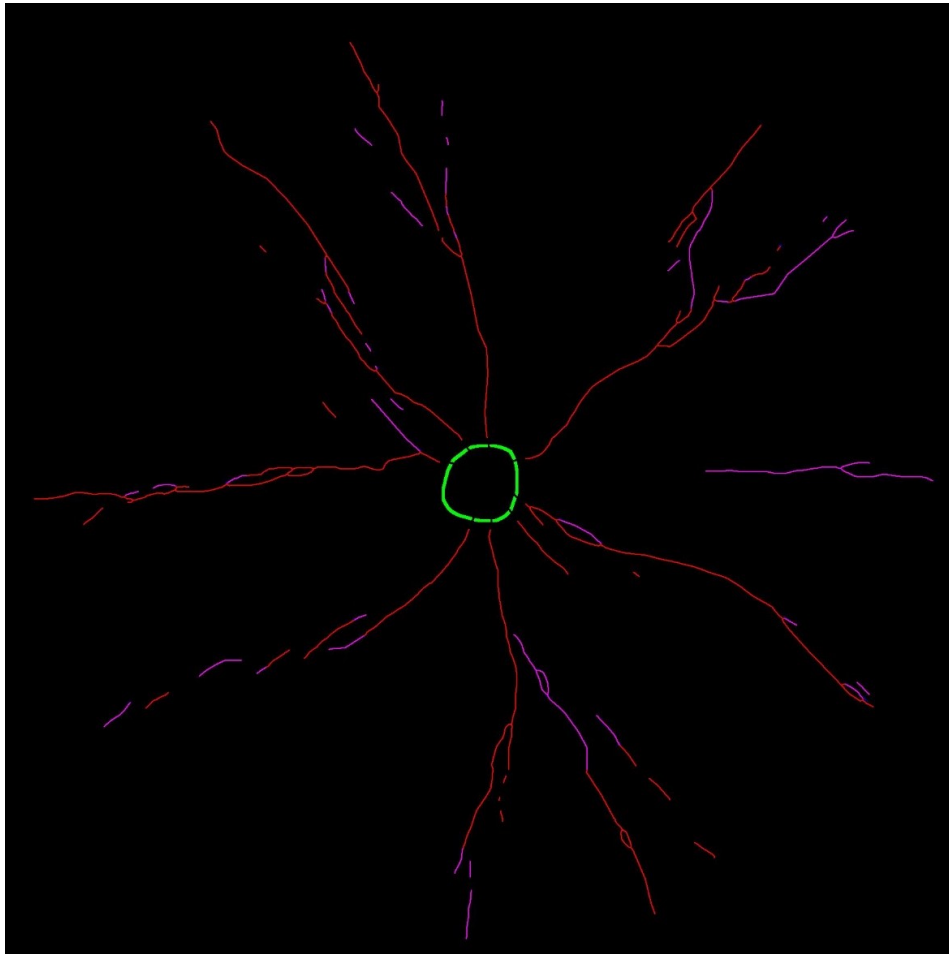


Figure 119: Example trace image with marked extensions - image 5 ($t+162.24 \mu\text{s}$), m12(21).

The trace images with extensions were used to note (probable) macro-mechanisms. Table 34 shows a summary of identified macro-mechanisms in the HSI set from blast test 21. All macro-mechanism data tables (i.e., event logs) are provided in Appendix 13.

Table 34: Summary of identified macro-mechanisms in HSI (m12(21)).

Elapsed time [μs]	Image	Propagation paths				Branching				Merging				Branching-merging			
		1.1	1.2	1.3	1.4	2.1	2.2	2.3	2.4	3.1	3.2	3.3	3.4	4.1	4.2	4.3	4.4
40.56	2	■	■														
81.12	3	■	■		■			■		■	■		■				
121.68	4	■	■			■		■					■	■			■
162.24	5	■	■			■		■			■		■	■			■
202.80	6	■					■	■			■		■				■
243.36	7	■					■				■						■
283.92	8	■						■	■							■	
324.48	9	■						■	■		■		■				
365.04	10	■				■							■				
405.60	11	■		■				■									■
446.16	12	■	■	■	■			■			■		■				

Mechanism notation:

- 1.1 – Crack extension ($l_{t,s}$)
- 1.2 – Discontinuous crack extension ($l_{t,si}$)
- 1.3 – Side crack arrest ($a-l_{t,s} \rightarrow Y_{m,sa}$)
- 1.4 – Side crack deflection ($d-l_{t,sk} \rightarrow Y_{m,sa}$)
- 2.1 – Primary in-line Y-branching ($l_{t,s} \rightarrow Y_{b,ps}$)
- 2.2 – Primary side Y-branching ($l_{t,s} \rightarrow Y_{b,pa}$)
- 2.3 – Secondary side Y-branching
- 2.4 – Secondary T-branching ($l_{t,s} \rightarrow T_{b,sp}$)
- 3.1 – Primary in-line Y-merging ($2l_{t,s} \rightarrow Y_{m,ps}$)
- 3.2 – Side Y-merging ($l_{t,s} \rightarrow Y_{m,sa}$)
- 3.3 – Secondary T-merging ($l_{t,s} \rightarrow T_{m,sp}$ or $l_{t,c} \rightarrow T_{m,sp}$)
- 3.4 – In-line merging ($l_{t,s} \rightarrow 0_{m,pi} \leftarrow l_{t,s}$)
- 4.1 – In-line 2Y-branching-merging ($l_{t,s} \rightarrow Y_{b,ps} + Y_{m,ps} \rightarrow l_{t,s}$)
- 4.2 – Double en-passant merging ($l_{t,c} \rightarrow T_{m,sp} + T_{m,sp} \leftarrow l_{t,c}$)
- 4.3 – En-passant tip deflection and merging ($l_{t,s} \rightarrow l_{t,ck} \rightarrow Y_{m,sa}$)
- 4.4 – Double en-passant tip deflection and merging ($l_{t,s} \rightarrow l_{t,ck} \rightarrow Y_{m,sa} + Y_{m,sa} \leftarrow l_{t,ck} \leftarrow l_{t,s}$)

In these tables, the macro-mechanisms are marked 1.1 through 4.4 according to Table 7, Table 8, Table 9, and Table 10 in Section 4.1.10. The result tables refer to HSI considering their original sequence number (image frame) in corresponding HSI set and the time elapsed from the detonation. All HSI sets are provided in Appendix 6. The elapsed time in the tables is also coloured to denote corresponding fracture phase (i.e., green for phase 1, yellow for phase 2, and red for phase 3). In each data row of the tables, the cells are coloured blue where a corresponding macro-mechanism was identified. The cells are coloured yellow where identification of a corresponding macro-mechanism was not clear.

For example, in the image in Figure 120, it is not clear if the macro-mechanisms shown by the arrows are 3.2 (side Y-merging, $I_{t,s} \rightarrow Y_{m,sa}$) or 2.3 (secondary side Y-branching, $I_{t,s} \rightarrow Y_{b,sa}$).

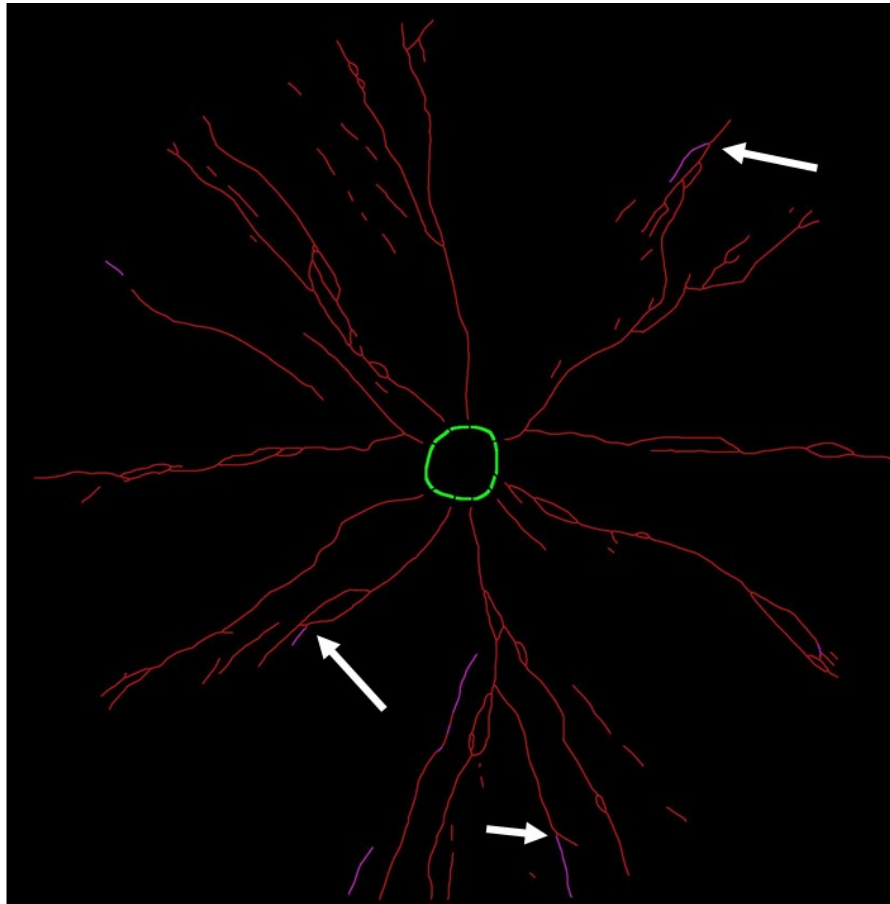


Figure 120: Example of indistinguishable macro-mechanisms (marked with white arrows). The trace image is image 12 ($t+446.16 \mu s$), m12(21).

In most cases, the macro-mechanisms related to the branching and merging occur during the second fracture phase. Side crack arrest (1.3) and side crack deflection (1.4) mostly occur at the end of the second and in the third fracture phase.

The macro-mechanisms often occur in a sequence (Table 35). For the branching and merging mechanisms (2.1 through 4.4), these sequences, on average, last longer with increasing linear charge concentration and they are more pronounced in the granite than in the mortar.

Table 35: Selected HSI event logs of the blasted cylinders.

I_c [g/m]	Mortar													Granite																												
	Elapsed time [µs]	Image	Propagation paths				Branching				Merging				Branching-merging				Elapsed time [µs]	Image	Propagation paths				Branching				Merging				Branching-merging									
			1.1	1.2	1.3	1.4	2.1	2.2	2.3	2.4	3.1	3.2	3.3	3.4	4.1	4.2	4.3	4.4			1.1	1.2	1.3	1.4	2.1	2.2	2.3	2.4	3.1	3.2	3.3	3.4	4.1	4.2	4.3	4.4						
6	40.56	6	█	█															40.56	2	█	█																				
	81.12	7	█	█																81.12	3	█	█																			
	121.68	8	█	█																121.68	4	█	█																			
	162.24	9	█	█																162.24	5	█	█																			
	202.80	10	█	█																202.80	6	█	█																			
	243.36	11	█	█																243.36	7	█	█																			
	283.92	12	█	█																283.92	8	█	█																			
	324.48	13	█	█																324.48	9	█	█																			
	365.04	14	█	█																365.04	10	█	█																			
	405.60	15	█	█																405.60	11	█	█																			
	Blast test 22.2													Blast test 26.1																												
	12	40.56	2	█	█															40.56	3	█	█																			
		81.12	3	█	█															81.12	4	█	█																			
		121.68	4	█	█															121.68	5	█	█																			
		162.24	5	█	█															162.24	6	█	█																			
202.80		6	█	█															202.80	7	█	█																				
243.36		7	█	█															243.36	8	█	█																				
283.92		8	█	█															283.92	9	█	█																				
324.48		9	█	█															324.48	10	█	█																				
365.04		10	█	█															365.04	11	█	█																				
405.60		11	█	█															405.60	12	█	█																				
446.16		12	█	█															446.16	12	█	█																				
Blast test 21													Blast test 25																													
20	40.56	8	█	█															40.56	3	█	█																				
	81.12	9	█	█															81.12	4	█	█																				
	121.68	10	█	█															121.68	5	█	█																				
	162.24	11	█	█															162.24	6	█	█																				
	202.80	12	█	█															202.80	7	█	█																				
	243.36	13	█	█															243.36	8	█	█																				
	283.92	14	█	█															283.92	14	█	█																				
	324.48	15	█	█															324.48	15	█	█																				
	365.04	16	█	█															365.04	16	█	█																				
	405.60	17	█	█															405.60	17	█	█																				
446.16	18	█	█															446.16	18	█	█																					
Blast test 23.1													Blast test 26.2																													

5.7 Blast-hole expansion, deformation zones, and radial swelling

This section provides a result overview of blast-hole expansion, radial swelling of blasted cylinders, and the deformation zones (see Section 4.2). The measurements and observations were carried out on the transverse CT sections (CTt), micro-CT scans (uCT), and the micrographs of the thin sections. The deformation zones are also described considering possible underlying mechanisms (see Section 5.8). Raw result-data sets are provided in Appendix 14.

5.7.1 Blast-hole expansion and cylinder swelling

The CTt sections were used to estimate the radius of the blast hole in blasted cylinders as normalized blast-hole radius ($r_{bh,norm}$), i.e., the difference between the average blast-hole radius and the cylinder swelling (see Equation 29 and Equation 30). Its value stays about the same in the axial direction of the cylinders when not affected by the end faces (Figure 121).

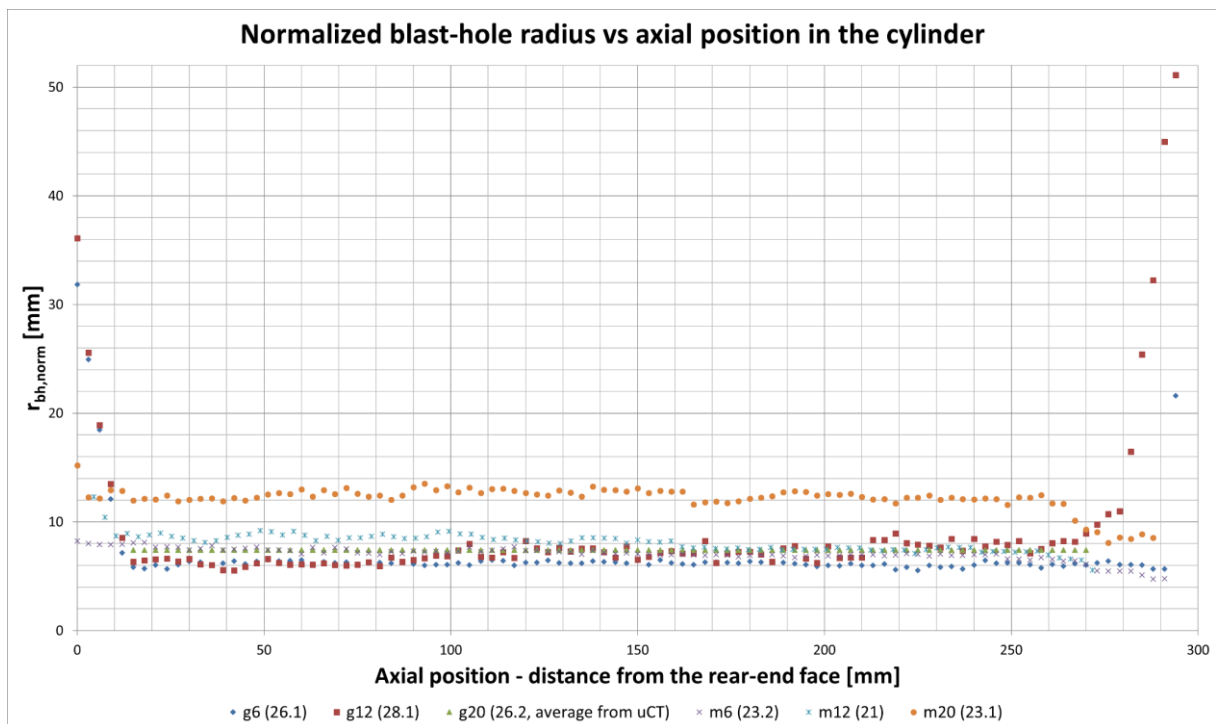


Figure 121: Normalized blast-hole radius along the axis of the blasted cylinders (CTt).

Figure 122 shows a summary of the measured normalized blast-hole radii.

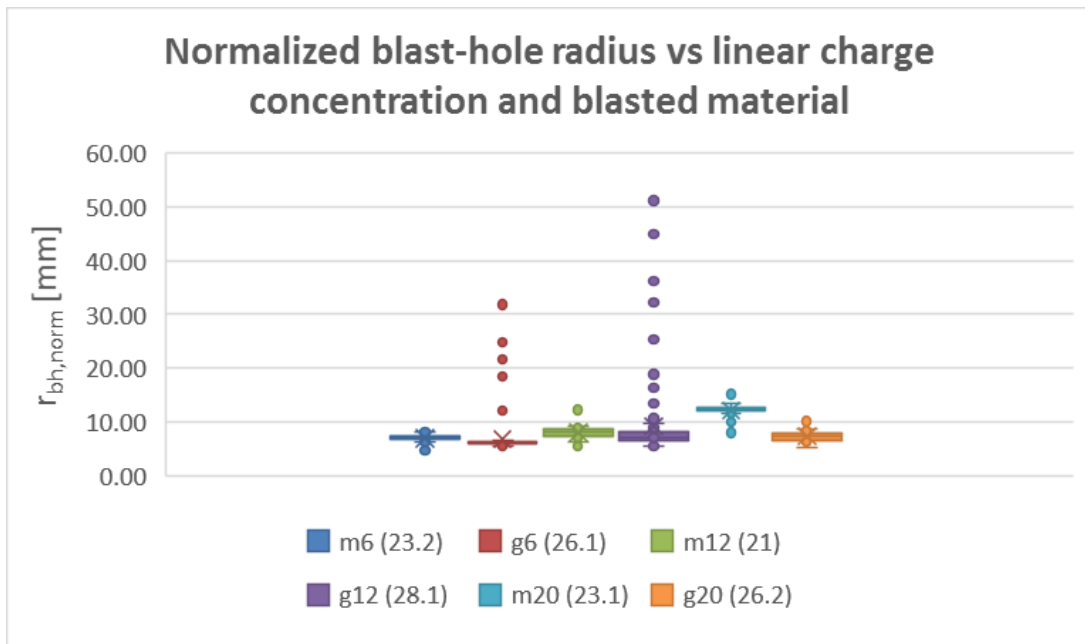


Figure 122: Normalized blast-hole radius ($r_{bh,norm}$) considering linear charge concentration and blasted material.

Table 36 shows a summary of measured blast-hole expansion, cylinder swelling, and normalized blast-hole radius.

Table 36: Summary of measured blast-hole expansion, cylinder swelling, and normalized blast-hole radius.

Material	I_c [g/m]	Blast test	δr_{bh} [mm]		δr_m [mm]		$r_{bh,norm}$ [mm]	
			Ave	Std	Ave	Std	Ave	Std
Mortar	6	23.2	3.05	0.66	1.00	0.05	7.05	0.56
	12	21	5.10	0.84	1.96	0.32	8.14	0.59
	20	23.1	8.03	1.11	0.73	0.03	12.30	1.12
Granite	6	26.1	2.66	0.25	1.50	0.04	6.16	0.24
	12	28.1	6.41	1.56	4.18	0.68	7.23	1.14
	20	26.2	-	-	-	-	7.43	1.17

The average values of $r_{bh,norm}$ are significantly different to each other considering both the linear charge concentration and the blasted material (Table 37).

Table 37: Statistical evaluation of $r_{bh,norm}$ with Two-way ANOVA ($\alpha = 0.05$).

	SS	df	MS	F	p-value	Sign. diff.
Material	265.423	1	265.423	855.526	8.51E-44	Yes
I_c [g/m]	24.490	2	12.245	39.469	1.44E-12	Yes
Between groups	292.996	2	146.498	472.200	2.61E-44	Yes
Within groups	24.199	78	0.310			
Total	607.109	83	7.315			

The values of the blast-hole expansion (δr_{bh}), the swelling (δr_m), and the normalized blast-hole radius ($r_{bh,norm}$) increase with increasing linear charge concentration, except for δr_m in the 20-g/m mortar shot. The blast hole expanded more in the mortar than in the granite. However, the blast cylinders swelled more in the granite than in the mortar.

5.7.2 Deformation zones

Table 38 shows a summary of the measured compaction-zone thickness ($\Delta r_{comp,a}$), thickness of the blasted-off layer ($\Delta r_{blast,b}$), thickness of the rest of the crushed-zone thickness ($\Delta r_{crush,non-c}$), and the estimated total crushed-zone thickness ($\Delta r_{crush,tot}$).

Table 38: Summary of obtained $\Delta r_{comp,a}$, $\Delta r_{blast,b}$, $\Delta r_{crush,non-c}$ and $\Delta r_{crush,tot}$.

Material	I_c [g/m]	Blast test	$\Delta r_{comp,a}$ [mm]	$\Delta r_{blast,b}$ [mm]	$\Delta r_{crush,non-c}$ [mm]	$\Delta r_{crush,tot}$ [mm]
Mortar	6	22.2	3.0	0.2	0	3.2
	12	20	3.7	0.4	0	4.1
	20	22.1	6.7	1.0	0	7.7
Granite	6	26.1	0	1.2	-	2.7
		27	0	-	1.5	
	12	28.1	0	2.2	-	4.1
		24	0	-	1.9	
	20	26.2	0	2.4	3.3	5.7

A compaction zone was found only in the mortar. The thickness of the zones increases with the linear charge concentration. The total crushed-zone thickness is about the same in both blasted materials for given linear charge concentrations, except in the 20-g/m shots. One possible reason for this is an error in the measurement of $\Delta r_{blast,b}$ (see Section 4.2 and Figure 55) in the uCT images for g20(26.2).

Figure 123 shows selected thin-section micrographs of the deformation zones in the mortar and the granite.

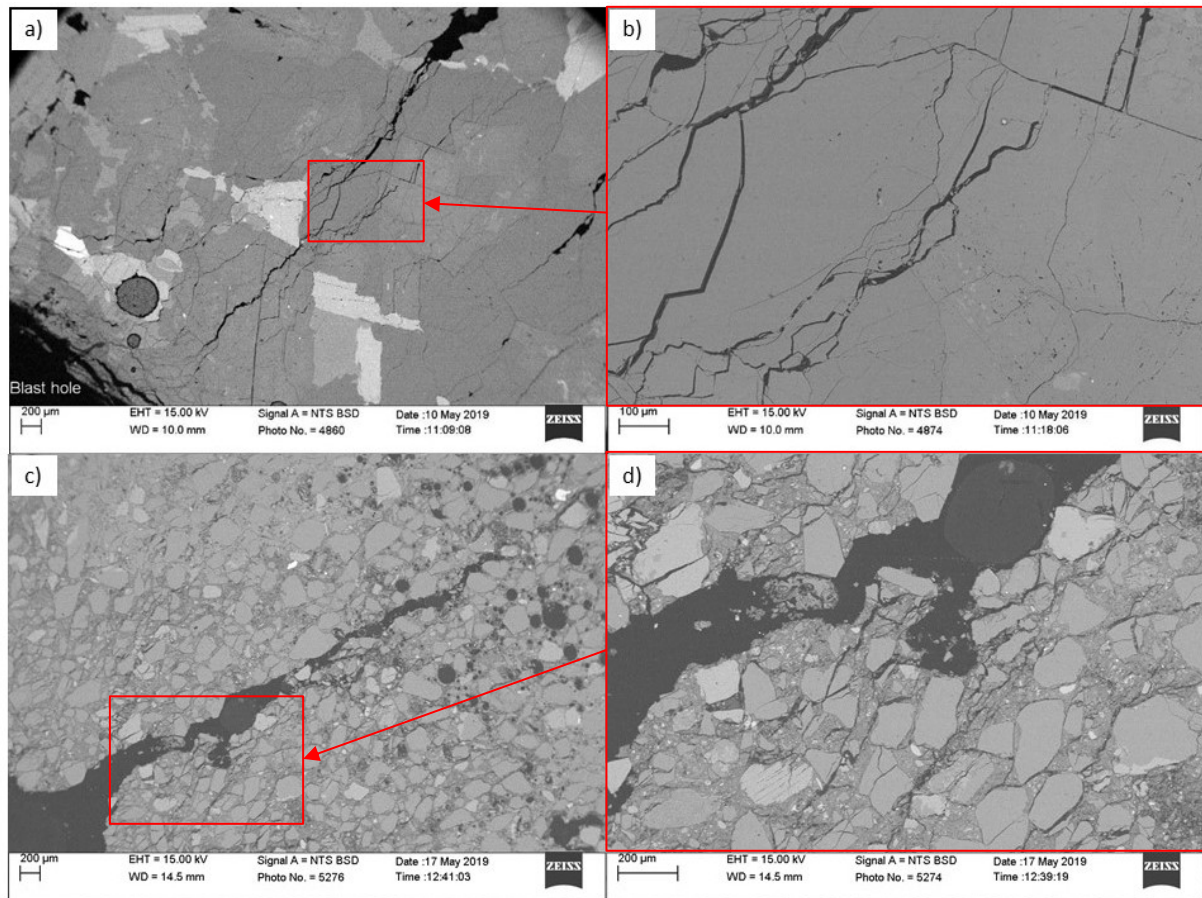


Figure 123: Deformation zones and crack patterns near the blast hole in the thin sections (SEM images): a), b) g12(24); c), d) m12(20). (Kukolj et al., 2019)

Figure 124 shows a typical arrangement of the deformation zones in the mortar.

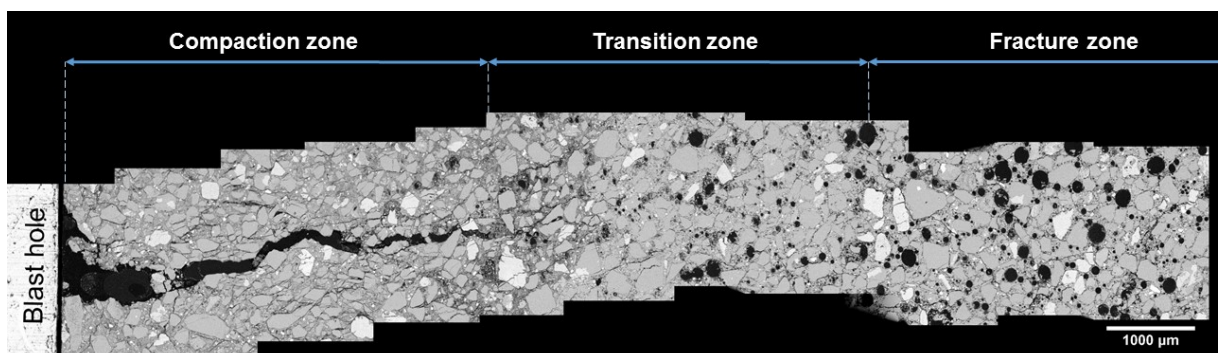


Figure 124: Deformation zones in the mortar. Fused SEM micrographs (m20(22.1)). The crushed zone includes the compaction zone and the transition zone (Kukolj et al., 2019)

The compaction zone was also observed in the uCT sections of larger fragments of the blasted mortar cylinders (Figure 125). A selected set of the uCT sections is provided in Appendix 15.

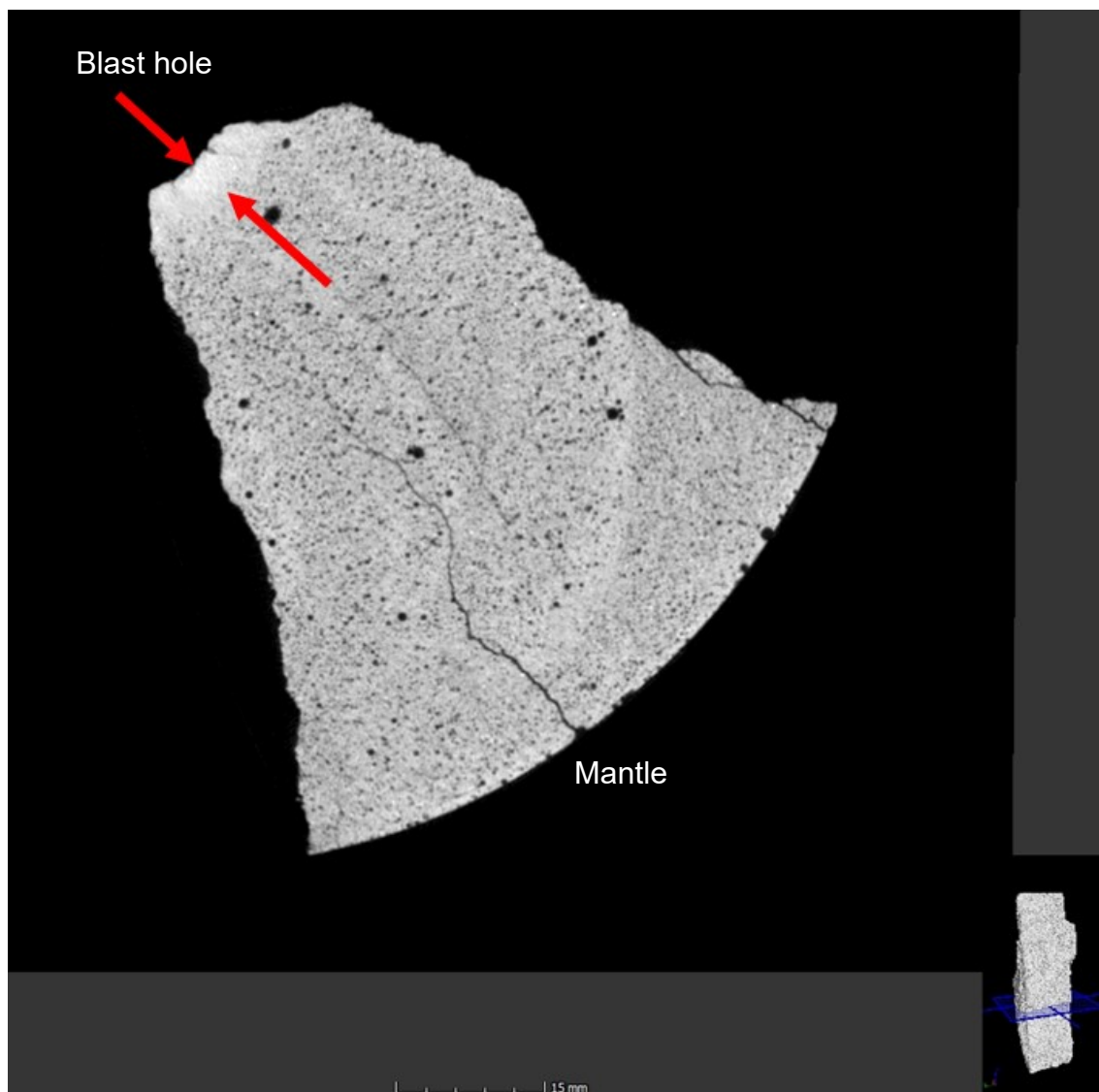


Figure 125: Transverse uCT section of a blast fragment (m12(20)). The compaction zone is denser and, hence, indicated by higher image intensity. The arrows mark the endpoints of the measured compaction-zone thickness.

The micrographs (see also Appendix 16) show that the blast-driven crushing around the blast hole in the mortar forms the compaction zone mostly by deforming the pores in the cement matrix and connecting them with the ongoing fracturing, including 'impact/impingement fractures' in the quartz grains (see Section 5.8.1). The initial porosity of the mortar is reduced due to the shearing and crushing failure around the blast hole (Figure 126).

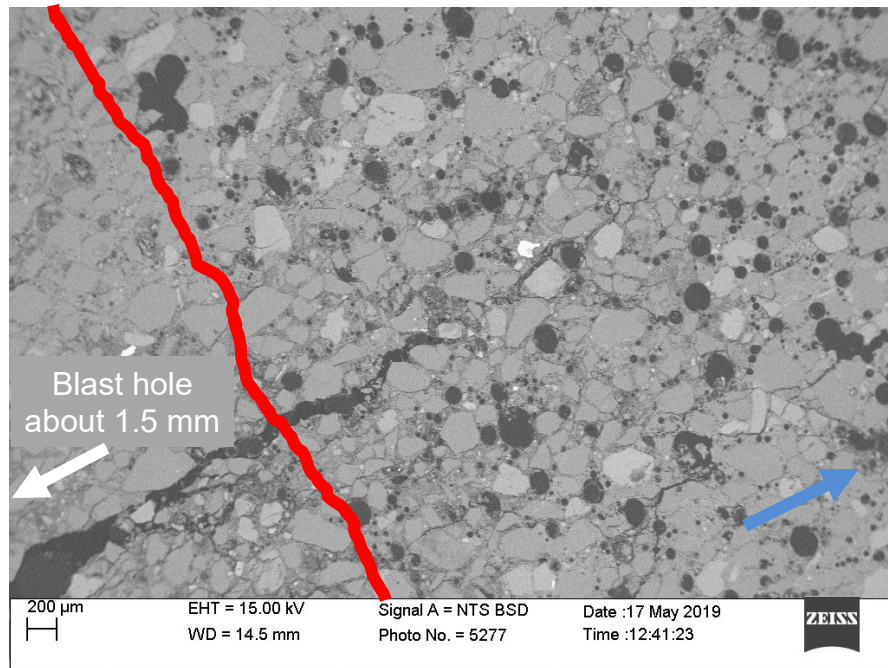


Figure 126: Outer boundary of the compaction zone (red line) in the mortar (m12(20)), about 1.5 mm from the blast hole. SEM micrograph of a thin section. The blue arrow marks the main direction of crack development.

Figure 127 shows the crushed zone around the blast hole in the granite.

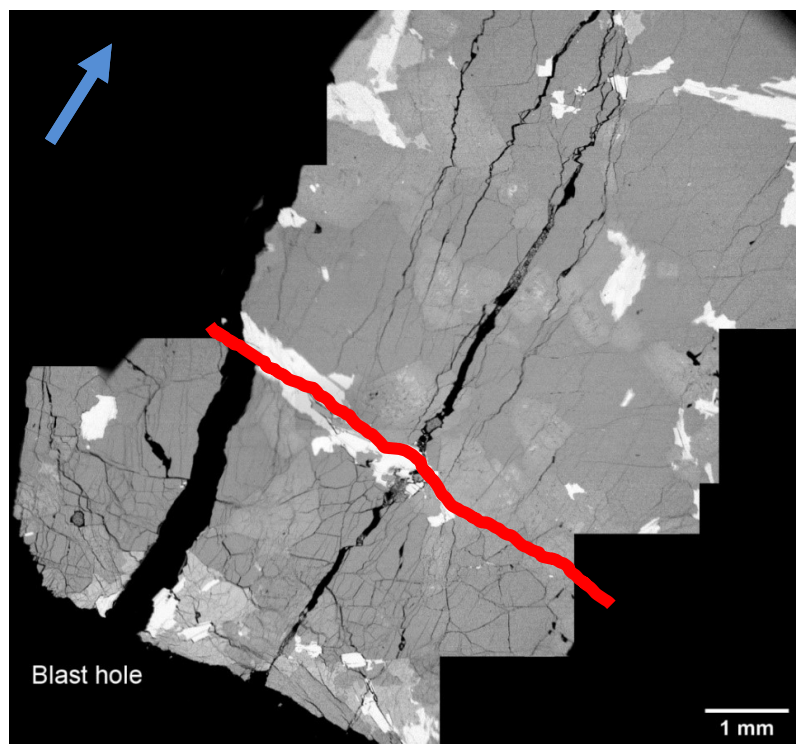


Figure 127: Deformation zones (crushed zone) in the granite. Fused SEM micrographs from (g20(26.2)). The red line marks the outer boundary of the crushed zone. The blue arrow marks the main direction of crack development.

Unlike in the mortar, the material near the blast hole in the granite contains more traces of tangential cracks. Farther in the radial direction, there is a zone with a mixture of tangential and radial cracks, followed up by a zone with mostly radial cracks. This transition in the granite (Figure 127) is comparable to that in the mortar (Figure 124 and Figure 126) considering the main acting fracture mechanisms.

The material compaction was not found in the wakes of the main radial cracks of either blasted material (Figure 128 and Figure 129).

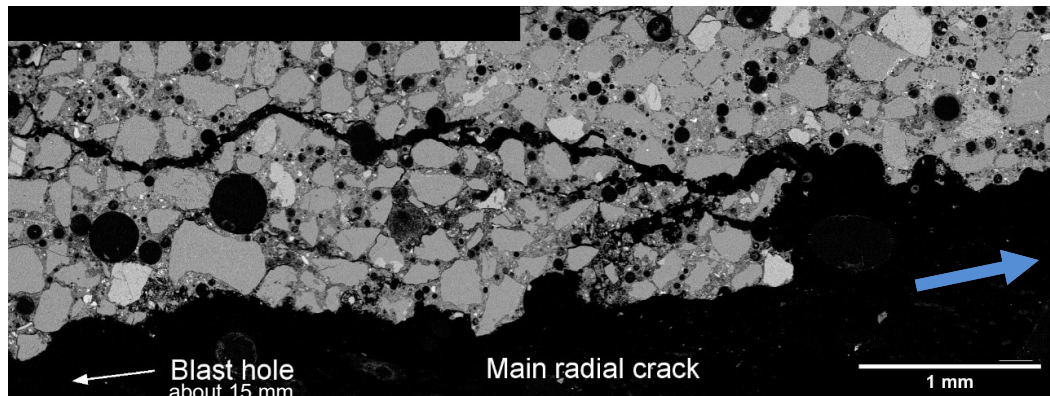


Figure 128: Flank of a main radial crack outside the deformation zones (about 15 mm from the blast hole) in the mortar (m12(20)). Stitched SEM micrographs of a thin section. The blue arrow marks the main direction of crack development.

However, multiple branching/merging of smaller cracks is often found in the wakes of the main radial cracks (Figure 129).

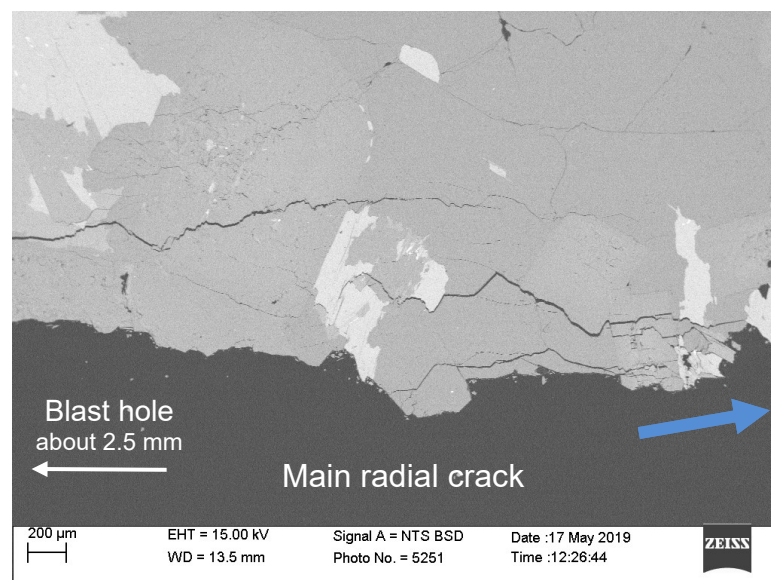


Figure 129: Flank of a main radial crack in the granite, outside the deformation zones (about 2.5 mm from the blast hole). SEM micrograph from g6(27). The blue arrow marks the main direction of crack development.

5.8 Micro- and meso-mechanisms

This section covers most frequently observed cracking-mechanism traces in the thin sections and in the surfaces of small fragments (see Section 4.4). Complete sets of micrographs are provided in Appendix 16. Mechanism descriptions in this section are provided with references to the mechanisms covered in Section 4.4.3:

- intergranular fracture – IG,
- transgranular fracture – TG,
- partial cleavage with lamellar steps - pcl,
- impingement cracking – ic,
- flaw-induced cracking – fc,
- refracturing – rc,
- cleavage – cc,
- elastic mismatch – em, and
- plastic mismatch - pm.

Deformations (i.e., structural anomalies) in the thin sections from non-blasted cylinders were recorded and considered in the analysis of the thin sections from the blasted cylinders (see Section “Preliminary deformation” in Appendix 2).

The notation for types of mineral crystals material features in the micrographs is as follows:

- bt, ms – mica (biotite or muscovite) (in the granite),
- cem - cement matrix (in the mortar),
- kfs – potassium (K) feldspar (in the granite),
- p – pore in the cement matrix (in the mortar),
- pg – plagioclase (in the granite), and
- qtz – quartz (in the granite and mortar).

5.8.1 Mortar thin sections

Figure 130 shows micrographs of the deformation zones in the mortar.

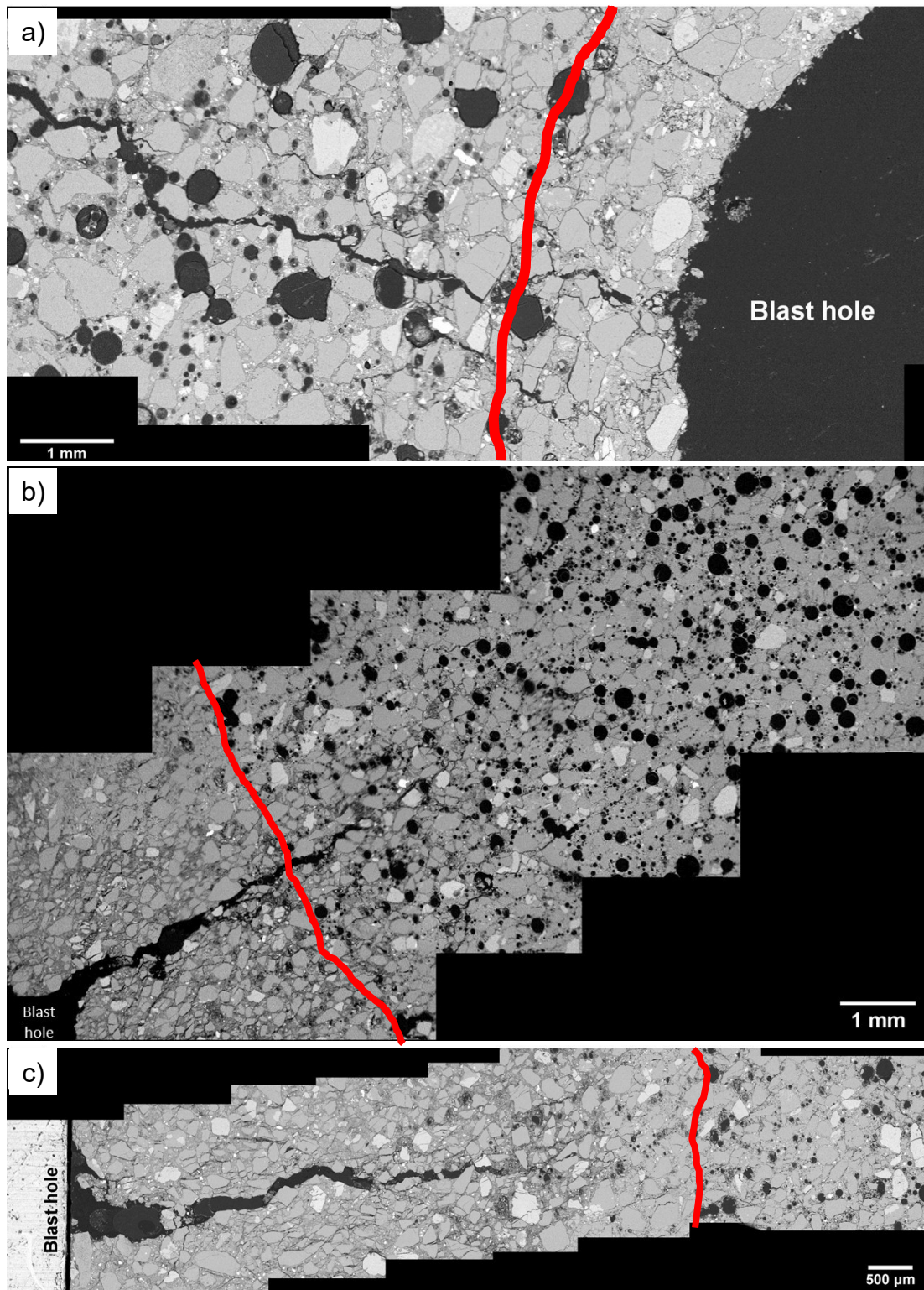


Figure 130: Crushed zone in the mortar: a) m6(22.2); b) m12(20); c) m20(22.1). The red line denotes the approximated outer boundary. Fused SEM micrographs.

The crushed zone measurements are covered in Section 5.7.2.

Quartz grains around the blast hole in the mortar are pushed away through the cement matrix. They collide with each other and break, leaving impingement (ic) traces (Figure 131 and Figure 132). This mechanism is more intensive closer to the blast hole, where the quartz grains are crushed and produced fines are trapped in the compacted cement matrix. In this region, the cement matrix shows traces of refracturing (rc) and air pores are squashed (see Figure 130 and Figure 133). The intensity of this mechanism is directly proportional to the linear charge concentration.

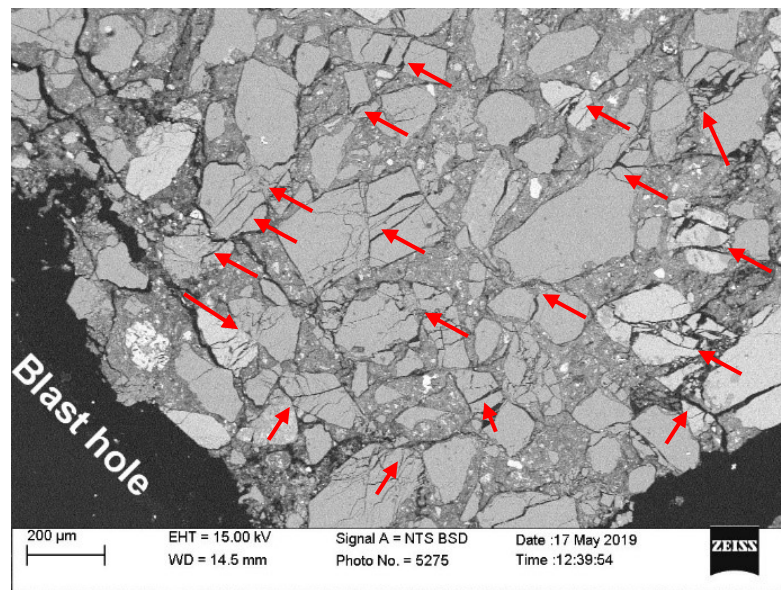


Figure 131: Crushed quartz grains with impingement fractures (ic) near the blast hole. SEM micrographs (m12(20)).

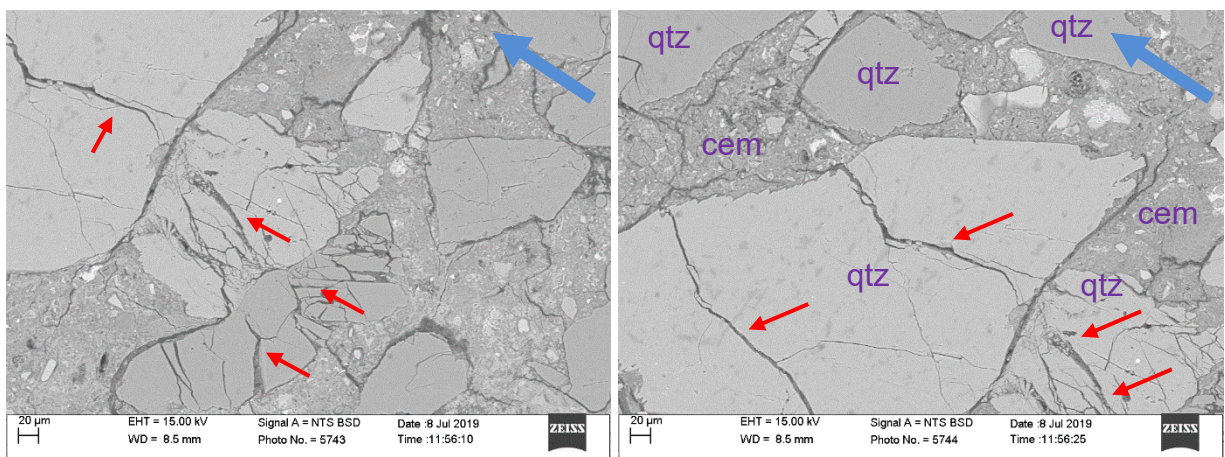


Figure 132: Impingement fractures (ic) in quartz grains in the compaction zone. SEM micrographs (m6(22.2)). The blue arrow marks the main direction of crack development.

These patterns remain farther out in the radial direction until the edge of the compaction zone (or the transition zone, see Section 5.7.2). The edge is defined by gradual “reappearance” of the pores and less frequent quartz-grain collisions (see Figure 130).

This gradual transition to the material unaffected by the compaction shows the direction of compaction, indicated by the orientation of partly closed pores (Figure 133).

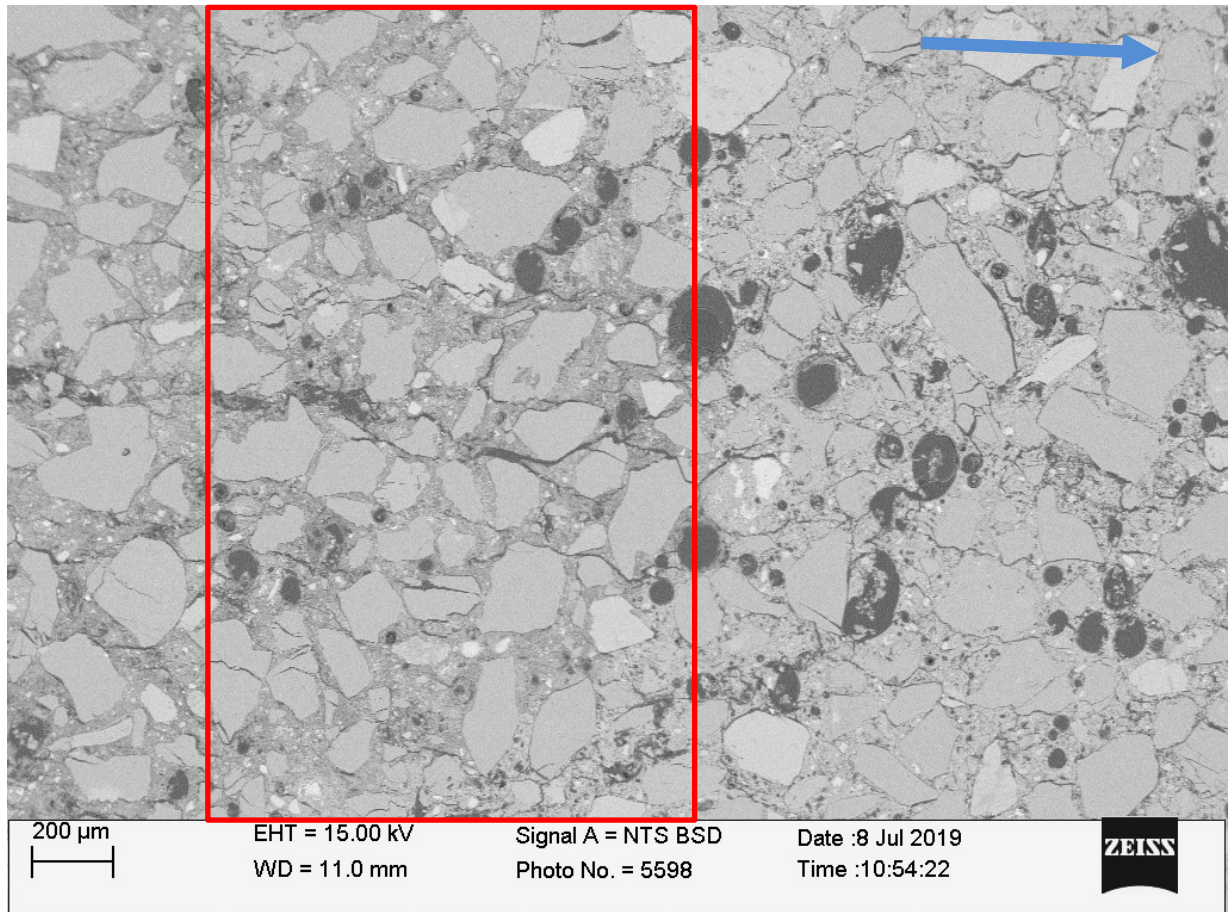


Figure 133: End of the compaction zone and beginning of the transition zone in the mortar (indicated by the red stripe). The blast hole is about 2 mm to the left from the image. SEM micrograph (m12(20)). The blue arrow marks the main direction of crack development.

The pores acted as stress-concentration points and, thus, attracted the propagating cracks. The cracks propagated through the pores, leaving mostly intergranular fractures (em, fc) (Figure 134).

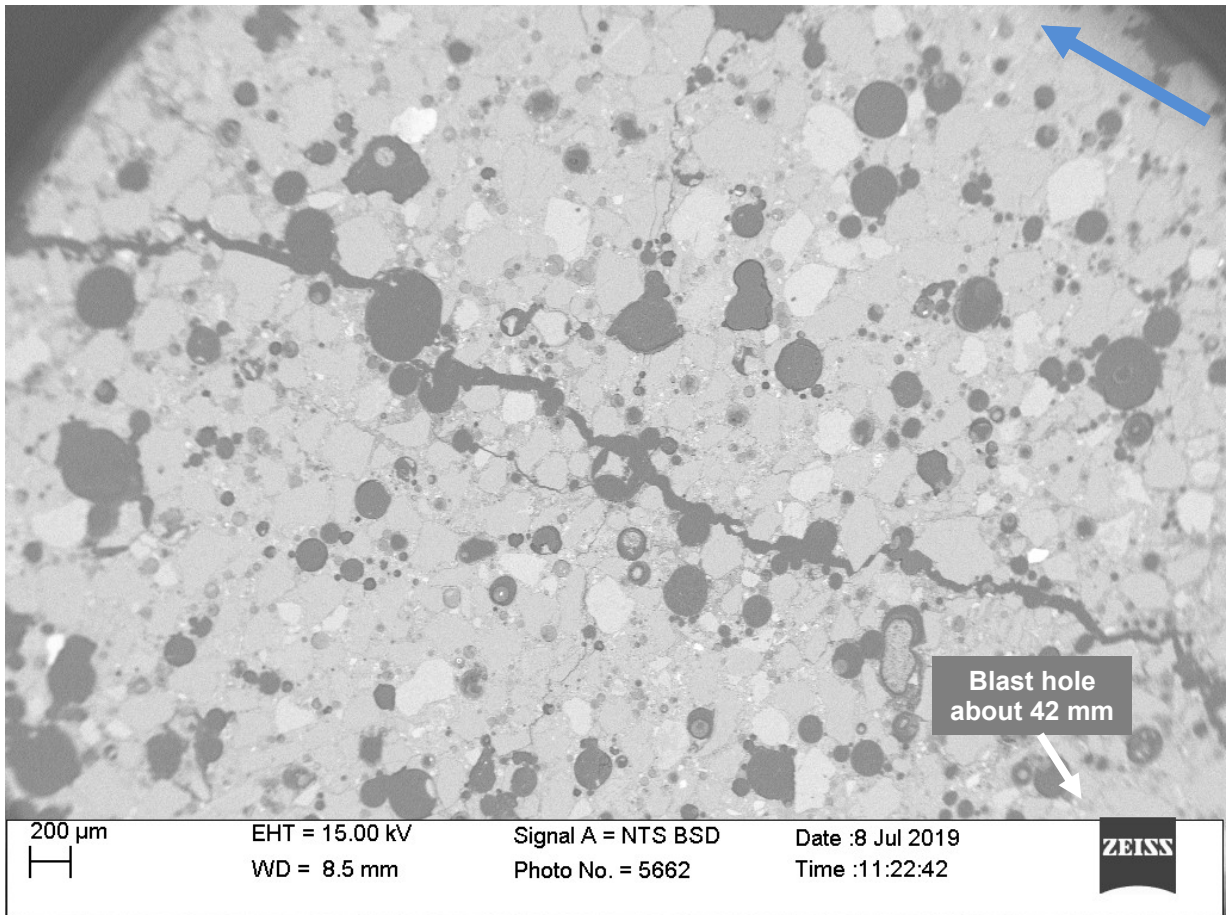


Figure 134. A crack composed of intergranular fractures in the mortar, about 42 mm from the blast hole. SEM micrograph (m6(22.2)). The blue arrow marks the main direction of crack development.

Transgranular fractures (pm and mc) of the quartz grains are very rare outside the compaction zone (Figure 134 and Figure 135).

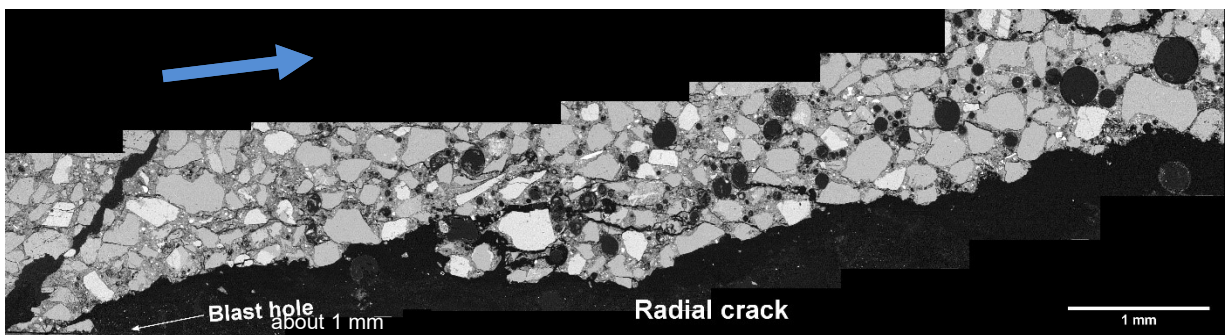


Figure 135: Flank of a main radial crack in the mortar (m12(20)). Fused SEM micrographs of a thin section. The blue arrow marks the main direction of crack development.

Smaller cracks (e.g., that branched from the larger radial cracks) are often arrested in the cement matrix or by reaching a pore or a quartz grain (Figure 136).

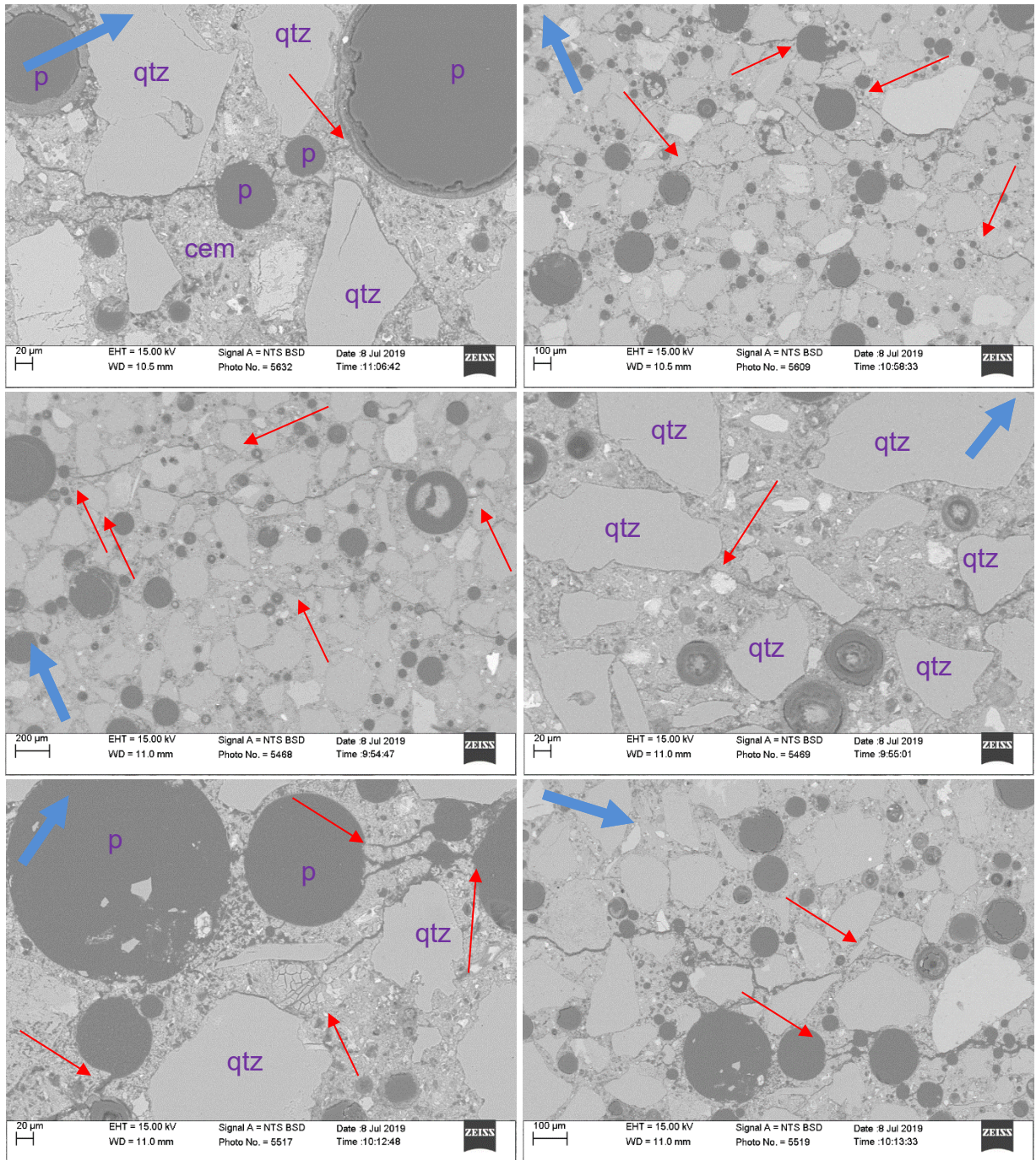


Figure 136: Examples of different crack-arrest marks in the mortar (indicated by the red arrows), about 30 mm from the blast hole. SEM micrographs from blast test (m20(22.1)). The blue arrow marks the main direction of crack development.

The wakes of even larger cracks and near the mantle do not show such traces of compaction. However, the fracture wakes in 12- and 20-g/m in the mortar shots show more intensive micro-cracking in the cement matrix. Fracture flanks (i.e., sides including the wakes) often show relative shearing displacement (Figure 137).

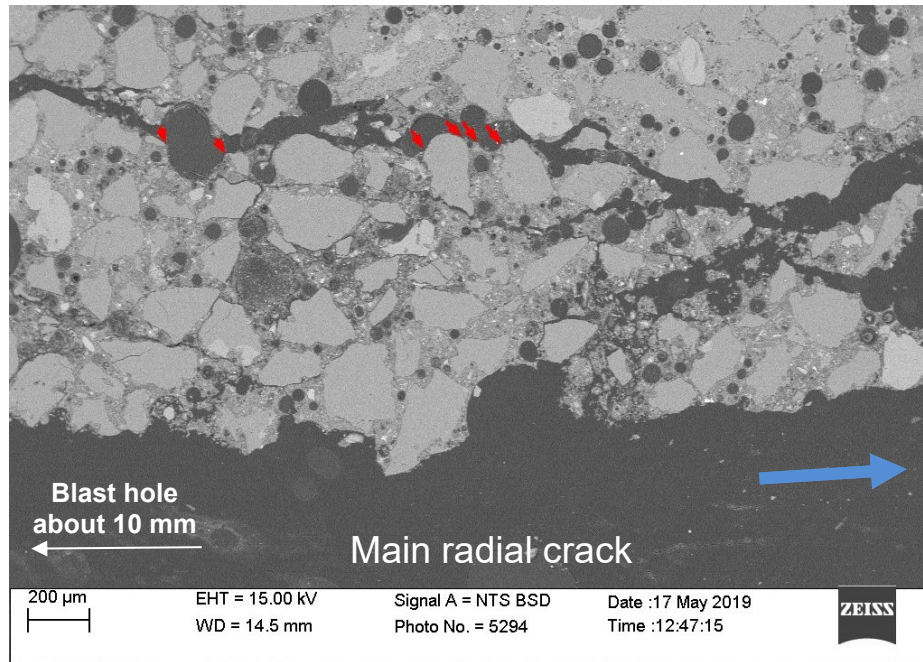


Figure 137: Relative shearing displacement in a crack flank (a flank of a main radial crack – bottom of the image), about 10 mm from the blast hole. Red arrows indicate the displacement. SEM micrograph (m12(20)). The blue arrow marks the main direction of crack development.

The mortar micrographs also show many different (crack) branching/merging patterns, more complex than those discussed in Section 5.6. Figure 138 shows complex branching/merging (fc, rc, and em) in the crushed/compaction zone in the mortar.

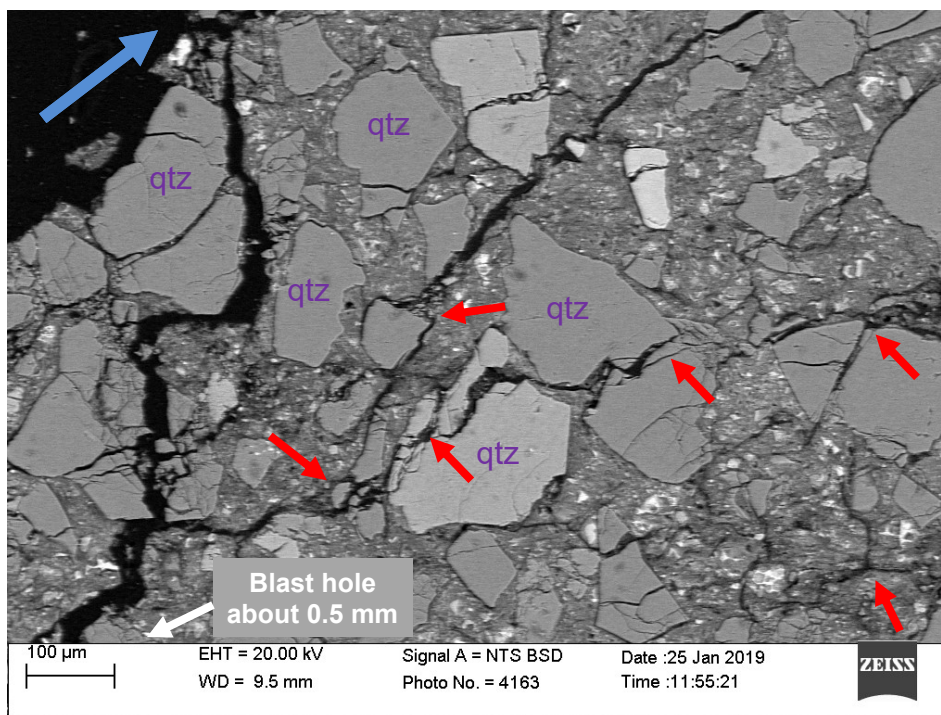


Figure 138: Complex branching/merging in the compaction zone of a mortar cylinder. SEM micrograph (m12(20)). The blue arrow marks the main direction of crack development.

The branching/merging covers different size scales, as these mechanisms occur as transgranular, intergranular, and intragranular fracturing of the quartz grains and fractures in the matrix. Figure 139 shows branching/merging patterns in a combination of transgranular and intergranular fractures of a quartz grain (fc, em, and pm), along with impingement crushing (multiple ic) of an adjacent quartz grain, and multiple crack-arrest marks in the matrix.

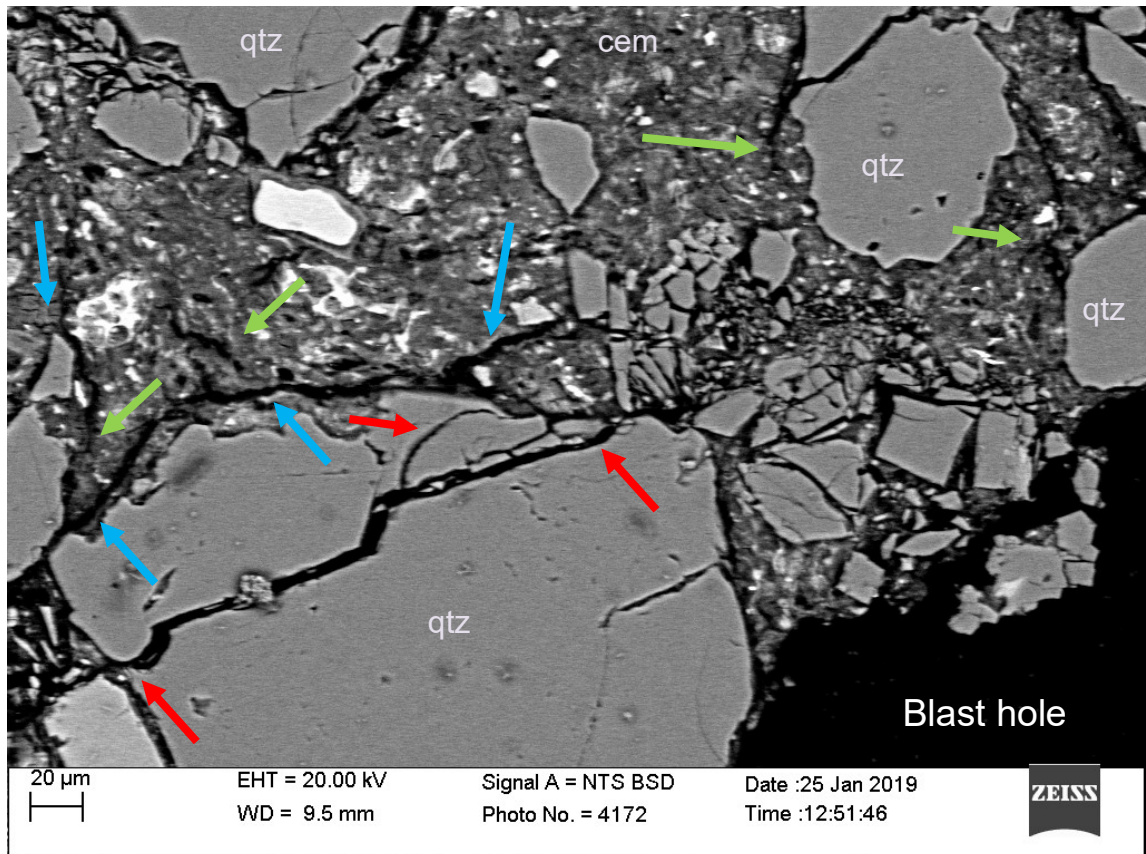


Figure 139: Branching/merging (in the compaction zone) on a micro-scale, showing transgranular (red arrows) and intergranular (blue arrows) fractures of the quartz grain in the lower-left corner, its crushed adjacent quartz grain, and multiple crack-arrest marks (green arrows) in the surrounding cement matrix. SEM micrograph (m12(20)).

Main radial cracks often show branching/merging patterns (em) in their wakes outside the crushed zone (Figure 140). In such cases, the pores affect crack propagation, and contribute to the development of branching/merging formations.

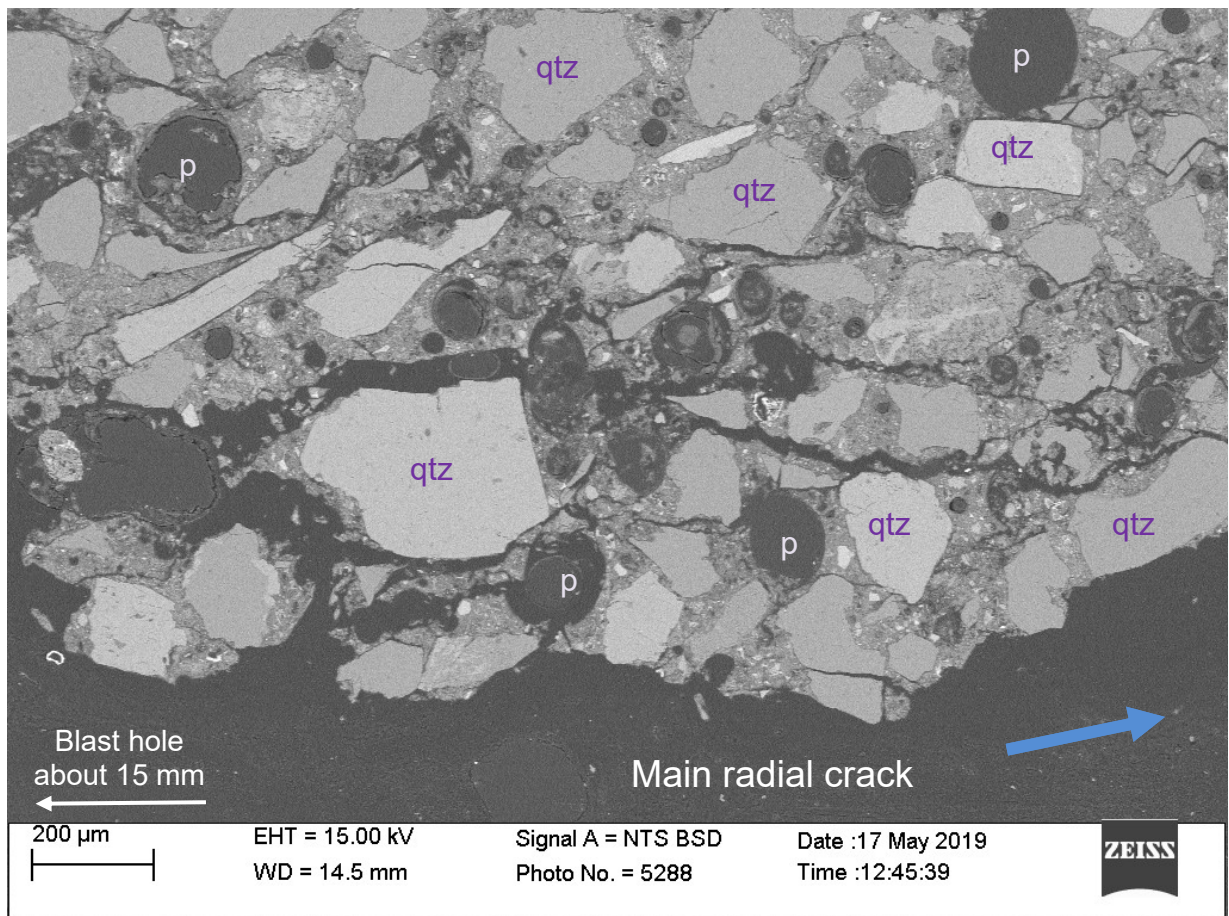


Figure 140: Branching/merging network formed in the wake of a main radial crack outside the crushed zone in the mortar. The radial crack is at the bottom of the image and the blast hole is about 15 mm to the left from the image. SEM micrograph (m12(20)). The blue arrow marks the main direction of crack development.

Even smaller cracks, at least 30 mm away from main radial cracks, blast hole, and mantle, also show traces of complex branching/merging, though in smaller scale (Figure 141).

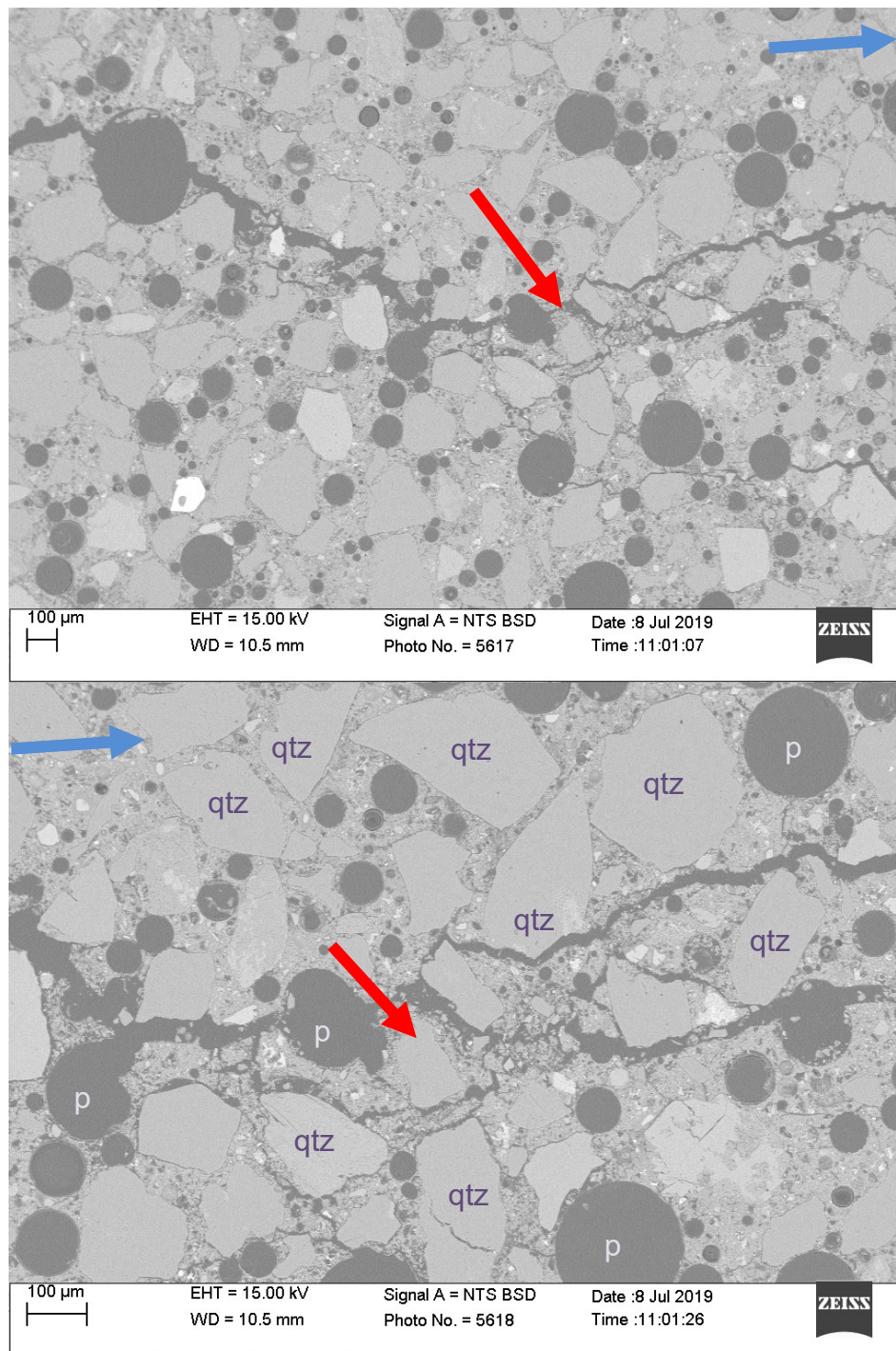


Figure 141: Seeming Y-branching (indicated by the red arrow) formed by a small crack in the intermediate region in the mortar (about 30 mm from the blast hole). The bottom image shows the branching area enlarged, with a complex branching/merging formation between pores and around quartz grains. SEM micrographs (m20(22.1)). The blue arrow marks the main direction of crack development.

Although rarely, also X-branching/merging patterns (fc, rc, and em) are found in the mortar (Figure 142).

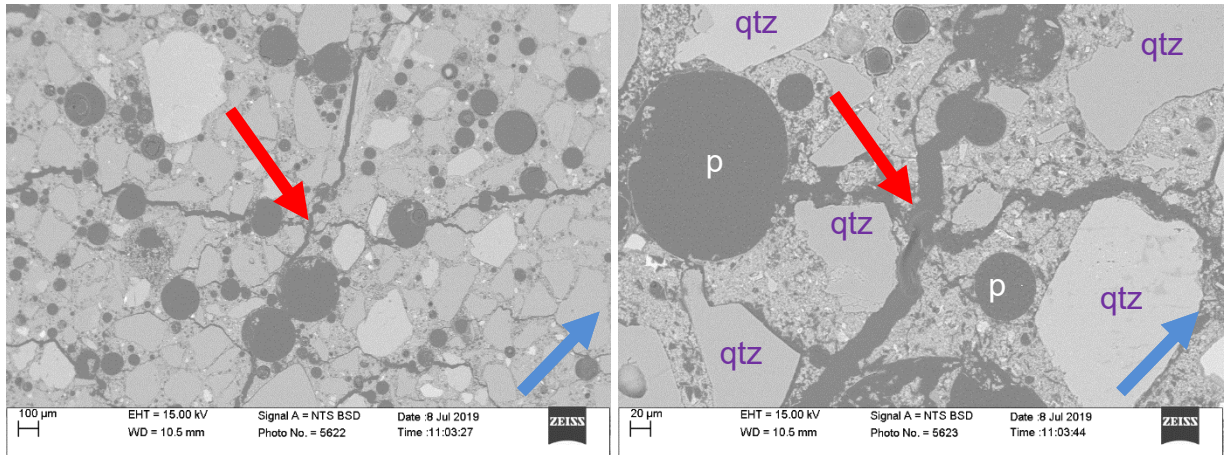


Figure 142: X-branching/merging pattern, showing an almost right-angle crossing of two cracks in the mortar (about 40 mm from the blast hole). SEM micrographs (m20(22.1)). The blue arrow marks the main direction of crack development.

At micro-scale, the branching/merging in the mortar occurs either at/in a pore (fc and em), at/through a quartz grain (fc, em, and pm), or as a combination of the two. Figure 143 shows a Y-branching/merging that occurred in between two adjacent closely spaced quartz grains (fc and em).

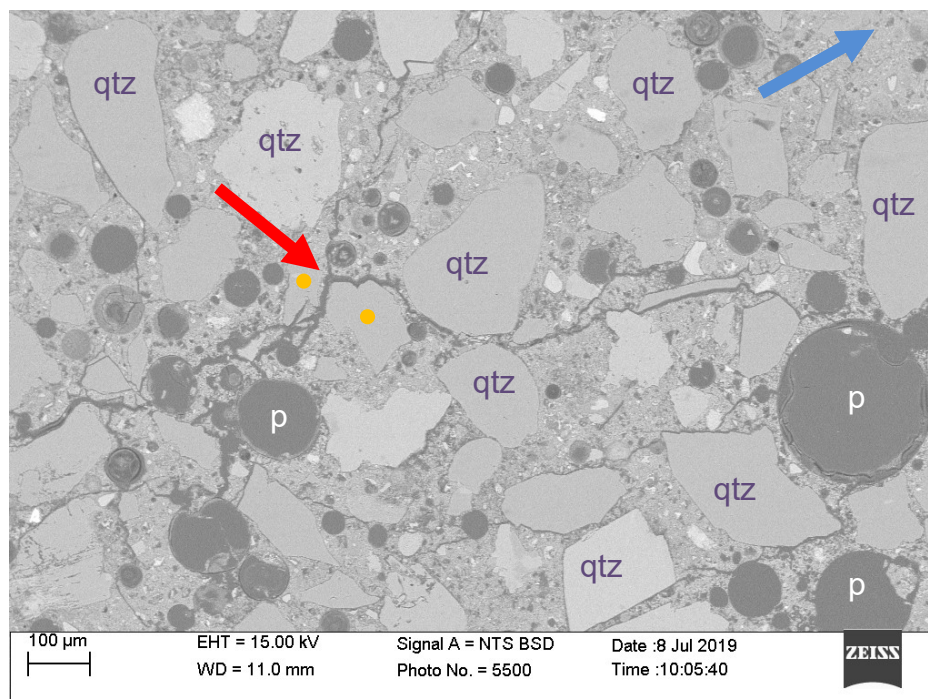


Figure 143: Y-branching/merging that occurred in between two adjacent closely spaced quartz grains (marked with orange points) (about 32 mm from the blast hole). SEM micrograph (m20(22.1)). The blue arrow marks the main direction of crack development.

Figure 144 shows a Y-branching/merging that occurred at a small pore just at an edge of a larger quartz grain (fc, em, and pm). One branch split the grain (transgranular fracture) and the other passed around the grain (intergranular fracture).

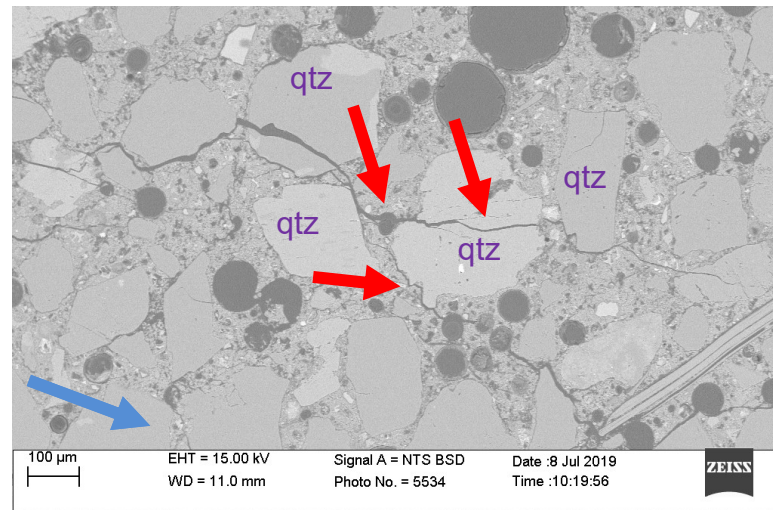


Figure 144: Y-branching/merging that occurred at a small pore right at the edge of a larger quartz grain in the mortar (about 35 mm from the blast hole). SEM micrograph (m20(22.1)). The blue arrow marks the main direction of crack development.

Figure 145 shows an example of a Y-branching/merging that occurred at a larger pore (fc and em). Another (fourth) smaller crack is also connected to the pore. However, this connection (branching or merging) most probably occurred after the Y-branching/merging.

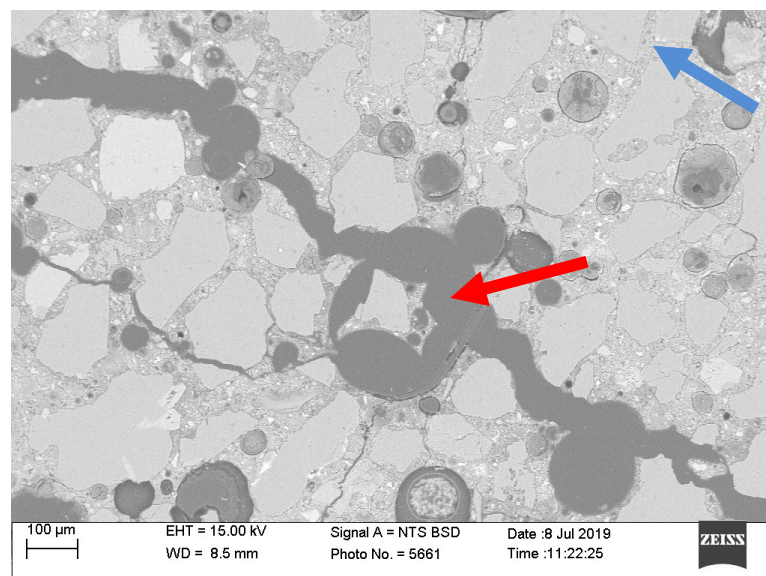


Figure 145: Y-branching/merging that that occurred at a larger pore (about 18 mm from the blast hole). SEM micrograph (m6(22.2)). The blue arrow marks the main direction of crack development.

Some of the micrographs also show intensive micro-fractures in the matrix (rc) around cracks (Figure 146).

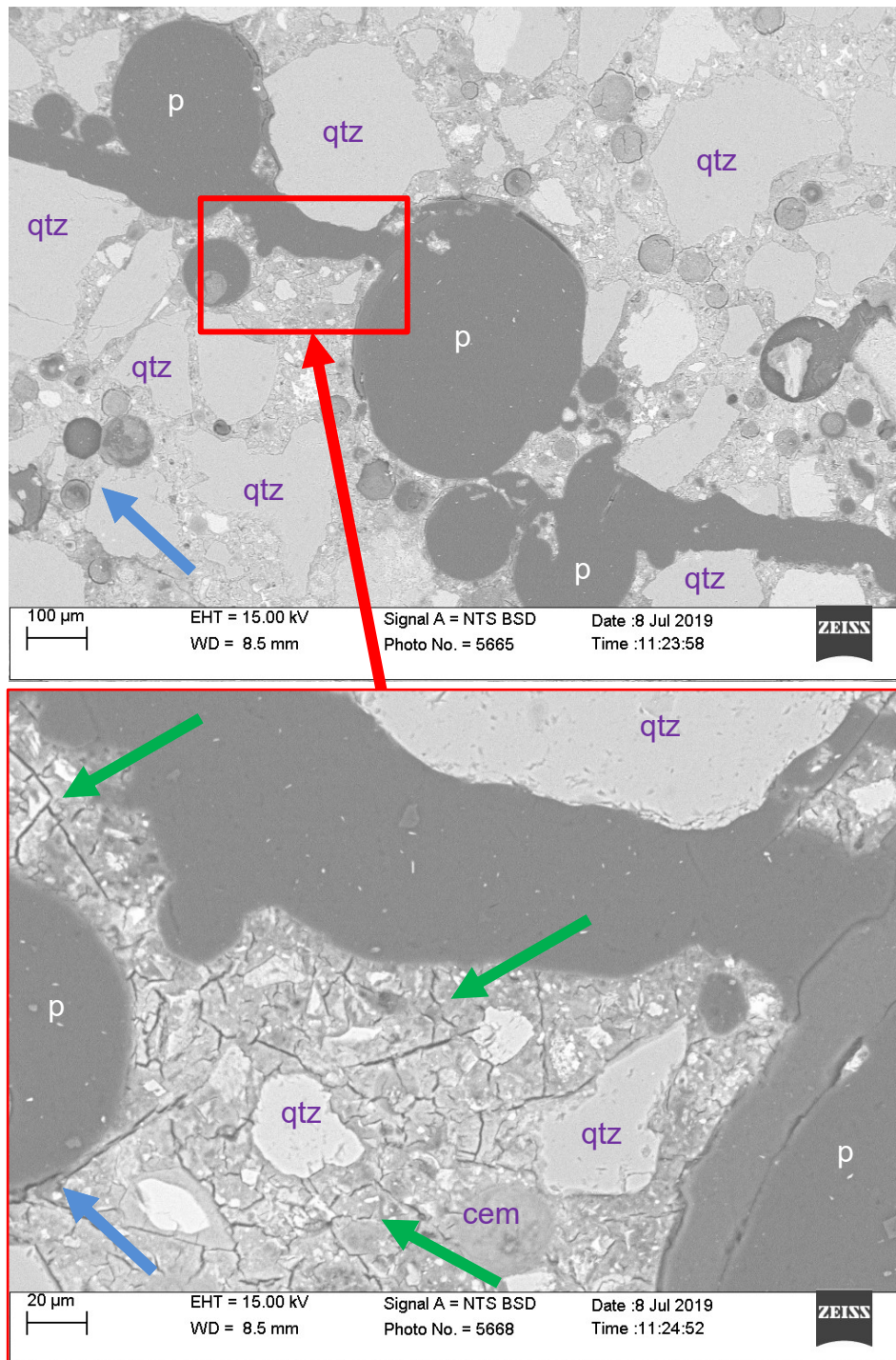


Figure 146: Intensive micro-fractures (rc) in the matrix (green arrows) around a crack crossing a pore (lower right corner), about 16 mm from the blast hole. The bottom image shows the severely fractured flank in the matrix enlarged. SEM micrographs (m6(22.2)). The blue arrow marks the main direction of crack development.

The branching/merging also can occur inside a quartz grain (Figure 147). This often occurs in the crushed zone in the mortar (fc, em, and pm).

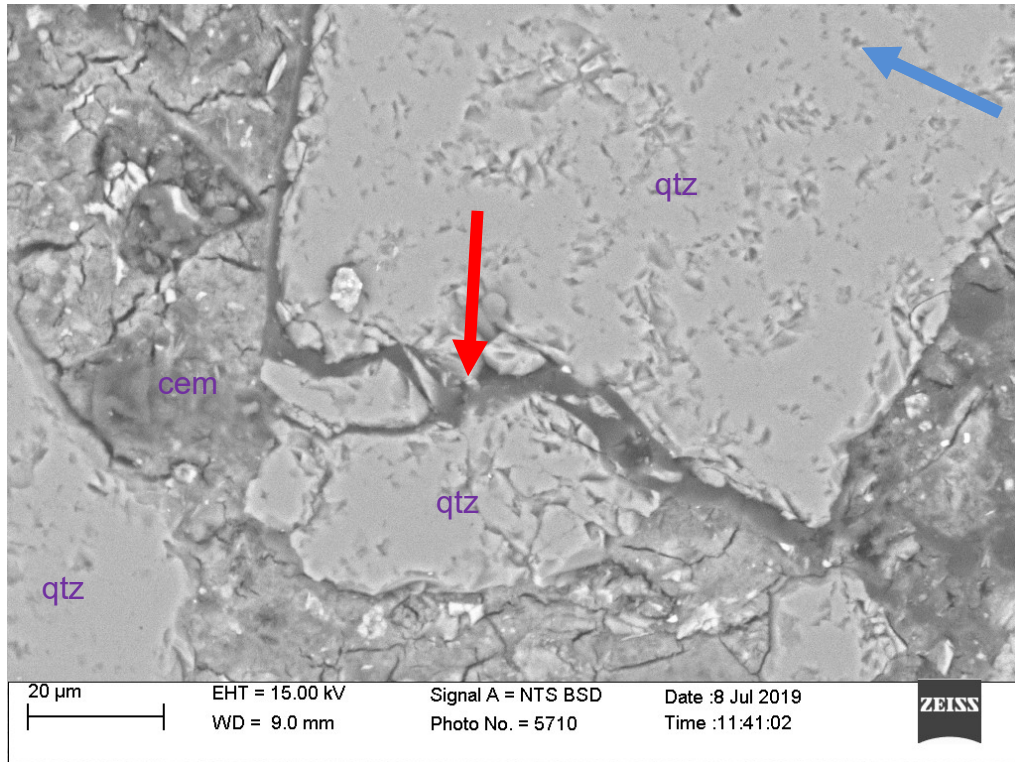


Figure 147: Intergranular branching/merging in a quartz grain in the mortar. SEM micrograph (m6(22.2)). The blue arrow marks the main direction of crack development.

5.8.2 Granite thin sections

Figure 148 and Figure 149 show micrographs of the crushed zone in the granite (see also Section 5.7.2).

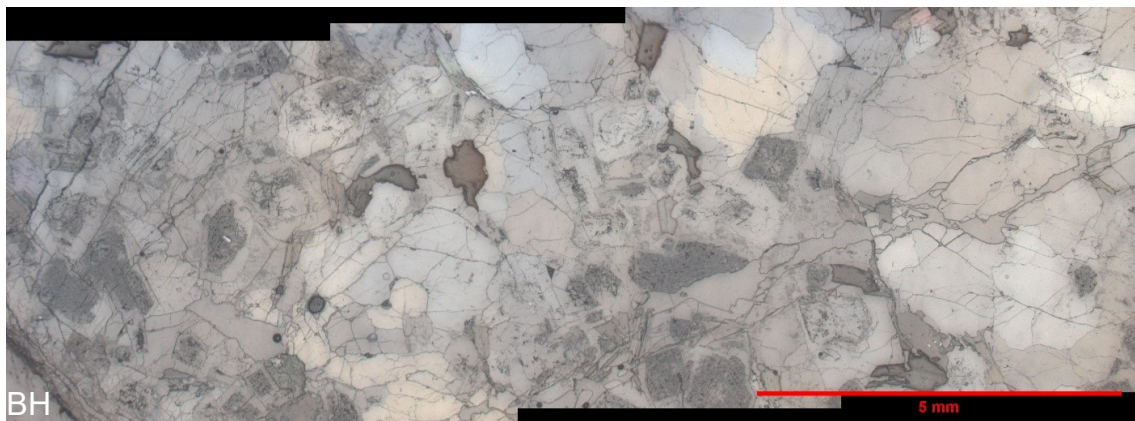


Figure 148: Deformation zones around the blast hole in the granite (the blast hole 'BH' is in the lower-left corner). Fused optical PPL micrographs (g12(24)).

These zones include many complex fracture forms due to the higher stresses in this region. Unlike in the mortar, impingement cracking (ic) is rare here.

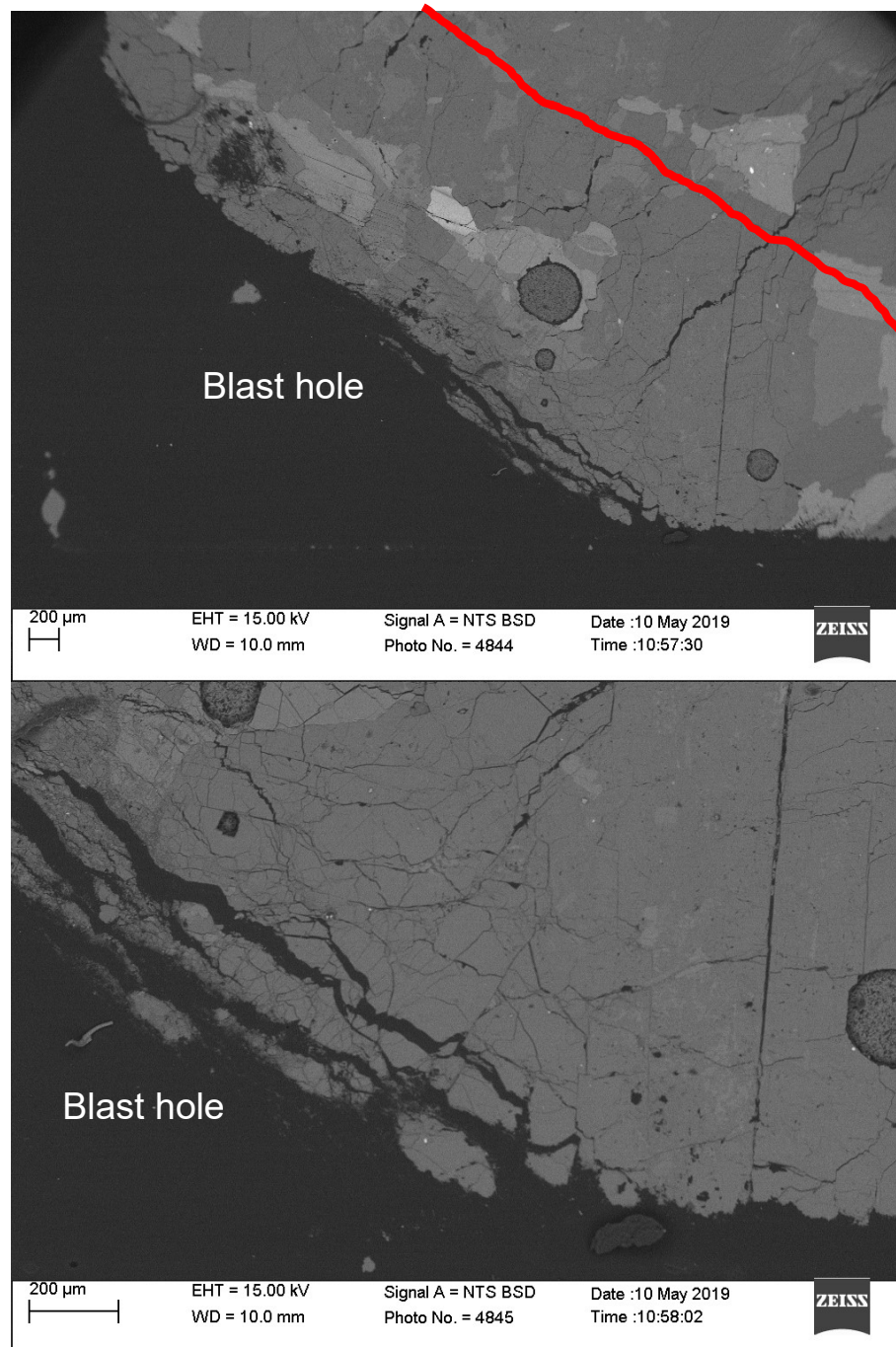


Figure 149: Crushed zone near the blast hole (lower-left corner in the images). SEM micrographs (g12(24)). The red line marks the outer boundary of the crushed zone.

Cleavage transgranular fractures (cc) appear often in the granite samples and are more pronounced with higher linear charge concentration (Figure 150). These are mostly found in mica and feldspar grains.

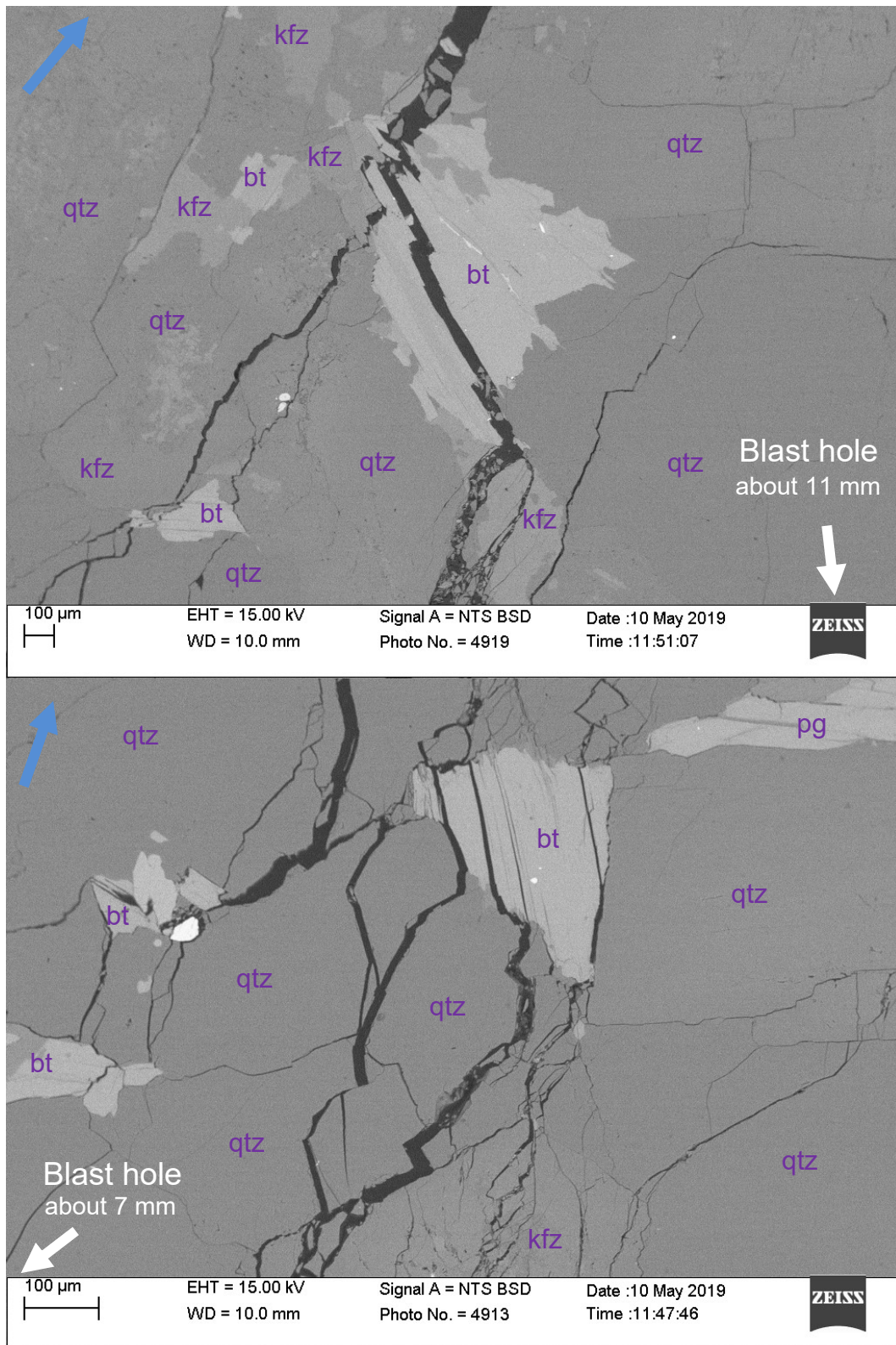


Figure 150: Cleavage fractures. SEM micrographs (g20(26.2)). The blue arrow marks the main direction of crack development.

Here, some of the grains acted as “shields” by arresting most of the propagating cracks depending on the grain structure, size, shape, and orientation (Figure 151). The grain shielding (fc, em, and pm) is usually related to mica and feldspar grains.

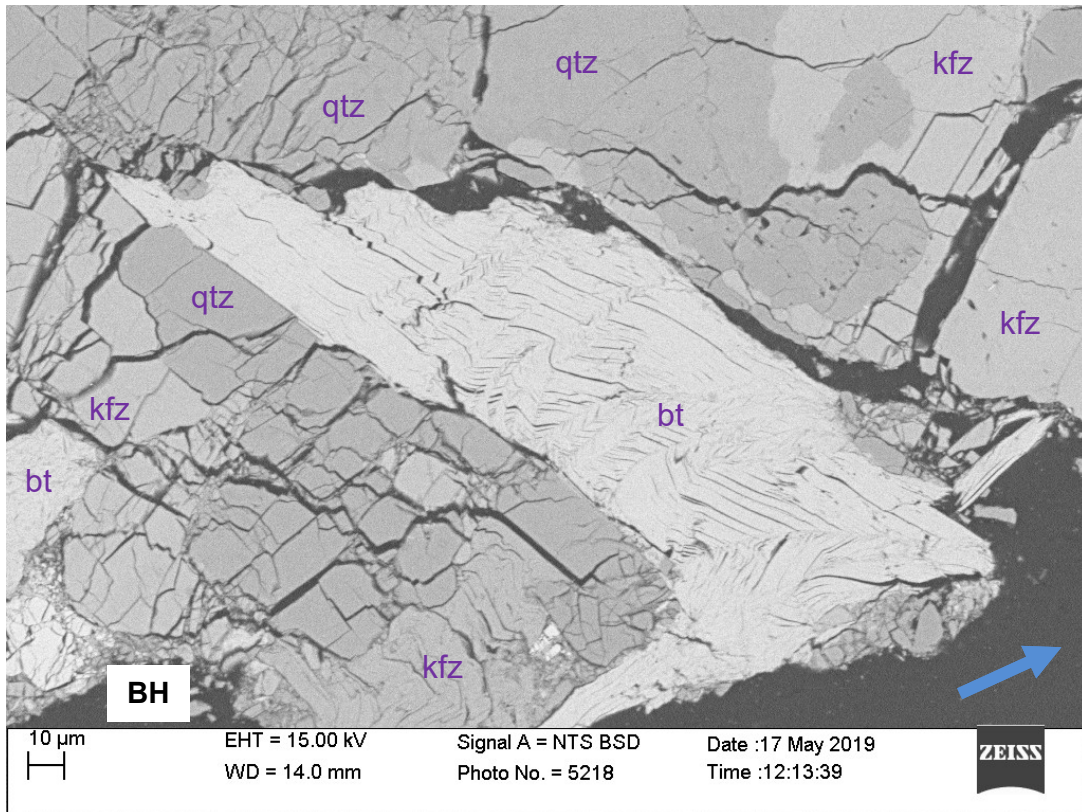


Figure 151: Grain shielding. Note the difference in fracturing below (nearer to the blast hole 'BH') and above the biotite grain (light grey). SEM micrograph (g6(27)). The blue arrow marks the main direction of crack development.

This is a form of intragranular crack arrest, i.e., a mechanism where a grain impedes and stops further propagation of a crack (Figure 152). This mechanism was observed in many forms and different grains.

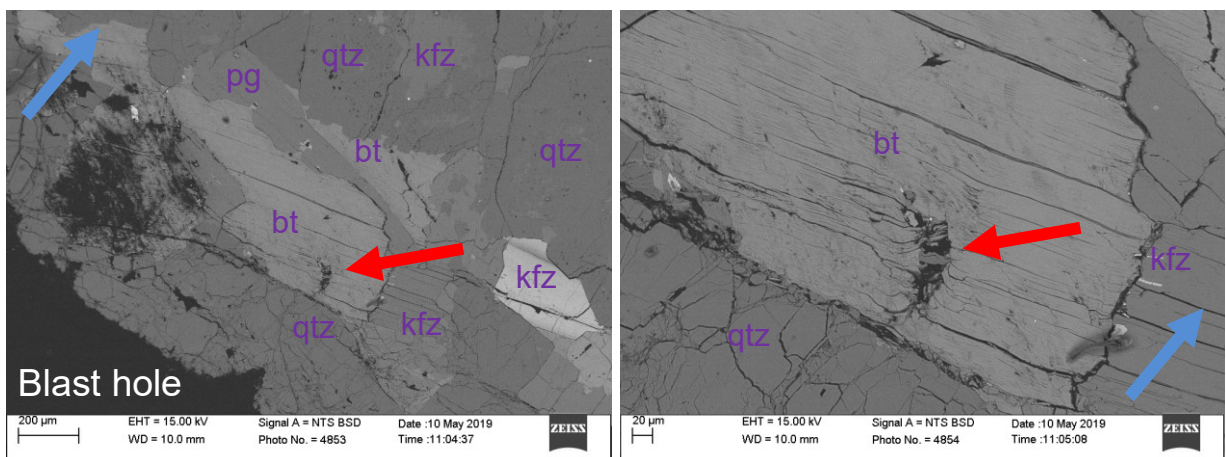


Figure 152: Intragranular crack arrest and partial rupture of a mica grain. SEM micrographs (g12(24)). The blue arrow marks the main direction of crack development.

If a propagating crack arrests at a mica grain, it usually penetrates through a few layers first, leaving rupture formations. Some grains act as branching/merging points.

Depending on the shape, orientation, and type, a grain could facilitate a propagating crack along its borders, cleavage planes, or both (fc, cc, em, and pm).

Quartz grains in most cases divide incoming cracks (em) and leave branched intergranular fractures. Here, the new crack branches can merge again at the other end of the grain. Mica and feldspar grains leave more complex fracture traces, as they often fracture along their cleavage planes (Figure 153 and Figure 154).

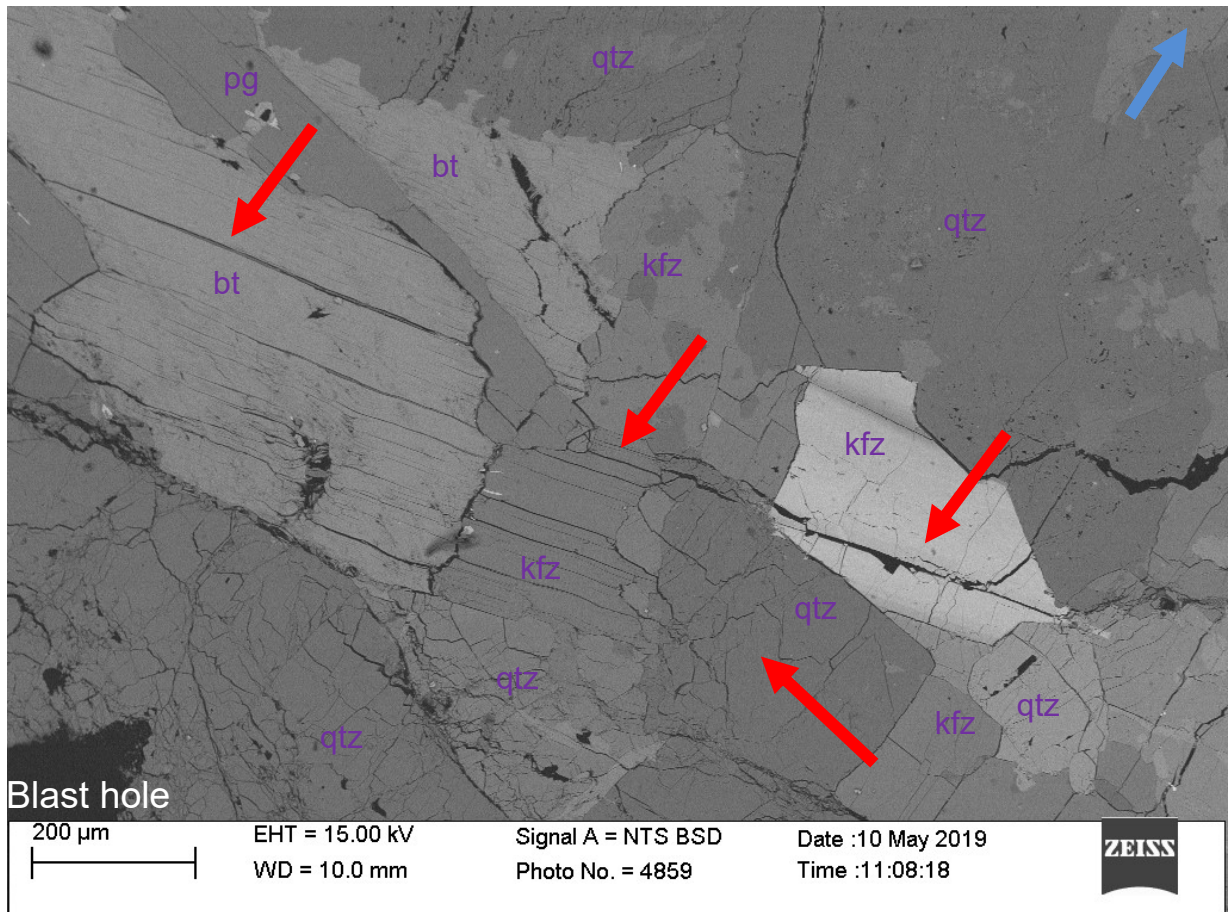


Figure 153: Complex fracturing and deformation in mica and feldspar grains. SEM micrographs (g12(24)). The blue arrow marks the main direction of crack development.

This fracturing can lead to further multimodal deformation of the grain layers surrounding the cleavage planes (em and pm). Such formations indicate combinations of shearing, bending, and folding of the grains and their parts (e.g., lamellae). These formations are also present along flanks of main radial cracks (Figure 154).

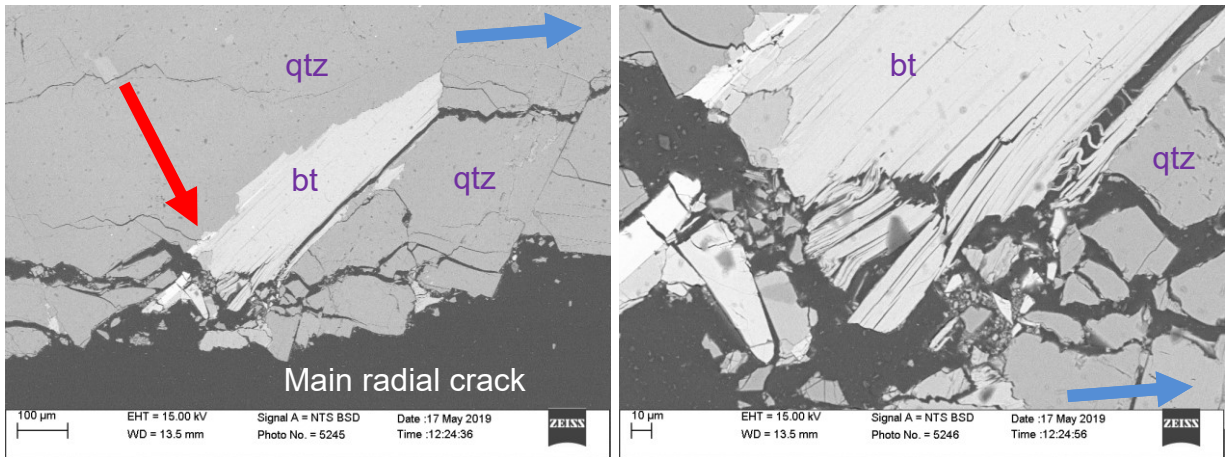


Figure 154: Fracture formations along the flanks of main radial cracks (about 5 mm from the blast hole). SEM micrographs from (g6(27)). The blue arrow marks the main direction of crack development.

These regions (i.e., crack wakes) include smaller cracks and occasional mica shearing/bending. The regions appear thicker and more intensive with higher linear charge concentration. Feldspar grains often fracture in “zig-zag” patterns (cc and em) due to their preferred cleavage planes (Figure 155).

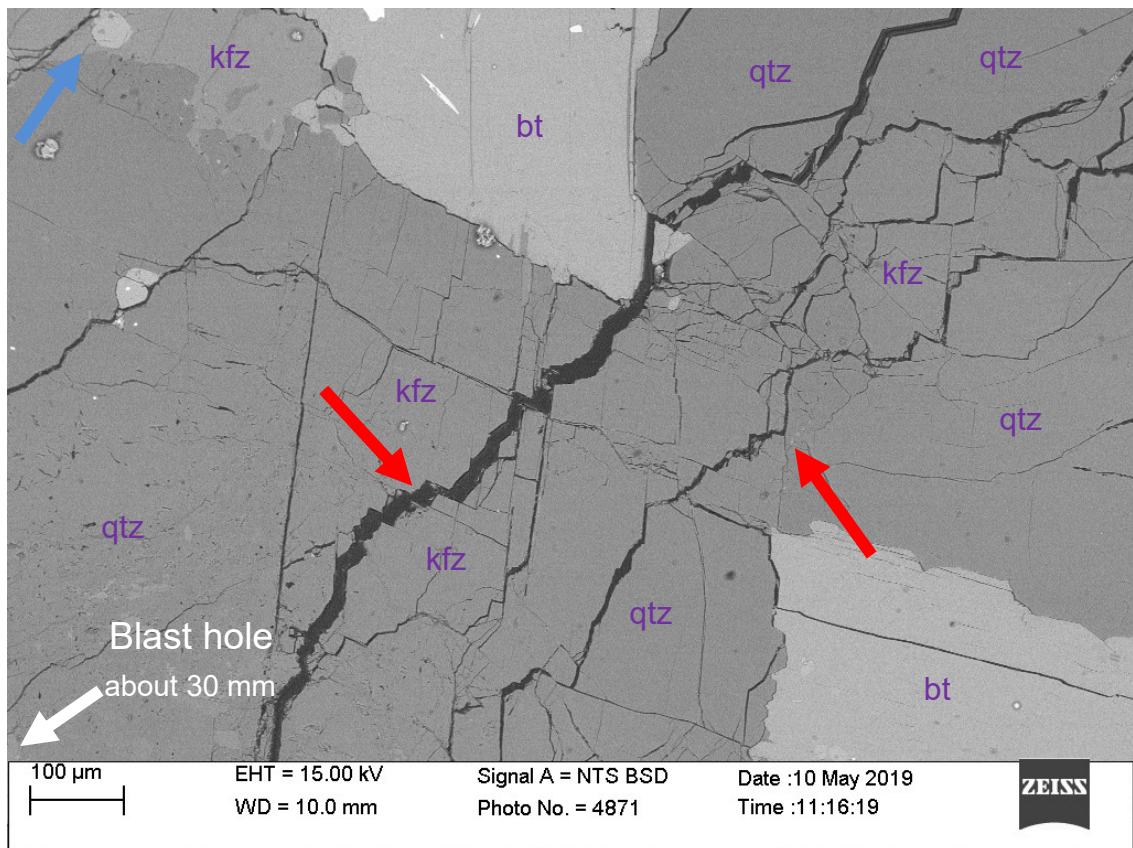


Figure 155: “Zig-zag” fracturing in feldspar with many branching/merging formations. SEM micrograph (g12(24)). The blue arrow marks the main direction of crack development.

Such fracturing leaves small branching/merging patterns along the cleavage paths and, especially, when the switching from one plane to another. Similar effects can be seen in mica grains (Figure 156). In that case, however, a crack ‘tried’ to propagate across the cleavage planes and the grain lamellae. This resulted in the crack-path deviation, looking like “side jumps” across the layers.

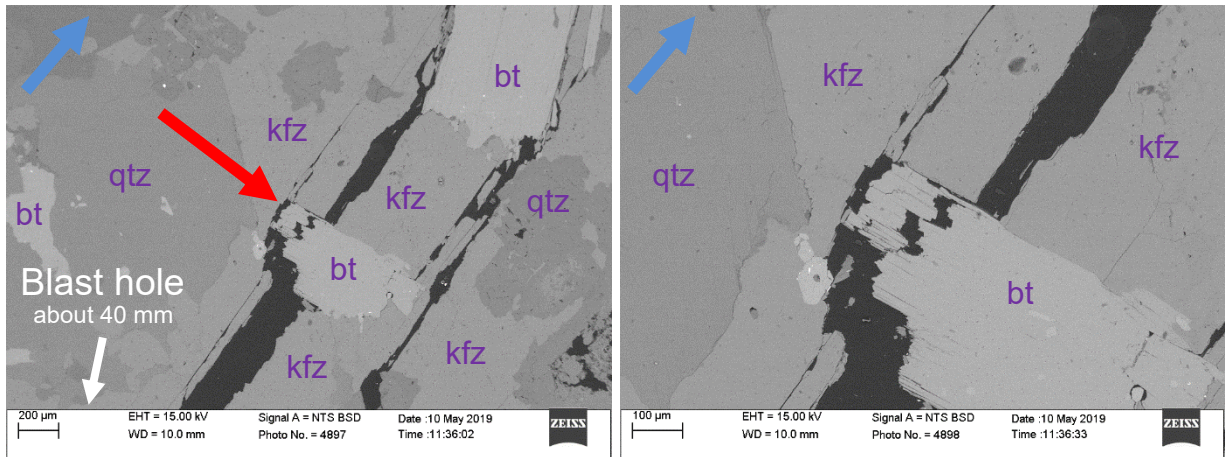


Figure 156: Seeming “zig-zag” fracturing in mica grains. SEM micrographs (g12(24)). The blue arrow marks the main direction of crack development.

Similar branching/merging is also present along some grain boundaries (Figure 157). These are probably related to the elastic mismatching (em) and corresponding unstable micro-crack propagation.

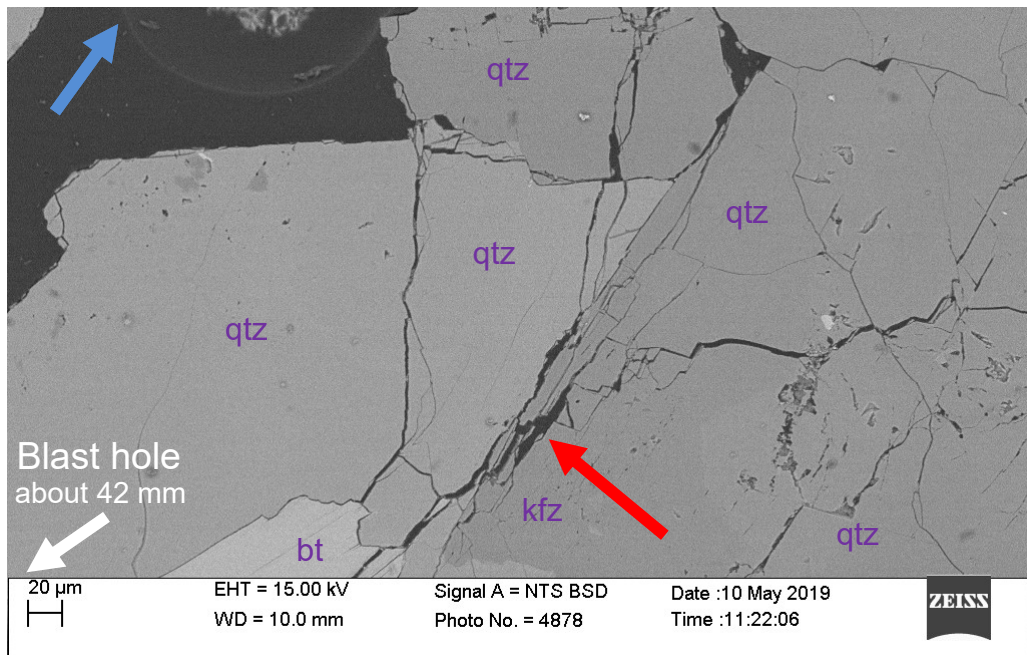


Figure 157: Branching/merging along grain boundaries. SEM micrograph (g12(24)). The blue arrow marks the main direction of crack development.

The fracturing along the grain boundaries can even lead to crushing if the contact grains are further subjected to relative motion (Figure 158). Such crushing formations are more probable between quartz grains and between quartz and feldspar grains.

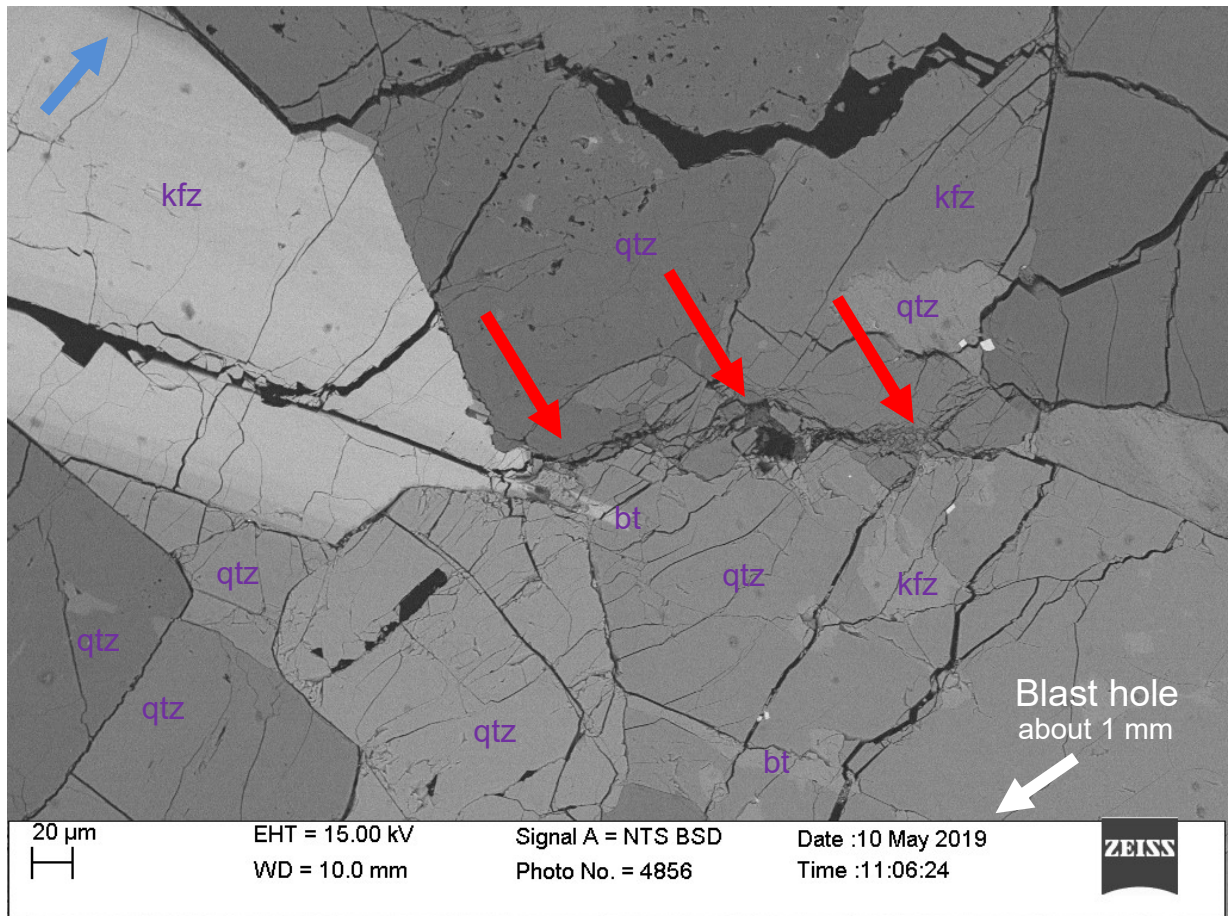


Figure 158: Crushing following branching/merging along grain boundaries. SEM micrograph (g12(24)). The blue arrow marks the main direction of crack development.

5.8.3 Small fragments

The observed small fragments were flat, up to about 30 mm in diameter (largest dimension). Their edges were considered as probable macroscopic branching/merging lines (mostly em). These edges are different from the rest of the fracture surfaces on these fragments (Figure 159 and Figure 160).

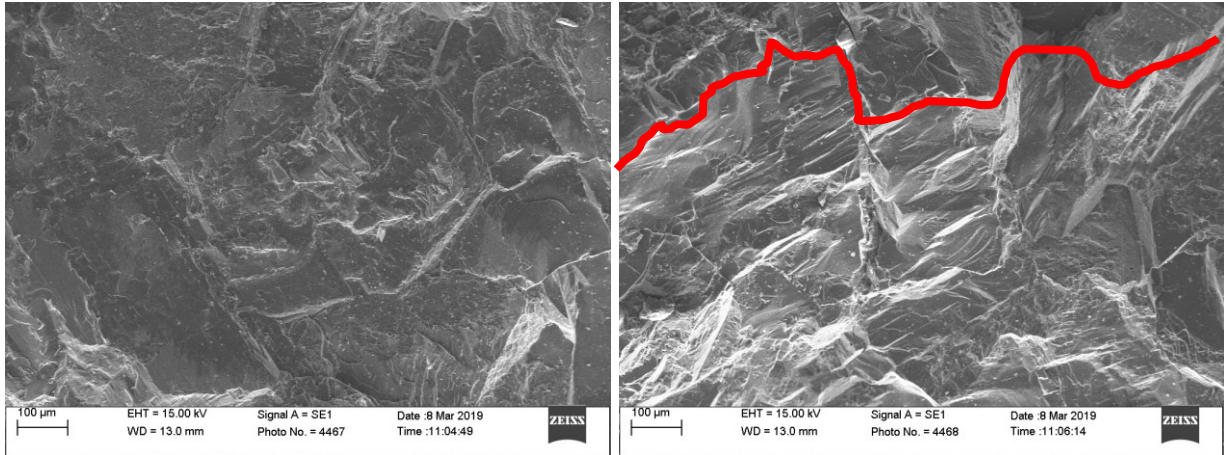


Figure 159: Fracture surfaces near the middle of a small fragment (left) and at its edge (right, red line) in the granite. SEM micrographs (g12(24)).

The edges in the granite and the mortar are rougher than the plane surfaces, with more traces of unstable crack propagation.

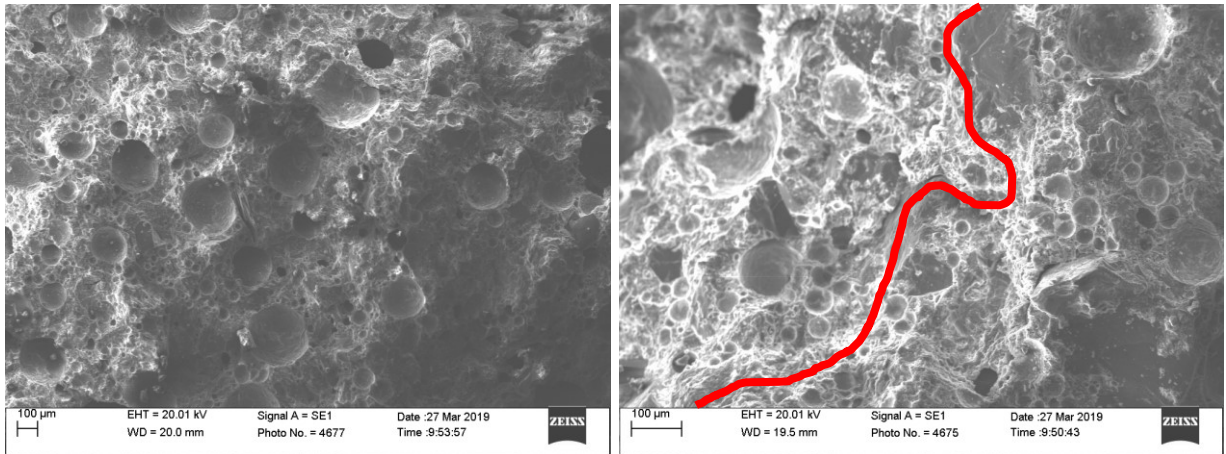


Figure 160: Fracture surfaces near the middle of a small fragment (left) and at its edge (right, red line) in the mortar. SEM micrographs (m12(20)).

Transgranular fractures are frequent at the edges in the granite (Figure 161).

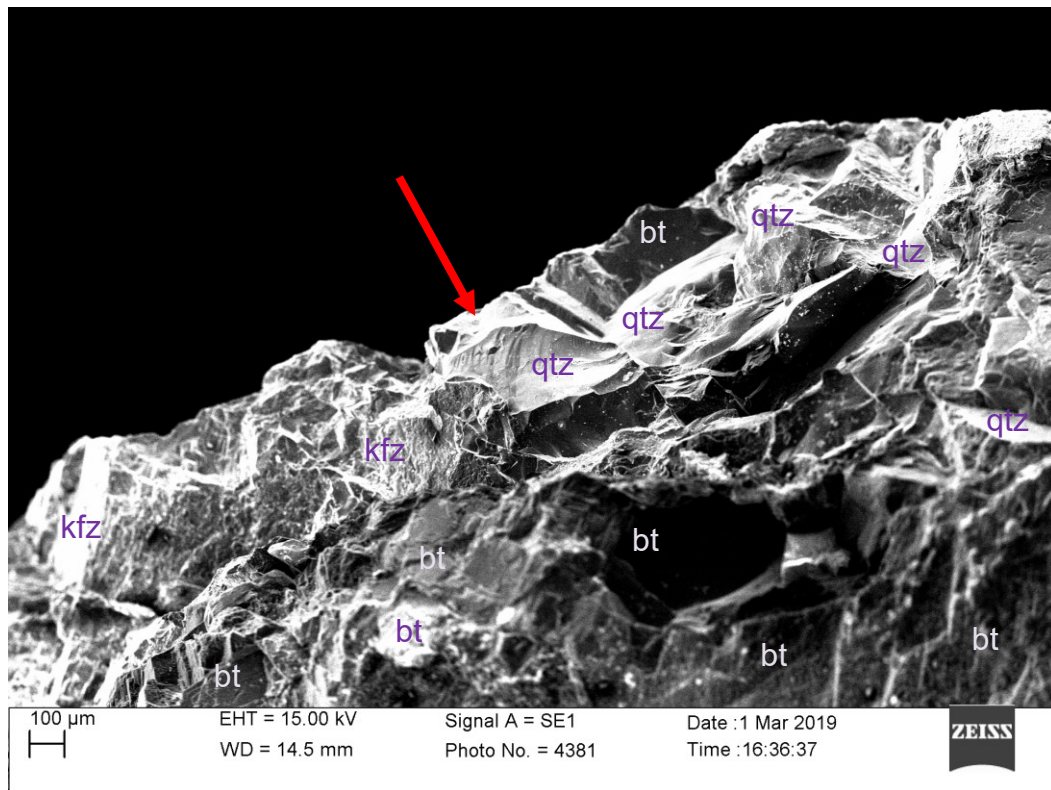


Figure 161: Transgranular fractures along a fragment edge in the granite. SEM micrograph (g12(24)).

The mortar fragments rarely show transgranular fractures (cc, em, or pm), i.e., shell-like (conchoidal) split surfaces of quartz grains (Figure 162). These fractures are more likely to occur near the edges.

In the rest of the surfaces in the mortar (e.g., near the middle of a flat side), the remnants of larger pores are often circular, indicating that they were most probably just split by the propagating crack that generated the observed fracture surface. The edges in the mortar, however, show less complete remnants of the larger pores (i.e., mostly spherical quarter segments), indicating that these pores had an important role in the branching/merging of the edges.

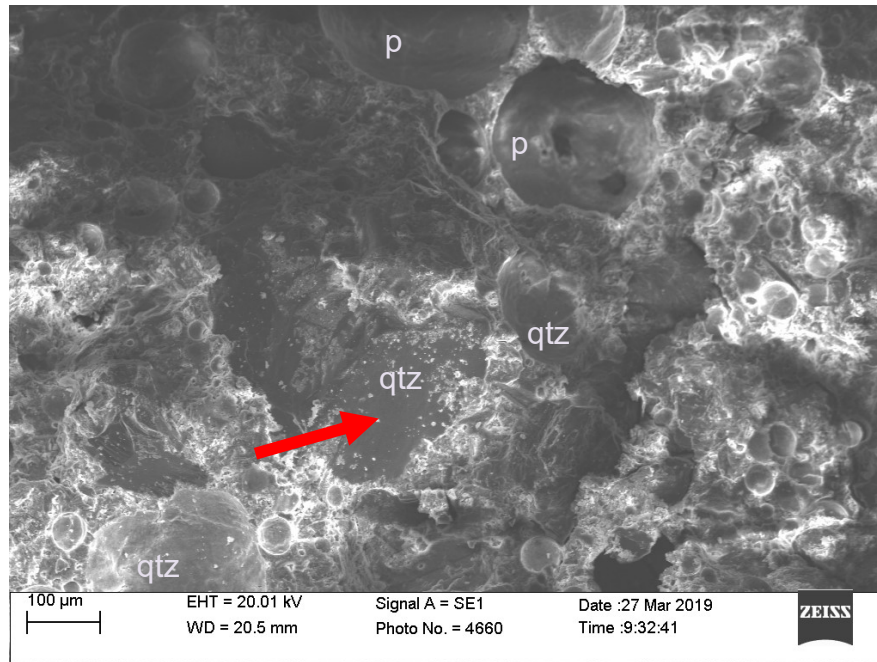


Figure 162: Transgranular fractures in quartz grains (dark surface near the centre of the image) in the mortar. SEM micrograph (g6(22.2)).

Transgranular fractures are also found at sudden changes in the plane inclination of fracture surfaces in both materials. These formations appear like those at the edges. Figure 163 shows such a case in the mortar.

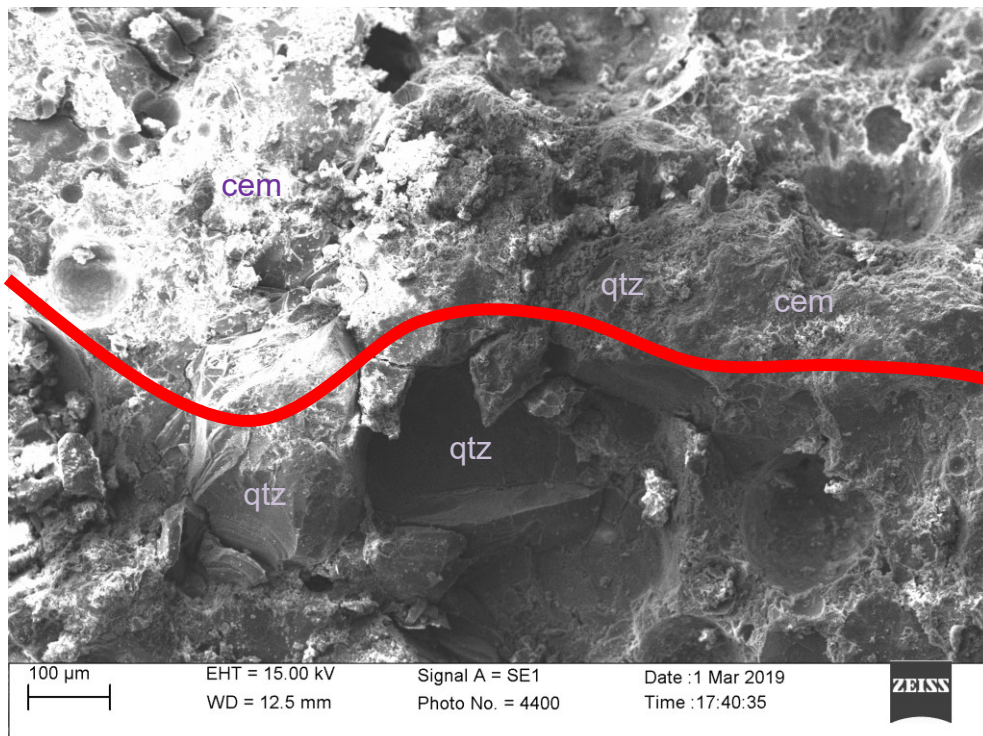


Figure 163: Transgranular fractures in quartz grains along a line of sudden change (indicated by the red line) in the mortar. SEM micrograph (m12(20)).

Figure 164 shows such a case with a branching/merging line in the granite.

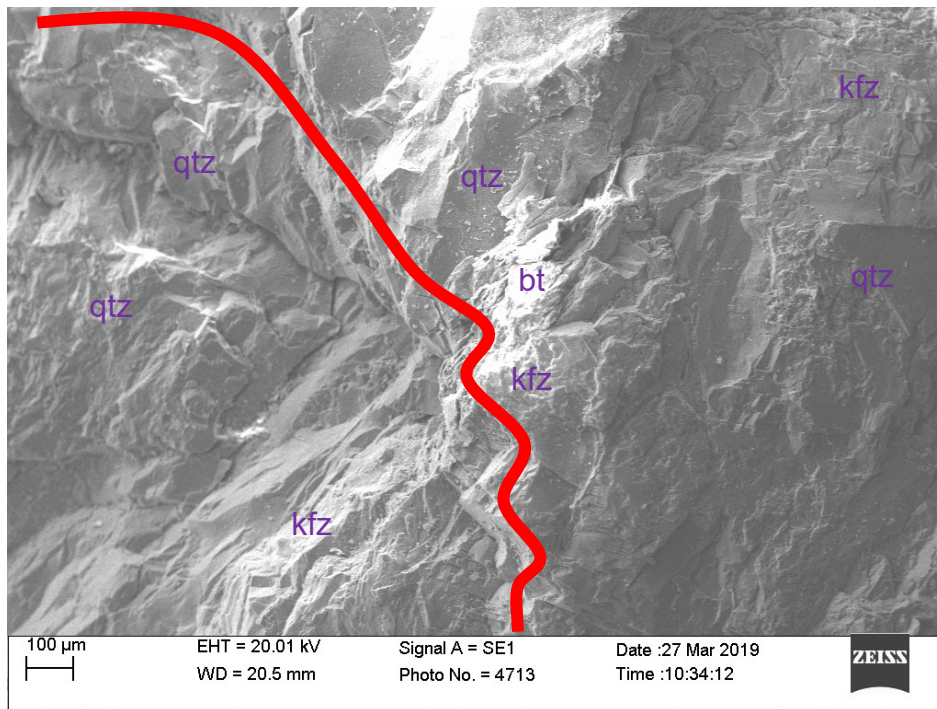


Figure 164: A line of sudden change (indicated by the red line) in the fracture surface in the granite. SEM micrograph (g20(26.2)).

Figure 165 shows a close-up image of a branching/merging fracture surface in the mortar.

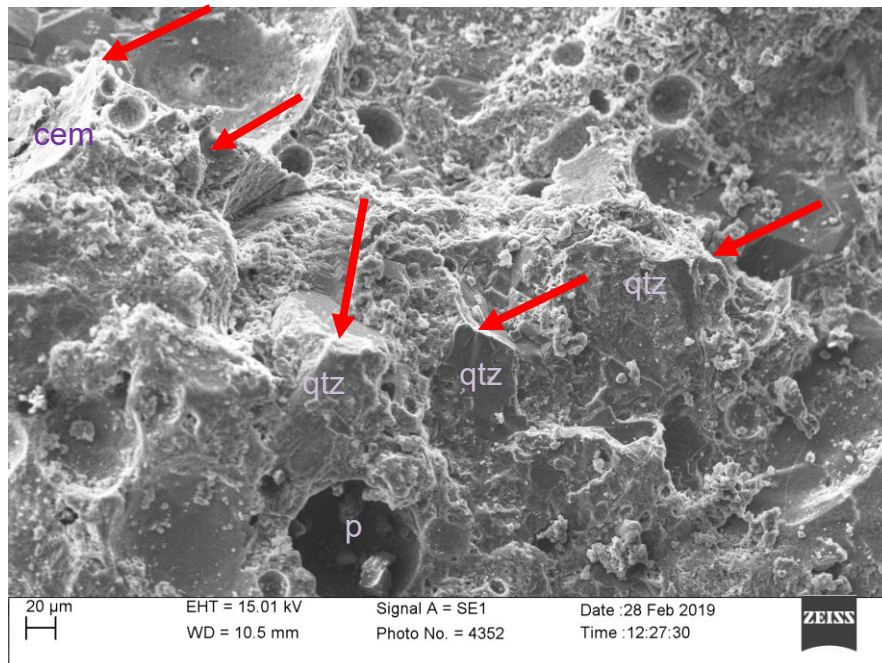


Figure 165: Branching/merging traces (indicated by the red arrows) at a fracture surface in the mortar. SEM micrograph (m12(20)).

The mortar fragment surfaces include many traces of micro-cracking at the pore edges (fc and em) (Figure 166), especially near the transition lines (i.e., probable branching/merging lines).

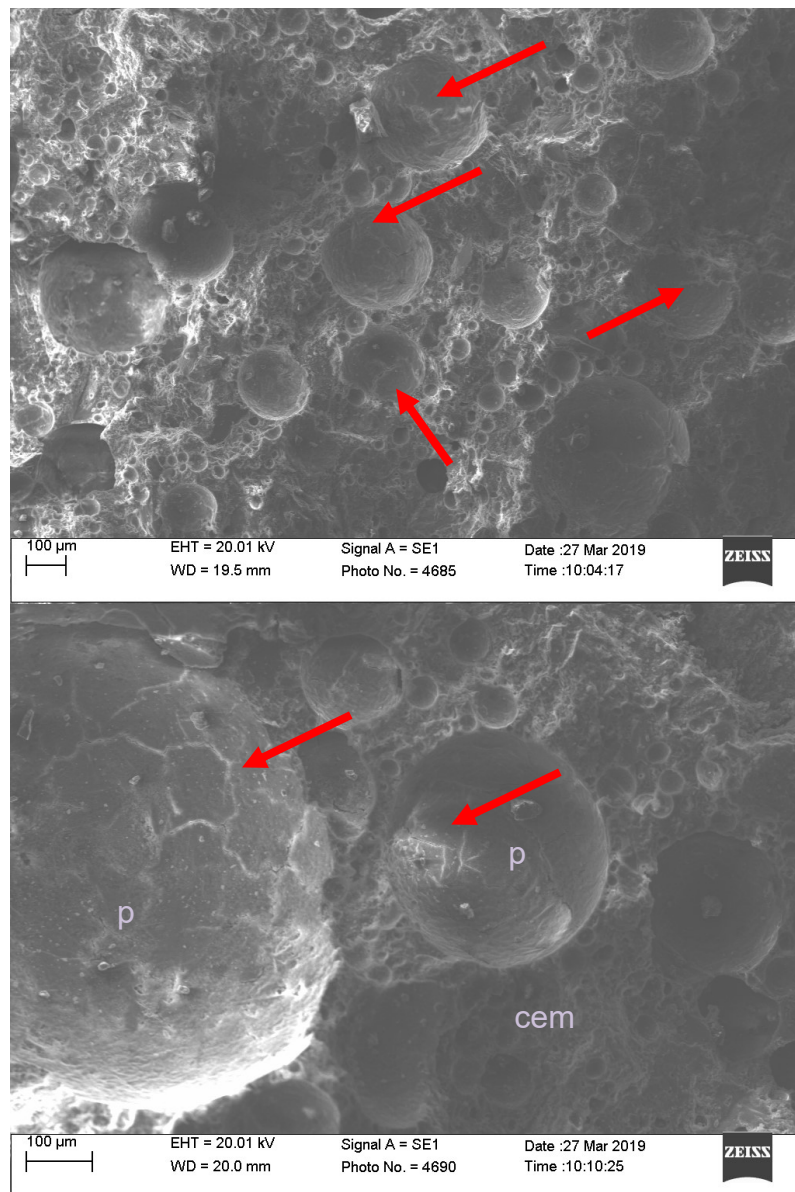


Figure 166: Intensive micro-cracking (indicated by the red arrows) at pore edges in the mortar. SEM micrographs (m20(22.1)).

The lines of sudden surface changes (i.e., probable branching/merging lines) in the granite, between mostly transgranular-fracture planes, often start from a single elongated crystal grain that sticks out from the fracture plane (Figure 167). Such grains (mostly mica or feldspar) are probable initiating or change points of branching/merging (fc and em).

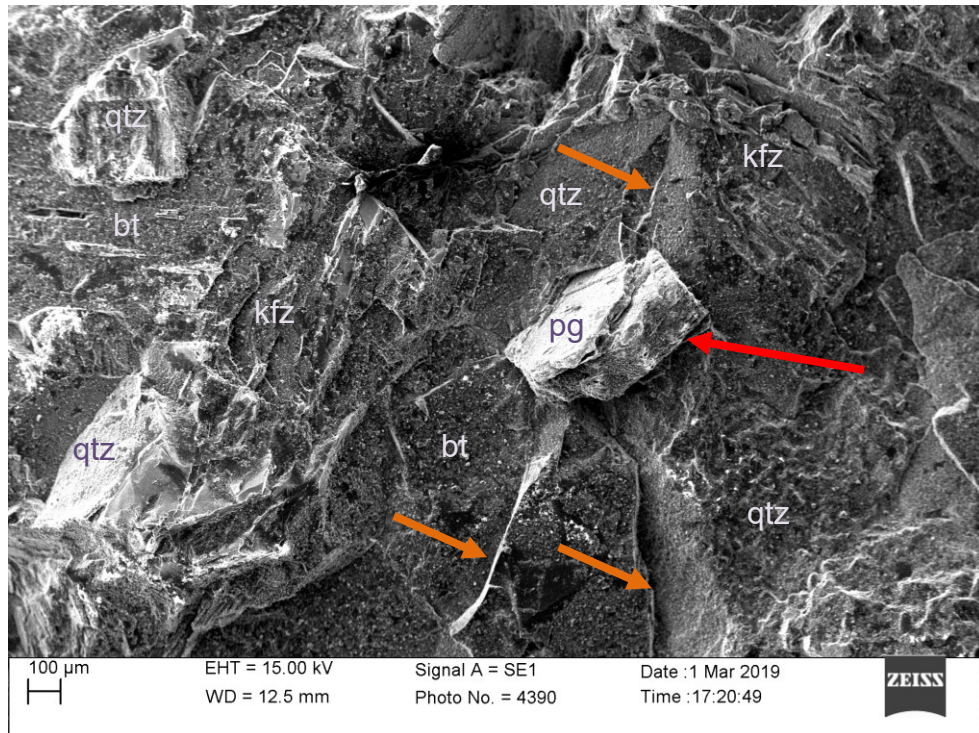


Figure 167: Branching/merging line (indicated by the orange arrows) starting at a single plagioclase crystal (indicated by the red arrow) in the granite. SEM micrograph (g12(24)).

5.9 Blast-induced fracture surfaces

This section presents results of measured roughness of blast-induced surfaces of larger fragments from the blast tests (see Section 4.3). The results cover images of height maps, roughness points, and summarized roughness results. Raw result data and images are provided in Appendix 17.

5.9.1 Height maps and surface-roughness images

The result maps were exported as colour-coded images based on histograms of the scan data and their spatial distribution. Figure 168 shows the height maps of the mortar fragments relative to a best-fit plane.

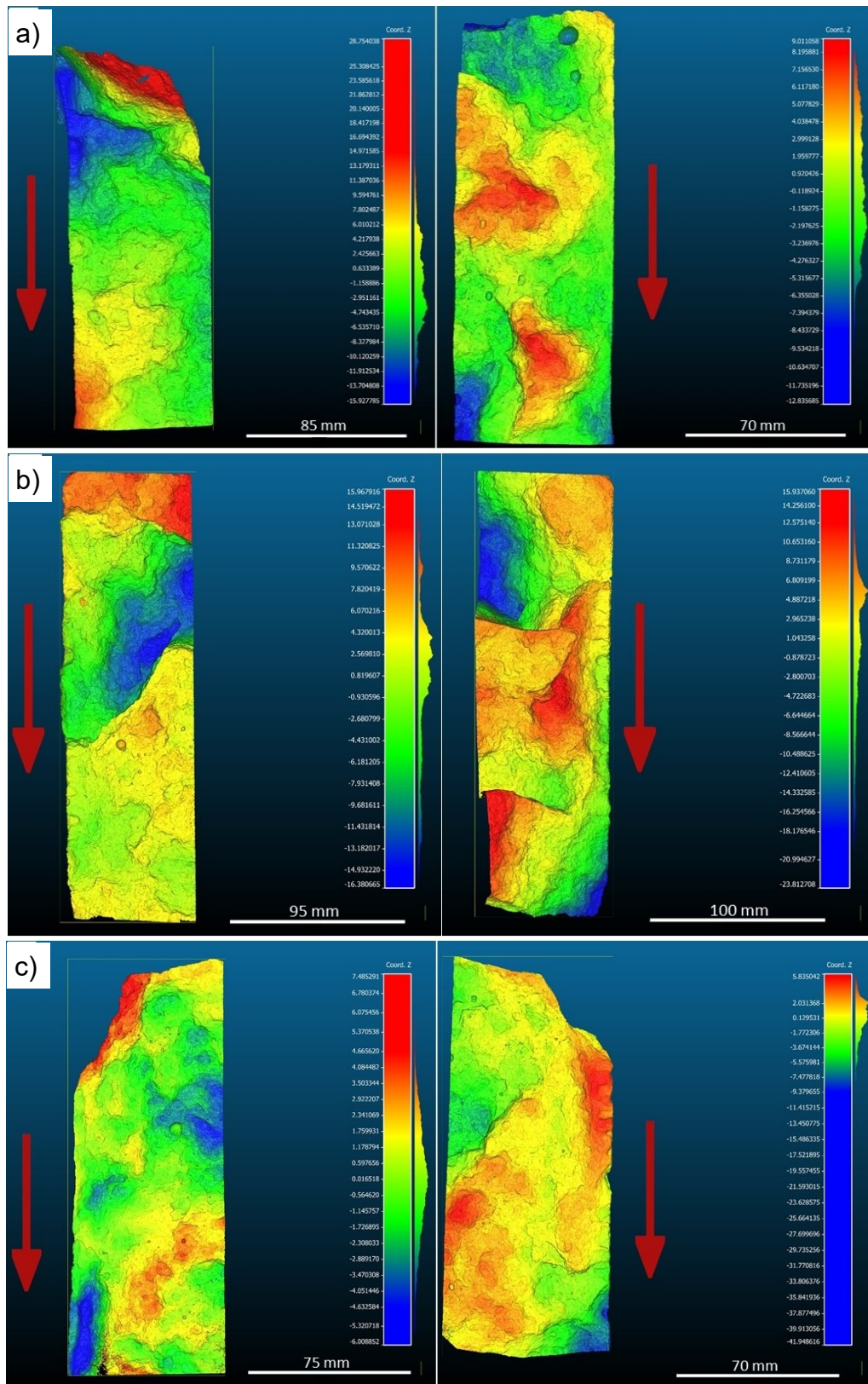


Figure 168: Height maps of scanned mortar fragments (left and right side): a) m6 (22.2), b) m12 (20); c) m20(22.1). The red arrow indicates the position of the blast hole and detonation direction.

Figure 169 shows height maps of the granite fragments relative to a best-fit plane.

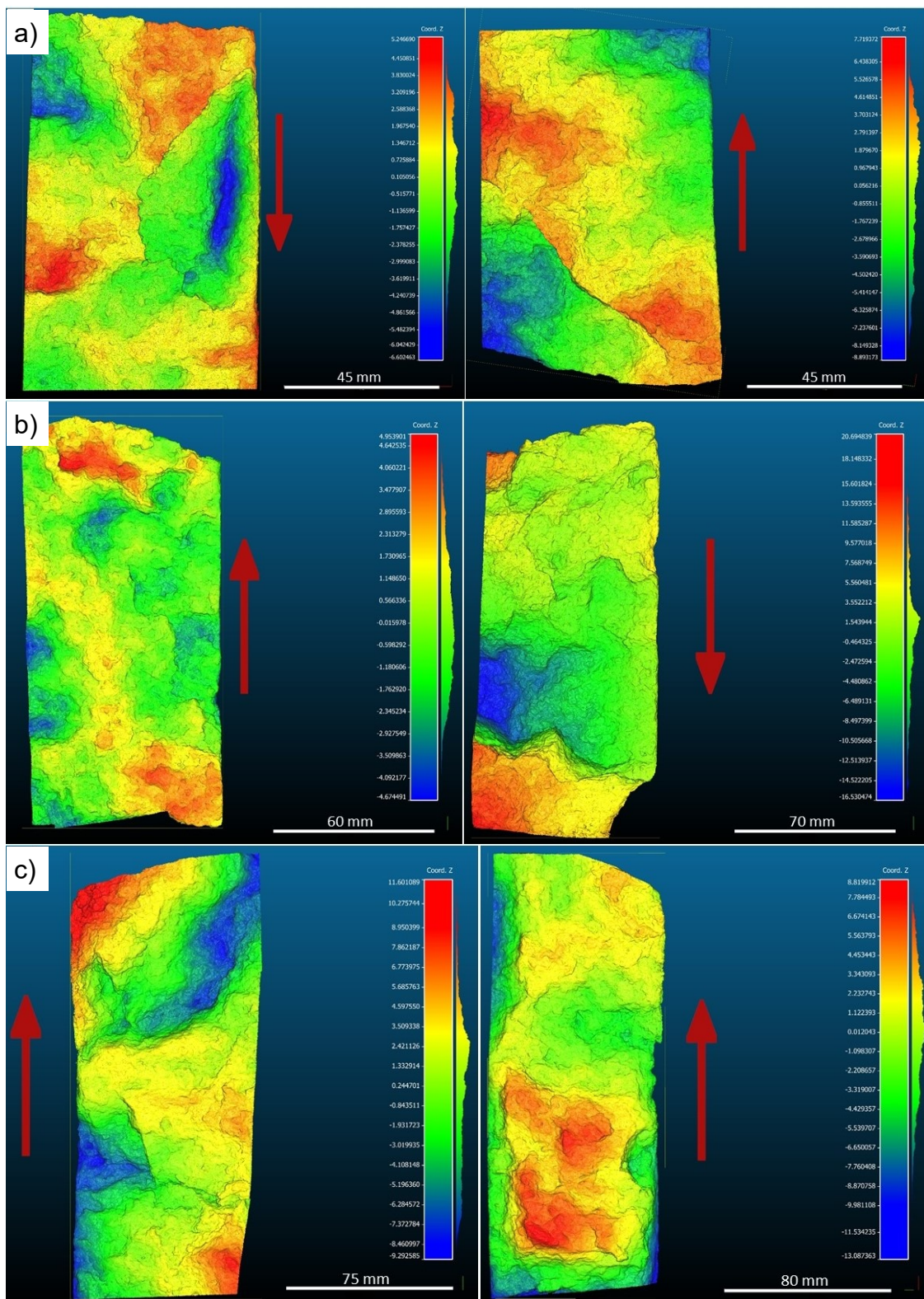


Figure 169: Height maps of scanned granite fragments (left and right side): a) g6(27); b) g12(25); c) g20(26.2). The red arrows indicate the position of the blast hole and detonation direction.

These images show distinct ridges and valleys, possibly indicating changes in fracture propagation due to the branching/merging mechanism. Such fractographic features are better shown in the colour-coded map images of the roughness of the fracture surfaces. Figure 170 shows examples of such images of the mortar and of the granite fragments.

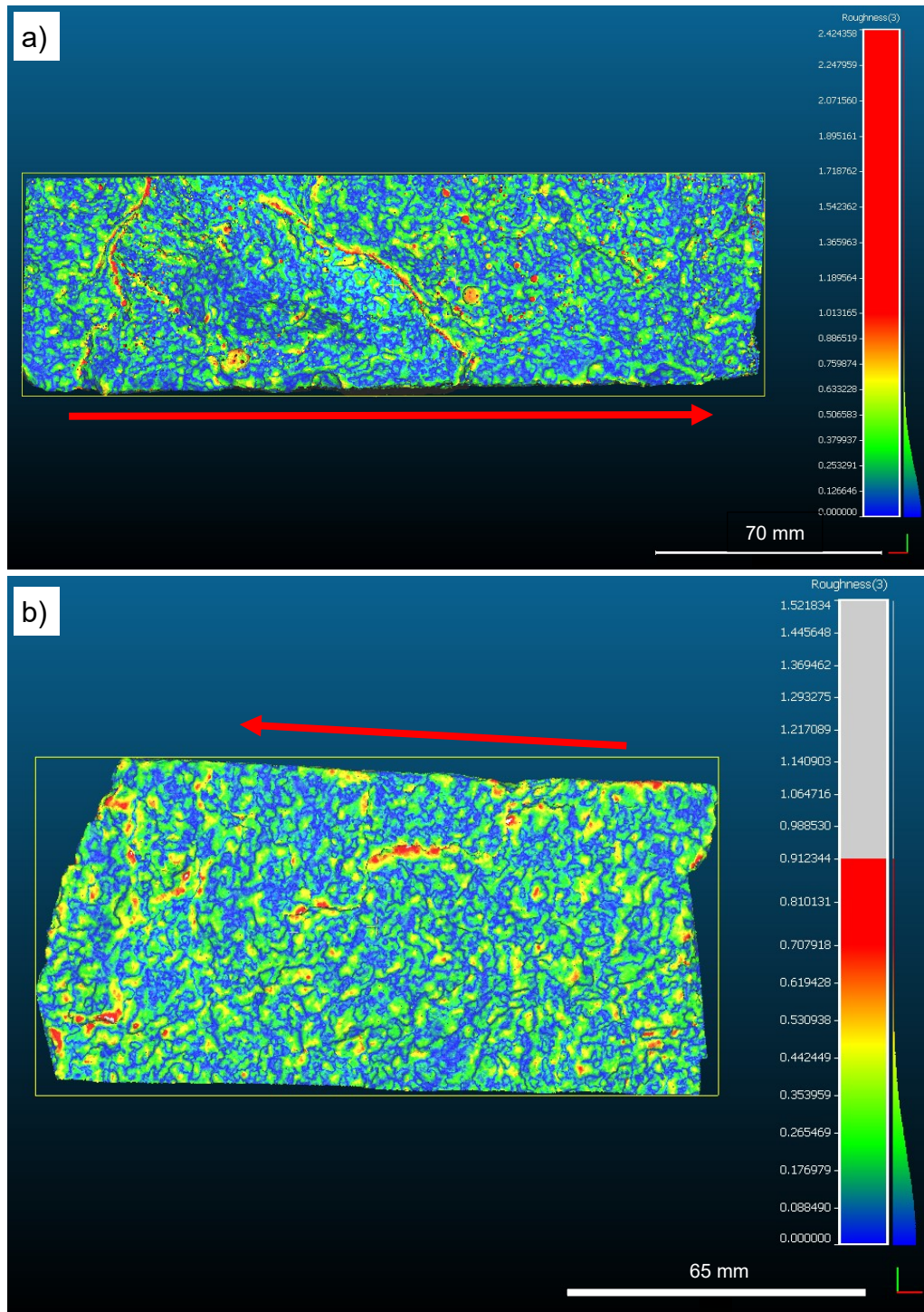


Figure 170: Map images of the fracture-surface roughness (kernel size 3 mm): a) the left side of a fragment from m12(20); b) the left side of a fragment from g12(25). The red arrows indicate the position of the blast hole and detonation direction.

In the mortar, the roughness values are highest at the edges of the pores and peaks of fracture ridges (Figure 171).

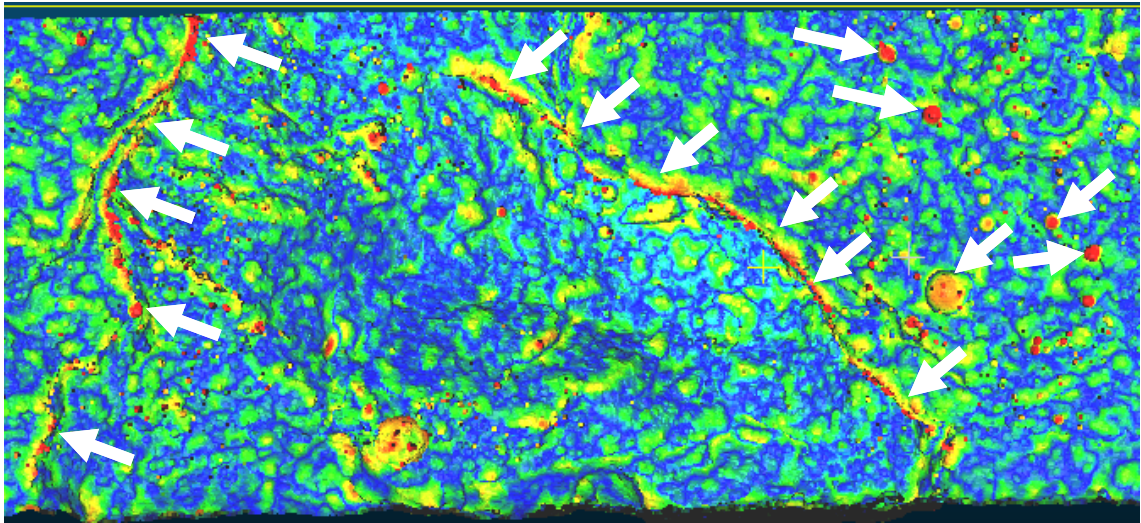


Figure 171: Enlarged portion of the map image from Figure 170a. Peak roughness values (marked with white arrows) are mostly positioned along ridge peaks and pore edges.

Ridges are well pronounced in the roughness maps for both materials. However, observed ridges, valleys, and other fractographic features in macro-scale could be related to only sudden changes in crack/fracture propagation, not necessarily to crack branching/merging. Furthermore, like in the work of Johnson (2014), these features do not seem to have regular orientation considering the detonation direction or the blast-hole position. They seem to be rather randomly distributed due to the complex interaction between blast-induced stress/strain waves and developing fractures (Fourney, 2015).

5.9.2 Fracture-surface roughness

Table 39 shows a summary of calculated average fracture-surface roughness considering kernel size, linear charge concentration (l_c), and blasted material (see also Table 159).

Table 39: Summary of the fracture-surface roughness, averaged for each scanned fragment.

Material	l_c [g/m]	Kernel size [mm]		
		1	3	5
Mortar	6	0.071	0.202	0.326
	12	0.073	0.218	0.371
	20	0.068	0.182	0.283
Granite	6	0.066	0.184	0.297
	12	0.070	0.198	0.321
	20	0.062	0.180	0.291

Figure 172 shows the influence of kernel size on average values of the fracture-surface roughness.

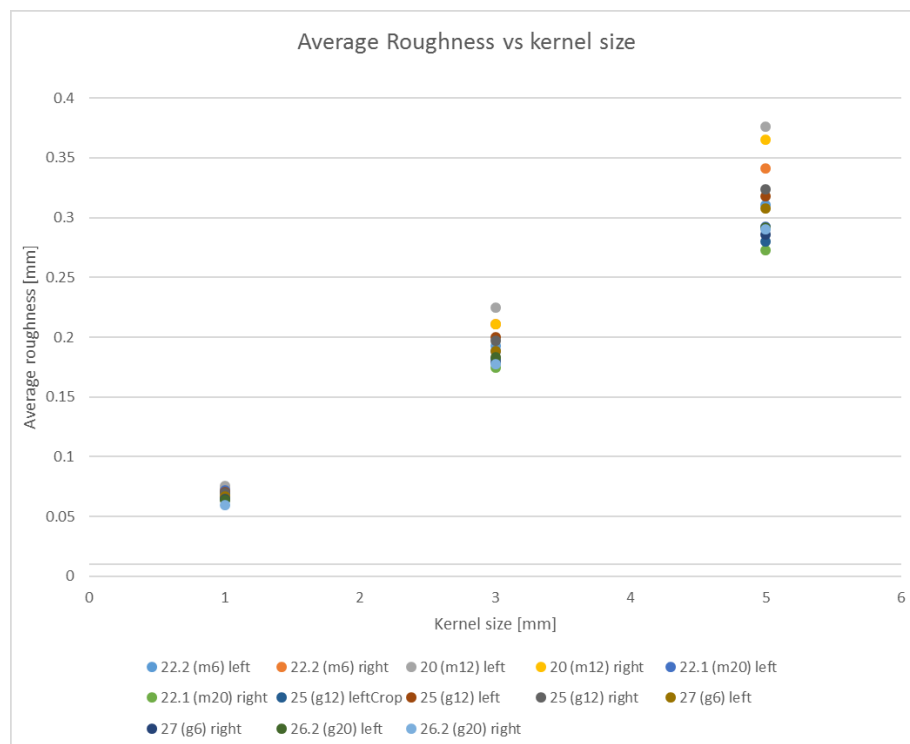


Figure 172: Average roughness of fracture surface concerning kernel size. The data points represent fracture surfaces (left and right) of scanned fragments.

The average roughness increases, and the data are more “spread out” (i.e., with higher absolute standard deviation) with the increase of the kernel size.

Figure 173 shows a summary of measured roughness of fracture surfaces, averaged per blast fragment.

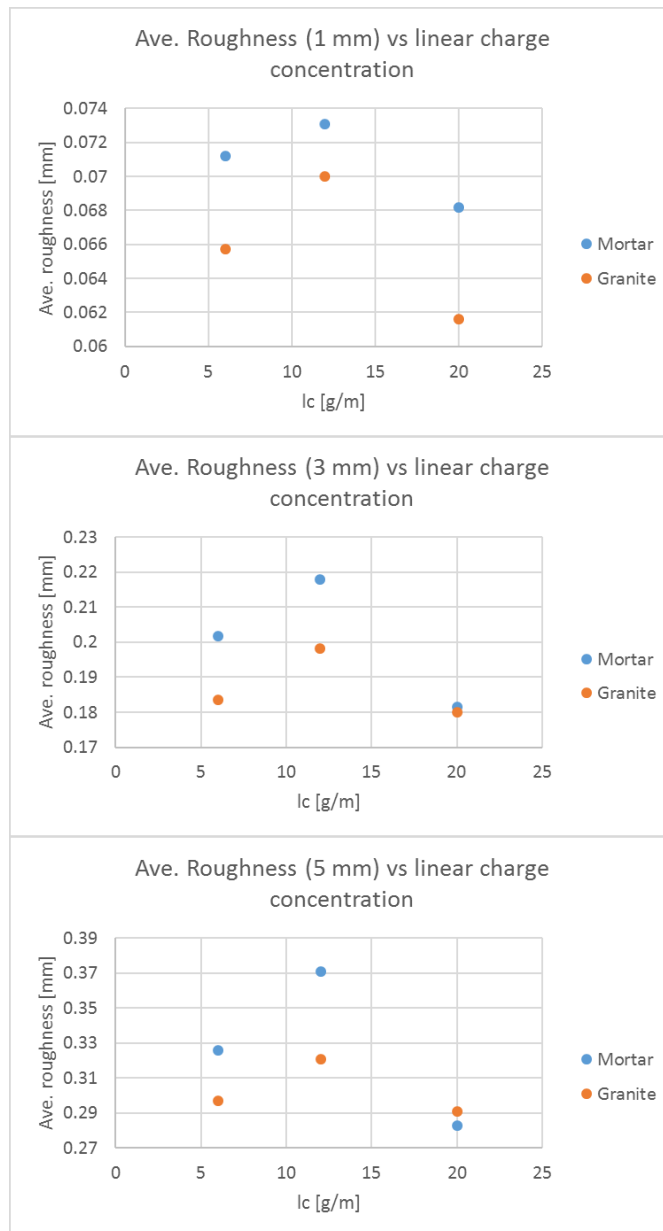


Figure 173: Summary of measured roughness of fracture surfaces, averaged per blast fragment. Kernel size is noted in the brackets in the graph titles.

For the kernel size of 1 mm, the average values of the fracture-surface roughness are significantly different to each other considering both linear charge concentration and blasted material (see Table 160). Conversely, the average values are not significantly different to each other considering the linear charge concentration for the kernel size of 3 mm (see Table 161), and considering blasted material for the kernel size of 5 mm (see Table 162). Such results indicate that the related data are “borderline.” This is due to the relatively large data sets - originally about 1E+06 data points for each fragment side, further randomly down-sampled to 100 data points each.

Furthermore, as shown in Figure 172, the relative standard deviation (Std) stays about the same for all kernel sizes (about 70-100%), indicating a relatively large system error compared to the random error(s) in the results. Therefore, even a small difference (i.e., otherwise negligible considering the average values) can result in the statistical evaluation showing a significant difference. To avoid such issues, these results were evaluated with box plots (Figure 174).

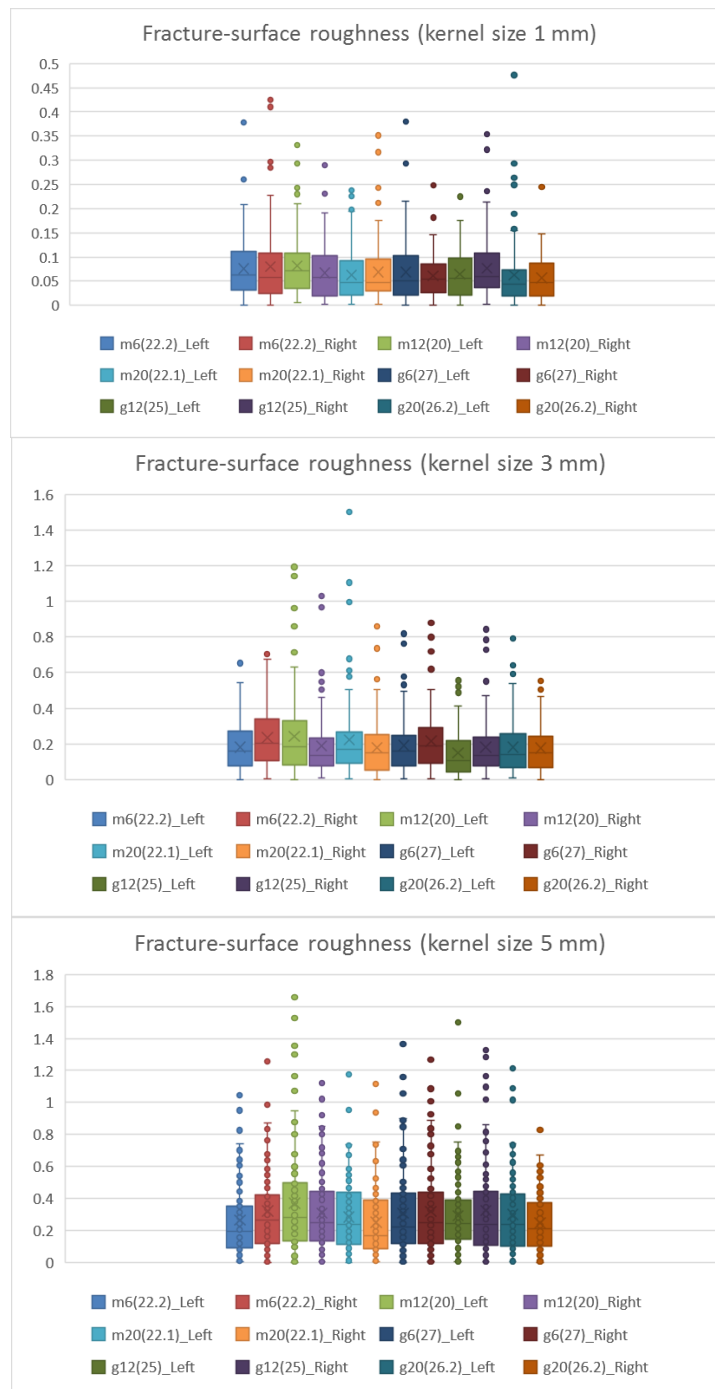


Figure 174: Box plots of data sets for fracture-surface roughness.

These plots show that the average values are about the same (for each kernel size).

5.10 Blast fragmentation

This section covers summarized results regarding screening (i.e., mechanical sieving and laser granulometry) of blasted cylinders, resulting cumulative fragment-size distributions (FSDs), and blast fines (see Section 4.5). The screening results were analysed as data sets from the sieving and as merged data sets from the sieving and the laser granulometry. Raw result data are provided in Appendix 18.

5.10.1 Screening results and fragment-size distributions (FSDs)

Figure 175 shows an overview of FSD data obtained by the sieving.

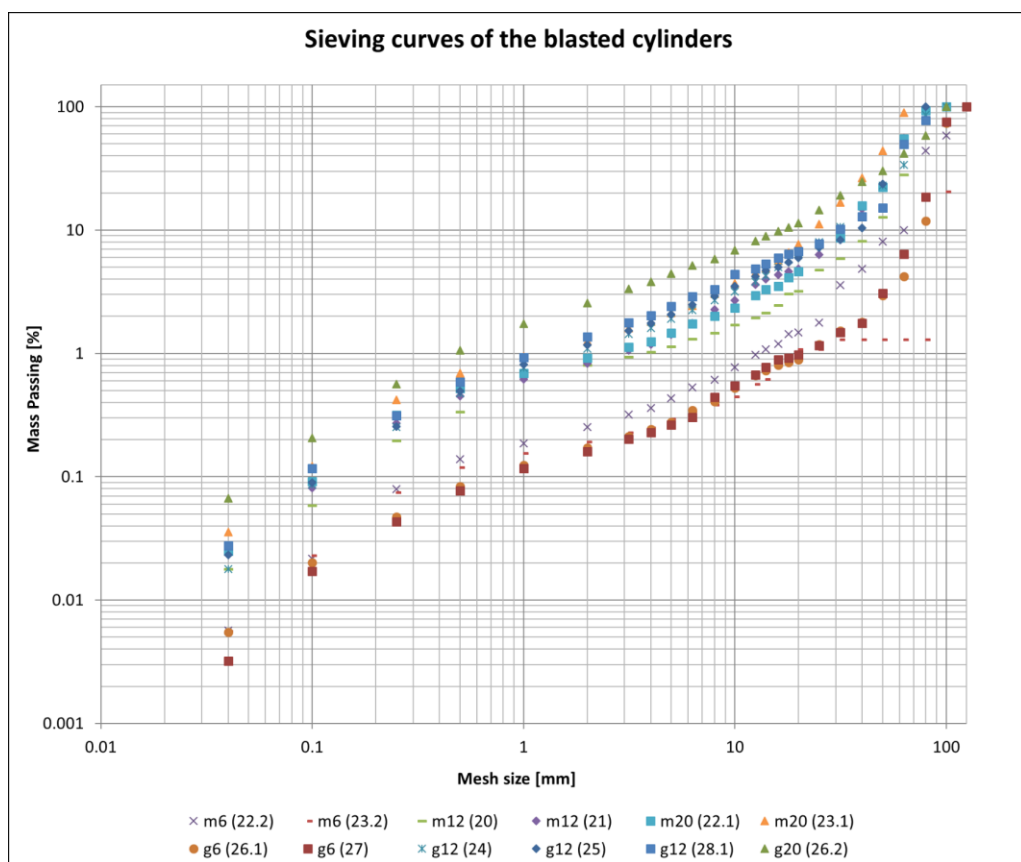


Figure 175: Sieving FSDs of blasted cylinders.

Figure 176 shows separate overviews of the sieving curves for the two blast materials.

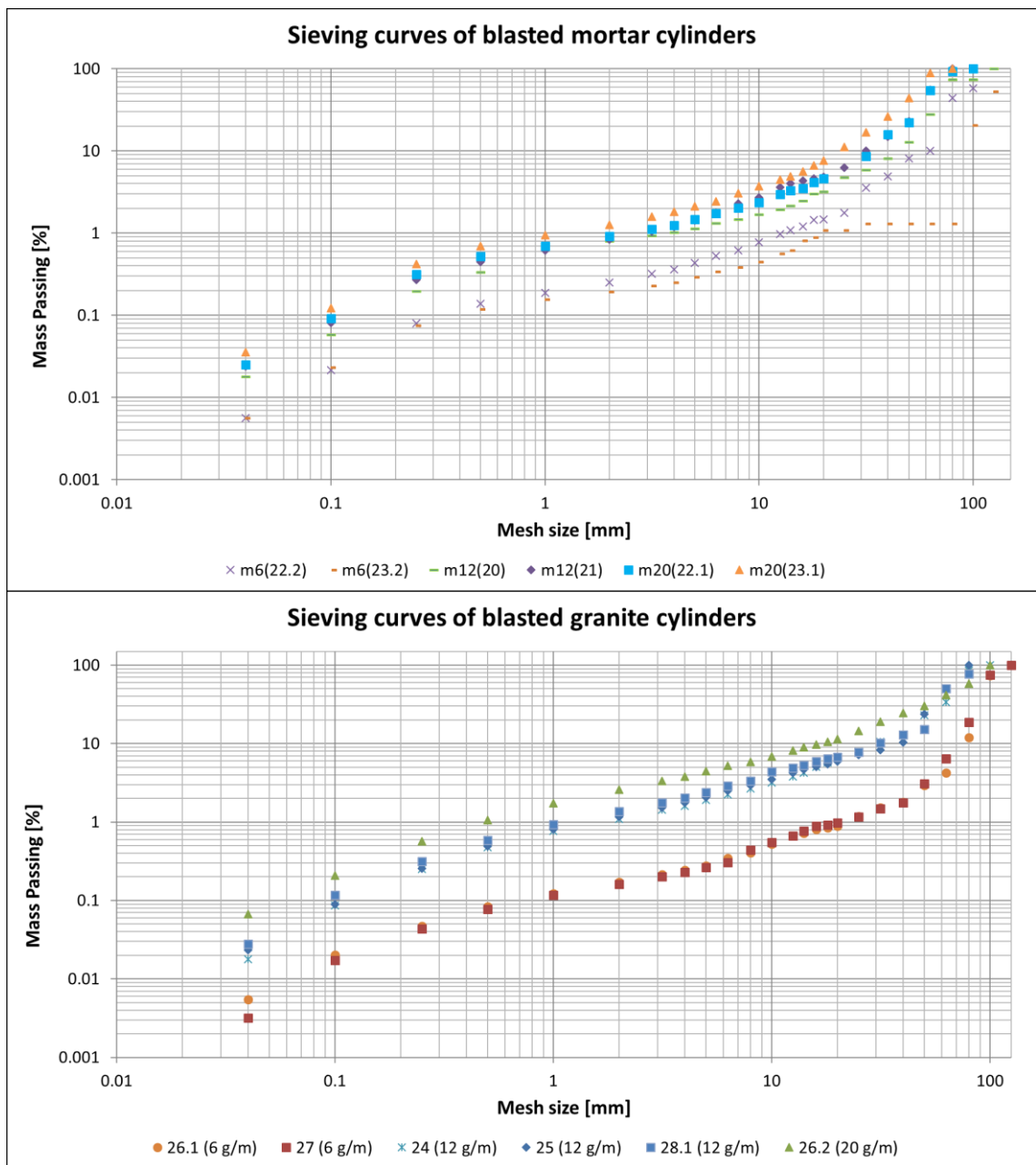


Figure 176: Sieving curves of blasted cylinders of mortar (top) and granite (bottom).

The sieving curves show the NBC parallel-upward shift with increasing linear charge concentration reasonably well. They also show the “dust-and-boulders” phenomenon, especially for the 6-g/m shots.

Figure 177 shows an overview of the curves obtained by the sieving and the laser-diffraction granulometry (merged screening data).

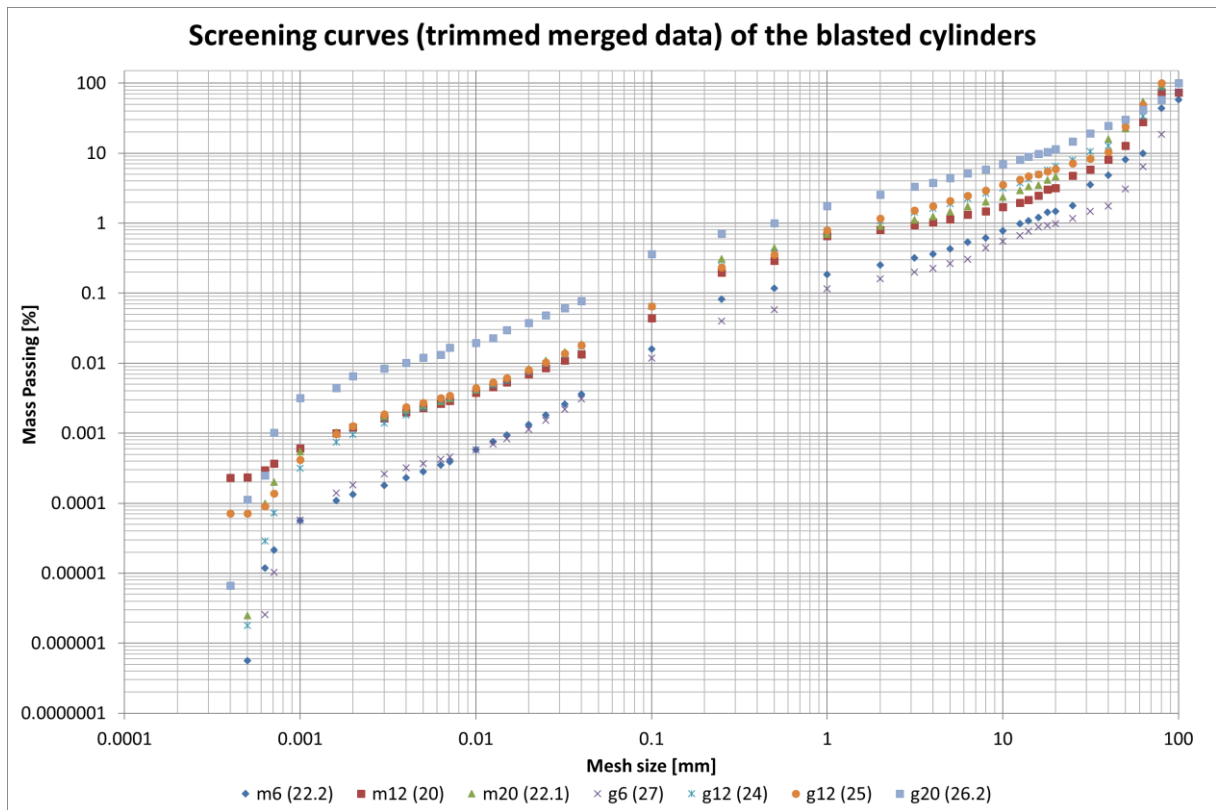


Figure 177: Curves of merged screening data of the blasted cylinders (> 1E-07% mass passing).

The curves indicate multimodal distributions with well-pronounced size ranges:

1. major fragments (mostly > 20 mm, and up to > 100 mm)
2. intermediate fragments (IF) (mostly 1–20 mm, and up to 80 mm)
3. fines (F), 0.04–1 mm
4. offset range (kink) (0.04–0.5 mm),
5. ultra-fines (UF) (1.6–40 μm), and
6. and ultra-fines tail (< 1.6 μm).

This means that the curve (i.e., fragment-size distribution) repeats itself (i.e., has a similar shape) at different fragment-size ranges.

Table 40 shows identified boundaries of the ranges in the sieving data and in the merged screening data.

Table 40: Identified fragment-size ranges in the FSDs. Offset

Material	Blast test	I_c [g/m]	x_{min} [μ m]	UF [μ m]	Fines [mm]	Offset [mm]	IF [mm]	x_{max} [mm]
Mortar	22.2	6	0.50	1.6–40.0	0.04–1	0.04–0.5	1–20	125–150
	23.2		40.00	-	0.04–1	0.04–0.5	1–20	125–150
	20	12	0.50	1.6–40.0	0.04–1	0.04–0.5	1–20	125–125
	21		40.00	-	0.04–1	0.04–0.5	1–20	63–80
	22.1	20	0.50	1.6–40.0	0.04–1	0.04–0.5	1–80	80–100
	23.1		40.00	-	0.04–1	0.04–0.5	1–63	63–80
Granite	26.1	6	40.00	-	0.04–1	0.04–0.5	1–20	100–125
	27		0.50	1.6–40.0	0.04–1	0.04–0.5	1–20	100–125
	24	12	0.50	1.6–40.0	0.04–1	0.04–0.5	1–40	80–100
	25		0.63	1.6–40.0	0.04–1	0.04–0.5	1–40	63–80
	28.1	20	40.00	-	0.04–1	0.04–0.5	1–20	80–100
	26.2		0.40	1.6–40.0	0.04–1	0.04–0.5	1–80	80–100

UF – Ultra-fines range,

IF – Intermediate-fragment-size range.

Table 41 shows the recorded material loss for all sieved cylinders.

Table 41: Total material loss in sieved blast cylinders.

Material	Blast test	Cylinder	I_c [g/m]	M_{cyl} [g]	m_{sieve} [g]	ΔM_{loss} [g]	ΔM_{loss} [%]
Mortar	22.2	mb71	6	8940	8858	81.92	0.92
	23.2	mb73		8920	8712	208.00	2.33
	20	mb72	12	8800	8707	93.21	1.06
	21	mb75		8980	8707	273.18	3.04
	22.1	mb74	20	9380	9213	167.15	1.78
	23.1	mb76		9020	8784	236.23	2.62
Granite	26.1	gb21	6	13880	13825	55.18	0.40
	27	gb25		14420	14385	35.19	0.24
	24	gb26	12	14040	13947	93.05	0.66
	25	gb22		13840	13744	96.22	0.70
	28.1	gb23	20	13840	13676	164.33	1.19
	26.2	gb24		13820	13736	83.84	0.61

These losses are mostly related to the water content in the cylinders during their initial weighing (i.e., after the cylinder processing and before the blasting). The cylinders had further dried, especially after the blast fragmentation, which resulted in such mass difference during the sieving. This can be seen, e.g., by comparing the losses of the cylinders blasted on the same day (e.g., from blast tests 23.1 and 23.2), or of those from the same processing series (i.e., processes on the same day), and by comparing the losses considering the blasted material. Cylinders blasted on the same day had

about the same drying time (i.e., the time between the processing and the blasting). Due to the difference in material porosity, more residual water remained in the mortar cylinders than in the granite ones after the same drying time.

The material loss due to drying was especially pronounced during the second sieving of the two largest fragments from m20(22.1). The additional sieving was carried out about 7 days after the initial sieving. Table 42 shows the recorded weight loss of these fragments. The material loss for both fragments is lower than 1%.

Table 42: Measured material loss due to drying in the largest two sieved fragments (m20 (22.1)).

Screening size class [mm]	$m_{\text{sieve f}}$ [g]		ΔM_{loss} [g]	ΔM_{loss} [%]
	Initial	Second		
100 80	2634	2612.07	21.93	0.83
80 63	4073	4048.95	24.05	0.59

Additionally, up to about 1% loss of the initial mass was expected due to the material blasted out of the chamber through the rear end and due to material handling after the blasting (D. Johansson & Ouchterlony, 2011).

The sieving data were used to calculate percentile fragment sizes x_{80} , x_{50} , and x_{30} (Equation 44 and Equation 45) and the ratio x_{80}/x_{30} . Table 43 shows a summary of these results.

Table 43: Summary of obtained percentile fragment sizes and the ratio x_{80}/x_{30} .

Material	Blast test	I_c [g/m]	x_{80} [mm]		x_{50} [mm]		x_{30} [mm]		x_{80}/x_{30} log
			lin	log	lin	log	lin	log	
Mortar	22.2	6	126.0	126.8	88.2	88.3	72.9	75.2	1.69
	23.2		139.4	140.8	122.9	123.4	107.4	109.4	1.29
	20	12	106.0	106.2	71.2	72.7	63.7	64.1	1.66
	21		72.3	73.0	60.7	61.2	52.8	53.6	1.36
	22.1	20	74.1	74.6	61.1	61.5	53.1	54.0	1.38
	23.1		60.3	60.8	51.7	52.2	42.0	42.3	1.44
Granite	26.1	6	106.0	106.2	92.3	95.4	85.8	89.6	1.19
	27		104.5	104.6	91.0	93.6	84.0	86.3	1.21
	24	12	78.1	78.6	68.3	69.7	58.6	58.8	1.34
	25		73.3	74.2	63.3	63.3	53.2	53.8	1.38
	28.1	20	81.8	81.8	63.0	63.0	55.6	57.1	1.43
	26.2		90.4	91.1	71.3	71.5	49.4	49.4	1.84

The Swebrec functions (Equation 46 and Equation 47) were fitted to the screening data sets to obtain comparable curve-describing parameters. Raw result data sets and fitting parameters are provided in Appendix 18. Table 44 shows a data-fitting summary of the “Swebrec 3p” function.

Table 44: Data-fitting summary (sieving) of the "Swebrec 3p" function (Equation 46).

Material	Blast test	I_c [g/m]	Size range [mm]	x_{max} [mm]	x_{50} [mm]	b	R ²
Mortar	22.2	6	0.5–20	150	96	2.72	0.9849
	23.2		0.5–20	74	67	1.75	0.9893
	20	12	0.5–20	69	62	1.43	0.9876
	21		0.5–20	150	81	2.42	0.9877
	22.1	20	0.5–80	87	62	2.06	0.9972
	23.1		0.5–63	68	52	1.68	0.9990
Granite	26.1	6	0.5–20	150	116	2.26	0.9901
	27		0.5–20	150	109	2.47	0.9884
	24	12	0.5–40	150	85	2.17	0.9923
	25		0.5–40	150	98	1.84	0.9804
	28.1	20	0.5–20	150	68	2.66	0.9677
	26.2		0.5–80	150	71	2.03	0.9987

Table 45 shows a result summary of the merged-data fitting to the “Swebrec 5p” function.

Table 45: Data-fitting summary (merged screening data) of the “Swebrec 5p” function (Equation 47).

Material	Blast test	I_c [g/m]	Size range [mm]	a	x_{max} [mm]	x_{50} [mm]	b	R ²
Granite	27	6	6.3E-4–20	0.99967	150	107.53	2.51	0.9947
	24	12	5E-4–40	0.99935	150	86.36	2.12	0.9967
	25		4 E-4–40	0.99951	150	98.62	1.80	0.9952
	26.2	20	4 E-4–80	0.99978	150	71.39	2.02	0.9994
Mortar	22.2	6	5 E-4–20	0.99980	150	104.31	2.42	0.9983
	20	12	3.6E-4–20	0.99999	36	35.31	0.87	0.9979
	22.1	20	5E-4–80	0.99992	87	62.14	2.06	0.9975

5.10.2 Blast fines

Figure 178 and Table 46 show an overview of the sieved fines proportions (mesh sizes 0.04–1 mm).

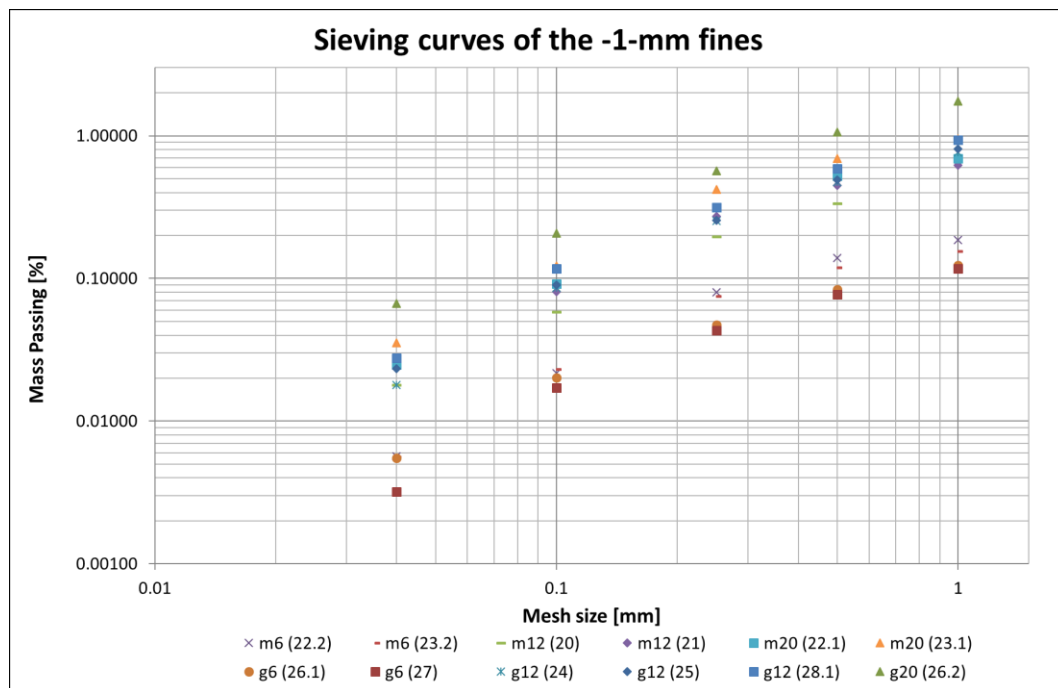


Figure 178: Overview of sieved fines proportions ($P(x)$) below 1-mm mesh size (m -1 mm, m -0.5 mm, m -0.25 mm, m -0.1 mm, and m -0.04 mm).

Table 46: Overview of sieved fines proportions P(x) below 1-mm mesh size.

Mortar							
Blast test:		22.2	23.2	20	21	22.1	23.1
I _c [g/m]:		6		12		20	
Symbol	Mesh size [mm]	Mass passing [%]					
m-1 mm	1	0.1865	0.1552	0.6562	0.6200	0.6934	0.9479
m-0.5 mm	0.5	0.1391	0.1190	0.3359	0.4501	0.5226	0.6929
m-0.25 mm	0.25	0.0797	0.0751	0.1962	0.2727	0.3156	0.4192
m-0.1 mm	0.1	0.0217	0.0231	0.0583	0.0811	0.0915	0.1222
m-0.04 mm	0.04	0.0056	0.0056	0.0179	0.0240	0.0250	0.0355
Granite							
Blast test:		27	26.1	24	25	28.1	26.2
I _c [g/m]:		6		12		20	
Symbol	Mesh size [mm]	Mass passing [%]					
m-1 mm	1	0.1169	0.1237	0.7655	0.8107	0.9325	1.7441
m-0.5 mm	0.5	0.0769	0.0835	0.4738	0.4921	0.5886	1.0599
m-0.25 mm	0.25	0.0433	0.0475	0.2521	0.2552	0.3138	0.5657
m-0.1 mm	0.1	0.0172	0.0201	0.0858	0.0899	0.1171	0.2073
m-0.04 mm	0.04	0.0032	0.0055	0.0179	0.0233	0.0277	0.0667

Relatively more fines were produced with increasing linear charge concentration, and more in the granite than in the mortar, except in the 6-g/m shots, in which more were produced in the mortar.

Figure 179 shows an overview of sieved blast-hole-wall fines, i.e., that material which was brushed off from the blast hole wall parts of larger fragments, see section 4.5.1 and Equation 42. These fines ($\Delta m_{bh,-1 \text{ mm}}$, $\Delta m_{bh,-0.5 \text{ mm}}$, $\Delta m_{bh,-0.25 \text{ mm}}$, $\Delta m_{bh,-0.1 \text{ mm}}$, and $\Delta m_{bh,-0.04 \text{ mm}}$) were included in m-1 mm, m-0.5 mm, m-0.25 mm, m-0.1 mm, and m-0.04 mm (see Section 5.10.2).

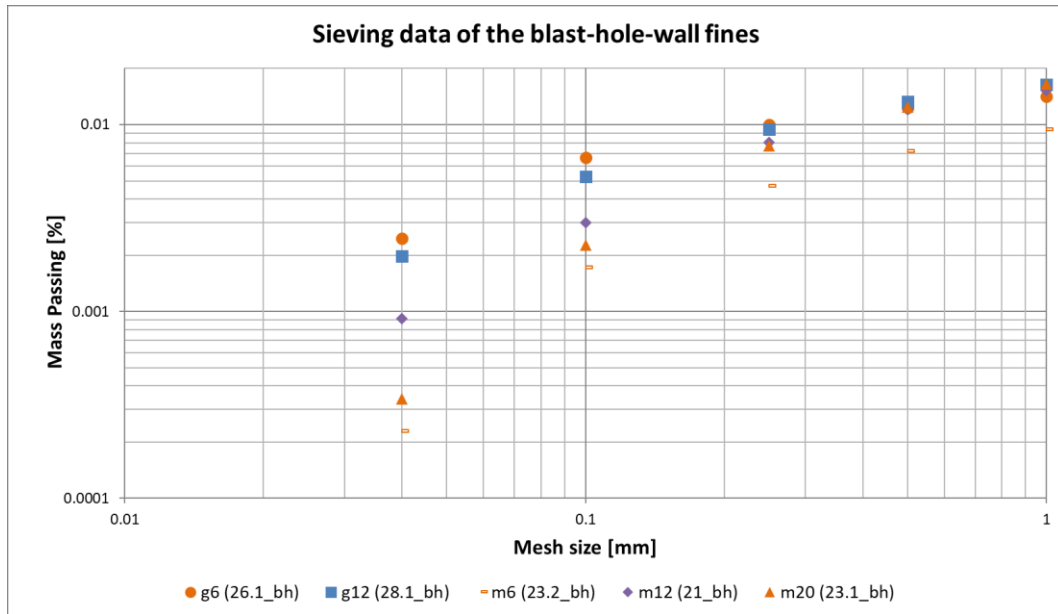


Figure 179: Overview of sieved blast-hole-wall fines.

Figure 180 shows plots of mass proportions (percentile values) of the blast-hole-wall fines (i.e., of those brushed off from the blast-hole wall) to the total of the sieved fines (see Equation 43). The related measurement uncertainty (i.e., the error bars in Figure 180) was determined based on the technical data of the measuring scales used to weigh the fines (see Appendix 11).

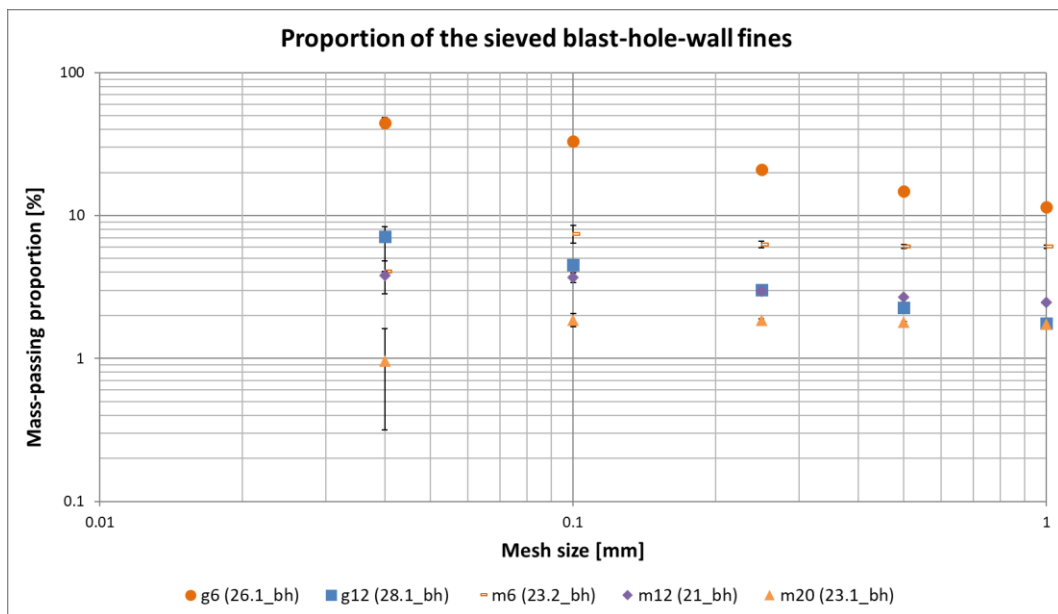


Figure 180: Relative mass proportions of the blast-hole-wall fines with the total mass proportions of the sieved fines as the reference.

A larger proportion of blast-hole-wall fines, relative to the total sieved fines for mesh sizes 0.04–1 mm, were produced in the granite than in the mortar, and less of them were produced with higher linear charge concentration.

Table 47 shows the measured mass of the blast-hole-wall fines smaller than 1 mm ($\Delta m_{bh,-1\text{ mm}}$) (see Section 4.5.1) and estimated mass of crack-generated fines (m_{CGF}), i.e., the difference between the total sieved mass passing 1-mm sieve ($m_{-1\text{ mm}}$) and $\Delta m_{bh,-1\text{ mm}}$ (Equation 36).

Table 47: Overview of measured blast-hole-wall fines and estimated CGF with their proportions considering total sieved mass.

Blast shot	m_{sieve} [g]	$m_{-1\text{ mm}}$ [g]	$\Delta m_{bh,-1\text{ mm}}$ [g]	$\Delta m_{bh,-1\text{ mm}}$ [%]	m_{CGF} [g]	m_{CGF_sieve} [%]
m6(23.2)	8712.0	13.52	0.82	0.009	12.70	0.146
m12(21)	8706.8	53.98	1.33	0.015	52.65	0.605
m20(23.1)	8783.8	83.26	1.45	0.017	81.81	0.931
g6(26.1)	13824.8	17.10	1.96	0.014	15.14	0.110
g12(28.1)	13675.7	127.52	2.24	0.016	125.28	0.916

Table 48 shows the estimated mass of compacted material (ΔM_{comp}) in the mortar cylinders (Equation 34). More compacted material is expected with a larger charge concentration in the mortar (see also Section 5.7.2).

Table 48: Estimated mass of compacted material.

Blast shot	$\Delta r_{comp,a}$ [mm]	l_{ch} [mm]	$r_{bh,norm}$ [mm]	$\Delta V_{comp,b}$ [cm ³]	M_{cyl} [g]	ΔM_{comp} [g]	ΔM_{comp} [%]
m6(22.2)	*2.99	274	*7.05	44.05	8940	103.97	1.163
m6(23.2)	2.99	274	7.05	44.05	8920	103.97	1.166
m12(20)	*3.67	267	*8.14	61.43	8800	144.98	1.647
m12(21)	3.67	268	8.14	61.66	8980	145.52	1.621
m20(22.1)	*6.69	278	*12.30	182.90	9380	431.65	4.602
m20(23.1)	6.69	267	12.30	175.51	9020	414.20	4.592

*Adopted measurements from a blasted cylinder of the same blasted material and l_c .

Table 49 shows the estimated mass of blasted-off material (ΔM_{blast}) (Equation 33).

Table 49: Estimated mass of the blasted-off material.

Blast shot	$\Delta r_{comp,a}$ [mm]	$\Delta r_{blast,b}$ [mm]	$\Delta V_{blast,b}$ [cm ³]	M_{cyl} [g]	ΔM_{blast} [g]	ΔM_{blast} [%]
m6(22.2)	2.99	0.16	1.41	8940	2.34	0.03
m12(20)	3.67	0.45	3.94	8800	6.54	0.07
m20(22.1)	6.69	1.03	9.96	9380	16.54	0.18
g6(26.1)	0	1.16	11.38	13880	31.29	0.23
g12(28.1)	0	2.23	25.31	13840	69.61	0.50
g20(26.2)	0	2.43	26.66	13820	73.35	0.53

More blasted-off material is expected from blasts with a larger linear charge concentration, and more in the granite than in the mortar.

Table 50 shows a summary of the total mass of fines smaller than 1 mm (m_{tot_fines}) (Equation 35), estimated CGF mass (Equation 36), including the maximum and minimum estimates (Equation 37 and Equation 38, respectively).

Table 50: Estimated masses of CGF and blasted-off material.

Blast shot	$r_{bh,norm}$ [mm]	m-1 mm		ΔM_{blast} [%]	m_{tot_fines} [%]	m_{CGF_cyl} [%]	m_{CGF}^+ [%]	m_{CGF}^- [%]
		[g]	[%]					
m6(22.2)	-	16.52	0.18	*0.03	0.21	-	-	-
m6(23.2)	7.06	13.52	0.15	0.03	0.18	0.142	93.93	10.53
m12(20)	-	57.13	0.65	*0.07	0.72	-	-	-
m12(21)	8.14	53.98	0.60	0.07	0.67	0.586	97.54	25.59
m20(22.1)	-	63.88	0.68	*0.18	0.86	-	-	-
m20(23.1)	12.30	83.26	0.92	0.18	1.10	0.907	98.26	15.93
g6(26.1)	6.16	17.10	0.12	0.23	0.35	0.109	88.54	30.88
g12(28.1)	7.23	127.52	0.92	0.50	1.42	0.905	98.24	63.68
g20(26.2)	7.43	239.57	1.73	0.53	2.26	-	-	-

*Adopted measurements from a blasted cylinder of the same blasted material and l_c

In the mortar, more CGF are produced than blast-hole fines with the considered linear charge concentrations. The same applies to the granite, except for the 6-g/m shots when neglecting the losses.

5.10.3 Specific surface area of the fines and blast-energy register (BER)

Table 51 shows a summary of the measured specific surface area (see Section 4.5.5). Raw measurement data of the specific surface areas are provided in Appendix 19. The a_s measurements obtained with the Blane method that exceed 13,000 were discarded. In such cases (marked red in Table 51), only the Permeran measurements were included in the average values (see Section 4.5.5).

Table 51: Summary of the measured specific surface area of the fines.

Material	Blast test	l_c [g/m]	Size class [μm]	Blane		Permeran		Average	
				a_s [cm ⁻¹]	a_m [cm ² /g]	a_s [cm ⁻¹]	a_m [cm ² /g]	a_s [cm ⁻¹]	a_m [cm ² /g]
Mortar	20	12	100 40	2390	1013	2162	916	2276	964
	20 + 21		-40	13660	5701	14137	5900	14137	5900
Granite	24		100 40	1434	539	1310	492	1372	515
	28.1		-40	7903	2875	8176	2974	8039	2924
Mortar	22.1	20	100 40	2255	939	2091	871	2173	905
	23.1		-40	13396	5633	14345	6032	14345	6032
Granite	26.2		100 40	1648	619	1778	668	1713	644
	26.2		-40	6381	2403	6611	2489	6496	2446

Table 52 shows a summary of calculated particle-shape factor (Equation 57) based on the measured specific surface area for the size class 0.1|0.04 mm.

Table 52: Summary of the calculated particle-shape factor.

Material	Blast test	l_c [g/m]	f_A
Mortar	20	12	15.20
	21		15.24
	22.1	20	14.64
	23.1		14.57
Granite	24	12	9.42
	25		9.19
	28.1	20	9.24
	26.2		11.40

The measured specific surface areas (a_s and a_m) are smaller in the granite than in the mortar for both investigated size classes. They stay about the same for all three values of linear charge concentration in the mortar. In the granite, the specific surface areas for the size class 0.1|0.04 mm increase and for the size class -0.04 mm decrease with increasing linear charge concentration.

However, in theory, the specific surface areas should not be significantly affected by the linear charge concentration, i.e., by the energy spent for the fragmentation (Steiner, 1991; Böhm et al., 2004; Niiranen, 2015).

Therefore, the obtained a_s and a_m for the 12- and 20-g/m blast shots could still be used to estimate these parameters for the 6-g/m blast shots by averaging (Table 53).

Table 53: Specific surface areas for the 6-g/m blast shots, obtained by averaging the corresponding data for 12- and 20-g/m blast shots in Table 51.

Material	Blast test	I_c [g/m]	Size class [μm]	Average	
				a_s [cm^{-1}]	a_m [cm^2/g]
Mortar	22.2, 23.2	6	100 40	2224	935
			-40	14241	5966
Granite	26.1, 27		100 40	1542	580
			-40	7268	2685

The particle-shape factor decreases in the mortar and increases in the granite with increasing linear charge concentration.

Table 54 shows calculated powder factor PF [g/t] and specific energy consumption E_c [J/g] (Equation 61).

Table 54: Overview of calculated powder factor (PF) and specific energy consumption (E_c).

Material	Blast test	I_c [g/m]	I_{ch} [mm]	q [kg/m^3]	M_{cyl} [g]	PF [g/t]	E_c [J/g]
Mortar	22.2	6	274.0	0.31	8940	183.893	0.766
	23.2		273.0	0.31	8920	183.632	0.765
	20	12	267.0	0.61	8800	364.091	1.518
	21		268.0	0.61	8980	358.129	1.493
	22.1	20	278.0	1.02	9380	592.751	2.471
	23.1		271.0	1.03	9020	600.887	2.504
Granite	26.1	6	280.2	0.32	13880	121.124	0.505
	27		275.0	0.32	14420	114.424	0.477
	24	12	281.3	0.64	14040	240.427	1.002
	25		276.6	0.63	13820	240.174	1.001
	28.1	20	295.0	0.64	13840	255.780	1.066
	26.2		281.3	1.07	13840	406.503	1.694

Notation:
 I_c – linear charge concentration
 I_{ch} – charge length
 q – specific charge
 M_{cyl} – Initial mass of a blast cylinder
PF – powder factor
 E_c – specific energy consumption ($\text{PF} \times 4.168 \text{ MJ/kg}$)

The plots of the blast-energy register (BER) (Figure 181) show that the Rittinger coefficients are about the same for the two blasted materials (i.e., 2.90 cm²/J for the granite and 2.80 cm²/J for the mortar). The corresponding data tables are provided in Appendix 18.

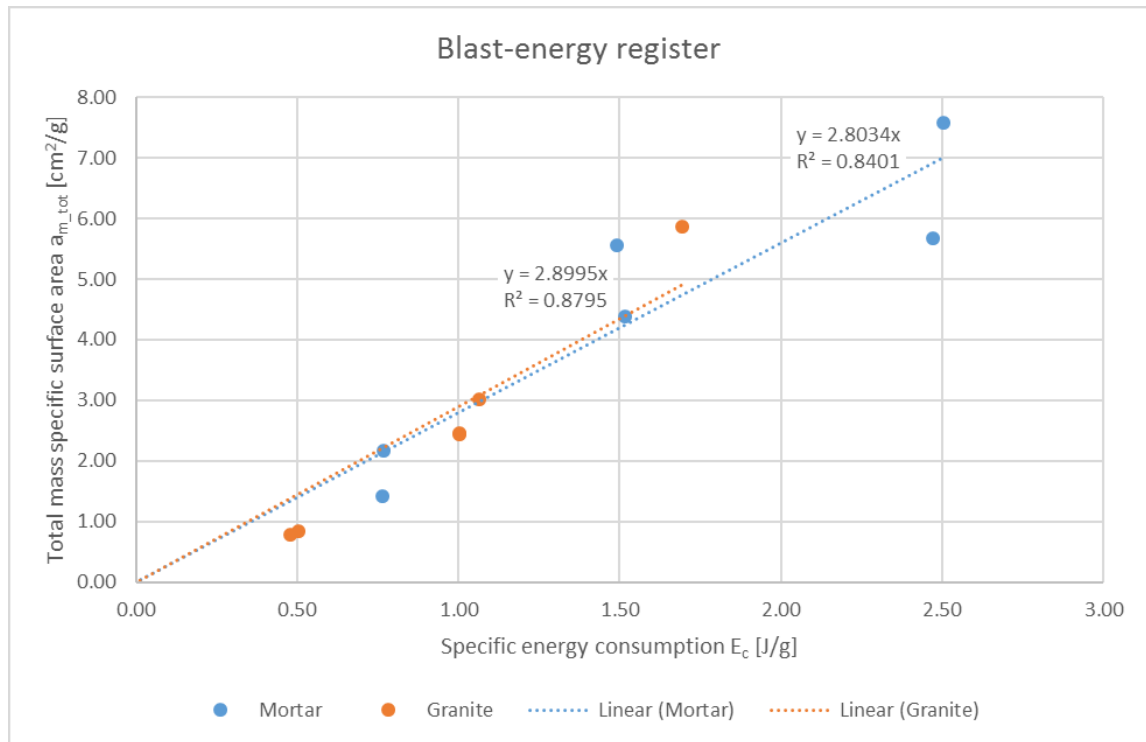


Figure 181: Blast-energy register – total mass specific surface area plotted against specific energy consumption. The regression lines have the intercept set point to (0,0).

5.10.4 Resulting “s-n(s)” curves

This section covers the s-n(s) curves (see Section 4.5.4) obtained by converting the screening data (see Section 5.10.1) using Equation 51, Equation 52, Equation 53, and Equation 54.

Table 55 shows a result summary of the s-n(s) fitting in log-log scale to the sieving data (see Table 163, Table 166, and Appendix 18).

Table 55: Summary from the fitting of the “s-n(s)” curves to the sieving data.
The values following ‘±’ represent standard error.

Material	I_c [g/m]	Blast test	$\ln(C_n)$	α, β	Size range (in FSD) [mm]	Data count	R^2	
Mortar	6	22.2	-7.36±0.43	1.65±0.03	1–14	10	0.998	
		23.2	-8.98±0.72	1.57±0.05	1–18	12	0.992	
	12	20	-7.00±0.64	1.63±0.04	1–16	11	0.994	
		21	-5.74±0.63	1.68±0.04	1–20	13	0.994	
	20	22.1	-6.49±0.62	1.63±0.04	1–20	13	0.994	
		23.1	-6.62±0.46	1.59±0.03	1–20	13	0.996	
Granite	6	26.1	-7.35±0.51	1.68±0.03	1–31.5	15	0.996	
		27	-7.41±0.66	1.67±0.04	1–31.5	15	0.993	
	12	24	-5.91±0.32	1.64±0.02	1–20	13	0.998	
		25	-4.81±0.28	1.72±0.02	1–20	13	0.999	
		28.1	-4.22±0.50	1.75±0.03	1–20	13	0.997	
	20	26.2	-5.08±0.36	1.65±0.02	1–63	18	0.997	
	Mortar	6	22.2	-5.11±0.53	1.81±0.09	0.04–0.5	4	0.995
			23.2	-4.98±0.47	1.86±0.08	0.04–0.5	4	0.996
12		20	-4.56±0.26	1.69±0.04	0.04–0.5	4	0.997	
		21	-3.87±0.45	1.81±0.04	0.04–0.5	4	0.996	
20		22.1	-3.66±0.50	1.83±0.09	0.04–0.5	4	0.996	
		23.1	-3.44±0.47	1.81±0.08	0.04–0.5	4	0.996	
Granite	6	26.1	-5.46±0.16	1.81±0.03	0.04–0.5	4	0.999	
		27	-5.52±0.13	1.81±0.02	0.04–0.5	4	0.999	
	12	24	-3.97±0.17	1.76±0.03	0.04–0.5	4	0.999	
		25	-4.02±0.17	1.74±0.03	0.04–0.5	4	0.999	
		28.1	-3.70±0.16	1.77±0.03	0.04–0.5	4	0.999	
	20	26.2	-3.26±0.17	1.78±0.03	0.04–0.5	4	0.999	

Table 56 shows a result summary of the s-n(s) fitting to the merged screening data (see Table 167, Table 170, and Appendix 18).

Table 56: Summary from the fitting of the merged screening data to the “s-n(s)” curves. The values following ‘±’ represent standard error.

Material	I_c [g/m]	Blast test	$\ln(C_n)$	α, β	Size range (in FSD) [mm]	Data count	R^2
Mortar	6	22.2	-11.12±1.61	1.69±0.05	1–20	13	0.989
	12	20	-13.67±1.66	1.58±0.06	2–20	12	0.988
	20	22.1	-12.22±1.43	1.60±0.05	2–20	12	0.991
Granite	6	27	-11.64±1.18	1.68±0.04	1–31.5	15	0.993
	12	24	-12.44±0.97	1.58±0.03	2–40	15	0.998
		25	-8.44±0.58	1.72±0.02	2–31.5	14	0.998
	20	26.2	-11.62±0.86	1.60±0.03	2–80	18	0.995
Mortar	6	22.2	-11.80±0.20	1.62±0.02	0.0005–0.5	21	0.998
	12	20	-9.73±0.18	1.67±0.02	0.0005–0.5	21	0.998
	20	22.1	-9.23±0.19	1.67±0.02	0.0005–0.5	21	0.998
Granite	6	27	-11.54±0.22	1.64±0.02	0.0005–0.5	21	0.997
	12	24	-9.64±0.16	1.64±0.01	0.0005–0.5	21	0.998
		25	-9.38±0.18	1.66±0.02	0.00063–0.5	20	0.998
	20	26.2	-7.90±0.25	1.70±0.02	0.0004–1	23	0.997

The statistical comparison of the s-n(s) slopes ($-\alpha, -\beta$) (see Appendix 10) indicates that:

- The s-n(s) slopes in the intermediate-fragment-size range are not significantly different to each other, aside from the slopes for g12(25) and g12(28.1) (see Table 165 and Table 169).
- The s-n(s) slopes in the fines-size range of the sieving data are not significantly different to each other (see Table 164).
- The s-n(s) slopes in the ultra-fines-size range of the merged-screening data are not significantly different to each other, aside from the slopes for g6(27), g12(24), and m6(22.2) (see Table 168). This relationship between the slopes indicates a possible influence of the linear charge concentration on the slopes (when increased from 6 to 12 g/m). In this case, this increase of the linear charge concentration steepens the slopes in this range.
- The s-n(s) slope from the (ultra-)fines-size range is not significantly different to that from the intermediate-fragment-size range (for the same blast shot) for 7 out of 12 blast shots (see Table 171). For the remaining 5 blast shots, the slopes are significantly different and mostly steeper in the (ultra-)fines range than in the intermediate-fragment-size range. However, the slopes do not show a clear effect of the linear charge concentration or the blasted material on this difference.

5.11 Correlation analysis

This analysis was carried out on different groups of result-data sets (A, B, C, D, and E), covering different groups of blast tests. Table 57 shows the correlated result parameters considering the correlation groups.

Table 57: Combinations of correlated result parameters and corresponding blast tests.

Symbol	Parameter Name	Unit	Compared blast tests				
			A: All	B: All without 28.1	C: 22.1, 20, 22.2, 26.2, 24, 25, 27	D: 23.1, 21, 23.2, 28.1, 26.1	E: 23.1, 21, 23.2, 26.1
C_p	P-wave velocity (identifier of blasted material)	[m/s]	*	*	*	*	*
q	Specific charge	[kg/m ³]	*	*	*	*	*
N (CTt)	Ave. count of main radial cracks in CTt	[-]				*	*
Std D_{cent} (CTt)	Std of topological-data scattering in CTt ternary diagrams	[-]				*	*
Std D_{cent} (CTnp)	Std of topological-data scattering in CTnp ternary diagrams	[-]				*	*
p_c (HSI) slope	Rate of change of the probability of a node being connected in HSI	[μs^{-1}]		*	*		*
Ave p_c (CTt)	Ave. probability of a node being connected in CTt	[-]				*	*
p_{20} (HSI) slope	Rate of change of the areal fracture frequency in HSI	[mm ⁻²]		*	*		*
p_{21} (HSI) slope	Rate of change of the fracture intensity in HSI	[mm ⁻¹]		*	*		*
p_{20} (CTt)	Ave. areal fracture frequency in CTt	[mm ⁻²]				*	*
p_{21} (CTt)	Ave. fracture intensity in CTt	[mm ⁻¹]				*	*
2D-frag. count (CTt)	Ave. count of in-plane fragments in CTt	[-]				*	*
2D-frag. Std D_{cent} (CTt)	Std of 2D-fragment-count scattering in CTt	[-]				*	*
C_{ave} [m/s]	Ave. crack-propagation speed	[m/s]		*	*	*	*
Ave $r_{bh,norm}$	Ave. normalized blast-hole radius	[mm]				*	*
Ave δr_m	Ave. mantle displacement (swelling)	[mm]				*	*
$m_{.1\text{ mm}}$	Sieved material below 1-mm sieve size	[g]	*	*	*	*	*
$x_{50\text{ log}}$	Median fragment size (P = 50%) (log-log scale)	[mm]	*	*	*	*	*
β (s-n(s)_F) sieving	Slope of sieved-data s-n(s) curve in the fines-size range	[mm ⁻¹]	*	*	*	*	*
α (s-n(s)_IF) sieving	Slope of sieved-data s-n(s) curve in the intermediate-fragment-size range	[mm ⁻¹]	*	*	*	*	*
β (s-n(s)_UF) merged	Slope of merged-data s-n(s) curve in the ultra-fines range	[mm ⁻¹]			*		
α (s-n(s)_IF) merged	Slope of merged-data s-n(s) curve in the intermediate-fragment range	[mm ⁻¹]			*		
Parameter count:			6	10	12	17	20

The results were correlated like this to allow their wider and more detailed comparison. Table 58 describes these groups (A to E).

Table 58: Description of the correlation groups (A to E).

Group	Blast-test count	Parameter count	Comment
A	12	6	Composed to cover all analysed blast tests.
B	11	10	Group A without g12(28.1) to include the HSI parameters.
C	7	12	Altered Group B to include all s-n(s) parameters.
D	5	17	Altered Group A to include most of the topological parameters (i.e., all except for the HSI ones).
E	4	20	Composed to provide maximum parameter count.

The highlighted parameters in Table 57, C_p and q , are inputs, and the rest are outputs (of the blast tests). Here, C_p (P-wave velocity) represents the type of blasted material (mortar or granite). This analysis was carried out by direct correlation (Linear, e.g., q vs x_{50}) and by correlating natural-logarithmic values (LN, e.g., $\ln(q)$ vs $\ln(x_{50})$) of the results. Complete correlation tables are provided in Appendix 20.

The results from these correlation tables were further summarized for q and for $m_{-1\text{ mm}}$ (the sieved mass passing the 1-mm mesh size). As in some cases the correlation coefficient (R) differs for different groups of result-data sets (A1, A2, B, C1, and C2), the final R score for a given parameter was taken from the group that covered the most blast tests. Finally, the summarized results were interpreted according to Table 59 (Dancey & Reidy, 2007).

Table 59: Interpretation of the Pearson's correlation coefficient (R) by Dancey & Reidy (2007).

Correlation coefficient (R)	Interpretation
$0.9 < R \leq 1$	Perfect
$0.6 < R \leq 0.9$	Strong
$0.3 < R \leq 0.6$	Moderate
$0 < R \leq 0.3$	Weak
0	Zero

Table 60 and Table 61 show the correlation summary for specific charge (q).

Table 60: Correlation summary for specific charge (q) (Linear correlation).
The bolded numbers represent the final R score for a given parameter.

Group:	A	B	C	D	E	
Blast-test count:	12	11	7	5	4	Interp.
C_p	-0.078	-0.088	0.036	-0.311	-0.486	Weak
N (CTt)				0.749	0.763	Strong
Std D_{cent} (CTt)				-0.920	-0.973	Perfect
Std D_{cent} (CTnp)				0.047	0.100	Weak
p_C (HSI) slope		0.468	0.419		0.914	Moderate
Ave p_C (CTt)				-0.496	-0.598	Moderate
p_{20} (HSI) slope		0.257	0.251		0.515	Weak
p_{21} (HSI) slope		0.589	0.565		0.975	Moderate
p_{20} (CTt)				0.873	0.878	Strong
p_{21} (CTt)				0.888	0.902	Strong
2D-frag. count (CTt)				0.805	0.882	Strong
2D-frag. Std D_{cent} (CTt)				-0.778	-0.832	Strong
C_{ave}		0.666	0.695	0.707	0.707	Strong
Ave $r_{bh,norm}$				0.920	0.976	Perfect
Ave δr_m				-0.016	-0.367	Weak
m_{-1mm} [%]	0.850	0.862	0.834	0.893	0.983	Strong
x_{50} log	-0.751	-0.764	-0.768	-0.856	-0.868	Strong
β (s-n(s)_F) sieving	-0.150	-0.149	0.035	-0.431	-0.514	Weak
α (s-n(s)_IF) sieving	-0.124	-0.169	-0.255	-0.063	-0.216	Weak
β (s-n(s)_UF) merged			0.860			Strong
α (s-n(s)_IF) merged			-0.566			Moderate

Table 61: Correlation summary for specific charge (q) (LN correlation). The bolded numbers represent the final R score for a given parameter.

Group:	A	B	C	D	E	
Blast-test count:	12	11	7	5	4	Interp.
C_p	-0.046	-0.075	0.063	-0.258	-0.511	Weak
N (CTt)				0.843	0.839	Strong
Std D_{cent} (CTt)				-0.971	-0.995	Perfect
Std D_{cent} (CTnp)				0.114	0.258	Weak
p_C (HSI) slope		0.553	0.649		0.823	Moderate
Ave p_C (CTt)				-0.450	-0.609	Moderate
p₂₀ (HSI) slope		0.488	0.539		0.562	Moderate
p₂₁ (HSI) slope		0.600	0.641		0.958	Moderate
p₂₀ (CTt)				0.863	0.856	Strong
p₂₁ (CTt)				0.913	0.913	Perfect
2D-frag. count (CTt)				0.860	0.877	Strong
2D-frag. Std D_{cent} (CTt)				-0.869	-0.900	Strong
C_{ave}		0.602	0.595	0.732	0.732	Strong
Ave r_{bh, norm}				0.864	0.949	Strong
Ave δr_m				-0.011	-0.355	Weak
m_{-1 mm} [%]	0.926	0.936	0.914	0.940	0.972	Perfect
x₅₀ log	-0.847	-0.851	-0.847	-0.954	-0.952	Strong
β (s-n(s)_F) sieving	-0.274	-0.266	-0.123	-0.533	-0.563	Weak
α (s-n(s)_IF) sieving	-0.024	-0.091	-0.218	0.085	-0.110	Weak
β (s-n(s)_UF) merged			0.854			Strong
α (s-n(s)_IF) merged			-0.596			Moderate

Table 62 shows the correlation for mass passing 1-mm sieve size ($m_{-1 \text{ mm}}$).

Table 62: Correlation summary for sieved mass passing 1-mm sieve size ($m_{-1 \text{ mm}}$) (Linear correlation). The bolded numbers represent the final R score for a given parameter.

Group:	A	B	C	D	E	
Blast-test count:	12	11	7	5	4	Interp.
C_p	0.229	0.182	0.348	-0.063	-0.570	Weak
q	0.850	0.862	0.834	0.893	0.983	Strong
N (CTt)				0.856	0.840	Strong
Std D_{cent} (CTt)				-0.981	-0.981	Perfect
Std D_{cent} (CTnp)				0.019	0.281	Weak
p_C (HSI) slope		0.750	0.803		0.871	Strong
Ave p_C (CTt)				-0.300	-0.656	Weak
p_{20} (HSI) slope		0.490	0.474		0.514	Moderate
p_{21} (HSI) slope		0.839	0.842		0.917	Strong
p_{20} (CTt)				0.912	0.947	Perfect
p_{21} (CTt)				0.945	0.965	Perfect
2D-frag. count (CTt)				0.964	0.951	Perfect
2D-frag. Std D_{cent} (CTt)				-0.937	-0.917	Perfect
C_{ave}		0.534	0.542	0.728	0.728	Moderate
Ave $r_{bh, norm}$				0.666	0.939	Strong
Ave δr_m				0.424	-0.229	Moderate
$x_{50} \log$	-0.646	-0.632	-0.584	-0.890	-0.901	Strong
β (s-n(s)_F) sieving	-0.372	-0.355	-0.222	-0.683	-0.516	Moderate
α (s-n(s)_IF) sieving	0.123	0.011	-0.039	0.297	-0.145	Weak
β (s-n(s)_UF) merged			0.859			Strong
α (s-n(s)_IF) merged			-0.438			Moderate

Table 63: Correlation summary for sieved mass passing 1-mm sieve size ($m_{-1\text{ mm}}$) (LN correlation). The bolded numbers represent the final R score for a given parameter.

Group:	A	B	C	D	E	
Blast-test count:	12	11	7	5	4	Interp.
C_p	0.060	-0.012	0.175	-0.156	-0.641	Weak
q	0.926	0.936	0.914	0.940	0.972	Perfect
N (CTt)				0.876	0.859	Strong
Std D_{cent} (CTt)				-0.955	-0.945	Perfect
Std D_{cent} (CTnp)				0.137	0.473	Weak
p_c (HSI) slope		0.448	0.538		0.818	Moderate
Ave p_c (CTt)				-0.369	-0.703	Moderate
p_{20} (HSI) slope		0.526	0.573		0.487	Moderate
p_{21} (HSI) slope		0.592	0.647		0.864	Moderate
p_{20} (CTt)				0.932	0.942	Perfect
p_{21} (CTt)				0.973	0.980	Perfect
2D-frag. count (CTt)				0.967	0.957	Perfect
2D-frag. Std D_{cent} (CTt)				-0.972	-0.964	Perfect
C_{ave}		0.394	0.327	0.682	0.682	Moderate
Ave $r_{\text{bh, norm}}$				0.687	0.904	Strong
Ave δr_m				0.281	-0.225	Weak
x_{50} log	-0.821	-0.812	-0.817	-0.922	-0.936	Strong
β (s-n(s)_F) sieving	-0.471	-0.456	-0.391	-0.642	-0.491	Moderate
α (s-n(s)_IF) sieving	0.145	0.010	-0.079	0.292	-0.079	Weak
β (s-n(s)_UF) merged			0.794			Strong
α (s-n(s)_IF) merged			-0.527			Moderate

5.11.1 Summary of the correlation results

The results of the correlation analysis (see Section 5.11), linear (lin) and logarithmic (LN), were summarized for the specific charge (q [kg/m^3]) and for the sieved mass passing 1-mm mesh ($m_{-1\text{ mm}}$ [%]).

Table 64 and Table 65 show those parameters that have “perfect” or “strong” correlation ($0.6 < |R| \leq 1$) (see Table 59) with q and with $m_{-1\text{ mm}}$.

Table 64: Summary of the correlation analysis for q [kg/m^3], considering only perfect and strong correlations.

Parameter		R	
Symbol	Name	lin	LN
N (CTt)	Ave. count of main radial cracks in CTt	0.749	0.843
Std D_{cent} (CTt)	Std of topological-data scattering in CTt ternary diagrams	-0.920	-0.971
p_{20} (CTt)	Ave. areal fracture frequency in CTt	0.873	0.863
p_{21} (CTt)	Ave. fracture intensity in CTt	0.888	0.913
2D-frag. count (CTt)	Ave. count of in-plane fragments in CTt	0.805	0.860
2D-frag. Std D_{cent} (CTt)	Std of 2D-fragment-count scattering in CTt	-0.778	-0.869
C_{ave}	Ave. crack-propagation speed	0.666	0.602
Ave $r_{\text{bh,norm}}$	Ave. normalized blast-hole radius	0.920	0.864
$m_{-1\text{ mm}}$	Sieved material below 1-mm sieve (mesh) size	0.850	0.926
χ_{50} log	Median fragment size ($P = 50\%$) (log-log scale)	-0.751	-0.847
β (s-n(s)_UF) merged	Slope of merged-data s-n(s) curve in the ultra-fines-size range	0.860	0.854

Table 65: Summary of the correlation analysis for $m_{-1\text{ mm}}$ [%], considering only perfect and strong correlations.

Parameter		R	
Symbol	Name	lin	LN
q	Specific charge	0.850	0.926
N (CTt)	Ave. count of main radial cracks in CTt	0.856	0.876
Std D_{cent} (CTt)	Std of topological-data scattering in CTt ternary diagrams	-0.981	-0.955
p_{c} (HSI) slope	Rate of change of the probability of a node being connected in HSI	0.750	$ R < 0.6$
p_{21} (HSI) slope	Rate of change of the fracture intensity in HSI	0.839	$ R < 0.6$
p_{20} (CTt)	Ave. areal fracture frequency in CTt	0.912	0.932
p_{21} (CTt)	Ave. fracture intensity in CTt	0.945	0.973
2D-frag. count (CTt)	Ave. count of in-plane fragments in CTt	0.964	0.967
2D-frag. Std D_{cent} (CTt)	Std of 2D-fragment-count scattering in CTt	-0.937	-0.972
Ave $r_{\text{bh,norm}}$	Ave. normalized blast-hole radius	0.666	0.687
χ_{50} log	Median fragment size ($P = 50\%$) (log-log scale)	-0.646	-0.821
β (s-n(s)_UF) merged	Slope of merged-data s-n(s) curve in the ultra-fines-size range	0.859	0.794

5.12 Summary of results

This section summarizes the results previously presented in Section 5 and provides a basis for the discussion points in Section 6.

5.12.1 Traced fracture patterns, topological features, and derived results

The blast fracturing of the frontal end face occurs in three phases considering crack-pattern development (see Section 5.1). The fracture phases are distinguished by:

- initial crack emerging and propagation (phase 1);
- increasingly complex branching and merging of running cracks (phase 2);
- spalling of the frontal end face and inrush of the blast fumes in front of it (phase 3).

The effect of the charge concentration on the duration of the phases is negligible considering the temporal resolution of the high-speed images (HSI). However, the third phase starts earlier in the granite than in the mortar cylinders.

The number of the main radial cracks (N) increases when increasing the charge concentration from 6 g/m to 12 g/m PETN in both materials (see Section 5.2). This number does not change when further increasing the charge to 20 g/m in the mortar. The blasted material does not significantly influence these results.

The absolute topological-node count in the HSI (N_I , J_{int} , N_{TB}) increases with the elapsed time and often levels out (see Section 5.3.1). The proportions P_I of the end nodes or crack tip nodes (I-nodes) develop differently than those of the boundary and internal intersection nodes (T_b and J_{int}). In general, the slopes of the linear-regression lines fitted to the node-count data (N_I , J_{int} , and N_{TB}) as a function of time steepen with increasing linear charge concentration, and they are steeper in the granite than in the mortar. Exceptions to this observation are for N_I (in the granite) and J_{int} , as their slopes decrease when further increasing the linear charge concentration from 12 to 20 g/m.

An I-node is converted to a joining node when the crack tip meets another crack or a boundary. The J_{int} -node proportion, in most cases, increases and levels out with time, opposite to the I-node proportion. This levelling-out (i.e., change in the curve slope) usually occurs during the transition between the first two fracture phases (see Section 5.1). The T_b -node proportions either increase at a relatively low rate or remain about the same over time.

The absolute node counts and their proportions in the transverse CT cross-sections (CTt) do not show a clear trend of development along the cylinder axis. The mean values of N_I in the CTt are about the same for the 12-g/m shots and 20-g/m shots in the mortar. The mean value of N_I increases with increasing linear charge concentration from 6 to 12 g/m. However, it is about the same in the two blasted materials for the 6- and for the 12-g/m shots. The mean values of J_{int} in the CTt are about the same for the 12-g/m shots in both materials and 20-g/m shot in the mortar. The mean values of J_{int} and of N_{TB} increase with increasing linear charge concentration from 6 to 12 g/m. However, they are about the same in the two blasted materials for the 6- and for the 12-g/m shots.

The node counts and their proportions in the non-planar CT cross-sections (CTnp) of the mortar show curves of a similar shape. The number of crack tip nodes (I-nodes) steadily increases with distance from the blast hole and seemingly levels out in the mortar CTnp. The number of internal intersections (J_{int} -nodes) steadily decreases with distance from the blast hole. The number of boundary intersections (T_b -nodes), where the boundaries are the cylinder end faces, stays about the same. In the granite, the counts of the I-nodes and the J_{int} -nodes in the CTnp drop with increasing distance from the blast hole, while the number of T_b -nodes stays about the same. The I-node proportion increases, though and that of the J_{int} -nodes decreases, with increasing distance, and the proportion of the T_b -nodes stays about the same.

The statistical evaluations and comparisons of the N_I results, of the J_{int} results, and of the N_{TB} results, for the CTnp (see Table 121, Table 122, and Table 123) show no significant difference in the slopes of the regression lines (see Table 117) considering the linear charge concentration (l_c). The same applies to the intercepts of the linear-regression lines for the 12- and 20-g/m shots. Both the slopes and the intercepts increase with increasing linear charge concentration from 6 to 12 g/m. The absolute values of the slopes and of the intercepts of N_I and J_{int} are larger for the granite than for the mortar. However, the slopes of N_I for the two blasted materials have mutually opposing trends.

The ternary diagrams of the node-count proportions show that the data points of the proportions in the HSI develop over time towards the clustered data points of the CTt. The data points of the post-mortem images (PMI) are also positioned inside the cluster, except in the cases of end-face spalling, which is more pronounced in the granite.

The clusters of CTt and CTnp data points in the ternary diagrams do not show any significant influence of the linear charge concentration or blasted material. However, the clusters of the CTt data do differ in the level of scatter as described by the standard deviation of D_{cent} (data-point distance from the cluster centroid). The scatter for the CTt decreases with increasing charge concentration and it is larger for the mortar than for the granite.

In most HSI sets, the number of crack lines and branches (N_L and N_B , see Appendix 9) do not differ much in the beginning, i.e., about until the second fracture phase (see Section 5.1). Later, N_B exceeds N_L due to multiple branching/merging. Both quantities steadily increase over time.

In the CTt, N_L and N_B increase when increasing the linear charge concentration from 6 g/m to 12 g/m. For the 6-g/m shots, the N_L values are larger in the mortar than in the granite, though the N_B is about the same in both materials. These numbers stay about the same for the 12-g/m shots in both blasted materials and for the 20-g/m shot in the mortar.

In all HSI, the curves of the number of connections per line or branch (C_L and C_B , see Section 5.3.3) have (about) the same initial values and firstly increase at about the same rate with time (like N_L and N_B , see Appendix 9). Then, C_L continues to increase at a higher rate. In some cases (for m6(22.2), m12(20), m12(21), m20(22.1), and g12(24)), at least one of the curves levels out in the second fracture phase.

In the CTt, C_L and C_B are larger in the granite than in the mortar and do not change significantly by changing the linear charge concentration.

In the HSI, the probability of a node being connected (p_C) increases with time (see Section 5.3.4). This increase usually follows a seemingly non-linear function – a bilinear function with a kink point positioned at the beginning of the second fracture phase. The slopes of the linear-regression lines of both p_I (the probability of a node not being connected) and p_C versus time do not significantly differ considering the blasted material. The slopes for p_I decrease, whilst for p_C they increase, with increasing linear charge concentration. These data for most blasted cylinders show a good linear fit for the second fracture phase. The linear-regression slopes for p_I and for p_C , in the second fracture phase, do not significantly differ from each other, both considering the blasted material and the linear charge concentration.

In the CTt, the probability p_c is higher in the granite than in the mortar. The scatter (IQR) of the result data decreases with increasing linear charge concentration. The average value of p_c does not significantly change with increasing linear charge concentration. Accordingly, the branch-connectivity probabilities show that over time more branches tend to become fully connected (p_{cc}), as the probability of the isolated ones (p_{ii}) decreases in the HSI. The probability of a branch being semi-connected (p_{ic}) stays nearly constant over time.

In the CTt, the probabilities p_{ii} and p_{ic} are very low compared to p_{cc} and independent of the linear charge concentration. These probabilities are lower in the granite than in the mortar. The probability p_{ic} is higher than p_{ii} for all blast shots. The probability p_{cc} is independent of the linear charge concentration, and it is higher in the granite than in the mortar.

Areal frequency p_{20} , fracture intensity p_{21} , and dimensionless fracture intensity p_{22} (see Section 5.3.5 and Appendix 9) in the HSI increase linearly over time, although the increase rate often differs from one fracture phase to another. The statistical evaluation of the linear-regression slopes of the p_{20} and p_{21} data indicates that the slopes are significantly different from each other, both considering the blasted material and the linear charge concentration. On average, the slopes become steeper with increasing linear charge concentration, and they are steeper in the granite than in the mortar.

These fracture-abundance parameters in the CTt increase with the linear charge concentration. Parameters p_{20} and p_{21} are lower in the granite than in the mortar for 6 g/m and about the same for the linear charge concentration of 12 and 20 g/m. Parameter p_{22} is independent of the linear charge concentration.

In the HSI, the total number of 2D fragments (see Section 5.4) increases linearly with elapsed time, except for m12(21), g6(26.1), and g12(25), where this trend seems to be non-linear. This, again, is the indicator of linear increase with the slope change (kink) between the first two fracture phases. The slopes of the linear-regression lines of the number of 2D fragments indicate that, on average, the slope (gradient) increases with increasing linear charge concentration and that it is larger in the granite than in the mortar. However, even for the same linear charge concentration and blasted material, some lines are significantly different to each other.

In the CTt, the total 2D-fragment count increases with the increase of the linear charge concentration from 6 g/m to 12 g/m, though it stays about the same with a further increase to 20 g/m. It is about the same in both blasted materials.

In the CTnp, the total 2D-fragment count is independent of the distance to the blast hole except near the blast hole. The only exception to this is for blast test 28.1 (granite, 12 g/m). Here, the count seems to linearly drop with the radial distance from the blast hole (i.e., from the centre of the initial borehole or the axis of the blast cylinder). The 2D-fragment count in the CTnp is not affected by the linear charge concentration and it is larger in the granite than in the mortar

The scatter in data-point clusters (D_{cent}) in the ternary diagrams of the 2D-fragment count in the CTt shows no significant variation except for blast test 26.1 (granite, 6 g/m).

The average crack-propagation speed (C_{ave} , see Section 5.5) does not significantly differ considering the blasted material. It increases with increasing linear charge concentration up to 12 g/m in the mortar. All other measured values are about the same in both blasted materials.

5.12.2 Identified mechanisms and deformation zones

The cracking macro-mechanisms (see Section 5.6) often occur in repetitive sequences in adjacent images. The branching and merging mechanisms (2.1 through 4.4, see Section 4.1.10), on average, last longer with increasing linear charge concentration and they are more frequent in the granite than in the mortar.

The normalized blast-hole radius ($r_{bh,norm}$) (see Section 5.7) is about the same in the axial direction of the cylinders outside the influence of the end faces (see Section 5.7.1). Both the blast-hole expansion (δr_{bh}) and the swelling (δr_m) increase with increasing linear charge concentration, except for δr_m in the 20-g/m mortar shot (m20(23.1)). The blast hole expanded more in the mortar than in the granite. However, the blast cylinders swelled more in the granite than in the mortar.

A compaction zone was found only in the mortar. The thickness of the deformation zones increases with increasing linear charge concentration. The total crushed-zone thickness ($\Delta r_{crush,tot}$) is about the same in both blasted materials for given linear charge concentrations, except in the 20-g/m shots (see Table 38). A possible reason for this could be an error in the estimation of the thickness of the blasted-off layer ($\Delta r_{blast,b}$) in

the micro-CT (uCT) images from g20(26.2), as this cylinder was measured differently (see Section 4.2).

The blast-driven crushing around the blast hole in the mortar forms the compaction zone mostly by deforming the pores in the cement matrix and connecting them with the ongoing fracturing, including ‘impact/impingement fractures’ in the quartz grains. The initial porosity of the mortar is reduced due to the shearing and crushing failure around the blast hole. Unlike in the mortar, the material near the blast hole in the granite contains more traces of tangential cracks. Farther out in the radial direction, there is a zone with a mixture of tangential and radial cracks, followed by a zone with mostly radial cracks. A material compaction was not found in the wakes of the main radial cracks of either blasted material. However, multiple branching-merging of smaller cracks is often found in these wakes.

The main micro-mechanisms (see Section 5.8) identified in the thin sections are:

- intergranular fracture – IG,
- transgranular fracture – TG,
- partial cleavage with lamellar steps - pcl,
- impingement cracking – ic,
- flaw-induced cracking – fc,
- refracturing – rc,
- cleavage – cc,
- elastic mismatch – em, and
- plastic mismatch - pm.

The mortar thin sections show mostly intergranular fractures outside the crushed zone. The air pores in the cement matrix influence the crack propagation by coalescence with running cracks, acting as branching/merging points, or acting as crack-arrest points.

In the granite, both transgranular and intergranular fracturing are present. The transgranular fracturing is more frequent near the blast hole and with higher linear charge concentration.

The thin sections in both materials show complex branching/merging at and near the main radial cracks. More complex mechanisms (i.e., combinations of the main ones, listed above) were identified at and below the grain-size level in both materials.

The branching/merging occurs on different size scales in both materials as a result of these complex mechanisms.

The SEM images of the small fragments (see Section 5.8.3) show rougher fracture surfaces with more transgranular fractures near and at the fragment edges in both materials. Although smoother than the fragment edges, the rest of the fracture surfaces on the fragments show sudden changes in the surface inclination with similar fracture traces to those identified at the edges. These features, identified as potential branching/merging lines, often start from larger pores in the mortar or elongated crystal grains (e.g., mica or feldspar) in the granite.

The half-split pores at the fracture surfaces in the mortar also show frequent micro-cracking at their edges. Such micro-cracks are also found in the granite as split mica or feldspar grains. These micro-cracks are a probable source of the ultra-fines following their liberation due to the propagation of a larger crack across them.

Mapped ridges and valleys in the fracture surfaces of the larger fragments (see Section 5.9) do not show any direct relation to the direction of the detonation or the assumed direction of the initial stress-wave front. These features seem to be rather randomly distributed. The maps suggest that the traces of the initial fracturing have been obscured by features of complex interaction between blast-induced stress/strain waves and developing fractures.

For the kernel size of 1 mm, the average values of the fracture-surface roughness are significantly different to each other considering both linear charge concentration and blasted material. Conversely, the average values are not significantly different to each other considering the linear charge concentration for the kernel size of 3 mm, and considering blasted material for the kernel size of 5 mm. The fracture-surface roughness is larger in the mortar than in the granite, except in the fragments from 20-g/m shots measured with 5-mm kernel, where the average roughness is larger in the granite. In both blasted materials, the surface roughness is largest in the fragments from the 12-g/m shots, smaller in the fragments from the 6-g/m shots, and smallest in the fragments from 20-g/m shots. Despite these results from the statistical evaluation, the corresponding box plots (Figure 174) do not show a significant difference between the data sets considering blasted material or the linear charge concentration.

5.12.3 Blast fragmentation

The FSD curves (see Section 5.10.1) show the expected NBC parallel-upward shift with increasing linear charge concentration. They also show the “dust-and-boulders” phenomenon, which is more pronounced in the 6-g/m shots.

The shape of the FSD curves of the merged screening data indicate a multimodal size distribution of the blast-fragmented material.

All obtained screening data were used for curve-fitting of the “Swebrec 3p” function, for the sieving data (Equation 46), and of the “Swebrec 5p” function, for the merged screening data (Equation 47). The fitting provided curve-description parameters and indicated the size limits of the ranges.

The identified ranges are:

- major fragments, ranging from the largest sieved fragment (original x_{max}) down to the largest fragment indicated by the fitting,
- intermediate fragments (IF), ranging from the lower major-fragment limit down to 1 mm fragment size,
- fines (F), ranging from 1 mm down to 0.04 mm fragment size, and
- ultra-fines (UF), ranging below 0.04 mm fragment size with
- the ultra-fines tail ($< 1.6 \mu\text{m}$).

More fines in the mesh-size range 0.04–1 mm (m-1 mm, m-0.5 mm, m-0.25 mm, m-0.1 mm, and m-0.04 mm, see Section 5.10.2) were produced with larger linear charge concentration, and more in the granite than in the mortar, except in the 6-g/m shots, for which more fines were produced in the mortar. A larger proportion of blast-hole-wall fines (relative to the total sieved fines passing through respective mesh size) were produced in the granite than in the mortar. Smaller relative quantities of these fines were produced with larger linear charge concentration (see Figure 180).

Based on the measurements of the thickness of the compaction zone ($\Delta r_{comp,a}$, see Section 5.7.2), more compacted material is expected with larger linear charge concentration in the mortar. More blasted-off material is expected with larger linear charge concentration, and more in the granite than in the mortar.

In both blasted materials, more crack-generated fines (CGF) passing 1 mm mesh size (m_{CGF}) were produced than blast-hole fines ($\Delta m_{bh,i}$) of corresponding size with the considered linear charge concentrations.

The measured specific surface areas (a_s and a_m , see Section 5.10.3) are smaller in the granite than in the mortar for both investigated size classes. They stay about the same for all three values of linear charge concentration in the mortar. In the granite, the specific surface areas for the size class 0.1|0.04 mm increase and for the size class - 0.04 mm decrease with increasing linear charge concentration. The obtained a_s and a_m for the 12- and 20-g/m blast shots could still be used to estimate these parameters by averaging for the 6-g/m blast shots. The particle-shape factor (f_A) decreases in the mortar and increases in the granite with increasing linear charge concentration. The plots of the blast-energy register (BER) show that the Rittinger coefficients (R_{BER}) are about the same for the two blasted materials (i.e., 2.90 cm²/J for the granite and 2.80 cm²/J for the mortar).

The s-n(s)-curve slope exponents ($-\alpha$, $-\beta$, see Section 5.10.4) were statistically evaluated and compared (see Appendix 10):

- The s-n(s) slope exponents in the intermediate-fragment-size range are not significantly different to each other, aside from the slopes for g12(25) and g12(28.1).
- The s-n(s) slope exponents in the fines-size range of the sieving data are not significantly different to each other.
- The s-n(s) slope exponents in the ultra-fines-size range of the merged-screening data are not significantly different to each other, aside from the slopes for g6(27), g12(24), and m6(22.2). This relationship between the slopes indicates a possible influence of the linear charge concentration on the slopes (when increased from 6 to 12 g/m). In this case, this increase of the linear charge concentration steepens the slopes in this range.
- The s-n(s) slope exponents from the (ultra-)fines-size range is not significantly different to that from the intermediate-fragment-size range (for the same blast shot) for 7 out of 12 blast shots. For the remaining 5 blast shots, the slopes are significantly different and mostly steeper in the (ultra-)fines range than in the intermediate-fragment-size range. However, the slopes do not show a clear effect of the linear charge concentration or the blasted material on this difference.

6 Discussion

This section discusses crucial aspects of the results (Section 5) and covers:

- the meaning of the presented results,
- accuracy and validity of the related methods and techniques,
- limitations, interpretations, implications, and significance of the results, and
- their relation to previously published (research) work.

6.1 Traced fracture patterns

The fracture patterns traced in the HSI all indicate the same development phases – fracture phases (see Section 5.1). The phases are delimited by the beginning of crack branching/merging and by the beginning of spalling of the frontal end face or intensive fumes leak (inrush) in front of it.

The initial cracks in the captured blast shots (HSI) are mostly radial. They further branch out and merge, forming new branches that may again branch/merge. This sequence of crack development at the frontal end face shows many complex patterns and also includes initiation and propagation of isolated cracks that, again, may branch and/or merge with other cracks.

The spalling at the frontal end face may occur even at this (early) stage (before the third phase) of crack development, especially in the granite. This effect is mostly a result of the acoustic-impedance mismatching between the protective window (PMMA) and rock/mortar at the frontal end face. The spalling starts with the circumferential boundary cracking induced by the reflected tensile waves. The movement of the frontal end face and the inrush (i.e., spill from the cylinder) of the blast fumes affect further propagation of the spalling cracks.

As was seen in the preliminary blast tests, different blast-test configurations lead to different resulting crack patterns. A weaker damping layer allows larger radial swelling and, hence, reduces the spalling at the frontal end face (see D. Johansson (2011) and the PMI from the preliminary test phase in Appendix 6). However, too weak a damping layer would in return induce spalling in the radial direction (i.e., at/near the cylinder mantle). The interaction of the frontal end face with the plug and the protective window is complex due to the window configuration. The final plug and the final window configuration worked well in the mortar. However, with larger linear charge concentration in the granite (even in some 20-g/m mortar shots), the spalling at the frontal end face became severe. The fume inrush obscured other mechanisms of crack-pattern development and crack patterns were very different to those from inside the cylinder, as observed with computer tomography (CTt, CTnp, and uCT). The spalling at the frontal end face rendered the HSI analysis useless after the second fracture phase. Even without the spalling at the frontal end face, the variability in the blasted material can make the crack patterns different even in blast shots of the same configuration.

The blast-induced fracture patterns in some cases are different for blast shots with the same linear charge concentration (l_c [g/m]) and in the same (blasted) material. This is the case for blast tests 20 (m12(20)) and 21 (m12(21)), and for blast tests 22.1 (m20(22.1)) and 23.1 (m20(23.1)) (Figure 182).

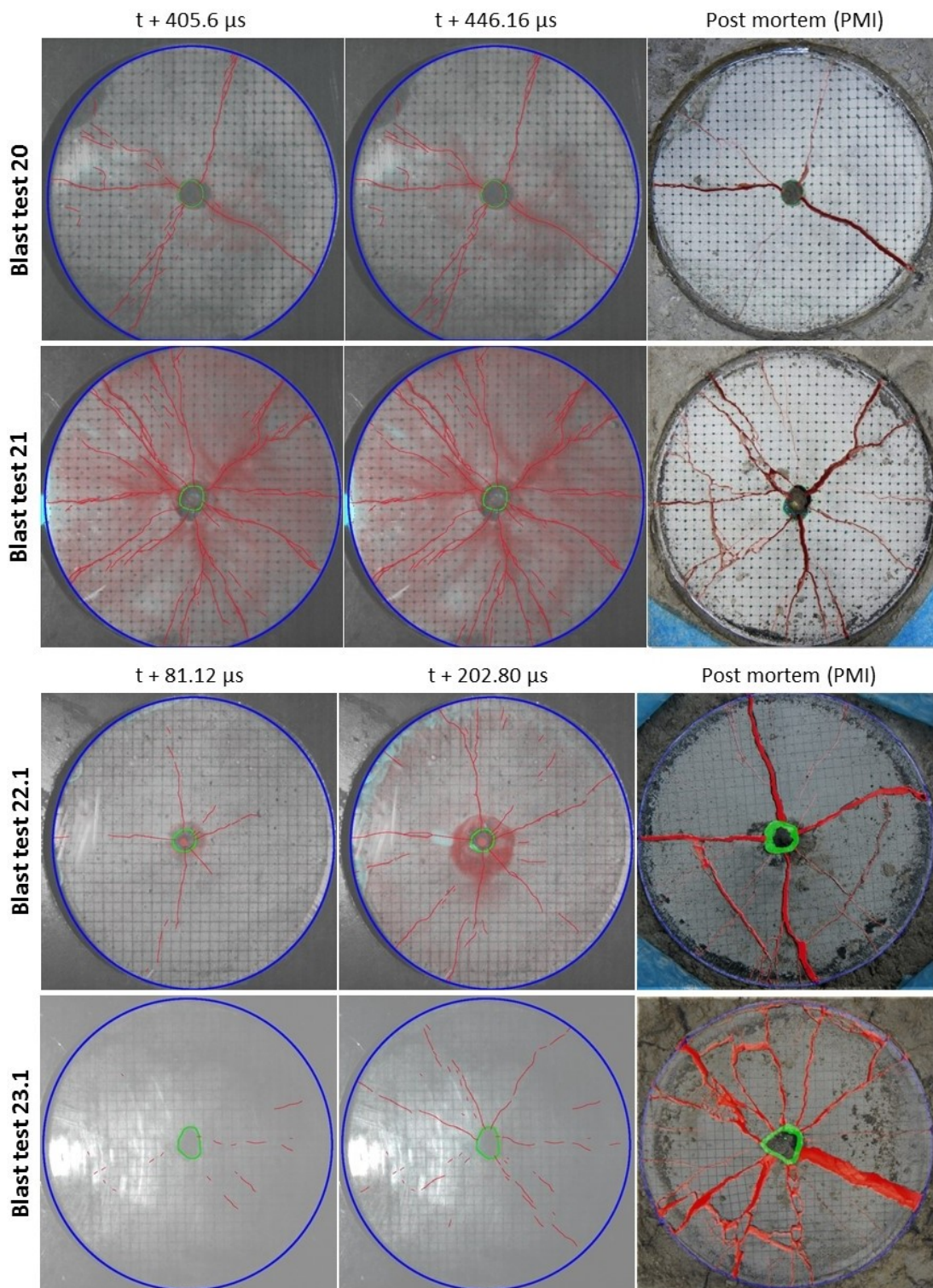


Figure 182. Crack-pattern difference between blast tests 20 and 21 and between blast test 22.1 and 23.1 (Selected HSI and PMI).

The crack patterns at the frontal end face in m12(21) clearly include more cracks and more crack intersections than in m12(20). The differences between m20(23.1) and m20(22.1) are less apparent in the HSI than in the PMI. A post-mortem analysis showed that the charging length was the same in all shots. Furthermore, the blast-test set-up

included the same type of the damping layer and the same plug configuration. Therefore, these crack pattern differences must depend on other factor(s).

The results concerning the internal crack patterns (CTt and CTnp) do not show such large differences. The fragmentation results also do not show significant difference between these compared blast tests. Different boundary conditions at the frontal end face are a probable cause for the differences in observed crack patterns. These boundary conditions could have been affected by:

- the interaction between the plug and the window,
- the interaction between the plug and the collar of the cylinder, and
- the interaction between the frontal end face with the window.

The differences in the spatial resolution of the HSI, PMI, and CTt suggests a systematic error in the comparison of these image sets.

Table 66: Spatial resolution (i.e., size in pixels) of analysed images of the frontal end face and of the internal cracks in transverse cross-sections.

Image type	Abbreviation	Covered part of blast cylinder	Original image size [pixel, px]
High-speed image	HSI	Frontal end face	336×336
Post-mortem image	PMI	Frontal end face	2675×2591
Transverse CT sections	CTt	Internal cracks	From 1400×1400 to 2000×2000

Contrary to expectations, although the HSI have lower spatial resolution than the PMI and the CTt, in many cases more topological features were detected in the HSI. Consequently, in many cases a larger topological parameter value was calculated for the last traced HSI than for the PMI or CTt. The difference between the HSI and the CTt or the PMI and the CTt can be explained as due to the complex boundary conditions at the frontal end face (Figure 183). However, this cannot be done for the difference between the last traced HSI and the corresponding PMI. Such results seem to contradict the basic assumption that the crack patterns at the frontal end face can only grow with time. A partial explanation may be that some cracks that are visible in the HSI have closed and remained undetectable in the PMI (see Section 5.1).

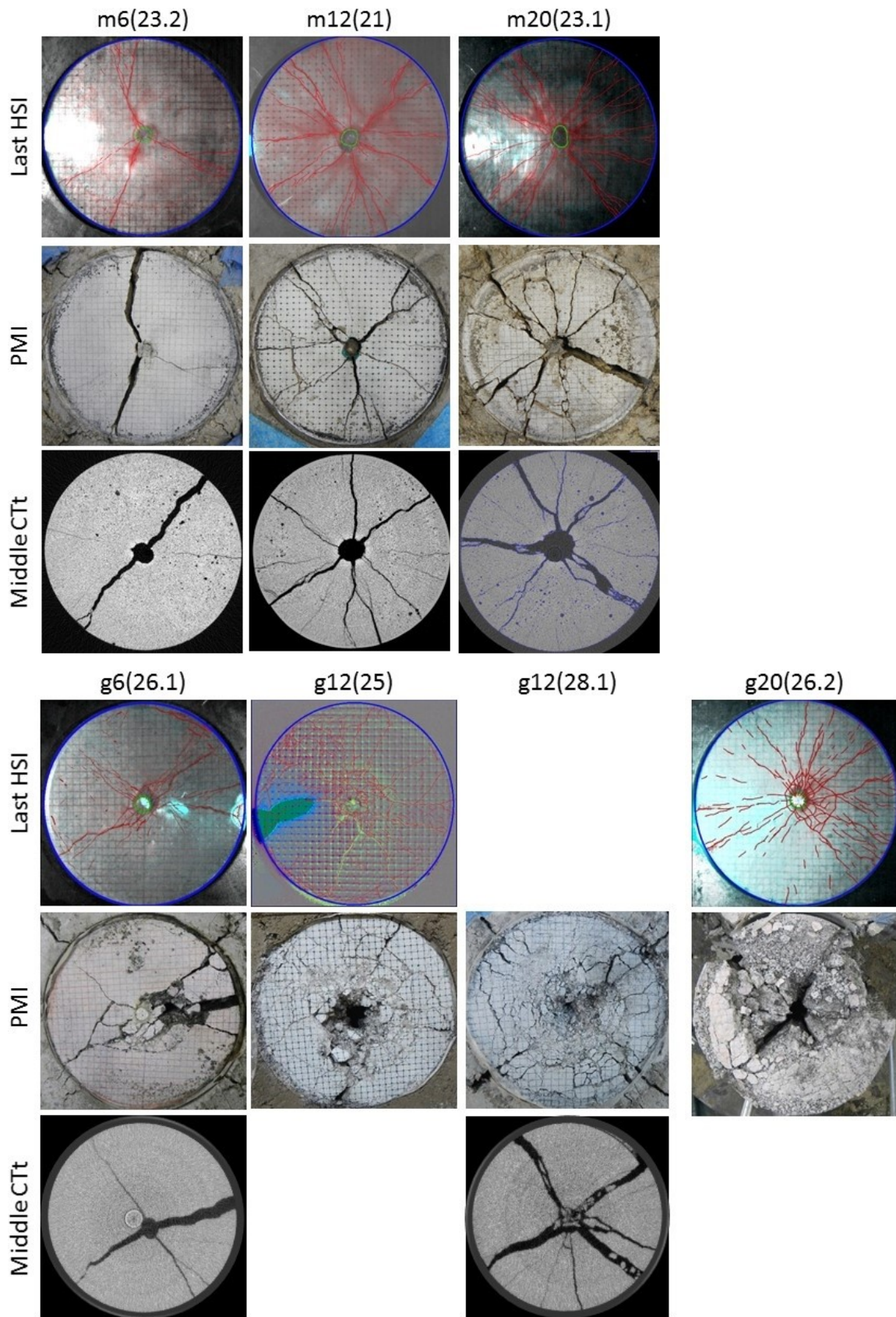


Figure 183: Overview of the last traced HSI, the PMI, and the middle CTt from selected blast tests. The empty fields indicate a lack of data.

6.2 Topological features

The topological analysis is based on branch and node counts (see Section 4.1.5). This analysis covers several features that are otherwise difficult to compare. A common crack-pattern development at the frontal end face initially covers an increase in the number of end nodes (N_I). Such behaviour is related to the generation of new cracks and to the crack branching. The branching increases N_I and the merging decreases it. The number of intersections (J_{int}) is increased by both the crack branching and the crack merging. As some of the cracks reach the radial boundaries (blast hole or mantle) the number of boundary (T_B) intersections increases and N_I decreases.

Therefore, as affected by the node counts, a decrease in some of the topological parameters from the last traced HSI to the PMI is not necessarily an indication of an error. The topological results show that the node counts are in most cases largest in the last traced HSI, than in the PMI, and the smallest in the CTt (see also Figure 183).

The number of main radial cracks (N) in the last traced HSI is, however, in most cases about the same as in the corresponding PMI of the blast shots. However, when this number is used to calculate the critical stress-intensity factor (K_{Ic} [MPa/m^{0.5}]) with Equation 19 (Grady & Kipp, 1987) and Equation 20 (Ouchterlony, 1997), the results are unrealistic.

As shown in Table 15, the estimated K_{Ic} values, in many cases, deviate considerably from the values obtained from the WST measurements (see Appendix 2). The results also show that for the mortar shots Equation 20 provides better estimates than those from Equation 19. The K_{Ic} estimates from these equations for the granite shots are about the same. Conversely, the statistical evaluation indicates that the blasted material does significantly affect N in the CTt (see Table 99, Table 100, and Table 101).

Given that the equations used for these estimations do not consider the specific boundary conditions in these blast tests, which are affected by the blasted material, an additional parameter (f_N) could be used as a conditional factor in Equation 19 and Equation 20:

$$N = f_N \cdot \pi \cdot \phi_h \left(\frac{\dot{p}}{6 \cdot C_p \cdot K_{Ic}} \right)^{2/3}, \quad \text{Equation 62}$$

$$N = f_N \cdot \frac{\pi}{3^{2/3}} \left(\frac{p_h \cdot \sqrt{\phi_h}}{K_{Ic}} \right)^{2/3}, \quad \text{Equation 63}$$

This conditional factor can be roughly estimated using these equations and the results in Table 15. However, as this factor could be described as a function of multiple parameters (e.g., related to size and shape of the blasted sample and to the impedance matching), more research is necessary before further conclusions on these equations. Another solution here would be to use a distribution-free fragmentation description based on percentile fragment sizes (Ouchterlony et al., 2017; Sanchidrián & Ouchterlony, 2017).

The CTt results of N suggest a non-linear correlation with the amount of the blast charge (i.e., linear charge concentration l_c or specific charge q) (see Figure 91). The correlation results (see Table 60 and Table 61) confirm this indication, as the log-log correlation coefficient R for q and N ($R = 0.843$) is larger than the lin-lin one ($R = 0.749$). Such behaviour could be related to the critical amount of the blast charge, as is the case for the “dust-and-boulders” phenomenon (see Section 5.10.1). This makes sense due to the physical relationship between the number of main radial cracks (N) and the number of main 2D fragments (i.e., those connected with both the blast hole and the mantle) and, consequently, with the number of (3D) boulders. Therefore, this non-linearity indicates that the critical value of the l_c is in the range from 6 to 12 g/m for both blasted materials.

The fracture-abundance parameters (p_{20} , p_{21} , and p_{22}) in the CTt also have such a non-linear correlation with l_c and with q (see Section 5.3.5). This also makes sense as all these parameters describe the degree of blast-induced fracturing.

In general, the absolute node counts in the HSI increase faster with time (i.e., with steeper slope) with increasing linear charge concentration. This behaviour can be related with the influence of the energy-release rate (Atkinson, 1987a). With more available energy being released per unit of time, more newly introduced nodes are expected, as their count reflects the crack-pattern development under the blast load. As higher energy-release rate is expected in stronger material, this interpretation agrees with the fact that these slopes are steeper in the granite than in the mortar.

However, exceptions to this observation were found for N_l (in the granite) and J_{int} , as their slopes decrease when further increasing the linear charge concentration from 12 to 20 g/m. Note here that the time range of useful HSI (i.e., before the third fracture phase) becomes considerably shorter with increasing linear charge concentration, especially in the granite shots. Such blast shots show more pronounced and earlier

spalling at the frontal end face. Therefore, it could be that in these shots the crack-pattern development at the frontal end face had not reached the stage when the rate would significantly increase when the spalling and the fumes already obscured it.

The number of I-nodes and of joining nodes should superficially increase with time. However, as an I-node is converted to a joining node when a crack tip meets another crack or a boundary, the I-node count may decrease. In most cases, the J_{int} -node proportion increases and levels out, in contrast to the I-node proportion. This levelling-out (i.e., decrease in the curve slope) usually occurs during the transition between the first two fracture phases (see Section 5.1). Note here that the fracture phases only indicate when the branching/merging becomes significant (start of the second phase) and when the frontal end face (i.e., the observed crack patterns) is no longer observable due to the spalling and/or the fumes inrush (start of the third phase). The T_b -node proportions either increase at a relatively low rate or remain about the same over time.

The ternary diagrams of the node-count proportions show that the data points of the proportions in the HSI move over time towards the clustered data points of the CTt. This behaviour shows a strong relationship (i.e., similarity) between the crack patterns at the frontal end face and the internal ones, though only before the third fracture phase. Furthermore, the data points of the PMI are also positioned inside the cluster, except in the case of the end-face spalling, which is more pronounced in the granite.

The clusters of CTt and CTnp data points in the ternary diagrams do not show any significant influence of the linear charge concentration or blasted material. However, the clusters of the CTt data do differ in the level of scatter as described by the standard deviation of D_{cent} (data-point distance from the cluster centroid). The scatter for the CTt decreases with increasing charge concentration and it is larger for the mortar than for the granite. This scatter can be interpreted as an inverse measure of uniformity of the crack patterns throughout blasted cylinder. Therefore, the crack patterns in the CTt are more uniform (i.e., show less variation) with increasing linear charge concentration, and they are more uniform in the granite than in the mortar.

This relationship with the linear charge concentration can also be observed considering the transition from below critical to enough charge amount to induce complete fragmentation and, thus, to the “dust-and-boulders” phenomenon. Here, boulders introduce larger crack-pattern variations along the axis of the scanned blasted cylinders, as they are not perfect radial segments.

Sanderson & Nixon (2015) explained that the average number of connections per branch (C_B [-]), a dimensionless number in the range 0–2, is a more reliable measure of crack branching than other similar measures (i.e., C_L , N_L , or N_B).

In the HSI, all C_B curves follow a non-linear trend (Figure 184). Here, the values firstly increase at a high rate and then, during the second fracture phase, the rate drops, making the curves almost level out towards the post-mortem state (i.e., in the PMI, here marked as $t+1000 \mu\text{s}$). Therefore, in all recorded blast shots the new branching/merging intersections initially appear much faster and then, during the second fracture phase, this rate drops significantly. Such behaviour could indicate a decrease of available fracture energy during the second fracture phase.

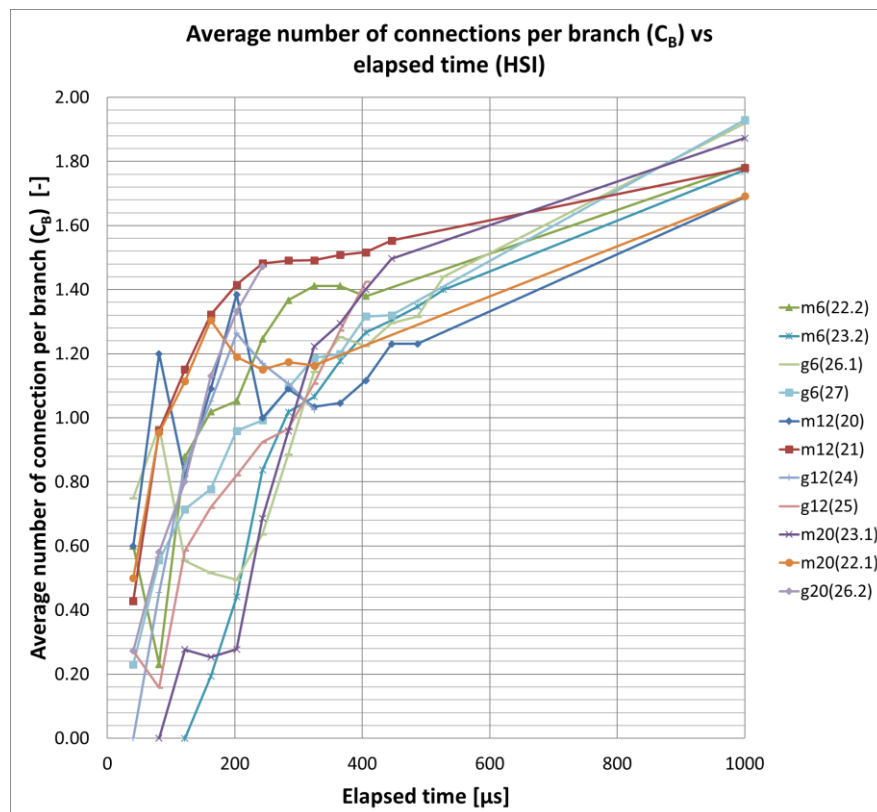


Figure 184: Development of the average number of connections per branch (C_B) in the HSI with the value from the PMI plotted at $t+1000 \mu\text{s}$.

As shown in Figure 102b, C_B result data in the CTt scatter less with increasing linear charge concentration, again indicating that the increase of the charge provides more uniform crack patterns in the CTt. The C_B values are larger in the granite than in the mortar and that they do not change significantly by changing the linear charge concentration.

More branching/merging was found in the granite than in the mortar, as the granite is more brittle, and its higher strength contributes to the energy release rate (i.e., its delayed failure, compared to that in the mortar, allows more energy to be built up before the release). The fact that the amount of charge does not significantly affect the amount of branching/merging in the CTt makes sense when observing Figure 184. The C_B curves look about the same with some deviation, and they seem to converge when approaching the post-mortem state.

The results of the probability of a node being connected (p_C), the branch-connectivity probabilities (p_{II} , p_{IC} , and p_{CC}), and the total 2D-fragment count agree with those for C_B , in the HSI and in the CTt.

6.3 Crack-propagation speed

The average crack-propagation speed (C_{ave} , see Section 5.5) does not significantly differ considering the blasted material. It increases with increasing linear charge concentration up to 12 g/m in the mortar. All other measured values remain about the same in both blasted materials when the linear charge concentration is changed. The correlation analysis shows that C_{ave} has a strong positive correlation with specific charge (q) (see Table 64) and a moderate positive correlation with sieved mass passing 1-mm mesh size ($m_{-1\text{ mm}}$). Therefore, C_{ave} depends on the linear charge concentration and on the blasted material in the same way as C_B does, at least in the mortar. This behaviour agrees with the theoretical relationship between the crack-propagation velocity and the branching/merging mechanism, in terms of the fracture toughness (Atkinson, 1987a).

6.4 Observed mechanisms

The macro- and meso-mechanisms, identified as specified features that compose crack patterns in the HSI (see Section 5.6), often occur in repetitive sequences in adjacent images. The branching and merging mechanisms (see Section 4.1.10), on average, last longer with increasing linear charge concentration and they are more frequent in the granite than in the mortar. This behaviour agrees with the results for C_B . The mechanisms generally considered as crack-tip branching/merging become more complex with the increasing linear charge concentration and in the granite, which is a more brittle and stronger material.

Such increase in complexity was also observed in the micro- and meso-mechanisms identified in the thin sections and in the uCT images. The traces of blast-induced crack propagation at this scale is associated with a frequent irregular band of microscopic cracks around and between macro-crack paths. Such formations show the influence of micro-structure of the blasted materials (e.g., granularity, porosity, grain orientation and relative position) to form fine fragments. Furthermore, the micro-cracking was frequently observed at the edges of half-split pores in the mortar micrographs and, similarly, as split mica or feldspar grains in the granite micrographs. Such formations indicate potential sources of fines at the lowest size scale detectible with this methodology (i.e., the ultra-fines). Therefore, the dynamic mechanism of branching/merging does occur at multiple size scales, as indicated by Michaux (2006, 2009) and Iravani (2020).

Furthermore, the fracture surfaces at the micro-level (see Section 5.8.3) are rougher near the edges of small fragments. As the thin sections show an increase of micro-cracks near the branching/merging points, the small-fragment edges could represent branching/merging lines. This agrees with the basic theory of crack-tip branching-merging (Åström, 2006; Kekäläinen et al., 2007), as can be shown on a simplified (penny-shaped) model of a small fragment (Figure 185). Adding the micro-cracks near the branching/merging points in a cross-section of the model explains why the small-fragment edges are rougher than the rest of the fragment surface. This roughness is also affected by the micro-structure, as mostly transgranular fractures are present at the edges.

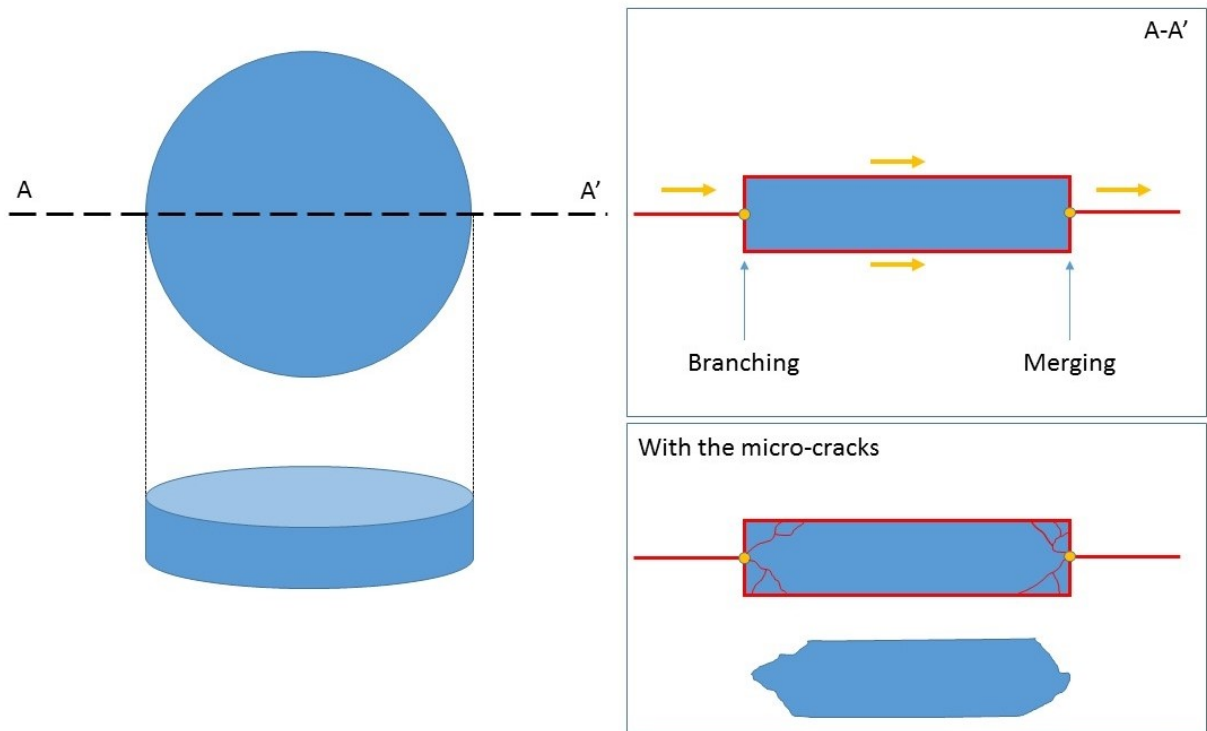


Figure 185: Crack-tip branching-merging on a penny-shaped model of a fragment with indicated effect of micro-cracks near the branching/merging points/lines on the surface roughness at the fragment edges. The yellow arrows indicate the direction of crack propagation.

6.5 Blast-hole expansion, mantle swelling, and deformation zones

Both the blast-hole expansion (δr_{bh}) and the swelling (δr_m) increase with increasing linear charge concentration. The normalized blast-hole radius ($r_{bh,norm}$) corresponds to the radius of the crushed zone r_c [mm] in the crushed-zone model (CZM) (Onederra et al., 2004).

Using Equation 4 and Equation 5, r_c was estimated for the results covered in this thesis as:

$$r_c = 0.812 \cdot r_{bh} \cdot \left(\frac{(p_h)^3}{\left(\frac{E_{dyn}}{1 + \mu_{dyn}} \right) \cdot UCS^2} \right)^{0.219} \quad \text{Equation 64}$$

Note here that r_o and P_b from Equation 4 are expressed as the initial borehole radius (r_{bh} , see Table 11) and the peak pressure level in the blast hole (p_h , see Figure 49), respectively. Table 67 shows the estimated r_c with the corresponding $r_{bh,norm}$ results (see Table 36).

Table 67: Summary of measured $r_{bh,norm}$ and estimated r_c (CZM).

Blast shot	p_h [MPa]	UCS [MPa]	E_{dyn} [GPa]	μ_{dyn} [-]	r_c [mm]	$r_{bh,norm}$ [mm]
m6(23.2)	35	27.7	14.5	0.17	1.24	7.05
m12(21)	85				2.23	8.14
m20(23.1)	166				3.46	12.30
g6(26.1)	35	171.5	57.9	0.22	0.42	6.16
g12(28.1)	85				0.75	7.23
g20(26.2)	166				1.16	7.43

The estimated r_c values are unrealistic, as all of them are smaller than the initial borehole radius (5 mm). Such outcome probably resulted from:

- the generally wrong assumption that the material around the blast hole is homogeneous and isotropic (see Equation 5),
- probable errors in measurement of E_{dyn} and μ_{dyn} , and
- limited or even wrong applicability of the constants 0.812 and 0.219 in Equation 64, considering the boundary conditions in these blast tests.

However, these results for r_c do agree with the observation that the blast hole expanded more in the mortar than in the granite and that the expansion increases with increasing linear charge concentration. Such relationship was also observed in other research work (Moser, 2005; Michaux, 2006; Banadaki, 2011; Sun, 2013; Chi, 2018).

In general, the swelling measurements agree with those provided by D. Johansson (2011), therein denoted as compaction [%]. The results from that research explain the effect of the damping layer on the swelling, including the impedance matching at the radial boundary of blast cylinder.

However, there are a few points to consider when referring to the swelling measurements. The swelling includes further radial movement (both rigid and elastic) of the blast fragments after they are formed (detached). The blast-hole wall can at first move without this being noticed at the surface. This also applies to the centre of gravity of a fragment. These fragments can move radially outwards during the blast (cylinder's radial expansion), and they can also move radially inwards (cylinder's radial retraction) upon the pressure drop in the blast hole. This rigid radial movement, both outwards and inwards, is a function of the blast loading, blast-cylinder material and size, damping-material material and size, and material and size of the segments of the blast chamber. The inertia and interactions of the initial fragments and the chamber components (e.g., the segments, the damping layer, and the connecting rods) during the blast determine the degree of the cylinder retraction upon the initial expansion.

In general, the swelling measurements agree with those provided by D. Johansson (2011), therein denoted as compaction [%]. The results from that research explain the effect of the damping layer on the swelling, including the impedance matching at the radial boundary of blast cylinder.

The compaction zone, as found only in the mortar cylinders, resembles the compaction observed by D. Johansson (2011). There, the blast loading broke the blast cylinder into mostly radial segments and further pushed them radially outwards into their radial boundary, compacting the damping material composing that boundary. The blast-induced compaction around the blast hole in the mortar blast cylinders (covered in this thesis) indicates a similar material behaviour upon the initial crushing-shearing of the borehole wall and interconnection of the air pores by propagating cracks near the blast hole.

Furthermore, the fact that the thickness of identified deformation zones around the blast hole (i.e., blasted-off material, the compaction zone, and the non-compacted crushed zone) increases with increasing linear charge concentration agrees with similar research with blast cylinders (Moser, 2005; Michaux, 2006; Banadaki, 2011; Sun, 2013; Chi, 2018; Iravani, 2020). However, the literature reviewed in this thesis is inconclusive to whether the total crushed-zone thickness ($\Delta r_{crush,tot}$) is independent of the blasted material, as indicated here.

The micrographs show that the crushed zone is not only formed by crushing-shearing, as the reviewed literature suggests, though also by microscopic variations of crack branching-merging.

6.6 Fracture-surface roughness

The results of the fracture-surface roughness and related topography (see Section 5.8.3 and Section 5.9.2) agree with the related findings of Zhang et al. (2000), Nukala et al. (2008), and Q. Zhang (2014). Generally, the fracture-surface roughness is larger in the mortar than in the granite. These results have a similar relationship with the linear charge concentration as for C_B , indicating the importance of the branching/merging or branching-merging on the fracture roughness. The kernel size of 1 mm was found more suitable than those of 3 and 5 mm to delineate the differences in the surface roughness between the two blasted materials and between the three levels of linear charge concentration. However, the topographic features (i.e., distribution and orientation of the ridges and valleys) of the fracture surfaces in macro-scale were inconclusive concerning their relationship with the direction of VOD, linear charge concentration, or the blasted material.

6.7 The fragment-size distribution (FSD) curves

The fragment-size distribution (FSD) curves agree with the NBC principle of the parallel-upward shift with increasing linear charge concentration (Steiner, 1991; Moser et al., 2000; Böhm et al., 2004; Ouchterlony & Moser, 2006; Ivanova, 2015; Schimek, 2015; Iravani, 2020).

However, the screening data show coarser fragmentation is the size range above 25 mm from g20(26.2) than those from the granite 12-g/m shots (g12(24), g12(25), and g12(28.1)) (see Figure 176 and Table 43). Such relationship is due to the “dust-and-boulders” phenomenon, with the “boulders” range covering x_{30} , x_{50} , and x_{80} . Although this phenomenon is not clear for the g20(26.2) data in Figure 176, photographs from the sieving of this cylinder show that the size class 100|80 mm is indeed composed of 3 boulders (Figure 186).



Figure 186: Fragments (boulders) from the size class 100|80 mm from g20(26.2).

The identified fragment-size ranges in the plots of the screening data agree with the findings of Iravani (2020) and with the general principle of self-similarity of size-distribution curves at different fragment-size ranges.

The results regarding the median fragment size (x_{50}) show similar relationship with specific charge (q [kg/m^3]) to that indicated by D. Johansson (2011), considering the influence of the damping layer on the blast fragmentation. Furthermore, the percentile fragments sizes from Table 43 can be presented with “fragmentation-energy-fan” plots (Figure 187), i.e., using a distribution-free fragmentation description based on percentile fragment sizes (Ouchterlony et al., 2017; Sanchidrián & Ouchterlony, 2017).

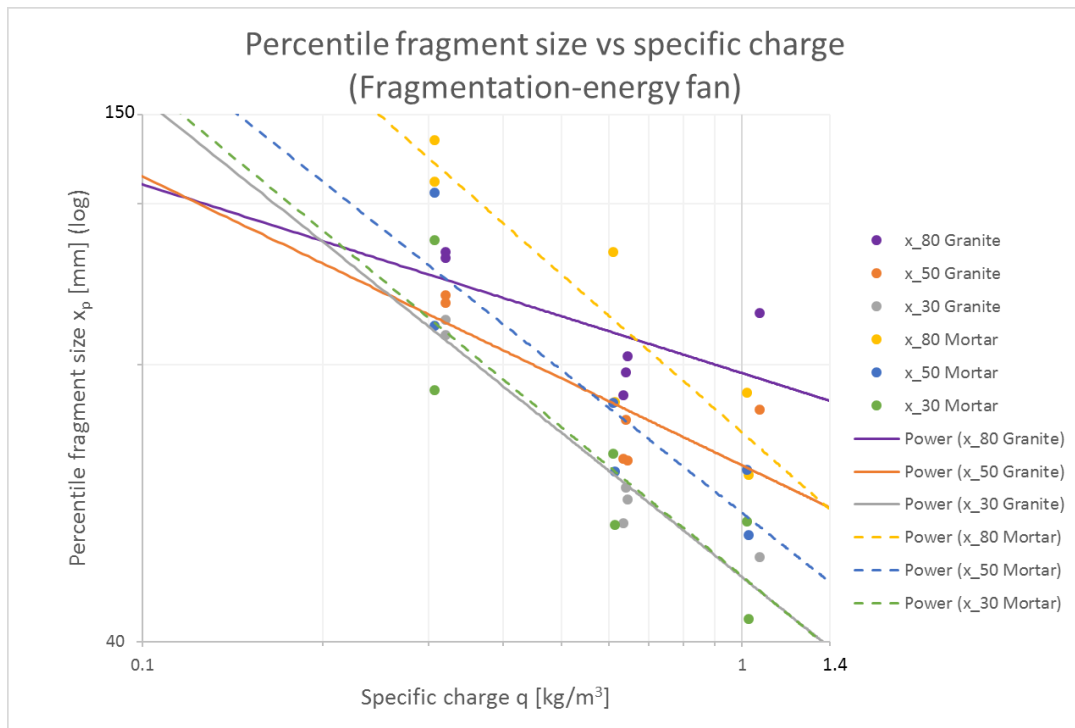


Figure 187: Percentile fragment sizes (x_{30} , x_{50} , and x_{80}) plotted against specific charge (q) (log-log scale).

The log-log fragmentation-energy-fan plots agree with the observations that the granite is stronger and more brittle than the mortar.

Such behaviour could be a result of the “dust-and-boulders” phenomenon and the related change in the nature of the blast fragmentation when increasing the linear charge concentration from 6, over 12, to 20 g/m in this blast-test set-up.

The Swebrec functions (Equation 46 and Equation 47) were confirmed as suitable for describing the FSD of the blasted cylinders. However, further improvement is required for describing the ultra-fines tail (fragment size below 1.6 μm).

6.8 Blast fines

More fines (size range 0.04–1 mm) are produced with increasing linear charge concentration, and more in the granite than in the mortar, except in the 6-g/m shots, for which more fines were produced in the mortar (see Section 5.10.2). This finding again shows the effect of the “dust-and-boulders” phenomenon.

A larger proportion of blast-hole-wall fines (relative to the total sieved fines passing through respective mesh size) were produced in the granite than in the mortar. This observation shows that less fines are produced around the blast hole in a more compliant and porous material due to ductile deformation. The compaction following the crushing around the blast hole entraps much of the initially formed fines. Smaller quantities of these fines compared to the total quantity of fines, for given mesh size, were produced with larger linear charge concentration. This behaviour confirms that the blast loading and the boundary conditions determine the major underlying mechanism for blast-induced fines. This observation is furthermore confirmed by the results regarding the estimated mass of the crack-generated fines (m_{CGF}). In the absolute terms, more m_{CGF} was produced than blast-hole fines ($\Delta m_{bh,i}$) of corresponding size with the considered linear charge concentrations.

The correlation analysis (Section 5.11) shows that the relationship of the fragmented mass passing 1 mm ($m_{-1\text{ mm}}$) with the specific charge (q) is better described as non-linear ($\ln(m_{-1\text{ mm}})$ vs $\ln(q)$) than linear ($m_{-1\text{ mm}}$ vs q), following the same relationship pattern as for C_B vs q (or linear charge concentration, l_c) (see Section 6.2). Aside for the parameters indirectly correlated with $m_{-1\text{ mm}}$ through the input parameter q , the correlation analysis (see Table 65) also has a strong positive linear correlation with the rate of change of the probability of a node being connected in the HSI (p_C slope) and with the rate of change of the fracture intensity in the HSI (p_{21} slope). This confirms the relationship of the macro-mechanisms with the blast-induced fines ($m_{-1\text{ mm}}$), as these slopes are directly linked to the crack-pattern development in the second fracture phase, especially considering crack branching/merging.

6.9 Specific surface area and blast-energy register (BER)

The measured specific surface area (a_s and a_m , see Section 5.10.3) generally agree with the related findings of Reichholf (2003) and Moser (2003, 2005).

The obtained blast-energy register (BER), however, shows that the Rittinger coefficients (R_{BER}) are about the same for the two blasted materials, i.e., that their “Blastability” (Reichholf, 2003) is about the same. This observation does not agree with the related findings of Reichholf (2003) and Moser (2003, 2005) about the Blastability of mortar/concrete and rock specimens. Table 68 shows the related R_{BER} results of Reichholf (2003).

Table 68: Summarized results of the calculated Rittinger coefficients for blasted samples by Reichholf (2003).

Material	Rittinger coefficient for BER R_{BER} [cm^2/J]
Dolomite	25.0
Iron ore	21.4
Limestone	96.1
Magnesite	21.6
Sandstone	33.0
Concrete 1	11.0

Here, he (Reichholf, 2003) demonstrated the “*A low Rittinger coefficient characterizes material difficult to break, a high coefficient a material easy to break*” (Böhm et al., 2004), which is not shown in the R_{BER} values for the granite and for the mortar shots (i.e., $2.90 \text{ cm}^2/\text{J}$ for the granite and $2.80 \text{ cm}^2/\text{J}$ for the mortar) (see Figure 181).

The R_{BER} results of Reichholf (2003) are about 10 times larger than those for the granite and the mortar shots. This is probably due to the charge decoupling (see Table 5) in the blast tests covered in this thesis, as Reichholf (2003) used fully coupled charge in his blast tests. Furthermore, Reichholf (2003) set up his experiment by remaining the amount of charge about the same, whilst varying the specific energy consumption (E_c [J/g]) by changing the specimen diameter for the blast tests. In this thesis, the charge amount was varied, and the specimen size remained about the same.

Furthermore, this relationship of the R_{BER} values in this thesis could be a result of the material properties and the micro-structure of the mortar compared to the granite. The mortar used in this thesis is much more porous compared to mortar/concrete material used in the work of Reichholf (2003) and Moser (2003, 2005). The observations and measurements of the compaction zone around the blast hole in the mortar (see Section 5.7.2) indicate larger energy dissipation than that during almost pure brittle fracturing like in the crushed zone of the granite. Furthermore, as some of the fine fragments are left “entrapped” in the compaction zone, they cannot be measured and further considered. Farther radially out from the blast hole, the mortar behaves more ductile than the granite due to the pores and micro-cracking in the cement matrix.

If the BER curves are plotted without setting the intercepts of the regression lines to (0,0), the R_{BER} values indicate that the mortar is more difficult to blast than the granite (Figure 188), which is even more contradictory to the results of Reichholf (2003) and Moser (2003, 2005).

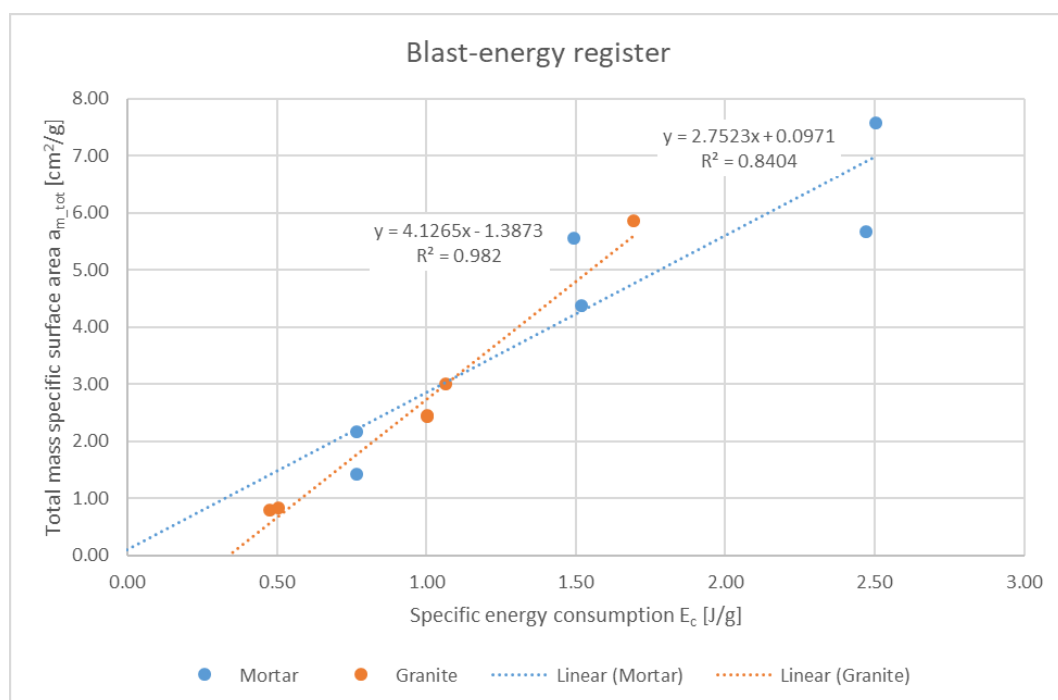


Figure 188: Blast-energy register – total mass specific surface area plotted against specific energy consumption. The regression lines do not have a set intercept point.

However, if the regression fitting is carried out with a polynomial function (Figure 189), the curves show that R_{BER} for the mortar is higher than for the granite for the 6- and 12-g/m shots, with change to the opposite relationship when for the 20-g/m shots. Note that the non-linearity is more pronounced in the mortar curve than for the granite one.

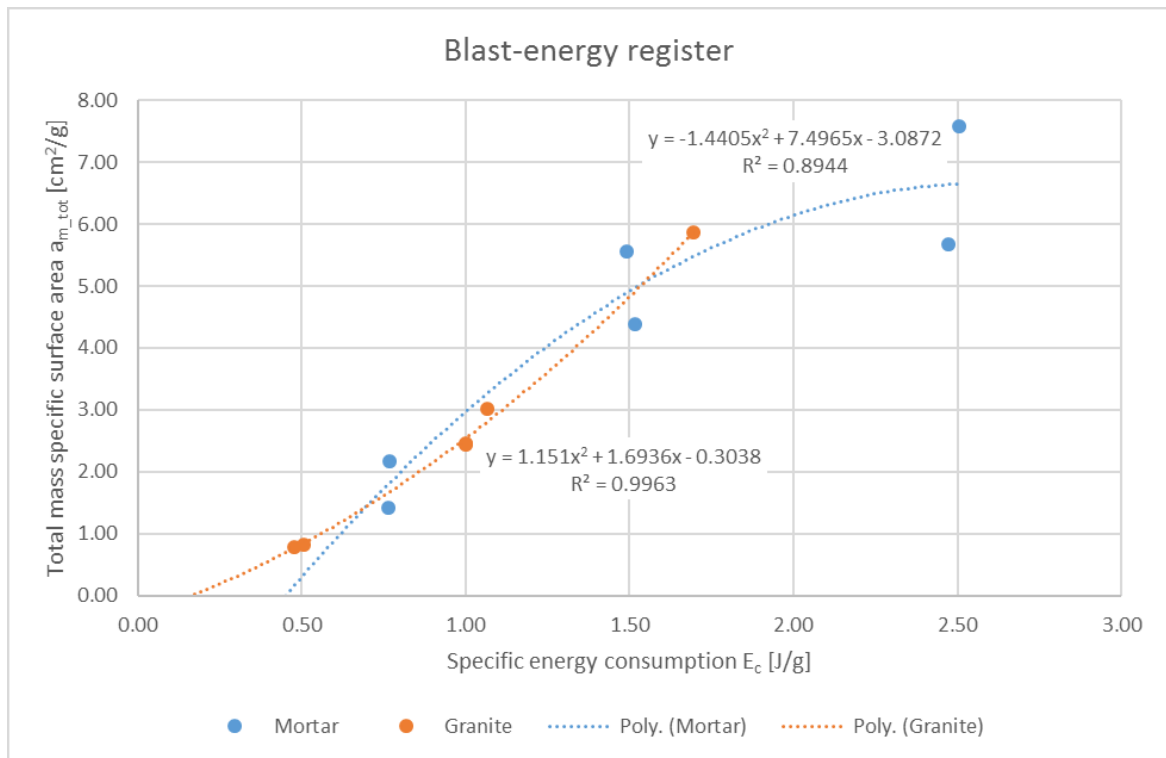


Figure 189: Blast-energy register – total mass specific surface area plotted against specific energy consumption. The regression is carried out with polynomial instead of linear functions and the fitted curves do not have a set intercept point.

Such representation indicates that the mortar is easier to blast than the granite for the linear charge density (l_c) of 6 and 12 g/m (for the given sample geometry), as expected. This relationship, however, is the opposite for the l_c of 20 g/m, i.e., the mortar is more difficult to blast than the granite. This could be a result of the compaction zone in the mortar, which increases with increasing l_c . Note that the compaction zone is directly affected by the confinement and coupling ratio, which increases non-linearly with increasing l_c (see Table 5).

Therefore, to be able to compare the R_{BER} results with those of Reichholf (2003) and Moser (2003, 2005), the coupling ratio and, more importantly, the radial boundary conditions should be considered. These factors are the main cause of the differences in the results.

6.10 Resulting “s-n(s)” curves

The s-n(s) plots and related statistical evaluations (see Section 5.10.4) confirm the indications of previous related work (Michaux, 2006, 2009; Iravani, 2020). The fitted regression lines to the s-n(s) data in log-log scale show piecewise straight lines (poly-line) across the observed size ranges, indicating “*different fragmentation processes with the kinks connecting these lines defining the size limits where the process of fragmentation changes*” (Iravani, 2020). The high correlation ($R > 0.9$) of the s-n(s) fitting confirm validity of the identified size-range limits and, generally, of those used by Iravani (2020) (see Table 55 and Table 56).

Referring to the Michaux’s (2006, 2009) observation of “*many branching-merging mechanisms that operate over fixed size ranges,*” Iravani (2020) concluded that the s-n(s) curves over these ranges have a slope (power-law exponent, $-\alpha$ or $-\beta$) of either -1.67, indicating the branching-merging as the dominating mechanism, or a higher absolute value, indicating the dominance of the crushing-shearing mechanism.

The s-n(s) slope exponents ($-\alpha$ and $-\beta$) (see Table 55 and Table 56) and the related statistical evaluation (see Section 5.10.4 and Appendix 10) generally agree with the indications of Ouchterlony & Moser (2013) and the conclusions of Iravani (2020).

All s-n(s) slope exponents in the intermediate-fragment-size range (for both the sieving data and the merged screening data) are about the same (except for those for g12(25) and g12(28.1)), covering the mechanism-specific value of -1.67. This confirms Iravani’s (2020) conclusion about the branching-merging being the dominating mechanism in this size range.

The s-n(s) slope exponents in the fines-size range of the sieving data are about the same and of larger than -1.67 (except for that of m12(20)). This confirms Iravani’s (2020) conclusion about the contribution of the crushing-shearing mechanism, additional to the branching-merging, in this size range.

Most of the s-n(s) slope exponents in the ultra-fines-size range of the merged-screening data are about the same, covering the mechanism-specific value of -1.67 and higher. This confirms Iravani’s (2020) conclusion about the simultaneous action of the branching-merging and the crushing-shearing mechanisms in this size range. These slopes are in most cases, however, flatter than those in the fines-size range for the sieving data. This could indicate that the branching-merging mechanism is more

pronounced than the crushing-shearing one in the size range below 0.04 mm. Further confirmation to this observation could be found in the micro-cracks around the pores in the mortar and in cleavage-split mica and feldspar grains in the granite (see Section 6.4).

However, the exceptions to this observation that the $s-n(s)$ slopes in the ultra-fines-size range of the merged-screening data are about the same was found for g6(27), g12(24), and m6(22.2). Furthermore, this resulted in the correlation analysis to show a strong positive linear correlation of the slopes with specific charge (q), and consequently with the fragmented mass passing 1 mm sieve size ($m_{-1 \text{ mm}}$) (see Table 64 and Table 65). Given the other results and statistical evaluations of the $s-n(s)$ slopes, this indication is more likely to be coincidental.

7 Summary and conclusions

The main objective of this thesis is to identify and quantify main mechanisms of dynamic blast-driven crack development in mortar and granite, and determine their relationship with the resulting blast fragmentation and fines. The commonly accepted blast-fragmentation theories presume crushing-shearing as the main mechanism behind the fines generation and that most of the fines are produced at or near blast holes. Dynamic branching and merging at the tips of dynamically propagating cracks was suggested and investigated in this thesis as another plausible source of blast fines.

This thesis covers development and implementation of small-scale blast tests on 12 confined $\text{Ø}150 \times 300$ -mm mortar and granite cylinders (a total of 40 with those from the preliminary test phase and additional tests) with different linear charge concentration l_c (6, 12, and 20 g/m) to investigate the effect of blast-driven crack development on the resulting fragmentation. The confinement was composed of radially positioned concrete segments around the blast cylinder with a damping layer in between. Metal covers were fixed on the frontal and on the rear side of the confinement, where the frontal one included an opening with a protective Polycarbonate window. The dynamic crack development at the frontal end face of the cylinder was observed through the window with high-speed photography. The crack patterns in their final (post-mortem) state were then recorded at the frontal end face with digital photography (post-mortem images, PMI) and inside the cylinder with computer tomography – in transverse cross-sections (CTt) and non-planar (tubular) cross-sections (CTnp). Investigations on the blast-induced cracks and fracture features at micro-level (i.e., micro-mechanisms) were carried out with micro-CT (uCT), optical microscopy, and SEM. Blast-induced fracture surfaces were investigated with uCT and SEM.

Captured high-speed images (HSI) were used to trace the blast-driven cracks and identify (dynamic) mechanisms related to the crack development. These macro-mechanisms were noted in “event logs,” records of their occurrence considering the time elapsed from the detonation (event initiation). The crack patterns in the HSI, PMI, CTt, and CTnp were analysed topologically by identifying and quantifying topological features – end nodes (I), Y-intersections, X-intersections, and intersections with the blast-hole wall and with the outer mantle of the cylinder. The results of this topological analysis were used to compare the blast-induced crack patterns in different blasted cylinders considering the effect of l_c and blasted material.

The blast-fragmented cylinders were then screened by sieving and laser-diffraction spectroscopy, and the screening results were compared to the mechanisms identified in the crack patterns and fracture surfaces.

The main conclusions of this thesis are provided as the following answers to the research questions stated in the introduction.

RQ1: What mechanisms can be identified in the development and in the final state of blast-induced cracks and fractures?

The captured crack patterns in the HSI show different macro-mechanisms regarding crack propagation, branching, and merging (see Section 5.8), defined as:

- Crack extension,
- Discontinuous crack extension,
- Side crack arrest,
- Side crack deflection,
- Primary in-line Y-branching,
- Primary side Y-branching,
- Secondary side Y-branching,
- Secondary T-branching,
- Primary in-line Y-merging,
- Side Y-merging,
- Secondary T-merging,
- In-line merging,
- In-line 2Y-branching-merging,
- Double en-passant merging,
- En-passant tip deflection and merging, and
- Double en-passant tip deflection and merging.

The SEM images of small fragments and thin-section images show micro-mechanisms, identified as:

- intergranular fracture – IG,
- transgranular fracture – TG,
- partial cleavage with lamellar steps - pcl,
- impingement cracking – ic,
- flaw-induced cracking – fc,
- refracturing – rc,
- cleavage – cc,
- elastic mismatch – em, and
- plastic mismatch - pm.

The micrographs and uCT images can also be used to investigate the deformation zones around the blast hole (i.e., the crushed zone and the compaction zone).

The external crack patterns from HSI and PMI and the internal crack patterns obtained by CT were used to identify and quantify the topological features, of which the intersection nodes (Y, X, and T_B) correspond to branching/merging of cracks.

RQ2: How can these mechanisms be identified and measured/quantified?

The macro-mechanisms can be counted in each image of an HSI sequence and presented as function of the time elapsed from the detonation to compose an “even log.” Furthermore, these mechanisms can be observed in a simplified form and quantified as the topological features in the HSI, PMI, CTt, and CTnp. Obtained quantities can be used to quantify the extent of branching/merging of the evaluated crack patterns and, hence, allow their comparison.

The deformation zones around the blast hole can be measured in the obtained CTt images and micrographs, with careful consideration to the position and orientation of the corresponding cross-sections and thin sections. The identified micro-mechanisms in the thin sections and SEM images could only be used for qualitative comparison.

RQ3: Which of these mechanisms are related to the generic mechanism of crack-tip branching-merging and how?

All identified macro-mechanisms concerning crack branching or merging are directly related to this mechanism, as they represent specific sub-variations of this mechanism considering dynamic crack development (i.e., the sequences of crack propagation and interaction). Furthermore, the, more general, branching-merging mechanism can be defined as different combinations of the identified macro-mechanisms. For example, a Y-branching and a following Y-merging compose the branching-merging formation by definition. In fact, the different combinations of all identified macro-mechanisms represent variations of branching-merging.

Considering the micro-structure of the blasted material, all identified micro-mechanisms represent variations of the crushing-shearing or of the branching-merging mechanism. It is, however, sometimes difficult to distinguish them in the micrographs due to the increasing complexity of related features with the decreasing size scale.

RQ4: How do these mechanisms affect the blast fragmentation and the generation of blast fines?

The branching/merging mechanisms, including the universal crack branching-merging, are directly affected by the blast loading and boundary conditions acting on the blasted sample. Depending on the amount of blasted explosive, the induced crack pattern ranges as follows:

- For a very low specific charge (q) – possible crushed zone around the blast hole (with or without compaction) with no cracks farther out;
- For a low (breakage) q – crushed zone around the blast hole (with or without compaction) and, farther out, up to 3-4 radial cracks and possible tangential cracks due to spalling (see HSI and PMI sets in Appendix 6), resulting in a few large fragments and fines (i.e., “dust and boulders”);
- For a medium q – crushed zone around the blast hole (with or without compaction) and the crack pattern shows more radial cracks and more intersections (i.e., branching/merging points), still resulting in the “dust and boulders,” though with also some fragments in the size range between the boulders and the fines;

- For a sufficient q – crushed zone around the blast hole (with compaction) with more radial cracks with many side branches, resulting in complete blast fragmentation with fragments filling out the whole fragment-size spectrum, showing an FSD that follows the Swebrec functions.

Therefore, both the extent of branching/merging in post-mortar crack patterns (average number of connections per branch, C_B) and blast fines (e.g., m^{-1} mm) are directly proportional to q . However, the HSI show that the rate at which the branching/merging occurs (i.e., the slope of plotted probability of a crack node being connected, p_C , against elapsed time) is highly correlated to the blast-induced fines, though less so to q .

The crushing-shearing mechanism was identified in the crushed zone around the blast hole in the blasted cylinders, especially in the compaction zone in the mortar. The micrographs show many forms of this mechanism at the micro-scale. However, some features (e.g., including impingement fractures in the mortar) can be treated as indications of both shearing and branching/merging. At this size scale, it is often difficult to distinguish the responsible mechanism for observed features due to the complexity of the fracture features and the micro-structure of the blasted material.

It can be concluded that the blast loading governs the crack/fracture development, manifested as crack branching/merging and crushing-shearing in different forms and at different scales, which then produce fragments of different sizes.

The FSD curves and the s - $n(s)$ curves of the blast-fragmented cylinders confirm the findings of Iravani (2020). The identified fragment-size regions generally match the size limits used by Iravani (2020) to delineate the fragment-size ranges of the fines-generating mechanisms. The obtained s - $n(s)$ slope exponents ($-\alpha$ and $-\beta$) confirm Iravani's (2020) hypothesis about the border value of 1.67, defining the size range with the s - $n(s)$ slope of this value as one with the branching-merging mechanism as the (main) source of the fines, and the size range with steeper s - $n(s)$ slope as one with crushing-shearing as the (main) source of the fines.

However, as these two main mechanisms (i.e., crack branching-merging and crushing-shearing) occur in different variations at the micro-scale, the s - $n(s)$ slope in the ultra-fines-size range (<0.04 mm) is probably also affected by the micro-structure of the blasted material. These variations, including possible combinations of the two main mechanisms, and their effect on the blast fragmentation (i.e., on the s - $n(s)$ slope) and fracture-surface roughness should be further investigated.

8 Future work

Further work on small-scale blast tests should include improvement of the blast-chamber design and the plug configuration to allow:

- application of a wider variety of blasted materials,
- application of stronger explosive charges (i.e., linear charge concentration of 20 g/m and larger, equally in all blast(ed) materials being investigated),
- better suppression of spalling and fumes at the frontal end face of the blast cylinder,
- investigation of different damping materials in the blast chamber according to the related findings of D. Johansson (2008, 2011),
- better control/prevention of the material losses during blasting.

The time of detonation, especially the initiation time, should be precisely measured/recorded (D. Johansson & Ouchterlony, 2011; Schimek, 2015) to prevent the issues with identifying the fracture phases at the frontal end face.

The high-speed photography could incorporate multiple high-speed cameras of higher spatial and temporal resolution to generate more precise HSI sets. Such configuration would allow for investigation of the crack-pattern development in 3D, using the principles of (stereo-) photogrammetry. Higher spatial and temporal resolutions of HSI would also provide sufficient information for a detailed analysis of the macro-mechanisms with minimized issues with determining crack-propagation direction and crack interactions. For example, this way the HSI could be also used to precisely determine whether a crack intersection has been caused by crack branching, merging, or a combination of these mechanisms.

The lighting system for this set-up should include light deflectors and reflectors to prevent the obscuring artefacts at the frontal end face caused by light reflection.

The blasted cylinders could be submitted to full micro-CT scanning (uCT) to improve the reconstruction and further measurements of the internal crack patterns. Furthermore, the scanning should be carried out before and after the blasting to allow for better evaluation of the crack-pattern development by 3D-model comparison.

Models of blasted samples could be used for a detailed fractography of the internal fracture surfaces. Furthermore, the models could be submitted to 3D segmentation to identify internal fragments, evaluate their geometry, and measure their size.

The microscopy should be carried out on more thin sections and on more small fragments in different blasted materials. The original position and orientation of the small fragments in the blast sample should be noted. The 3D segmentation of the blasted sample could be used here to precisely mark the position of the corresponding small fragments and determine their orientation in the sample.

The blast samples (e.g., cylinders) and the damping layer in the blast chamber should be thoroughly dried before the blasting.

The material losses due to material handling during the screening should be minimized by using a transparent enclosure for the fragmented material during the handling and the measurement.

9 Bibliography

- Agisoft. (2019). Agisoft Metashape. *Agisoft Metashape*, September, 1–2. <https://www.agisoft.com/>
- Åström, J. A. (2006). Statistical models of brittle fragmentation. *Advances in Physics*, 55(3–4), 247–278. <https://doi.org/10.1080/00018730600731907>
- Åström, J. A., Linna, R. P., Timonen, J., Møller, P. F., & Oddershede, L. (2004a). Exponential and power-law mass distributions in brittle fragmentation. *Physical Review E - Statistical Physics, Plasmas, Fluids, and Related Interdisciplinary Topics*, 70(2), 7. <https://doi.org/10.1103/PhysRevE.70.026104>
- Åström, J. A., Ouchterlony, F., Linna, R. P., & Timonen, J. (2004b). Universal dynamic fragmentation in D dimensions. *Physical Review Letters*, 92(24). <https://doi.org/10.1103/PhysRevLett.92.245506>
- Åström, J. A., & Timonen, J. (2012). Spontaneous formation of densely packed shear bands of rotating fragments. *European Physical Journal E*, 35(5). <https://doi.org/10.1140/epje/i2012-12040-y>
- Atkinson, B. K. (1987a). Fracture Mechanics of Rock. In *Fracture Mechanics of Rock*. Elsevier. <https://doi.org/10.1016/c2009-0-21691-6>
- Atkinson, B. K. (1987b). Introduction To Fracture Mechanics And Its Geophysical Applications. In *Fracture Mechanics of Rock* (pp. 1–26). Elsevier. <https://doi.org/10.1016/b978-0-12-066266-1.50006-5>
- Banadaki, M. M. D. (2011). *Stress-wave Induced Fracture in Rock due to Explosive Action*. Doctoral thesis. University of Toronto, Department of Civil Engineering, Toronto, Canada.
- Barton, N. (1982). Shear strength investigations for surface mining. In O. Brawner, C (Ed.), *Proceedings of the 23rd US Rock Mechanics Symposium* (pp. 178–180). Society of Mining Engineers of the American Institute of Mining, Metallurgical, and Petroleum Engineers.
- Barton, N., & Choubey, V. (1977). The shear strength of rock joints in theory and practice. *Rock Mechanics Felsmechanik Mécanique Des Roches*, 10(1–2), 1–54. <https://doi.org/10.1007/BF01261801>

- Blenkinsop, T. (2007). *Deformation Microstructures and Mechanisms in Minerals and Rocks*. Kluwer Academic Publishers.
- Böhm, A., Mayerhofer, R., & Öfner, W. (2004). *Energy for rock breakage*. [https://pure.unileoben.ac.at/portal/en/publications/energy-for-rock-breakage\(14a226fd-fd06-4fe3-816b-921697707b0b\).html](https://pure.unileoben.ac.at/portal/en/publications/energy-for-rock-breakage(14a226fd-fd06-4fe3-816b-921697707b0b).html)
- Brinkmann, J. R. (1987). Separating shock wave and gas expansion breakage mechanisms. In L. Fournery, William & D. Dick, Richard (Eds.), *Proceedings Second International Symposium on Rock Fragmentation by Blasting, FRAGBLAST 2* (pp. 6–15). Society for Experimental Mechanics.
- Chastain, S., & Pfaffman, J. (2006). GIMP: GNU Image Manipulation Program. *Learning & Leading with Technology*, 33(5), 54–55. <https://www.gimp.org/>
- Chi, L. Y. (2018). *Shock compression and fractures in laboratory rock blasting*. Doctoral thesis. Norwegian University of Science and Technology, Longyearbyen, Norway.
- Chi, L. Y., Zhang, Z.-X., Aalberg, A., & Li, C. C. (2019). Experimental Investigation of Blast-Induced Fractures in Rock Cylinders. *Rock Mechanics and Rock Engineering*, 52(8), 2569–2584. <https://doi.org/10.1007/s00603-019-01749-0>
- Cignoni, P., Callieri, M., Corsini, M., Dellepiane, M., Ganovelli, F., & Ranzuglia, G. (2008). MeshLab: An open-source mesh processing tool. *6th Eurographics Italian Chapter Conference 2008 – Proceedings* (pp. 129–136). Salerno, Italy
- CloudCompare [GPL software]* (2.6.3). (2019). <http://www.cloudcompare.org/>
- Dalmas, D., Guerra, C., Scheibert, J., & Bonamy, D. (2013). Damage mechanisms in the dynamic fracture of nominally brittle polymers. *International Journal of Fracture*, 184(1–2), 93–111. <https://doi.org/10.1007/s10704-013-9839-y>
- Dancey, C. P., & Reidy, J. (2007). *Statistics without Maths for Psychology*. Pearson Education.
- Djordjevic, N. (1999). A two-component model of blast fragmentation. *The AusIMM Proceedings*, 304(2) (pp. 9–13). The Australasian Institute of Mining and Metallurgy, Australia.

- Djordjevic, N. (2002). Origin of blast-induced fines. *Institution of Mining and Metallurgy. Transactions. Section A: Mining Technology*, 111(MAY/AUG), 143–146. <https://doi.org/10.1179/mnt.2002.111.2.143>
- Esen, S., Onederra, I. A., & Bilgin, H. A. (2003). Modelling the size of the crushed zone around a blasthole. *International Journal of Rock Mechanics and Mining Sciences*, 40(4), 485–495. [https://doi.org/10.1016/S1365-1609\(03\)00018-2](https://doi.org/10.1016/S1365-1609(03)00018-2)
- Ferreira, T., & Rasband, W. (2012). ImageJ User Guide User Guide ImageJ. In *Image J user Guide: Vol. 1.46r*. <https://doi.org/10.1038/nmeth.2019>
- Fourney, W. L. (1993). Mechanisms of rock fragmentation by blasting. *Comprehensive Rock Engineering. Vol. 4*, 39–69. <https://doi.org/10.1016/b978-0-08-042067-7.50009-x>
- Fourney, W. L. (2015). The role of stress waves and fracture mechanics in fragmentation. In T. Spathis, A. P. Gribble, D. C. Torrance, A. & N. Little, T (Eds.), *11th International Symposium on Rock Fragmentation by Blasting* (pp. 27–39). AusIMM.
- Gallagher, J. J., Friedman, M., Handin, J., & Sowers, G. M. (1974). Experimental studies relating to microfracture in sandstone. *Tectonophysics*, 21(3), 203–247. [https://doi.org/10.1016/0040-1951\(74\)90053-5](https://doi.org/10.1016/0040-1951(74)90053-5)
- Grady, D. E., & Kipp, M. E. (1987). Dynamic rock fragmentation. In *Fracture Mechanics of Rock* (pp. 429–475). Elsevier. <https://doi.org/10.1016/b978-0-12-066266-1.50015-6>
- Grasedieck, A. (2006). *Die natürliche Bruchcharakteristik (NBC) von Gesteinen in der Sprengtechnik*. Doctoral thesis. Montanuniversitaet Leoben.
- Grimshaw, H. C. (1958). The fragmentation produced by explosive detonated in stone blocks. In H. Walton, W (Ed.), *Mechanical properties of non-metallic materials* (p. 380-388). Butterworths.
- Hippertt, J. F. M. (1994). Grain boundary microstructures in micaceous quartzite: significance for fluid movement and deformation processes in low metamorphic grade shear zones. *Journal of Geology*, 102(3), 331–348. <https://doi.org/10.1086/629675>

- Hohl, W. (2013). Test report - *Prüfbericht TR_2013_007*. Chair of Mining Engineering and Mineral Economics, Montanuniversitaet, Leoben.
- Horii, H., & Nemat-Nasser, S. (1985). Compression-induced microcrack growth in brittle solids: Axial splitting and shear failure. *Journal of Geophysical Research*, *90*(B4), 3105. <https://doi.org/10.1029/jb090ib04p03105>
- Instruments Malvern Ltd. (2007). *Mastersizer 2000 User Manual* (p. 154). https://www.labmakelaar.com/fjc_documents/mastersizer-2000-2000e-manual-eng1.pdf
- Iravani, A. (2020). *Simulation of dynamic fracturing in rock like materials. Fines creation from branching-merging of blast loaded cracks in general and in cylindrical specimens*. Doctoral thesis. Montanuniversitaet Leoben.
- Iravani, A., Åström, J. A., & Ouchterlony, F. (2018a). Physical Origin of the Fine-Particle Problem in Blasting Fragmentation. *Physical Review Applied*, *10*(3). <https://doi.org/10.1103/PhysRevApplied.10.034001>
- Iravani, A., Kukolj, I., Ouchterlony, F., Antretter, T., & Åström, J. A. (2018b). Modelling blast fragmentation of cylinders of mortar and rock. In H. Schunnesson & D. Johansson (Eds.), *12th International Symposium on Rock Fragmentation by Blasting* (pp. 597–610). Luleå Univ. of Technology.
- Iravani, A., Ouchterlony, F., Kukolj, I., & Åström, J. A. (2020). Generation of fine fragments during dynamic propagation of pressurized cracks. *Physical Review E*, *101*(2), 23002. <https://doi.org/10.1103/PhysRevE.101.023002>
- Isakov, M., Hiermaier, S., & Kuokkala, V. T. (2014). Improved specimen recovery in tensile split Hopkinson bar. *Philosophical Transactions of the Royal Society A: Mathematical, Physical and Engineering Sciences*, *372*(2023), 20130194. <https://doi.org/10.1098/rsta.2013.0194>
- Ivanova, R. (2015). *Investigation on fragmentation by blasting. The influence of distorted blasthole patterns on fragmentation, roughness of the remaining bench face and blast damage behind it in model scale blasting*. Doctoral thesis. Montanuniversitaet Leoben.
- Jaeger, J. C., Cook, N. G. W., & Zimmerman, R. (2007). *Fundamentals of rock mechanics* (4th ed.). Wiley-Blackwell.

- Janesick, J. R. (2004). Charge-coupled CMOS and hybrid detector arrays. *Focal Plane Arrays for Space Telescopes*, 5167, 1. <https://doi.org/10.1117/12.511864>
- Johansson, C. H., & Persson, P. A. (1970). *Detonics of high explosives*. Academic Press.
- Johansson, D. (2011). *Effects of confinement and initiation delay on fragmentation and waste rock compaction*. Doctoral thesis. Luleå University of Technology.
- Johansson, D. (2008). *Fragmentation and waste rock compaction in small-scale confined blasting*. Licenciate thesis. Luleå University of Technology. <https://www.diva-portal.org/smash/get/diva2:990096/FULLTEXT01.pdf>
- Johansson, D., & Ouchterlony, F. (2011). Fragmentation in small-scale confined blasting. *International Journal of Mining and Mineral Engineering*, 3(1), 72–94. <https://doi.org/10.1504/IJMME.2011.041450>
- Johansson, D., & Ouchterlony, F. (2013). Shock wave interactions in rock blasting: The use of short delays to improve fragmentation in model-scale. *Rock Mechanics and Rock Engineering*, 46(1), 1–18. <https://doi.org/10.1007/s00603-012-0249-7>
- Johansson, D., Villegas, T., & Ouchterlony, F. (2010). Dynamic blast compaction of some granular materials: small-scale tests and numerical modelling of a mining-related problem. *International Journal of Mining and Mineral Engineering*, 2(2), 79–100. <https://doi.org/10.1504/IJMME.2010.035311>
- Johnson, C. E. (2014). Fragmentation Analysis in the Dynamic Stress Wave Collision Regions in Bench Blasting [University of Kentucky]. In *Theses and Dissertations--Mining Engineering 16*. https://uknowledge.uky.edu/mng_etds/16
- Kanninen, M. F., Popelar, C. A., & Saunders, H. (1988). Advanced Fracture Mechanics. *Journal of Vibration and Acoustics*, 110(3), 419–420. <https://doi.org/10.1115/1.3269540>
- Kekäläinen, P., Åström, J. A., & Timonen, J. (2007). Solution for the fragment-size distribution in a crack-branching model of fragmentation. *Physical Review E - Statistical, Nonlinear, and Soft Matter Physics*, 76(2), 1–7. <https://doi.org/10.1103/PhysRevE.76.026112>

- Khormali, R. (2012). *An investigation into the natural breakage characteristics (NBC) of rock and rock-like materials in blasting, and model correlations in fragmentation phenomena*. Technical report. Montanuniversitaet Leoben.
- Kukulj, I., Iravani, A., Ouchterlony, F., Weiss, C., & Lubensky, J. (2018a). Filming blast fragmentation of rock and mortar cylinders. In Schunnesson, H.; Johansson, D. (Eds.), *Rock Fragmentation by Blasting, Proceedings of 12th International Symposium on Rock Fragmentation by Blasting* (pp. 483–494). Luleå University of Technology, Luleå.
- Kukulj, I., Iravani, A., & Ouchterlony, F. (2018b). Using Small-scale Blast Tests and Numerical Modelling to Trace the Origin of Fines Generated in Blasting. *BHM Berg- Und Hüttenmännische Monatshefte*, 163(10), 427–436. <https://doi.org/10.1007/s00501-018-0778-9>
- Kukulj, I., Oberdorfer, B., & Ouchterlony, F. (2019). Internal Fractures After Blasting Confined Rock and Mortar Cylinders. *BHM Berg- Und Hüttenmännische Monatshefte*, 164(10), 422–430. <https://doi.org/10.1007/s00501-019-00899-6>
- Kutter, H. K., & Fairhurst, C. (1971). On the fracture process in blasting. *International Journal of Rock Mechanics and Mining Sciences And*, 8(3), 181–202. [https://doi.org/10.1016/0148-9062\(71\)90018-0](https://doi.org/10.1016/0148-9062(71)90018-0)
- Lajtai, E. Z., Schmidtke, R. H., & Bielus, L. P. (1987). The effect of water on the time-dependent deformation and fracture of a granite. *International Journal of Rock Mechanics and Mining Sciences*, 24(4), 247–255. [https://doi.org/10.1016/0148-9062\(87\)90179-3](https://doi.org/10.1016/0148-9062(87)90179-3)
- Littell, R. C., Stroup, W. W., & Fround, R. J. (2002). *SAS for linear models* (4th ed.). SAS Institute.
- López, L. M. (2002). *Personal communication*.
- Mali, H. (2019). *Personal communication*.
- Malvern. (1999). Manual sample dispersion unit for mastersizer 2000. *Pigment & Resin Technology*, 28(3), 374–380. <https://doi.org/10.1108/prt.1999.12928cad.018>
- Manzocchi, T. (2002). The connectivity of two-dimensional networks of spatially correlated fractures. *Water Resources Research*, 38(9), 1-1-1–20. <https://doi.org/10.1029/2000wr000180>

- Maxam. (2019). *Riocord Detonating Cord*. Maxam. www.maxam.net
- McDonald, J. H. (2014). *Handbook of biological statistics* (3rd ed.). Sparky House Publishing.
- Michaux, S. P. (2006). *Analysis of fines generation in blasting*. Doctoral thesis. The University of Queensland.
- Michaux, S. P. (2009). Sub-populations and patterns in blast induced fine fragmentation. *Minerals Engineering*, 22(7–8), 576–586. <https://doi.org/10.1016/j.mineng.2009.04.005>
- Michaux, S. P., & Djordjevic, N. (2005). Influence of explosive energy on the strength of the rock fragments and SAG mill throughput. *Minerals Engineering*, 18(4), 439–448. <https://doi.org/10.1016/j.mineng.2004.07.003>
- Miklautsch, A. (2002). *Experimental investigation of the blast fragmentation behaviour of rock and concrete*. Montanuniversitaet Leoben.
- Morel, S., Bouchaud, E., Schmittbuhl, J., & Valentin, G. (2002). R-curve behavior and roughness development of fracture surfaces. *International Journal of Fracture*, 114(4), 307–325. <https://doi.org/10.1023/A:1015727911242>
- Moser, P. (2005). Less fines in aggregate and industrial minerals production. *3rd European Federation of Explosives*, 567–574.
- Moser, P. (2003). Less fines production in aggregate and industrial minerals industry. In Roger Holmberg (Ed.), *Explosives and Blasting Technique* (pp. 335–343). Lisse: Balkema. <https://doi.org/10.1201/9781439833476.ch40>
- Moser, P., Cheimanoff, N., Ortiz, R., & Hochholdinger, R. (2000). Breakage characteristics in rock blasting. In R Holmberg (Ed.), *Explosives and Blasting Technique* (pp. 165–170). A. A. Balkema Publishers.
- Moser, P., Grasedieck, A., Arsic, V., & Reichholf, G. (2003a). Charakteristik der Korngrößenverteilung von Sprenghauwerk im Feinbereich. *Berg- Und Hüttenmännische Monatshefte : BHM*, 217–225.
- Moser, P., Olsson, M., Ouchterlony, F., & Grasedieck, A. (2003b). Comparison of the blast fragmentation from lab-scale and full-scale tests at Bårarp. In R Holmberg (Ed.), *Explosives and Blasting Technique* (pp. 449–458). Balkema. <https://doi.org/10.1201/9781439833476.ch55>

- Napier-Munn, T. (2014). *Statistical methods for mineral engineers how to design experiments and analyse data*. JKMRC Julius Kruttschnitt Mineral Research Centre.
- Nasseri, M. H. B., Grasselli, G., & Mohanty, B. (2010). Fracture toughness and fracture roughness in anisotropic granitic rocks. *Rock Mechanics and Rock Engineering*, 43(4), 403–415. <https://doi.org/10.1007/s00603-009-0071-z>
- Niiranen, K. (2015). *Characterization of the Kiirunavaara Iron Ore*. Montanuniversitaet Leoben, Austria.
- Nukala, P. K. V. V., Zapperi, S., Alava, M. J., & Šimunović, S. (2008). Crack roughness in the two-dimensional random threshold beam model. *Physical Review E - Statistical, Nonlinear, and Soft Matter Physics*, 78(4). <https://doi.org/10.1103/PhysRevE.78.046105>
- Olsson, M., Nie, S., Bergqvist, I., & Ouchterlony, F. (2002). What causes cracks in rock blasting? *Fragblast*, 6(2), 221–233. <https://doi.org/10.1076/frag.6.2.221.8668>
- Onederra, I. A., Esen, S., & Jankovic, A. (2004). Estimation of fines generated by blasting - Applications for the mining and quarrying industries. *Institution of Mining and Metallurgy. Transactions. Section A: Mining Technology*, 113(4), 237–247. <https://doi.org/10.1179/037178404225006191>
- Ouchterlony, F. (1974). Fracture mechanics applied to rock blasting. *Advances in Rock Mechanics: Proceedings of the Third Congress of the International Society for Rock Mechanics*, 2B, 1377–1383.
- Ouchterlony, F. (2010). Fragmentation characterization; The Swebrec function and its use in blast engineering. In J. A. Sanchidrián (Ed.), *Rock Fragmentation by Blasting - Proceedings of the 9th International Symposium on Rock Fragmentation by Blasting, FRAGBLAST 9* (pp. 3–22). CRC Press/Taylor & Francis Group.
- Ouchterlony, F. (2009). Fragmentation characterization; The Swebrec function and its use in blast engineering. *Rock Fragmentation by Blasting - Proceedings of the 9th International Symposium on Rock Fragmentation by Blasting, FRAGBLAST 9*, 3–22.

- Ouchterlony, F. (1997). Prediction of crack lengths in rock after cautious blasting with zero inter-hole delay. *Fragblast*, 1(4), 417–444. <https://doi.org/10.1080/13855149709408407>
- Ouchterlony, F. (2005). The Swebrec© function: Linking fragmentation by blasting and crushing. *Institution of Mining and Metallurgy. Transactions. Section A: Mining Technology*, 114(1). <https://doi.org/10.1179/037178405X44539>
- Ouchterlony, F., & Moser, P. (2006). Likenesses and differences in the fragmentation of full-scale and model-scale blasts. *8th International Symposium on Rock Fragmentation by Blasting, May*, 207–220.
- Ouchterlony, F., & Moser, P. (2013). On the branching-merging mechanism during dynamic crack growth as a major source of fines in rock blasting. *Rock Fragmentation by Blasting, FRAGBLAST 10 - Proceedings of the 10th International Symposium on Rock Fragmentation by Blasting*, 65–75. <https://doi.org/10.1201/b13759-9>
- Ouchterlony, F., Nyberg, U., Bergman, P., & Esen, S. (2007). Monitoring the blast fragmentation in Boliden Mineral's Aitik mine. *4th EFEE World Conference on Explosives and Blasting*, 47-62.
- Ouchterlony, F., Nyberg, U., Olsson, M., Bergqvist, I., Granlund, L., & Grind, H. (2003). The energy balance of production blasts at Nordkalk's Klinthagen quarry. In *Explosives and Blasting Technique* (pp. 193–203). Taylor & Francis. <https://doi.org/10.1201/9781439833476.ch24>
- Ouchterlony, F., Sanchidrián, J. A., & Moser, P. (2017). Percentile Fragment Size Predictions for Blasted Rock and the Fragmentation–Energy Fan. *Rock Mechanics and Rock Engineering*, 50(4), 751–779. <https://doi.org/10.1007/s00603-016-1094-x>
- Ouchterlony, F., Sifferlinger, N. A., & Brechelmacher, A. (2018). Das europäische Horizon 2020-Forschungsprojekt „Sustainable Low Impact Mining – SLIM“The European Horizon 2020 Research Project “Sustainable Low Impact Mining Solution for Exploitation of Small Mineral Deposits Based On Advanced Rock Blasting and Environm. *BHM Berg- Und Hüttenmännische Monatshefte*, 163(2), 52–56. <https://doi.org/10.1007/s00501-018-0701-4>

- Reichholf, G. (2003). *Experimental investigation into the characteristic of particle size distributions of blasted material*. Doctoral thesis. Montanuniversitaet Leoben.
- Restner, U. (1999). *Test report (Meßbericht) from the Department of Geophysics – internal paper*. Montanuniversitaet Leoben.
- Rice, J. R. (1964). A path independent integral and the approximate analysis of strain concentration by notches and cracks. *Journal of Applied Mechanics, Transactions ASME*, 35(2), 379–388. <https://doi.org/10.1115/1.3601206>
- Rossmannith, H. P., & Uenishi, K. (2005). On size and boundary effects in scaled model blasts spatial problems. *Fragblast*, 9(3), 139–174. <https://doi.org/10.1080/13855140500298339>
- Rossmannith, H. P., & Uenishi, K. (2006). The mechanics of spall fracture in rock and concrete. *Fragblast*, 10(3–4), 111–162. <https://doi.org/10.1080/13855140600874005>
- Saiang, D., & Nordlund, E. (2009). Numerical analyses of the influence of blast-induced damaged rock around shallow tunnels in brittle rock. *Rock Mechanics and Rock Engineering*, 42(3), 421–448. <https://doi.org/10.1007/s00603-008-0013-1>
- Sampaleanu, C. (2017). *The role of intact rock fracture in rockfall initiation*. 152–153.
- Sanchidrián, J. A. (2018). SLIM: Technology for blasting to improve mining. In H. Schunnesson & D. Johansson (Eds.), *Proceedings of 12th International Symposium on Rock Fragmentation by Blasting* (pp. 783–793). Luleå University of Technology.
- Sanchidrián, J. A., & López, L. M. (2003). Calculation of explosives useful work – comparison with cylinder test data. *EFEE 2nd World Conference Explosives and Blasting Technique*, 357–361. <https://doi.org/10.1201/9781439833476.ch42>
- Sanchidrián, J. A., & Ouchterlony, F. (2017). A Distribution-Free Description of Fragmentation by Blasting Based on Dimensional Analysis. *Rock Mechanics and Rock Engineering*, 50(4), 781–806. <https://doi.org/10.1007/s00603-016-1131-9>

- Sanchidrián, J. A., Ouchterlony, F., Moser, P., Segarra, P., & López, L. M. (2012). Performance of some distributions to describe rock fragmentation data. *International Journal of Rock Mechanics and Mining Sciences*, 53, 18–31. <https://doi.org/10.1016/j.ijrmms.2012.04.001>
- Sanchidrián, J. A., Ouchterlony, F., Segarra, P., & Moser, P. (2014). Size distribution functions for rock fragments. *International Journal of Rock Mechanics and Mining Sciences*, 71, 381–394. <https://doi.org/10.1016/j.ijrmms.2014.08.007>
- Sanchidrián, J. A., Segarra, P., López, L. M., Ouchterlony, F., & Moser, P. (2013). On the performance of truncated distributions to describe rock fragmentation. *Measurement and Analysis of Blast Fragmentation: Workshop Hosted by FRAGBLAST 10 - The 10th International Symposium on Rock Fragmentation by Blasting*, 87–96. <https://doi.org/10.1201/b13761-13>
- Sanchidrián, J. A., Segarra, P., Ouchterlony, F., & López, L. M. (2009). On the accuracy of fragment size measurement by image analysis in combination with some distribution functions. *Rock Mechanics and Rock Engineering*, 42(1), 95–116. <https://doi.org/10.1007/s00603-007-0161-8>
- Sanderson, D. J., & Nixon, C. W. (2015). The use of topology in fracture network characterization. *Journal of Structural Geology*, 72, 55–66. <https://doi.org/10.1016/j.jsg.2015.01.005>
- Sanderson, D. J., Peacock, D. C. P., Nixon, C. W., & Rotevatn, A. (2019). Graph theory and the analysis of fracture networks. *Journal of Structural Geology*, 125, 155–165. <https://doi.org/10.1016/j.jsg.2018.04.011>
- Schimek, P. (2015). *Improvement of Fragmentation by Blasting Investigation. Investigation of the influence of delay-times on the crack development in the surrounding rock, the characteristics of the blasted bench face and the fragmentation of the further rows*. Doctoral thesis. Montanuniversitaet Leoben.
- Schuhmann, R. (1940). Principles of comminution. I-size distribution and surface calculation. *Technical Publications AIME*, 1189(11).
- Scott, A., David, D., Alvarez, A., & Veloso, L. (1998). Managing fines generation in the blasting and crushing operations at Cerro Colorado Mine. *Mine To Mill 1998 Conference*, 141–148.

- Sinkala, T. (1989). *Hole deviations in percussion drilling and control measures: theoretical and field studies*. Luleå Tekniska Universitet.
- Snedecor, G., & Cochran, W. (1989). *Statistical methods*. Iowa State University Press.
- Steiner, H. J. (1991). The significance of the Rittinger equation in present-day comminution technology. *XVIIth International Mineral Processing Congress*, 177–188.
- Strickland, J. (2014). *Predictive modelling and analytics*. Lulu Press, Inc. Colorado.
- Sun, C. (2013). *Damage zone prediction for rock blasting* [The University of Utah]. <https://collections.lib.utah.edu/details?id=196208>
- Svahn, V. (2003). *Generation of Fines in Bench Blasting* [Chalmers University of Technology]. <http://www.minfo.se/minbas/7-Lic-Thesis-Victoria-Svahn.pdf>
- Tapponnier, P., & Brace, W. F. (1976). Development of stress-induced microcracks in Westerly Granite. *International Journal of Rock Mechanics and Mining Sciences And*, 13(4), 103–112. [https://doi.org/10.1016/0148-9062\(76\)91937-9](https://doi.org/10.1016/0148-9062(76)91937-9)
- Tarasov, M. D., Karpenko, I. I., Sudovtsov, V. A., & Tolshmyakov, A. I. (2007). Measuring the brightness temperature of a detonation front in a porous explosive. *Combustion, Explosion and Shock Waves*, 43(4), 465–467. <https://doi.org/10.1007/s10573-007-0063-9>
- Teipel, U., & Winter, H. (2011). Reduzierte Abweichung – Less deviation. *AT Mineral Processing*, 52(06–2011), 45–5.
- Thornton, D., Kanchibotla, S. S., & Brunton, I. (2002). Modelling the impact of rockmass and blast design variation on blast fragmentation. *Fragblast*, 6(2), 169–188. <https://doi.org/10.1076/frag.6.2.169.8663>
- Ulusay, R., & Hudson, J. A. (2011). *The Complete ISRM Suggested Methods for Rock Characterization, Testing and Monitoring*. (R. Ulusay & J. A. Hudson (Eds.)). ISRM. <https://www.isrm.net/gca/index.php?id=935>
- Vernon, R. H. (2018). A Practical Guide to Rock Microstructure. In *A Practical Guide to Rock Microstructure*. Cambridge University Press. <https://doi.org/10.1017/9781108654609>

- Whittaker, B. N., Singh, R. N., & Gexin Sun. (1992). Rock fracture mechanics: principles, design and applications. *Rock Fracture Mechanics: Principles, Design and Applications*, 568.
- Wilson, W. H., & Holloway, D. C. (1987). Fragmentation studies in instrumented concrete models. In G. Herget & S. Vongpaisal (Eds.), *6th ISRM Congress* (pp. 735–741). Balkema. [https://doi.org/10.1016/0148-9062\(88\)91705-6](https://doi.org/10.1016/0148-9062(88)91705-6)
- Wong, T. F., & Biegel, R. (1985). Effects of pressure on the micromechanics of faulting in San Marcos gabbro. *Journal of Structural Geology*, 7(6), 737–749. [https://doi.org/10.1016/0191-8141\(85\)90149-X](https://doi.org/10.1016/0191-8141(85)90149-X)
- Xia, K., & Yao, W. (2015). Dynamic rock tests using split Hopkinson (Kolsky) bar system - A review. In *Journal of Rock Mechanics and Geotechnical Engineering* (Vol. 7, Issue 1, pp. 27–59). Chinese Academy of Sciences. <https://doi.org/10.1016/j.jrmge.2014.07.008>
- Zaiontz, C. (2020a). *Comparing slopes & intercepts | Real Statistics Using Excel*. © Real Statistics 2020. <http://www.real-statistics.com/multiple-regression/comparing-slopes-and-intercepts/>
- Zaiontz, C. (2020b). *Regression approach to ANCOVA | Real Statistics Using Excel*. © Real Statistics 2020. <http://www.real-statistics.com/analysis-of-covariance-ancova/regression-approach-ancova/>
- Zellner, M. B., Randow, C. L., Cantrell, R., & Yonce, C. E. (2016). *Blast Loading Assessment of Multi-Energy Flash Computed Tomography (MEFCT) Diagnostic*.
- Zhang, Q. (2014). *Mechanical Behaviour of Materials under Dynamic Loading Rock* (Issue November). Swiss Federal Institute of Technology in Lausanne.
- Zhang, Z.-X. (2016). Single-Hole Blasting. *Rock Fracture and Blasting*, 217–236. <https://doi.org/10.1016/b978-0-12-802688-5.00010-5>
- Zhang, Z.-X., Kou, S. Q., Jiang, L. G., & Lindqvist, P. A. (2000). Effects of loading rate on rock fracture: Fracture characteristics and energy partitioning. *International Journal of Rock Mechanics and Mining Sciences*, 37(5), 745–762. [https://doi.org/10.1016/s1365-1609\(00\)00008-3](https://doi.org/10.1016/s1365-1609(00)00008-3)

10 List of Figures

Figure 1: Blast-driven stress-wave front and induced crack propagation. The high-speed image captured supersonic explosive detonation and resulting deformation in a PMMA sample (C. H. Johansson & Persson, 1970).	9
Figure 2: Conceptual sketch of deformation zones around a blast hole, modified figure from Whittaker et al. (1992) and Saiang & Nordlund (2009).	10
Figure 3: Parallel shifting of sieving curves in NBC concept (Moser et al., 2003a). ...	13
Figure 4: Volume of crushed material around 2D blast-hole (Ouchterlony & Moser, 2013) in CZM (Onederra et al., 2004).	16
Figure 5: Conceptual sketch (Ouchterlony & Moser, 2013) of the layered mortar cylinder used in the blast tests (Svahn, 2003).	19
Figure 6: Sieving FSDs for each coloured layer in Svahn’s (2003) blast cylinders. (Ouchterlony & Moser, 2013).	19
Figure 7: Results from simulated blast fragmentation by Kukolj et al. (2018a): a) FSD curves of modelled cylinders; b) mass of fine particles concerning the radius from the blast hole and peak blast-hole pressure.	21
Figure 8: FSD curve for Darley Dale sandstone shot B (Grimshaw, 1958): a) $n(x)$ data; b) curve fit to the corresponding $P(x)$ function. Note the “bump” in the region 0.1-5 mm. (Ouchterlony & Moser, 2013).	23
Figure 9: Selected plots of $x-A(x)$ and $x-N(x)$ with fixed indicated size ranges (Michaux, 2006): a) The plot of $x - A(x)$ in a log-lin scale for monzonite with three regions of different curve slope; b) The plot of $x - N(x)$ in a log-log scale for grout with three regions with different curve slopes.	24
Figure 10: An $s-n(s)$ curves fitted to different sieving data with identified fragment-size ranges (Iravani, 2020): a) from D. Johansson (2008), b) from data covered in this thesis.	26
Figure 11: Micro-mechanical model: a) Hexagonal crystal system of the dolomite in the marble; b) schematic diagram showing the microscopic model of intergranular and transgranular fractures; c) formation of secondary micro-cracks nearly parallel to the twinning (i.e., cleavage); d) formation of secondary micro-cracks almost normal to the twinning (i.e., lamellar steps). (Q. Zhang, 2014)	28

Figure 12: Identified dynamic-fracture mechanisms in fine-grained marble. (Q. Zhang, 2014)	28
Figure 13: Cleavages and lamellar steps in: a), b) sandstone and c), d) gabbro. (Q. Zhang, 2014)	29
Figure 14: Captured SEM micrographs of fracture surfaces, generated at different loading rates (increasing from left to right), in marble specimens. (Q. Zhang, 2014). 29	
Figure 15: Symbolic workflow of the experimental method.....	30
Figure 16: Experimental set-up for the blast-tests, showing the frontal end face.....	31
Figure 17: Blast cylinders before blasting.	32
Figure 18: Casting moulds for the mortar blast cylinders.....	33
Figure 19: Original granite block and final granite blast cylinders.....	33
Figure 20: Blast cylinder ready for the blasting test.	34
Figure 21: Blast-cylinder mantle wrapped in layers of aluminium tape and LLDPE foil.	34
Figure 22: Blast-chamber segments with the damping layer and the cylinder inside. a) transverse cross-section: 1 – blast cylinder wrapped in aluminium and LLDPE foil; 2 – damping layer; 3 – chamber segments; b) fresh damping material between the cylinder and the segments.	35
Figure 23: Nomenclature for blast cylinders and material-test samples. Note that the marking in position 3 (marked red) applies only to material-test samples.....	37
Figure 24: Shorter notation for "blast configuration" (blasted material, linear charge concentration, and blast test).....	37
Figure 25: Plug configuration and positioning: a) aluminium plug parts; b) positioning of the shorter plug part, wrapped in masking tape, in the borehole; c) added layer of silicone on top of the shorter part; d) final placement of the longer part in the borehole.	39
Figure 26: Comparison of two plug configurations and resulting filming (two sets of sequential frames capturing the blast detonation): Blast test 12.3 (bottom row) included the final plug configuration and blast test 12.2 (top row) included a shorter wooden dowel as the plug.....	40

Figure 27: Axial half-cross sections of the prepared blast chamber: a) frontal view; b) rear view (1 – Frontal end face, steel plate; 2 – Protective window; 3 – Borehole with stem plug; 4 – Chamber segment; 5 –Damping layer; 6 – Shock tube and detonator; 7 – PETN cord; 8 – Blast cylinder Detonator; 9 – Rear-end face, steel plate; 10 – Detonator opening; 11 – Wooden disk; 12 – Rubber disc). 41

Figure 28: Cross-section of the blast chamber with the radial blast-induced movement of the segments. The arrows indicate the movement direction; the red circles indicate the resulting gap. 42

Figure 29: Blast chamber just before a blast test. 43

Figure 30: Blast-fracturing phases at the filmed end face of the cylinder. Selected HSI of tests m12(21) (left column) and g12(25) (right column). The notes (t) refer to the time elapsed from the detonation. 46

Figure 31: Selected HSI from m12(21). The three images show how a minor spill of the fumes escalates to massive inrush (283.92 μ s). The inrush indicates the beginning of the third phase. 47

Figure 32: Removal of protective foils from blast cylinder mb-72, m12(20). 47

Figure 33: Photogrammetry set-up – the turning table, the programmed stepper-motor drive, and the digital camera. 48

Figure 34: Principle of the photogrammetry procedure: a) process workflow; b) resulting image of blast cylinder mb-72, m12(20). 49

Figure 35: Principle of the CT procedure 50

Figure 36: Definitions of the cylinder cross-sections - transverse and non-planar. 51

Figure 37: Tracing process in GIMP. Original image and different trace types (i.e., cracks, the blast hole, and the mantle) are traced with different colours. 52

Figure 38: Principle of the topological analysis: a) Original fracture-pattern image (HSI, CT section, or PMI); b) Trace image with fracture paths coloured red; c) Resulting topological image with fracture lines (thinned fracture paths) and different topological nodes (tips and intersections). 53

Figure 39: Fracture path (A-B) with intersecting fracture lines (dashed lines), showing topological nodes and branches: I-nodes (circles), Y-nodes (triangles), and X-nodes (diamonds). (Sanderson & Nixon, 2015). 53

Figure 40: Conceptual sketch of the topological nodes and marking.....	55
Figure 41: Ternary diagram of node-type (I, Y, and X) proportions for different fracture patterns. (Sanderson & Nixon, 2015).....	56
Figure 42: Example of the ternary diagram used for plotting proportions of the topological nodes. It covers a sequence of HSI, marked in sequence numbers, and the corresponding PMI (pm). The blue arrows indicate the values for plotting point 'pm.'	56
Figure 43: Determination of the data scatter (D_{cent}) in the CT ternary diagrams.....	57
Figure 44: Ternary diagrams of node proportions with the comparative parameters: a) ratio of the number of branches to lines (N_B/N_L); b) the average number of connections per line (C_L). (Sanderson & Nixon, 2015)	58
Figure 45: Proportions of fracture branches plotted in a ternary diagram (Sanderson & Nixon, 2015): a) " <i>proportions of different branch types with numbers 0 to 2.0 indicating connections per branch (C_B);</i> " b) values of C_B on the original triangular plot.	59
Figure 46: In-plane (2D) fragmentation - definition and preparation for counting of 2D fragments. The fragment patterns are obtained by deleting non-connected and semi-connected branches.	61
Figure 47: Determination of 2D-fragment size.	62
Figure 48: Example a ternary diagram used to describe in-plane (2D) fragmentation in HSI. It covers a sequence of HSI, marked in sequence numbers, and the corresponding PMI (pm). The number in the upper-right corner denotes the reference blast-test number.	63
Figure 49: Estimated blast-hole pressure levels concerning elapsed time and the linear charge concentration. (Iravani et al., 2018b)	64
Figure 50: Examples of difficulties in determining influencing mechanisms based on observed crack patterns in HSI.....	70
Figure 51: Example of the deformation zones in the mortar (CT sections): a) longitudinal (side) section of a fragment (m12(20)); b) transverse section of a fragment (m12(20)); c) transverse section of a blasted cylinder (m12(21)). The compaction zone and the crushed zone appear lighter in the images due to the higher material density.	72
Figure 52: Wedge-shaped fragment section with deformation zones.	73

Figure 53: Application of the “lasso/blow” tool in ImageJ to trace the blast-hole wall in the binary image of a CTt section. The resulting yellow contour was used to calculate the area of the blast hole. 76

Figure 54: Measurement of the compacted zone ($\Delta r_{comp, a}$) in a uCT image from m12(20). 77

Figure 55: Transverse section of the uCT scan from g20(26.2) with a best-fitted circle to the blast-hole contour. 77

Figure 56: Difference between the measured average radii in the CTt of blasted cylinders and that of a single fragment: a) cross-section of a fragmented cylinder and the same cross-section with radially displaced fragments; b) enlarged sections from a), with notation..... 78

Figure 57: Example of the analysed fracture surfaces (side images) of a larger fragment, m20(22.1). 81

Figure 58: Processing of fracture-surface models in MeshLab..... 82

Figure 59: Process of sampling and model transformation in CloudCompare: a) initial imported mesh model of a fracture surface; b) the model is sampled into a point cloud (data points are coloured white), which is then used for fitting a plane; c) the position parameters of the plane are used to transform (i.e., reposition) the point cloud into the X-Y plane..... 83

Figure 60: Height map obtained by analysing Z-axis values of the data points. The results are presented as colour-coded maps with a histogram bar. The provided scale is in [mm]. 84

Figure 61: Principle of local-roughness measurement on point cloud in CloudCompare. 85

Figure 62: Example of a colour-coded image of local surface roughness with a kernel of 5 mm. The provided scale is in [mm]. Note the green-to-red ridges and blue valleys. 85

Figure 63: Microscopy equipment: a) optical light-reflection microscope Olympus BX60, b) SEM system Evo MA 10..... 86

Figure 64: Principle of the thin-section production..... 87

Figure 65: Terminology used for observed cracks/fractures in the thin sections..... 88

Figure 66: Measurement of the average grain size (“Average-grain intercept” method) in mortar micrographs. Only red segments (intersections with the grains) of the whole scan line are considered.....	89
Figure 67: Application of the “particle analysis” on a mortar optical micrograph in ImageJ. The mortar pores were detected and filtered out considering their shape circularity.	89
Figure 68: Illustration of uncertainty issues of grain-size measurement due to grain-figure projection. Note the difference between diameters D2 and D1.....	90
Figure 69: Example thin-section micrographs of complex fracture patterns at the meso/micro-level from blast test 26.2 (granite, 20 g/m): a) SEM image; b) CPL optical microscopy.....	90
Figure 70: Spatial origin(s) of the small blast fragments (shown on a larger fragment).	91
Figure 71: Small blast fragments prepared for SEM.	91
Figure 72: Impingement micro-cracks. An example SEM micrograph (Blenkinsop, 2007).	93
Figure 73: Conceptual sketches of: a) to d) basic impingement-crack patterns; e) basic failure modes for their further description (Blenkinsop, 2007).....	93
Figure 74: Conceptual sketch of flaw-induced micro-cracks (Blenkinsop, 2007): a) principle of the analytical solution of Horii and Nemat-Nasser (1985). The flaw length is $2c$ at angle γ to load direction (arrows), and the micro-crack length is l at angle θ to the flaw; b) examples of flaw-induced micro-cracks; c) examples of interaction between micro-cracks and pores.	94
Figure 75: Conceptual sketches (Tapponnier & Brace, 1976) of: a) refractured micro-crack, fractured cement on both fracture flanks; b) elastic-mismatch micro-cracks at the contact between mica and quartz.	94
Figure 76: Conceptual sketches of elastic-mismatch micro-cracks: a) intensive micro-cracking in plagioclase between kinked biotite grains; b) a micro-crack initiated at the end of a lamella displaces a grain boundary. (Blenkinsop, 2007).....	95
Figure 77: Conceptual sketch of micro-fault-induced micro-cracks. (Blenkinsop, 2007)	96

Figure 78: Overview of the sieving procedure.	97
Figure 79: Blasted cylinder taken apart and prepared for sieving (g12(25)).	98
Figure 80: Mechanical sieve shaker HAVER EML Digital Plus (laboratory of the Chair of Mineral Processing, IZR, MUL).	99
Figure 81: A potential through-going interlocked crack in a larger fragment from m6(22.2).	100
Figure 82: Overview of the laser-diffraction granulometry.	101
Figure 83: Example of results obtained by the laser-diffraction granulometry for a single size class (e.g., 0.5 0.25 mm).	102
Figure 84: Example log-log plot of screening data. Sieving data for blast test 27 (granite, 6 g/m).	103
Figure 85: Definition of local (GGS) slopes (sn) in the sieving curves.	109
Figure 86: Local (GGS) slope (sn) over a range of empty data points.	110
Figure 87: Images of crack-pattern development captured with the high-speed camera and PMI of the frontal end face. The cracks were traced in red (HSI) and orange (PMI) colour. The numbers in the brackets mark corresponding blast tests.	115
Figure 88: Tangential cracks in the first phase at at $t+121.68 \mu s$ (g12(24)).	116
Figure 89: Example of crack closure. A crack marked with red arrows firstly propagates (a to c) and then closes when another crack (marked with yellow arrow) propagates nearby (d and e). Selected HSI (m12(9)).	117
Figure 90: Effect of the “radial spall wave” at the frontal end face in the granite (g12(25)) and bending of the protective window (note the light reflection on the left side in the images).	118
Figure 91: Main-radial-crack count relative to blast material and linear charge concentration in CTt.	120
Figure 92: Node counts from the high-speed images (HSI) concerning elapsed time from the detonation in the mortar (m12(21)). The orange box marks the second fracture phase.	121

Figure 93: Node counts from the high-speed images (HSI) concerning elapsed time from the detonation in the granite (g12(24)). The orange box marks the second fracture phase.....	122
Figure 94: Node counts and their proportions from the CTt relative to the axial position in the mortar (m12(21))......	123
Figure 95: Node counts and their proportions from the CTt relative to the axial position in the granite (g12(28.1)).	123
Figure 96: Node counts and their proportions from the CTnp concerning the radial position in the mortar (m12(21))......	125
Figure 97: Node counts and their proportions from the CTnp concerning the radial position in the granite (g12(28.1)).	125
Figure 98: Node-count proportions (set of ternary diagrams). Red and orange points represent the HSI with numbers indicating their time sequence with time steps of 40.56 μ s and 'pm' representing the PMI. Blue points indicate the CTt with numbers indicating the sequence in their axial position starting from the rear end face.....	127
Figure 99: Node-count proportions (set of ternary diagrams) from transverse CT sections. The data points are marked with numbers that indicate the sequence in the axial position of the sections starting from the rear end face. Point 'pm' represents the PMI and point 'C' the geometrical centre of the data points marked with numbers.	128
Figure 100: Node-count proportions (set of ternary diagrams) from CTnp. The data points are marked with numbers that indicate the sequence in the radial position of the sections starting from the cylinder axis. Point 'M' represents the PMM and point 'C' the geometrical centre of the data points marked with numbers.....	130
Figure 101: Average number of connections per line (C_L) and per branch (C_B) concerning time elapsed from the detonation (HSI): a) m12(21); b) g12(25). The orange box marks the second fracture phase.....	132
Figure 102: Summary of the average number of connections: a) per line (C_L) in the CTt; b) per branch (C_B) in the CTt.	133
Figure 103: Development of node-connectivity probabilities (p_l and p_c) in the HSI: a) m12(21); b) g12(25). The orange box marks the second fracture phase.....	135

Figure 104: Development of node-connectivity probability (p_c) in the HSI: a) m12(21); b) m6(23.2); c) g6(27). The data points of the second fracture phase are marked blue.	136
Figure 105: Summary of the node-connectivity probability (p_c) in the CTt.....	138
Figure 106: Fracture abundance (p_{20} and p_{21}) in HSI and PMI (m12(21)). The data points of the second fracture phase are marked blue.	139
Figure 107: Fracture abundance (p_{20} and p_{21}) in HSI and PMI (g6(27)). The data points of the second fracture phase are marked blue.	140
Figure 108: Summary of the calculated fracture abundance parameters (p_{20} and p_{21}) in the CTt.....	143
Figure 109: Total in-plane (2D) fragment count in the HSI: a) m6(23.2); b) m12(20). The red horizontal line shows the count value in the corresponding PMI. The orange box marks the second fracture phase.....	144
Figure 110: Total in-plane (2D) fragment count in the HSI: a) m12(21); b) g12(25). The red horizontal line shows the count value in the corresponding PMI. The orange box marks the second fracture phase.....	145
Figure 111: Summary of the total 2D-fragment count in CTt.	146
Figure 112: Total 2D-fragment count concerning radial distance from the cylinder axis in CTnp.	147
Figure 113: In-plane 2D-fragment proportions (set of ternary diagrams) of the HSI and the PMI in the mortar. Orange circles represent the HSI with numbers indicating their time sequence with time steps of 40.56 μ s and 'pm' representing the PMI.	148
Figure 114: In-plane 2D-fragment proportions (set of ternary diagrams) of the HSI and the PMI in the granite. Orange circles represent the HSI with numbers indicating their time sequence with time steps of 40.56 μ s and 'pm' representing the PMI.	149
Figure 115: In-plane 2D-fragment proportions (set of ternary diagrams) from CTt. The data points are marked with numbers that indicate the sequence in the axial position of the sections starting from the rear end face. Point 'pm' represents the post-mortem state at the frontal end face and point 'C' the geometrical centre of the data points marked with numbers.	150

Figure 116: Maximum crack-propagation speed per frame (HSI): a) m12(21); b) g12(25). The graphs show maximum (C_{max}) and average (C_{ave}) values. The orange box marks the second fracture phase.....	152
Figure 117: Summary of measured average crack-propagation speed (CTt).	153
Figure 118: Excerpt from the HSI set (m12 (21)) of HSI images with fractures marked red and the corresponding trace images (green – blast-hole wall, red – cracks from the previous image, and violet – new cracks, extensions).	155
Figure 119: Example trace image with marked extensions - image 5 ($t+162.24 \mu s$), m12(21).	156
Figure 120: Example of indistinguishable macro-mechanisms (marked with white arrows). The trace image is image 12 ($t+446.16 \mu s$), m12(21).	158
Figure 121: Normalized blast-hole radius along the axis of the blasted cylinders (CTt).	160
Figure 122: Normalized blast-hole radius ($r_{bh,norm}$) considering linear charge concentration and blasted material.	161
Figure 123: Deformation zones and crack patterns near the blast hole in the thin sections (SEM images): a), b) g12(24); c), d) m12(20). (Kukolj et al., 2019)	163
Figure 124: Deformation zones in the mortar. Fused SEM micrographs (m20(22.1)). The crushed zone includes the compaction zone and the transition zone (Kukolj et al., 2019)	163
Figure 125: Transverse uCT section of a blast fragment (m12(20)). The compaction zone is denser and, hence, indicated by higher image intensity. The arrows mark the endpoints of the measured compaction-zone thickness.	164
Figure 126: Outer boundary of the compaction zone (red line) in the mortar (m12(20)), about 1.5 mm from the blast hole. SEM micrograph of a thin section. The blue arrow marks the main direction of crack development.....	165
Figure 127: Deformation zones (crushed zone) in the granite. Fused SEM micrographs from (g20(26.2)). The red line marks the outer boundary of the crushed zone. The blue arrow marks the main direction of crack development.....	165

Figure 128: Flank of a main radial crack outside the deformation zones (about 15 mm from the blast hole) in the mortar (m12(20)). Stitched SEM micrographs of a thin section. The blue arrow marks the main direction of crack development. 166

Figure 129: Flank of a main radial crack in the granite, outside the deformation zones (about 2.5 mm from the blast hole). SEM micrograph from g6(27). The blue arrow marks the main direction of crack development. 166

Figure 130: Crushed zone in the mortar: a) m6(22.2); b) m12(20); c) m20(22.1). The red line denotes the approximated outer boundary. Fused SEM micrographs. 168

Figure 131: Crushed quartz grains with impingement fractures (ic) near the blast hole. SEM micrographs (m12(20)). 169

Figure 132: Impingement fractures (ic) in quartz grains in the compaction zone. SEM micrographs (m6(22.2)). The blue arrow marks the main direction of crack development. 169

Figure 133: End of the compaction zone and beginning of the transition zone in the mortar (indicated by the red stripe). The blast hole is about 2 mm to the left from the image. SEM micrograph (m12(20)). The blue arrow marks the main direction of crack development. 170

Figure 134. A crack composed of intergranular fractures in the mortar, about 42 mm from the blast hole. SEM micrograph (m6(22.2)). The blue arrow marks the main direction of crack development. 171

Figure 135: Flank of a main radial crack in the mortar (m12(20)). Fused SEM micrographs of a thin section. The blue arrow marks the main direction of crack development. 171

Figure 136: Examples of different crack-arrest marks in the mortar (indicated by the red arrows), about 30 mm from the blast hole. SEM micrographs from blast test (m20(22.1)). The blue arrow marks the main direction of crack development. 172

Figure 137: Relative shearing displacement in a crack flank (a flank of a main radial crack – bottom of the image), about 10 mm from the blast hole. Red arrows indicate the displacement. SEM micrograph (m12(20)). The blue arrow marks the main direction of crack development..... 173

Figure 138: Complex branching/merging in the compaction zone of a mortar cylinder. SEM micrograph (m12(20)). The blue arrow marks the main direction of crack development. 173

Figure 139: Branching/merging (in the compaction zone) on a micro-scale, showing transgranular (red arrows) and intergranular (blue arrows) fractures of the quartz grain in the lower-left corner, its crushed adjacent quartz grain, and multiple crack-arrest marks (green arrows) in the surrounding cement matrix. SEM micrograph (m12(20)). 174

Figure 140: Branching/merging network formed in the wake of a main radial crack outside the crushed zone in the mortar. The radial crack is at the bottom of the image and the blast hole is about 15 mm to the left from the image. SEM micrograph (m12(20)). The blue arrow marks the main direction of crack development. 175

Figure 141: Seeming Y-branching (indicated by the red arrow) formed by a small crack in the intermediate region in the mortar (about 30 mm from the blast hole). The bottom image shows the branching area enlarged, with a complex branching/merging formation between pores and around quartz grains. SEM micrographs (m20(22.1)). The blue arrow marks the main direction of crack development. 176

Figure 142: X-branching/merging pattern, showing an almost right-angle crossing of two cracks in the mortar (about 40 mm from the blast hole). SEM micrographs (m20(22.1)). The blue arrow marks the main direction of crack development. 177

Figure 143: Y-branching/merging that occurred in between two adjacent closely spaced quartz grains (marked with orange points) (about 32 mm from the blast hole). SEM micrograph (m20(22.1)). The blue arrow marks the main direction of crack development. 177

Figure 144: Y-branching/merging that occurred at a small pore right at the edge of a larger quartz grain in the mortar (about 35 mm from the blast hole). SEM micrograph (m20(22.1)). The blue arrow marks the main direction of crack development. 178

Figure 145: Y-branching/merging that that occurred at a larger pore (about 18 mm from the blast hole). SEM micrograph (m6(22.2)). The blue arrow marks the main direction of crack development. 178

Figure 146: Intensive micro-fractures (rc) in the matrix (green arrows) around a crack crossing a a pore (lower right corner), about 16 mm from the blast hole. The bottom

image shows the severely fractured flank in the matrix enlarged. SEM micrographs (m6(22.2)). The blue arrow marks the main direction of crack development. 179

Figure 147: Intergranular branching/merging in a quartz grain in the mortar. SEM micrograph (m6(22.2)). The blue arrow marks the main direction of crack development. 180

Figure 148: Deformation zones around the blast hole in the granite (the blast hole 'BH' is in the lower-left corner). Fused optical PPL micrographs (g12(24)). 180

Figure 149: Crushed zone near the blast hole (lower-left corner in the images). SEM micrographs (g12(24)). The red line marks the outer boundary of the crushed zone. 181

Figure 150: Cleavage fractures. SEM micrographs (g20(26.2)). The blue arrow marks the main direction of crack development. 182

Figure 151: Grain shielding. Note the difference in fracturing below (nearer to the blast hole 'BH') and above the biotite grain (light grey). SEM micrograph (g6(27)). The blue arrow marks the main direction of crack development. 183

Figure 152: Intragranular crack arrest and partial rupture of a mica grain. SEM micrographs (g12(24)). The blue arrow marks the main direction of crack development. 183

Figure 153: Complex fracturing and deformation in mica and feldspar grains. SEM micrographs (g12(24)). The blue arrow marks the main direction of crack development. 184

Figure 154: Fracture formations along the flanks of main radial cracks (about 5 mm from the blast hole). SEM micrographs from (g6(27)). The blue arrow marks the main direction of crack development. 185

Figure 155: "Zig-zag" fracturing in feldspar with many branching/merging formations. SEM micrograph (g12(24)). The blue arrow marks the main direction of crack development. 185

Figure 156: Seeming "zig-zag" fracturing in mica grains. SEM micrographs (g12(24)). The blue arrow marks the main direction of crack development. 186

Figure 157: Branching/merging along grain boundaries. SEM micrograph (g12(24)). The blue arrow marks the main direction of crack development. 186

Figure 158: Crushing following branching/merging along grain boundaries. SEM micrograph (g12(24)). The blue arrow marks the main direction of crack development.	187
Figure 159: Fracture surfaces near the middle of a small fragment (left) and at its edge (right, red line) in the granite. SEM micrographs (g12(24)).	188
Figure 160: Fracture surfaces near the middle of a small fragment (left) and at its edge (right, red line) in the mortar. SEM micrographs (m12(20)).	188
Figure 161: Transgranular fractures along a fragment edge in the granite. SEM micrograph (g12(24)).	189
Figure 162: Transgranular fractures in quartz grains (dark surface near the centre of the image) in the mortar. SEM micrograph (g6(22.2)).	190
Figure 163: Transgranular fractures in quartz grains along a line of sudden change (indicated by the red line) in the mortar. SEM micrograph (m12(20)).	190
Figure 164: A line of sudden change (indicated by the red line) in the fracture surface in the granite. SEM micrograph (g20(26.2)).	191
Figure 165: Branching/merging traces (indicated by the red arrows) at a fracture surface in the mortar. SEM micrograph (m12(20)).	191
Figure 166: Intensive micro-cracking (indicated by the red arrows) at pore edges in the mortar. SEM micrographs (m20(22.1)).	192
Figure 167: Branching/merging line (indicated by the orange arrows) starting at a single plagioclase crystal (indicated by the red arrow) in the granite. SEM micrograph (g12(24)).	193
Figure 168: Height maps of scanned mortar fragments (left and right side): a) m6 (22.2), b) m12 (20); c) m20(22.1). The red arrow indicates the position of the blast hole and detonation direction.	194
Figure 169: Height maps of scanned granite fragments (left and right side): a) g6(27); b) g12(25); c) g20(26.2). The red arrows indicate the position of the blast hole and detonation direction.	195
Figure 170: Map images of the fracture-surface roughness (kernel size 3 mm): a) the left side of a fragment from m12(20); b) the left side of a fragment from g12(25). The red arrows indicate the position of the blast hole and detonation direction.	196

Figure 171: Enlarged portion of the map image from Figure 170a. Peak roughness values (marked with white arrows) are mostly positioned along ridge peaks and pore edges.....	197
Figure 172: Average roughness of fracture surface concerning kernel size. The data points represent fracture surfaces (left and right) of scanned fragments.	198
Figure 173: Summary of measured roughness of fracture surfaces, averaged per blast fragment. Kernel size is noted in the brackets in the graph titles.	199
Figure 174: Box plots of data sets for fracture-surface roughness.....	200
Figure 175: Sieving FSDs of blasted cylinders.	201
Figure 176: Sieving curves of blasted cylinders of mortar (top) and granite (bottom).	202
Figure 177: Curves of merged screening data of the blasted cylinders (> 1E-07% mass passing).	203
Figure 178: Overview of sieved fines proportions (P(x)) below 1-mm mesh size (m-1 mm, m-0.5 mm, m-0.25 mm, m-0.1 mm, and m-0.04 mm).	207
Figure 179: Overview of sieved blast-hole-wall fines.	209
Figure 180: Relative mass proportions of the blast-hole-wall fines with the total mass proportions of the sieved fines as the reference.	209
Figure 181: Blast-energy register – total mass specific surface area plotted against specific energy consumption. The regression lines have the intercept set point to (0,0).	214
Figure 182. Crack-pattern difference between blast tests 20 and 21 and between blast test 22.1 and 23.1 (Selected HSI and PMI).	236
Figure 183: Overview of the last traced HSI, the PMI, and the middle CTt from selected blast tests. The empty fields indicate a lack of data.	238
Figure 184: Development of the average number of connections per branch (C _B) in the HSI with the value from the PMI plotted at t+1000 μs.	242
Figure 185: Crack-tip branching-merging on a penny-shaped model of a fragment with indicated effect of micro-cracks near the branching/merging points/lines on the surface	

roughness at the fragment edges. The yellow arrows indicate the direction of crack propagation.....	245
Figure 186: Fragments (boulders) from the size class 100 80 mm from g20(26.2)..	249
Figure 187: Percentile fragment sizes (x_{30} , x_{50} , and x_{80}) plotted against specific charge (q) (log-log scale).....	250
Figure 188: Blast-energy register – total mass specific surface area plotted against specific energy consumption. The regression lines do not have a set intercept point.	253
Figure 189: Blast-energy register – total mass specific surface area plotted against specific energy consumption. The regression is carried out with polynomial instead of linear functions and the fitted curves do not have a set intercept point.....	254
Figure 190: Equipment used for mixing the mortar.....	311
Figure 191: Confinements for casting the mortar cylinders.....	312
Figure 192: Sealed mortar-casting confinement.....	313
Figure 193: Radial drying-induced cracking around the sticks at the end-face surfaces.	313
Figure 194: Equipment used for transverse cutting of the cylinders.....	314
Figure 195: Graphical definition of the borehole deviation (Sinkala, 1989).....	314
Figure 196: Block for producing material-testing samples of mortar (left) and the samples after core-drilling (right).	315
Figure 197: Technical drawing of the WST samples.....	315
Figure 198: Mortar WST samples.....	316
Figure 199: Original granite block (left) and cylindrical material-testing samples (right).	316
Figure 200: Sample for testing material properties of the damping layer.....	317
Figure 201: Gas pycnometer Micrometrics AccuPyc 1330 (laboratory of the Chair of Mineral Processing, IZR, MUL).....	323
Figure 202: UCS-test set-up.....	325
Figure 203: BTS-test set-up.....	327

Figure 204: Ultrasound-test set-up.	328
Figure 205: Aligned measurement signals for sample gt1-104 (granite). The noted data points indicate T_p (left) and T_s (right). These time values were further corrected by subtracting the time of signal initiation (t_i) from them.	330
Figure 206: WST set-up.	332
Figure 207: Measurement plots from the WSTs	333
Figure 208: Typical resulting fracture surfaces from WSTs on the granite (top) and the mortar (bottom).	334
Figure 209: Fracture surfaces in WST samples of magnetic mortar – water-saturated sample (left) and dry sample (right) (Khormali, 2012).	335
Figure 210: Oscillatory concentric zoning (indicated by the red arrow) in a plagioclase grain induced fracturing in adjacent quartz and feldspar grains (about 20 mm from the borehole). CPL optical micrographs.	337
Figure 211: Solidified intrusions (light yellow, indicated by the red arrows) in preceding fractures in quartz and feldspar grains (about 10 mm from the borehole). CPL optical micrograph.	338
Figure 212: Fractures in host quartz grains formed by growth of smaller feldspar and plagioclase grains therein (indicated by the red arrows) (about 15 mm from the borehole). Sharp boundary interfaces between crystals can also induce impingement fractures and elastic-mismatch cracking. CPL optical micrograph.	339
Figure 213: Lamellar fractures (indicated by the orange arrows) in quartz and feldspar grains and fractures around corners of elongated mica grains (red and brown, indicated by the red arrow) (about 25 mm from the borehole). CPL optical micrograph.	340
Figure 214: Complex failure including longitudinal rupture and shearing of a biotite grain (light grey, indicated by the red arrows), surrounded by quartz grains (dark grey) (about 18 mm from the borehole). SEM micrograph.	341
Figure 215: A biotite grain (light grey) split in half during the material genesis and filled-up by later crystalized feldspar (darker grey, indicated by the red arrow), surrounded by quartz grains (dark grey) (about 20 mm from the borehole). SEM micrograph.	342

Figure 216: A biotite grain (light grey) positioned in line with a crack (indicated by the red arrows) in the adjacent feldspar grain (darker grey), both surrounded by quartz grains (dark grey) (about 30 mm from the borehole). SEM micrograph..... 342

Figure 217: Shrinkage micro-cracks in the cement matrix around a large quartz grain (about 15 mm from the borehole). PPL optical micrograph. 343

Figure 218: Shrinkage micro-cracks in the cement matrix between quartz grains (about 10 mm from the borehole). PPL optical micrograph..... 344

Figure 219: Already fractured quartz grain in the cement matrix in a non-blasted mortar sample (about 25 mm from the borehole). PPL optical micrograph. 345

Figure 220: Segment of a borehole wall in a non-blasted granite sample. The near-borehole zone already includes some damage prior to blasting. CPL optical micrograph. 346

Figure 221: Segment of a borehole wall in a non-blasted granite sample. The traces of intensive fracturing in the large feldspar grains (light grey/blue) indicate possible drilling-induced damage. CPL optical micrograph. 346

Figure 222: Drill-induced cracks propagated from the borehole (upper right corner of the image) through quartz grains (dark grey) and were attracted to a sharp corner of an elongated mica grain (light grey). SEM micrograph. 347

Figure 223: Severely-fractured mica and feldspar grains (light grey) near the borehole (dark grey/black, upper side of the image). SEM micrograph. 348

Figure 224: Internally fractured quartz grains near the borehole of a non-blasted sample. PPL optical micrographs. 348

Figure 225: Internally fractured quartz grains near the borehole of a non-blasted sample. SEM micrograph. 349

Figure 226: Tangential cracks around the borehole in a non-blasted mortar sample. The cracks were probably generated by the material shrinking during mortar curing. SEM micrograph..... 350

Figure 227: Grain-size measurement: a) mortar (optical micrograph with its binary version for measuring the grains); b) granite (fused image with red intercept lines). 351

Figure 228: Selected mortar micrograph images (left column) with corresponding binary images used to measure the average grain size (right column). 353

Figure 229: Selected granite micrographs used to measure the average grain size. The intersection lines are coloured red.....	354
Figure 230: Blast set-up used in blast test 1.....	356
Figure 231: Common blast set-up with the blast chamber and the HSI camera inside an enclosed transport container.	357
Figure 232: Experimental set-up outside the container.....	357
Figure 233: An earlier cylinder-wrapping solution with an aluminium sheet bent around the cylinder and held together with a tightened steel wire (blast test 9).....	360
Figure 234: Replaceable polycarbonate disk: a) being manufactured; b) placed directly on a blast cylinder; c) covered with the protective window prior to a blast test.	362
Figure 235: Wooden stick used to align the borehole with the opening in rear steel plate	362
Figure 236: An HSI image from blast test 28.1 (granite, 12 g/m).....	374
Figure 237: Crack-line count (N_L) and branch count (N_B) concerning time elapsed from the detonation (HSI): a) m12(21); b) g12(24). The orange box marks the second fracture phase.....	401
Figure 238: Crack-line count concerning time elapsed from the detonation (HSI and PMI): a) m6(22.2); b) g6(26.1). The post-mortem state is plotted at $t+1000 \mu s$, as after this time no further change is expected. The orange box marks the second fracture phase.....	402
Figure 239: Summary of the crack-line count (N_L) and of the branch count (N_B) in the CTt.....	403
Figure 240: Development of branch-connectivity probabilities (p_{II} , p_{IC} , and p_{CC}) in the HSI: a) m12(21); b) g12(25). The orange box marks the second fracture phase.....	405
Figure 241: Summary of branch-connectivity probability (p_{CC}) in CTt.....	406
Figure 242: Dimensionless fracture intensity (p_{22}) in HSI and PMI: a) m12(21); b) g6(27). The data points of the second fracture phase are marked blue.....	408
Figure 243: Summary of calculated dimensionless fracture intensity (p_{22}) in the CTt.	409
Figure 244: Shaker-configuration interface (controller).....	458

Figure 245: Apparatus for air-jet screening (laboratory of the Chair of Mineral Processing, IZR, MUL). 459

Figure 246: Malvern Mastersizer 2000 control software. Sample-adding procedure. 459

11 List of Tables

Table 1: Overview of the thesis structure and corresponding research tasks.....	5
Table 2: Ingredients of the mortar mixture.....	32
Table 3: Measured material properties.....	36
Table 4: Properties of PETN cords (Maxam™) used for the blast tests.....	38
Table 5: Calculated coupling ratio.....	38
Table 6: Short overview of the blast tests in the final test phase.....	44
Table 7: Macro-mechanisms (Crack-propagation paths).....	66
Table 8: Macro-mechanisms (Crack interactions - Branching).....	67
Table 9: Macro-mechanisms (Crack interactions - Merging).....	68
Table 10: Macro-mechanisms (Crack interactions - Branching-merging).....	69
Table 11: Terminology of symbols in Figure 52, related to a single fragment or fragment assembly. The subscript letters after comma denote: o - outer, i - inner, b - before, and a - after.....	74
Table 12: Micro- and meso-mechanisms of deformation in minerals and rock.....	92
Table 13: Determination of the material density used in the BER calculations (i.e., the calculation density).....	111
Table 14: Fracture-phase distribution in the captured blast shots (HSI).....	116
Table 15: Summary of counted main radial cracks with estimated stress-intensity factor. The values marked red indicate spalling, where “sp” stands for “unknown due to spalling.”.....	119
Table 16: Average values (means) of N in CTt.....	120
Table 17: Average values (means) of N_I , J_{int} , and N_{TB} in CTt.....	124
Table 18: Measured scatter of the node counts in the CTt.....	129
Table 19: Statistical evaluation of average D_{cent} in CTt with One-way ANOVA ($\alpha = 0.05$).	129
Table 20: Measured scatter of the topological results D_{cent} for the CTnp.....	131

Table 21: Statistical evaluation of average D_{cent} in CTnp with One-way ANOVA ($\alpha = 0.05$).	131
Table 22: Summary of C_B and C_L in CTt and PMI (or the last traced HSI).	134
Table 23: Summary of the estimated p_c slopes in the second fracture phase of the HSI.	137
Table 24: Summary of p_i and p_c in CTt and PMI (or the last traced HSI).	137
Table 25: Summary of estimated fracture abundance (p_{20} and p_{21}) regression-line slopes in the second fracture phase of the HSI.	141
Table 26: Summary of the fracture-abundance (p_{20} and p_{21}) results.	142
Table 27: Summary of the slopes of the linear-regression lines for 2D-fragment count in HSI with 95%-confidence limits.	145
Table 28: Summary of the slopes of the linear-regression lines for 2D-fragment count for the second fracture phase in HSI with 95%-confidence limits.	146
Table 29: Measured scatter of the 2D-fragment proportions in the CTt.	151
Table 30: Statistical evaluation of measured scatter D_{cent} of the 2D-fragment proportions in CTt with One-way ANOVA ($\alpha = 0.05$).	151
Table 31: Overview of calculated average crack-propagation speed.	153
Table 32: Statistical evaluation of average crack-propagation speed in HSI with One-way ANOVA ($\alpha = 0.05$).	154
Table 33: Statistical evaluation of average crack-propagation speed in HSI with Two-way ANOVA ($\alpha = 0.05$).	154
Table 34: Summary of identified macro-mechanisms in HSI (m12(21)).	157
Table 35: Selected HSI event logs of the blasted cylinders.	159
Table 36: Summary of measured blast-hole expansion, cylinder swelling, and normalized blast-hole radius.	161
Table 37: Statistical evaluation of $r_{bh, norm}$ with Two-way ANOVA ($\alpha = 0.05$).	161
Table 38: Summary of obtained $\Delta r_{comp, a}$, $\Delta r_{blast, b}$, $\Delta r_{crush, non - c}$, and $\Delta r_{crush, tot}$	162

Table 39: Summary of the fracture-surface roughness, averaged for each scanned fragment.	198
Table 40: Identified fragment-size ranges in the FSDs. Offset	204
Table 41: Total material loss in sieved blast cylinders.	204
Table 42: Measured material loss due to drying in the largest two sieved fragments (m20 (22.1)).	205
Table 43: Summary of obtained percentile fragment sizes and the ratio x_{80}/x_{30} . ..	206
Table 44: Data-fitting summary (sieving) of the "Swebrec 3p" function (Equation 46).	206
Table 45: Data-fitting summary (merged screening data) of the "Swebrec 5p" function (Equation 47).	207
Table 46: Overview of sieved fines proportions $P(x)$ below 1-mm mesh size.	208
Table 47: Overview of measured blast-hole-wall fines and estimated CGF with their proportions considering total sieved mass.	210
Table 48: Estimated mass of compacted material.	210
Table 49: Estimated mass of the blasted-off material.	210
Table 50: Estimated masses of CGF and blasted-off material.	211
Table 51: Summary of the measured specific surface area of the fines.	212
Table 52: Summary of the calculated particle-shape factor.	212
Table 53: Specific surface areas for the 6-g/m blast shots, obtained by averaging the corresponding data for 12- and 20-g/m blast shots in Table 51.	213
Table 54: Overview of calculated powder factor (PF) and specific energy consumption (E_c).	213
Table 55: Summary from the fitting of the "s-n(s)" curves to the sieving data. The values following '±' represent standard error.	215
Table 56: Summary from the fitting of the merged screening data to the "s-n(s)" curves. The values following '±' represent standard error.	216
Table 57: Combinations of correlated result parameters and corresponding blast tests.	217

Table 58: Description of the correlation groups (A to E).	218
Table 59: Interpretation of the Pearson's correlation coefficient (R) by Dancey & Reidy (2007).	218
Table 60: Correlation summary for specific charge (q) (Linear correlation). The bolded numbers represent the final R score for a given parameter.	219
Table 61: Correlation summary for specific charge (q) (LN correlation). The bolded numbers represent the final R score for a given parameter.	220
Table 62: Correlation summary for sieved mass passing 1-mm sieve size ($m_{-1 \text{ mm}}$) (Linear correlation). The bolded numbers represent the final R score for a given parameter.	221
Table 63: Correlation summary for sieved mass passing 1-mm sieve size ($m_{-1 \text{ mm}}$) (LN correlation). The bolded numbers represent the final R score for a given parameter.	222
Table 64: Summary of the correlation analysis for q [kg/m^3], considering only perfect and strong correlations.	223
Table 65: Summary of the correlation analysis for $m_{-1 \text{ mm}}$ [%], considering only perfect and strong correlations.	223
Table 66: Spatial resolution (i.e., size in pixels) of analysed images of the frontal end face and of the internal cracks in transverse cross-sections.	237
Table 67: Summary of measured $r_{\text{bh,norm}}$ and estimated r_c (CZM).	246
Table 68: Summarized results of the calculated Rittinger coefficients for blasted samples by Reichholf (2003).	252
Table 69: Overview of initial measurements (size and weight) of the blast cylinders.	320
Table 70: Overview of initial measurements (size and weight) of the material-testing samples.	321
Table 71: Overview of initial measurements (size and weight) of the material-testing samples. (Cont.)	322
Table 72: Measured grain-level densities of the blasted materials.	323

Table 73: Average values of the measured densities in Table 70, Table 71, and Table 72.....	324
Table 74: Final UCS-test results.....	326
Table 75: Final BTS-test results.....	327
Table 76: Results of the ultrasound-tests on the mortar samples.....	328
Table 77: Results of the ultrasound-tests on the granite samples. The rows marked blue are repeated measurements with an additional layer of ultrasound paste. The rows marked red were excluded as outliers.	329
Table 78: Results of the ultrasound-tests on the damping-material samples. The row marked red was excluded as an outlier.	331
Table 79: Summary of calculated sound impedance (Z_{bm}), impedance-matching index (i), wave-transfer coefficient (CT), and wave-reflection coefficient (CR), for the blasted materials.	331
Table 80: Summary of calculated values for the dynamic Poisson ratio (μ_{dyn}), the dynamic Young's modulus (E_{dyn}), and the dynamic shear modulus (G_{dyn}).	332
Table 81: Final WST results.	335
Table 82: Calculated critical stress-intensity factors.	336
Table 83: Summary of measured average grain size in the thin sections.....	352
Table 84: Summary of measured average pore size in the mortar.	352
Table 85: Result data of measured average grain size d_g in the mortar	354
Table 86: Measured average grain size d_g in the granite.....	355
Table 87: Overview of the blast test from the final development phase.....	358
Table 88: Overview of all conducted blast tests.....	359
Table 89: Used materials for the damping layer in the blast test.	361
Table 90: Plug configurations and plug lengths used in the blast tests.....	363
Table 91: Typical settings of recording parameters for the high-speed filming.	373
Table 92: Statistical evaluation of average N_L and N_B in CTt of 6-g/m shots and of 12- and 20-g/m shots with One-way ANOVA ($\alpha = 0.05$).	404

Table 93: Summary of N_B , N_L , and N_B/N_L in CTt and PMI (or the last traced HSI)...	404
Table 94: Statistical evaluation of average p_{cc} in CTt of mortar and granite shots with One-way ANOVA ($\alpha = 0.05$).	406
Table 95: Summary of the branch-connectivity probabilities in CTt and PMI (or the last traced HSI).	407
Table 96: Summary of estimated fracture abundance (p_{22}) curve slopes in the second fracture phase of the HSI.	409
Table 97: Summary of the p_{22} results.	410
Table 98: Statistical evaluation of dimensionless fracture intensity (p_{22}) in CTt with One-way ANOVA ($\alpha = 0.05$).	411
Table 99: Statistical evaluation of average N in CTt with One-way ANOVA ($\alpha = 0.05$).	412
Table 100: Statistical evaluation of average N in CTt with Two-way ANOVA ($\alpha = 0.05$). Data from m6(23.2), g6(26.1), m12(21), and g12(28.1).	412
Table 101: Statistical evaluation of average N in CTt with Two-way ANOVA ($\alpha = 0.05$) through multiple linear regression with m20(23.1) as the reference. Data from m6(23.2), g6(26.1), m12(21), g12(28.1), and m20(23.1).	412
Table 102: Overview of slopes and intercepts of linear-regression lines for N_i in CTt.	413
Table 103: Overview of slopes and intercepts of linear-regression lines for J_{int} in CTt.	413
Table 104: Overview of slopes and intercepts of linear-regression lines for N_{TB} in CTt.	414
Table 105: Statistical evaluation of absolute values of N_i in HSI with One-way ANOVA through multiple linear regression with g20(26.2) as the reference. Data from m6(22.2), m6(23.2), g6(26.1), g6(27), m12(20), m12(21), g12(24), g12(25), g12(28.1), m20(22.1), m20(23.1), and g20(26.2).	415
Table 106: Statistical evaluation of absolute values of J_{int} in HSI with One-way ANOVA through multiple linear regression with g20(26.2) as the reference. Data from m6(22.2), m6(23.2), g6(26.1), g6(27), m12(20), m12(21), g12(24), g12(25), g12(28.1), m20(22.1), m20(23.1), and g20(26.2).	416

Table 107: Statistical evaluation of absolute values of N_{TB} in HSI with One-way ANOVA through multiple linear regression with g20(26.2) as the reference. Data from m6(22.2), m6(23.2), g6(26.1), g6(27), m12(20), m12(21), g12(24), g12(25), g12(28.1), m20(22.1), m20(23.1), and g20(26.2).	417
Table 108: Statistical evaluation of absolute values of N_I in HSI with ANCOVA (Two-way ANOVA of regression residuals, $\alpha = 0.05$). Data from m6(22.2), m6(23.2), g6(26.1), g6(27), m12(20), m12(21), g12(24), g12(25), g12(28.1), m20(22.1), m20(23.1), and g20(26.2).	418
Table 109: Statistical evaluation of absolute values of J_{int} in HSI with ANCOVA (Two-way ANOVA of regression residuals, $\alpha = 0.05$). Data from m6(22.2), m6(23.2), g6(26.1), g6(27), m12(20), m12(21), g12(24), g12(25), g12(28.1), m20(22.1), m20(23.1), and g20(26.2).	418
Table 110: Statistical evaluation of absolute values of N_{TB} (T_b count) in HSI with ANCOVA (Two-way ANOVA of regression residuals, $\alpha = 0.05$). Data from m6(22.2), m6(23.2), g6(26.1), g6(27), m12(20), m12(21), g12(24), g12(25), g12(28.1), m20(22.1), m20(23.1), and g20(26.2).	418
Table 111: Statistical evaluation of absolute values of N_I in CTt with multiple linear regression ($\alpha = 0.05$) with m20(23.1) as the reference. Data from m6(23.2), g6(26.1), m12(21), g12(28.1), and m20(23.1).	419
Table 112: Statistical evaluation of absolute values of N_I in CTt with Two-way ANOVA ($\alpha = 0.05$) through multiple linear regression. Data from m6(23.2), g6(26.1), m12(21), and g12(28.1).	419
Table 113: Statistical evaluation of absolute values of J_{int} in CTt with multiple linear regression ($\alpha = 0.05$) with m20(23.1) as the reference. Data from m6(23.2), g6(26.1), m12(21), g12(28.1), and m20(23.1).	420
Table 114: Statistical evaluation of absolute values of J_{int} in CTt with Two-way ANOVA ($\alpha = 0.05$) through multiple linear regression. Data from m6(23.2), g6(26.1), m12(21), and g12(28.1).	420
Table 115: Statistical evaluation of absolute values of N_{TB} in CTt with multiple linear regression ($\alpha = 0.05$) with m20(23.1) as the reference. Data from m6(23.2), g6(26.1), m12(21), g12(28.1), and m20(23.1).	421

Table 116: Statistical evaluation of absolute values of N_{TB} in CTt with Two-way ANOVA ($\alpha = 0.05$) through multiple linear regression. Data from m6(23.2), g6(26.1), m12(21), and g12(28.1).	421
Table 117: Overview of slopes and intercepts of linear-regression lines for N_i , J_{int} , and N_{TB} in the CTnp.	422
Table 118: Statistical evaluation of absolute values of N_i in CTnp with multiple linear regression ($\alpha = 0.05$) with m20(23.1) as the reference. Data from m6(23.2), g6(26.1), m12(21), g12(28.1), and m20(23.1).....	423
Table 119: Statistical evaluation of absolute values of J_{int} in CTnp with multiple linear regression ($\alpha = 0.05$) with m20(23.1) as the reference. Data from m6(23.2), g6(26.1), m12(21), g12(28.1), and m20(23.1).....	424
Table 120: Statistical evaluation of N_{TB} in CTnp with multiple linear regression ($\alpha = 0.05$) with m20(23.1) as the reference. Data from m6(23.2), g6(26.1), m12(21), g12(28.1), and m20(23.1).	425
Table 121: Statistical evaluation of absolute values of N_i in CTnp with multiple linear regression ($\alpha = 0.05$) with m20(23.1) as the reference. Data from m6(23.2), g6(26.1), m12(21), g12(28.1), and m20(23.1).....	425
Table 122: Statistical evaluation of absolute values of J_{int} in CTnp with multiple linear regression ($\alpha = 0.05$) with m20(23.1) as the reference. Data from m6(23.2), g6(26.1), m12(21), g12(28.1), and m20(23.1).....	426
Table 123: Statistical evaluation of absolute values of N_{TB} in CTnp with multiple linear regression ($\alpha = 0.05$) with m20(23.1) as the reference. Data from m6(23.2), g6(26.1), m12(21), g12(28.1), and m20(23.1).....	426
Table 124: Statistical evaluation of average C_L and C_B in CTt of mortar and granite shots with One-way ANOVA ($\alpha = 0.05$).	427
Table 125: Statistical evaluation of C_L in CTt with multiple linear regression ($\alpha = 0.05$) with m20(23.1) as the reference. Data from m6(23.2), g6(26.1), m12(21), g12(28.1), and m20(23.1).	428
Table 126: Statistical evaluation of C_L in CTt with Two-way ANOVA ($\alpha = 0.05$) through multiple linear regression. Data from m6(23.2), g6(26.1), m12(21), and g12(28.1).	428

Table 127: Statistical evaluation of C_B in CTt with multiple linear regression ($\alpha = 0.05$) with m20(23.1) as the reference. Data from m6(23.2), g6(26.1), m12(21), g12(28.1), and m20(23.1).	429
Table 128: Statistical evaluation of C_B in CTt with Two-way ANOVA ($\alpha = 0.05$) through multiple linear regression. Data from m6(23.2), g6(26.1), m12(21), and g12(28.1).	429
Table 129: Statistical evaluation of p_i in HSI with multiple linear regression with g20(26.2) as the reference. Data from m6(22.2), m6(23.2), g6(26.1), g6(27), m12(20), m12(21), g12(24), g12(25), g12(28.1), m20(22.1), m20(23.1), and g20(26.2).....	430
Table 130: Statistical evaluation of p_c in HSI with multiple linear regression with g20(26.2) as the reference. Data from m6(22.2), m6(23.2), g6(26.1), g6(27), m12(20), m12(21), g12(24), g12(25), g12(28.1), m20(22.1), m20(23.1), and g20(26.2).....	431
Table 131: Statistical evaluation of p_i and p_c in HSI with ANCOVA (Two-way ANOVA of regression residuals, $\alpha = 0.05$). Data from m6(22.2), m6(23.2), g6(26.1), g6(27), m12(20), m12(21), g12(24), g12(25), g12(28.1), m20(22.1), m20(23.1), and g20(26.2).	432
Table 132: Statistical evaluation of p_i in the second fracture phase in HSI with multiple linear regression (Two-way ANOVA) with g20(26.2) as the reference. Data from m6(22.2), m6(23.2), g6(26.1), g6(27), m12(20), m12(21), g12(24), g12(25), g12(28.1), m20(22.1), m20(23.1), and g20(26.2).....	432
Table 133: Statistical evaluation of p_i in the second fracture phase in HSI with multiple linear regression with g20(26.2) as the reference. Data from m6(22.2), m6(23.2), g6(26.1), g6(27), m12(20), m12(21), g12(24), g12(25), g12(28.1), m20(22.1), m20(23.1), and g20(26.2).	433
Table 134: Statistical evaluation of p_c in the second fracture phase in HSI with multiple linear regression (Two-way ANOVA) with g20(26.2) as the reference. Data from m6(22.2), m6(23.2), g6(26.1), g6(27), m12(20), m12(21), g12(24), g12(25), g12(28.1), m20(22.1), m20(23.1), and g20(26.2).....	434
Table 135: Statistical evaluation of p_c in the second fracture phase in HSI with multiple linear regression with g20(26.2) as the reference. Data from m6(22.2), m6(23.2), g6(26.1), g6(27), m12(20), m12(21), g12(24), g12(25), g12(28.1), m20(22.1), m20(23.1), and g20(26.2).	435

Table 136: Statistical evaluation of p_l and p_c in the second fracture phase in HSI with ANCOVA (Two-way ANOVA of regression residuals, $\alpha = 0.05$). Data from m6(22.2), m6(23.2), g6(26.1), g6(27), m12(20), m12(21), g12(24), g12(25), g12(28.1), m20(22.1), m20(23.1), and g20(26.2).	436
Table 137: Statistical evaluation of p_l in CTt with multiple linear regression with m20(23.1) as the reference. Data from m6(23.2), g6(26.1), m12(21), g12(28.1), and m20(23.1).	436
Table 138: Statistical evaluation of p_l in CTt with Two-way ANOVA. Data from m6(23.2), g6(26.1), m12(21), and g12(28.1).	436
Table 139: Overview and statistical evaluation of average p_c in CTt of mortar and of granite shots with One-way ANOVA ($\alpha = 0.05$).	437
Table 140: Statistical evaluation of p_c in CTt with multiple linear regression ($\alpha = 0.05$) with m20(23.1) as the reference. Data from m6(23.2), g6(26.1), m12(21), g12(28.1), and m20(23.1).	437
Table 141: Statistical evaluation of p_c in CTt with Two-way ANOVA. Data from m6(23.2), g6(26.1), m12(21), and g12(28.1).	437
Table 142: Statistical evaluation of p_{20} in HSI with multiple linear regression with g20(26.2) as the reference. Data from m6(22.2), m6(23.2), g6(26.1), g6(27), m12(20), m12(21), g12(24), g12(25), g12(28.1), m20(22.1), m20(23.1), and g20(26.2).	438
Table 143: Statistical evaluation of p_{21} in HSI with multiple linear regression with g20(26.2) as the reference. Data from m6(22.2), m6(23.2), g6(26.1), g6(27), m12(20), m12(21), g12(24), g12(25), g12(28.1), m20(22.1), m20(23.1), and g20(26.2).	439
Table 144: Statistical evaluation of p_{22} in HSI with multiple linear regression with g20(26.2) as the reference. Data from m6(22.2), m6(23.2), g6(26.1), g6(27), m12(20), m12(21), g12(24), g12(25), g12(28.1), m20(22.1), m20(23.1), and g20(26.2).	440
Table 145: Statistical evaluation of p_{20} , p_{21} , and p_{22} in the second fracture phase in HSI with ANCOVA (Two-way ANOVA of regression residuals, $\alpha = 0.05$). Data from m6(22.2), m6(23.2), g6(26.1), g6(27), m12(20), m12(21), g12(24), g12(25), g12(28.1), m20(22.1), m20(23.1), and g20(26.2).	441
Table 146: Overview and statistical evaluation of average p_{20} and p_{21} in CTt with One-way ANOVA ($\alpha = 0.05$).	441

Table 147: Statistical evaluation of p_{20} in CTt with multiple linear regression ($\alpha = 0.05$) with m20(23.1) as the reference. Data from m6(23.2), g6(26.1), m12(21), g12(28.1), and m20(23.1).	442
Table 148: Statistical evaluation of p_{21} in CTt with multiple linear regression ($\alpha = 0.05$) with m20(23.1) as the reference. Data from m6(23.2), g6(26.1), m12(21), g12(28.1), and m20(23.1).	442
Table 149: Statistical evaluation of p_{22} in CTt with multiple linear regression ($\alpha = 0.05$) with m20(23.1) as the reference. Data from m6(23.2), g6(26.1), m12(21), g12(28.1), and m20(23.1).	443
Table 150: Statistical evaluation of the fracture abundance (p_{20} , p_{21} , and p_{22}) in CTt with Two-way ANOVA ($\alpha = 0.05$). Data from m6(23.2), g6(26.1), m12(21), g12(28.1), and m20(23.1).	443
Table 151: Statistical evaluation of the 2D-fragment count in HSI with multiple linear regression with g20(26.2) as the reference. Data from m6(22.2), m6(23.2), g6(26.1), g6(27), m12(20), m12(21), g12(24), g12(25), g12(28.1), m20(22.1), m20(23.1), and g20(26.2).	444
Table 152: Statistical evaluation of the 2D-fragment count in the second fracture phase in HSI with multiple linear regression with g20(26.2) as the reference. Data from m6(22.2), m6(23.2), g6(26.1), g6(27), m12(20), m12(21), g12(24), g12(25), g12(28.1), m20(22.1), m20(23.1), and g20(26.2).	445
Table 153: Statistical evaluation of the 2D-fragment count in HSI with ANCOVA (One-way ANOVA of linear-regression residuals). Data from m6(22.2), m6(23.2), g6(26.1), g6(27), m12(20), m12(21), g12(24), g12(25), g12(28.1), m20(22.1), m20(23.1), and g20(26.2).	446
Table 154: Statistical evaluation of the 2D-fragment count in the second fracture phase in HSI with ANCOVA (One-way ANOVA of linear-regression residuals). Data from m6(22.2), m6(23.2), g6(26.1), g6(27), m12(20), m12(21), g12(24), g12(25), g12(28.1), m20(22.1), m20(23.1), and g20(26.2).	446
Table 155: Statistical evaluation of average total 2D-fragment count in CTt with One-way ANOVA ($\alpha = 0.05$).	447

Table 156: Statistical evaluation of 2D-fragment count in CTt with multiple linear regression ($\alpha = 0.05$) with m20(23.1) as the reference. Data from m6(23.2), g6(26.1), m12(21), g12(28.1), and m20(23.1).....	447
Table 157: Statistical evaluation of the 2D-fragment count in CTt with Two-way ANOVA ($\alpha = 0.05$). Data from m6(23.2), g6(26.1), m12(21), g12(28.1), and m20(23.1).	447
Table 158: Statistical evaluation of 2D-fragment count in CTnp with multiple linear regression ($\alpha = 0.05$) with m20(23.1) as the reference. Data from m6(23.2), g6(26.1), m12(21), g12(28.1), and m20(23.1).....	448
Table 159: Overview of average fracture-surface roughness.	449
Table 160: Statistical evaluation of fracture-surface roughness (kernel size - 1 mm) with Two-way ANOVA ($\alpha = 0.05$). Data from m6(22.2), m12(20), m20(22.1), g6(27), g12(25), and g20(26.2).	449
Table 161: Statistical evaluation of fracture-surface roughness (kernel size - 3 mm) with Two-way ANOVA ($\alpha = 0.05$). Data from m6(22.2), m12(20), m20(22.1), g6(27), g12(25), and g20(26.2).	450
Table 162: Statistical evaluation of fracture-surface roughness (kernel size - 5 mm) with Two-way ANOVA ($\alpha = 0.05$). Data from m6(22.2), m12(20), m20(22.1), g6(27), g12(25), and g20(26.2).	450
Table 163: Summary of the slopes and intercepts of the s-n(s) linear-regression lines with 95%-confidence limits for the fines-size range of the sieving data.	451
Table 164: Statistical evaluation of s-n(s) regression lines for the sieving data in the fines-size range with multiple linear regression ($\alpha = 0.05$) with m20(23.1) as the reference. Data from m6(22.2), m6(23.2), g6(26.1), g6(27), m12(20), m12(21), g12(24), g12(25), g12(28.1), m20(22.1), m20(23.1), and g20(26.2).	452
Table 165: Statistical evaluation of s-n(s) regression lines for the sieving data in the intermediate-fragment-size range with multiple linear regression ($\alpha = 0.05$) with m20(23.1) as the reference. Data from m6(22.2), m6(23.2), g6(26.1), g6(27), m12(20), m12(21), g12(24), g12(25), g12(28.1), m20(22.1), m20(23.1), and g20(26.2).....	453
Table 166: Summary of the slopes and intercepts of the s-n(s) linear-regression lines with 95%-confidence limits for the intermediate-fragment-size range of the sieving data.	454

Table 167: Summary of the slopes and intercepts of the s-n(s) linear-regression lines with 95%-confidence limits for the ultra-fines-size range of the merged screening data.	454
Table 168: Statistical evaluation of s-n(s) regression lines for the merged-screening data in the ultra-fines-size range with multiple linear regression ($\alpha = 0.05$) with g20(26.2) as the reference. Data from m6(22.2), g6(27), m12(20), g12(24), g12(25), m20(22.1), and g20(26.2).	455
Table 169: Statistical evaluation of s-n(s) regression lines for the merged-screening data in the intermediate-fragment-size range with multiple linear regression ($\alpha = 0.05$) with g20(26.2) as the reference. Data from m6(22.2), g6(27), m12(20), g12(24), g12(25), m20(22.1), and g20(26.2).	456
Table 170: Summary of the slopes and intercepts of the s-n(s) linear-regression lines with 95%-confidence limits for the intermediate-fragment-size range of the merged screening data.	457
Table 171: Results of a statistical comparison of the intermediate-fragment-size slopes with the (ultra-)fines slopes per blast shot.	457
Table 172: Raw measurements of average $r_{bh,a}$ from the CTt images (1 of 3).....	480
Table 173: Raw measurements of average $r_{bh,a}$ from the CTt images (2 of 3).....	481
Table 174: Raw measurements of average $r_{bh,a}$ from the CTt images (3 of 3).....	482
Table 175: Raw measurements of average $r_{m,a}$ from the CTt images (1 of 3).	483
Table 176: Raw measurements of average $r_{m,a}$ from the CTt images (2 of 3).....	484
Table 177: Raw measurements of average $r_{m,a}$ from the CTt images (3 of 3).....	485
Table 178: Measured $r_{bh,norm}$ for blast test 26.2 (granite, 20 g/m).	486
Table 179: Correlation of results from group A, covering all blast tests from the final test phase.	535
Table 180: Correlation of results from group B, covering blast test from group A without g12(28.1)	536
Table 181: Correlation of results from group C, covering blast tests m20(22.1), m12(20), m6(22.2), g20(26.2), g12(24), g12(25), and g6(27).	537

Table 182: Correlation of results from group D, covering blast tests m20(23.1), m12(21), m6(23.2), g12(28.1), and g6(26.1)..... 538

Table 183: Correlation of results from group E, covering blast tests m20(23.1), m12(21), m6(23.2), and g6(26.1). 539

Appendix 1 **Sample production**

Blast cylinders and samples for testing material properties (test samples) were manufactured in the laboratory facilities of “Impuls Zentrum für Rohstoffe” (IZR) at the Chair of Mining Engineering and Mineral economics at the Montanuniversitaet Leoben (MUL). Samples of the damping material were made separately from the mortar and granite batches.

The mortar blast cylinders and material-testing samples were made by following a similar procedure (Figure 190) to the one that Schimek (2015) and Ivanova (2015) used.

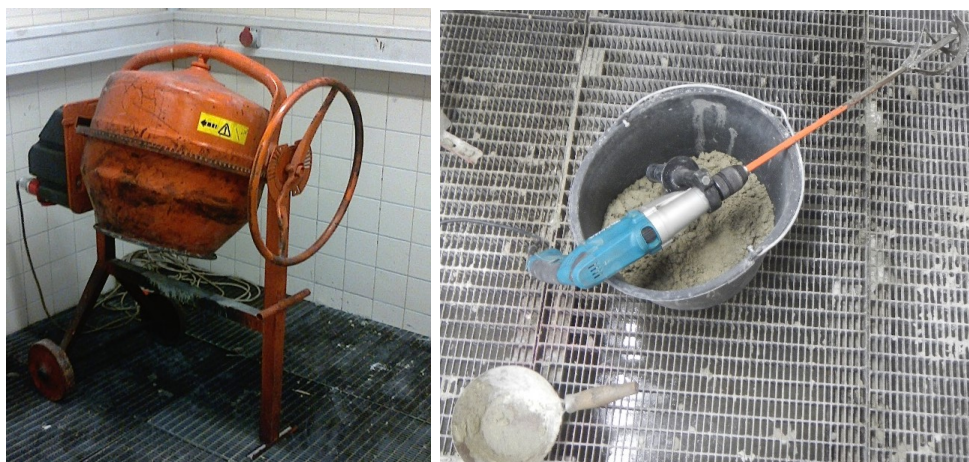


Figure 190: Equipment used for mixing the mortar.

This included preparation of the mixture ingredients (i.e., by measuring the weight dosage), mixing them in a concrete mixer for about 20 minutes, fine mixing for about 10 min, and pouring in cast confinements along with vibration treatment, tamping, and gentle knocking on the confinement with a rubber hammer. Casting oil (Schalöl, Avenarius Agro) was applied to internal walls of the confinements prior to casting. The mixed mortar was poured in the confinements successively in 3 to 5 layers, and the poured mixture was each time tamped with a wooden stick about 30 times along a circular path. After one day, the mortar blast cylinders were submerged in water and left to cure at room temperature. The blocks for material testing were watered every day during the initial curing period of 7 days. Finally, the specimens were released from the confinements and left to cure for at least another 21 days at room temperature.

The recipe was changed in the preliminary test phase due to difficulties with the quartz-sand supply, like in the research of Schimek (2015) and Ivanova (2015). Although the final procedure also included careful water dosage and fine mixing of the fresh mortar

with chemical additives (i.e., defoamer and plasticizer), the cured samples were very porous (i.e., air pores made 25-30% volume). This resulted in relatively low material density of the mortar specimens in the final test phase (Table 3).

It was suspected that material sedimentation during the curing of the mortar cylinders could cause a density gradient along the axis. However, CT-analysis of cured non-blasted cylinders showed only minor axial fluctuations in the density-related porosity.

The casting confinement for the mortar blast cylinders consisted of a plastic pipe ($\varnothing 152 \times 330$ mm) with a wall thickness of 5 mm, of wooden disks ($\varnothing 152 \times 20$ mm) with a central $\varnothing 10$ -mm borehole for closing of the pipe on the top and bottom side, and of a rod ($\varnothing 10 \times 330$ mm) secured in the boreholes of the disks in the central axial position of the pipe (Figure 191).



Figure 191: Confinements for casting the mortar cylinders.

The upper disk was made of cardboard (about 5-mm thick) for producing mortar batches 6 and 7. The disks were fixed to the pipe with duct tape (Figure 192).



Figure 192: Sealed mortar-casting confinement.

The central rod was pulled out from each mortar blast cylinder one day after casting. The rod was of aluminium in the final test phase (6 cylinders) and of wood in the preliminary test phase. This change was made because the wooden sticks swelled and sometimes caused radial cracking around the sticks at the end-face surfaces (Figure 193). The cracks were not detected further inside the cylinder after processing the end faces.



Figure 193: Radial drying-induced cracking around the sticks at the end-face surfaces.

The blast cylinders (mortar and granite) were then transversally cut to about $\text{\O}150 \times 310$ mm (Figure 194). This was different for the mortar blast cylinders in the preliminary test phase as they were mostly $\text{\O}140 \times 280$ mm in size. The end faces of the cylinders were evened out by trimming and milling to ± 0.1 mm.



Figure 194: Equipment used for transverse cutting of the cylinders.

The borehole in the granite blast cylinders was drilled with water cooling. In some cases, the drilling path deviated and/or some material on the borehole collar at the opposite end face would spall off due to errors in the drilling procedure. The borehole deviation (Sinkala, 1989) was kept in a specified range and recorded for all granite blast cylinders (Figure 195). The range was set to total borehole deviation of $d_{tot} = 15 \text{ mm}$.

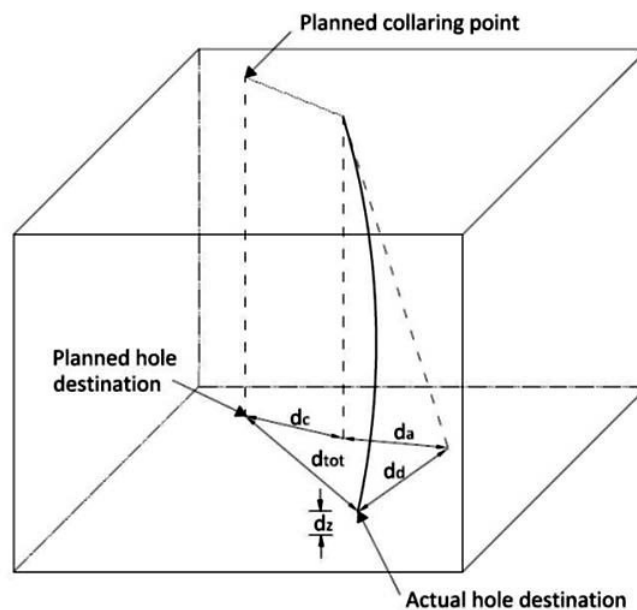


Figure 195: Graphical definition of the borehole deviation (Sinkala, 1989).

As the end face with the drilling-induced spalling also had the borehole out of centre due to the deviation, the blast cylinder was oriented with this end face towards the detonator side of the blast chamber prior to the blasting. In this way, the spalled borehole collar compensated for excessive blast damage from the detonator. The borehole deviation in the mortar cylinders was insignificant (below 5 mm).

After being processed, the blast cylinders were left to dry for at least 7 days at room temperature.

The casting confinement for the material-testing samples of mortar was a rectangular wooden box, 350×350×150 mm in size. The resulting mortar blocks were carefully cut and core-drilled to provide the test samples (Figure 196). All core-drilling was done in the vertical direction (curing orientation).



Figure 196: Block for producing material-testing samples of mortar (left) and the samples after core-drilling (right).

The cubical mortar and granite specimens (Figure 197) for the wedge-splitting tests (WST) were produced at the Chair of Ceramics (MUL) from a part of the mortar blocks and from one of the granite cylinders (ø150×350 mm in size).

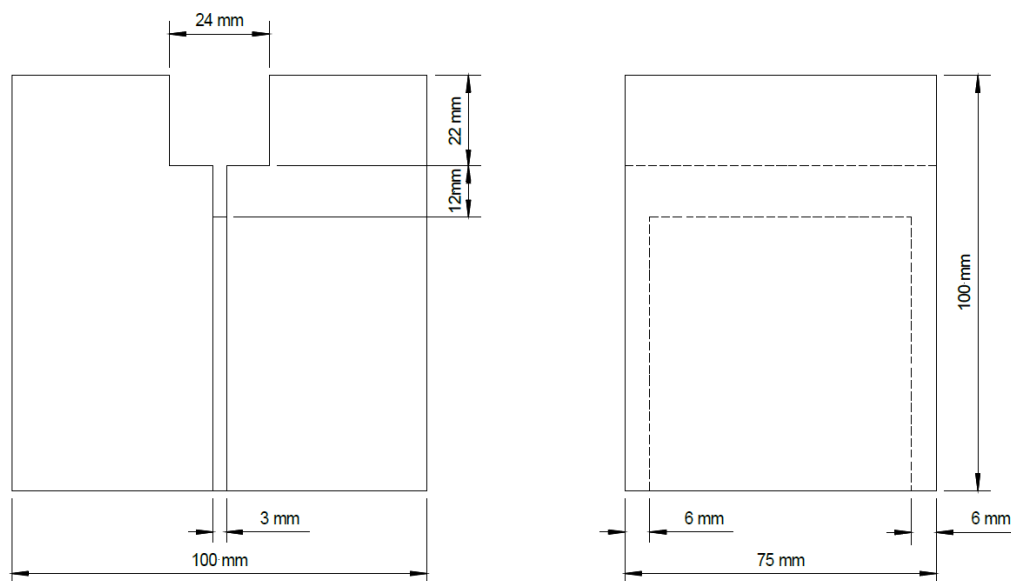


Figure 197: Technical drawing of the WST samples.

The WST mortar samples (Figure 198) were oriented with the loading direction (i.e., the notch) in the horizontal plane of the mortar sample blocks or perpendicular to the core-drilling direction of the granite samples.



Figure 198: Mortar WST samples.

The granite blast cylinders and material-testing samples of the same batches were core-drilled with water cooling in the same direction from the same original block (Figure 199).



Figure 199: Original granite block (left) and cylindrical material-testing samples (right).

Material-testing samples of the damping layer were produced when the damping material was mixed and poured in the blast chamber. In the final test phase, this was one day before blasting.

For each blast test in the final test phase, the samples were made as some of the damping material was poured in four glass tubes, $\varnothing 50 \times 100$ mm in size (Figure 200). These samples were tested on the same day when the respective blast test was conducted.



Figure 200: Sample for testing material properties of the damping layer.

Datasheets of materials used for sample production

[Appendix 1 - Datasheets of materials for sample production](#)

Appendix 2 **Material properties (procedure and result data)**

The material-properties testing of the mortar and the granite specimens covered:

- material density,
- uniaxial compressive strength (UCS) tests,
- uniaxial tensile strength (Brazilian UTS - BTS) tests,
- ultrasound tests (measurement of P- and S-wave propagation speed), and
- Wedge-splitting tests (WST).

Material properties of the damping layer were tested 24 hours after casting, and they covered:

- material density (initial measurements) and
- P- and S-wave propagation speeds.

The initial density measurements, UCS tests, BTS tests, and ultrasound tests were conducted in the laboratory of the Chair of Mining Engineering and Mineral Economics (IZR, MUL).

Density

Following the sample production and a 7-days drying period, each specimen's weight and size were measured. These initial measurements were used for a basic density calculation, i.e., by dividing the volume of the sample by its mass. The blast cylinders were measured with a measuring scale FG-150KAL (A&D Company, Limited). The material-testing samples (excluding those for WST) were measured with a measuring scale FZ-3000i (A&D Company, Limited).

Table 69 and Table 70/Table 71 show the ensuing data for the blast cylinders and the material-testing samples, respectively, where:

- D – Sample diameter,
- Db – Borehole diameter (for the blast cylinders),
- H – Sample height/length,
- V – Calculated sample volume,
- m – Sample mass, and
- ρ – Calculated material density.

Here, the rows highlighted yellow are related to the final test phase.

Table 69: Overview of initial measurements (size and weight) of the blast cylinders.

Blast test	Sample	D [mm]	Db [mm]	H [mm]	V [cm³]	m [g]	ρ [g/cm³]
1	mb-11	142.0	10	280	4410.067	9100	2.06
2	mb-12	142.0	10	280	4410.067	9080	2.06
3	mb-13	142.0	10	280	4410.067	9120	2.07
4	mb-14	142.0	10	280	4410.067	9040	2.05
5	mb-15	142.0	10	280	4410.067	9100	2.06
6	mb-21	142.0	10	274	4315.566	8600	1.99
7	mb-22	142.0	10	275	4331.316	8640	1.99
8	mb-23	142.0	10	275	4331.316	8660	2.00
9	mb-24	142.0	10	270	4252.565	8380	1.97
10	mb-25	142.0	10	271	4268.315	8420	1.97
11.1	mb-31	142.0	10	282	4441.568	9150	2.06
11.2	mb-32	142.0	10	284	4473.068	8880	1.99
12.1	mb-42//	142.0	10				
12.2	mb-45	142.0	10	280	4410.067	8028	1.82
12.3	mb-41	142.0	10	280	4410.067	8023	1.82
13.1	mb-5//	152.0	10				
13.2	mb-5//	152.0	10				
14.1	gb-12	149.0	10	298	5171.213	13720	2.65
14.2	gb-13	149.0	10	298	5165.227	13700	2.65
15	gb-14	149.0	10	298	5138.546	13640	2.65
16	gb-11	149.0	10	298	5155.818	13680	2.65
17	mb-43	142.0	10	286	4504.569	7480	1.66
18.1	gb-15//	149.0	10				
18.2	mb-44	142.0	10	288	4536.069	7500	1.65
19	gb-15//	149.0	10				
20	mb-72	151.7	10	292	5252	8800	1.68
21	mb-75	151.7	10	291	5234	8980	1.72
22.1	mb-74	151.7	10	303	5450	9380	1.72
22.2	mb-71	151.4	10	299	5356	8940	1.67
23.1	mb-76	151.0	10	296	5283	9020	1.71
23.2	mb-73	151.4	10	298	5345	8920	1.67
24	gb-26	148.5	10	306.3	5278	14040	2.66
25	gb-22	149.0	10	301.6	5233	13820	2.64
26.1	gb-21	149.0	10	302.2	5243	13880	2.65
26.2	gb-24	149.0	10	303.3	5262	13840	2.63
27	gb-25	149.0	10	297	5153	14420	2.80
28.1	gb-23	149.0	10	317	5500	13840	2.52
28.2	gb-23, gb-25//	149.0	10				
29.1	gb-21//	149.0	10				
29.2	gb-26//	149.0	10				

The angle values in Table 70 and Table 71 denote three equally spaced measurement positions.

Table 70: Overview of initial measurements (size and weight) of the material-testing samples.

Sample	D [mm]				H [mm]				V [cm ³]	m [g]	ρ [g/cm ³]
	0°	120°	240°	Ave	0°	120°	240°	Ave			
mt0-701	48.4	48.0	48.6	48.31	28.1	27.9	27.9	27.96	51.22	85.50	1.67
mt0-702	49.2	49.3	49.3	49.24	25.6	26.0	26.2	25.96	49.41	82.18	1.66
mt0-703	48.9	49.1	49.0	48.99	29.2	28.8	29.0	29.01	54.65	90.70	1.66
mt0-704	49.0	49.0	49.0	48.99	26.8	26.7	26.8	26.74	50.38	84.41	1.68
mt0-705	48.6	48.8	48.9	48.78	27.7	27.5	27.5	27.56	51.48	85.20	1.66
mt0-706	48.9	49.3	49.3	49.17	23.6	23.4	23.5	23.52	44.63	73.83	1.65
mt0-707	49.1	49.2	49.0	49.10	26.3	26.5	26.7	26.50	50.14	82.47	1.64
mt0-708	49.1	49.1	49.1	49.08	26.3	26.4	26.5	26.39	49.90	81.85	1.64
mt0-709	48.5	48.0	48.1	48.19	27.5	27.4	27.2	27.38	49.93	83.41	1.67
mt0-710	48.7	48.5	48.7	48.65	28.0	27.8	27.9	27.89	51.82	86.50	1.67
mt0-711	49.0	48.9	49.1	48.98	28.3	28.2	29.0	28.48	53.63	87.18	1.63
mt0-712	48.6	48.7	48.8	48.71	26.6	26.8	26.8	26.72	49.76	83.38	1.68
mt0-713	48.7	48.8	48.7	48.72	26.3	26.3	26.4	26.33	49.07	80.90	1.65
mt0-714	48.8	49.0	48.9	48.92	28.3	28.2	28.3	28.26	53.08	89.12	1.68
mt0-715	48.3	48.7	48.3	48.44	26.1	26.5	26.3	26.30	48.45	80.19	1.66
gt0-107	50.9	51.3	51.2	51.15	28.1	28.4	28.5	28.32	58.16	157.44	2.71
gt0-108	50.8	51.3	51.5	51.19	28.5	28.6	28.4	28.49	58.62	158.37	2.70
gt0-117	51.1	51.4	51.4	51.32	28.9	29.0	28.9	28.94	59.83	160.81	2.69
gt0-118	51.4	51.4	51.4	51.40	28.6	28.9	28.9	28.79	59.71	160.93	2.70
gt0-202	49.3	49.2	49.5	49.31	27.7	27.6	28.1	27.80	53.07	143.83	2.71
gt0-203	48.6	49.5	49.1	49.08	28.3	28.2	28.0	28.18	53.29	143.58	2.69
gt0-204	49.0	49.2	49.2	49.13	25.8	26.3	26.0	26.01	49.29	133.27	2.70
mt1-701	49.3	49.2	49.3	49.26	96.9	96.5	96.8	96.73	184.27	302.70	1.64
mt1-702	48.8	49.0	48.8	48.88	103.3	103.3	103.2	103.24	193.65	318.92	1.65
mt1-703	49.2	49.3	49.4	49.31	101.5	101.4	101.4	101.45	193.61	318.38	1.64
mt1-704	48.9	49.0	49.0	48.98	100.9	100.8	100.8	100.85	189.90	313.65	1.65
mt1-705	49.0	49.1	49.0	49.04	102.1	102.2	102.1	102.13	192.77	318.48	1.65
mt1-706	48.8	48.7	48.7	48.75	99.0	99.0	99.0	98.99	184.67	304.63	1.65
mt1-707	48.5	48.6	48.6	48.57	103.7	103.7	103.7	103.71	192.06	318.79	1.66
mt1-708	49.3	49.2	49.2	49.20	101.4	101.6	101.5	101.50	192.88	318.79	1.65
mt1-709	49.1	49.2	49.1	49.14	105.8	105.8	105.9	105.82	200.61	331.72	1.65
mt1-710	48.7	48.9	49.0	48.85	95.6	96.1	96.0	95.88	179.57	300.78	1.68
mt1-711	49.0	49.0	49.0	48.97	102.8	103.1	103.3	103.07	194.03	326.11	1.68
mt1-712	48.5	49.1	48.8	48.78	100.0	100.3	100.3	100.21	187.19	311.71	1.67
mt1-713	48.4	48.6	48.5	48.50	101.0	101.2	101.2	101.14	186.78	311.09	1.67

Table 71: Overview of initial measurements (size and weight) of the material-testing samples. (Cont.)

Sample	D [mm]				L [mm]				V [cm ³]	m [g]	ρ [g/cm ³]
	0°	120°	240°	Ave	0°	120°	240°	Ave			
gt1-101	50.8	50.7	50.7	50.70	100.2	100.1	100.1	100.17	202.15	555.12	2.75
gt1-102	50.6	50.7	50.5	50.61	99.1	99.2	99.0	99.08	199.25	549.31	2.76
gt1-103	50.7	50.6	50.6	50.62	100.5	100.5	100.4	100.49	202.14	556.30	2.75
gt1-104	50.8	50.7	50.7	50.76	104.5	104.6	104.4	104.49	211.36	577.18	2.73
gt1-105	50.7	50.8	50.6	50.71	101.5	101.4	101.3	101.36	204.58	561.17	2.74
gt1-106	50.7	50.7	50.7	50.71	97.9	97.9	97.7	97.83	197.49	541.97	2.74
gt1-107	50.7	50.8	50.7	50.75	99.0	99.0	99.1	99.05	200.24	550.5	2.75
gt1-108	50.8	50.9	50.8	50.82	99.5	99.5	99.6	99.53	201.77	552.42	2.74
gt1-109	50.8	50.9	50.8	50.85	102.6	102.6	102.6	102.60	208.26	569.03	2.73
gt1-110	50.8	50.8	50.8	50.82	100.1	100.1	100.2	100.14	203.00	555.94	2.74
gt1-111	50.8	50.5	50.6	50.64	101.0	101.0	101.1	101.03	203.33	559.36	2.75
gt1-112	50.7	50.7	50.6	50.67	101.4	101.4	101.4	101.39	204.34	562.02	2.75
gt1-211	48.7	48.7	48.8	48.74	102.8	102.8	102.8	102.81	191.76	528.89	2.76
gt1-212	48.8	48.9	49.0	48.91	102.6	102.7	102.8	102.70	192.87	532.77	2.76
gt1-213	48.9	48.8	48.8	48.82	101.9	101.9	101.9	101.89	190.61	526.33	2.76
gt0-102	50.7	50.8	50.8	50.77	28.2	27.9	27.9	28.00	56.66	157.84	2.79
gt0-103	50.9	50.9	50.9	50.89	27.6	27.5	27.6	27.54	55.99	154.98	2.77
gt0-104	50.9	50.8	50.8	50.86	29.0	29.0	29.0	28.97	58.83	162.82	2.77
gt0-105	50.9	50.8	50.8	50.83	28.7	28.7	28.9	28.78	58.37	161.12	2.76
gt0-106	50.7	50.8	50.7	50.71	27.2	26.9	26.9	26.98	54.46	152.77	2.81
gt0-107	50.8	50.8	50.7	50.74	28.5	28.6	28.4	28.48	57.57	160.89	2.79
gt0-108	50.6	50.6	50.8	50.66	27.9	27.7	27.8	27.82	56.05	157.42	2.81
gt0-109	50.6	50.8	50.6	50.66	25.7	26.0	25.9	25.88	52.13	147.03	2.82

Although the blast cylinders had been left to dry for at least 7 days at room temperature, some of them had higher density than that of the material-test samples (see Table 3 and Table 6). This was due to incomplete drying of these blast cylinders. This was especially pronounced in the mortar blast cylinders due to their porosity. As the water saturation does not significantly influence the blast fragmentation of such specimens (Lajtai et al., 1987; D. Johansson, 2011; Z.-X. Zhang, 2016), the blast tests were still conducted on these cylinders. It was also noted that the expected post-blast drying of fragmented material would appear as material (weight) loss after the sieving analysis.

Grain-level density (ρ_g) of sieved material from the blasted cylinders was measured with a gas pycnometer Micrometrics Accupyc 1330 with cell volume of 10 cm³ (Figure 201). The measurement covered two smallest grain-size categories of the sieved material (i.e. '-40 μ m' and '100-40 μ m').



Figure 201: Gas pycnometer Micromeritics AccuPyc 1330 (laboratory of the Chair of Mineral Processing, IZR, MUL).

Table 72 shows the measured grain-level densities.

Table 72: Measured grain-level densities of the blasted materials.

Material	Sample (blast test)	Fragment-size range [μm]	Grain-level density ρ _g [g/cm ³]
Granite	g12(28.1)	-40	2.749
	g12(24)	100 40	2.662
	g20(26.2)	-40	2.656
	g20(26.2)	100 40	2.661
	Ave:		2.682
	Std:		0.039
Mortar	m12(20) and m12(21)	-40	2.396
	m12(20)	100 40	2.360
	m20(23.1)	-40	2.378
	m20(22.1)	100 40	2.400
	Ave:		2.384
	Std:		0.016

Table 73 shows the average values of the measured material (bulk) densities (ρ_b [g/cm³]) (see Table 70 and Table 71) and of the grain-level densities (ρ_g [g/cm³]) (see Table 72).

Table 73: Average values of the measured densities in Table 70, Table 71, and Table 72.

Material	Bulk density ρ_b [g/cm ³]			Grain-level density ρ_g [g/cm ³]		
	Ave	Std	Data count	Ave	Std	Data count
Granite	2.748	0.035	30	2.682	0.039	4
Mortar	1.658	0.013	28	2.384	0.016	4

Note here that for the granite ρ_b is higher than ρ_g , although it should be the opposite. As the porosity of the granite is about 0.5% (see the technical report on the granite material in Appendix 1), this contradiction is probably a result of a variation in material properties of the corresponding samples and measurement error.

Uniaxial compressive strength (UCS) tests

The UCS tests were conducted according to the testing standard ÖNORM B 3124 Teil 3 and the ISRM Suggested Methods (Ulusay & Hudson, 2011). Figure 202 shows the test set-up.

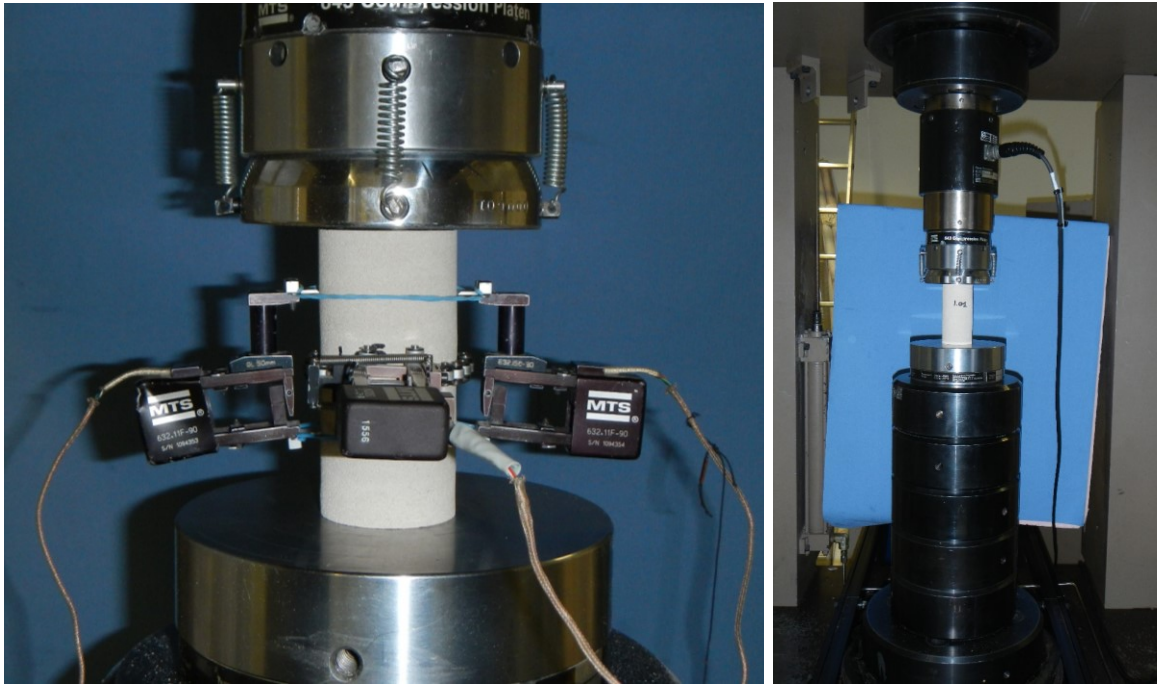


Figure 202: UCS-test set-up.

The modulus of elasticity (Young's modulus, E) was calculated using the stress–strain diagrams recorded during the UCS tests. Poisson ratio (μ) was determined as a ratio of the lateral strain to the axial strain within the linear elastic region (Hohl, 2013).

A detailed description of the methods and related testing procedures is provided in a technical report (Restner, 1999).

Table 74 shows the UCS results.

Table 74: Final UCS-test results.

Sample		F_{max} [N]	σ_c [MPa]	E [MPa]	μ [-]
Mortar	mt1-706	56589.2	30.318	11955.69	0.119131
	mt1-707	49823.2	26.891	11887.99	0.201396
	mt1-708	52685.5	27.645	12498.80	0.248378
	mt1-709	52809.1	27.789	12542.24	0.220107
	mt1-710	50573.6	26.984	12366.52	0.229186
	mt1-711	52019.3	27.619	12399.08	0.217004
	mt1-712	50758.3	27.160	11761.03	0.303388
	mt1-713	50639.8	27.411	12425.42	0.266556
Ave:		27.727	12229.60	0.225643	
Std:		1.096	308.75	0.053833	
Std [%]:		3.95	2.52	23.86	
Granite	gt1-101	334718.3	165.796	65905.17	0.245691
	gt1-102	360956.4	179.429	-	-
	gt1-103	325898.7	160.792	64480.17	0.201591
	gt1-104	366375.7	181.405	-	-
	gt1-105	333057.2	164.583	64525.34	0.242076
	gt1-106	372066.5	183.498	-	-
	gt1-107	346611.0	170.944	65153.83	0.238108
	gt1-108	365494.4	181.469	-	-
	gt1-201	304130.1	162.404	66349.28	0.253788
	gt1-202	308717.5	164.315	-	-
	Ave:		171.464	65282.76	0.236251
Std:		9.031	830.56	0.020220	
Std [%]:		5.27	1.27	8.56	

Indirect uniaxial tensile strength (Brazilian UTS - BTS) tests

The BTS tests were conducted according to the testing standard ÖNORM B3124 Teil 4 and the ISRM Suggested Methods (Ulusay & Hudson, 2011). Figure 203 shows the test set-up.

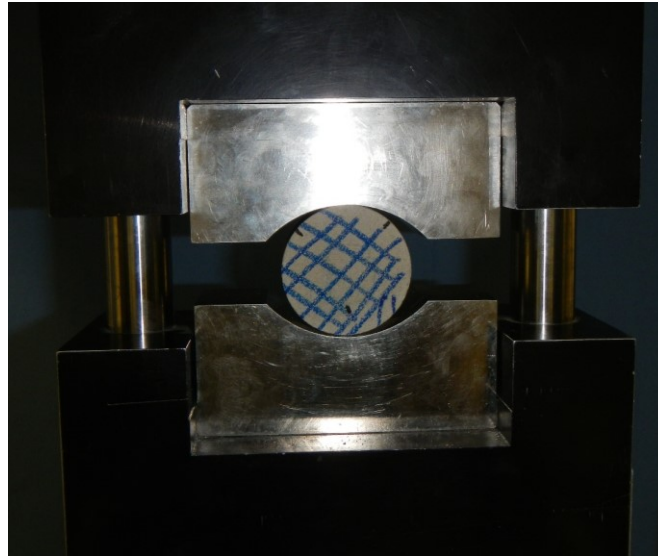


Figure 203: BTS-test set-up.

Table 75 shows the BTS results.

Table 75: Final BTS-test results.

Mortar			Granite		
Sample	F_{max} [N]	σ_t [MPa]	Sample	F_{max} [N]	σ_t [MPa]
mt0-701	6351.6	3.00	gt0-107	27559.39	12.12
mt0-702	6097.9	3.04	gt0-108	27401.74	11.97
mt0-703	4575.1	2.05	gt0-117	25211.60	10.81
mt0-704	6685.3	3.25	gt0-118	25122.21	10.81
mt0-705	6099.4	2.89	gt0-202	27050.25	12.57
mt0-706	6153.5	3.39	gt0-203	19356.92	8.91
mt0-707	8105.8	3.97	gt0-204	17637.2	8.79
mt0-708	4572.2	2.25			
mt0-709	5713.3	2.76			
mt0-710	6104.0	2.87			
mt0-711	6077.8	2.78			
mt0-712	6630.2	3.24			
mt0-713	6028.7	2.99			
mt0-714	4802.1	2.21			
mt0-715	5617.0	2.81			
Ave:	2.90		Ave:	10.85	
Std:	0.49		Std:	1.52	
Std [%]:	16.81		Std [%]:	13.97	

Ultrasound tests

The P-wave (C_p) and the S-wave velocity (C_s) were measured with instrumentation (Figure 204) that constitutes sample-securing support, ultrasound signal generator (USG 40, Geotron Elektronik), two ultrasound probes (UPG-S/UPE-S), USB-oscilloscope, and a PC computer with software Light House UMPC. This was done according to the ASTM testing standard D2845-00. The measurement configuration was set to signal amplitude (u) of 200 mV, signal frequency (F_s) of 100 MHz, and sampling frequency (F_c) of 250 kHz.

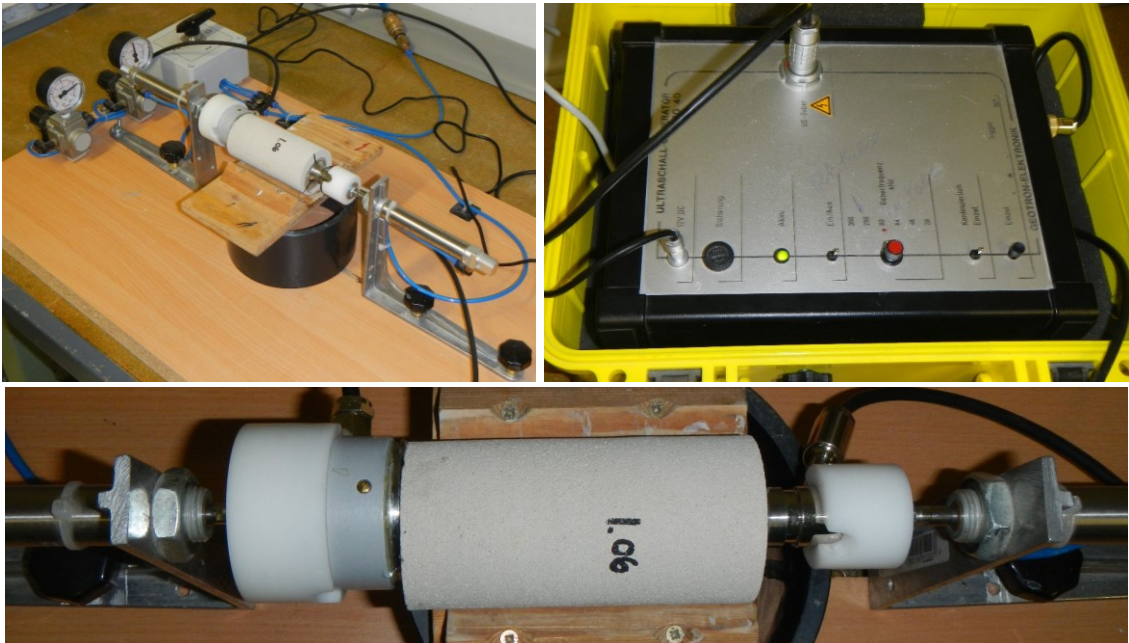


Figure 204: Ultrasound-test set-up.

Table 76 shows the measurement results of the mortar samples.

Table 76: Results of the ultrasound-tests on the mortar samples.

Sample	L [mm]	T _p [μs]	T _s [μs]	C _p [m/s]	C _s [m/s]	C _s /C _p
mt1-705	102.17	34.9	50.6	2928	2019	0.69
mt1-707	103.76	33.3	51.1	3116	2030	0.65
mt1-708	101.64	32.9	48.6	3089	2091	0.68
mt1-709	105.87	34.1	49.8	3105	2128	0.69
mt1-710	96.13	31.1	46.7	3091	2058	0.67
mt1-711	103.59	33.4	50.7	3101	2043	0.66
mt1-712	100.50	33.1	49.3	3036	2039	0.67
mt1-713	101.44	32.9	48.1	3083	2111	0.68
Ave:				3069	2065	
Std:				61.8	40.2	
Std [%]:				2.0	1.9	

Table 77 shows the measurement results of the granite samples.

Table 77: Results of the ultrasound-tests on the granite samples. The rows marked blue are repeated measurements with an additional layer of ultrasound paste. The rows marked red were excluded as outliers.

Sample	L [mm]	T _p [μs]	T _s [μs]	C _p [m/s]	C _s [m/s]	C _s /C _p
gt1-101	100.17	20.4	37.6	4910	2664	0.54
gt1-102	99.08	20.3	30.8	4881	3217	0.66
gt1-103	100.49	20.5	32.4	4902	3101	0.63
gt1-103	101.06	20.4	30.4	4954	3324	0.67
gt1-104	104.49	21.8	31.7	4793	3296	0.69
gt1-105	101.36	20.8	31.5	4873	3218	0.66
gt1-105	101.99	20.7	31.1	4927	3279	0.67
gt1-106	97.83	20.2	31.2	4843	3135	0.65
gt1-107	99.05	20.4	30.5	4855	3247	0.67
gt1-108	99.53	21.0	31.5	4739	3160	0.67
gt1-109	102.60	21.4	32.0	4795	3206	0.67
gt1-109	103.17	20.7	31.8	4984	3244	0.65
gt1-110	100.14	21.0	31.0	4769	3230	0.68
gt1-111	101.03	20.7	31.4	4881	3217	0.66
gt1-112	101.39	21.0	32.2	4828	3149	0.65
gt1-112	102.00	20.7	30.3	4928	3366	0.68
gt1-211	102.81	20.6	30.4	4991	3382	0.68
gt1-212	102.70	20.4	31.8	5034	3230	0.64
gt1-213	101.89	19.6	31.6	5198	3224	0.62
gt1-213	102.52	20.2	30.6	5075	3350	0.66
Ave:				4892	3242	
Std:				92	80	
Std [%]:				1.9	2.5	

The arrival times of the P-wave (T_p) and the S-wave (T_s) were measured two to three times per sample with different relative position of the probes. This change in the probe position altered the signal phase. The measured signals were exported and further processed (i.e., submitted to noise filtering and data-point read-out) in MATLAB®.

For each sample, the signals were filtered from noise and aligned on the same graph (Figure 205). This allowed for determining the arrival times more precisely.

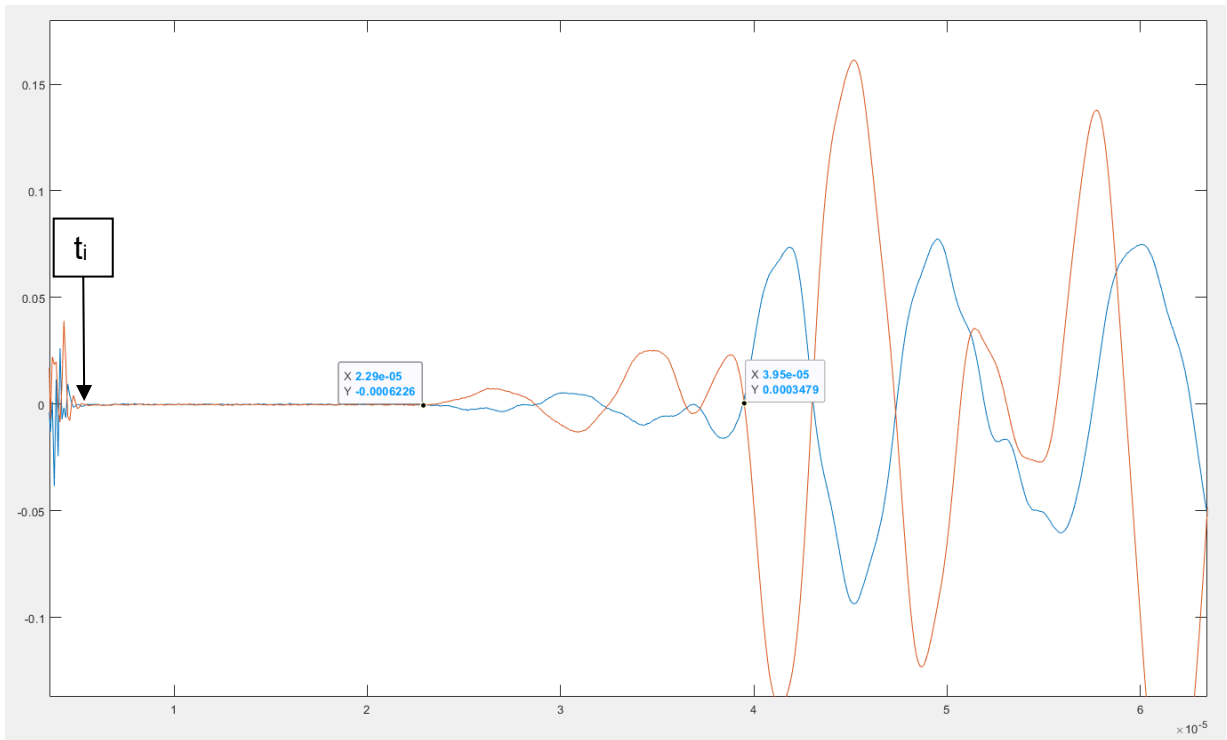


Figure 205: Aligned measurement signals for sample gt1-104 (granite). The noted data points indicate T_p (left) and T_s (right). These time values were further corrected by subtracting the time of signal initiation (t_i) from them.

Sound impedance was calculated for the blasted materials (Z_{bm}) and for the damping material (Z_{damp} [kg/m²s]) from the corresponding material density (ρ) and P-wave velocity (C_p) as (Z.-X. Zhang, 2016):

$$Z = \rho \cdot C_p$$

Equation 65

Table 78 shows the measurement results of the damping-material samples.

Table 78: Results of the ultrasound-tests on the damping-material samples. The row marked red was excluded as an outlier.

Sample	L [mm]	Tp [μs]	Ts [μs]	ρ [g/cm ³]	C _p [m/s]	C _s [m/s]	C _s /C _p	Z _{damp} [kg/m ² s]
d1	150.80	130.4	228.8	2.20	1166.82	603.43	0.52	2556189.2
d2	152.64	135.2	260.0	2.18	1314.91	765.51	0.58	2880607.7
d3	155.82	100.0	244.4	2.21	1545.21	648.22	0.42	3385129.3
d4	150.04	185.6	284.8	2.18	813.50	554.54	0.68	1782143.8
Ave:				2.19	1098	641	0.59	2406314
Std:				0.01	257.6	110.4	0.08	564360
Std [%]:				0.7	23.5	17.2	14.0	23.5

The impedance-matching index (*i*) was calculated for both blasted materials as (Z.-X. Zhang, 2016):

$$i = \frac{Z_{bm}}{Z_{damp}} \quad \text{Equation 66}$$

The values of *i* were then used to calculate the wave-transfer (CT) and the wave-reflection (CR) coefficients (Z.-X. Zhang, 2016):

$$CT = \frac{2i}{i + 1} \quad \text{Equation 67}$$

$$CR = \frac{i - 1}{i + 1} \quad \text{Equation 68}$$

Table 79 shows calculated values of Z_{bm}, *i*, CT, and CR for the blasted materials, considering the stress-wave interaction with the surrounding damping layer (i.e., the outer boundary, mantle, of the blasted cylinders).

Table 79: Summary of calculated sound impedance (Z_{bm}), impedance-matching index (*i*), wave-transfer coefficient (CT), and wave-reflection coefficient (CR), for the blasted materials.

Material	ρ [g/cm ³]	C _p [m/s]	Z _{bm} [kg/m ² s]	<i>i</i> [-]	CT [-]	CR [-]
Granite	2.75	4892	13452296	0.179	0.30	-0.70
Mortar	1.66	3069	5093979	0.472	0.64	-0.36

Equation 1 and Equation 2 were used to calculate the dynamic Poisson ratio (μ_{dyn}), the dynamic Young's modulus (E_{dyn}), and the dynamic shear modulus (G_{dyn}), as follows:

$$\mu_{dyn} = \frac{2 \cdot \left(\frac{C_s}{C_p}\right)^2 - 1}{2 \cdot \left(\left(\frac{C_s}{C_p}\right)^2 - 1\right)} \quad \text{Equation 69}$$

$$E_{dyn} = C_p^2 \cdot \rho \left[\frac{(1 + \mu_{dyn})(1 - 2\mu_{dyn})}{1 - \mu_{dyn}} \right] \quad \text{Equation 70}$$

$$G_{dyn} = \frac{E_{dyn}}{2 \cdot (1 + \mu_{dyn})} = C_s^2 \cdot \rho \quad \text{Equation 71}$$

Table 80 shows a summary of calculated values for μ_{dyn} , E_{dyn} , and G_{dyn} .

Table 80: Summary of calculated values for the dynamic Poisson ratio (μ_{dyn}), the dynamic Young's modulus (E_{dyn}), and the dynamic shear modulus (G_{dyn}).

Material	μ_{dyn} [-]	E_{dyn} [GPa]	G_{dyn} [GPa]
Granite	0.108	64.076	28.904
Mortar	0.086	15.380	7.079
Damping	0.187	2.266	0.954

Wedge splitting test (WST)

The WSTs were carried out at the Chair of Ceramics (MUL). Figure 206 shows the test set-up.

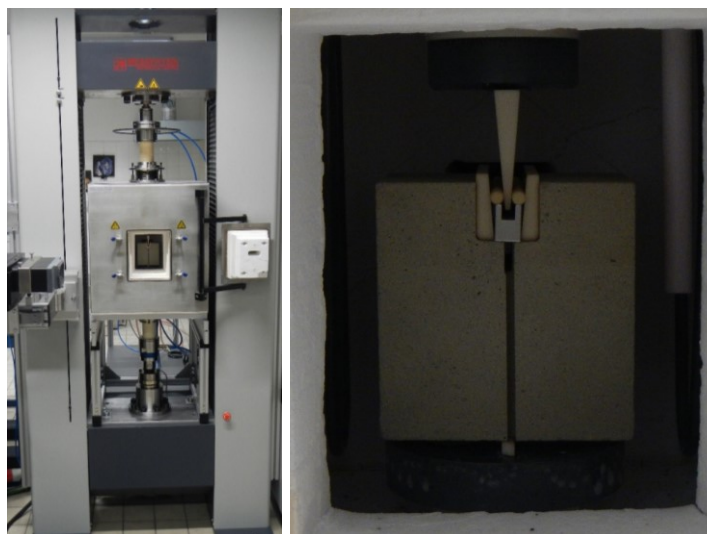


Figure 206: WST set-up.

Figure 207 shows measurement plots from the WSTs.

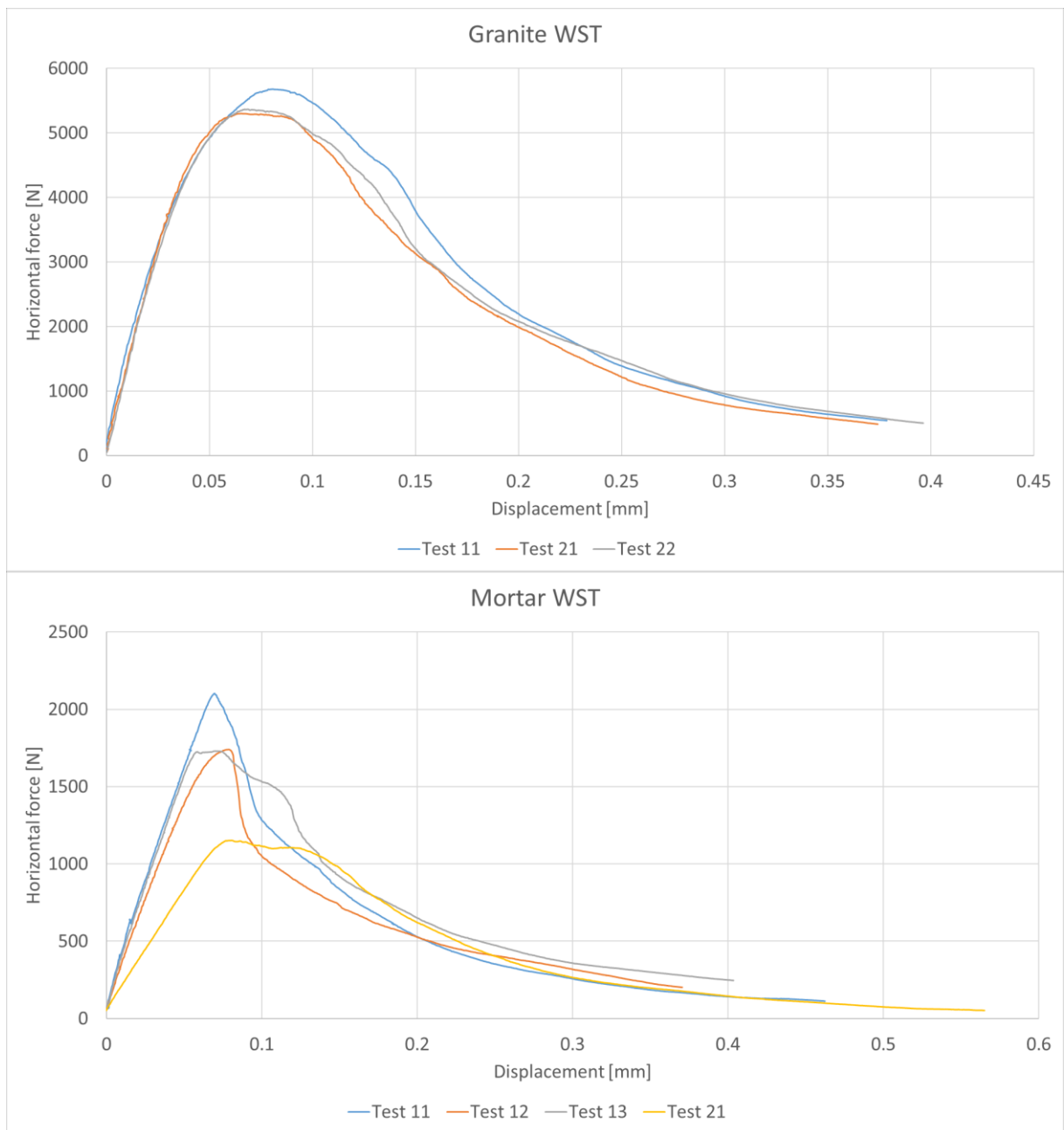


Figure 207: Measurement plots from the WSTs

As shown by the measurement plots in Figure 207, some difficulties were encountered during the tests on the mortar samples. Compared to those for the granite, the mortar test result deviate more from their average value. Accordingly, the resulting fracture surfaces in the mortar samples are different to those in the granite ones (Figure 208).



Figure 208: Typical resulting fracture surfaces from WSTs on the granite (top) and the mortar (bottom).

Such fracture surfaces resulting from WSTs have already been reported regarding a similar material. Khormali (2012) indicated this phenomenon in the magnetic mortar used in the research of Schimek (2015) and Ivanova (2015). He pointed out that the crack deviation (i.e., the resulting fracture-surface roughness) was smaller in water-saturated samples than the dry ones of this material (Figure 209). This relation indicates the effect of material porosity on crack propagation in such materials.

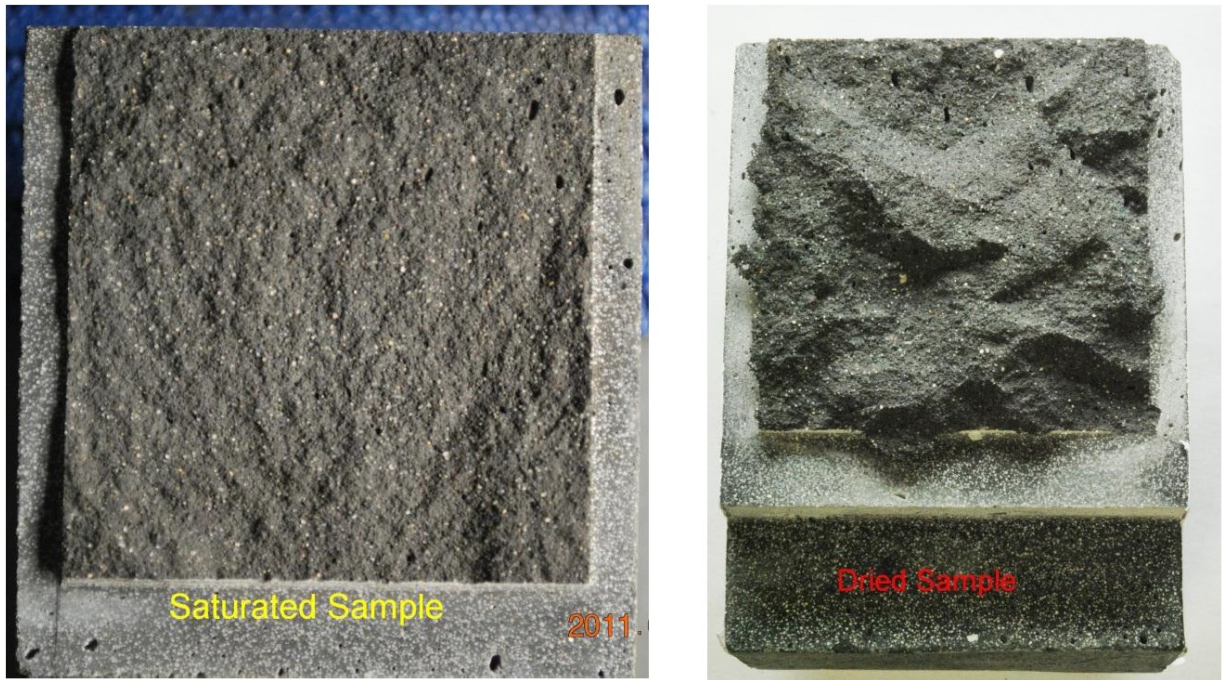


Figure 209: Fracture surfaces in WST samples of magnetic mortar – water-saturated sample (left) and dry sample (right) (Khormali, 2012).

Table 81 shows obtained results from the WSTs.

Table 81: Final WST results.

Material	Test	Sample	σ [N/mm ²]	G_f [N/m]	F_{max} [N]	$F_{h,max}$ [N]
Mortar	11	mtc-703	9.85	245.96	993.28	5676.59
	21	mtc-701	9.20	220.98	927.21	5299.03
	22	mtc-702	9.31	235.31	939.01	5366.47
Average:			9.45	234.08	953.17	5447.36
Granite	11	gtc-101	3.65	63.5	367.89	2102.47
	12	gtc-102	3.02	60.9	304.55	1740.51
	13	gtc-103	3.00	77.2	302.72	1730.02
	21	gtc-201	3.41	67.2	201.67	1152.52
Average (11;12;13):			3.27	67.22	294.20	1681.38

Static (K_{F-s}) and dynamic (K_{F-d}) critical stress-intensity factors were calculated as (Rice, 1964; Kanninen et al., 1988):

$$K_{F-s} = \sqrt{G_{f'} \cdot \frac{E}{1 - \mu^2}} \quad \text{Equation 72}$$

$$K_{F-d} = \sqrt{G_{f'} \cdot \frac{E_{dyn}}{1 - \mu_{dyn}^2}} \quad \text{Equation 73}$$

where:

E – static Young’s modulus (from UCS tests),

μ – static Poisson ratio,

E_{dyn} - dynamic Young’s modulus (from the ultrasound tests), and

μ_{dyn} – dynamic Poisson ratio.

Table 82 shows calculated K_{F-s} and K_{F-d} .

Table 82: Calculated critical stress-intensity factors.

Material	$G_{f'}$ [N/m]	E [GPa]	E_{dyn} [GPa]	μ [-]	μ_{dyn} [-]	K_{F-s} [MPa/\sqrt{m}]	K_{F-d} [MPa/\sqrt{m}]
Granite	67.22	65.30	64.08	0.24	0.11	2.16	2.09
Mortar	234.08	12.2	15.38	0.23	0.09	1.74	1.91

Preliminary deformation

Although the blast loading induces fracturing and other deformation in the blasted material, the resulting traces of fracturing/deformation mechanisms might have been there even before the blasting process.

Preliminary (before the blasting) deformation in the granite on this scale of observation was affected by complex mechanisms and stress/strain transitions during the genesis of the material due to complex tectonics and metamorphic processes (Vernon, 2018). Figure 210 shows an example of fracturing in adjacent quartz and feldspar grains induced by oscillatory concentric zoning in a plagioclase grain.

“Most of the plagioclase grains are actually anhedral, despite the euhedral growth zoning produced when the crystal was growing freely in a liquid. Irregularities in the boundaries of plagioclase against other minerals are due to fortuitous impingement and mutual interference of these minerals as they crystallized from interstitial melt. Some solid-state adjustment during cooling may have contributed to the irregularities in an attempt to minimize local interfacial energies, but the evidence is not clear.” (Vernon, 2018)

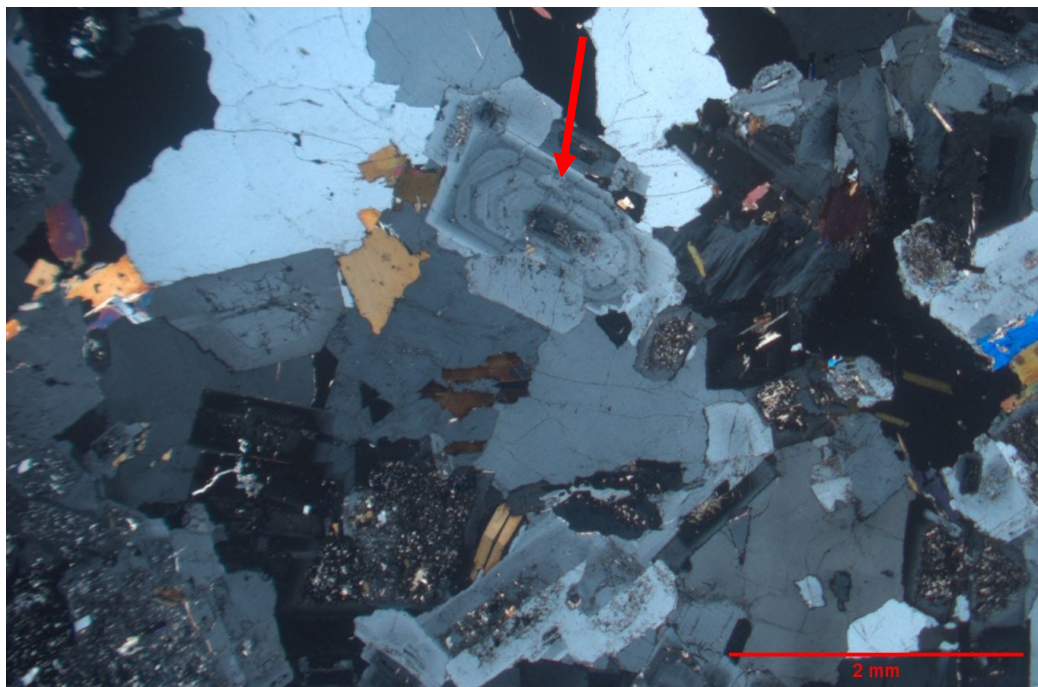


Figure 210: Oscillatory concentric zoning (indicated by the red arrow) in a plagioclase grain induced fracturing in adjacent quartz and feldspar grains (about 20 mm from the borehole). CPL optical micrographs.

This Figure also shows that most of this fracturing in the quartz grains occurred near sharp edges of the intergranular boundaries and around intermediate grains of different Young's modulus (brown mica grains in the Figure), i.e., due to elastic mismatch covered in Section 4.4.4 (Blenkinsop, 2007).

Figure 211 shows an example of fractures filled up with intrusive material. These light-coloured fractures in the micrograph are prone to affecting blast fracturing due to their orientation and elastic mismatch.

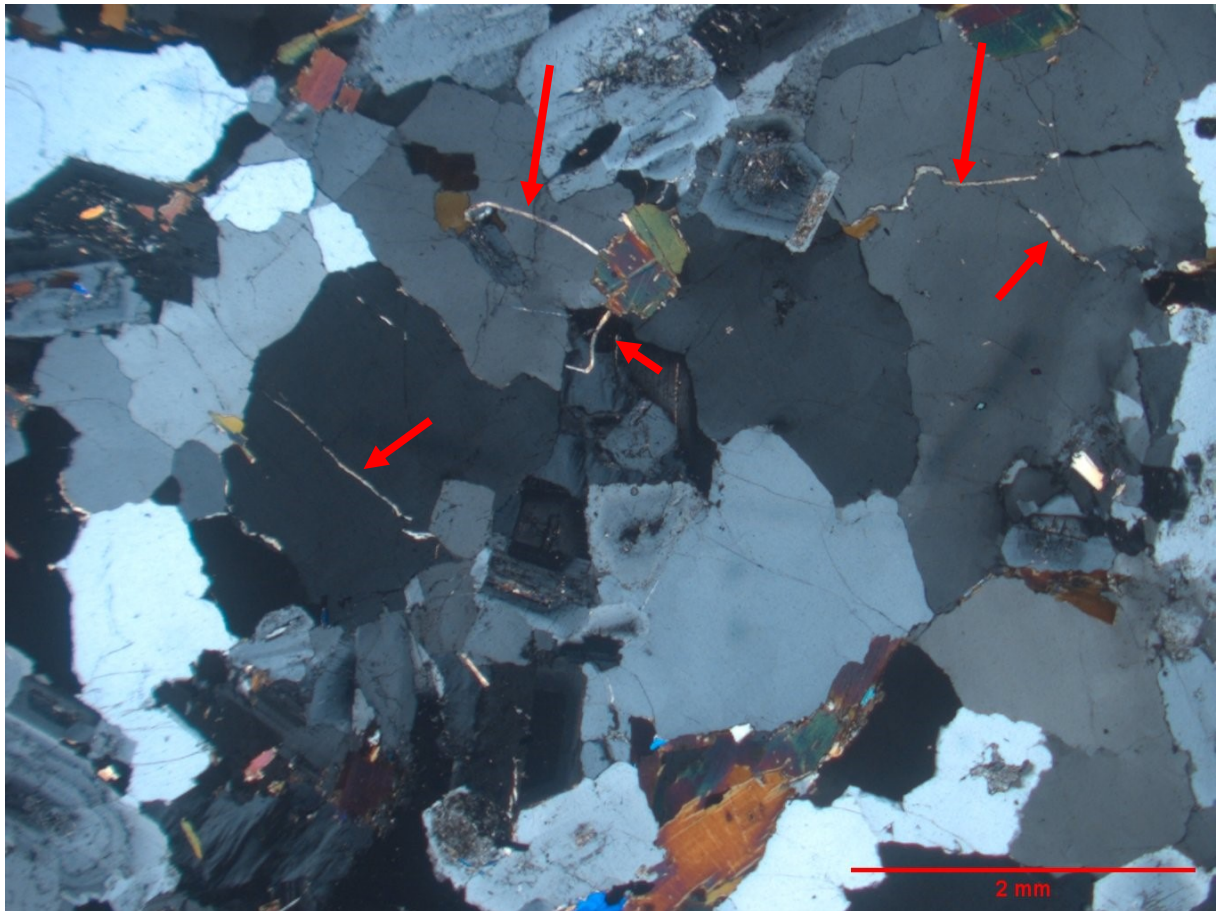


Figure 211: Solidified intrusions (light yellow, indicated by the red arrows) in preceding fractures in quartz and feldspar grains (about 10 mm from the borehole). CPL optical micrograph.

Figure 212 shows another example of inclusion-induced fracturing. Here, grains of plagioclase and feldspar had been nucleated in larger host quartz grains. Further growth these internal grains induced fractures in the host grains. This figure also shows fracturing around sharp corners of the boundaries between elongated feldspar/plagioclase grains and larger surrounding quartz grains.

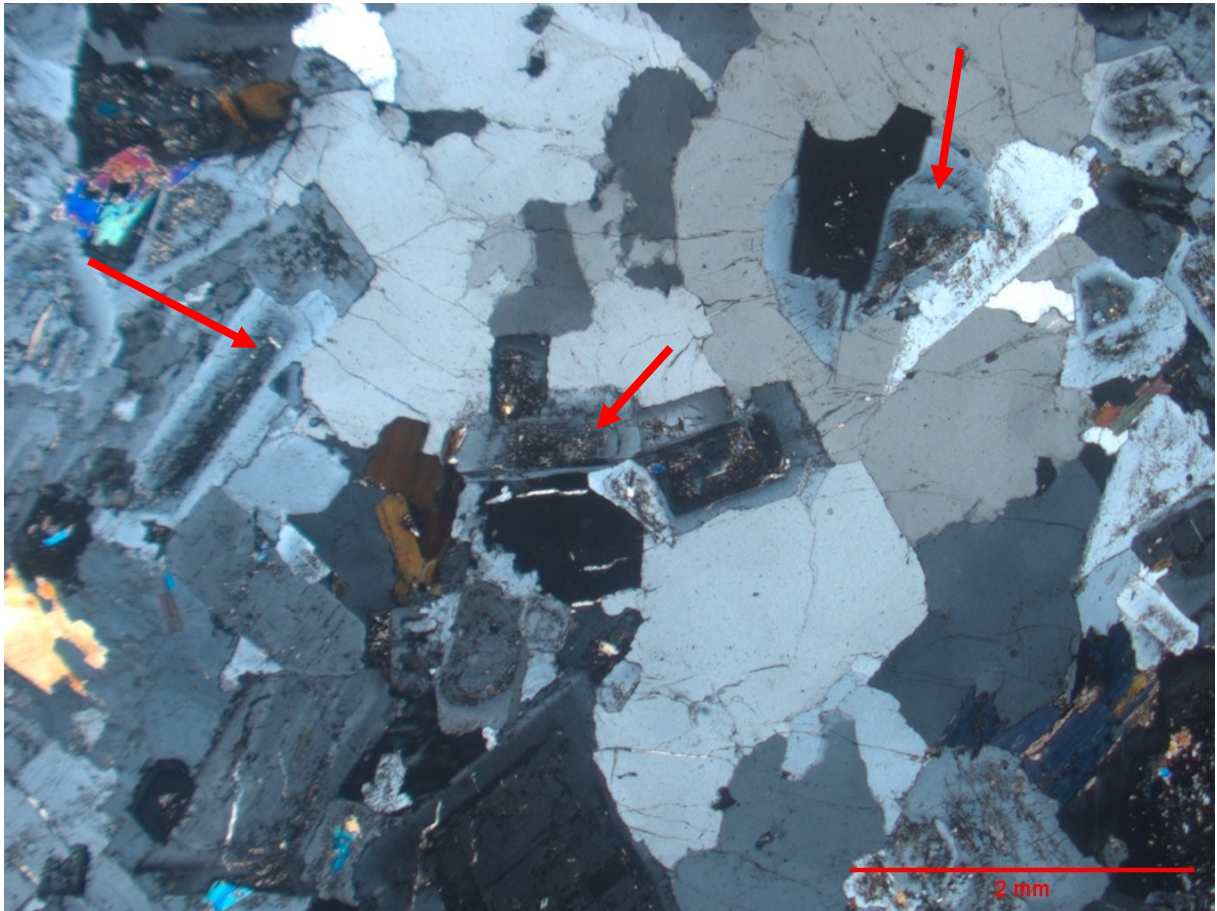


Figure 212: Fractures in host quartz grains formed by growth of smaller feldspar and plagioclase grains therein (indicated by the red arrows) (about 15 mm from the borehole). Sharp boundary interfaces between crystals can also induce impingement fractures and elastic-mismatch cracking. CPL optical micrograph.

Figure 213 and show examples of lamellar fractures in quartz and feldspar grains and fractures around corners of elongated mica grains.

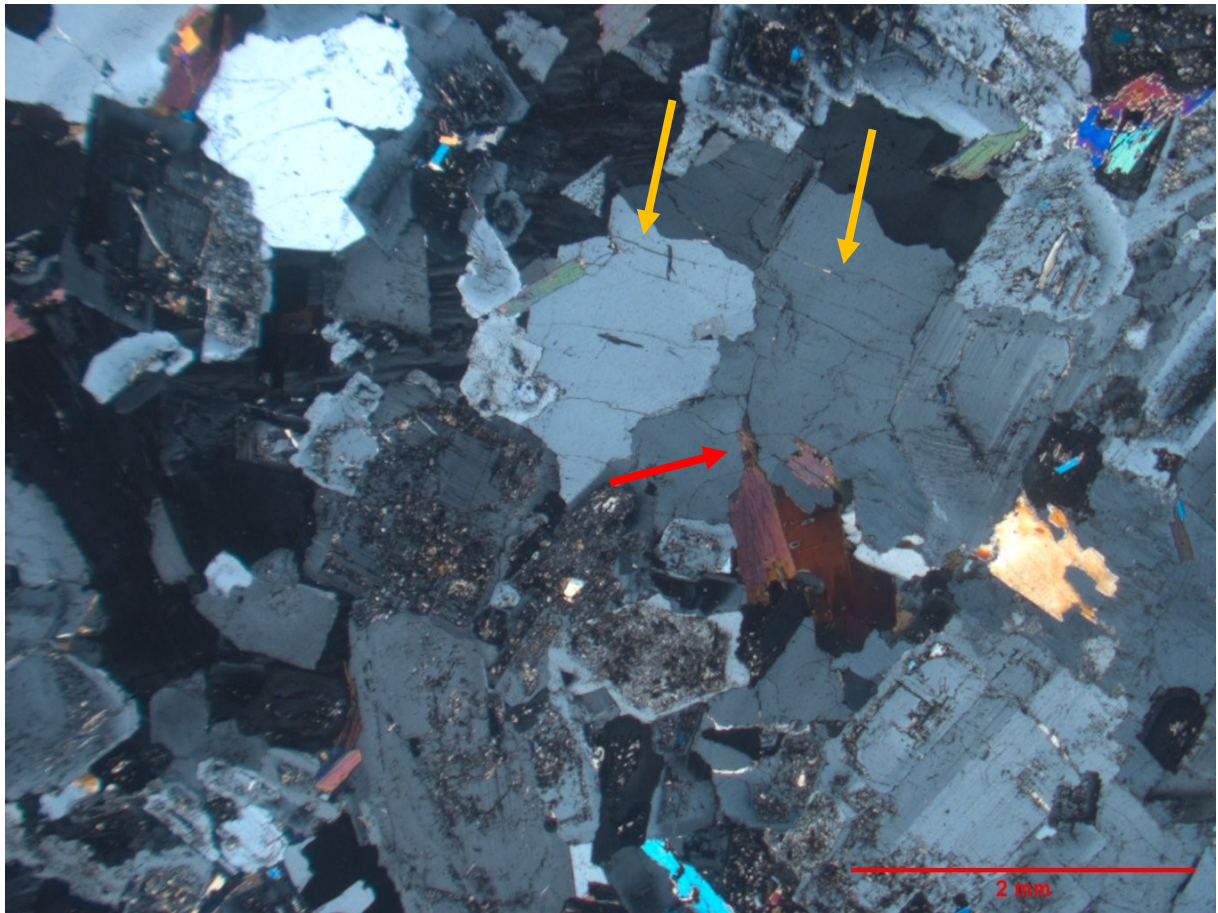


Figure 213: Lamellar fractures (indicated by the orange arrows) in quartz and feldspar grains and fractures around corners of elongated mica grains (red and brown, indicated by the red arrow) (about 25 mm from the borehole). CPL optical micrograph.

These fractures can also pass through multiple crystal grains seemingly without changing the propagation orientation.

Relative movement of crystal grains in the granite during its genesis might lead to rupture of softer lamellar (mica) grains. Figure 214 shows such an example, where a mica grain, surrounded by quartz grains, was stretched and bent. Such traces of rupture failure might seem like a result of blast-induced fracturing in the post-blast samples. To avoid such misinterpretation, a wider range around such deformation features was carefully observed to evaluate if they could have been generated by blast-induced cracking.

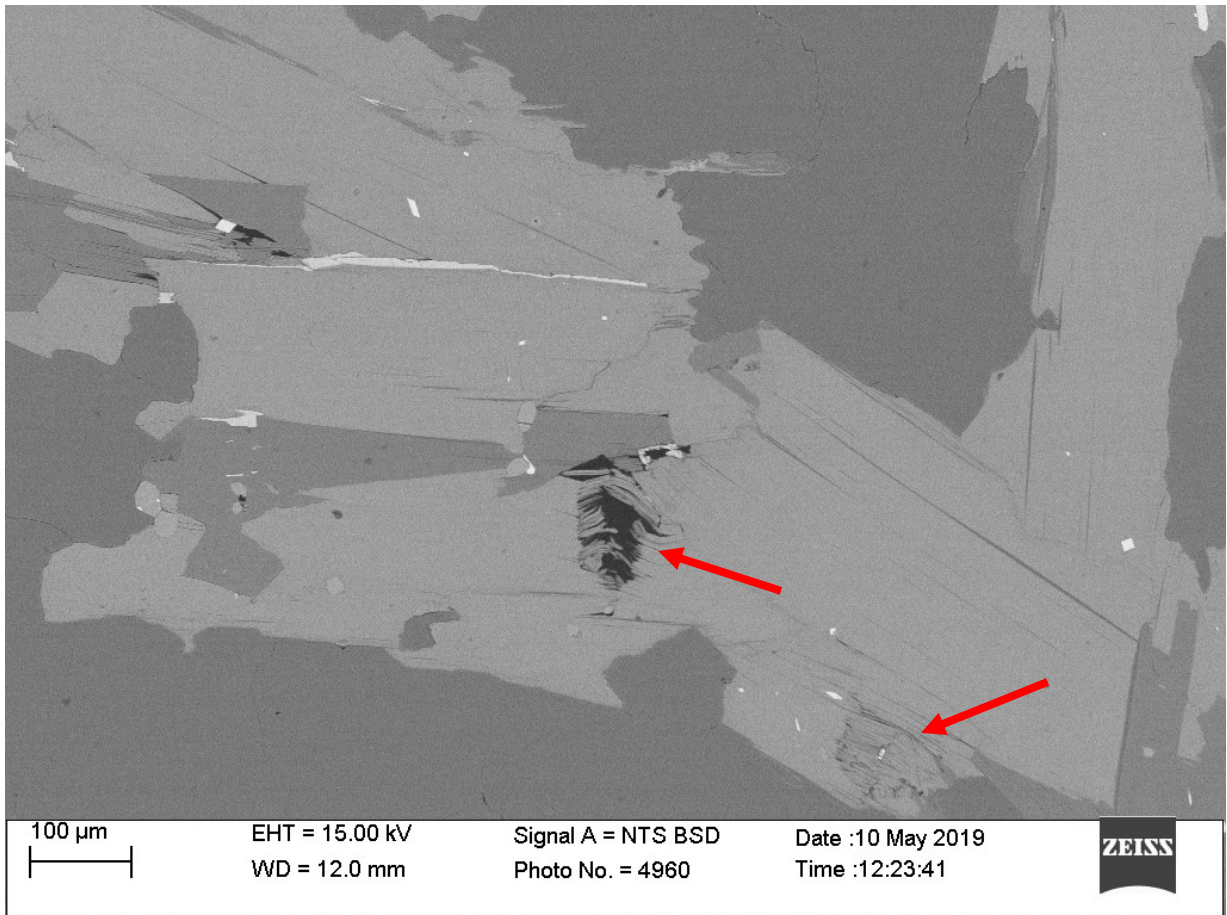


Figure 214: Complex failure including longitudinal rupture and shearing of a biotite grain (light grey, indicated by the red arrows), surrounded by quartz grains (dark grey) (about 18 mm from the borehole). SEM micrograph.

In a similar case, a mica grain can be split apart along one of its cleavage planes, leaving a gap in between that is further filled up by intrusion, later crystalized as, e.g., feldspar or quartz (Figure 215). Due to the difference in the elastic properties of these grains, a blast-induced crack may most likely propagate through such a gap during blast, and make it seem like the mica grain was directly split in half by the crack.

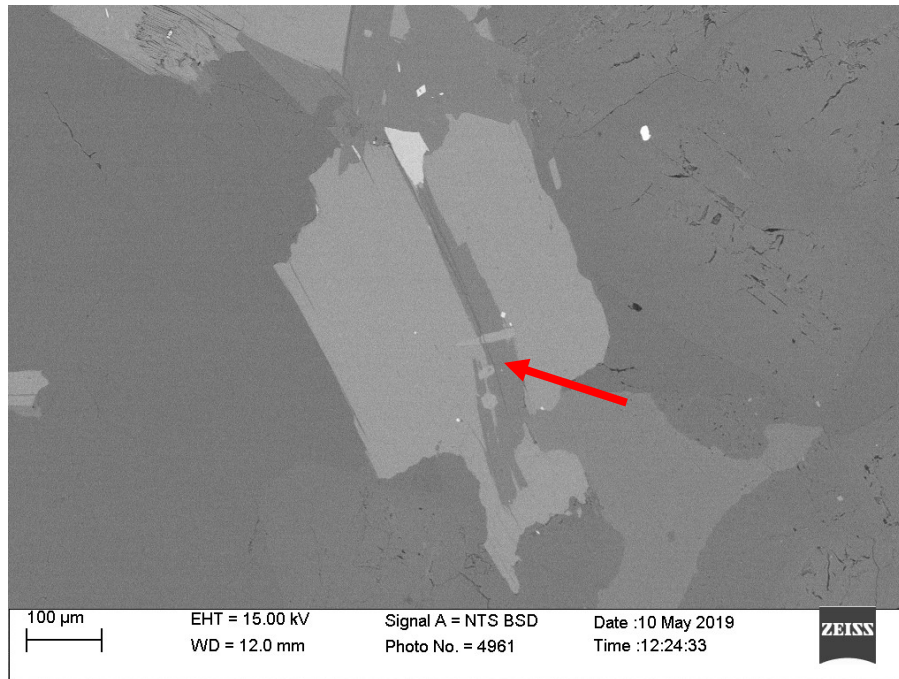


Figure 215: A biotite grain (light grey) split in half during the material genesis and filled-up by later-crystallized feldspar (darker grey, indicated by the red arrow), surrounded by quartz grains (dark grey) (about 20 mm from the borehole). SEM micrograph.

Therefore, the arrangement of crystal grains in the granite directly affects blast-induced fracturing and may result in misleading appearance of the post-blast fractures.

The grains can be arranged to provide a favourable path for a propagating blast-induced crack. Figure 216 shows such a case, where a mica grain is in contact with an already cracked feldspar grain. The feldspar crack is in line (i.e., probably also in plane in 3D) with the cleavage planes of the mica grain.

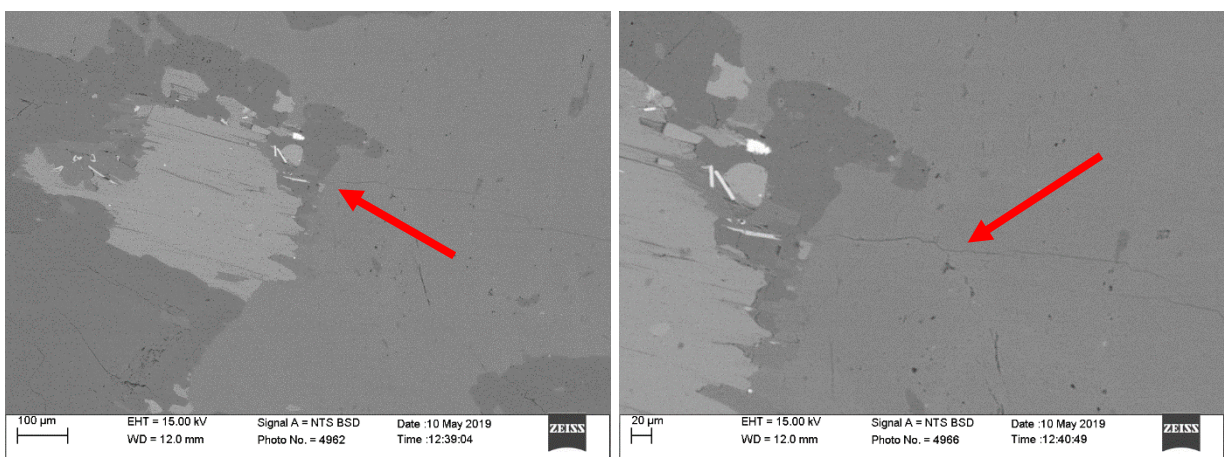


Figure 216: A biotite grain (light grey) positioned in line with a crack (indicated by the red arrows) in the adjacent feldspar grain (darker grey), both surrounded by quartz grains (dark grey) (about 30 mm from the borehole). SEM micrograph.

In the mortar, shrinking cracks are generated due to uneven hardening during the cement curing of the material (Figure 217).

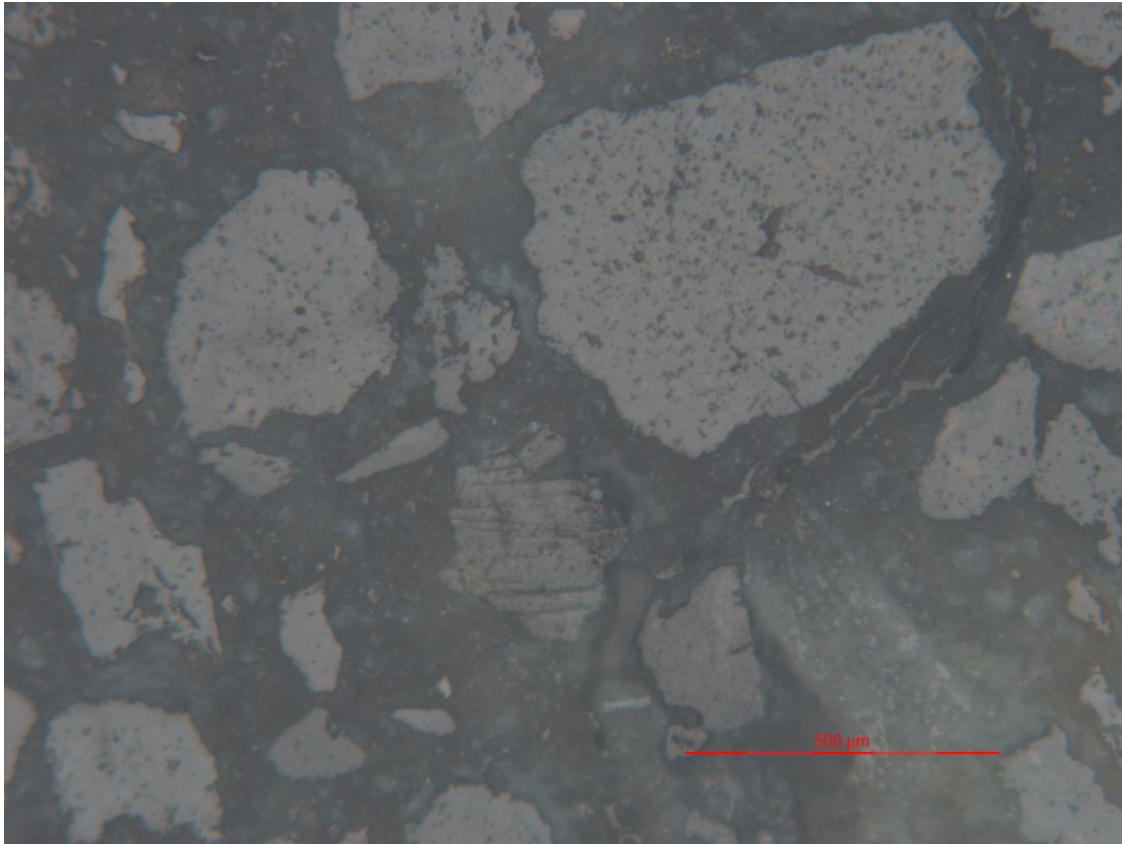


Figure 217: Shrinkage micro-cracks in the cement matrix around a large quartz grain (about 15 mm from the borehole). PPL optical micrograph.

The porosity of the mortar further increases the final preliminary deformation as the shrinkage micro-cracks interconnect with the pores and weaken the material's structure (Figure 218).

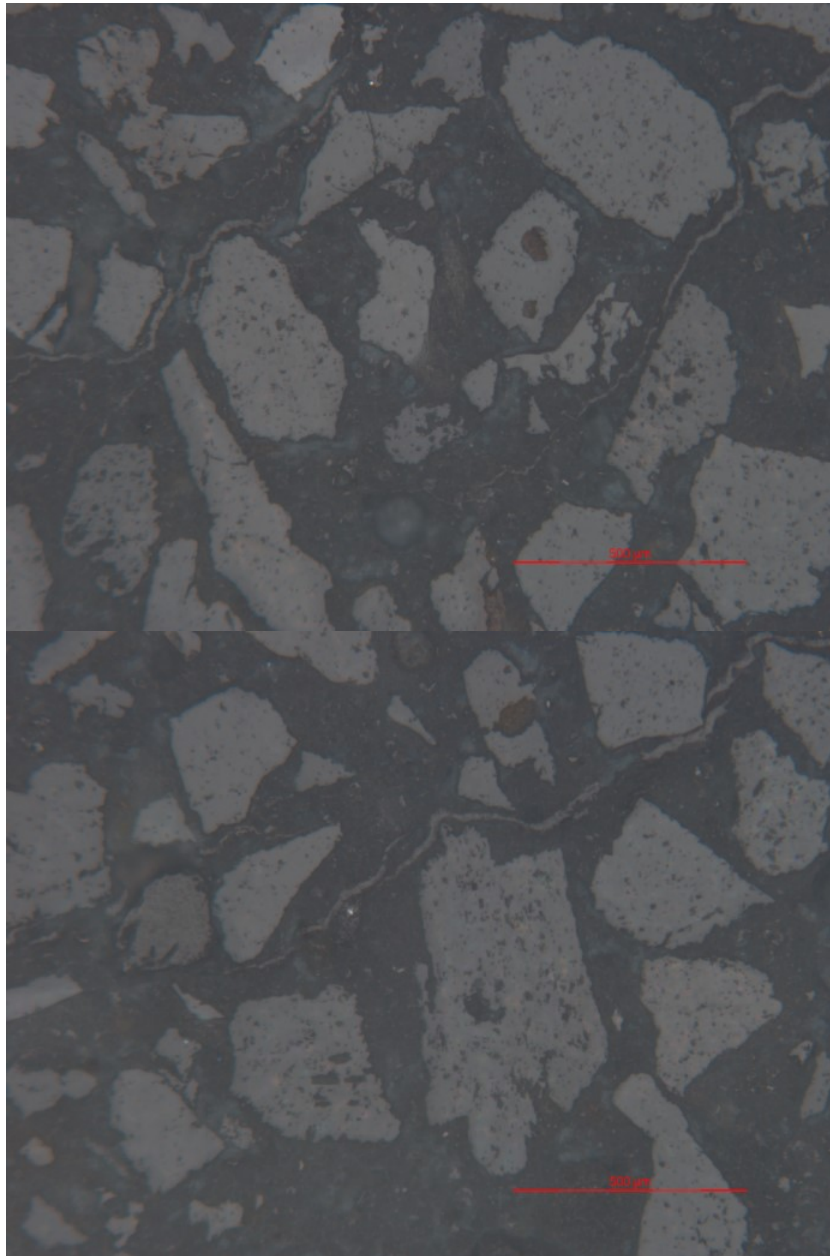


Figure 218: Shrinkage micro-cracks in the cement matrix between quartz grains (about 10 mm from the borehole). PPL optical micrograph.

Some quartz grains may already be cracked before the cylinder production due to, e.g., prior material handling of the quartz sand (Figure 219).

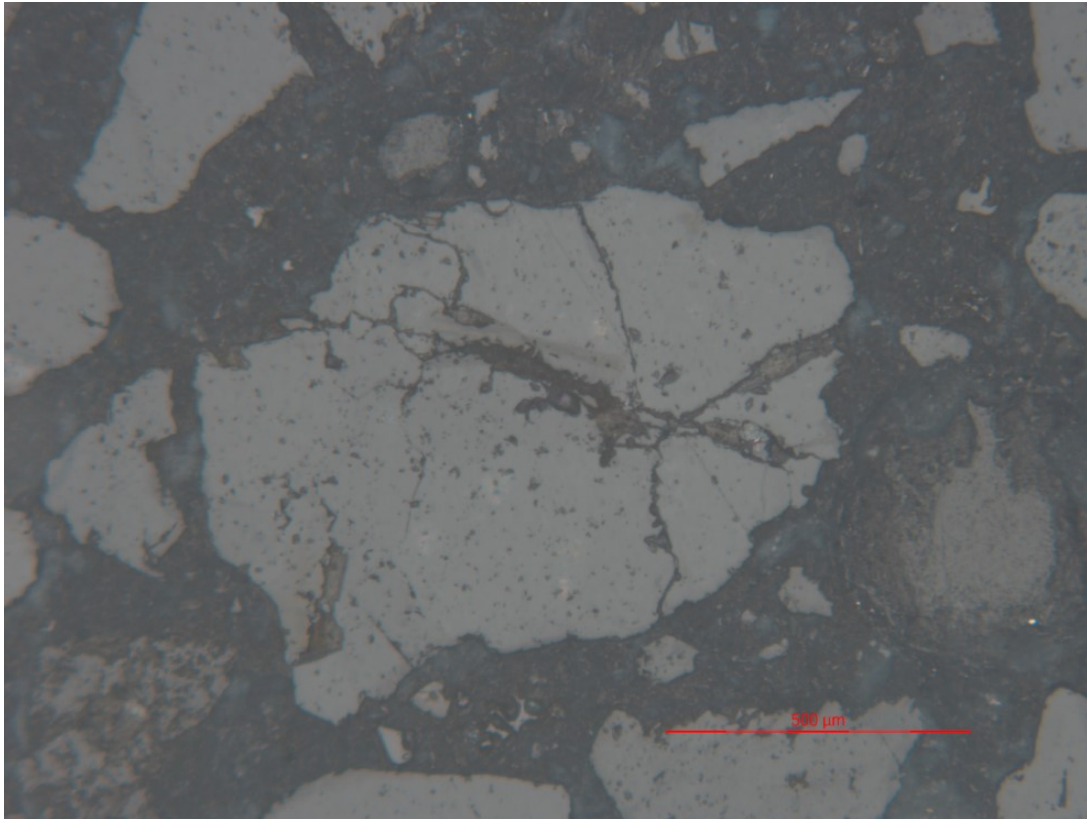


Figure 219: Already fractured quartz grain in the cement matrix in a non-blasted mortar sample (about 25 mm from the borehole). PPL optical micrograph.

The production and processing of the blasted cylinders potentially increase this deformation due to the core drilling of the cylinders and the borehole drilling in the granite and due to the casing of the cylinders and formation of the borehole in the mortar.

Figure 220 shows a segment of the borehole wall in a thin section of a non-blasted granite sample.

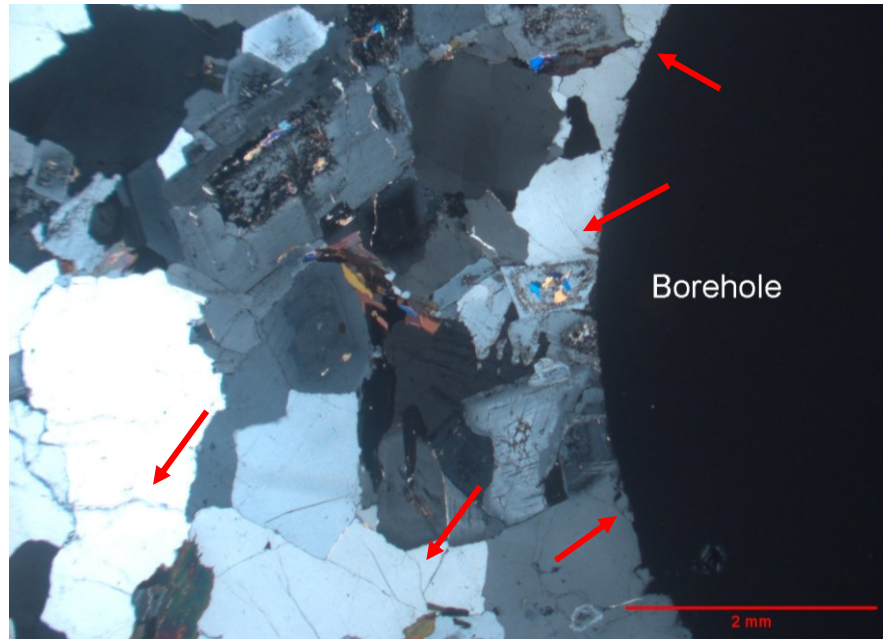


Figure 220: Segment of a borehole wall in a non-blasted granite sample. The near-borehole zone already includes some damage prior to blasting. CPL optical micrograph.

The pre-blast near-borehole damage in the granite is shown by denser fracture networks therein (e.g., in feldspar in Figure 221).

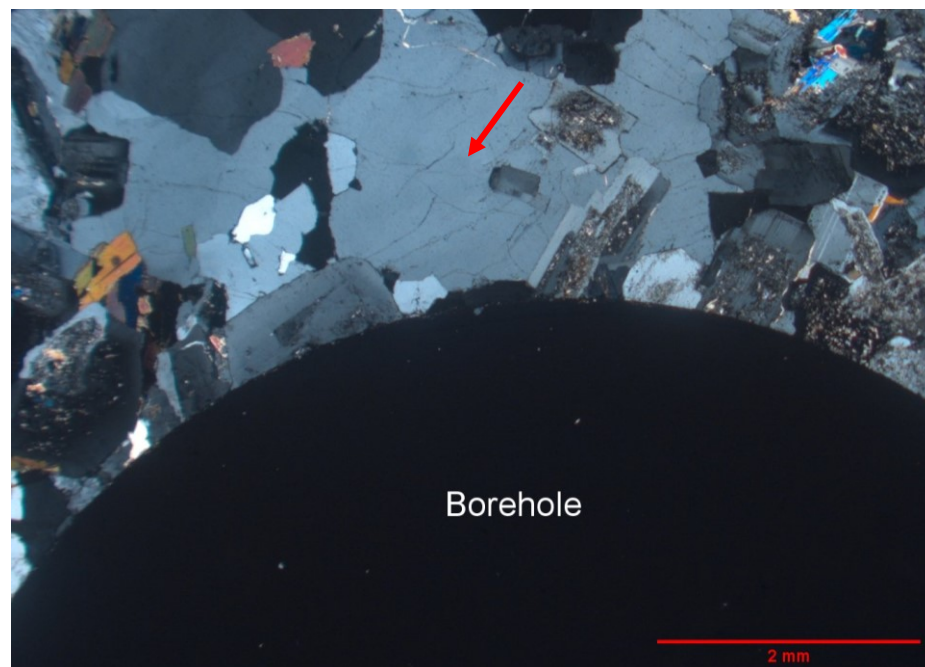


Figure 221: Segment of a borehole wall in a non-blasted granite sample. The traces of intensive fracturing in the large feldspar grains (light grey/blue) indicate possible drilling-induced damage. CPL optical micrograph.

The drill-induced cracks can also propagate radially and interact with different crystal grains. Figure 222 shows an example, where drill-induced cracks were attracted to a sharp corner of an elongated mica grain.

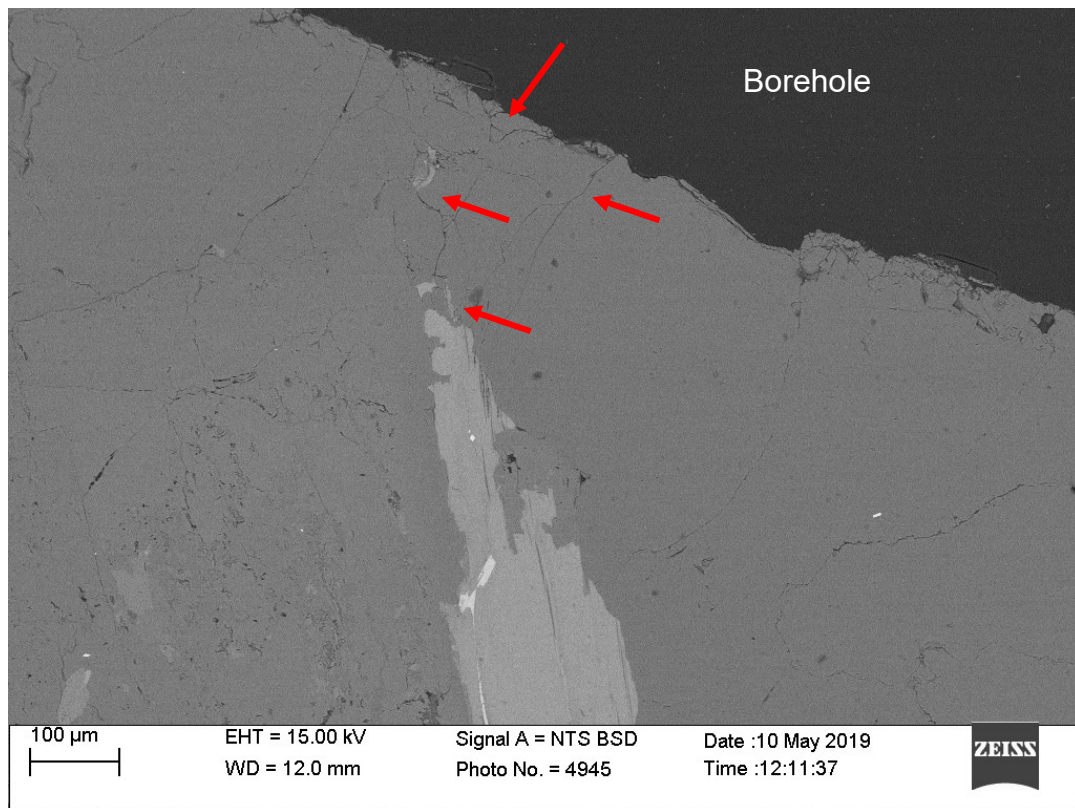


Figure 222: Drill-induced cracks propagated from the borehole (upper right corner of the image) through quartz grains (dark grey) and were attracted to a sharp corner of an elongated mica grain (light grey). SEM micrograph.

Depending on the arrangement of crystal grains, the drill-induced damage in the granite may already seem like the crushed zone before blasting (Figure 223).

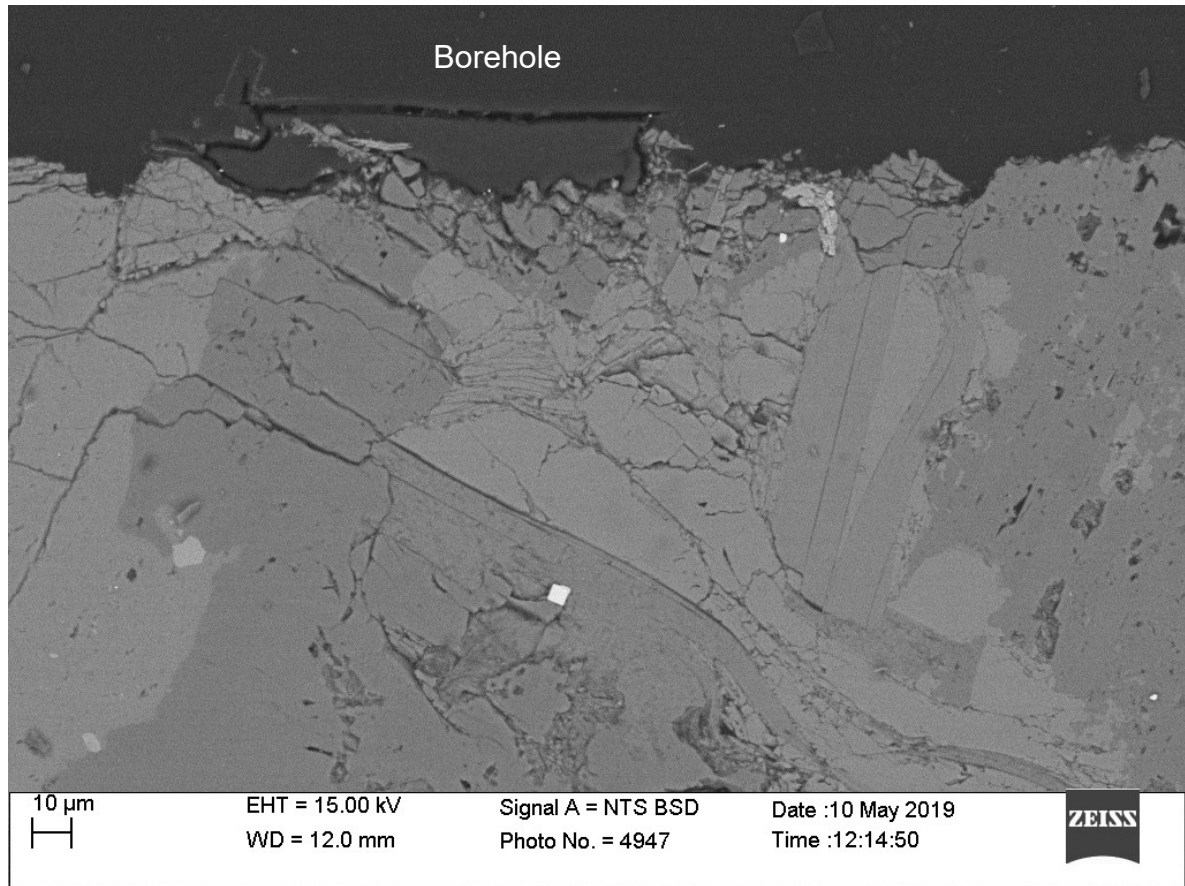


Figure 223: Severely-fractured mica and feldspar grains (light grey) near the borehole (dark grey/black, upper side of the image). SEM micrograph.

In the mortar, the near-borehole zone of non-blasted samples already includes some quartz grains with intergranular cracks/fractures (Figure 224). This damage could be a result of how the aluminium rod was extracted from the borehole during the cylinder casting (see Appendix 1).

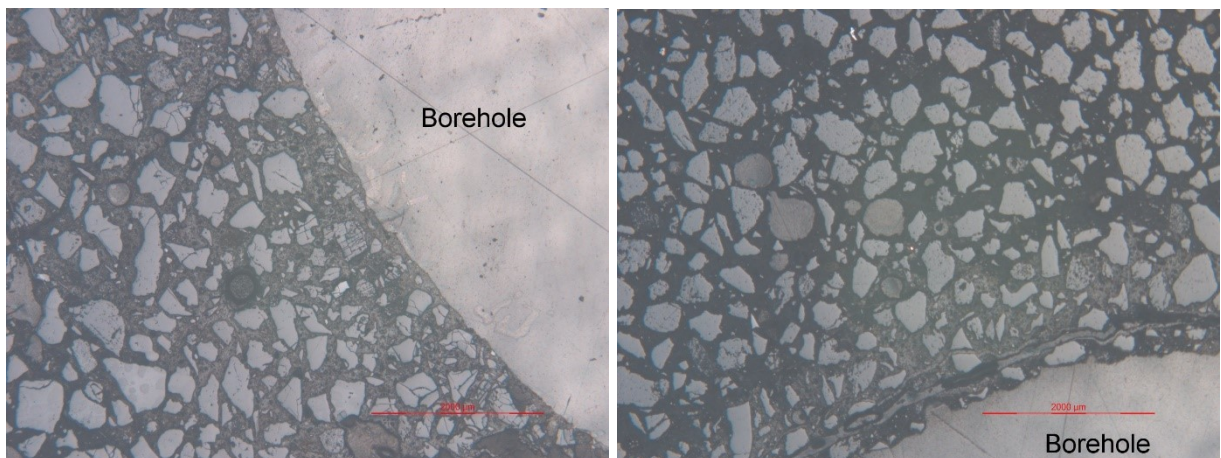


Figure 224: Internally fractured quartz grains near the borehole of a non-blasted sample. PPL optical micrographs.

However, this zone rarely exceeds 1 mm in thickness, it does not seem to have affected material porosity, and most of the contained quartz grains are not in contact with each other (Figure 225).

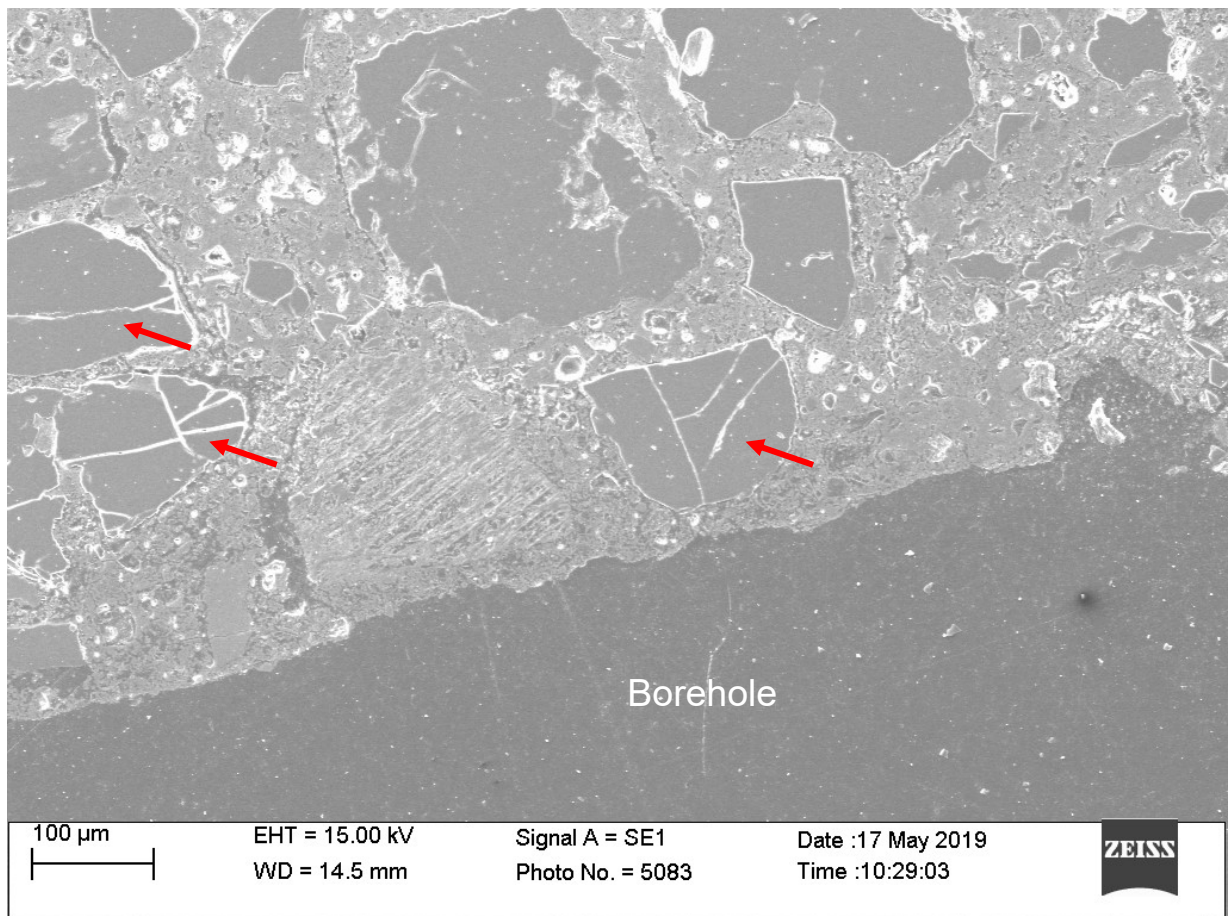


Figure 225: Internally fractured quartz grains near the borehole of a non-blasted sample. SEM micrograph.

In several cases, the thin sections of non-blasted mortar samples also show concentric tangential cracks around the borehole (Figure 226). These could have resulted during the curing due to the cement interaction with the aluminium rod. The cement material in direct contact with the rod wall could stick to it, leading to tensile stresses in its radial vicinity due to the subsequent material shrinking (i.e., surrounding material moving radially away from the borehole) or rather due to the thin-section production.

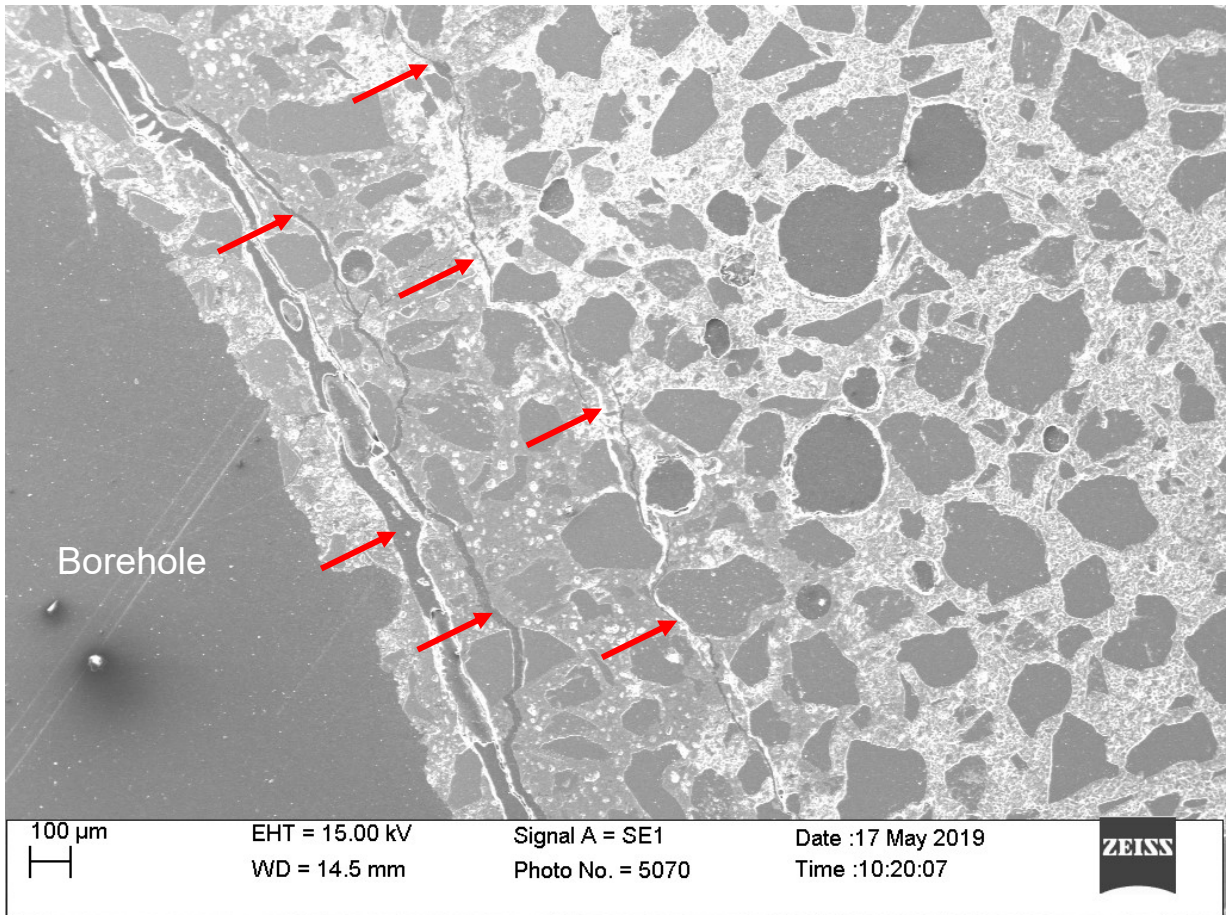


Figure 226: Tangential cracks around the borehole in a non-blasted mortar sample. The cracks were probably generated by the material shrinking during mortar curing. SEM micrograph.

Average grain size and average pore size (mortar)

This section covers the procedure and processed micrograph images to calculate the average grain size in the mortar and in the granite, with the corresponding result tables.

The results are presented with the following parameters:

- Image – Specific micrograph processed into a binary image to measure the average grain size;
- Line count – Number of lines randomly distributed in the images to export and measure their intersections with material grains;
- Grain count – Number of grains in the images intersected by the lines;
- L_{tot} – Total length of the lines per image;
- L_{line} – Total length the line intersections with the grains per image;
- d_g – Calculated average grain size per image.

Figure 227 shows example images in which grain size was measured.

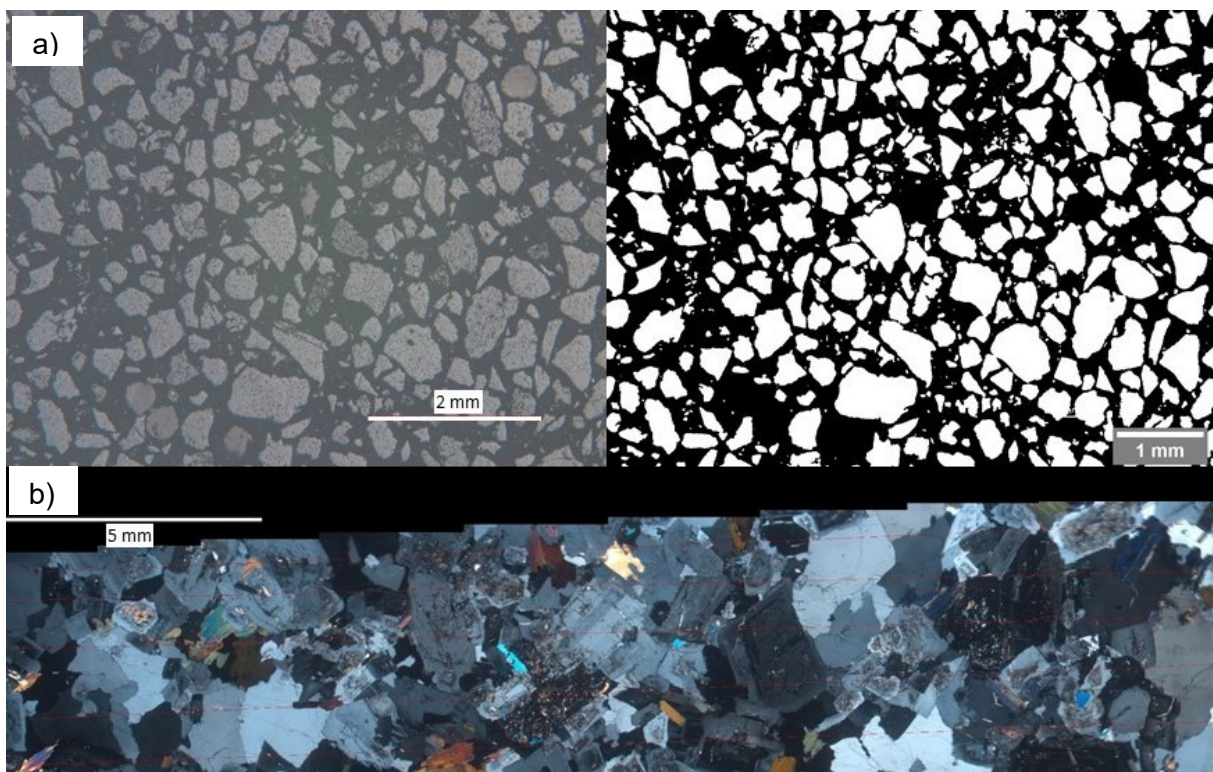


Figure 227: Grain-size measurement: a) mortar (optical micrograph with its binary version for measuring the grains); b) granite (fused image with red intercept lines).

Table 83 shows measured average grain size in thin sections of undisturbed samples of both materials. Raw result data are provided in Appendix 2. The grain size in the granite was measured as crystal size.

Table 83: Summary of measured average grain size in the thin sections.

Material	Grain size d_g [mm]		Number of images	Num. of intersection lines per image	Num. of intersected grains
	Ave	Std			
Mortar	0.137	0.042	7	5	589
Granite	0.422	0.067	5	5	1468

The average pore size in the mortar (Table 84) was measured as a part of the micro-CT (uCT) procedure (see Section 4.1.3). Here, voids of filtered ‘sphericity’ (>0.5) were measured as pores, yielding the average pore size to be 0.62 mm in the scanned mortar fragments.

Table 84: Summary of measured average pore size in the mortar.

Blast test	I_c [g/m]	Pore diameter d_p [mm]		
		Ave	Std	Data count
22.2	6	0.68	0.26	70406
20	12	0.57	0.18	49310
22.1	20	0.61	0.22	30011
Average pore size:		0.62 mm		

Figure 228 shows selected mortar images used to measure the average grain size.

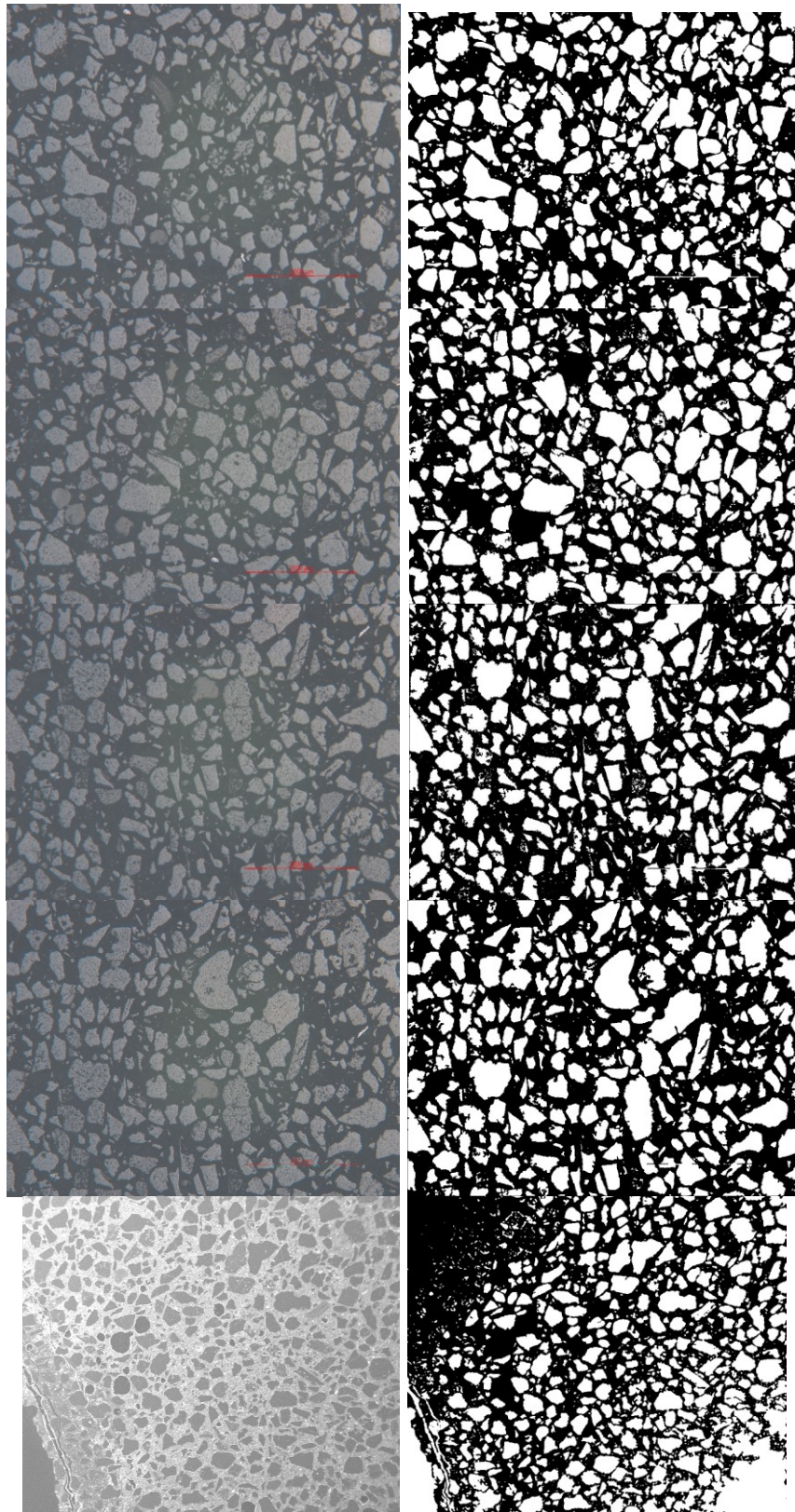


Figure 228: Selected mortar micrograph images (left column) with corresponding binary images used to measure the average grain size (right column).

Table 85 shows result data of measured average grain size in the mortar.

Table 85: Result data of measured average grain size d_g in the mortar

Image	im01	im02	im03	im04	im05	im06	im07	Ave	Std
Line count [-]	5	5	5	5	5	5	5		
Grain count [-]	105	117	67	73	82	69	76		
L_{tot} [mm]	14.34	14.49	11.09	9.52	10.18	9.73	5.98		
L_{line} [mm]	31.08	34.03	23.66	23.74	24.08	23.91	14.44		
d_g [mm]	0.14	0.12	0.17	0.13	0.12	0.14	0.08	0.14	0.04

Figure 229 shows selected granite images used to measure the average grain size.

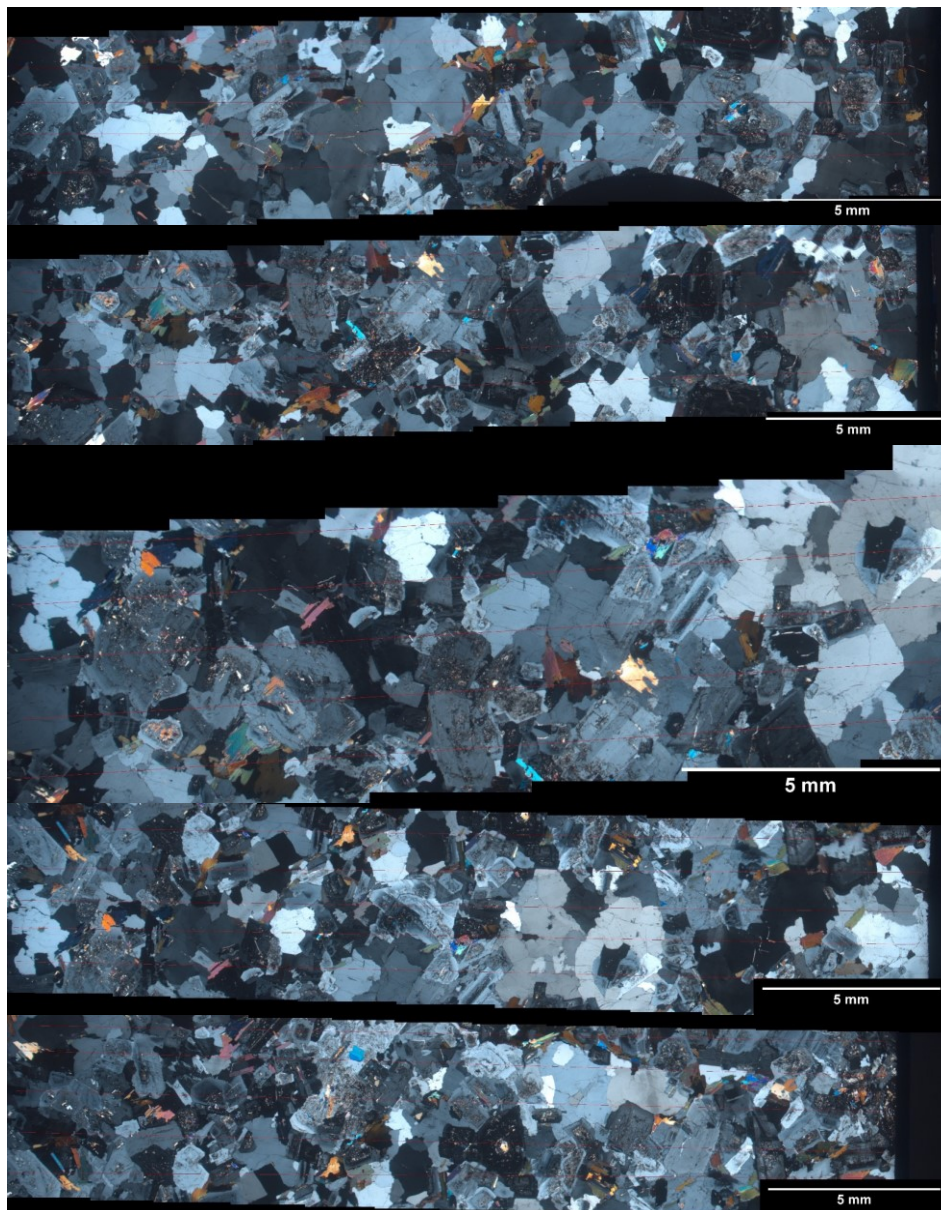


Figure 229: Selected granite micrographs used to measure the average grain size. The intersection lines are coloured red.

Table 86 shows result data of measured average grain size in the granite.

Table 86: Measured average grain size d_g in the granite

Image	im01	im02	im03	im04	im05	Ave	Std
Line count [-]	5	5	5	5	5		
Grain count [-]	325	338	200	323	282		
L_{line} [mm]	126.48	126.82	89.51	127.05	126.80		
d_g [mm]	0.40	0.38	0.45	0.39	0.45	0.42	0.08

Appendix 3 **Blast-test set-up**

Test site

The blast tests were conducted at a blast site at the Erzberg iron mine, about 25 km north-west of Leoben, Styria, Austria. The blast site belongs to the Chair of Mining Engineering and Mineral Economics, MUL. The site has been also used for other experimental work of the Chair (e.g., Grasedieck, 2006; Ivanova, 2015; Reichholf, 2003; Schimek, 2015).

Blast test 1 was conducted outside (i.e., in an open area) to make preliminary vibration and noise measurements (Figure 230).



Figure 230: Blast set-up used in blast test 1.

In the following blast tests, the blasting was carried out inside a transport container (Figure 231). The blast chamber was secured on a support table and the camera and the lighting placed in front of the chamber.



Figure 231: Common blast set-up with the blast chamber and the HSI camera inside an enclosed transport container.

This arrangement was enclosed in the container during the blasting. The blast was initiated from outside the container where the data-acquisition equipment and a laptop PC for filming were set (Figure 232).



Figure 232: Experimental set-up outside the container.

Conducted blast tests

The blast tests are labelled considering the sequence number of corresponding blast day (i.e., 1 to 29). The blast tests blasted on the same day are labelled with additional number following a full stop (e.g., '29.2').

Table 87 shows the blast tests from the final phase with dates.

Table 87: Overview of the blast test from the final development phase.

Blas t test	Date	Sample	Ic [g/m]
20	25.08.2017	mb-72	12
21	1.09.2017	mb-75	12
22.1	8.09.2017	mb-74	20
22.2	8.09.2017	mb-71	6
23.1	12.09.2017	mb-76	20
23.2	12.09.2017	mb-73	6
24	15.09.2017	gb-26	12
25	22.09.2017	gb-22	12
26.1	3.10.2017	gb-21	6
26.2	3.10.2017	gb-24	20
27	6.10.2017	gb-23	6
28.1	20.10.2017	gb-25	12

The blast tests preceding blast test 20 are considered preliminary as they served for developing the test methodology, i.e., the materials used and the set-up arrangement changed from test to test, which makes a detailed comparison of results prone to errors.

Blast tests 12.1, 13.1, 13.2, 18.1, 19, 28.2, 29.1 and 29.2 were conducted with axially-stacked shorter cylinders. This was used to observe the blast-induced crack patterns in blast cylinders with transverse discontinuities. Here, the cylinders were not weighed as they were not intended for further fragmentation analysis. The HSI configuration in blast tests 28.1, 28.2, 29.1 and 29.2 was with smaller ROI to allow filming at higher temporal and spatial resolution (see Appendix 4).

Blast tests 28.2, 29.1, and 29.2 were conducted for investigating the influence of the blast fumes on the crack development.

Table 88 lists all conducted blast tests within this research.

Table 88: Overview of all conducted blast tests.

Blast test	l_c [g/m]	Blast cylinder	Cylinder size [mm]	q [kg/m ³]	Damping material	HSI	Test phase
1	20	mb-11	Ø142×282	1.179	gravel	No	Preliminary test (development) phase
2	6	mb-12	Ø142×283	0.354	c-mix1	PD1	
3	12	mb-13	Ø142×281	0.707			
4	12	mb-14	Ø142×283	0.707			
5	6	mb-15	Ø142×282	0.354	m-mix1	PD2	
6	12	mb-21	Ø142×284	0.706	tb20+wool	No	
7	12	mb-22	Ø142×285	0.706	tb20+foam		
8	12	mb-23	Ø142×285	0.706	tb20+m-mix1	PD3.1	
9	12	mb-24	Ø142×280	0.691		PD3.2	
10	12	mb-25	Ø142×281	0.692	tb20+m-mix2	PD3.3	
11.1	12	mb-31	Ø142×282	0.694	tb20+Al-pipe	PD3.4	
11.2	12	mb-32	Ø142×284	0.695	gypsum	PD3.5	
12.1	12	mb-42//	Ø142×52	-	tb20f13	No	
12.2	12	mb-45	Ø142×284	0.735	tb20f20	FD	
12.3	12	mb-41	Ø142×281	0.707			
13.1	12	mb-51//	Ø152×55	-	tb20+fer	PD3.6	
13.2	12	mb-52//	Ø152×52	-			
14.1	12	gb-12	Ø149×298	0.646	tb20	PD3.7	
14.2	12	gb-13	Ø149×298	0.645			
15	6	gb-14	Ø149×299	0.319			
16	12	gb-11	Ø149×298	0.635			
17	12	mb-43	Ø149×298	0.669	tb20+silicone		
18.1	12	gb-15//	Ø149×103	-			
18.2	12	mb-44	Ø142×288	0.696	FD	FD	
19	12	gb-15//	Ø149×195	-			
20	12	mb-72	Ø152×292	0.610			
21	12	mb-75	Ø152×291	0.614			
22.1	20	mb-74	Ø152×303	1.020			
22.2	6	mb-71	Ø151×299	0.307			
23.1	20	mb-76	Ø151×296	1.028			
23.2	6	mb-73	Ø151×298	0.307			
24	12	gb-26	Ø149×306	0.640			
25	12	gb-22	Ø149×302	0.634			
26.1	6	gb-21	Ø149×302	0.321			
26.2	20	gb-24	Ø149×303	1.069			
27	6	gb-25	Ø149×297	0.320			
28.1	12	gb-23	Ø149×317	0.644			AD1
28.2	6	gb-23//	Ø149×105	-			AD2
29.1	12	gb-21//	Ø149×102	-			AD1
29.2	6	gb-26//	Ø149×103	-			AD2

Notation:
 l_c – linear charge concentration of PETN cord [g/m];
 q – specific charge [kg/m³];
 PD(sequence number) – preliminary design/configuration;
 FD – final design/configuration;
 AD(sequence number) – additional design/configuration.

Blast cylinders and the damping layer

The production procedure for the blast cylinders is described in Appendix 1. The Ø140×280-mm mortar cylinders (preliminary test phase) were not sieved after blasting. Only the Ø150×300-mm blast cylinders (mortar and granite) were subjected to the whole analysis scope.

The wrapping around blast cylinder was not applied before blast test 6. For the blast tests 6 through 9, the cylinders were wrapped in 1-mm-thick aluminium sheet, held together by a 1-mm-gauge steel wire (Figure 233). Starting with blast test 10, the wrapping consisted of two layers of aluminium tape (Tesa® 56223) and a layer of linear low-density polyethylene (LLDPE) foil.



Figure 233: An earlier cylinder-wrapping solution with an aluminium sheet bent around the cylinder and held together with a tightened steel wire (blast test 9).

This change in the wrapping was carried out to preserve the fractured/fragmented cylinder after the blasting.

Different materials were tried for the damping layer (Table 88 and Table 89). These trials were carried out to decrease the influence of the cylinder's radial boundary on the blast-fragmentation outcome and to keep the fragmented material in place for the analyses after blasting. The same material was used for the damping layer in the final test phase to allow result comparison despite the influence of the layer on the blast fragmentation.

Table 89: Used materials for the damping layer in the blast test.

Blast test	Blast cylinder	Damping material		Test phase	
1	mb-11	gravel	Commercial mixture 3-5 mm.	Preliminary test (development) phase	
2	mb-12	c-mix1	Portland cement (cured for 3 days)		
3	mb-13				
4	mb-14				
5	mb-15	m-mix1	Mortar: quartz sand (0.1-0.3 mm), Portland cement, and water (3:1:0.5)		
6	mb-21	tb20+wool	"Trocken beton 20" with a layer of insulation wool around the cylinder.		
7	mb-22	tb20+foam	"Trocken beton 20" with a layer of insulation foam around the cylinder.		
8	mb-23	tb20+m-mix1	"Trocken beton 20" with a layer of m-mix1 around the cylinder.		
9	mb-24				
10	mb-25	tb20+m-mix2	"Trocken beton 20" with a layer of m-mix2 (included more cement) around the cylinder.		
11.1	mb-31	tb20+Al-pipe	"Trocken beton 20" with an aluminium pipe around the cylinder.		
11.2	mb-32	gypsum	Gypsum, quartz sand, and water (4:2:0.5).		
12.1	mb-42//	tb20f13	"Trocken beton 20" (7.5 kg) with 13 g of fibreglass threads.		
12.2	mb-45	tb20f20	"Trocken beton 20" (7.5 kg) with 20 g of fibreglass threads.		
12.3	mb-41	tb20f30	"Trocken beton 20" (7.5 kg) with 30 g of fibreglass threads.		
13.1	mb-51//	tb20+fer	"Trocken beton 20" with magnetite powder (Feroxon) (1:1)		
13.2	mb-52//				
14.1	gb-12	tb20	"Trocken beton 20"		
14.2	gb-13				
15	gb-14				
16	gb-11				
17	mb-43	tb20+silicone	"Trocken beton 20" with a layer of silicone around the cylinder.		
18.1	gb-15//				
18.2	mb-44				
19	gb-15//	FD	"Trocken beton 20" (7.5 kg) with fiberglass threads (0.13 % of mass).		Final test phase
20	mb-72				
21	mb-75				
22.1	mb-74				
22.2	mb-71				
23.1	mb-76				
23.2	mb-73				
24	gb-26				
25	gb-22				
26.1	gb-21				
26.2	gb-24				
27	gb-25				
28.1	gb-23				
28.2	gb-23//				
29.1	gb-21//				
29.2	gb-26//				

In the preliminary test phase, the protective window was frequently scratched and discoloured by fragments and blast fumes. The frontal end face of the cylinder was, therefore, also covered with a replaceable polycarbonate (Lexan®) disk (Ø150×3 mm) in the final test phase. The disk (Figure 234) was secured between the protective window and the frontal end face of the cylinder.



Figure 234: Replaceable polycarbonate disk: a) being manufactured; b) placed directly on a blast cylinder; c) covered with the protective window prior to a blast test.

The rear end face of the cylinder was directly covered with a Ø160×5-mm rubber disc, made of blast-mat material, and a Ø160×10-mm wooden disc, both with a central Ø10-mm borehole. These disks were mounted on the blast cylinder prior to it being positioned in the blast chamber. A wooden stick (Ø10 mm in diameter) was used to align the borehole with the rear steel plate (Figure 235).

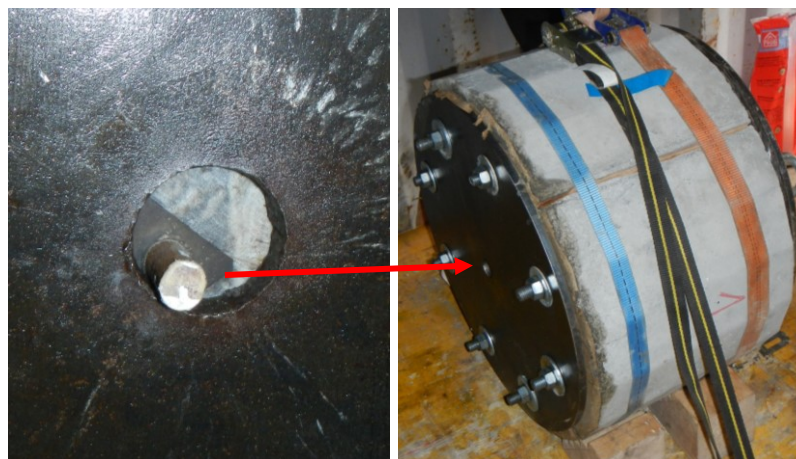


Figure 235: Wooden stick used to align the borehole with the opening in rear steel plate

Charge coupling and stemming

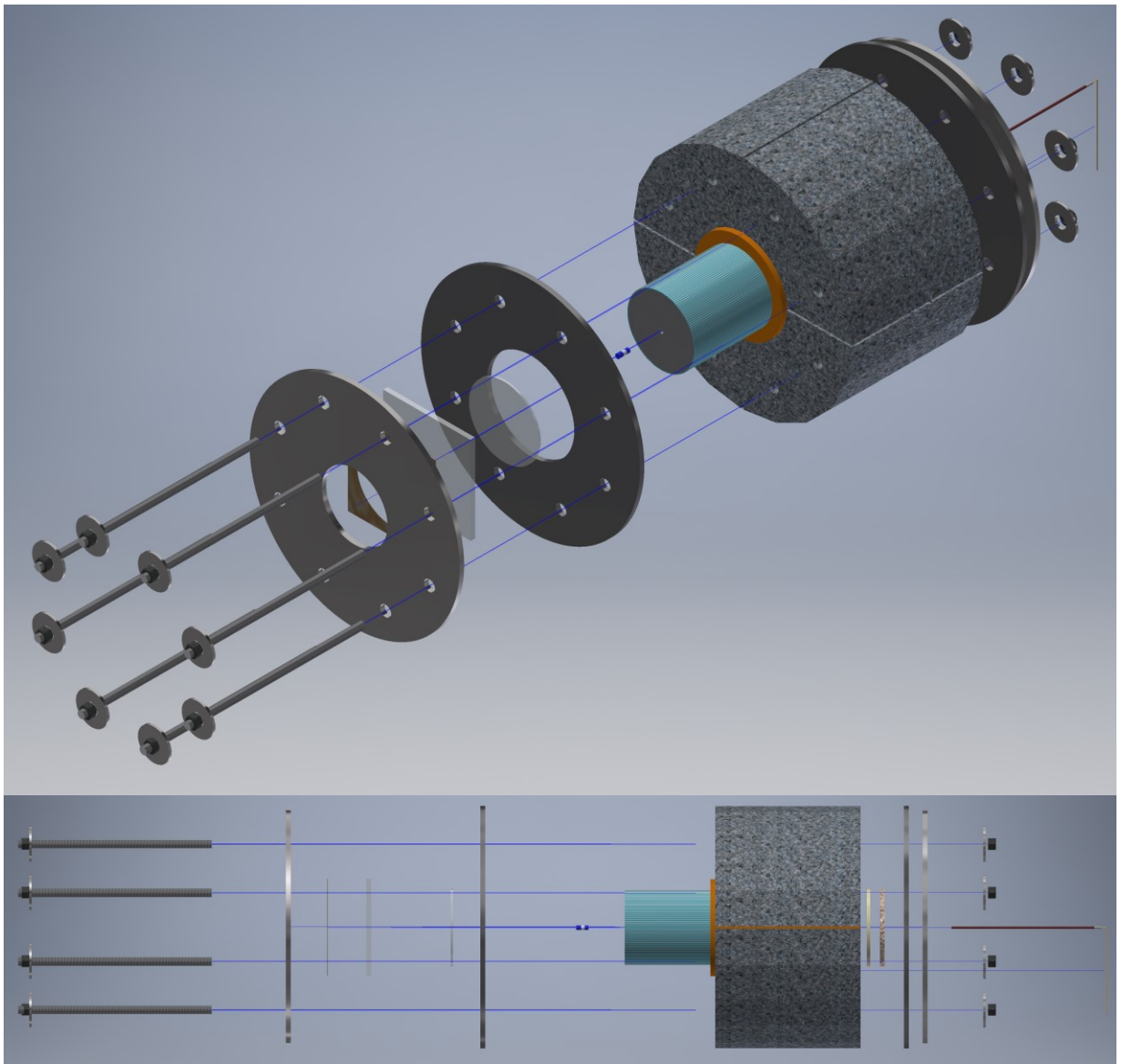
The PETN cord was secured in the borehole without coupling. A couple of turns of electrical-insulation tape were applied at three equidistant points along the cord to assure a more consistent radial coupling ratio in the axial direction of the cylinder.

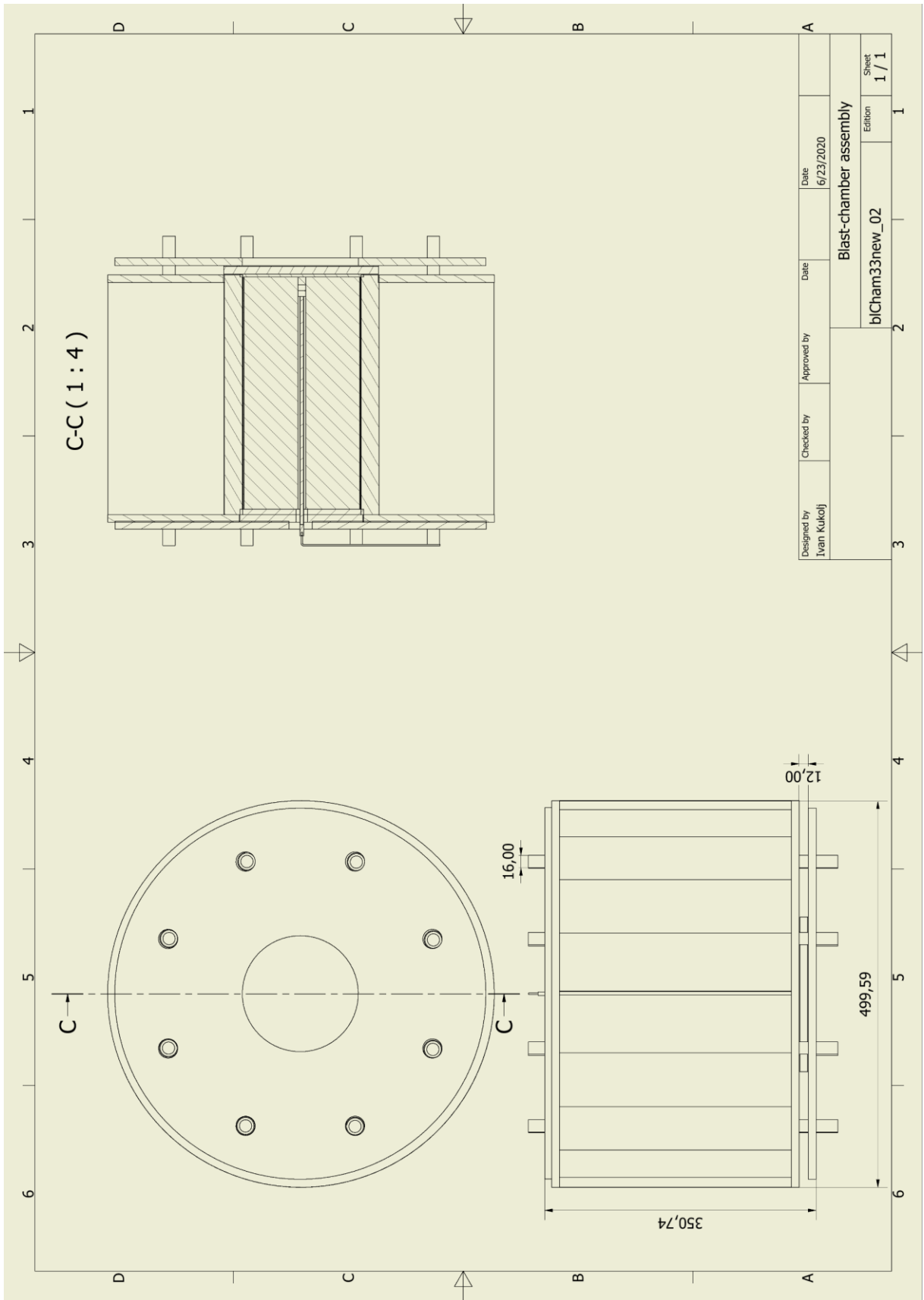
Different plug configurations were used in the blast tests (Table 90).

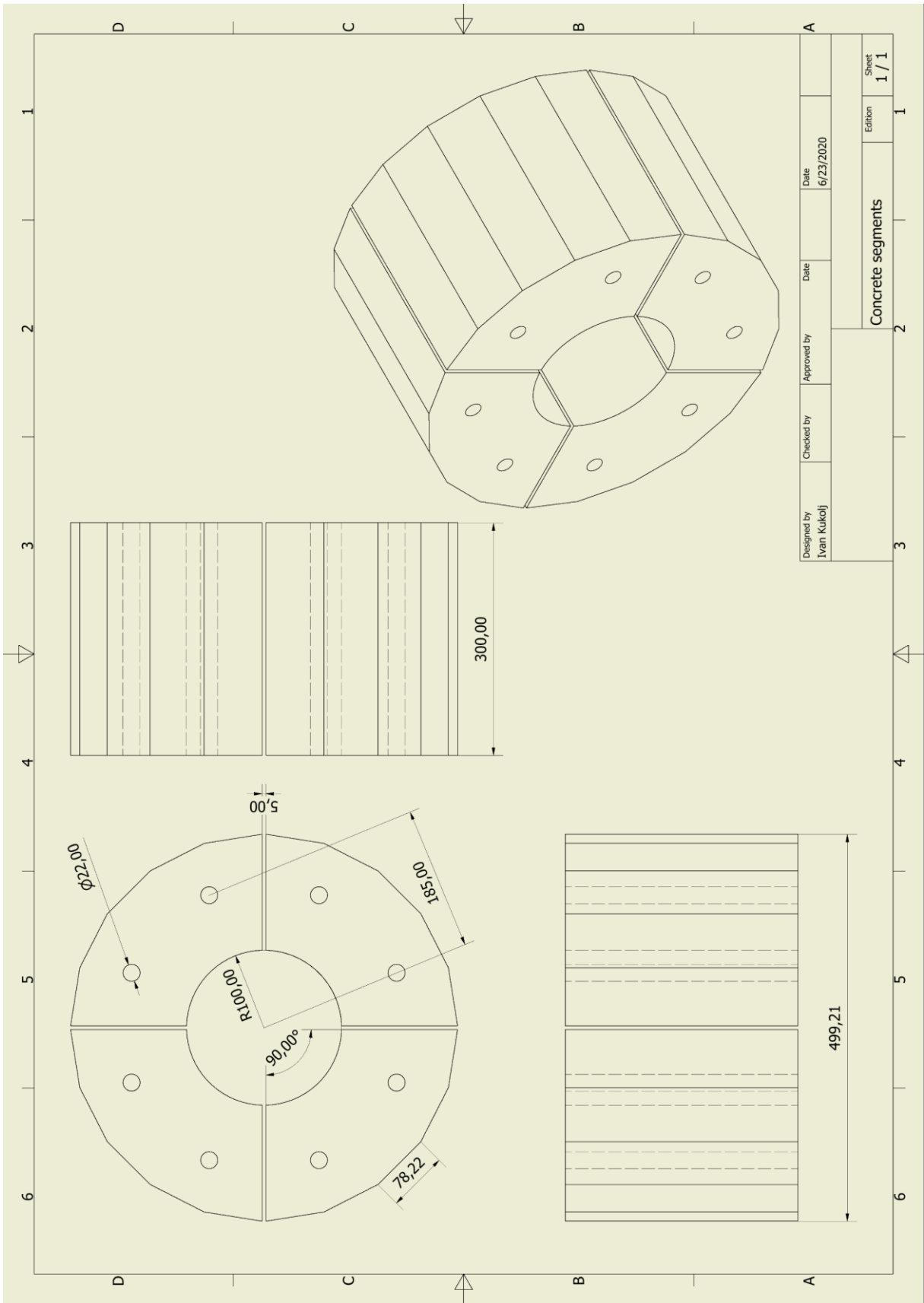
Table 90: Plug configurations and plug lengths used in the blast tests.

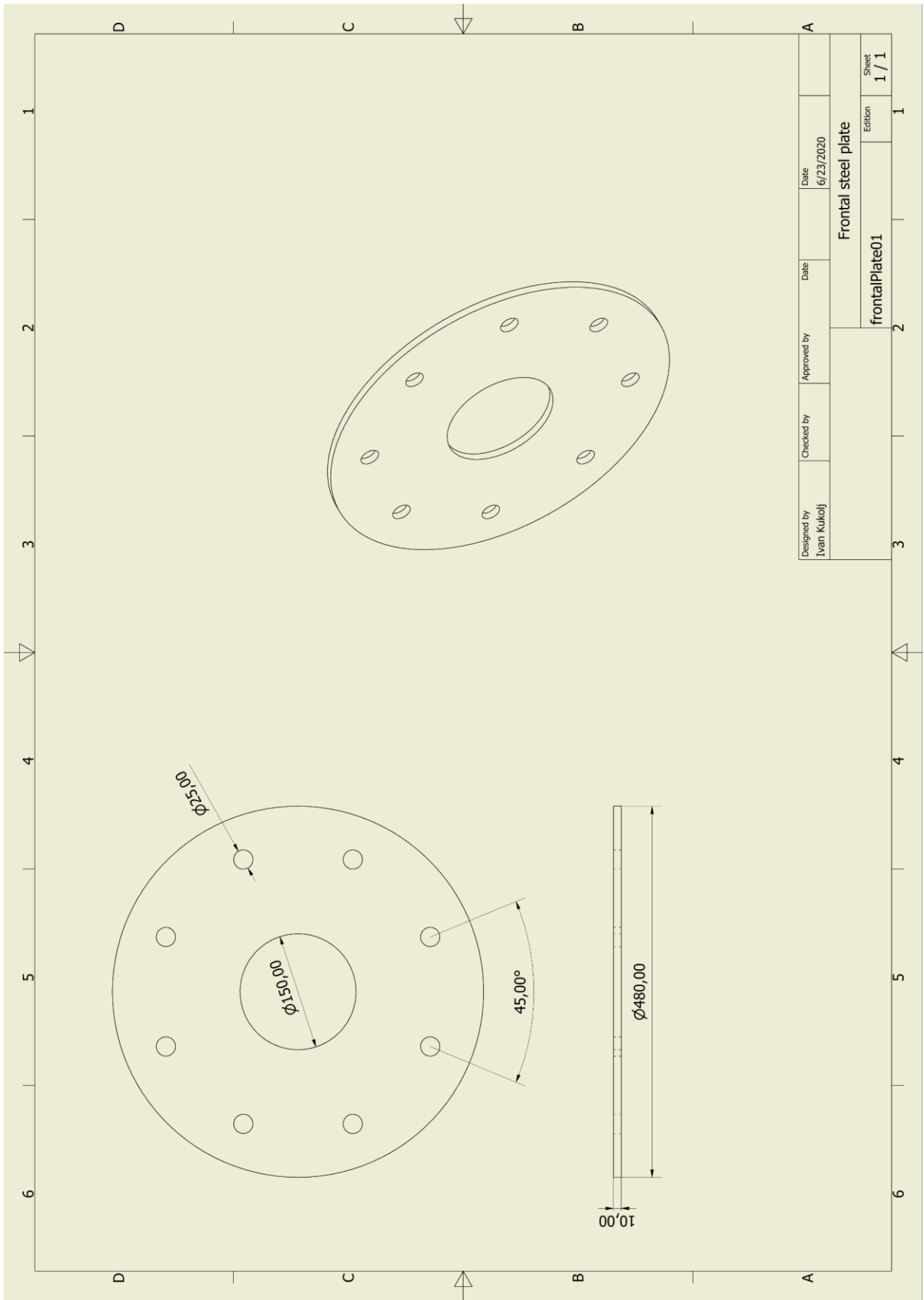
Blast test	Blast cylinder	Length [mm]	Plug configuration
1	mb-11	20	Silicone Ø10×20 mm (PolyMax, UHU).
2	mb-12	20	
3	mb-13	20	
4	mb-14	20	
5	mb-15	20	
6	mb-21	20	Ear plug Ø10×18 mm + gypsum
7	mb-22	20	Silicone Ø10×20 mm (PolyMax, UHU).
8	mb-23	20	
9	mb-24	25	Portland cement (32.5R) Ø10×25 mm.
10	mb-25	25	
11.1	mb-31	25	
11.2	mb-32	25	
12.1	mb-42//	10	Brass pipe (60-mm long)
12.2	mb-45	10	Brass pipe (60-mm long) with a silicone cap (Ø10×5 mm) at the collar.
12.3	mb-41	20	Brass pipe (60-mm long) with a silicone cap and a 15-mm wooden stick at the collar.
13.1	mb-51//	10	Wooden stick (Ø8×10 mm) in a brass pipe (Ø10 mm) in an aluminium pipe (Ø12 mm), 56-mm long. (Configuration plugS01).
13.2	mb-52//	15	plugS01 with the wooden stick of Ø8×15 mm.
14.1	gb-12	20	55-mm long brass pipe with a Ø8×20-mm wooden dowel.
14.2	gb-13	20	
15	gb-14	25	40-mm brass pipe with Ø8×15-mm wooden stick (masking tape was added radially for better coupling). Aluminium Ø10×10-mm cylinder was positioned behind the plug (Configuration plugS02).
16	gb-11	25	
17	mb-43	35	plugS02 without the cylinder and with a 20-mm column of silicone, added above the pipe at the collar of the borehole.
18.1	gb-15//	25	Ø10×10 wooden stick with radially-applied masking tape, followed by a 15-mm long silicon column (Configuration plugS03).
18.2	mb-44	25	
19	gb-15//	20	plugS03 with a 10-mm long silicon column.
20	mb-72	25	Ø10×10-mm wooden stick with radially-applied masking tape, followed by a silicon column (PolyMax, UHU) (Configuration plugS04).
21	mb-75	23	
22.1	mb-74	25	
22.2	mb-71	25	
23.1	mb-76	25	
23.2	mb-73	25	
24	gb-26	25	
25	gb-22	25	
26.1	gb-21	22	
26.2	gb-24	22	
27	gb-25	22	Ø10×7-mm aluminium cylinder with radially-applied masking tape, followed by another 10-mm aluminium cylinder and a layer of silicon (PolyMax, UHU) in between (Configuration plugS05).
28.1	gb-23	22	
28.2	gb-23//	22	Ø10×10-mm aluminium cylinder with radially-applied masking tape, in front of a Ø8×5-mm wooden dowel inside the brass pipe and a layer of silicon (PolyMax, UHU) in between (Configuration plugS06).
29.1	gb-21//	25	
29.2	gb-26//	25	

Technical drawings and model details of the blast chamber

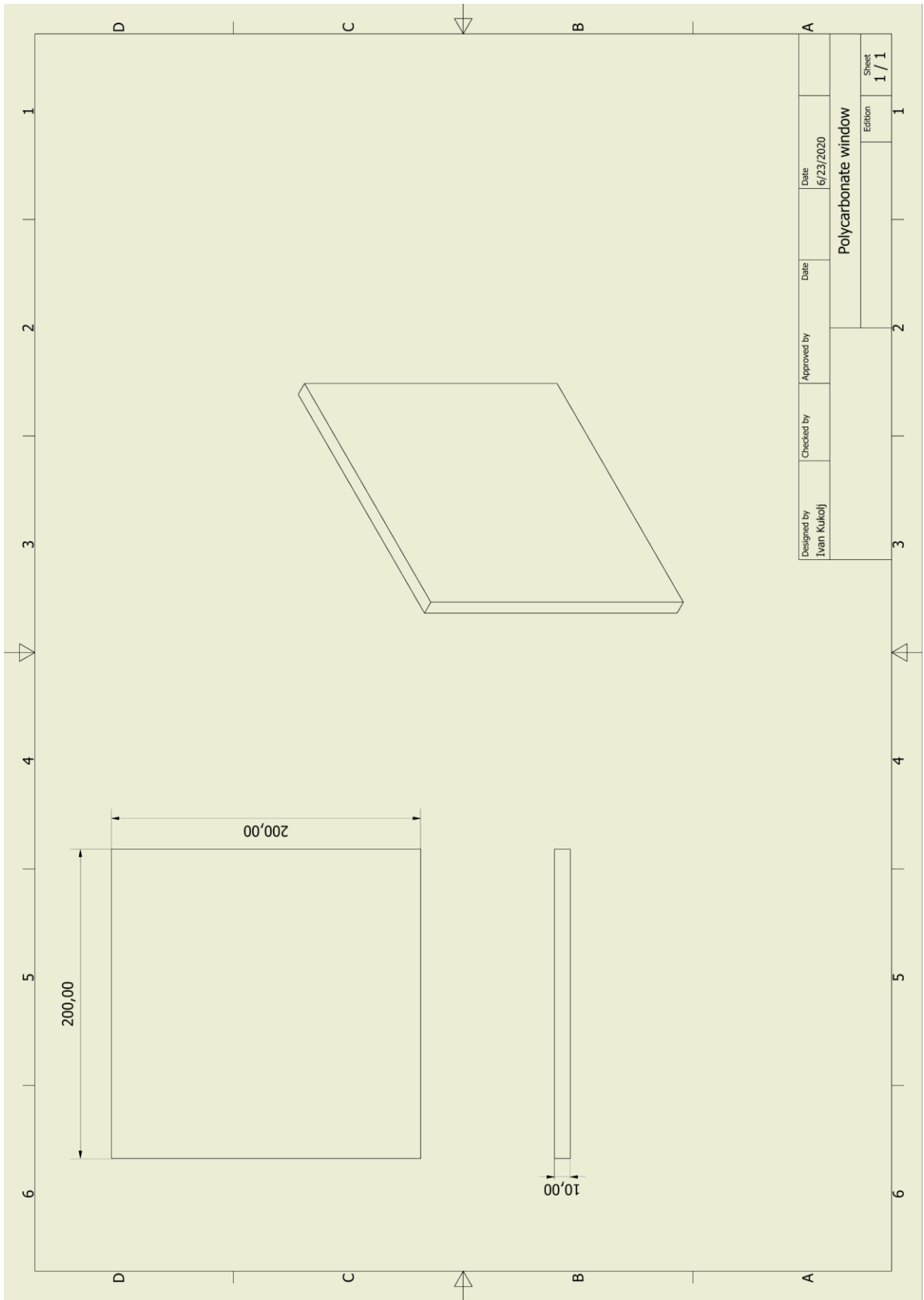


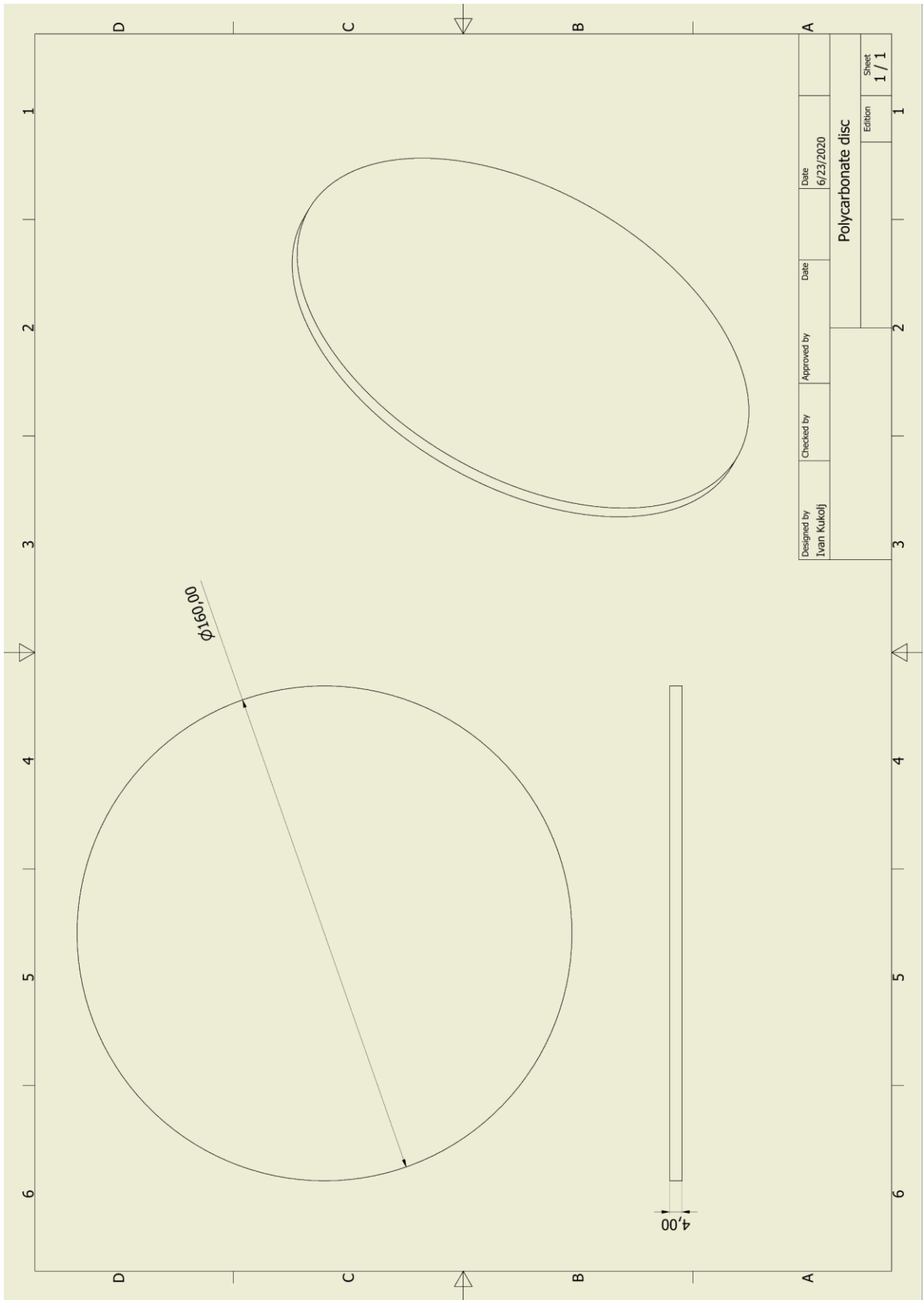


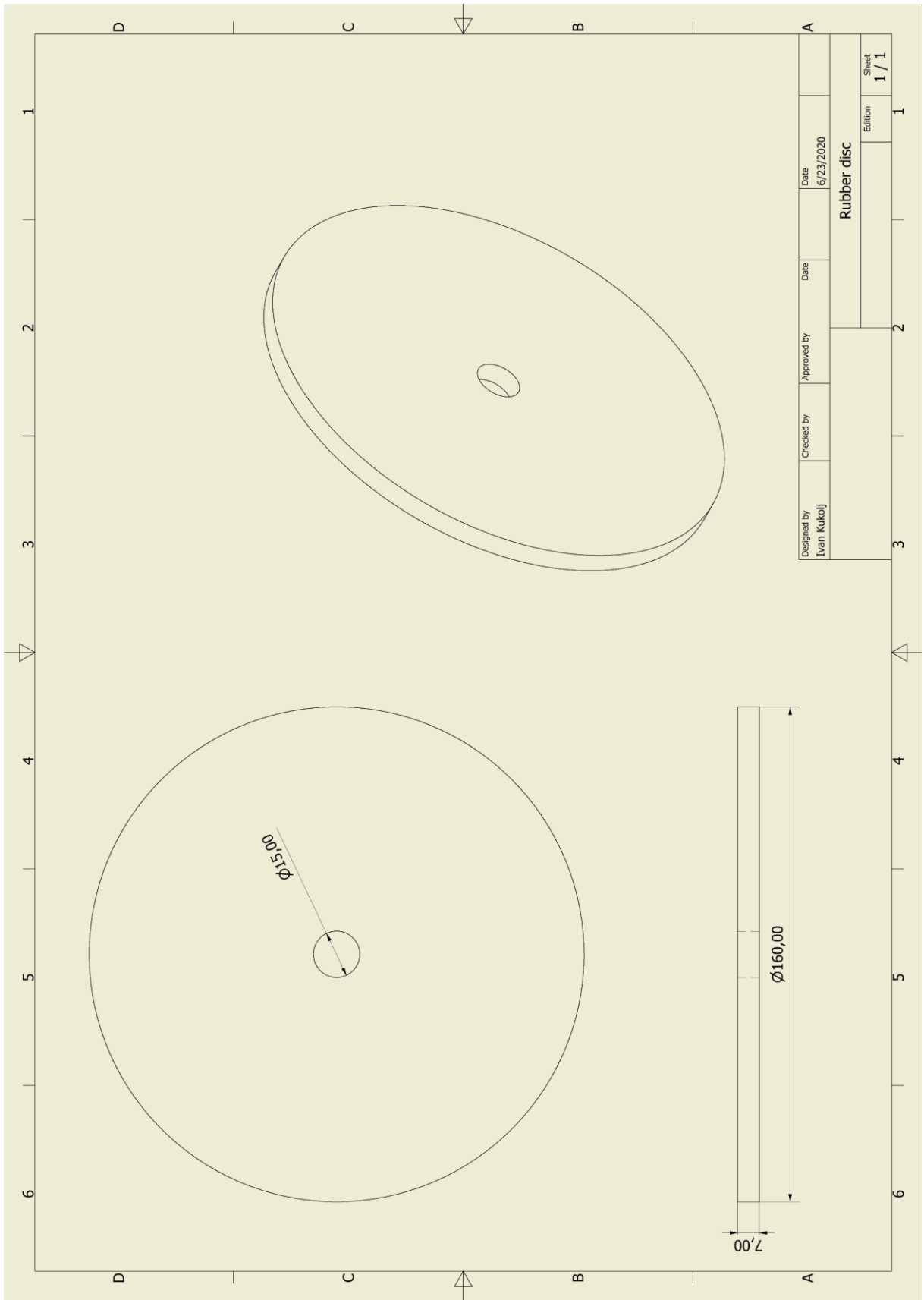














Appendix 4 High-speed-imaging (HSI) equipment and configuration

The cracking at the filmed frontal end face starts about when the detonation front reaches the stemming plug, which was observed as a slight movement of the plug and occasionally a dimmed detonation-flash around it.

The filming set-up utilized a 12-bit CMOS high-speed camera Imager HS 4M (LA Vision GmbH, Göttingen, Germany) and a high-performance LED-lighting system Constellation 120 (Imaging Solutions, Emingen, Germany). The set-up also included a laptop computer with a camera-specific software package (DaVIS[®], LA Vision GmbH) for controlling operation of the camera with synchronized lighting and an external data-acquisition system (high-speed controller). The camera captures images with a minimum inter-frame time of 3.15 μ s. The high-speed controller (La Vision GmbH) adjusts the filming process in real-time and performs image acquisition with temporal resolution of 10 ns. As the internal memory of the camera has limited capacity (36 GB), each pre-set frame rate (images per second) necessitated a trade-off between image resolution and maximum duration of the recording sequence.

The obtained filming results were first processed in the DaVIS[®] software to ‘increase’ the image resolution. The filming sequences were separated into single frames in .bmp format. Visible cracks on each filming image were traced in the GIMP (GNU Image Manipulation Program) to allow analysis of the crack development (see Section 4.1.4).

A video sequence with sufficiently high spatial and temporal resolution exceeds the available memory capacity for capturing the whole crack initiation and propagation process. Therefore, to provide enough filming time a compromise was made prior to the filming to fulfil the requirements for the spatial and temporal resolution. The set-up uses different parameter arrangements to achieve this (Table 91).

Table 91: Typical settings of recording parameters for the high-speed filming.

Setting	Recording rate [fps]	Recording time [s]	Image size [pixel]	Image size [mm]
1	24,656	4.6	336×336	160.0×160.0
2	30,122	5.1	288×288	151.8×151.8
3	37,585	5.9	240×240	141.2×141.2

The observation distance between the camera objective and the blast-chamber window is about 1.5 to 2 m. The camera is equipped with a 35-mm lens (AF Nikkor f/2D, Nikon).

In some blast tests, the filming covered only a part of the end face (Figure 236). By decreasing the region of interest, this allowed a higher frame rate (i.e., up to about 36,000 fps at the resolution of 336x212 pixels).

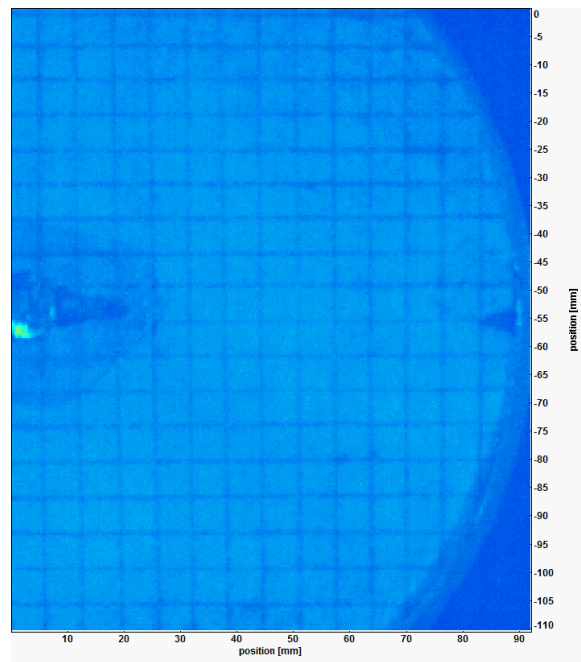


Figure 236: An HSI image from blast test 28.1 (granite, 12 g/m).

Here, the aim was to achieve higher frame rate with lowest possible decrease of the spatial resolution. These arrangements are marked in Table 88 as 'AD' (additional design/configuration) followed by a sequence number (e.g., 'AD1').

The lighting system has maximum electrical-power consumption of 120 W. It can operate in continuous or pulsed mode, producing light intensity of up to 15,000 lm. The lighting system was positioned slightly off-axis to the perpendicular orientation of the camera with respect to the frontal end face of the cylinder. This provided a more uniform illumination of filmed surface. Fine adjustment of the off-axis arrangement prevented local light overexposure in video frames caused by direct light reflection from the window surface.

After establishing the optical set-up, scaling was carried out prior to the filming. The scaling procedure used the grid mesh at the end face as the measurement reference. The high-speed controller is connected to the camera and the computer generates the timing sequence for acquisition of the HSI. Human-initiated triggering is used to start the filming sequence with a temporal offset of 0.5 to 1.5 s prior to the blast initiation.

Appendix 5 **CT scanning and pre-processing**

Blasted cylinders were scanned in a “GE/Phoenix x|argos” scanner with a two-pole 320kV fan-beam X-ray tube and an NTB line detector. The tube parameters were 300 kV and 2500 μ A using Cu and Sn prefilters of 1-mm thickness each. For every sample rotation, 2622 images were recorded. The voxel size in the radial direction was set to 130 μ m. The voxel size in the axial direction was set to 3 mm to increase the number of scanned cylinders and reduce the scanning time. As the initial granite-cylinder scans had shown significant noise, the volume reconstruction process included not only beam-hardening correction but also a noise-reduction filtering.

The high-resolution scanning (uCT) covered 8 samples using a “GE/Phoenix v|tome|x” scanner with a 240 kV micro-focus cone beam X-ray tube and a “GE dynamic 41|100” flat-panel detector with 4000 \times 4000 px. The samples were larger fragments from the blast cylinders and smaller undisturbed samples. The scanning parameters were set to 160–200 kV and 200 μ A with different combination of Sn and Cu filters, resulting in different voxel sizes ranging from 60 to 120 μ m. All parameters were chosen considering sample size and thickness to be penetrated by the X-rays. The reconstruction was also performed with a medium beam-hardening correction. The CT-data of all samples were analysed with the software Volume Graphics Studio Max 3.2.

For the cylindrical samples, the data sets were aligned to an outer best-fitted cylinder. The volume for the porosity analysis was limited to the fitted cylinder in order to avoid deviations due to open cracks or pores. The cracks and pores were segmented by setting the grey-value histogram with the iso-50% threshold and by adapting the threshold manually where necessary.

The minimal pore size for the detection was set to 8 voxels. The detected cracks were exported in the form of plane transverse and non-planar sections. The former followed the scanning resolution in the axial direction. The latter were obtained by virtually cutting and unrolling the fitted cylinder at different radii.

Appendix 6 **Image sets (HSI, PMI, PMM, CTt, CTnp)**

[Appendix 6 -Image sets \(HSI, PMI, PMM, CTt, CTnp\)](#)

Appendix 7 **MATLAB[®] scripts for processing the crack patterns**

[Appendix 7 - Matlab scripts](#)

Appendix 8 Crack-pattern analysis – result-data sets

Sets from HSI and PMI

Bl. Shot:	m6(22.2)											
Frame:	6	7	8	9	10	11	12	13	14	15	PMI	
t [μs]:	40.56	81.12	121.68	162.24	202.80	243.36	283.92	324.48	365.04	405.60	1000	
N _I	7	23	23	26	27	29	25	25	25	27	9	
N _Y	0	0	3	5	5	10	11	13	13	13	15	
N _R	0	0	0	0	0	0	0	0	0	0	0	
N _{TH}	1	1	2	2	3	3	3	3	3	3	4	
N _{TM}	0	0	1	2	2	3	4	4	4	4	6	
N _X	0	0	0	0	0	0	0	0	0	0	0	
N _{TB}	1	1	3	4	5	6	7	7	7	7	10	
J _{int}	0	0	3	5	5	10	11	13	13	13	15	
C _{max} [m/s]	70	325	492	224	379	420	375	112	131	235		
C _{ave} [m/s]	48	128	156	78	107	110	92	32	46	63		
# Extensions	4	8	17	17	10	14	7	4	3	4		
N _{-tot}	8	24	29	35	37	45	43	45	45	47	34	
N _I +N _Y +N _R +N _X	7	23	26	31	32	39	36	38	38	40	24	
N _L	4	12	15	18	19	23	22	23	23	24	17	
N _B	4	12	17.5	22.5	23.5	32.5	32.5	35.5	35.5	36.5	32	
N _B /N _L	1.00	1.00	1.21	1.29	1.27	1.44	1.51	1.58	1.58	1.55	1.88	
# 2D fragments	1	1	2	2	2	4	4	5	5	5	11	
C _L	0.50	0.17	0.83	1.03	1.08	1.42	1.67	1.78	1.78	1.70	2.94	
C _B	0.60	0.23	0.88	1.02	1.05	1.25	1.37	1.41	1.41	1.38	1.79	
p _I	0.70	0.88	0.56	0.49	0.47	0.38	0.32	0.29	0.29	0.31	0.11	
p _C	0.30	0.12	0.44	0.51	0.53	0.62	0.68	0.71	0.71	0.69	0.89	
p _{II}	0.49	0.78	0.31	0.24	0.22	0.14	0.10	0.09	0.09	0.10	0.01	
p _{IC}	0.21	0.10	0.25	0.25	0.25	0.23	0.22	0.21	0.21	0.21	0.10	
p _{CC}	0.09	0.01	0.19	0.26	0.28	0.39	0.47	0.50	0.50	0.48	0.80	

Grapher:													
Bl. Shot:	22.2		Frame										
axis	degree	nodes	6	7	8	9	10	11	12	13	14	15	PMI
x	0	I	0.875	0.958	0.793	0.743	0.730	0.644	0.581	0.556	0.556	0.574	0.265
y	120	TH+TM	0.125	0.042	0.103	0.114	0.135	0.133	0.163	0.156	0.156	0.149	0.294
z	240	J _{int}	0.000	0.000	0.103	0.143	0.135	0.222	0.256	0.289	0.289	0.277	0.441
check		sum	1.000	1.000	1.000	1.000	1.000	1.000	1.000	1.000	1.000	1.000	1.000

Grapher:													
Bl. Shot:	22.2		Frame										
axis	degree	nodes	6	7	8	9	10	11	12	13	14	15	PMI
x	0	I	1.000	1.000	0.885	0.839	0.844	0.744	0.694	0.658	0.658	0.675	0.375
y	120	Y	0.000	0.000	0.115	0.161	0.156	0.256	0.306	0.342	0.342	0.325	0.625
z	240	X + R	0.000	0.000	0.000	0.000	0.000	0.000	0.000	0.000	0.000	0.000	0.000
check		sum	1.000	1.000	1.000	1.000	1.000	1.000	1.000	1.000	1.000	1.000	1.000

Bl. Shot:	m6 23.2														
Frame:	6	7	8	9	10	11	12	13	14	15	16	17	18	PMI	
t [μs]:	40.56	81.12	121.68	162.24	202.80	243.36	283.92	324.48	365.04	405.60	446.16	486.72	527.28	1000	
N _I	6	10	20	56	53	50	55	71	65	66	64	64	63	10	
N _V	0	0	0	0	1	6	10	15	19	25	26	30	34	14	
N _R	0	0	0	0	0	0	0	0	0	0	0	0	0	0	
N _{TH}	0	0	0	1	3	4	6	6	6	6	6	6	6	3	
N _{TM}	0	0	0	1	1	2	3	6	6	7	8	8	9	9	
N _X	0	0	0	0	0	0	0	0	0	0	0	0	0	0	
N _{TB}	0	0	0	2	4	6	9	12	12	13	14	14	15	12	
J _{int}	0	0	0	0	1	6	10	15	19	25	26	30	34	14	
Cmax [m/s]	382	81	78	372	338	383	163	258	262	740	179	107	155		
Cave [m/s]	165	62	50	87	120	129	58	130	79	148	44	46	50		
# Extensions	3	2	5	25	23	13	11	18	24	14	5	7	14		
N-tot	6	10	20	58	58	62	74	98	96	104	104	108	112	36	
N _I +N _V +N _R +N _X	6	10	20	56	54	56	65	86	84	91	90	94	97	24	
N _L	3	5	10	29	29	31	37	49	48	52	52	54	56	18	
N _B	3	5	10	29	30	37	47	64	67	77	78	84	90	32	
N _B /N _L	1.00	1.00	1.00	1.00	1.03	1.19	1.27	1.31	1.40	1.48	1.50	1.56	1.61	1.78	
# 2D fragments	1	1	1	1	1	3	4	6	9	11	13	16	18	7	
C _L	0.00	0.00	0.00	0.14	0.34	0.77	1.03	1.10	1.29	1.46	1.54	1.63	1.75	2.89	
C _B	0.00	0.00	0.00	0.19	0.44	0.84	1.02	1.07	1.18	1.27	1.30	1.35	1.40	1.77	
p _I	1.00	1.00	1.00	0.90	0.78	0.58	0.49	0.47	0.41	0.37	0.35	0.33	0.30	0.11	
p _C	0.00	0.00	0.00	0.10	0.22	0.42	0.51	0.53	0.59	0.63	0.65	0.67	0.70	0.89	
p _{II}	1.00	1.00	1.00	0.82	0.61	0.34	0.24	0.22	0.17	0.13	0.12	0.11	0.09	0.01	
p _{IC}	0.00	0.00	0.00	0.09	0.17	0.24	0.25	0.25	0.24	0.23	0.23	0.22	0.21	0.10	
p _{CC}	0.00	0.00	0.00	0.01	0.05	0.18	0.26	0.28	0.35	0.40	0.43	0.45	0.49	0.79	

Grapher:																
Bl. Shot:	23.2															
axis	degree	nodes	6	7	8	9	10	11	12	13	14	15	16	17	18	PMI
x	0	I	1.000	1.000	1.000	0.966	0.914	0.806	0.743	0.724	0.677	0.635	0.615	0.593	0.563	0.278
y	120	TH+TM	0.000	0.000	0.000	0.034	0.069	0.097	0.122	0.122	0.125	0.125	0.135	0.130	0.134	0.333
z	240	J _{int}	0.000	0.000	0.000	0.000	0.017	0.097	0.135	0.153	0.198	0.240	0.250	0.278	0.304	0.389
check		sum	1.000	1.000	1.000	1.000	1.000	1.000	1.000	1.000	1.000	1.000	1.000	1.000	1.000	1.000

Grapher:																
Bl. Shot:	23.2															
axis	degree	nodes	6	7	8	9	10	11	12	13	14	15	16	17	18	PMI
x	0	I	1.000	1.000	1.000	1.000	0.981	0.893	0.846	0.826	0.774	0.725	0.711	0.681	0.649	0.417
y	120	Y	0.000	0.000	0.000	0.000	0.019	0.107	0.154	0.174	0.226	0.275	0.289	0.319	0.351	0.583
z	240	X+R	0.000	0.000	0.000	0.000	0.000	0.000	0.000	0.000	0.000	0.000	0.000	0.000	0.000	0.000
check		sum	1.000	1.000	1.000	1.000	1.000	1.000	1.000	1.000	1.000	1.000	1.000	1.000	1.000	1.000

Bl. Shot:	m12(20)													
Frame:	6	7	8	9	10	11	12	13	14	15	16	17	PMI	
t [μs]:	40.56	81.12	121.68	162.24	202.80	243.36	283.92	324.48	365.04	405.60	446.16	486.72	1000	
N _I	14	4	13	10	8	24	30	42	52	57	45	45	14	
N _V	0	0	0	1	3	3	4	7	9	12	12	12	12	
N _R	0	0	0	0	0	0	0	0	0	0	0	0	0	
N _{TH}	1	1	2	2	2	2	4	4	4	5	5	5	4	
N _{TM}	1	1	1	1	1	3	4	4	6	7	7	7	8	
N _X	0	0	0	0	0	0	0	0	0	0	0	0	1	
N _{TB}	2	2	3	3	3	5	8	8	10	12	12	12	12	
J _{int}	0	0	0	1	3	3	4	7	9	12	12	12	13	
C _{max} [m/s]	274	207	169	248	75	831	411	439	400	295	187	2		
C _{ave} [m/s]	146	143	77	164	41	242	113	143	121	90	82	2		
# Extensions	8	5	6	7	3	11	16	13	18	12	11	1		
N-tot	16	6	16	14	14	32	42	57	71	81	69	69	39	
N _I +N _V +N _R +N _X	14	4	13	11	11	27	34	49	61	69	57	57	27	
N _L	8	3	8	7	7	16	21	29	36	41	35	35	19	
N _B	8	3	8	8	10	19	25	35.5	44.5	52.5	46.5	46.5	33	
N _B /N _L	1.00	1.00	1.00	1.14	1.43	1.19	1.19	1.25	1.25	1.30	1.35	1.35	1.74	
# 2D fragments	1	1	1	1	6	7	7	7	9	13	14	14	8	
C _L	0.50	1.33	0.75	1.14	1.71	1.00	1.14	1.05	1.07	1.19	1.39	1.39	2.63	
C _B	0.60	1.20	0.82	1.09	1.38	1.00	1.09	1.03	1.05	1.12	1.23	1.23	1.69	
p _I	0.70	0.40	0.59	0.45	0.31	0.50	0.45	0.48	0.48	0.44	0.38	0.38	0.16	
p _C	0.30	0.60	0.41	0.55	0.69	0.50	0.55	0.52	0.52	0.56	0.62	0.62	0.84	
p _{II}	0.49	0.16	0.35	0.21	0.09	0.25	0.21	0.23	0.23	0.20	0.15	0.15	0.02	
p _{IC}	0.21	0.24	0.24	0.25	0.21	0.25	0.25	0.25	0.25	0.25	0.24	0.24	0.13	
p _{CC}	0.09	0.36	0.17	0.30	0.48	0.25	0.30	0.27	0.27	0.31	0.38	0.38	0.71	

Grapher:															
Bl. Shot:	20	Frame													
axis	degree	nodes	6	7	8	9	10	11	12	13	14	15	16	17	PMI
x	0	I	0.875	0.667	0.813	0.714	0.571	0.750	0.714	0.737	0.732	0.704	0.652	0.652	0.359
y	120	TH+TM	0.125	0.333	0.188	0.214	0.214	0.156	0.190	0.140	0.141	0.148	0.174	0.174	0.308
z	240	J _{int}	0.000	0.000	0.000	0.071	0.214	0.094	0.095	0.123	0.127	0.148	0.174	0.174	0.333
check		sum	1.000	1.000	1.000	1.000	1.000	1.000	1.000	1.000	1.000	1.000	1.000	1.000	1.000

Grapher:															
Bl. Shot:	20	Frame													
axis	degree	nodes	6	7	8	9	10	11	12	13	14	15	16	17	PMI
x	0	I	1.000	1.000	1.000	0.909	0.727	0.889	0.882	0.857	0.852	0.826	0.789	0.789	0.519
y	120	Y	0.000	0.000	0.000	0.091	0.273	0.111	0.118	0.143	0.148	0.174	0.211	0.211	0.444
z	240	X + R	0.000	0.000	0.000	0.000	0.000	0.000	0.000	0.000	0.000	0.000	0.000	0.000	0.037
check		sum	1.000	1.000	1.000	1.000	1.000	1.000	1.000	1.000	1.000	1.000	1.000	1.000	1.000

Bl. Shot:	m12(21)											
Frame:	2	3	4	5	6	7	8	9	10	11	12	PMI
t [μs]:	40.56	81.12	121.68	162.24	202.80	243.36	283.92	324.48	365.04	405.60	446.16	1000
N _I	44	52	62	80	83	85	84	89	87	89	88	28
N _V	0	5	14	33	48	58	59	62	63	66	73	47
N _R	0	0	0	0	0	0	0	0	0	0	0	0
N _{TH}	4	8	8	8	8	8	8	9	9	9	9	7
N _{TM}	0	3	6	11	11	15	15	16	17	18	20	20
N _X	0	0	0	0	0	0	0	0	0	0	0	1
N _{TB}	4	11	14	19	19	23	23	25	26	27	29	27
J _{int}	0	5	14	33	48	58	59	62	63	66	73	48
C _{max} [m/s]	469	1169	472	575	296	713	510	629	151	855	296	
C _{ave} [m/s]	114	204	99	130	99	113	264	211	63	164	143	
# Extensions	24	41	38	50	30	22	4	11	4	10	11	
N-tot	48	68	90	132	150	166	166	176	176	182	190	103
N _I +N _V +N _R +N _X	44	57	76	113	131	143	143	151	150	155	161	76
N _L	24	34	45	66	75	83	83	88	88	91	95	51
N _B	24	39	59	99	123	141	142	150	151	157	168	100
N _B /N _L	1.00	1.15	1.31	1.50	1.64	1.70	1.71	1.70	1.72	1.73	1.77	1.96
# 2D fragments	1	1	4	11	19	28	29	32	33	35	38	27
C _L	0.33	0.94	1.24	1.58	1.79	1.95	1.98	1.98	2.02	2.04	2.15	2.94
C _B	0.43	0.96	1.15	1.32	1.42	1.48	1.49	1.49	1.51	1.52	1.55	1.78
p _I	0.79	0.52	0.42	0.34	0.29	0.26	0.25	0.25	0.25	0.24	0.22	0.11
p _C	0.21	0.48	0.58	0.66	0.71	0.74	0.75	0.75	0.75	0.76	0.78	0.89
p _{II}	0.62	0.27	0.18	0.11	0.09	0.07	0.06	0.06	0.06	0.06	0.05	0.01
p _{IC}	0.17	0.25	0.24	0.22	0.21	0.19	0.19	0.19	0.19	0.18	0.17	0.10
p _{CC}	0.05	0.23	0.33	0.44	0.50	0.55	0.56	0.56	0.57	0.57	0.60	0.79

Grapher:														
Bl. Shot:	21	Frame												
axis	degree	nodes	2	3	4	5	6	7	8	9	10	11	12	PMI
x	0	I	0.917	0.765	0.689	0.606	0.553	0.512	0.506	0.506	0.494	0.489	0.463	0.272
y	120	TH+TM	0.083	0.162	0.156	0.144	0.127	0.139	0.139	0.142	0.148	0.148	0.153	0.262
z	240	J _{int}	0.000	0.074	0.156	0.250	0.320	0.349	0.355	0.352	0.358	0.363	0.384	0.466
check		sum	1.000	1.000	1.000	1.000	1.000	1.000	1.000	1.000	1.000	1.000	1.000	1.000
Grapher:														
Bl. Shot:	21	Frame												
axis	degree	nodes	2	3	4	5	6	7	8	9	10	11	12	PMI
x	0	I	1.000	0.912	0.816	0.708	0.634	0.594	0.587	0.589	0.580	0.574	0.547	0.368
y	120	Y	0.000	0.088	0.184	0.292	0.366	0.406	0.413	0.411	0.420	0.426	0.453	0.618
z	240	X + R	0.000	0.000	0.000	0.000	0.000	0.000	0.000	0.000	0.000	0.000	0.000	0.013
check		sum	1.000	1.000	1.000	1.000	1.000	1.000	1.000	1.000	1.000	1.000	1.000	1.000

Bl. Shot:	m20(22.1)								
Frame:	2	3	4	5	6	7	8	9	PMI
t [μ s]:	40.56	81.12	121.68	162.24	202.80	243.36	283.92	324.48	1000
N _I	27	23	31	32	49	62	76	82	120
N _V	1	0	3	8	9	9	16	17	127
N _R	0	0	0	0	0	0	0	0	32
N _{TH}	2	6	6	7	7	8	8	8	9
N _{TM}	0	1	4	5	8	11	12	13	29
N _X	0	0	0	0	0	0	0	0	9
N _{TB}	2	7	10	12	15	19	20	21	38
J _{int}	1	0	3	8	9	9	16	17	168
C _{max} [m/s]	376	661	728	374	398	284	454	412	
C _{ave} [m/s]	78	201	213	108	208	138	139	121	
# Extensions	16	20	15	19	18	18	19	19	
N-tot	30	30	44	52	73	90	112	120	326
N _I +N _V +N _R +N _X	28	23	34	40	58	71	92	99	288
N _L	15	15	22	26	37	45	56	60	143
N _B	16	15	25	34	45.5	54	72	77	351.5
N _B /N _L	1.07	1.00	1.14	1.31	1.25	1.20	1.29	1.28	2.47
# 2D fragments	1	1	2	4	5	6	9	10	59
C _L	0.40	0.93	1.18	1.54	1.32	1.24	1.29	1.27	2.89
C _B	0.50	0.95	1.11	1.30	1.19	1.15	1.17	1.16	1.69
p _I	0.75	0.52	0.44	0.35	0.40	0.42	0.41	0.42	0.15
p _C	0.25	0.48	0.56	0.65	0.60	0.58	0.59	0.58	0.85
p _{II}	0.56	0.27	0.20	0.12	0.16	0.18	0.17	0.18	0.02
p _{IC}	0.19	0.25	0.25	0.23	0.24	0.24	0.24	0.24	0.13
p _{CC}	0.06	0.23	0.31	0.43	0.35	0.33	0.34	0.34	0.72

Grapher:											
Bl. Shot:	22.1	Frame									
axis	degree	nodes	2	3	4	5	6	7	8	9	PMI
x	0	I	0.900	0.767	0.705	0.615	0.671	0.689	0.679	0.683	0.368
y	120	TH+TM	0.067	0.233	0.227	0.231	0.205	0.211	0.179	0.175	0.117
z	240	J _{int}	0.033	0.000	0.068	0.154	0.123	0.100	0.143	0.142	0.515
check		sum	1.000	1.000	1.000	1.000	1.000	1.000	1.000	1.000	1.000

Grapher:											
Bl. Shot:	22.1	Frame									
axis	degree	nodes	2	3	4	5	6	7	8	9	PMI
x	0	I	0.964	1.000	0.912	0.800	0.845	0.873	0.826	0.828	0.417
y	120	Y	0.036	0.000	0.088	0.200	0.155	0.127	0.174	0.172	0.441
z	240	X + R	0.000	0.000	0.000	0.000	0.000	0.000	0.000	0.000	0.142
check		sum	1.000	1.000	1.000	1.000	1.000	1.000	1.000	1.000	1.000

Bl. Shot:	m20(23.1)												
Frame:	8	9	10	11	12	13	14	15	16	17	18	PMI	
t [μs]:	40.56	81.12	121.68	162.24	202.80	243.36	283.92	324.48	365.04	405.60	446.16	1000	
N _I	16	36	56	62	93	109	101	105	108	113	104	40	
N _V	0	0	0	0	0	6	11	27	32	44	57	115	
N _R	0	0	0	0	0	0	0	0	0	0	0	1	
N _{TH}	0	0	3	3	4	8	9	11	11	14	14	9	
N _{TM}	0	0	0	0	1	5	11	17	23	30	32	60	
N _X	0	0	0	0	0	0	0	0	0	0	0	8	
N _{TB}	0	0	3	3	5	13	20	28	34	44	46	69	
J _{int}	0	0	0	0	0	6	11	27	32	44	57	124	
C _{max} [m/s]	277	407	202	406	775	1224	275	1631	524	1050	345		
C _{ave} [m/s]	92	119	72	109	237	196	125	225	136	163	119		
# Extensions	8	12	12	6	27	34	31	42	26	41	23		
N-tot	16	36	59	65	98	128	132	160	174	201	207	233	
N _I +N _V +N _R +N _X	16	36	56	62	93	115	112	132	140	157	161	164	
N _L	8	18	30	33	49	64	66	80	87	101	104	112	
N _B	8	18	29.5	32.5	49	70	77	107	119	144.5	160.5	245	
N _B /N _L	1.00	1.00	1.00	1.00	1.00	1.09	1.17	1.34	1.37	1.44	1.55	2.19	
# 2D fragments	1	1	1	1	1	2	5	13	17	27	36	66	
C _L	0.00	0.00	0.20	0.18	0.20	0.59	0.94	1.38	1.52	1.75	1.99	3.45	
C _B	0.00	0.00	0.28	0.25	0.28	0.69	0.96	1.22	1.29	1.40	1.50	1.87	
p _I	1.00	1.00	0.86	0.87	0.86	0.66	0.52	0.39	0.35	0.30	0.25	0.06	
p _C	0.00	0.00	0.14	0.13	0.14	0.34	0.48	0.61	0.65	0.70	0.75	0.94	
p _{II}	1.00	1.00	0.74	0.76	0.74	0.43	0.27	0.15	0.12	0.09	0.06	0.00	
p _{IC}	0.00	0.00	0.12	0.11	0.12	0.23	0.25	0.24	0.23	0.21	0.19	0.06	
p _{CC}	0.00	0.00	0.02	0.02	0.02	0.12	0.23	0.37	0.42	0.49	0.56	0.88	

Grapher:														
Bl. Shot:	23.1		Frame											
axis	degree	nodes	8	9	10	11	12	13	14	15	16	17	18	PMI
x	0	I	1.000	1.000	0.949	0.954	0.949	0.852	0.765	0.656	0.621	0.562	0.502	0.172
y	120	TH+TM	0.000	0.000	0.051	0.046	0.051	0.102	0.152	0.175	0.195	0.219	0.222	0.296
z	240	J _{int}	0.000	0.000	0.000	0.000	0.000	0.047	0.083	0.169	0.184	0.219	0.275	0.532
check		sum	1.000	1.000	1.000	1.000	1.000	1.000	1.000	1.000	1.000	1.000	1.000	1.000

Grapher:														
Bl. Shot:	23.1		Frame											
axis	degree	nodes	8	9	10	11	12	13	14	15	16	17	18	PMI
x	0	I	1.000	1.000	1.000	1.000	1.000	0.948	0.902	0.795	0.771	0.720	0.646	0.244
y	120	Y	0.000	0.000	0.000	0.000	0.000	0.052	0.098	0.205	0.229	0.280	0.354	0.701
z	240	X + R	0.000	0.000	0.000	0.000	0.000	0.000	0.000	0.000	0.000	0.000	0.000	0.055
check		sum	1.000	1.000	1.000	1.000	1.000	1.000	1.000	1.000	1.000	1.000	1.000	1.000

Bl. Shot:	g6(26.1)													
Frame:	2	3	4	5	6	7	8	9	10	11	12	13	14	PMI
t [μs]:	40.56	81.12	121.68	162.24	202.80	243.36	283.92	324.48	365.04	405.60	446.16	486.72	527.28	1000
N _I	10	19	47	69	73	77	83	92	96	116	120	127	130	24
N _V	0	1	2	2	2	2	9	27	33	36	42	50	76	127
N _R	0	0	0	0	0	0	0	0	0	0	0	0	0	22
N _{TH}	0	0	0	0	0	4	6	7	10	12	15	16	18	11
N _{TM}	2	5	4	6	6	6	7	7	8	9	10	10	11	18
N _X	0	0	0	0	0	0	0	0	2	3	5	4	5	3
N _{TB}	2	5	4	6	6	10	13	14	18	21	25	26	29	29
J _{int}	0	1	2	2	2	2	9	27	35	39	47	54	81	152
Cmax [m/s]	362	279	170	535	189	396	470	349	328	498	312	172	343	
Cave [m/s]	183	107	63	189	86	130	238	100	111	134	105	90	70	
# Extensions	6	10	16	17	15	13	14	23	20	21	19	14	31	
N-tot	12	25	53	77	81	89	105	133	149	176	192	207	240	205
N _I +N _V +N _R +N _X	10	20	49	71	75	79	92	119	131	155	167	181	211	176
N _L	6	13	27	39	41	45	53	67	74	87	94	102	118	90
N _B	6	13.5	28.5	40.5	42.5	46.5	61.5	93.5	110.5	128.5	145.5	159.5	203.5	267
N _B /N _L	1.00	1.08	1.08	1.05	1.05	1.04	1.17	1.41	1.50	1.49	1.56	1.57	1.73	2.97
# 2D fragments	1	3	3	3	3	4	6	16	19	21	27	32	44	77
C _L	0.67	0.96	0.45	0.42	0.40	0.54	0.84	1.23	1.44	1.39	1.54	1.58	1.87	4.02
C _B	0.75	0.97	0.55	0.52	0.49	0.64	0.89	1.14	1.25	1.22	1.30	1.32	1.44	1.92
p _I	0.63	0.51	0.72	0.74	0.75	0.68	0.56	0.43	0.37	0.39	0.35	0.34	0.28	0.04
p _C	0.38	0.49	0.28	0.26	0.25	0.32	0.44	0.57	0.63	0.61	0.65	0.66	0.72	0.96
p _{II}	0.39	0.26	0.52	0.55	0.57	0.46	0.31	0.18	0.14	0.15	0.12	0.12	0.08	0.00
p _{IC}	0.23	0.25	0.20	0.19	0.19	0.22	0.25	0.24	0.23	0.24	0.23	0.23	0.20	0.04
p _{CC}	0.14	0.24	0.08	0.07	0.06	0.10	0.20	0.33	0.39	0.37	0.42	0.43	0.52	0.92

Grapher:																
Bl. Shot:	26.1															
axis	degree	nodes	Frame												PMI	
x	0	I	0.833	0.760	0.887	0.896	0.901	0.865	0.790	0.692	0.644	0.659	0.625	0.614	0.542	0.117
y	120	TH+TM	0.167	0.200	0.075	0.078	0.074	0.112	0.124	0.105	0.121	0.119	0.130	0.126	0.121	0.141
z	240	J _{int}	0.000	0.040	0.038	0.026	0.025	0.022	0.086	0.203	0.235	0.222	0.245	0.261	0.338	0.741
check		sum	1.000	1.000	1.000	1.000	1.000	1.000	1.000	1.000	1.000	1.000	1.000	1.000	1.000	1.000

Grapher:																
Bl. Shot:	26.1															
axis	degree	nodes	Frame												PMI	
x	0	I	1.000	0.950	0.959	0.972	0.973	0.975	0.902	0.773	0.733	0.748	0.719	0.702	0.616	0.136
y	120	Y	0.000	0.050	0.041	0.028	0.027	0.025	0.098	0.227	0.252	0.232	0.251	0.276	0.360	0.722
z	240	X + R	0.000	0.000	0.000	0.000	0.000	0.000	0.000	0.000	0.015	0.019	0.030	0.022	0.024	0.142
check		sum	1.000	1.000	1.000	1.000	1.000	1.000	1.000	1.000	1.000	1.000	1.000	1.000	1.000	1.000

Bl. Shot:	g6(27)												
Frame:	4	5	6	7	8	9	10	11	12	13	14	PMI	
t [μs]:	40.56	81.12	121.68	162.24	202.8	243.36	283.92	324.48	365.04	405.60	446.16	1000	
N _I	23	39	81	99	128	138	156	170	192	203	217	38	
N _V	0	0	7	10	16	20	30	47	57	82	91	127	
N _R	0	0	0	0	0	0	0	0	0	0	0	127	
N _{TH}	0	4	4	5	6	6	9	10	11	11	11	8	
N _{TM}	1	1	4	6	16	18	21	23	24	32	33	31	
N _X	0	0	0	0	1	1	2	2	3	4	4	8	
N _{TB}	1	5	8	11	22	24	30	33	35	43	44	39	
J _{int}	0	0	7	10	17	21	32	49	60	86	95	262	
C _{max} [m/s]	253	204	891	236	1235	384	639	373	437	725	425		
C _{ave} [m/s]	106	116	276	98	165	130	142	119	111	135	106		
# Extensions	12	10	31	20	32	13	29	29	29	36	19		
N-tot	24	44	96	120	167	183	218	252	287	332	356	339	
N _I +N _V +N _R +N _X	23	39	88	109	145	159	188	219	252	289	312	300	
N _L	12	22	48	60	83	91	108	125	142	164	176	102	
N _B	12	22	55	70	101	113	142	176	205	254	275	499	
N _B /N _L	1.00	1.00	1.15	1.17	1.22	1.24	1.31	1.41	1.44	1.55	1.56	4.89	
# 2D fragments	1	1	3	4	6	7	14	18	22	37	43	187	
C _L	0.17	0.45	0.63	0.70	0.94	0.99	1.15	1.31	1.34	1.57	1.58	5.90	
C _B	0.23	0.56	0.71	0.78	0.96	0.99	1.09	1.19	1.20	1.32	1.32	1.93	
p _I	0.88	0.72	0.64	0.61	0.52	0.50	0.45	0.41	0.40	0.34	0.34	0.04	
p _C	0.12	0.28	0.36	0.39	0.48	0.50	0.55	0.59	0.60	0.66	0.66	0.96	
p _{II}	0.78	0.52	0.41	0.37	0.27	0.25	0.21	0.17	0.16	0.12	0.12	0.00	
p _{IC}	0.10	0.20	0.23	0.24	0.25	0.25	0.25	0.24	0.24	0.22	0.22	0.03	
p _{CC}	0.01	0.08	0.13	0.15	0.23	0.25	0.30	0.35	0.36	0.43	0.44	0.93	

Grapher:														
Bl. Shot:	27		Frame											
axis	degree	nodes	4	5	6	7	8	9	10	11	12	13	14	PMI
x	0	I	0.958	0.886	0.844	0.825	0.766	0.754	0.716	0.675	0.669	0.611	0.610	0.112
y	120	TH+TM	0.042	0.114	0.083	0.092	0.132	0.131	0.138	0.131	0.122	0.130	0.124	0.115
z	240	J _{int}	0.000	0.000	0.073	0.083	0.102	0.115	0.147	0.194	0.209	0.259	0.267	0.773
check		sum	1.000	1.000	1.000	1.000	1.000	1.000	1.000	1.000	1.000	1.000	1.000	1.000

Grapher:														
Bl. Shot:	27		Frame											
axis	degree	nodes	4	5	6	7	8	9	10	11	12	13	14	PMI
x	0	I	1.000	1.000	0.920	0.908	0.883	0.868	0.830	0.776	0.762	0.702	0.696	0.127
y	120	Y	0.000	0.000	0.080	0.092	0.110	0.126	0.160	0.215	0.226	0.284	0.292	0.423
z	240	X + R	0.000	0.000	0.000	0.000	0.007	0.006	0.011	0.009	0.012	0.014	0.013	0.450
check		sum	1.000	1.000	1.000	1.000	1.000	1.000	1.000	1.000	1.000	1.000	1.000	1.000

Bl. Shot:	g12(24)							
Frame:	4	5	6	7	8	9	10	11
t [μs]:	40.56	81.12	121.68	162.24	202.80	243.36	283.92	324.48
N _I	8	102	260	431	532	682	813	974
N _Y	0	3	52	127	127	127	127	127
N _R	0	0	0	8	117	127	127	127
N _{TH}	0	3	8	7	7	7	7	7
N _{TM}	0	4	4	9	9	9	15	13
N _X	0	0	0	4	4	6	13	19
N _{TB}	0	7	12	16	16	16	22	20
J _{int}	0	3	52	139	248	260	267	273
C _{max} [m/s]	91	785	1043	735	389	483	499	258
Cave [m/s]	73	194	173	110	63	91	68	52
# Extensions	4	52	106	127	113	89	83	44
N-tot	8	112	324	586	796	958	1102	1267
N _I +N _Y +N _R +N _X	8	105	312	570	780	942	1080	1247
N _L	4	56	162	287	338	413	481	561
N _B	4	59	214	438	706.5	805.5	888	979.5
N _B /N _L	1.00	1.05	1.32	1.53	2.09	1.95	1.85	1.75
# 2D fragments	1	1	19	36	77	111	145	142
C _L	0.00	0.36	0.79	1.08	1.56	1.34	1.20	1.05
C _B	0.00	0.45	0.85	1.05	1.26	1.17	1.11	1.03
P _I	1.00	0.77	0.58	0.47	0.37	0.42	0.45	0.49
P _C	0.00	0.23	0.42	0.53	0.63	0.58	0.55	0.51
P _{II}	1.00	0.60	0.33	0.23	0.14	0.17	0.20	0.24
P _{IC}	0.00	0.18	0.24	0.25	0.23	0.24	0.25	0.25
P _{CC}	0.00	0.05	0.18	0.28	0.40	0.34	0.31	0.26

Grapher:										
Bl. Shot:	24	Frame								
axis	degree	nodes	4	5	6	7	8	9	10	11
x	0	I	1.000	0.911	0.802	0.735	0.668	0.712	0.738	0.769
y	120	TH+TM	0.000	0.063	0.037	0.027	0.020	0.017	0.020	0.016
z	240	J _{int}	0.000	0.027	0.160	0.237	0.312	0.271	0.242	0.215
check		sum	1.000	1.000	1.000	1.000	1.000	1.000	1.000	1.000
Grapher:										
Bl. Shot:	24	Frame								
axis	degree	nodes	4	5	6	7	8	9	10	11
x	0	I	1.000	0.971	0.833	0.756	0.682	0.724	0.753	0.781
y	120	Y	0.000	0.029	0.167	0.223	0.163	0.135	0.118	0.102
z	240	X + R	0.000	0.000	0.000	0.021	0.155	0.141	0.130	0.117
check		sum	1.000	1.000	1.000	1.000	1.000	1.000	1.000	1.000

Bl. Shot:	g12(25)										
Frame:	3	4	5	6	7	8	9	10	11	12	
t [μs]:	40.56	81.12	121.68	162.24	202.80	243.36	283.92	324.48	365.04	405.60	
N _I	19	35	123	263	303	371	461	462	477	455	
N _Y	0	0	3	19	34	61	98	127	127	127	
N _R	0	0	0	0	0	0	0	9	70	127	
N _{TH}	1	1	2	4	5	10	12	14	16	16	
N _{TM}	0	0	12	25	30	34	32	34	35	41	
N _X	0	0	0	1	1	1	1	3	5	17	
N _{TB}	1	1	14	29	35	44	44	48	51	57	
J _{int}	0	0	3	20	35	62	99	139	202	271	
C _{max} [m/s]	116	151	348	992	573	592	440	467	410	299	
C _{ave} [m/s]	72	74	123	136	109	132	81	95	102	85	
# Extensions	10	8	55	110	62	85	77	58	73	111	
N-tot	20	36	140	312	373	477	604	649	730	783	
N _I +N _Y +N _R +N _X	19	35	126	283	338	433	560	601	679	726	
N _L	10	18	70	156	186	238	302	319	328	320	
N _B	10	18	73	176.5	222	301	401.5	469.5	604.5	734.5	
N _B /N _L	1.00	1.00	1.04	1.14	1.19	1.26	1.33	1.47	1.85	2.30	
# 2D fragments	1	1	6	10	15	18	32	38	60	123	
C _L	0.20	0.11	0.49	0.63	0.75	0.89	0.95	1.17	1.55	2.05	
C _B	0.27	0.16	0.59	0.72	0.82	0.92	0.97	1.11	1.27	1.43	
p _I	0.86	0.92	0.71	0.64	0.59	0.54	0.52	0.45	0.36	0.29	
p _C	0.14	0.08	0.29	0.36	0.41	0.46	0.48	0.55	0.64	0.71	
p _{II}	0.75	0.85	0.50	0.41	0.35	0.29	0.27	0.20	0.13	0.08	
p _{IC}	0.12	0.07	0.21	0.23	0.24	0.25	0.25	0.25	0.23	0.20	
p _{CC}	0.02	0.01	0.09	0.13	0.17	0.21	0.23	0.31	0.40	0.51	

Grapher:												
Bl. Shot:	25	Frame										
axis	degree	nodes	3	4	5	6	7	8	9	10	11	12
x	0	I	0.950	0.972	0.879	0.843	0.812	0.778	0.763	0.712	0.653	0.581
y	120	TH+TM	0.050	0.028	0.100	0.093	0.094	0.092	0.073	0.074	0.070	0.073
z	240	J _{int}	0.000	0.000	0.021	0.064	0.094	0.130	0.164	0.214	0.277	0.346
check		sum	1.000	1.000	1.000	1.000	1.000	1.000	1.000	1.000	1.000	1.000

Grapher:											
Bl. Shot:	25	Frame									
axis	degree	nodes	4	5	6	7	8	9	10	11	12
x	0	I	1.000	1.000	0.976	0.929	0.896	0.857	0.823	0.769	0.703
y	120	Y	0.000	0.000	0.024	0.067	0.101	0.141	0.175	0.211	0.187
z	240	X + R	0.000	0.000	0.000	0.004	0.003	0.002	0.002	0.020	0.110
check		sum	1.000	1.000	1.000	1.000	1.000	1.000	1.000	1.000	1.000

Bl. Shot:	g20(26.2)					
Frame:	3	4	5	6	7	8
t [μs]:	40.56	81.12	121.68	162.24	202.80	243.36
N _I	19	44	90	140	160	167
N _V	0	0	5	29	62	102
N _R	0	0	0	0	0	0
N _{TH}	1	4	9	17	18	18
N _{TM}	0	2	6	12	21	26
N _X	0	0	0	2	4	7
N _{TB}	1	6	15	29	39	44
J _{int}	0	0	5	31	66	109
C _{max} [m/s]	329	510	608	539	671	481
C _{ave} [m/s]	112	192	198	200	124	151
# Extensions	10	15	41	67	58	50
N-tot	20	50	110	200	265	320
N _I +N _V +N _R +N _X	19	44	95	171	226	276
N _L	10	25	55	99	131	157
N _B	10	25	60	132	200.5	272.5
N _B /N _L	1.00	1.00	1.09	1.33	1.54	1.74
# 2D fragments	1	1	2	14	29	53
C _L	0.20	0.48	0.73	1.21	1.61	1.96
C _B	0.27	0.58	0.80	1.13	1.33	1.47
p _I	0.86	0.71	0.60	0.43	0.33	0.26
p _C	0.14	0.29	0.40	0.57	0.67	0.74
p _{II}	0.75	0.50	0.36	0.19	0.11	0.07
p _{IC}	0.12	0.21	0.24	0.25	0.22	0.19
p _{CC}	0.02	0.08	0.16	0.32	0.44	0.54

Grapher:								
Bl. Shot:	26.2	Frame						
axis	degree	nodes	3	4	5	6	7	8
x	0	I	0.950	0.880	0.818	0.700	0.604	0.522
y	120	TH+TM	0.050	0.120	0.136	0.145	0.147	0.138
z	240	J _{int}	0.000	0.000	0.045	0.155	0.249	0.341
check		sum	1.000	1.000	1.000	1.000	1.000	1.000

Grapher:								
Bl. Shot:	26.2	Frame						
axis	degree	nodes	3	4	5	6	7	8
x	0	I	1.000	1.000	0.947	0.819	0.708	0.605
y	120	Y	0.000	0.000	0.053	0.170	0.274	0.370
z	240	X + R	0.000	0.000	0.000	0.012	0.018	0.025
check		sum	1.000	1.000	1.000	1.000	1.000	1.000

Bl. Shot:	m12 8		narrow			
Frame:	17	18	19	20	21	22
t [μ s]	28	56	84	112	140	168
N _I	18	29	38	65	70	82
N _Y	0	1	10	18	34	40
N _R	0	0	0	0	0	0
N _{TB}	0	0	0	4	4	6
N _X	0	0	0	1	3	3
N _Y +N _R +N _X	0	1	10	19	37	43
Cmax [m/s]	39	81	122	998	462	523
Cave [m/s]	27	34	53	133	134	148
N-tot	18	30	48	88	111	131

Bl. Shot:	8		t [μ s]					
axis	degree	nodes	28	56	84	112	140	168
x	0	I	1.000	0.967	0.792	0.739	0.631	0.626
y	120	TH+TM	0.000	0.000	0.000	0.045	0.036	0.046
z	240	Y+R+X	0.000	0.033	0.208	0.216	0.333	0.328
check		sum	1.000	1.000	1.000	1.000	1.000	1.000

Bl. Shot:	m12 9		narrow				
Frame:	3	4	5	6	7	8	9
t [μ s]	28	56	84	112	140	168	196
N _I	28	92	188	284	364	404	464
N _Y	1	36	87	105	127	127	127
N _R	0	0	0	0	40	85	127
N _{TB}	5	11	14	12	16	20	22
N _X	0	0	1	3	4	10	9
N _Y +N _R +N _X	1	36	88	108	171	222	263
Cmax [m/s]	1465	1418	370	341	794	310	644
Cave [m/s]	252	205	119	111	103	72	83.12
N-tot	34	139	290	404	551	646	749

Bl. Shot:	9		t [μ s]						
axis	degree	nodes	28	56	84	112	140	168	196
x	0	I	0.824	0.662	0.648	0.703	0.661	0.625	0.619
y	120	TH+TM	0.147	0.079	0.048	0.030	0.029	0.031	0.029
z	240	Y+R+X	0.029	0.259	0.303	0.267	0.310	0.344	0.351
check		sum	1.000	1.000	1.000	1.000	1.000	1.000	1.000

Bl. Shot:	m12 10		narrow							
Frame:	3	4	5	6	7	8	9			
t [μ s]	28	56	84	112	140	168	196			
N _I	22	65	132	214	308	398	459			
N _Y	1	23	74	127	127	127	127			
N _R	0	0	0	15	45	86	127			
N _{TB}	1	12	18	26	28	27	33			
N _X	0	0	3	6	7	7	12			
N _Y +N _R +N _X	1	23	77	148	179	220	266			
Cmax [m/s]	794	893	702	1386	368	400	1168			
Cave [m/s]	271	179	148	177	115	114	140.33			
N-tot	24	100	227	388	515	645	758			

Bl. Shot:	10		t [μ s]						
axis	degree	nodes	28	56	84	112	140	168	196
x	0	I	0.917	0.650	0.581	0.552	0.598	0.617	0.606
y	120	TH+TM	0.042	0.120	0.079	0.067	0.054	0.042	0.044
z	240	Y+R+X	0.042	0.230	0.339	0.381	0.348	0.341	0.351
check		sum	1.000	1.000	1.000	1.000	1.000	1.000	1.000

Bl. Shot:	g12 28.1		narrow								
Frame:	5	6	7	8	9	10	11	12	13		
t [μ s]	30.83	61.66	92.49	123.32	154.15	184.98	215.81	246.64	277.47		
N _I	14	42	101	205	316	431	553	694	889		
N _Y	0	2	12	44	107	127	127	127	127		
N _R	0	0	0	0	0	65	127	127	127		
N _{TB}	0	0	0	2	5	7	8	13	13		
N _X	0	0	0	0	0	6	8	14	17		
N _Y +N _R +N _X	0	2	12	44	107	198	262	268	271		
Cmax [m/s]	94	513	555	859	434	544	518	565.81	351.79		
Cave [m/s]	57	116	102	125	62	85	79.68	77.62	64.35		
N-tot	14	44	113	251	428	636	823	975	1173		

Bl. Shot:	28.1		t [μ s]								
axis	degree	nodes	30.83	61.66	92.49	123.32	154.15	184.98	215.81	246.64	277.47
x	0	I	1.000	0.955	0.894	0.817	0.738	0.678	0.672	0.712	0.758
y	120	TH+TM	0.000	0.000	0.000	0.008	0.012	0.011	0.010	0.013	0.011
z	240	Y+R+X	0.000	0.045	0.106	0.175	0.250	0.311	0.318	0.275	0.231
check		sum	1.000	1.000	1.000	1.000	1.000	1.000	1.000	1.000	1.000

Bl. Shot:	g12 28.2		narrow				
Frame:	8	9	10	11	12	13	14
t [μ s]	27.66	55.32	82.98	110.64	138.3	165.96	193.62
N_I	10	63	152	231	281	356	385
N_Y	0	4	31	85	127	127	127
N_R	0	0	0	0	25	72	118
N_{TB}	0	7	14	15	17	20	25
N_X	0	0	0	1	3	6	8
$N_Y+N_R+N_X$	0	4	31	86	155	205	253
C_{max} [m/s]	432	1322	1813	553	827	954	890
Cave [m/s]	236	295	313	154	153	186	141.42
N-tot	10	74	197	332	453	581	663

Bl. Shot:	28.2		t [μ s]						
axis	degree	nodes	27.66	55.32	82.98	110.64	138.3	165.96	193.62
x	0	I	1.000	0.851	0.772	0.696	0.620	0.613	0.581
y	120	TH+TM	0.000	0.095	0.071	0.045	0.038	0.034	0.038
z	240	Y+R+X	0.000	0.054	0.157	0.259	0.342	0.353	0.382
check		sum	1.000	1.000	1.000	1.000	1.000	1.000	1.000

Bl. Shot:	g12 29.1		narrow		
Frame:	7	8	9	10	11
t [μ s]	30.83	61.66	92.49	123.32	154.15
N_I	44	170	377	568	720
N_Y	0	49	127	127	127
N_R	0	0	73	127	127
N_{TB}	0	9	12	11	12
N_X	0	0	3	14	16
$N_Y+N_R+N_X$	0	49	203	268	270
C_{max} [m/s]	351	774	344	687	439
Cave [m/s]	105	165	49	64	46
N-tot	44	228	592	847	1002

Bl. Shot:	29.1		t [μ s]				
axis	degree	nodes	30.83	61.66	92.49	123.32	154.15
x	0	I	1.000	0.746	0.637	0.671	0.719
y	120	TH+TM	0.000	0.039	0.020	0.013	0.012
z	240	Y+R+X	0.000	0.215	0.343	0.316	0.269
check		sum	1.000	1.000	1.000	1.000	1.000

Bl. Shot:	g6 29.2		narrow		
Frame:	7	8	9	10	11
t [μs]	27.66	55.32	82.98	110.64	138.3
N_I	39	71	102	126	151
N_Y	0	8	22	30	45
N_R	0	0	0	0	0
N_{TB}	3	5	6	7	8
N_X	0	0	1	1	2
N_Y+N_R+N_X	0	8	23	31	47
C_{max} [m/s]	722	1280	381	940	549
C_{ave} [m/s]	255	268	102	246	193
N-tot	42	84	131	164	206

Bl. Shot:	29.2		t [μs]				
axis	degree	nodes	27.66	55.32	82.98	110.64	138.3
x	0	I	0.929	0.845	0.779	0.768	0.733
y	120	TH+TM	0.071	0.060	0.046	0.043	0.039
z	240	Y+R+X	0.000	0.095	0.176	0.189	0.228
check		sum	1.000	1.000	1.000	1.000	1.000

Crack-propagation data sets

Bl. shot		t [μ s]												
		40.56	81.12	121.68	162.24	202.8	243.36	283.92	324.48	365.04	405.6	446.16	486.72	527.28
m6(22.2)	Count	4	8	17	17	10	14	7	4	3	4			
	Cmax	70	325	492	224	379	458	375	111	131	235			
	Cave	48	128	149	78	107	113	72	32	46	63			
m6(23.2)	Count	3	2	5	25	23	13	11	18	24	14	5	7	14
	Cmax	382	81	78	372	338	383	163	258	262	740	179	107	155
	Cave	165	62	50	87	120	128	58	130	79	148	44	46	50
m12(20)	Count	8	5	6	7	3	11	16	13	18	12	11	1	
	Cmax	274	207	169	248	74	554	411	439	378	295	187	2	
	Cave	146	143	77	164	41	198	118	142	110	89	74	2	
m12(21)	Count	24	41	38	50	30	22	4	11	4	10	11		
	Cmax	469	1169	472	575	296	713	510	629	142	855	296		
	Cave	114	205	97	132	99	105	264	204	61	164	115		
m20(22.1)	Count	16	20	15	19	18	18	19	19					
	Cmax	376	661	690	374	387	284	454	412					
	Cave	78	203	227	105	186	139	137	115					
m20(23.1)	Count	8	12	12	6	27	34	31	42	26	41	23		
	Cmax	277	407	202	406	775	1224	275	1631	524	1050	345		
	Cave	92	119	72	109	229	195	124	229	138	161	120		
g6(26.1)	Count	6	10	16	17	15	13	14	23	20	21	19	14	31
	Cmax	374	288	176	553	195	409	486	361	339	514	323	178	354
	Cave	191	122	64	196	89	135	246	103	114	139	103	94	72
g6(27)	Count	12	10	31	20	32	13	29	29	29	36	19		
	Cmax	253	204	891	236	1235	384	639	373	437	725	425		
	Cave	106	116	276	98	165	130	142	119	111	134	106		
g12(24)	Count	4	52	106	127	113	89	83	44					
	Cmax	91	785	1043	735	389	483	499	263					
	Cave	73	189	175	111	62	89	69	45					
g12(25)	Count	10	8	55	110	62	85	77	58	73	111			
	Cmax	116	151	348	992	573	592	440	467	410	299			
	Cave	72	74	123	136	109	132	81	95	102	85			
g20(26.2)	Count	10	15	41	67	58	50							
	Cmax	329	510	608	539	671	481							
	Cave	112	192	198	200	124	151							

Sets from CTt

Bl. Shot:	m12(21)										top
Axial position [mm]:	1.47	34.14	60.86	90.56	120.26	149.96	179.66	209.36	239.06	268.76	
Image:	101	111	121	131	141	151	161	171	181	191	
N_I	50	64	64	33	17	40	42	32	30	31	
N_Y	49	107	61	43	57	34	54	58	41	65	
N_R	0	0	0	0	0	0	0	0	0	0	
N_{TH}	8	8	9	9	10	10	10	9	7	7	
N_{TM}	25	25	28	17	17	20	19	21	20	23	
N_X	0	1	3	0	0	0	0	0	0	0	
N_{TB}	33	33	37	26	27	30	29	30	27	30	
px/mm	9.40	9.40	9.40	9.40	9.40	9.40	9.40	9.40	9.40	9.40	
J_{int}	49	108	64	43	57	34	54	58	41	65	
N-tot	132	205	165	102	101	104	125	120	98	126	
N_I+N_Y+N_R+N_X	99	172	128	76	74	74	96	90	71	96	
N_L	66	102	81	51	51	52	63	60	49	63	
N_B	115	211	148	94	107.5	86	116.5	118	90	128	
N_B/N_L	1.74	2.07	1.83	1.84	2.13	1.65	1.86	1.97	1.84	2.03	
# 2D fragments	27	49	27	23	35	20	28	33	18	31	
C_L	2.48	2.76	2.49	2.71	3.33	2.46	2.66	2.93	2.78	3.02	
C_B	1.66	1.74	1.65	1.73	1.87	1.66	1.71	1.78	1.74	1.80	
p_I	0.17	0.13	0.17	0.14	0.06	0.17	0.14	0.11	0.13	0.10	
p_C	0.83	0.87	0.83	0.86	0.94	0.83	0.86	0.89	0.87	0.90	
p_{II}	0.03	0.02	0.03	0.02	0.00	0.03	0.02	0.01	0.02	0.01	
p_{IC}	0.14	0.11	0.14	0.12	0.06	0.14	0.12	0.10	0.11	0.09	
p_{CC}	0.69	0.75	0.68	0.74	0.88	0.68	0.73	0.80	0.76	0.81	

Grapher:												
Bl. Shot:	21	ct	Axial position [mm]									
axis	degree	nodes	1.47	34.14	60.86	90.56	120.26	149.96	179.66	209.36	239.06	268.76
x	0	I	0.379	0.312	0.388	0.324	0.168	0.385	0.336	0.267	0.306	0.246
y	120	TH+TM	0.250	0.161	0.224	0.255	0.267	0.288	0.232	0.250	0.276	0.238
z	240	J_{int}	0.371	0.527	0.388	0.422	0.564	0.327	0.432	0.483	0.418	0.516
check		sum	1.000	1.000	1.000	1.000	1.000	1.000	1.000	1.000	1.000	1.000

Bl. Shot:	m20(23.1)										top
Axial position [mm]:	3	33	63	93	123	153	183	213	243	273	
Image:	1	11	21	31	41	51	61	71	81	91	
N_I	36	69	55	40	35	44	54	34	39	62	
N_Y	48	58	68	66	68	62	50	32	39	78	
N_R	0	0	0	0	0	0	0	0	0	0	
N_{TH}	9	9	15	8	7	10	10	8	10	6	
N_{TM}	23	26	24	20	24	16	22	24	25	28	
N_X	0	1	0	0	0	0	1	1	0	2	
N_{TB}	106	141	149	133	135	128	120	83	95.5	169	
px/mm	7.80	7.80	7.80	7.80	7.80	7.80	7.80	7.80	7.80	7.80	
J_{int}	48	59	68	66	68	62	51	33	39	80	
N-tot	116	163	162	134	134	132	137	99	113	176	
N_I+N_Y+N_R+N_X	84	128	123	106	103	106	105	67	78	142	
N_L	58	81	81	67	67	66	68	49	57	87	
N_B	106	141	149	133	135	128	120	83	96	169	
N_B/N_L	1.83	1.74	1.84	1.99	2.01	1.94	1.76	1.69	1.69	1.94	
# 2D fragments	27	33	37	39	37	34	30	20	20	39	
C_L	2.76	2.32	2.64	2.81	2.96	2.67	2.44	2.65	2.62	2.62	
C_B	1.74	1.61	1.71	1.75	1.79	1.71	1.64	1.70	1.70	1.69	
p_I	0.13	0.20	0.15	0.12	0.11	0.14	0.18	0.15	0.15	0.15	
p_C	0.87	0.80	0.85	0.88	0.89	0.86	0.82	0.85	0.85	0.85	
p_{II}	0.02	0.04	0.02	0.02	0.01	0.02	0.03	0.02	0.02	0.02	
p_{IC}	0.11	0.16	0.12	0.11	0.09	0.12	0.15	0.13	0.13	0.13	
p_{CC}	0.76	0.65	0.73	0.77	0.80	0.73	0.68	0.73	0.72	0.72	

Grapher:												
Bl. Shot:	23.1	ct	Axial position [mm]									
axis	degree	nodes	3	33	63	93	123	153	183	213	243	273
x	0	I	0.310	0.423	0.340	0.299	0.261	0.333	0.394	0.343	0.345	0.352
y	120	TH+TM	0.276	0.215	0.241	0.209	0.231	0.197	0.234	0.323	0.310	0.193
z	240	J _{int}	0.414	0.362	0.420	0.493	0.507	0.470	0.372	0.333	0.345	0.455
check		sum	1.000	1.000	1.000	1.000	1.000	1.000	1.000	1.000	1.000	1.000

Bl. Shot: m6(23.2)											top
Axial position [mm]:	0.5	30.5	60.5	90.5	120.5	150.5	180.5	210.5	240.5	270.5	
Image:	2003	2013	2023	2033	2043	2053	2063	2073	2083	2093	
N_I	44	21	11	10	10	12	11	16	15	16	
N_Y	104	20	23	16	17	19	17	7	23	10	
N_R	0	0	0	0	0	0	0	0	0	0	
N_{TH}	7	7	6	5	3	5	7	4	4	5	
N_{TM}	15	6	11	7	12	4	9	7	8	5	
N_X	3	0	0	0	0	0	1	0	0	0	
N_{TB}	22	13	17	12	15	9	16	11	12	10	
px/mm	11.86	11.86	11.86	11.86	11.86	11.86	11.86	11.86	11.86	11.86	
J_{int}	107	20	23	16	17	19	18	7	23	10	
N-tot	173	54	51	38	42	40	45	34	50	36	
$N_I+N_Y+N_R+N_X$	151	41	34	26	27	31	29	23	38	26	
N_L	85	27	26	19	21	20	22	17	25	18	
N_B	195	47	48.5	35	38	39	41	24	48	28	
N_B/N_L	2.29	1.74	1.90	1.84	1.81	1.95	1.86	1.41	1.92	1.56	
# 2D fragments	55	9	14	11	11	12	11	6	14	7	
C_L	3.04	2.44	3.14	2.95	3.05	2.80	3.09	2.12	2.80	2.22	
C_B	1.80	1.65	1.83	1.79	1.81	1.75	1.81	1.54	1.75	1.58	
p_I	0.10	0.18	0.08	0.11	0.09	0.13	0.10	0.23	0.13	0.21	
p_C	0.90	0.83	0.92	0.89	0.91	0.88	0.90	0.77	0.88	0.79	
p_{II}	0.01	0.03	0.01	0.01	0.01	0.02	0.01	0.05	0.02	0.04	
p_{IC}	0.09	0.14	0.08	0.10	0.09	0.11	0.09	0.18	0.11	0.17	
p_{CC}	0.81	0.68	0.84	0.80	0.82	0.77	0.82	0.60	0.77	0.62	

Grapher:												
Bl. Shot:	23.2	ct	Axial position [mm]									
axis	degree	nodes	0.5	30.5	60.5	90.5	120.5	150.5	180.5	210.5	240.5	270.5
x	0	I	0.254	0.389	0.216	0.263	0.238	0.300	0.244	0.471	0.300	0.444
y	120	TH+TM	0.127	0.241	0.333	0.316	0.357	0.225	0.356	0.324	0.240	0.278
z	240	J_{int}	0.618	0.370	0.451	0.421	0.405	0.475	0.400	0.206	0.460	0.278
check		sum	1.000	1.000	1.000	1.000	1.000	1.000	1.000	1.000	1.000	1.000

Bl. Shot:	g6(26.1)												top
Axial position [mm]:	0.5	3.5	6.5	30.5	60.5	90.5	120.5	150.5	180.5	210.5	240.5	270.5	
Image:	1	2	3	11	21	31	41	51	61	71	81	91	
N_I	14	4	5	5	4	0	6	8	2	3	4	7	
N_V	18	10	14	9	14	9	9	7	10	13	15	22	
N_R	0	0	0	0	0	0	0	0	0	0	0	0	
N_{TH}	12	5	7	5	4	4	5	4	5	3	3	5	
N_{TM}	8	5	7	5	4	7	8	7	7	9	10	13	
N_X	0	0	0	0	0	0	0	0	0	0	0	0	
N_{TB}	20	10	14	10	8	11	13	11	12	12	13	18	
px/mm	7.80	7.80	7.80	7.80	7.80	7.80	7.80	7.80	7.80	7.80	7.80	7.80	
J_{int}	18	10	14	9	14	9	9	7	10	13	15	22	
N-tot	52	24	33	24	26	20	28	26	24	28	32	47	
$N_I+N_V+N_R+N_X$	32	14	19	14	18	9	15	15	12	16	19	29	
N_L	26	12	17	12	13	10	14	13	12	14	16	24	
N_B	44	22	30.5	21	27	19	23	20	22	27	31	45.5	
N_B/N_L	1.69	1.83	1.85	1.75	2.08	1.90	1.64	1.54	1.83	1.93	1.94	1.94	
# 2D fragments	11	9	9	9	10	6	6	5	6	10	12	14	
C_L	2.92	3.33	3.39	3.17	3.38	4.00	3.14	2.77	3.67	3.57	3.50	3.40	
C_B	1.78	1.88	1.89	1.84	1.89	2.00	1.83	1.74	1.94	1.92	1.91	1.89	
p_I	0.11	0.06	0.06	0.08	0.06	0.00	0.08	0.13	0.03	0.04	0.05	0.06	
p_C	0.89	0.94	0.94	0.92	0.94	1.00	0.92	0.87	0.97	0.96	0.95	0.94	
p_{II}	0.01	0.00	0.00	0.01	0.00	0.00	0.01	0.02	0.00	0.00	0.00	0.00	
p_{IC}	0.10	0.06	0.05	0.07	0.05	0.00	0.08	0.11	0.03	0.04	0.04	0.05	
p_{CC}	0.79	0.88	0.89	0.85	0.89	1.00	0.84	0.76	0.94	0.92	0.91	0.89	

Grapher:														
Bl. Shot:	26.1	ct	Axial position [mm]											
axis	degree	nodes	0.5	3.5	6.5	30.5	60.5	90.5	120.5	150.5	180.5	210.5	240.5	270.5
x	0	I	0.269	0.167	0.152	0.208	0.154	0.000	0.214	0.308	0.083	0.107	0.125	0.149
y	120	TH+TM	0.385	0.417	0.424	0.417	0.308	0.550	0.464	0.423	0.500	0.429	0.406	0.383
z	240	J_{int}	0.346	0.417	0.424	0.375	0.538	0.450	0.321	0.269	0.417	0.464	0.469	0.468
check		sum	1.000	1.000	1.000	1.000	1.000	1.000	1.000	1.000	1.000	1.000	1.000	1.000

Bl. Shot: g12(28.1)										top
Axial position [mm]:	3	33	63	93	123	153	183	213	243	273
Image:	1	11	21	31	41	51	61	71	81	91
N_I	14	18	34	13	19	29	41	24	34	39
N_V	40	42	55	55	66	35	83	70	66	71
N_R	0	0	0	0	0	0	0	0	0	0
N_{TH}	11	8	8	12	5	11	7	8	9	7
N_{TM}	13	20	29	25	24	21	27	31	36	34
N_X	0	0	0	0	0	0	1	1	0	0
N_{TB}	24	28	37	37	29	32	34	39	45	41
px/mm	7.80	7.80	7.80	7.80	7.80	7.80	7.80	7.80	7.80	7.80
J_{int}	40	42	55	55	66	35	84	71	66	71
N-tot	78	88	126	105	114	96	159	134	145	151
N_I+N_V+N_R+N_X	54	60	89	68	85	64	125	95	100	110
N_L	39	44	63	53	57	48	79	67	73	76
N_B	79	86	118	107.5	123	83	164	138.5	138.5	146.5
N_B/N_L	2.03	1.95	1.87	2.05	2.16	1.73	2.08	2.08	1.91	1.94
# 2D fragments	25	26	33	38	37	23	42	41	41	38
C_L	3.28	3.18	2.92	3.50	3.33	2.79	2.99	3.31	3.06	2.97
C_B	1.86	1.84	1.78	1.91	1.88	1.75	1.79	1.86	1.81	1.79
p_I	0.07	0.08	0.11	0.04	0.06	0.13	0.10	0.07	0.09	0.10
p_C	0.93	0.92	0.89	0.96	0.94	0.87	0.90	0.93	0.91	0.90
p_{II}	0.00	0.01	0.01	0.00	0.00	0.02	0.01	0.00	0.01	0.01
p_{IC}	0.06	0.07	0.10	0.04	0.06	0.11	0.09	0.06	0.08	0.09
p_{CC}	0.87	0.85	0.79	0.91	0.88	0.76	0.80	0.87	0.82	0.80

Grapher:												
Bl. Shot:	28.1	ct	Axial position [mm]									
axis	degree	nodes	3	33	63	93	123	153	183	213	243	273
x	0	I	0.179	0.205	0.270	0.124	0.167	0.302	0.258	0.179	0.234	0.258
y	120	TH+TM	0.308	0.318	0.294	0.352	0.254	0.333	0.214	0.291	0.310	0.272
z	240	J_{int}	0.513	0.477	0.437	0.524	0.579	0.365	0.528	0.530	0.455	0.470
check		sum	1.000	1.000	1.000	1.000	1.000	1.000	1.000	1.000	1.000	1.000

Sets from CTnp

Bl. Shot:		m6(23.2)												
Radial position [mm]:		11.4	16.4	21.4	26.4	31.4	36.4	41.4	46.4	51.4	56.4	61.4	66.4	
Image:		0	1	2	3	4	5	6	7	8	9	10	11	PMM
N _I		25	12	10	10	10	14	11	6	7	21	29	27	25
N _V		44	12	13	12	13	14	4	8	10	15	15	19	62
N _R		0	0	0	0	0	0	0	0	0	0	0	0	0
N _{Tub}		2	2	2	2	2	2	3	2	2	2	2	3	5
N _{Tlb}		5	2	3	2	3	2	2	4	3	2	2	3	10
N _X		3	0	0	0	0	0	0	0	0	0	0	0	0
N _{TB}		7	4	5	4	5	4	5	6	5	4	4	6	15
px/mm		7.82	7.82	7.82	7.82	7.82	7.82	7.82	7.82	7.82	7.82	7.82	7.82	5.02
J _{int}		47	12	13	12	13	14	4	8	10	15	15	19	62
N-tot		79	28	28	26	28	32	20	20	22	40	48	52	102
# 2D fragments		15	3	4	4	4	1	2	4	4	6	6	5	34

Grapher:		Radial position [mm]:													
Bl. Shot:	23.2	CTnp	11.4	16.4	21.4	26.4	31.4	36.4	41.4	46.4	51.4	56.4	61.4	66.4	PMM
axis	degree	nodes	0	1	2	3	4	5	6	7	8	9	10	11	
x	0	I	0.316	0.429	0.357	0.385	0.357	0.438	0.550	0.300	0.318	0.525	0.604	0.519	0.245
y	120	Tub+Tlb	0.089	0.143	0.179	0.154	0.179	0.125	0.250	0.300	0.227	0.100	0.083	0.115	0.147
z	240	J _{int}	0.595	0.429	0.464	0.462	0.464	0.438	0.200	0.400	0.455	0.375	0.313	0.365	0.608
check		sum	1.000	1.000	1.000	1.000	1.000	1.000	1.000	1.000	1.000	1.000	1.000	1.000	1.000

Bl. Shot:		m12(21)														
Radial position [mm]:		7	12	17	22	27	32	37	42	47	52	57	62	67	72	
Image:		0	1	2	3	4	5	6	7	8	9	10	11	12	13	PMM
N _I		15	119	117	121	112	126	119	156	174	149	158	162	155	181	138
N _V		82	70	36	45	54	42	45	39	39	45	39	30	29	39	127
N _R		0	0	0	0	0	0	0	0	0	0	0	0	0	0	117
N _{Tub}		2	9	7	6	6	7	7	6	7	7	9	11	6	7	5
N _{Tlb}		7	4	4	6	4	5	7	7	6	11	6	7	8	9	26
N _X		0	2	0	0	0	4	0	1	2	1	0	0	1	0	11
N _{TB}		9	13	11	12	10	12	14	13	13	18	15	18	14	16	31
px/mm		7.78	7.78	7.78	7.78	7.78	7.78	7.78	7.78	7.78	7.78	7.78	7.78	7.78	7.78	3.96
J _{int}		82	72	36	45	54	46	45	40	41	46	39	30	30	39	255
N-tot		106	204	164	178	176	184	178	209	228	213	212	210	199	236	424
# 2D fragments		29	16	4	5	8	7	8	5	4	7	5	4	3	4	72

Grapher:		Radial position [mm]:															
Bl. Shot:	21	CTnp	7	12	17	22	27	32	37	42	47	52	57	62	67	72	PMM
axis	degree	nodes	0	1	2	3	4	5	6	7	8	9	10	11	12	13	m12(21)
x	0	I	0.142	0.583	0.713	0.680	0.636	0.685	0.669	0.746	0.763	0.700	0.745	0.771	0.779	0.767	0.325
y	120	Tub+Tlb	0.085	0.064	0.067	0.067	0.057	0.065	0.079	0.062	0.057	0.085	0.071	0.086	0.070	0.068	0.073
z	240	J _{int}	0.774	0.353	0.220	0.253	0.307	0.250	0.253	0.191	0.180	0.216	0.184	0.143	0.151	0.165	0.601
check		sum	1.000	1.000	1.000	1.000	1.000	1.000	1.000	1.000	1.000	1.000	1.000	1.000	1.000	1.000	1.000

Bl. Shot:		m20(23.1)												
Radial position [mm]:		16.45	21.45	26.45	31.45	36.45	41.45	46.45	51.45	56.45	61.45	66.45	71.45	
Image:		0	1	2	3	4	5	6	7	8	9	10	11	PMM
N _I		108	115	115	151	193	185	147	163	165	143	176	184	162
N _V		127	103	127	107	127	109	87	87	85	94	76	74	127
N _R		11	0	7	1	7	0	0	0	0	0	0	0	127
N _{Tub}		9	9	10	9	10	11	13	11	14	11	13	11	24
N _{Tlb}		8	7	6	8	6	7	8	9	10	10	7	9	24
N _X		3	1	3	1	5	5	4	1	0	1	1	2	4
N _{TB}		17	16	16	17	16	18	21	20	24	21	20	20	48
px/mm		7.84	7.84	7.84	7.84	7.84	7.84	7.84	7.84	7.84	7.84	7.84	7.84	4.79
J _{int}		141	104	137	109	139	114	91	88	85	95	77	76	258
N-tot		266	235	268	277	348	317	259	271	274	259	273	280	468
# 2D fragments		39	22	30	20	26	19	21	17	23	29	17	24	108

Grapher:		Radial position [mm]:													
Bl. Shot:	23.1	CTnp	16.45	21.45	26.45	31.45	36.45	41.45	46.45	51.45	56.45	61.45	66.45	71.45	PMM
axis	degree	nodes	0	1	2	3	4	5	6	7	8	9	10	11	
x	0	I	0.406	0.489	0.429	0.545	0.555	0.584	0.568	0.601	0.602	0.552	0.645	0.657	0.346
y	120	Tub+Tlb	0.064	0.068	0.060	0.061	0.046	0.057	0.081	0.074	0.088	0.081	0.073	0.071	0.103
z	240	J _{int}	0.530	0.443	0.511	0.394	0.399	0.360	0.351	0.325	0.310	0.367	0.282	0.271	0.551
check		sum	1.000	1.000	1.000	1.000	1.000	1.000	1.000	1.000	1.000	1.000	1.000	1.000	1.000

Bl. Shot:		g6(26.1)											
Radial position [mm]:		17.62	22.62	27.62	32.62	37.62	42.62	47.62	52.62	57.62	62.62	67.62	
Image:		0	1	2	3	4	5	6	7	8	9	10	PMM
N _I		58	82	72	62	42	41	47	41	54	48	56	3
N _Y		56	53	49	59	41	26	34	24	19	18	29	37
N _R		0	0	0	0	0	0	0	0	0	0	0	0
N _{Tub}		5	2	3	3	4	4	6	3	5	5	4	7
N _{Tlb}		3	3	4	6	7	5	5	4	4	3	3	5
N _X		0	2	0	0	1	0	0	0	0	0	0	1
N _{TB}		8	5	7	9	11	9	11	7	9	8	7	12
px/mm		8.76	8.76	8.76	8.76	8.76	8.76	8.76	8.76	8.76	8.76	8.76	4.95
J _{int}		56	55	49	59	42	26	34	24	19	18	29	38
N-tot		122	142	128	130	95	76	92	72	82	74	92	53
# 2D fragments		14	11	6	16	11	6	5	5	3	3	7	23

Grapher:		Radial position [mm]:													
Bl. Shot:		26.1	CTnp	17.62	22.62	27.62	32.62	37.62	42.62	47.62	52.62	57.62	62.62	67.62	PMM
axis		degree	nodes	0	1	2	3	4	5	6	7	8	9	10	
x		0	I	0.475	0.577	0.563	0.477	0.442	0.539	0.511	0.569	0.659	0.649	0.609	0.057
y		120	Tub+Tlb	0.066	0.035	0.055	0.069	0.116	0.118	0.120	0.097	0.110	0.108	0.076	0.226
z		240	J _{int}	0.459	0.387	0.383	0.454	0.442	0.342	0.370	0.333	0.232	0.243	0.315	0.717
check			sum	1.000	1.000	1.000	1.000	1.000	1.000	1.000	1.000	1.000	1.000	1.000	1.000

Bl. Shot:		g12(28.1)												
Radial position [mm]:		13.09	18.09	23.09	28.09	33.09	38.09	43.09	48.09	53.09	58.09	63.09	g12(24)	g12(25)
Image:		0	1	2	3	4	5	6	7	8	9	10	PMM	PMM
N _I		144	148	204	170	149	126	138	155	119	160	135	56	54
N _Y		127	127	127	127	127	127	127	127	127	127	110	127	127
N _R		127	127	127	127	123	67	38	41	21	6	0	64	45
N _{Tub}		0	7	8	7	11	14	12	9	11	10	11	6	2
N _{Tlb}		18	16	11	6	8	7	9	8	9	7	8	10	9
N _X		9	7	5	6	9	3	2	3	3	2	3	7	1
N _{TB}		18	23	19	13	19	21	21	17	20	17	19	16	11
px/mm		7.83	7.83	7.83	7.83	7.83	7.83	7.83	7.83	7.83	7.83	7.83		
J _{int}		263	261	259	260	259	197	167	171	151	135	113	198	173
N-tot		425	432	482	443	427	344	326	343	290	312	267	270	238
# 2D fragments		108	97	70	70	68	57	40	34	41	25	21	70	63

Grapher:		Radial position [mm]:														
Bl. Shot:		28.1	CTnp	13.09	18.09	23.09	28.09	33.09	38.09	43.09	48.09	53.09	58.09	63.09	PMM	
axis		degree	nodes	0	1	2	3	4	5	6	7	8	9	10	g12(24)	g12(25)
x		0	I	0.339	0.343	0.423	0.384	0.349	0.366	0.423	0.452	0.410	0.513	0.506	0.207	0.227
y		120	Tub+Tlb	0.042	0.053	0.039	0.029	0.044	0.061	0.064	0.050	0.069	0.054	0.071	0.059	0.046
z		240	J _{int}	0.619	0.604	0.537	0.587	0.607	0.573	0.512	0.499	0.521	0.433	0.423	0.733	0.727
check			sum	1.000	1.000	1.000	1.000	1.000	1.000	1.000	1.000	1.000	1.000	1.000	1.000	1.000

Appendix 9 Additional results of the topological analysis

Crack-line count (N_L) and branch count (N_B)

Figure 237 shows an example of calculated crack-line count (N_L [-]) and the branch count (N_B [-]) concerning the elapsed time from the detonation in the HSI (see Section 4.1.5).

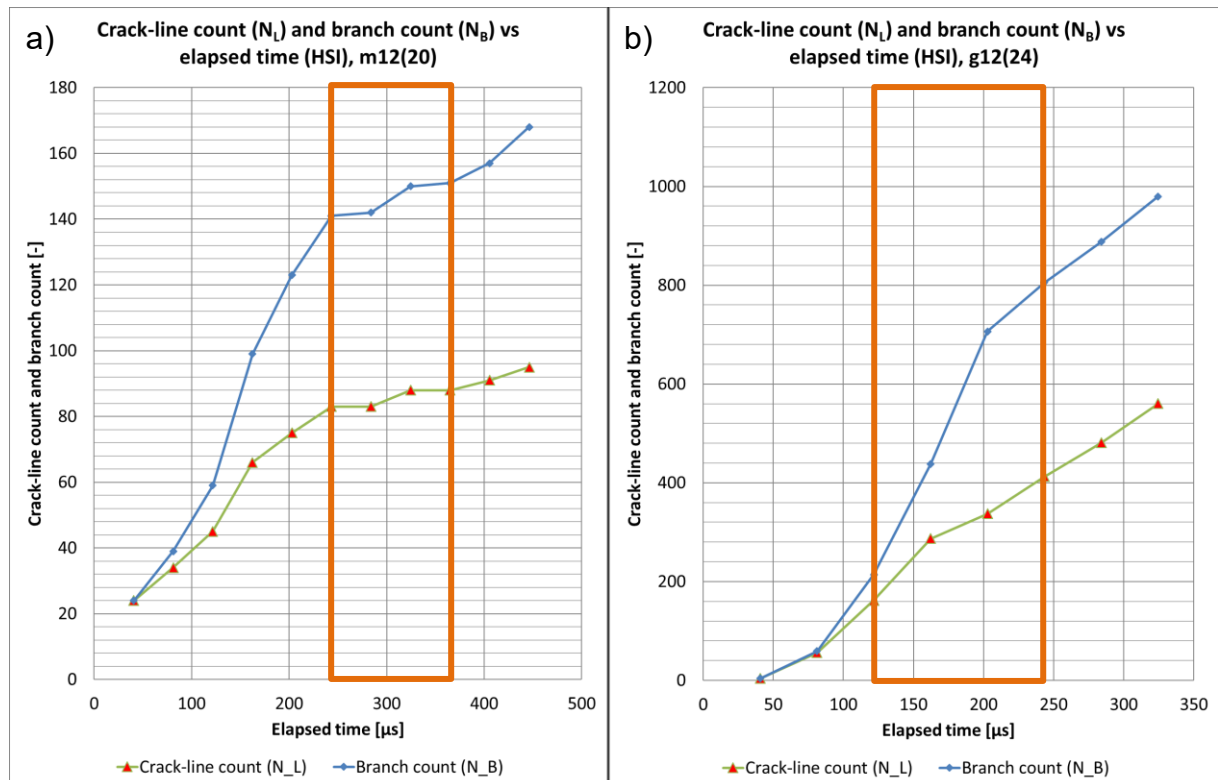


Figure 237: Crack-line count (N_L) and branch count (N_B) concerning time elapsed from the detonation (HSI): a) m12(21); b) g12(24). The orange box marks the second fracture phase.

In most cases, N_L and N_B do not differ much in the beginning, i.e., about until the second fracture phase starts (see Section 5.1). Later, N_B significantly exceeds N_L due to multiple branching/merging. Both quantities steadily increase over time with the change in the rate at the beginning of the second fracture phase.

However, for m6(22.2), m6(23.2), m12(20), m12(21), g6(26.1), and g6(27), one or both quantities suddenly drop in the late second fracture phase or later (i.e., in the post-mortem state, shown in PMI). Figure 238 shows such a case.

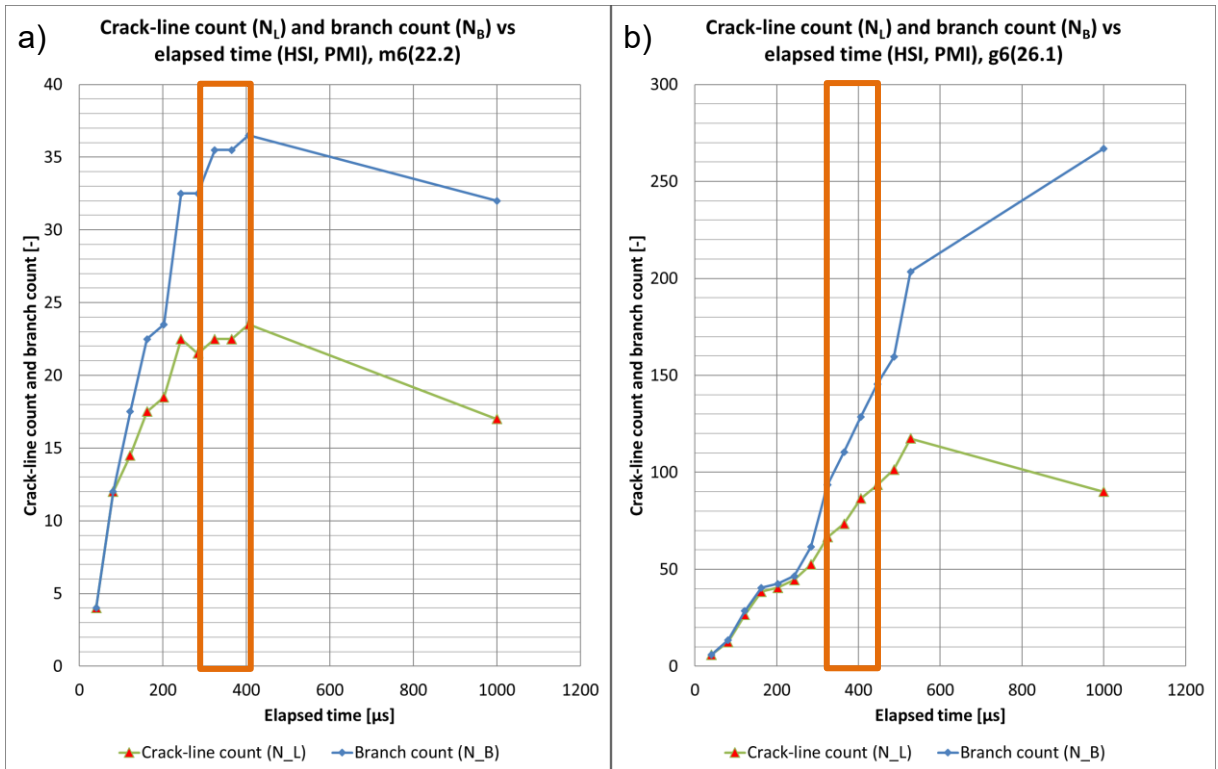


Figure 238: Crack-line count concerning time elapsed from the detonation (HSI and PMI): a) m6(22.2); b) g6(26.1). The post-mortem state is plotted at $t+1000 \mu$ s, as after this time no further change is expected. The orange box marks the second fracture phase.

Such behaviour could be a result of the closure of previously developed cracks at the frontal end face of the cylinder. Here, some of the opened-up cracks in the later stage of development close and seemingly disappear (see Figure 89).

Figure 239 shows the calculated N_L and N_B in the CTt.

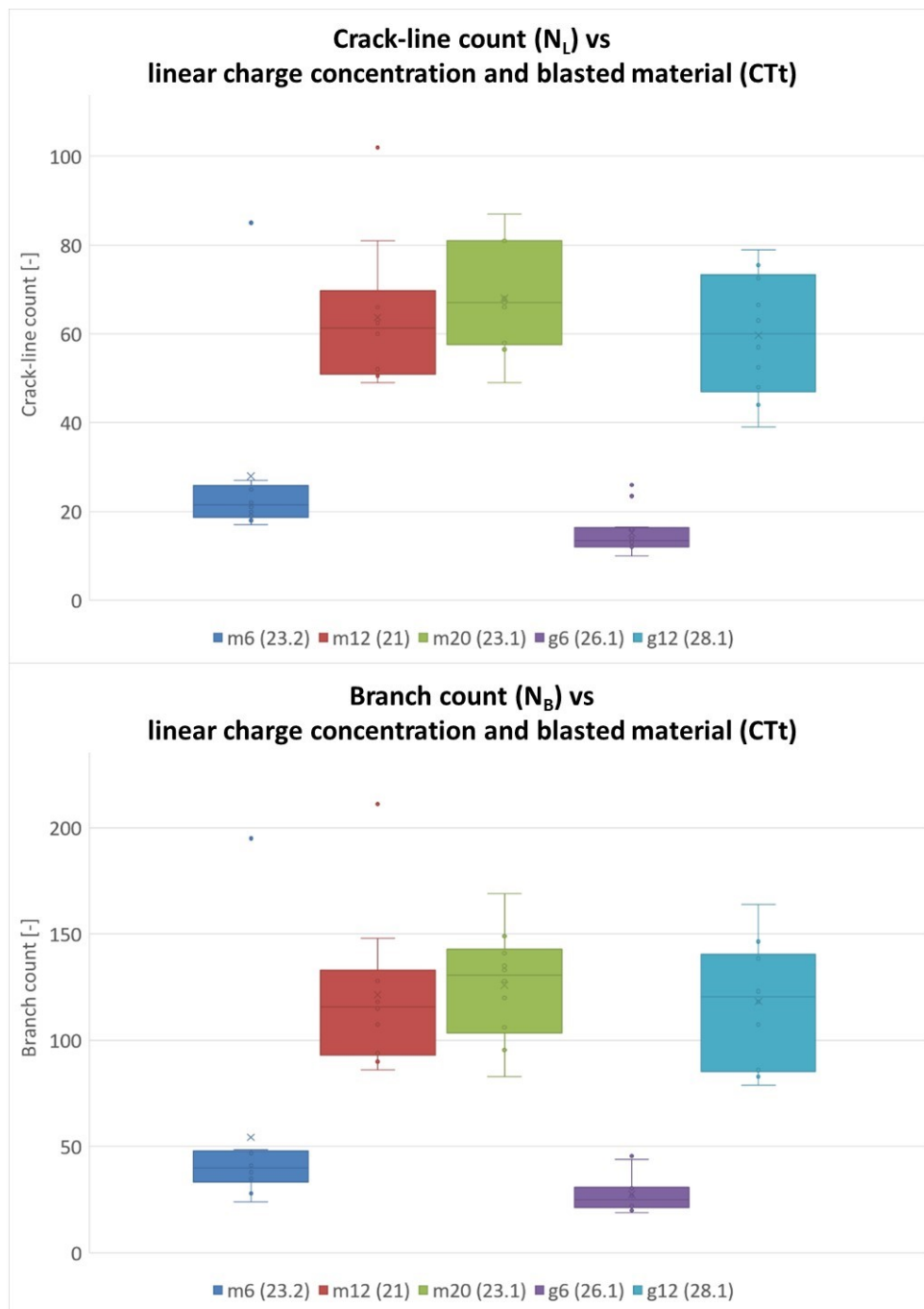


Figure 239: Summary of the crack-line count (N_L) and of the branch count (N_B) in the CTt.

The CTt data show that N_L and N_B increase when increasing the linear charge concentration from 6 g/m to 12 g/m. For the 6-g/m shots, N_L is larger in the mortar than in the granite, though N_B is about the same in both materials (Table 92).

These numbers stay about the same for the 12-g/m shots in both blasted materials and for the 20-g/m shot in the mortar.

Table 92: Statistical evaluation of average N_L and N_B in CTt of 6-g/m shots and of 12- and 20-g/m shots with One-way ANOVA ($\alpha = 0.05$).

Variable		Ave	Std	Data count	F	F_{crit}	p-value	Sign. diff.
N_L	m6(23.2)	27.95	20.32	10	4.49	4.35	0.05	Yes
	g6(26.1)	15.17	4.84	12				
	m12(21)	63.70	16.59	10	0.86	3.35	0.44	No
	g12(28.1)	59.70	13.80	10				
	m20(23.1)	68.05	12.01	10				
N_B	m6(23.2)	54.35	50.09	10	3.31	4.35	0.08	No
	g6(26.1)	27.67	8.89	12				
	m12(21)	121.40	36.57	10	0.15	3.35	0.86	No
	g12(28.1)	118.40	29.20	10				
	m20(23.1)	125.95	25.72	10				

Table 93 shows a summary of N_B , N_L , and N_B/N_L in CTt (average values) and PMI (or the last traced HSI).

Table 93: Summary of N_B , N_L , and N_B/N_L in CTt and PMI (or the last traced HSI).

Materi	I_c [g/m]	Blast test	N_B	N_L	N_B/N_L	Source
Mortar	6	22.2	32.0	17.0	1.88	PMI
		23.2	32.0	18.0	1.78	PMI
			54.4	28.0	1.83	CTt
	12	20	33.0	19.0	1.74	PMI
		21	100.0	51.0	1.96	PMI
			121.4	63.7	1.90	CTt
	20	22.1	351.5	142.5	2.47	PMI
		23.1	245.0	112.0	2.19	PMI
			126.0	68.1	1.84	CTt
Granite	6	26.1	267.0	90.0	2.97	PMI
			27.7	15.2	1.83	CTt
		27	499.0	102.0	4.89	PMI
	12	24	979.5	560.5	1.75	HSI (324.48 μ s)
		25	734.5	319.5	2.30	HSI (405.60 μ s)
		28.1	118.4	59.7	1.98	CTt
	20	26.2	272.5	156.5	1.74	HSI (243.36 μ s)

The difference in the results in Table 93 between the PMI (or the last traced HSI before the spalling) and the CTt can be associated with the end-face effects (e.g., spalling and cratering) and differences in feature detectability (i.e., the spatial resolution of the images) (see Section 5.1).

Branch-connectivity probabilities (p_{II} , p_{IC} , and p_{CC})

The branch-connectivity probabilities (see Section 4.1.5 and Section 5.3.4) show that over time more branches are probable to become fully connected (p_{CC} [-]) as the probability of the isolated ones (p_{II} [-]) decreases in the HSI (Figure 240). The probability of a branch being semi-connected (p_{IC} [-]) stays nearly constant over time.

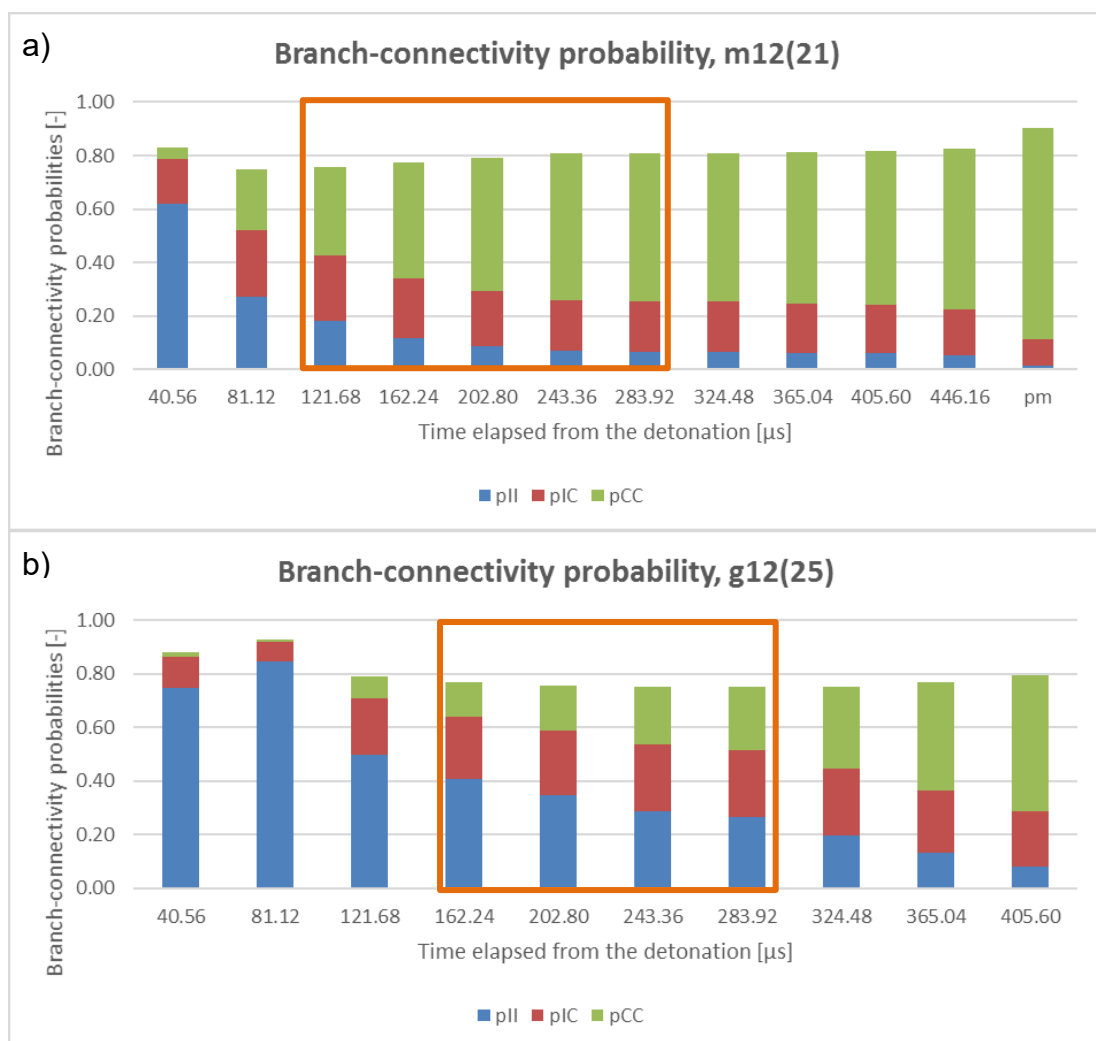


Figure 240: Development of branch-connectivity probabilities (p_{II} , p_{IC} , and p_{CC}) in the HSI: a) m12(21); b) g12(25). The orange box marks the second fracture phase.

In the CTt, the probabilities p_{II} and p_{IC} are very low compared to p_{CC} and stay nearly constant for all three quantities of linear charge concentration. These probabilities are lower in the granite than in the mortar. The probability p_{IC} is higher than p_{II} for all blast shots.

Figure 241 shows a summary of branch-connectivity probability (p_{CC}) in the CTt.

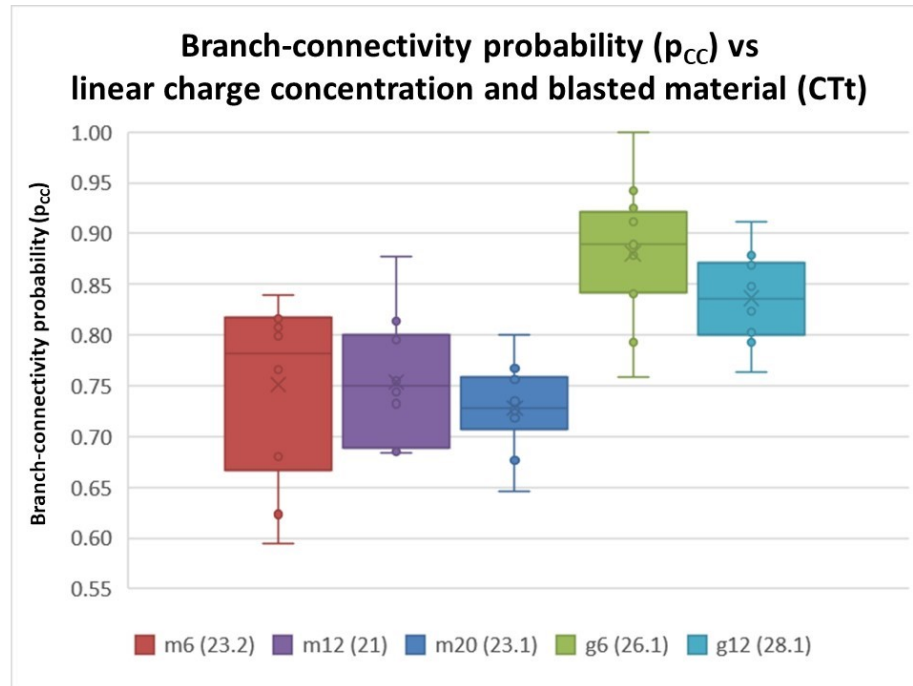


Figure 241: Summary of branch-connectivity probability (p_{CC}) in CTt.

The probability p_{CC} stays about the same for all three linear charge concentrations (Table 94) and it is higher in the granite than in the mortar.

Table 94: Statistical evaluation of average p_{CC} in CTt of mortar and granite shots with One-way ANOVA ($\alpha = 0.05$).

Variable	Ave	Std	Data count	F	F _{crit}	p-value	Sign. diff.
m6(23.2)	0.75	0.09	10	0.46	3.35	0.64	No
m12(21)	0.75	0.06	10				
m20(23.1)	0.73	0.04	10				
g6(26.1)	0.88	0.07	12	3.23	4.35	0.09	No
g12(28.1)	0.84	0.05	10				
m6(23.2)	0.75	0.09	10	11.76	2.57	1E-06	Yes
m12(21)	0.75	0.06	10				
m20(23.1)	0.73	0.04	10				
g6(26.1)	0.88	0.07	12				
g12(28.1)	0.84	0.05	10				

Table 24 shows a summary of the branch-connectivity probabilities in CTt (average values) and PMI (or the last traced HSI before the spalling).

Table 95: Summary of the branch-connectivity probabilities in CTt and PMI (or the last traced HSI).

Material	I_c [g/m]	Blast test	p_{II}	p_{IC}	p_{CC}	Source
Mortar	6	22.2	0.011	0.096	0.797	PMI
		23.2	0.013	0.101	0.786	PMI
			0.021	0.114	0.751	CTt
	12	20	0.024	0.131	0.713	PMI
		21	0.012	0.098	0.792	PMI
			0.019	0.114	0.754	CTt
	20	22.1	0.024	0.130	0.716	PMI
		23.1	0.004	0.060	0.877	PMI
			0.022	0.125	0.728	CTt
Granite	6	26.1	0.002	0.039	0.921	PMI
			0.005	0.057	0.881	CTt
		27	0.001	0.034	0.931	PMI
	12	24	0.237	0.250	0.263	HSI (324.48 μ s)
		25	0.083	0.205	0.508	HSI (405.6 μ s)
		28.1	0.008	0.078	0.836	CTt
	20	26.2	0.070	0.194	0.542	HSI (243.36 μ s)

Fracture abundance – dimensionless fracture intensity (p_{22})

Dimensionless fracture intensity p_{22} [-] (see Section 4.1.6) was calculated based on the trace images of HSI, PMI, and CTt. These values increase over time in the HSI and then, in most cases, drop in the PMI and the CTt (Figure 242).

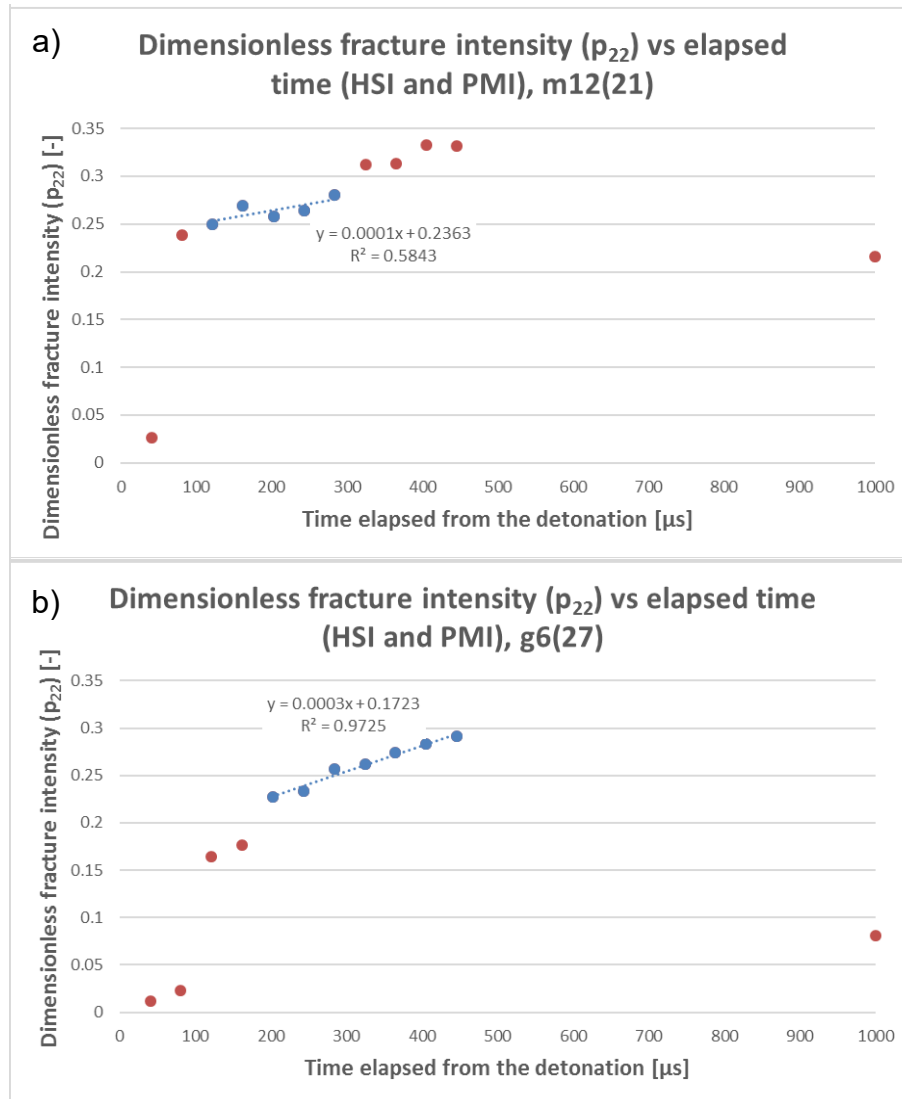


Figure 242: Dimensionless fracture intensity (p_{22}) in HSI and PMI: a) m12(21); b) g6(27). The data points of the second fracture phase are marked blue.

The trend of the value increase in the HSI is in most cases bilinear, similarly as for p_1 and p_c (see Section 5.3.4). The bilinear trend of these curves reflects a kink (i.e., change in the gradient) between the first two fracture phases.

Table 25 shows a summary of the estimated curve slopes of p_{22} , in the second fracture phase.

Table 96: Summary of estimated fracture abundance (p_{22}) curve slopes in the second fracture phase of the HSI.

Material	Ic [g/m]	Blast test	Data	p_{22}	
				Slope	R ²
Mortar	6	22.2	4	-1.8E-05	0.994
		23.2	4	5.6E-04	0.980
	12	20	4	6.2E-04	0.911
		21	5	1.4E-04	0.584
	20	22.1	5	1.0E-03	0.789
		23.1	5	2.2E-03	0.970
Granite	6	26.1	4	4.3E-04	0.962
		27	7	2.7E-04	0.972
	12	24	4	-7.5E-04	0.841
		25	4	1.3E-03	0.808
	20	26.2	2	3.6E-03	

These values increase with more linear charge concentration in the CTt (Figure 244).

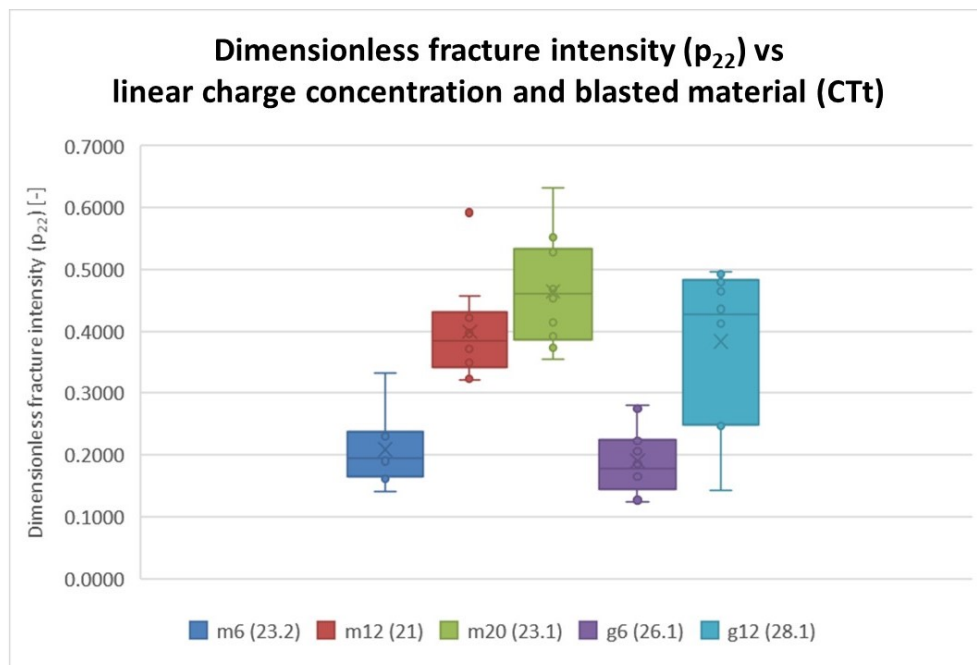


Figure 243: Summary of calculated dimensionless fracture intensity (p_{22}) in the CTt.

Table 26 shows a summary of the p_{22} results in CTt (average values) and PMI (or the last traced HSI before the spalling).

Table 97: Summary of the p_{22} results.

Material	I_c [g/m]	Blast test	p_{22} [-]	Source
Mortar	6	22.2	0.049	PMI
			0.126	HSI (405.60 μ s)
		23.2	0.106	PMI
			0.152	HSI (527.28 μ s)
			0.208	CTt
		12	20	0.080
	0.259			HSI (486.72 μ s)
	21		0.216	PMI
			0.332	HSI (446.16 μ s)
			0.399	CTt
	20	22.1	0.162	PMI
			0.390	HSI (324.48 μ s)
		23.1	0.183	PMI
			0.642	HSI (446.16 μ s)
0.464			CTt	
Granite	6	26.1	0.129	PMI
			0.206	HSI (527.28 μ s)
			0.190	CTt
		27	0.081	PMI
			0.291	HSI (446.16 μ s)
		12	24	0.161
	25		0.274	HSI (405.60 μ s)
	28.1		0.384	CTt
20	26.2	0.353	HSI (243.36 μ s)	

Values of p_{22} are about the same in both materials for the same linear charge concentration (Table 175).

Table 98: Statistical evaluation of dimensionless fracture intensity (p_{22}) in CTt with One-way ANOVA ($\alpha = 0.05$).

Variable	Ave	Std	Data count	F	F _{crit}	p-value	Sign. diff.	
p_{22}	m6(23.2)	0.2084	0.0520	10	0.68	4.35	0.42	No
	g6(26.1)	0.1903	0.0503	12				
	m12(21)	0.3990	0.0765	10	2.07	3.35	0.15	No
	g12(28.1)	0.3837	0.1181	10				
	m20(23.1)	0.4644	0.0827	10				
	m6(23.2)	0.2084	0.0520	10	25.64	2.57	3E-11	Yes
	g6(26.1)	0.1903	0.0503	12				
	m12(21)	0.3990	0.0765	10				
	g12(28.1)	0.3837	0.1181	10				
	m20(23.1)	0.4644	0.0827	10				

Appendix 10 Results of statistical analyses

This section covers those results of statistical analyses (see Section 4.6) that are not presented in Section 5.

The coloured highlighting in the tables denotes “not significantly different” (yellow colour) and “significantly different” (orange colour) p-values and indications.

Number of main radial cracks (N)

This section covers results of the statistical analyses corresponding to Section 5.2.

Table 99: Statistical evaluation of average N in CTt with One-way ANOVA ($\alpha = 0.05$).

Variable	Ave	Std	Data count	F	F _{crit}	p-value	Sign. diff.
m6(23.2)	2.90	0.70	10	12.19	4.35	2E-03	Yes
g6(26.1)	3.83	0.55	12				
m12(21)	5.70	1.19	10	0.36	3.35	0.70	No
g12(28.1)	5.40	1.02	10				
m20(23.1)	5.30	1.10	10				
m6(23.2)	2.90	0.70	10				
g6(26.1)	3.83	0.55	12	17.13	2.57	9E-09	Yes
m12(21)	5.70	1.19	10				
g12(28.1)	5.40	1.02	10				
m20(23.1)	5.30	1.10	10				

**Table 100: Statistical evaluation of average N in CTt with Two-way ANOVA ($\alpha = 0.05$).
Data from m6(23.2), g6(26.1), m12(21), and g12(28.1).**

	SS	df	MS	F	p-value	Sign. diff.
Material	0.90	1	0.90	0.98	3.28E-01	No
I_c [g/m]	48.40	1	48.40	52.80	1.47E-08	Yes
Between groups	3.60	1	3.60	3.93	5.52E-02	No
Within groups	33.00	36	0.92			
Total	85.90	39	2.20			

**Table 101: Statistical evaluation of average N in CTt with Two-way ANOVA ($\alpha = 0.05$) through multiple linear regression with m20(23.1) as the reference.
Data from m6(23.2), g6(26.1), m12(21), g12(28.1), and m20(23.1).**

	Coeff.	Std. err.	t Stat	p-value	Sign. diff.
Intercept	5.30	0.325	16.289	1.00E-20	Yes
6 g/m	-2.10	0.430	-4.879	1.32E-05	Yes
12 g/m	0.10	0.430	0.232	8.17E-01	No
Material	0.30	0.325	0.922	3.61E-01	No

Absolute node counts (N_i , J_{int} , N_{TB})

This section covers results of the statistical analyses corresponding to Section 5.3.1.

Table 102: Overview of slopes and intercepts of linear-regression lines for N_i in CTt.

N_i	Slope	Std. err.	Intercept	Std. err.	R^2	df
m6(22.2)	0.030	0.014	16.933	3.543	0.367	8
m6(23.2)	0.117	0.024	16.269	7.718	0.684	11
m12(20)	0.115	0.019	-1.697	5.526	0.795	10
m12(21)	0.104	0.020	51.436	5.555	0.745	9
m20(22.1)	0.223	0.027	7.036	5.595	0.917	6
m20(23.1)	0.224	0.038	27.655	10.459	0.794	9
g6(26.1)	0.238	0.017	14.000	5.529	0.946	11
g6(27)	0.477	0.024	15.327	6.640	0.977	9
g12(24)	3.429	0.072	-150.679	14.671	0.997	6
g12(25)	1.401	0.161	-15.600	40.430	0.905	8
g20(26.2)	0.802	0.089	-10.467	14.109	0.953	4

Table 103: Overview of slopes and intercepts of linear-regression lines for J_{int} in CTt.

J_{int}	Slope	Std. err.	Intercept	Std. err.	R^2	df
m6(22.2)	0.042	0.004	-2.067	0.930	0.942	8
m6(23.2)	0.078	0.006	-9.462	1.981	0.936	11
m12(20)	0.032	0.003	-3.318	0.820	0.933	10
m12(21)	0.185	0.021	-1.273	5.851	0.894	9
m20(22.1)	0.062	0.007	-3.429	1.418	0.930	6
m20(23.1)	0.139	0.021	-17.836	5.823	0.828	9
g6(26.1)	0.153	0.019	-20.423	6.238	0.851	11
g6(27)	0.240	0.024	-24.145	6.736	0.914	9
g12(24)	1.163	0.160	-57.107	32.757	0.898	6
g12(25)	0.717	0.096	-76.800	24.222	0.874	8
g20(26.2)	0.542	0.108	-41.733	17.133	0.862	4

Table 104: Overview of slopes and intercepts of linear-regression lines for N_{TB} in CTt.

N_{TB}	Slope	Std. err.	Intercept	Std. err.	R^2	df
m6(22.2)	0.019	0.002	0.600	0.566	0.898	8
m6(23.2)	0.037	0.003	-2.654	0.847	0.947	11
m12(20)	0.027	0.002	-0.515	0.677	0.935	10
m12(21)	0.054	0.006	6.855	1.613	0.904	9
m20(22.1)	0.067	0.005	1.036	1.010	0.968	6
m20(23.1)	0.126	0.012	-12.945	3.196	0.929	9
g6(26.1)	0.057	0.003	-2.538	1.072	0.964	11
g6(27)	0.112	0.005	-4.000	1.354	0.983	9
g12(24)	0.067	0.011	1.464	2.319	0.852	6
g12(25)	0.161	0.016	-3.533	3.975	0.929	8
g20(26.2)	0.231	0.016	-10.467	2.567	0.981	4

Table 105: Statistical evaluation of absolute values of N_i in HSI with One-way ANOVA through multiple linear regression with g20(26.2) as the reference. Data from m6(22.2), m6(23.2), g6(26.1), g6(27), m12(20), m12(21), g12(24), g12(25), g12(28.1), m20(22.1), m20(23.1), and g20(26.2).

OVERALL FIT						
Multiple R		0.993				
R Square		0.986				
Adjusted R Square		0.983				
Standard Error		20.763				
Observations		113				
ANOVA				Alpha	0.05	
	df	SS	MS	F	p-value	Sign. diff.
Regression	21	2857198.44	136057.07	315.60	1.21E-75	yes
Residual	91	39230.11	431.10			
Total	112	2896428.55				
	Coeff.	Std. err.	t stat	p-value		
Intercept	-10.467	19.329	-0.541	5.89E-01		
t [μ s]	0.802	0.122	6.551	3.35E-09		
m6(22.2)	27.400	23.975	1.143	2.56E-01		
m6(23.2)	26.736	22.866	1.169	2.45E-01		
m12(20)	8.770	23.171	0.378	7.06E-01		
m12(21)	61.903	23.535	2.630	1.00E-02		
m20(22.1)	17.502	25.206	0.694	4.89E-01		
m20(23.1)	38.121	23.535	1.620	1.09E-01		
g6(26.1)	24.467	22.866	1.070	2.87E-01		
g6(27)	25.794	23.535	1.096	2.76E-01		
g12(24)	-140.212	25.206	-5.563	2.65E-07		
g12(25)	-5.133	23.975	-0.214	8.31E-01		
*m6(22.2)	-0.771	0.135	-5.725	1.32E-07		
*m6(23.2)	-0.685	0.128	-5.345	6.67E-07		
*m12(20)	-0.686	0.130	-5.295	8.20E-07		
*m12(21)	-0.698	0.132	-5.299	8.07E-07		
*m20(22.1)	-0.579	0.146	-3.972	1.42E-04		
*m20(23.1)	-0.578	0.132	-4.387	3.09E-05		
*g6(26.1)	-0.564	0.128	-4.402	2.91E-05		
*g6(27)	-0.324	0.132	-2.463	1.57E-02		
*g12(24)	2.628	0.146	18.042	8.27E-32		
*g12(25)	0.599	0.135	4.448	2.45E-05		

* Statistical effects (slope coefficients).

Table 106: Statistical evaluation of absolute values of J_{int} in HSI with One-way ANOVA through multiple linear regression with g20(26.2) as the reference. Data from m6(22.2), m6(23.2), g6(26.1), g6(27), m12(20), m12(21), g12(24), g12(25), g12(28.1), m20(22.1), m20(23.1), and g20(26.2).

OVERALL FIT						
Multiple R	0.967					
R Square	0.936					
Adjusted R Square	0.921					
Standard Error	16.862					
Observations	113					
ANOVA				Alpha	0.05	
	df	SS	MS	F	p-value	Sign. diff.
Regression	21	377498.67	17976.13	63.22	3.97E-45	yes
Residual	91	25873.36	284.32			
Total	112	403372.04				
	Coeff.	Std. err.	t stat	p-value		
Intercept	-41.733	15.698	-2.659	9.27E-03		
t [μ s]	0.542	0.099	5.451	4.26E-07		
m6(22.2)	39.667	19.470	2.037	4.45E-02		
m6(23.2)	32.272	18.570	1.738	8.56E-02		
m12(20)	38.415	18.818	2.041	4.41E-02		
m12(21)	40.461	19.113	2.117	3.70E-02		
m20(22.1)	38.305	20.470	1.871	6.45E-02		
m20(23.1)	23.897	19.113	1.250	2.14E-01		
g6(26.1)	21.310	18.570	1.148	2.54E-01		
g6(27)	17.588	19.113	0.920	3.60E-01		
g12(24)	-15.374	20.470	-0.751	4.55E-01		
g12(25)	-35.067	19.470	-1.801	7.50E-02		
*m6(22.2)	-0.500	0.109	-4.567	1.55E-05		
*m6(23.2)	-0.463	0.104	-4.454	2.39E-05		
*m12(20)	-0.509	0.105	-4.837	5.35E-06		
*m12(21)	-0.357	0.107	-3.335	1.24E-03		
*m20(22.1)	-0.480	0.118	-4.056	1.05E-04		
*m20(23.1)	-0.402	0.107	-3.760	3.00E-04		
*g6(26.1)	-0.388	0.104	-3.731	3.31E-04		
*g6(27)	-0.302	0.107	-2.819	5.90E-03		
*g12(24)	0.622	0.118	5.257	9.63E-07		
*g12(25)	0.175	0.109	1.600	1.13E-01		

* Statistical effects (slope coefficients).

Table 107: Statistical evaluation of absolute values of N_{TB} in HSI with One-way ANOVA through multiple linear regression with g20(26.2) as the reference. Data from m6(22.2), m6(23.2), g6(26.1), g6(27), m12(20), m12(21), g12(24), g12(25), g12(28.1), m20(22.1), m20(23.1), and g20(26.2).

OVERALL FIT						
Multiple R	0.982					
R Square	0.964					
Adjusted R Square	0.955					
Standard Error	2.884					
Observations	113					
ANOVA				Alpha	0.05	
	df	SS	MS	F	p-value	Sign. diff.
Regression	21	20029.45	953.78	114.69	3.36E-56	yes
Residual	91	756.78	8.32			
Total	112	20786.23				
	Coeff.	Std. err.	t stat	p-value		
Intercept	-10.467	2.685	-3.899	1.85E-04		
t [μ s]	0.231	0.017	13.594	1.24E-23		
m6(22.2)	11.067	3.330	3.323	1.28E-03		
m6(23.2)	7.813	3.176	2.460	1.58E-02		
m12(20)	9.952	3.218	3.092	2.64E-03		
m12(21)	17.321	3.269	5.299	8.07E-07		
m20(22.1)	11.502	3.501	3.286	1.45E-03		
m20(23.1)	-2.479	3.269	-0.758	4.50E-01		
g6(26.1)	7.928	3.176	2.496	1.43E-02		
g6(27)	6.467	3.269	1.978	5.09E-02		
g12(24)	11.931	3.501	3.408	9.77E-04		
g12(25)	6.933	3.330	2.082	4.01E-02		
*m6(22.2)	-0.212	0.019	-11.342	4.20E-19		
*m6(23.2)	-0.194	0.018	-10.921	3.09E-18		
*m12(20)	-0.204	0.018	-11.319	4.67E-19		
*m12(21)	-0.177	0.018	-9.675	1.22E-15		
*m20(22.1)	-0.164	0.020	-8.114	2.23E-12		
*m20(23.1)	-0.105	0.018	-5.719	1.35E-07		
*g6(26.1)	-0.174	0.018	-9.757	8.23E-16		
*g6(27)	-0.119	0.018	-6.503	4.17E-09		
*g12(24)	-0.164	0.020	-8.128	2.08E-12		
*g12(25)	-0.070	0.019	-3.739	3.22E-04		

* Statistical effects (slope coefficients).

Table 108: Statistical evaluation of absolute values of N_i in HSI with ANCOVA (Two-way ANOVA of regression residuals, $\alpha = 0.05$). Data from m6(22.2), m6(23.2), g6(26.1), g6(27), m12(20), m12(21), g12(24), g12(25), g12(28.1), m20(22.1), m20(23.1), and g20(26.2).

N_i	SS	df	MS	F	p-value	Sign. diff.
Material	460092	1	460092.02	17.61	1.09E-04	Yes
I_c [g/m]	546923.9	2	273461.97	10.46	1.56E-04	Yes
Between groups	525228.9	2	262614.44	10.05	2.09E-04	Yes
Within groups	1332696	51	26131.29			
Total	1379446	56	24632.96			

Table 109: Statistical evaluation of absolute values of J_{int} in HSI with ANCOVA (Two-way ANOVA of regression residuals, $\alpha = 0.05$). Data from m6(22.2), m6(23.2), g6(26.1), g6(27), m12(20), m12(21), g12(24), g12(25), g12(28.1), m20(22.1), m20(23.1), and g20(26.2).

J_{int}	SS	df	MS	F	p-value	Sign. diff.
Material	57168.39	1	57168.39	16.89	1.44E-04	Yes
I_c [g/m]	74822.10	2	37411.05	11.05	1.03E-04	Yes
Between groups	66854.82	2	33427.41	9.87	2.37E-04	Yes
Within groups	172639.10	51	3385.08			
Total	177853.40	56	3175.95			

Table 110: Statistical evaluation of absolute values of N_{TB} (T_b count) in HSI with ANCOVA (Two-way ANOVA of regression residuals, $\alpha = 0.05$). Data from m6(22.2), m6(23.2), g6(26.1), g6(27), m12(20), m12(21), g12(24), g12(25), g12(28.1), m20(22.1), m20(23.1), and g20(26.2).

N_{TB}	SS	df	MS	F	p-value	Sign. diff.
Material	3210.08	1	3210.08	41.74	3.15E-09	Yes
I_c [g/m]	2368.93	2	1184.46	15.40	1.32E-06	Yes
Between groups	48.78	2	24.39	0.32	7.29E-01	No
Within groups	8228.18	107	76.90			
Total	13866.52	112	123.81			

Table 111: Statistical evaluation of absolute values of N_I in CTt with multiple linear regression ($\alpha = 0.05$) with m20(23.1) as the reference. Data from m6(23.2), g6(26.1), m12(21), g12(28.1), and m20(23.1).

Regression Statistics					
Multiple R	0.833				
R Square	0.693				
Adjusted R Square	0.674				
Standard Error	10.713				
Observations	52				
ANOVA					
	df	SS	MS	F	Significance F
Regression	3	12448.35	4149.45	36.16	2.28E-12
Residual	48	5508.88	114.77		
Total	51	17957.23			
N_I	Coeff.	Std. err.	t Stat	p-value	Sign. diff.
Intercept	46.80	3.39	13.814	2.40E-18	Yes
6 g/m	-29.58	4.47	-6.622	2.80E-08	Yes
12 g/m	-7.12	4.47	-1.593	1.18E-01	No
Material	-12.57	3.31	-3.792	4.17E-04	Yes

Table 112: Statistical evaluation of absolute values of N_I in CTt with Two-way ANOVA ($\alpha = 0.05$) through multiple linear regression. Data from m6(23.2), g6(26.1), m12(21), and g12(28.1).

N_I	SS	df	MS	F	p-value	Sign. diff.
Material	87.02	1	87.02	0.59	4.49E-01	No
I_c [g/m]	15171.03	1	15171.03	102.29	4.58E-12	Yes
Between groups	2325.63	1	2325.63	15.68	3.39E-04	Yes
Within groups	5339.10	36	148.31			
Total	22922.78	39	587.76			

Table 113: Statistical evaluation of absolute values of J_{int} in CTt with multiple linear regression ($\alpha = 0.05$) with m20(23.1) as the reference. Data from m6(23.2), g6(26.1), m12(21), g12(28.1), and m20(23.1).

Regression Statistics					
Multiple R	0.742				
R Square	0.550				
Adjusted R Square	0.522				
Standard Error	18.389				
Observations	52				
ANOVA					
	df	SS	MS	F	Significance F
Regression	3	19840.36	6613.45	19.56	2.01E-08
Residual	48	16231.71	338.16		
Total	51	36072.08			
J_{int}	Coeff.	Std. err.	t Stat	p-value	Sign. diff.
Intercept	57.400	5.815	9.871	3.87E-13	Yes
6 g/m	-35.235	7.669	-4.595	3.16E-05	Yes
12 g/m	3.735	7.669	0.487	6.28E-01	No
Material	-6.470	5.687	-1.138	2.61E-01	No

Table 114: Statistical evaluation of absolute values of J_{int} in CTt with Two-way ANOVA ($\alpha = 0.05$) through multiple linear regression. Data from m6(23.2), g6(26.1), m12(21), and g12(28.1).

J_{int}	SS	df	MS	F	p-value	Sign. diff.
Material	422.50	1	422.50	1.11	3.00E-01	No
I_c [g/m]	15210.00	1	15210.00	39.87	2.65E-07	Yes
Between groups	592.90	1	592.90	1.55	2.21E-01	No
Within groups	13734.20	36	381.51			
Total	29959.60	39	768.19			

Table 115: Statistical evaluation of absolute values of N_{TB} in CTt with multiple linear regression ($\alpha = 0.05$) with m20(23.1) as the reference. Data from m6(23.2), g6(26.1), m12(21), g12(28.1), and m20(23.1).

Regression Statistics					
Multiple R	0.914				
R Square	0.835				
Adjusted R Square	0.824				
Standard Error	4.421				
Observations	52				
ANOVA					
	df	SS	MS	F	Significance F
Regression	3	4735.572	1578.524	80.762	8.99E-19
Residual	48	938.178	19.545		
Total	51	5673.750			
N_{TB}	Coeff.	Std. err.	t Stat	p-value	Sign. diff
Intercept	32.40	1.40	23.18	1.03E-27	Yes
6 g/m	-20.12	1.84	-10.91	1.35E-14	Yes
12 g/m	-0.78	1.84	-0.42	6.73E-01	No
Material	1.57	1.37	1.14	2.58E-01	No

Table 116: Statistical evaluation of absolute values of N_{TB} in CTt with Two-way ANOVA ($\alpha = 0.05$) through multiple linear regression. Data from m6(23.2), g6(26.1), m12(21), and g12(28.1).

N_{TB}	SS	df	MS	F	p-value	Sign. diff.
Material	15.625	1	15.625	0.832	3.68E-01	No
I_c [g/m]	3861.225	1	3861.225	205.719	1.85E-16	Yes
Between groups	99.225	1	99.225	5.287	2.74E-02	Yes
Within groups	675.700	36	18.769			
Total	4651.775	39	119.276			

Table 117: Overview of slopes and intercepts of linear-regression lines for N_I , J_{int} , and N_{TB} in the CTnp.

N_I	Slope	Std. err.	Intercept	Std. err.	R^2	df
m6(23.2)	0.155	0.133	9.128	5.674	0.119	10
m12(21)	1.575	0.338	70.915	15.001	0.644	12
m20(23.1)	1.065	0.387	106.942	18.265	0.431	10
g6(26.1)	-0.431	0.224	73.184	10.179	0.292	9
g12(28.1)	-0.533	0.431	170.110	17.794	0.145	9
<hr/>						
J_{int}	Slope	Std. err.	Intercept	Std. err.	R^2	df
m6(23.2)	-0.211	0.176	23.382	7.473	0.126	10
m12(21)	-0.517	0.137	66.507	6.089	0.542	12
m20(23.1)	-1.083	0.236	152.243	11.150	0.678	10
g6(26.1)	-0.820	0.147	72.312	6.686	0.775	9
g12(28.1)	-3.360	0.361	331.255	14.880	0.906	9
<hr/>						
N_{TB}	Slope	Std. err.	Intercept	Std. err.	R^2	df
m6(23.2)	-0.006	0.017	5.161	0.739	0.013	10
m12(21)	0.100	0.023	9.470	1.023	0.611	12
m20(23.1)	0.108	0.029	14.100	1.372	0.579	10
g6(26.1)	0.016	0.036	7.575	1.620	0.023	9
g12(28.1)	-0.011	0.053	19.234	2.182	0.005	9

Table 118: Statistical evaluation of absolute values of N_I in CTnp with multiple linear regression ($\alpha = 0.05$) with m20(23.1) as the reference. Data from m6(23.2), g6(26.1), m12(21), g12(28.1), and m20(23.1).

Regression Statistics							
Multiple R		0.946					
R Square		0.895					
Adjusted R Square		0.881					
Standard Error		21.267					
Observations		60					
ANOVA							
	df	SS	MS	F	Significance F		
Regression	7	201498.90	28785.56	63.64	2.95E-23		
Residual	52	23519.03	452.29				
Total	59	225017.93					
		Coeff.	Std. err.	t Stat	p-value	Sign. diff.	
Intercept		106.942	16.795	6.368	5.04E-08	Yes	
Radial position [mm]		1.065	0.356	2.994	4.20E-03	Yes	
6 g/m		-106.367	21.423	-4.965	7.78E-06	Yes	
12 g/m		-32.248	20.340	-1.585	1.19E-01	No	
Material		82.550	15.704	5.257	2.79E-06	Yes	
*6 g/m		-0.529	0.472	-1.121	2.68E-01	No	
*12 g/m		0.279	0.441	0.633	5.29E-01	No	
*Material		-1.360	0.363	-3.743	4.56E-04	Yes	

* Statistical effects (slope coefficients).

Table 119: Statistical evaluation of absolute values of J_{int} in CTnp with multiple linear regression ($\alpha = 0.05$) with m20(23.1) as the reference. Data from m6(23.2), g6(26.1), m12(21), g12(28.1), and m20(23.1).

Regression Statistics						
Multiple R	0.898					
R Square	0.807					
Adjusted R Square	0.781					
Standard Error	33.822					
Observations	60					
ANOVA						
	df	SS	MS	F	Significance F	
Regression	7	248352.43	35478.92	31.02	2.00E-16	
Residual	52	59483.90	1143.92			
Total	59	307836.33				
		Coeff.	Std. err.	t Stat	p-value	Sign. diff.
Intercept		152.243	26.709	5.700	5.71E-07	Yes
Radial position [mm]		-1.083	0.566	-1.914	6.12E-02	No
6 g/m		-176.420	34.069	-5.178	3.68E-06	Yes
12 g/m		-47.049	32.348	-1.454	1.52E-01	No
Material		175.335	24.975	7.020	4.59E-09	Yes
*6 g/m		1.297	0.751	1.727	9.00E-02	No
*12 g/m		0.258	0.701	0.368	7.14E-01	No
*Material		-2.092	0.578	-3.619	6.69E-04	Yes

* Statistical effects (slope coefficients).

Table 120: Statistical evaluation of N_{TB} in CTnp with multiple linear regression ($\alpha = 0.05$) with m20(23.1) as the reference. Data from m6(23.2), g6(26.1), m12(21), g12(28.1), and m20(23.1).

Regression Statistics						
Multiple R	0.950					
R Square	0.902					
Adjusted R Square	0.889					
Standard Error	1.986					
Observations	60					
ANOVA						
	df	SS	MS	F	Significance F	
Regression	7	1884.58	269.23	68.27	5.84E-24	
Residual	52	205.07	3.94			
Total	59	2089.65				
		Coeff.	Std. err.	t Stat	p-value	Sign. diff.
Intercept		14.100	1.568	8.991	3.58E-12	Yes
Radial position [mm]		0.108	0.033	3.242	2.07E-03	Yes
6 g/m		-10.599	2.000	-5.298	2.41E-06	Yes
12 g/m		-3.438	1.899	-1.810	7.60E-02	No
Material		6.615	1.466	4.511	3.71E-05	Yes
*6 g/m		-0.084	0.044	-1.904	6.24E-02	No
*12 g/m		-0.027	0.041	-0.655	5.15E-01	No
*Material		-0.054	0.034	-1.602	1.15E-01	No

* Statistical effects (slope coefficients).

Table 121: Statistical evaluation of absolute values of N_I in CTnp with multiple linear regression ($\alpha = 0.05$) with m20(23.1) as the reference. Data from m6(23.2), g6(26.1), m12(21), g12(28.1), and m20(23.1).

	Coeff.	Std. err.	t Stat	p-value	Sign. diff.
Intercept	106.942	16.795	6.368	5.04E-08	Yes
Radial position [mm]	1.065	0.356	2.994	4.20E-03	Yes
6 g/m	-106.367	21.423	-4.965	7.78E-06	Yes
12 g/m	-32.248	20.340	-1.585	1.19E-01	No
Material	82.550	15.704	5.257	2.79E-06	Yes
*6 g/m	-0.529	0.472	-1.121	2.68E-01	No
*12 g/m	0.279	0.441	0.633	5.29E-01	No
*Material	-1.360	0.363	-3.743	4.56E-04	Yes

* Statistical effects (slope coefficients).

Table 122: Statistical evaluation of absolute values of J_{int} in CTnp with multiple linear regression ($\alpha = 0.05$) with m20(23.1) as the reference. Data from m6(23.2), g6(26.1), m12(21), g12(28.1), and m20(23.1).

	Coeff.	Std. err.	t Stat	p-value	Sign. diff
Intercept	152.243	26.709	5.700	5.71E-07	Yes
Radial position [mm]	-1.083	0.566	-1.914	6.12E-02	No
6 g/m	-176.420	34.069	-5.178	3.68E-06	Yes
12 g/m	-47.049	32.348	-1.454	1.52E-01	No
Material	175.335	24.975	7.020	4.59E-09	Yes
*6 g/m	1.297	0.751	1.727	9.00E-02	No
*12 g/m	0.258	0.701	0.368	7.14E-01	No
*Material	-2.092	0.578	-3.619	6.69E-04	Yes

* Statistical effects (slope coefficients).

Table 123: Statistical evaluation of absolute values of N_{TB} in CTnp with multiple linear regression ($\alpha = 0.05$) with m20(23.1) as the reference. Data from m6(23.2), g6(26.1), m12(21), g12(28.1), and m20(23.1).

	Coeff.	Std. err.	t Stat	p-value	Sign. diff
Intercept	14.100	1.568	8.991	3.58E-12	Yes
Radial position [mm]	0.108	0.033	3.242	2.07E-03	Yes
6 g/m	-10.599	2.000	-5.298	2.41E-06	Yes
12 g/m	-3.438	1.899	-1.810	7.60E-02	No
Material	6.615	1.466	4.511	3.71E-05	Yes
*6 g/m	-0.084	0.044	-1.904	6.24E-02	No
*12 g/m	-0.027	0.041	-0.655	5.15E-01	No
*Material	-0.054	0.034	-1.602	1.15E-01	No

* Statistical effects (slope coefficients).

Average number of connections per line (C_L) and per branch (C_B)

This section covers results of the statistical analyses corresponding to Section 5.3.3.

Table 124: Statistical evaluation of average C_L and C_B in CTt of mortar and granite shots with One-way ANOVA ($\alpha = 0.05$).

Variable		Ave	Std	Data count	F	F _{crit}	p-value	Sign. diff.
C_L	m6(23.2)	2.76	0.37	10	0.54	3.35	0.59	No
	m12(21)	2.76	0.27	10				
	m20(23.1)	2.65	0.18	10				
	g6(26.1)	3.35	0.33	12	3.23	4.35	0.09	No
	g12(28.1)	3.13	0.22	10				
C_B	m6(23.2)	1.73	0.10	10	0.42	3.35	0.66	No
	m12(21)	1.74	0.07	12				
	m20(23.1)	1.71	0.05	10				
	g6(26.1)	1.88	0.07	10	3.16	4.35	0.09	No
	g12(28.1)	1.83	0.05	10				
C_L	m6(23.2)	2.76	0.37	10	11.96	2.57	9E-07	Yes
	m12(21)	2.76	0.27	10				
	m20(23.1)	2.65	0.18	10				
	g6(26.1)	3.35	0.33	12				
	g12(28.1)	3.13	0.22	10				
C_B	m6(23.2)	1.73	0.10	10	11.35	2.57	2E-06	Yes
	m12(21)	1.74	0.07	12				
	m20(23.1)	1.71	0.05	10				
	g6(26.1)	1.88	0.07	10				
	g12(28.1)	1.83	0.05	10				

Table 125: Statistical evaluation of C_L in CTt with multiple linear regression ($\alpha = 0.05$) with m20(23.1) as the reference. Data from m6(23.2), g6(26.1), m12(21), g12(28.1), and m20(23.1).

Regression Statistics					
Multiple R	0.704				
R Square	0.496				
Adjusted R Square	0.463				
Standard Error	0.288				
Observations	50				
ANOVA					
	df	SS	MS	F	Significance F
Regression	3	3.75	1.25	15.09	5.66E-07
Residual	46	3.81	0.08		
Total	49	7.55			
C_L	Coeff.	Std. err.	t Stat	p-value	Sign. diff
Intercept	2.648	0.091	29.109	2.81E-31	Yes
6 g/m	0.180	0.120	1.498	1.41E-01	No
12 g/m	0.049	0.120	0.408	6.86E-01	No
Material	0.501	0.091	5.505	1.59E-06	Yes

Table 126: Statistical evaluation of C_L in CTt with Two-way ANOVA ($\alpha = 0.05$) through multiple linear regression. Data from m6(23.2), g6(26.1), m12(21), and g12(28.1).

	SS	df	MS	F	p-value	Sign. diff.
Material	2.51	1	2.51	26.89	8.52E-06	Yes
l_c [g/m]	0.17	1	0.17	1.85	1.83E-01	No
Between groups	0.17	1	0.17	1.78	1.91E-01	No
Within groups	3.36	36	0.09			
Total	6.21	39	0.16			

Table 127: Statistical evaluation of C_B in CTt with multiple linear regression ($\alpha = 0.05$) with m20(23.1) as the reference. Data from m6(23.2), g6(26.1), m12(21), g12(28.1), and m20(23.1).

Regression Statistics					
Multiple R	0.693				
R Square	0.480				
Adjusted R Square	0.446				
Standard Error	0.072				
Observations	50				
ANOVA					
	df	SS	MS	F	Significance F
Regression	3	0.22	0.07	14.13	1.16E-06
Residual	46	0.24	0.01		
Total	49	0.46			
C_B	Coeff.	Std. err.	t Stat	p-value	Sign. diff
Intercept	1.705	0.023	74.563	1.24E-49	Yes
6 g/m	0.040	0.030	1.327	1.91E-01	No
12 g/m	0.015	0.030	0.484	6.30E-01	No
Material	0.123	0.023	5.389	2.36E-06	Yes

Table 128: Statistical evaluation of C_B in CTt with Two-way ANOVA ($\alpha = 0.05$) through multiple linear regression. Data from m6(23.2), g6(26.1), m12(21), and g12(28.1).

	SS	df	MS	F	p-value	Sign. diff.
Material	0.15	1	0.15	26.29	1.02E-05	Yes
I_c [g/m]	0.01	1	0.01	1.13	2.96E-01	No
Between groups	0.01	1	0.01	1.54	2.22E-01	No
Within groups	0.21	36	0.01			
Total	0.38	39	0.01			

Node-connectivity probabilities (p_i and p_c)

This section covers results of the statistical analyses corresponding to Section 5.3.4.

Table 129: Statistical evaluation of p_i in HSI with multiple linear regression with g20(26.2) as the reference. Data from m6(22.2), m6(23.2), g6(26.1), g6(27), m12(20), m12(21), g12(24), g12(25), g12(28.1), m20(22.1), m20(23.1), and g20(26.2).

OVERALL FIT						
Multiple R	0.927					
R Square	0.858					
Adjusted R Square	0.826					
Standard Error	0.088					
Observations	113					
ANOVA				Alpha	0.05	
	df	SS	MS	F	p-value	Sign. diff
Regression	21	4.30	0.20	26.28	7.81E-30	yes
Residual	91	0.71	0.01			
Total	112	5.01				
	Coeff.	Std. err.	t Stat	p-value	Sign. diff.	
Intercept	9.63E-01	8.22E-02	11.725	6.87E-20	Yes	
t [μ s]	-3.02E-03	5.20E-04	-5.811	9.05E-08	Yes	
m6(22.2)	-1.73E-01	1.02E-01	-1.702	9.21E-02	No	
m6(23.2)	1.36E-01	9.72E-02	1.399	1.65E-01	No	
m12(20)	-4.06E-01	9.85E-02	-4.125	8.19E-05	Yes	
m12(21)	-3.60E-01	1.00E-01	-3.595	5.26E-04	Yes	
m20(22.1)	-3.44E-01	1.07E-01	-3.213	1.82E-03	Yes	
m20(23.1)	1.90E-01	1.00E-01	1.903	6.01E-02	No	
g6(26.1)	-1.94E-01	9.72E-02	-1.997	4.88E-02	Yes	
g6(27)	-1.37E-01	1.00E-01	-1.365	1.76E-01	No	
g12(24)	-8.49E-02	1.07E-01	-0.792	4.30E-01	No	
g12(25)	-1.58E-02	1.02E-01	-0.155	8.77E-01	No	
*m6(22.2)	1.59E-03	5.73E-04	2.775	6.70E-03	Yes	
*m6(23.2)	1.31E-03	5.45E-04	2.407	1.81E-02	Yes	
*m12(20)	2.67E-03	5.51E-04	4.850	5.07E-06	Yes	
*m12(21)	1.98E-03	5.60E-04	3.529	6.56E-04	Yes	
*m20(22.1)	2.18E-03	6.19E-04	3.523	6.70E-04	Yes	
*m20(23.1)	9.21E-04	5.60E-04	1.645	1.03E-01	No	
*g6(26.1)	2.14E-03	5.45E-04	3.937	1.61E-04	Yes	
*g6(27)	1.80E-03	5.60E-04	3.217	1.79E-03	Yes	
*g12(24)	1.32E-03	6.19E-04	2.130	3.59E-02	Yes	
*g12(25)	1.41E-03	5.73E-04	2.458	1.59E-02	Yes	

* Statistical effects (slope coefficients).

Table 130: Statistical evaluation of p_c in HSI with multiple linear regression with g20(26.2) as the reference. Data from m6(22.2), m6(23.2), g6(26.1), g6(27), m12(20), m12(21), g12(24), g12(25), g12(28.1), m20(22.1), m20(23.1), and g20(26.2).

OVERALL FIT							
Multiple R	0.927						
R Square	0.858						
Adjusted R Square	0.826						
Standard Error	0.088						
Observations	113						
ANOVA				Alpha	0.05		
	df	SS	MS	F	p-value	Sign. diff.	
Regression	21	4.30	0.20	26.28	7.80961E-30	yes	
Residual	91	0.71	0.01				
Total	112	5.01					
	Coeff.	Std. err.	t Stat	p-value	Sign. diff.		
Intercept	3.66E-02	8.22E-02	0.445	6.57E-01	No		
t [μ s]	3.02E-03	5.20E-04	5.811	9.05E-08	Yes		
m6(22.2)	1.73E-01	1.02E-01	1.702	9.21E-02	No		
m6(23.2)	-1.36E-01	9.72E-02	-1.399	1.65E-01	No		
m12(20)	4.06E-01	9.85E-02	4.125	8.19E-05	Yes		
m12(21)	3.60E-01	1.00E-01	3.595	5.26E-04	Yes		
m20(22.1)	3.44E-01	1.07E-01	3.213	1.82E-03	Yes		
m20(23.1)	-1.90E-01	1.00E-01	-1.903	6.01E-02	No		
g6(26.1)	1.94E-01	9.72E-02	1.997	4.88E-02	Yes		
g6(27)	1.37E-01	1.00E-01	1.365	1.76E-01	No		
g12(24)	8.49E-02	1.07E-01	0.792	4.30E-01	No		
g12(25)	1.58E-02	1.02E-01	0.155	8.77E-01	No		
*m6(22.2)	-1.59E-03	5.73E-04	-2.775	6.70E-03	Yes		
*m6(23.2)	-1.31E-03	5.45E-04	-2.407	1.81E-02	Yes		
*m12(20)	-2.67E-03	5.51E-04	-4.850	5.07E-06	Yes		
*m12(21)	-1.98E-03	5.60E-04	-3.529	6.56E-04	Yes		
*m20(22.1)	-2.18E-03	6.19E-04	-3.523	6.70E-04	Yes		
*m20(23.1)	-9.21E-04	5.60E-04	-1.645	1.03E-01	No		
*g6(26.1)	-2.14E-03	5.45E-04	-3.937	1.61E-04	Yes		
*g6(27)	-1.80E-03	5.60E-04	-3.217	1.79E-03	Yes		
*g12(24)	-1.32E-03	6.19E-04	-2.130	3.59E-02	Yes		
*g12(25)	-1.41E-03	5.73E-04	-2.458	1.59E-02	Yes		

* Statistical effects (slope coefficients).

Table 131: Statistical evaluation of p_i and p_c in HSI with ANCOVA (Two-way ANOVA of regression residuals, $\alpha = 0.05$). Data from m6(22.2), m6(23.2), g6(26.1), g6(27), m12(20), m12(21), g12(24), g12(25), g12(28.1), m20(22.1), m20(23.1), and g20(26.2).

p_i, p_c	SS	df	MS	F	p-value	Sign. diff.
Material	0.002	1	0.002	0.092	7.62E-01	No
I_c [g/m]	0.170	2	0.085	4.562	1.26E-02	Yes
Between groups	0.193	2	0.097	5.194	7.03E-03	Yes
Within groups	1.989	107	0.019			
Total	2.356	112	0.021			

Table 132: Statistical evaluation of p_i in the second fracture phase in HSI with multiple linear regression (Two-way ANOVA) with g20(26.2) as the reference. Data from m6(22.2), m6(23.2), g6(26.1), g6(27), m12(20), m12(21), g12(24), g12(25), g12(28.1), m20(22.1), m20(23.1), and g20(26.2).

Regression Statistics					
Multiple R	0.516				
R Square	0.267				
Adjusted R Square	0.142				
Standard Error	0.093				
Observations	49				
ANOVA					
	df	SS	MS	F	Significance F
Regression	7	0.128	0.018	2.131	6.16E-02
Residual	41	0.353	0.009		
Total	48	0.481			
	Coeff.	Std. err.	t Stat	p-value	Sign. diff.
Intercept	0.4321	0.0996	4.3389	9.12E-05	Yes
t [μ s]	-0.0002	0.0004	-0.4433	6.60E-01	No
6 g/m	0.0824	0.1485	0.5551	5.82E-01	No
12 g/m	-0.0406	0.1164	-0.3492	7.29E-01	No
Material	0.1587	0.0927	1.7115	9.45E-02	No
*6 g/m	-0.0002	0.0005	-0.4638	6.45E-01	No
*12 g/m	0.0002	0.0005	0.5212	6.05E-01	No
*Material	-0.0004	0.0003	-1.2233	2.28E-01	No

* Statistical effects (slope coefficients).

Table 133: Statistical evaluation of p_i in the second fracture phase in HSI with multiple linear regression with g20(26.2) as the reference. Data from m6(22.2), m6(23.2), g6(26.1), g6(27), m12(20), m12(21), g12(24), g12(25), g12(28.1), m20(22.1), m20(23.1), and g20(26.2).

OVERALL FIT						
Multiple R	0.977					
R Square	0.955					
Adjusted R Square	0.920					
Standard Error	0.028					
Observations	49					
ANOVA				Alpha	0.05	
	df	SS	MS	F	p-value	Sign. diff.
Regression	21	0.459	0.022	27.238	4.43E-13	yes
Residual	27	0.022	0.001			
Total	48	0.481				
	Coeff.	Std. err.	t Stat	p-value	Sign. diff.	
Intercept	0.90734	0.05875	15.44491	6.33E-15	Yes	
t [μ s]	-0.00273	0.00031	-8.75546	2.27E-09	Yes	
m6(22.2)	-0.58799	0.12349	-4.76155	5.78E-05	Yes	
m6(23.2)	-0.10869	0.12349	-0.88016	3.87E-01	No	
m12(20)	-0.39830	0.11261	-3.53697	1.49E-03	Yes	
m12(21)	-0.38339	0.07495	-5.11496	2.24E-05	Yes	
m20(22.1)	-0.62816	0.09224	-6.81032	2.58E-07	Yes	
m20(23.1)	0.24159	0.09353	2.58300	1.55E-02	Yes	
g6(26.1)	-0.31910	0.13468	-2.36935	2.52E-02	Yes	
g6(27)	-0.22136	0.07349	-3.01229	5.58E-03	Yes	
g12(24)	-0.18495	0.08308	-2.22617	3.45E-02	Yes	
g12(25)	-0.10559	0.09224	-1.14473	2.62E-01	No	
*m6(22.2)	0.00269	0.00044	6.08873	1.68E-06	Yes	
*m6(23.2)	0.00168	0.00044	3.79715	7.55E-04	Yes	
*m12(20)	0.00263	0.00044	5.96449	2.32E-06	Yes	
*m12(21)	0.00170	0.00038	4.44171	1.36E-04	Yes	
*m20(22.1)	0.00327	0.00044	7.39295	5.94E-08	Yes	
*m20(23.1)	0.00056	0.00038	1.46821	1.54E-01	No	
*g6(26.1)	0.00221	0.00044	4.99901	3.05E-05	Yes	
*g6(27)	0.00193	0.00034	5.68158	4.92E-06	Yes	
*g12(24)	0.00129	0.00044	2.91558	7.06E-03	Yes	
*g12(25)	0.00170	0.00044	3.85070	6.56E-04	Yes	

* Statistical effects (slope coefficients).

Table 134: Statistical evaluation of p_c in the second fracture phase in HSI with multiple linear regression (Two-way ANOVA) with g20(26.2) as the reference. Data from m6(22.2), m6(23.2), g6(26.1), g6(27), m12(20), m12(21), g12(24), g12(25), g12(28.1), m20(22.1), m20(23.1), and g20(26.2).

Regression Statistics						
Multiple R	0.516					
R Square	0.267					
Adjusted R Square	0.142					
Standard Error	0.093					
Observations	49					
ANOVA		df	SS	MS	F	Significance F
Regression		7	0.128	0.018	2.131	6.16E-02
Residual		41	0.353	0.009		
Total		48	0.481			
	Coeff.	Std. err.	t Stat	p-value	Sign. diff.	
Intercept	0.5679	0.0996	5.7030	1.14E-06	Yes	
t [μ s]	0.0002	0.0004	0.4433	6.60E-01	No	
6 g/m	-0.0824	0.1485	-0.5551	5.82E-01	No	
12 g/m	0.0406	0.1164	0.3492	7.29E-01	No	
Material	-0.1587	0.0927	-1.7115	9.45E-02	No	
*6 g/m	0.0002	0.0005	0.4638	6.45E-01	No	
*12 g/m	-0.0002	0.0005	-0.5212	6.05E-01	No	
*Material	0.0004	0.0003	1.2233	2.28E-01	No	

* Statistical effects (slope coefficients).

Table 135: Statistical evaluation of p_c in the second fracture phase in HSI with multiple linear regression with g20(26.2) as the reference. Data from m6(22.2), m6(23.2), g6(26.1), g6(27), m12(20), m12(21), g12(24), g12(25), g12(28.1), m20(22.1), m20(23.1), and g20(26.2).

OVERALL FIT						
Multiple R	0.977					
R Square	0.955					
Adjusted R Square	0.920					
Standard Error	0.028					
Observations	49					
ANOVA				Alpha	0.05	
	df	SS	MS	F	p-value	Sign. diff.
Regression	21	0.4591	0.0219	27.238	4.43E-13	yes
Residual	27	0.0217	0.0008			
Total	48	0.4808				
	Coeff.	Std. err.	t Stat	p-value	Sign. diff.	
Intercept	0.09266	0.05875	1.57734	1.26E-01	No	
t [μ s]	0.00273	0.00031	8.75546	2.27E-09	Yes	
m6(22.2)	0.58799	0.12349	4.76155	5.78E-05	Yes	
m6(23.2)	0.10869	0.12349	0.88016	3.87E-01	No	
m12(20)	0.39830	0.11261	3.53697	1.49E-03	Yes	
m12(21)	0.38339	0.07495	5.11496	2.24E-05	Yes	
m20(22.1)	0.62816	0.09224	6.81032	2.58E-07	Yes	
m20(23.1)	-0.24159	0.09353	-2.58300	1.55E-02	Yes	
g6(26.1)	0.31910	0.13468	2.36935	2.52E-02	Yes	
g6(27)	0.22136	0.07349	3.01229	5.58E-03	Yes	
g12(24)	0.18495	0.08308	2.22617	3.45E-02	Yes	
g12(25)	0.10559	0.09224	1.14473	2.62E-01	No	
*m6(22.2)	-0.00269	0.00044	-6.08873	1.68E-06	Yes	
*m6(23.2)	-0.00168	0.00044	-3.79715	7.55E-04	Yes	
*m12(20)	-0.00263	0.00044	-5.96449	2.32E-06	Yes	
*m12(21)	-0.00170	0.00038	-4.44171	1.36E-04	Yes	
*m20(22.1)	-0.00327	0.00044	-7.39295	5.94E-08	Yes	
*m20(23.1)	-0.00056	0.00038	-1.46821	1.54E-01	No	
*g6(26.1)	-0.00221	0.00044	-4.99901	3.05E-05	Yes	
*g6(27)	-0.00193	0.00034	-5.68158	4.92E-06	Yes	
*g12(24)	-0.00129	0.00044	-2.91558	7.06E-03	Yes	
*g12(25)	-0.00170	0.00044	-3.85070	6.56E-04	Yes	

* Statistical effects (slope coefficients).

Table 136: Statistical evaluation of p_i and p_c in the second fracture phase in HSI with ANCOVA (Two-way ANOVA of regression residuals, $\alpha = 0.05$). Data from m6(22.2), m6(23.2), g6(26.1), g6(27), m12(20), m12(21), g12(24), g12(25), g12(28.1), m20(22.1), m20(23.1), and g20(26.2).

p_i, p_c	SS	df	MS	F	p-value	Sign. diff.
Material	0.0101	1	0.010	1.295	2.61E-01	No
I_c [g/m]	0.0075	2	0.004	0.479	6.23E-01	No
Between groups	0.0461	2	0.023	2.958	6.25E-02	No
Within groups	0.3350	43	0.008			
Total	0.4044	48	0.008			

Table 137: Statistical evaluation of p_i in CTt with multiple linear regression with m20(23.1) as the reference. Data from m6(23.2), g6(26.1), m12(21), g12(28.1), and m20(23.1).

Regression Statistics	
Multiple R	0.693
R Square	0.480
Adjusted R Square	0.446
Standard Error	0.036
Observations	50

ANOVA					
	df	SS	MS	F	Significance F
Regression	3	0.055	0.018	14.135	1.16E-06
Residual	46	0.060	0.001		
Total	49	0.116			

	Coeff.	Std. err.	t Stat	p-value	Sign. diff.
Intercept	0.147	0.011	12.879	7.30E-17	Yes
6 g/m	-0.020	0.015	-1.327	1.91E-01	No
12 g/m	-0.007	0.015	-0.484	6.30E-01	No
Material	-0.062	0.011	-5.389	2.36E-06	Yes

Table 138: Statistical evaluation of p_i in CTt with Two-way ANOVA. Data from m6(23.2), g6(26.1), m12(21), and g12(28.1).

	SS	df	MS	F	p-value	Sign. diff.
Material	0.0380	1	0.0380	26.2858	1.02E-05	Yes
I_c [g/m]	0.0016	1	0.0016	1.1258	2.96E-01	No
Between groups	0.0022	1	0.0022	1.5429	2.22E-01	No
Within groups	0.0520	36	0.0014			
Total	0.0938	39	0.0024			

Table 139: Overview and statistical evaluation of average p_c in CTt of mortar and of granite shots with One-way ANOVA ($\alpha = 0.05$).

Variable	Ave	Std	Data count	F	F _{crit}	p-value	Sign. diff.
m6(23.2)	0.87	0.05	10	0.42	3.35	0.66	No
m12(21)	0.87	0.04	10				
m20(23.1)	0.85	0.03	10				
g6(26.1)	0.94	0.03	12	3.16	4.35	0.09	No
g12(28.1)	0.91	0.03	10				
All data				11.35	2.57	2E-06	Yes

Table 140: Statistical evaluation of p_c in CTt with multiple linear regression ($\alpha = 0.05$) with m20(23.1) as the reference. Data from m6(23.2), g6(26.1), m12(21), g12(28.1), and m20(23.1).

Regression Statistics	
Multiple R	0.693
R Square	0.480
Adjusted R Square	0.446
Standard Error	0.036
Observations	50

ANOVA					
	df	SS	MS	F	Significance F
Regression	3	0.055	0.018	14.135	1.16E-06
Residual	46	0.060	0.001		
Total	49	0.116			

	Coeff.	Std. err.	t Stat	p-value	Sign. diff.
Intercept	0.853	0.011	74.563	1.24E-49	Yes
6 g/m	0.020	0.015	1.327	1.91E-01	No
12 g/m	0.007	0.015	0.484	6.30E-01	No
Material	0.062	0.011	5.389	2.36E-06	Yes

Table 141: Statistical evaluation of p_c in CTt with Two-way ANOVA. Data from m6(23.2), g6(26.1), m12(21), and g12(28.1).

	SS	df	MS	F	p-value	Sign. diff.
Material	0.0380	1	0.0380	26.2858	1.02E-05	Yes
l_c [g/m]	0.0016	1	0.0016	1.1258	2.96E-01	No
Between groups	0.0022	1	0.0022	1.5429	2.22E-01	No
Within groups	0.0520	36	0.0014			
Total	0.0938	39	0.0024			

Fracture abundance (p_{20} , p_{21} , and p_{22})

This section covers results of the statistical analyses corresponding to Section 5.3.5 and p_{22} (see Appendix 9).

Table 142: Statistical evaluation of p_{20} in HSI with multiple linear regression with $g_{20}(26.2)$ as the reference. Data from $m_6(22.2)$, $m_6(23.2)$, $g_6(26.1)$, $g_6(27)$, $m_{12}(20)$, $m_{12}(21)$, $g_{12}(24)$, $g_{12}(25)$, $g_{12}(28.1)$, $m_{20}(22.1)$, $m_{20}(23.1)$, and $g_{20}(26.2)$.

Regression Statistics						
Multiple R	0.9976					
R Square	0.9952					
Adjusted R Square	0.9914					
Standard Error	0.0004					
Observations	49					
ANOVA				Alpha	0.05	
	df	SS	MS	F	p-value	Sign. diff.
Regression	21	8.98E-04	4.27E-05	265.057	5.08E-26	yes
Residual	27	4.35E-06	1.61E-07			
Total	48	9.02E-04				
	Coeff.	Std. err.	t Stat	p-value	Sign. diff.	
Intercept	-2.04E-03	8.33E-04	-2.446	2.13E-02	Yes	
t [μ s]	4.12E-05	4.43E-06	9.305	6.51E-10	Yes	
$m_6(22.2)$	2.90E-03	1.75E-03	1.658	1.09E-01	No	
$m_6(23.2)$	2.49E-03	1.75E-03	1.422	1.66E-01	No	
$m_{12}(20)$	8.31E-04	1.60E-03	0.520	6.07E-01	No	
$m_{12}(21)$	3.23E-03	1.06E-03	3.036	5.26E-03	Yes	
$m_{20}(22.1)$	1.38E-03	1.31E-03	1.052	3.02E-01	No	
$m_{20}(23.1)$	2.25E-03	1.33E-03	1.697	1.01E-01	No	
$g_6(26.1)$	1.57E-03	1.91E-03	0.825	4.17E-01	No	
$g_6(27)$	1.83E-03	1.04E-03	1.757	9.02E-02	No	
$g_{12}(24)$	-1.00E-03	1.18E-03	-0.853	4.01E-01	No	
$g_{12}(25)$	-4.13E-04	1.31E-03	-0.316	7.55E-01	No	
* $m_6(22.2)$	-4.05E-05	6.26E-06	-6.462	6.32E-07	Yes	
* $m_6(23.2)$	-3.58E-05	6.26E-06	-5.718	4.46E-06	Yes	
* $m_{12}(20)$	-3.31E-05	6.26E-06	-5.287	1.41E-05	Yes	
* $m_{12}(21)$	-2.98E-05	5.42E-06	-5.495	8.09E-06	Yes	
* $m_{20}(22.1)$	-2.91E-05	6.26E-06	-4.651	7.78E-05	Yes	
* $m_{20}(23.1)$	-2.97E-05	5.42E-06	-5.472	8.59E-06	Yes	
* $g_6(26.1)$	-2.97E-05	6.26E-06	-4.739	6.14E-05	Yes	
* $g_6(27)$	-2.11E-05	4.81E-06	-4.389	1.57E-04	Yes	
* $g_{12}(24)$	5.71E-05	6.26E-06	9.125	9.74E-10	Yes	
* $g_{12}(25)$	1.89E-05	6.26E-06	3.016	5.53E-03	Yes	

* Statistical effects (slope coefficients).

Table 143: Statistical evaluation of p_{21} in HSI with multiple linear regression with g20(26.2) as the reference. Data from m6(22.2), m6(23.2), g6(26.1), g6(27), m12(20), m12(21), g12(24), g12(25), g12(28.1), m20(22.1), m20(23.1), and g20(26.2).

OVERALL FIT						
Multiple R	0.997					
R Square	0.994					
Adjusted R Square	0.989					
Standard Error	0.003					
Observations	49					
ANOVA				Alpha	0.05	
	df	SS	MS	F	p-value	Sign. diff.
Regression	21	3.16E-02	1.51E-03	210.318	1.12E-24	yes
Residual	27	1.93E-04	7.16E-06			
Total	48	3.18E-02				
	Coeff.	Std. err.	t Stat	p-value	Sign. diff.	
Intercept	-3.10E-02	5.55E-03	-5.587	6.32E-06	Yes	
t [μ s]	4.92E-04	2.95E-05	16.669	9.75E-16	Yes	
m6(22.2)	4.67E-02	1.17E-02	4.001	4.41E-04	Yes	
m6(23.2)	1.75E-02	1.17E-02	1.501	1.45E-01	No	
m12(20)	1.90E-02	1.06E-02	1.790	8.48E-02	No	
m12(21)	4.62E-02	7.08E-03	6.525	5.37E-07	Yes	
m20(22.1)	3.09E-02	8.71E-03	3.551	1.43E-03	Yes	
m20(23.1)	-1.01E-02	8.84E-03	-1.142	2.64E-01	No	
g6(26.1)	2.18E-02	1.27E-02	1.712	9.84E-02	No	
g6(27)	3.07E-02	6.94E-03	4.423	1.44E-04	Yes	
g12(24)	3.47E-02	7.85E-03	4.415	1.47E-04	Yes	
g12(25)	7.27E-03	8.71E-03	0.835	4.11E-01	No	
*m6(22.2)	-4.84E-04	4.17E-05	-11.587	5.51E-12	Yes	
*m6(23.2)	-3.83E-04	4.17E-05	-9.173	8.75E-10	Yes	
*m12(20)	-3.91E-04	4.17E-05	-9.363	5.72E-10	Yes	
*m12(21)	-3.29E-04	3.61E-05	-9.115	9.96E-10	Yes	
*m20(22.1)	-3.48E-04	4.17E-05	-8.332	6.09E-09	Yes	
*m20(23.1)	-1.86E-04	3.61E-05	-5.144	2.07E-05	Yes	
*g6(26.1)	-3.59E-04	4.17E-05	-8.609	3.19E-09	Yes	
*g6(27)	-3.16E-04	3.20E-05	-9.862	1.91E-10	Yes	
*g12(24)	-5.80E-06	4.17E-05	-0.139	8.91E-01	No	
*g12(25)	-5.75E-05	4.17E-05	-1.378	1.80E-01	No	

* Statistical effects (slope coefficients).

Table 144: Statistical evaluation of p_{22} in HSI with multiple linear regression with g20(26.2) as the reference. Data from m6(22.2), m6(23.2), g6(26.1), g6(27), m12(20), m12(21), g12(24), g12(25), g12(28.1), m20(22.1), m20(23.1), and g20(26.2).

OVERALL FIT						
Multiple R	0.988					
R Square	0.976					
Adjusted R Square	0.956					
Standard Error	0.024					
Observations	49					
ANOVA				Alpha	0.05	
	df	SS	MS	F	p-value	Sign. diff.
Regression	21	0.6339	0.0302	51.193	1.42E-16	yes
Residual	27	0.0159	0.0006			
Total	48	0.6498				
	Coeff.	Std. err.	t Stat	p-value	Sign. diff.	
Intercept	9.63E-02	5.04E-02	1.912	6.65E-02	No	
t [μ s]	1.18E-03	2.68E-04	4.410	1.48E-04	Yes	
m6(22.2)	3.37E-02	1.06E-01	0.318	7.53E-01	No	
m6(23.2)	-1.55E-01	1.06E-01	-1.462	1.55E-01	No	
m12(20)	-1.10E-01	9.65E-02	-1.137	2.65E-01	No	
m12(21)	1.40E-01	6.42E-02	2.180	3.82E-02	Yes	
m20(22.1)	-9.08E-03	7.91E-02	-0.115	9.09E-01	No	
m20(23.1)	-3.13E-01	8.02E-02	-3.904	5.70E-04	Yes	
g6(26.1)	-5.22E-02	1.15E-01	-0.452	6.55E-01	No	
g6(27)	7.60E-02	6.30E-02	1.207	2.38E-01	No	
g12(24)	2.54E-01	7.12E-02	3.562	1.39E-03	Yes	
g12(25)	-6.83E-02	7.91E-02	-0.864	3.95E-01	No	
*m6(22.2)	-1.20E-03	3.79E-04	-3.167	3.80E-03	Yes	
*m6(23.2)	-6.24E-04	3.79E-04	-1.649	1.11E-01	No	
*m12(20)	-5.64E-04	3.79E-04	-1.491	1.48E-01	No	
*m12(21)	-1.04E-03	3.28E-04	-3.182	3.66E-03	Yes	
*m20(22.1)	-1.72E-04	3.79E-04	-0.455	6.53E-01	No	
*m20(23.1)	1.02E-03	3.28E-04	3.114	4.34E-03	Yes	
*g6(26.1)	-7.52E-04	3.79E-04	-1.987	5.71E-02	No	
*g6(27)	-9.07E-04	2.91E-04	-3.122	4.26E-03	Yes	
*g12(24)	-1.94E-03	3.79E-04	-5.111	2.26E-05	Yes	
*g12(25)	1.16E-04	3.79E-04	0.305	7.63E-01	No	

* Statistical effects (slope coefficients).

**Table 145: Statistical evaluation of p_{20} , p_{21} , and p_{22} in the second fracture phase in HSI with ANCOVA (Two-way ANOVA of regression residuals, $\alpha = 0.05$).
Data from m6(22.2), m6(23.2), g6(26.1), g6(27), m12(20), m12(21), g12(24), g12(25), g12(28.1), m20(22.1), m20(23.1), and g20(26.2).**

p_{20}	SS	df	MS	F	p-value	Sign. diff.
Material	2.91E-04	1	2.91E-04	45.051	3.37E-08	Yes
I_c [g/m]	1.12E-04	2	5.58E-05	8.641	7.01E-04	Yes
Between groups	1.44E-04	2	7.22E-05	11.179	1.23E-04	Yes
Within groups	2.78E-04	43	6.46E-06			
Total	8.75E-04	48	1.82E-05			
p_{21}	SS	df	MS	F	p-value	Sign. diff.
Material	9.43E-03	1	9.43E-03	26.442	6.35E-06	Yes
I_c [g/m]	3.92E-03	2	1.96E-03	5.504	7.44E-03	Yes
Between groups	2.23E-03	2	1.12E-03	3.129	5.39E-02	No
Within groups	1.53E-02	43	3.56E-04			
Total	3.17E-02	48	6.61E-04			
p_{22}	SS	df	MS	F	p-value	Sign. diff.
Material	0.0038	1	0.0038	0.6316	4.31E-01	No
I_c [g/m]	0.2308	2	0.1154	19.0174	1.21E-06	Yes
Between groups	0.0792	2	0.0396	6.5241	3.35E-03	Yes
Within groups	0.2610	43	0.0061			
Total	0.6493	48	0.0135			

Table 146: Overview and statistical evaluation of average p_{20} and p_{21} in CTt with One-way ANOVA ($\alpha = 0.05$).

Variable	Ave	Std	Data count	F	F_{crit}	p-value	Sign. diff.	
p_{20}	m6(23.2)	0.0016	0.0011	10	5.15	4.35	0.03	Yes
	g6(26.1)	0.0008	0.0003	12				
	m12(21)	0.0033	0.0008	10	1.99	3.35	0.16	No
	g12(28.1)	0.0030	0.0007	10				
	m20(23.1)	0.0036	0.0006	10				
p_{21}	m6(23.2)	0.0316	0.0141	10	5.70	4.35	0.03	Yes
	g6(26.1)	0.0218	0.0022	12				
	m12(21)	0.0669	0.0084	10	1.54	3.35	0.23	No
	g12(28.1)	0.0648	0.0157	10				
	m20(23.1)	0.0736	0.0098	10				
p_{20}	m6(23.2)	0.0016	0.0011	10	30.49	2.57	3E-12	Yes
	g6(26.1)	0.0008	0.0003	12				
	m12(21)	0.0033	0.0008	10				
	g12(28.1)	0.0030	0.0007	10				
	m20(23.1)	0.0036	0.0006	10				
p_{21}	m6(23.2)	0.0316	0.0141	10	49.78	2.57	2E-16	Yes
	g6(26.1)	0.0218	0.0022	12				
	m12(21)	0.0669	0.0084	10				
	g12(28.1)	0.0648	0.0157	10				
	m20(23.1)	0.0736	0.0098	10				

Table 147: Statistical evaluation of p_{20} in CTt with multiple linear regression ($\alpha = 0.05$) with m20(23.1) as the reference. Data from m6(23.2), g6(26.1), m12(21), g12(28.1), and m20(23.1).

Regression Statistics					
Multiple R	0.8321				
R Square	0.6924				
Adjusted R Square	0.6651				
Standard Error	0.0008				
Observations	50				
ANOVA			Alpha	0.05	
	df	SS	MS	F	Significance F
Regression	4	6.00E-05	1.50E-05	25.326	4.99E-11
Residual	45	2.66E-05	5.92E-07		
Total	49	8.66E-05			
	Coeff.	Std. err.	t Stat	p-value	Sign. diff.
Intercept	3.74E-03	3.00E-04	12.478	3.28E-16	Yes
Axial position [mm]	-1.02E-06	1.27E-06	-0.804	4.26E-01	No
6 g/m	-2.15E-03	3.22E-04	-6.695	2.89E-08	Yes
12 g/m	-1.62E-04	3.22E-04	-0.502	6.18E-01	No
Material	-5.70E-04	2.43E-04	-2.344	2.36E-02	Yes

Table 148: Statistical evaluation of p_{21} in CTt with multiple linear regression ($\alpha = 0.05$) with m20(23.1) as the reference. Data from m6(23.2), g6(26.1), m12(21), g12(28.1), and m20(23.1).

Regression Statistics					
Multiple R	0.882				
R Square	0.779				
Adjusted R Square	0.759				
Standard Error	0.012				
Observations	50				
ANOVA			Alpha	0.05	
	df	SS	MS	F	Significance F
Regression	4	2.20E-02	5.50E-03	39.562	3.42E-14
Residual	45	6.25E-03	1.39E-04		
Total	49	2.82E-02			
	Coeff.	Std. err.	t Stat	p-value	Sign. diff.
Intercept	7.18E-02	4.59E-03	15.637	8.27E-20	Yes
Axial position [mm]	1.29E-05	1.94E-05	0.666	5.09E-01	No
6 g/m	-4.40E-02	4.93E-03	-8.913	1.68E-11	Yes
12 g/m	-4.57E-03	4.93E-03	-0.928	3.59E-01	No
Material	-6.27E-03	3.73E-03	-1.681	9.96E-02	No

Table 149: Statistical evaluation of p_{22} in CTt with multiple linear regression ($\alpha = 0.05$) with m20(23.1) as the reference. Data from m6(23.2), g6(26.1), m12(21), g12(28.1), and m20(23.1).

Regression Statistics	
Multiple R	0.8327
R Square	0.6933
Adjusted R Square	0.6661
Standard Error	0.0789
Observations	50

ANOVA		Alpha		0.05	
	df	SS	MS	F	Significance F
Regression	4	6.34E-01	1.58E-01	25.436	4.67E-11
Residual	45	2.80E-01	6.23E-03		
Total	49	9.14E-01			
	Coeff.	Std. err.	t Stat	p-value	Sign. diff.
Intercept	4.19E-01	3.07E-02	13.634	1.38E-17	Yes
Axial position [mm]	3.28E-04	1.30E-04	2.522	1.53E-02	Yes
6 g/m	-2.55E-01	3.30E-02	-7.727	8.62E-10	Yes
12 g/m	-6.46E-02	3.30E-02	-1.956	5.67E-02	No
Material	-1.61E-02	2.50E-02	-0.646	5.22E-01	No

Table 150: Statistical evaluation of the fracture abundance (p_{20} , p_{21} , and p_{22}) in CTt with Two-way ANOVA ($\alpha = 0.05$). Data from m6(23.2), g6(26.1), m12(21), g12(28.1), and m20(23.1).

p_{20}	SS	df	MS	F	p-value	Sign. diff.
Material	3.27E-06	1	3.27E-06	5.135	2.96E-02	Yes
I_c [g/m]	3.97E-05	1	3.97E-05	62.363	2.27E-09	Yes
Between groups	4.77E-07	1	4.77E-07	0.750	3.92E-01	No
Within groups	2.29E-05	36	6.36E-07			
Total	6.63E-05	39	1.7E-06			
p_{21}	SS	df	MS	F	p-value	Sign. diff.
Material	3.90E-04	1	3.90E-04	2.707	1.09E-01	No
I_c [g/m]	1.55E-02	1	1.55E-02	107.572	2.32E-12	Yes
Between groups	1.65E-04	1	1.65E-04	1.144	2.92E-01	No
Within groups	5.19E-03	36	1.44E-04			
Total	2.13E-02	39	5.45E-04			
p_{22}	SS	df	MS	F	p-value	Sign. diff.
Material	2.45E-03	1	2.45E-03	0.3505	5.58E-01	No
I_c [g/m]	3.64E-01	1	3.64E-01	52.1558	1.68E-08	Yes
Between groups	1.32E-06	1	1.32E-06	0.0002	9.89E-01	No
Within groups	2.52E-01	36	6.99E-03			
Total	6.19E-01	39	1.59E-02			

In-plane (2D) fragmentation

This section covers results of the statistical analyses corresponding to Section 5.4.

Table 151: Statistical evaluation of the 2D-fragment count in HSI with multiple linear regression with g20(26.2) as the reference. Data from m6(22.2), m6(23.2), g6(26.1), g6(27), m12(20), m12(21), g12(24), g12(25), g12(28.1), m20(22.1), m20(23.1), and g20(26.2).

OVERALL FIT						
Multiple R	0.967					
R Square	0.936					
Adjusted R Square	0.918					
Standard Error	7.976					
Observations	95					
ANOVA				Alpha	0.05	
	df	SS	MS	F	p-value	Sign. diff.
Regression	21	67861.172	3231.484	50.799	3.20E-35	yes
Residual	73	4643.733	63.613			
Total	94	72504.905				
	Coeff.	Std. err.	t Stat	p-value	Sign. diff.	
Intercept	-32.600	10.701	-3.047	3.22E-03	Yes	
t [μ s]	0.323	0.062	5.194	1.79E-06	Yes	
m6(22.2)	32.633	12.639	2.582	1.18E-02	Yes	
m6(23.2)	22.100	14.403	1.534	1.29E-01	No	
m12(20)	29.267	13.763	2.126	3.68E-02	Yes	
m12(21)	28.024	12.387	2.262	2.67E-02	Yes	
m20(22.1)	30.207	13.431	2.249	2.75E-02	Yes	
m20(23.1)	-0.686	16.401	-0.042	9.67E-01	No	
g6(26.1)	23.638	11.684	2.023	4.67E-02	Yes	
g6(27)	18.594	12.387	1.501	1.38E-01	No	
g12(24)	-25.471	13.431	-1.896	6.19E-02	No	
g12(25)	-6.033	12.639	-0.477	6.35E-01	No	
*m6(22.2)	-0.309	0.067	-4.607	1.69E-05	Yes	
*m6(23.2)	-0.270	0.067	-4.013	1.43E-04	Yes	
*m12(20)	-0.286	0.067	-4.258	6.05E-05	Yes	
*m12(21)	-0.218	0.066	-3.317	1.42E-03	Yes	
*m20(22.1)	-0.285	0.072	-3.936	1.87E-04	Yes	
*m20(23.1)	-0.176	0.072	-2.429	1.76E-02	Yes	
*g6(26.1)	-0.242	0.064	-3.791	3.07E-04	Yes	
*g6(27)	-0.211	0.066	-3.205	2.00E-03	Yes	
*g12(24)	0.337	0.072	4.658	1.40E-05	Yes	
*g12(25)	-0.026	0.067	-0.385	7.01E-01	No	

* Statistical effects (slope coefficients).

Table 152: Statistical evaluation of the 2D-fragment count in the second fracture phase in HSI with multiple linear regression with g20(26.2) as the reference.
Data from m6(22.2), m6(23.2), g6(26.1), g6(27), m12(20), m12(21), g12(24), g12(25), g12(28.1), m20(22.1), m20(23.1), and g20(26.2).

OVERALL FIT						
Multiple R	0.992					
R Square	0.984					
Adjusted R Square	0.972					
Standard Error	3.329					
Observations	49					
ANOVA				Alpha	0.05	
	df	SS	MS	F	p-value	Sign. diff.
Regression	21	18616.944	886.521	80.006	4.18E-19	yes
Residual	27	299.179	11.081			
Total	48	18916.122				
	Coeff.	Std. err.	t Stat	p-value	Sign. diff.	
Intercept	-51.100	6.903	-7.403	5.80E-08	Yes	
t [μs]	0.414	0.037	11.285	9.98E-12	Yes	
m6(22.2)	53.300	14.510	3.673	1.04E-03	Yes	
m6(23.2)	38.200	14.510	2.633	1.38E-02	Yes	
m12(20)	54.100	13.232	4.089	3.50E-04	Yes	
m12(21)	35.800	8.807	4.065	3.73E-04	Yes	
m20(22.1)	48.300	10.838	4.457	1.31E-04	Yes	
m20(23.1)	14.300	10.990	1.301	2.04E-01	No	
g6(26.1)	38.600	15.825	2.439	2.16E-02	Yes	
g6(27)	20.957	8.635	2.427	2.22E-02	Yes	
g12(24)	-30.800	9.762	-3.155	3.91E-03	Yes	
g12(25)	31.900	10.838	2.943	6.60E-03	Yes	
*m6(22.2)	-0.407	0.052	-7.837	1.99E-08	Yes	
*m6(23.2)	-0.355	0.052	-6.840	2.39E-07	Yes	
*m12(20)	-0.399	0.052	-7.695	2.82E-08	Yes	
*m12(21)	-0.249	0.045	-5.540	7.17E-06	Yes	
*m20(22.1)	-0.375	0.052	-7.220	9.15E-08	Yes	
*m20(23.1)	-0.261	0.045	-5.814	3.46E-06	Yes	
*g6(26.1)	-0.328	0.052	-6.317	9.21E-07	Yes	
*g6(27)	-0.257	0.040	-6.440	6.70E-07	Yes	
*g12(24)	0.367	0.052	7.077	1.31E-07	Yes	
*g12(25)	-0.244	0.052	-4.702	6.78E-05	Yes	

* Statistical effects (slope coefficients).

Table 153: Statistical evaluation of the 2D-fragment count in HSI with ANCOVA (One-way ANOVA of linear-regression residuals). Data from m6(22.2), m6(23.2), g6(26.1), g6(27), m12(20), m12(21), g12(24), g12(25), g12(28.1), m20(22.1), m20(23.1), and g20(26.2).

	SS	df	MS	F	p-value	Sign. diff.
Material	9713.2	1	9713.2	23.03	6.37E-06	Yes
I_c [g/m]	12658.9	2	6329.5	15.01	2.41E-06	Yes
Between groups	4411.9	2	2206.0	5.23	7.11E-03	Yes
Within groups	37529.0	89	421.7			
Total	65190.4	94	693.5			

Table 154: Statistical evaluation of the 2D-fragment count in the second fracture phase in HSI with ANCOVA (One-way ANOVA of linear-regression residuals).

Data from m6(22.2), m6(23.2), g6(26.1), g6(27), m12(20), m12(21), g12(24), g12(25), g12(28.1), m20(22.1), m20(23.1), and g20(26.2).

	SS	df	MS	F	p-value	Sign. diff.
Material	5355.476	1	5355.476	21.008	3.91E-05	Yes
I_c [g/m]	4233.963	2	2116.982	8.304	8.92E-04	Yes
Between groups	493.073	2	246.537	0.967	3.88E-01	No
Within groups	10961.769	43	254.925			
Total	20560.195	48	428.337			

Table 155: Statistical evaluation of average total 2D-fragment count in CTt with One-way ANOVA ($\alpha = 0.05$).

Variable	Ave	Std	Data count	F	F _{crit}	p-value	Sign. diff.
m6(23.2)	15.00	14.30	10.00	2.10	4.35	0.16	No
g6(26.1)	8.92	2.75	12.00				
m12(21)	29.10	8.84	10.00	1.16	3.35	0.33	No
g12(28.1)	34.40	7.21	10.00				
m20(23.1)	31.60	7.21	10.00				
All data				17.90	2.57	5E-09	Yes

Table 156: Statistical evaluation of 2D-fragment count in CTt with multiple linear regression ($\alpha = 0.05$) with m20(23.1) as the reference. Data from m6(23.2), g6(26.1), m12(21), g12(28.1), and m20(23.1).

Regression Statistics	
Multiple R	0.746
R Square	0.557
Adjusted R Square	0.518
Standard Error	9.213
Observations	50

ANOVA		df	SS	MS	F	Significance F
Regression	4	4805.764	1201.441	14.155	1.48E-07	
Residual	45	3819.356	84.875			
Total	49	8625.120				

	Coeff.	Std. err.	t Stat	p-value	Sign. diff.
Intercept	33.567	3.588	9.355	4.03E-12	Yes
Axial position [mm]	-0.014	0.015	-0.939	3.53E-01	No
6 g/m	-19.544	3.854	-5.071	7.27E-06	Yes
12 g/m	0.371	3.854	0.096	9.24E-01	No
Material	-0.479	2.913	-0.165	8.70E-01	No

Table 157: Statistical evaluation of the 2D-fragment count in CTt with Two-way ANOVA ($\alpha = 0.05$). Data from m6(23.2), g6(26.1), m12(21), g12(28.1), and m20(23.1).

	SS	df	MS	F	p-value	Sign. diff.
Material	2.5	1	2.50	0.029	8.65E-01	No
I_c [g/m]	3960.1	1	3960.10	46.146	6.14E-08	Yes
Between groups	336.4	1	336.40	3.920	5.54E-02	No
Within groups	3089.4	36	85.82			
Total	7388.4	39	189.45			

Table 158: Statistical evaluation of 2D-fragment count in CTnp with multiple linear regression ($\alpha = 0.05$) with m20(23.1) as the reference. Data from m6(23.2), g6(26.1), m12(21), g12(28.1), and m20(23.1).

Regression Statistics					
Multiple R	0.857				
R Square	0.735				
Adjusted R Square	0.699				
Standard Error	12.659				
Observations	60				
ANOVA					
	df	SS	MS	F	Significance F
Regression	7	23100.253	3300.036	20.594	5.95E-13
Residual	52	8332.681	160.244		
Total	59	31432.933			
	Coeff.	Std. err.	t Stat	p-value	Sign. diff.
Intercept	30.893	9.997	3.090	3.21E-03	Yes
Radial position [mm]	-0.159	0.212	-0.750	4.57E-01	No
6 g/m	-45.343	12.751	-3.556	8.13E-04	Yes
12 g/m	1.633	12.107	0.135	8.93E-01	No
Material	64.292	9.348	6.878	7.75E-09	Yes
*6 g/m	0.384	0.281	1.365	1.78E-01	No
*12 g/m	-0.239	0.262	-0.912	3.66E-01	No
*Material	-0.939	0.216	-4.344	6.51E-05	Yes

* Statistical effects (slope coefficients).

Fracture-surface roughness

This section covers results of the statistical analyses corresponding to the results in Section 5.9.2.

Table 159 shows an overview of calculated average fracture-surface roughness for the three kernel sizes.

Table 159: Overview of average fracture-surface roughness.

Variable		Kernel 1 mm			Kernel 3 mm			Kernel 5 mm		
		Ave	Std	Data	Ave	Std	Data	Ave	Std	Data
m6(22.2)	l	0.0694	0.0634	1000199	0.1927	0.1614	1000199	0.3107	0.2541	1000199
	r	0.0730	0.0672	1000765	0.2108	0.1736	1000765	0.3413	0.2845	1000765
m12(20)	l	0.0753	0.0672	1000201	0.2247	0.1891	1000264	0.3764	0.3241	1000266
	r	0.0708	0.0616	1000462	0.2111	0.1767	1000463	0.3651	0.3103	1000463
m20(22.1)	l	0.0716	0.0694	999970	0.1884	0.1668	999970	0.2925	0.2449	999970
	r	0.0648	0.0588	1000038	0.1747	0.1409	1000038	0.2728	0.2154	1000038
g6(27)	l	0.0665	0.0554	1000152	0.1882	0.1575	1000153	0.3079	0.2714	1000153
	r	0.0650	0.0539	999546	0.1791	0.1494	999546	0.2858	0.2410	999546
g12(25)	l	0.0706	0.0611	1000011	0.1999	0.1689	1000013	0.3176	0.2670	1000013
	r	0.0694	0.0580	1000525	0.1967	0.1643	1000533	0.3238	0.2694	1000534
g20(26.2)	l	0.0640	0.0559	999475	0.1831	0.1576	999481	0.2917	0.2482	999481
	r	0.0592	0.0494	999475	0.1771	0.1417	999481	0.2904	0.2313	999481

* l – left fragment side

r – right fragment side

Table 160 shows results of the statistical evaluation (Two-way ANOVA) of fracture-surface roughness for the kernel size of 1 mm.

Table 160: Statistical evaluation of fracture-surface roughness (kernel size - 1 mm) with Two-way ANOVA ($\alpha = 0.05$). Data from m6(22.2), m12(20), m20(22.1), g6(27), g12(25), and g20(26.2).

	SS	df	MS	F	p-value	Sign. diff.
Material	0.0167	1	0.0167	4.640	3.14E-02	Yes
I_c [g/m]	0.0224	2	0.0112	3.108	4.51E-02	Yes
Between groups	0.0046	2	0.0023	0.635	5.30E-01	No
Within groups	4.3023	1194	0.0036			
Total	4.3460	1199	0.0036			

Table 161 shows results of the statistical evaluation (Two-way ANOVA) of fracture-surface roughness for the kernel size of 3 mm.

Table 161: Statistical evaluation of fracture-surface roughness (kernel size - 3 mm) with Two-way ANOVA ($\alpha = 0.05$). Data from m6(22.2), m12(20), m20(22.1), g6(27), g12(25), and g20(26.2).

	SS	df	MS	F	p-value	Sign. diff.
Material	0.1864	1	0.1864	6.369	1.17E-02	Yes
I_c [g/m]	0.0672	2	0.0336	1.148	3.18E-01	No
Between groups	0.0961	2	0.0481	1.642	1.94E-01	No
Within groups	34.9450	1194	0.0293			
Total	35.2947	1199	0.0294			

Table 162 shows results of the statistical evaluation (Two-way ANOVA) of fracture-surface roughness for the kernel size of 5 mm.

Table 162: Statistical evaluation of fracture-surface roughness (kernel size - 5 mm) with Two-way ANOVA ($\alpha = 0.05$). Data from m6(22.2), m12(20), m20(22.1), g6(27), g12(25), and g20(26.2).

	SS	df	MS	F	p-value	Sign. diff.
Material	0.0011	1	0.0011	0.017	8.98E-01	No
I_c [g/m]	0.6013	2	0.3006	4.593	1.03E-02	Yes
Between groups	0.1364	2	0.0682	1.042	3.53E-01	No
Within groups	78.1581	1194	0.0655			
Total	78.8969	1199	0.0658			

Regression lines of the s-n(s) data

This section covers results of the statistical analyses corresponding to Section 5.10.4.

Table 163 shows a summary of the slopes and intercepts of the s-n(s) linear-regression lines for the sieving data in the fines-size range (F).

Table 163: Summary of the slopes and intercepts of the s-n(s) linear-regression lines with 95%-confidence limits for the fines-size range of the sieving data.

Variable	Slope ($-\alpha, -\beta$)	<i>lower</i>	<i>upper</i>	Intercept ($\ln(C_n)$)	<i>lower</i>	<i>upper</i>
g6(26.1)_F	-1.812	-2.104	-1.520	-5.460	-5.830	-3.759
g6(27)_F	-1.808	-2.100	-1.516	-5.521	-7.161	-3.819
g12(24)_F	-1.756	-2.048	-1.464	-3.966	-7.222	-2.265
g12(25)_F	-1.739	-2.031	-1.447	-4.018	-5.668	-2.317
g12(28.1)_F	-1.768	-2.060	-1.476	-3.698	-5.720	-1.997
m6(22.2)_F	-1.808	-2.100	-1.516	-5.105	-5.400	-3.404
m6(23.2)_F	-1.861	-2.153	-1.569	-4.980	-6.807	-3.278
m12(20)_F	-1.692	-1.984	-1.401	-4.561	-6.681	-2.860
m12(21)_F	-1.812	-2.104	-1.521	-3.872	-6.262	-2.170
m20(22.1)_F	-1.830	-2.122	-1.538	-3.663	-5.573	-1.962
m20(23.1)_F	-1.814	-2.106	-1.522	-3.441	-5.365	-1.740
g20(26.2)_F	-1.739	-1.698	-1.618	-3.265	-3.970	-2.560

Table 164 shows linear-regression results of s-n(s) regression lines for the sieving data in the fines-size range.

Table 164: Statistical evaluation of s-n(s) regression lines for the sieving data in the fines-size range with multiple linear regression ($\alpha = 0.05$) with m20(23.1) as the reference. Data from m6(22.2), m6(23.2), g6(26.1), g6(27), m12(20), m12(21), g12(24), g12(25), g12(28.1), m20(22.1), m20(23.1), and g20(26.2).

OVERALL FIT						
Multiple R	0.999					
R Square	0.998					
Adjusted R Square	0.996					
Standard Error	0.317					
Observations	48					
ANOVA	df	SS	MS	F	p-value	Sign. diff.
Regression	23	1156.73	50.29	500.87	6.01E-27	yes
Residual	24	2.41	0.10			
Total	47	1159.15				
	Coeff.	Std. err.	t Stat	p-value	Sign. diff.	
Intercept	-3.2650	0.3415	-9.5615	1.17E-09	Yes	
ln(s)	-1.7389	0.0586	-29.6806	1.98E-20	Yes	
g6(26.1)_F	-2.1950	0.4829	-4.5454	1.32E-04	Yes	
g6(27)_F	-2.2557	0.4829	-4.6710	9.59E-05	Yes	
g12(24)_F	-0.7014	0.4829	-1.4524	1.59E-01	No	
g12(25)_F	-0.7531	0.4829	-1.5595	1.32E-01	No	
g12(28.1)_F	-0.4331	0.4829	-0.8968	3.79E-01	No	
m6(22.2)_F	-1.8403	0.4829	-3.8108	8.49E-04	Yes	
m6(23.2)_F	-1.7148	0.4829	-3.5510	1.62E-03	Yes	
m12(20)_F	-1.2960	0.4829	-2.6837	1.30E-02	Yes	
m12(21)_F	-0.6066	0.4829	-1.2561	2.21E-01	No	
m20(22.1)_F	-0.3984	0.4829	-0.8250	4.17E-01	No	
m20(23.1)_F	-0.1761	0.4829	-0.3646	7.19E-01	No	
*g6(26.1)_F	-0.0731	0.0829	-0.8822	3.86E-01	No	
*g6(27)_F	-0.0693	0.0829	-0.8369	4.11E-01	No	
*g12(24)_F	-0.0167	0.0829	-0.2013	8.42E-01	No	
*g12(25)_F	-0.0004	0.0829	-0.0050	9.96E-01	No	
*g12(28.1)_F	-0.0288	0.0829	-0.3480	7.31E-01	No	
*m6(22.2)_F	-0.0687	0.0829	-0.8296	4.15E-01	No	
*m6(23.2)_F	-0.1219	0.0829	-1.4716	1.54E-01	No	
*m12(20)_F	0.0465	0.0829	0.5607	5.80E-01	No	
*m12(21)_F	-0.0736	0.0829	-0.8878	3.83E-01	No	
*m20(22.1)_F	-0.0912	0.0829	-1.1001	2.82E-01	No	
*m20(23.1)_F	-0.0749	0.0829	-0.9034	3.75E-01	No	

* Statistical effects (slope coefficients).

Table 165 shows linear-regression results of s-n(s) regression lines for the sieving data in the intermediate-fragment-size range.

Table 165: Statistical evaluation of s-n(s) regression lines for the sieving data in the intermediate-fragment-size range with multiple linear regression ($\alpha = 0.05$) with m20(23.1) as the reference. Data from m6(22.2), m6(23.2), g6(26.1), g6(27), m12(20), m12(21), g12(24), g12(25), g12(28.1), m20(22.1), m20(23.1), and g20(26.2).

Regression Statistics					
Multiple R	0.998				
R Square	0.997				
Adjusted R Square	0.996				
Standard Error	0.289				
Observations	87				
ANOVA	df	SS	MS	F	Significance F
Regression	23	3062.434	133.149	1467.628	3.17E-150
Residual	135	12.248	0.091		
Total	158	3074.682			
	Coeff.	Std. err.	t Stat	p-value	Sign. diff.
Intercept	-6.624	0.546	-12.125	2.39E-23	Yes
ln(s)	-1.587	0.034	-46.355	8.65E-85	Yes
g6(26.1)_IF	-0.725	0.726	-0.999	3.19E-01	No
g6(27)_IF	-0.781	0.726	-1.076	2.84E-01	No
g12(24)_IF	0.712	0.773	0.921	3.59E-01	No
g12(25)_IF	1.811	0.773	2.344	2.05E-02	Yes
g12(28.1)_IF	2.400	0.773	3.106	2.31E-03	Yes
g20(26.2)_IF	1.540	0.671	2.294	2.33E-02	Yes
m6(22.2)_IF	-0.733	0.858	-0.854	3.95E-01	No
m6(23.2)_IF	-2.355	0.797	-2.955	3.69E-03	Yes
m12(20)_IF	-0.371	0.824	-0.451	6.53E-01	No
m12(21)_IF	0.883	0.773	1.143	2.55E-01	No
m20(22.1)_IF	0.134	0.768	0.174	8.62E-01	No
*g6(26.1)_IF	-0.091	0.045	-2.039	4.34E-02	Yes
*g6(27)_IF	-0.087	0.045	-1.947	5.36E-02	No
*g12(24)_IF	-0.056	0.048	-1.165	2.46E-01	No
*g12(25)_IF	-0.130	0.048	-2.693	7.97E-03	Yes
*g12(28.1)_IF	-0.163	0.048	-3.369	9.85E-04	Yes
*g20(26.2)_IF	-0.067	0.041	-1.634	1.05E-01	No
*m6(22.2)_IF	-0.059	0.056	-1.062	2.90E-01	No
*m6(23.2)_IF	0.015	0.050	0.302	7.63E-01	No
*m12(20)_IF	-0.038	0.053	-0.722	4.71E-01	No
*m12(21)_IF	-0.087	0.048	-1.807	7.30E-02	No
*m20(22.1)_IF	-0.042	0.048	-0.884	3.78E-01	No

* Statistical effects (slope coefficients).

Table 166 shows a summary of the slopes and intercepts of the s-n(s) linear-regression lines for the sieving data in the intermediate-fragment-size range (IF).

Table 166: Summary of the slopes and intercepts of the s-n(s) linear-regression lines with 95%-confidence limits for the intermediate-fragment-size range of the sieving data.

Variable	Slope (- α , - β)	<i>lower</i>	<i>upper</i>	Intercept ($\ln(C_n)$)	<i>lower</i>	<i>upper</i>
g6(26.1)_IF	-1.678	-1.835	-1.522	-7.350	-9.866	-4.834
g6(27)_IF	-1.674	-1.831	-1.518	-7.405	-9.922	-4.889
g12(24)_IF	-1.643	-1.807	-1.480	-5.913	-8.521	-3.304
g12(25)_IF	-1.717	-1.881	-1.554	-4.813	-7.422	-2.205
g12(28.1)_IF	-1.750	-1.914	-1.587	-4.224	-6.833	-1.616
g20(26.2)_IF	-1.654	-1.802	-1.505	-5.084	-7.492	-2.675
m6(22.2)_IF	-1.646	-1.824	-1.468	-7.358	-10.136	-4.579
m6(23.2)_IF	-1.572	-1.739	-1.404	-8.979	-11.636	-6.323
m12(20)_IF	-1.625	-1.797	-1.453	-6.996	-9.706	-4.286
m12(21)_IF	-1.675	-1.838	-1.511	-5.741	-8.349	-3.132
m20(22.1)_IF	-1.630	-1.792	-1.467	-6.491	-9.089	-3.892
m20(23.1)_IF	-1.587	-1.655	-1.519	-6.624	-7.705	-5.544

Table 167 shows a summary of the slopes and intercepts of the s-n(s) linear-regression lines for the merged screening data in the ultra-fines-size range.

Table 167: Summary of the slopes and intercepts of the s-n(s) linear-regression lines with 95%-confidence limits for the ultra-fines-size range of the merged screening data.

Variable	Slope (- α , - β)	<i>lower</i>	<i>upper</i>	Intercept ($\ln(C_n)$)	<i>lower</i>	<i>upper</i>
g6(27)_UF	-1.639	-1.717	-1.560	-11.545	-12.449	-10.640
g12(24)_UF	-1.643	-1.721	-1.564	-9.636	-10.541	-8.732
g12(25)_UF	-1.661	-1.741	-1.580	-9.382	-10.312	-8.452
m6(22.2)_UF	-1.617	-1.695	-1.538	-11.802	-12.721	-10.882
m12(20)_UF	-1.670	-1.749	-1.592	-9.729	-10.649	-8.809
m20(22.1)_UF	-1.673	-1.752	-1.595	-9.227	-10.132	-8.323
g20(26.2)_UF	-1.698	-1.728	-1.667	-7.902	-8.268	-7.535

Table 168 shows linear-regression results of s-n(s) regression lines for the merged screening data in the ultra-fines-size range (UF).

Table 168: Statistical evaluation of s-n(s) regression lines for the merged-screening data in the ultra-fines-size range with multiple linear regression ($\alpha = 0.05$) with g20(26.2) as the reference. Data from m6(22.2), g6(27), m12(20), g12(24), g12(25), m20(22.1), and g20(26.2).

OVERALL FIT							
Multiple R	0.999						
R Square	0.998						
Adjusted R Square	0.998						
Standard Error	0.494						
Observations	148						
ANOVA				Alpha	0.05		
	df	SS	MS	F	p-value	Sign. diff.	
Regression	13	14480.029	1113.848	4559.781	2.28E-170	yes	
Residual	134	32.733	0.244				
Total	147	14512.762					
	Coeff.	Std. err.	t Stat	p-value	Sign. diff.		
Intercept	-7.902	0.185	-42.643	7.94E-80	Yes		
ln(s)	-1.698	0.016	-109.470	5.85E-133	Yes		
g6(27)_UF	-3.643	0.272	-13.393	1.72E-26	Yes		
g12(24)_UF	-1.735	0.272	-6.377	2.71E-09	Yes		
g12(25)_UF	-1.480	0.285	-5.196	7.41E-07	Yes		
m6(22.2)_UF	-3.900	0.280	-13.938	7.57E-28	Yes		
m12(20)_UF	-1.827	0.280	-6.531	1.25E-09	Yes		
m20(22.1)_UF	-1.326	0.272	-4.873	3.06E-06	Yes		
*g6(27)_UF	0.059	0.024	2.427	1.65E-02	Yes		
*g12(24)_UF	0.055	0.024	2.266	2.51E-02	Yes		
*g12(25)_UF	0.037	0.025	1.474	1.43E-01	No		
*m6(22.2)_UF	0.081	0.024	3.352	1.04E-03	Yes		
*m12(20)_UF	0.028	0.024	1.141	2.56E-01	No		
*m20(22.1)_UF	0.024	0.024	1.002	3.18E-01	No		

* Statistical effects (slope coefficients).

Table 169 shows linear-regression results of s-n(s) regression lines for the merged screening data in the intermediate-fragment-size range.

Table 169: Statistical evaluation of s-n(s) regression lines for the merged-screening data in the intermediate-fragment-size range with multiple linear regression ($\alpha = 0.05$) with g20(26.2) as the reference. Data from m6(22.2), g6(27), m12(20), g12(24), g12(25), m20(22.1), and g20(26.2).

OVERALL FIT						
Multiple R	0.997					
R Square	0.994					
Adjusted R Square	0.993					
Standard Error	0.359					
Observations	99					
ANOVA				Alpha	0.05	
	df	SS	MS	F	p-value	Sign. diff.
Regression	13	1749.008	134.539	1041.927	8.73E-88	yes
Residual	85	10.976	0.129			
Total	98	1759.983				
	Coeff.	Std. err.	t Stat	p-value	Sign. diff.	
Intercept	-11.615	0.888	-13.077	4.69E-22	Yes	
ln(s)	-1.597	0.028	-57.349	9.91E-70	Yes	
g6(27)_IF	-0.022	1.352	-0.016	9.87E-01	No	
g12(24)_IF	-0.820	1.440	-0.570	5.70E-01	No	
g12(25)_IF	3.173	1.530	2.074	4.11E-02	Yes	
m6(22.2)_IF	0.497	1.503	0.331	7.42E-01	No	
m12(20)_IF	-2.060	1.774	-1.161	2.49E-01	No	
m20(22.1)_IF	-0.606	1.720	-0.352	7.25E-01	No	
*g6(27)_IF	-0.079	0.044	-1.773	7.99E-02	No	
*g12(24)_IF	0.017	0.047	0.360	7.20E-01	No	
*g12(25)_IF	-0.123	0.050	-2.464	1.58E-02	Yes	
*m6(22.2)_IF	-0.090	0.049	-1.813	7.33E-02	No	
*m12(20)_IF	0.022	0.058	0.374	7.10E-01	No	
*m20(22.1)_IF	-0.004	0.057	-0.063	9.50E-01	No	

* Statistical effects (slope coefficients).

Table 170 shows a summary of the slopes and intercepts of the s-n(s) linear-regression lines for the sieving data in the intermediate-fragment-size range.

Table 170: Summary of the slopes and intercepts of the s-n(s) linear-regression lines with 95%-confidence limits for the intermediate-fragment-size range of the merged screening data.

Variable	Slope (- α , - β)	lower	upper	Intercept (ln(C _n))	lower	upper
g6(27)_IF	-1.676	-1.819	-1.532	-11.6374	-16.092	-7.183
g12(24)_IF	-1.581	-1.729	-1.432	-12.4352	-17.064	-7.807
g12(25)_IF	-1.721	-1.875	-1.566	-8.4418	-13.250	-3.634
m6(22.2)_IF	-1.687	-1.841	-1.533	-11.1184	-15.873	-6.364
m12(20)_IF	-1.576	-1.747	-1.405	-13.6749	-18.969	-8.381
m20(22.1)_IF	-1.601	-1.770	-1.432	-12.2213	-17.408	-7.035
g20(26.2)_IF	-1.597	-1.653	-1.542	-11.615	-13.381	-9.849

Table 171 shows results of the statistical comparison (see Appendix 12) of the s-n(s) regression-line slopes for the intermediate-fragment-size range with those for the (ultra-)fines-size range (Table 163 and Table 166; see also Table 55) per blast shot.

Table 171: Results of a statistical comparison of the intermediate-fragment-size slopes with the (ultra-)fines slopes per blast shot.

Blast shot	Std. error	t-value	df	p-value	Sign. diff.
g20(26.2)	0.054	1.588	18	0.130	No
g12(28.1)	0.056	0.313	13	0.759	No
g12(25)	0.034	0.651	13	0.526	No
g12(24)	0.038	2.985	13	0.011	Yes
g6(27)	0.081	1.655	15	0.119	No
g6(26.1)	0.064	2.098	15	0.053	No
m20(23.1)	0.063	3.627	13	0.003	Yes
m20(22.1)	0.080	2.509	13	0.026	Yes
m12(21)	0.078	1.766	13	0.101	No
m12(20)	0.069	0.981	11	0.347	No
m6(23.2)	0.086	3.380	12	0.005	Yes
m6(22.2)	0.066	2.442	10	0.035	Yes

Appendix 11 **Blast-fragmentation measurement (additional details)**

Manual and mechanical sieving

The mechanical sieving was carried out using a pre-defined configuration. Figure 244 shows a control interface used for setting the shaker configuration.



Figure 244: Shaker-configuration interface (controller).

A fine brush was used to obtain residual material from the sieve mesh after the sieving. The material was added to corresponding size class right above the size of the sieve being cleaned (e.g., the residual material from the 1-mm sieve was added to the 2|1-mm class). All used sieves were with rectangular mesh, clean and dry before each sieving. The sieved material was neither pushed/crushed through the sieve mesh nor further processed (e.g., by additional manual sieving). Some measurement error had been expected due to trapped fines in sieve mesh. This was additionally investigated by air-jet screening of some of the sieved material. Figure 245 shows the air-jet screening assembly.



Figure 245: Apparatus for air-jet screening (laboratory of the Chair of Mineral Processing, IZR, MUL).

Laser-diffraction granulometry

The mortar material was analysed in a 5-% NaOH-solution with distilled water, whilst the granite material was analysed in pure distilled water. The solution for the mortar increases the sample's PH value and prevents flocculation due to the cement content. Solutions were prepared in 600-ml portions in beakers. After adding the solution in the apparatus' stirrer, sample dispersion was carried out according to the control software (Figure 246).

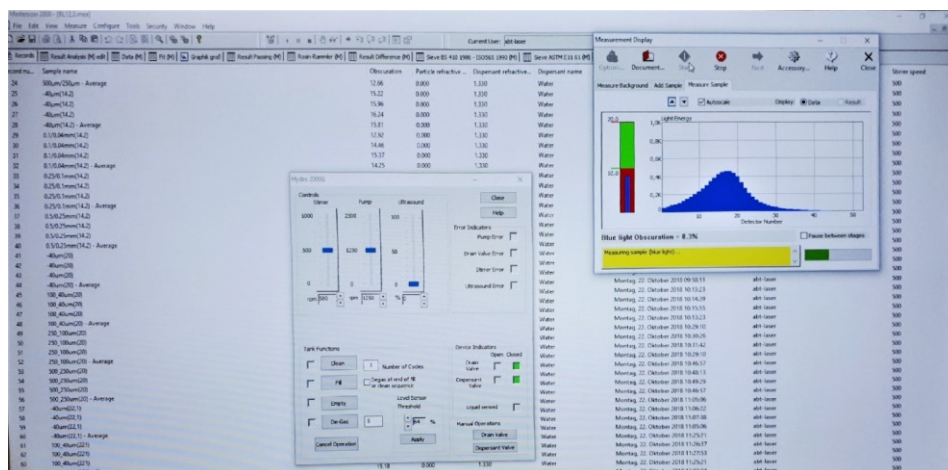


Figure 246: Malvern Mastersizer 2000 control software. Sample-adding procedure.

The fragmented material was added with a micro-spoon until reaching an acceptable concentration, which is signalled by the controlled software. The stirrer speed was set to 500 rpm and the pump speed to 1250 rpm.

The process of collating the laser-screening results (i.e., the four mass-passing data sub-sets per each analysed blasted cylinder) and merging them with the sieving results used the following procedure:

1. Assume no laser-screening measurements when $x > x_5$ (2 mm).
2. Assume all sieving data to be correct.
3. For intervals $x \in (0, 0.04) \cup [0.04, 0.01] \cup [0.1, 0.25] \cup [0.25, 0.5][mm]$, there are laser-screening samples provided by the sieving:

L_1 : from x_0 to x_1 ,

L_2 : from x_1 to x_2 ,

L_3 : from x_2 to x_3 ,

L_4 : from x_3 to x_4 .

4. All these samples contain material from the sieving range though there are no laser-screening measurements for $x > 2$ mm.
5. The laser-screening samples are assumed to be representative of the original bin contents.
6. The density of material in a bin is assumed to constant, allowing equivalence of mass data from the sieving and volume data from the laser granulometry.
7. The laser-screening curves are assumed to be continuous, $L_i(x)$ is expressed as unit volume for $i = 1, 2, 3, 4$.
8. The sieving data is assumed given as $M_0 \cdot P(x)$, where M_0 is the total sieved mass and $P(x)$ is the cumulative distribution function (CDF).
9. Then, the sieved bin contents are given by:

$$M_{56} = M_6(x) - M_5(x),$$

$$M_{45} = M_5(x) - M_4(x),$$

$$M_{34} = M_4(x) - M_3(x),$$

$$M_{23} = M_3(x) - M_2(x),$$

$$M_{12} = M_2(x) - M_1(x),$$

$$M_{01} = M_1(x).$$

10. Assumptions 4 to 7 imply the normalisation $\alpha_4 \int_0^1 L_4(x) dx = M_{45}$, $\alpha_3 \int_0^1 L_3(x) dx = M_{34}$, etc.

11. $L_4(x)$ contains material outside the bin range 0.25–0.5 mm, writing $x_3 = 0.25$ mm and $x_4 = 0.5$ mm. Therefore, $L_4(x)$ can be partitioned into sub-volumes corresponding to each bin:

$$\int_{x_0}^{x_1} L_4(x)dx, \int_{x_1}^{x_2} L_4(x)dx, \int_{x_2}^{x_3} L_4(x)dx, \int_{x_3}^{x_4} L_4(x)dx, \int_{x_4}^{x_5} L_4(x)dx, \int_{x_5}^{x_6} L_4(x)dx.$$

In short, this can be written as: $L_{4,01}, L_{4,12}, L_{4,23}, L_{4,34}, L_{4,45}, L_{4,56}$.

Here, $L_1, L_2,$ and L_3 are also partitioned like this.

12. Mass balance for the bins can be written in a matrix form:

$$M'_{56} = M_{56} + \alpha_1 L_{1,56} + \alpha_2 L_{2,56} + \alpha_3 L_{3,56} + \alpha_4 L_{4,56}; M'_5 = M_6 - M'_{56}$$

$$M'_{45} = M_{45} + \alpha_1 L_{1,45} + \alpha_2 L_{2,45} + \alpha_3 L_{3,45} + \alpha_4 L_{4,45}; M'_4 = M'_5 - M'_{45}$$

$$M'_{34} = M_{34} + \alpha_1 L_{1,34} + \alpha_2 L_{2,34} + \alpha_3 L_{3,34} + \alpha_4 L_{4,34}; M'_3 = M'_4 - M'_{34}$$

$$M'_{23} = M_{23} + \alpha_1 L_{1,23} + \alpha_2 L_{2,23} + \alpha_3 L_{3,23} + \alpha_4 L_{4,23}; M'_2 = M'_3 - M'_{23}$$

$$M'_{12} = M_{12} + \alpha_1 L_{1,12} + \alpha_2 L_{2,12} + \alpha_3 L_{3,12} + \alpha_4 L_{4,12}; M'_1 = M'_2 - M'_{12}$$

$$M'_{01} = M_{01} + \alpha_1 L_{1,01} + \alpha_2 L_{2,01} + \alpha_3 L_{3,01} + \alpha_4 L_{4,01}; M'_0 = M'_1 - M'_{01}$$

13. Summing all equations yields:

$$\begin{aligned} M'_5 + M'_4 + M'_3 + M'_2 + M'_1 + M'_0 \\ = M_6 + M'_5 + M'_4 + M'_3 + M'_2 + M'_1 - M'_{56} - M'_{45} - M'_{34} - M'_{23} \\ - M'_{12} - M'_{01} \end{aligned}$$

or simplified:

$$M'_0 = M_6 - M'_{56} - M'_{45} - M'_{34} - M'_{23} - M'_{12} - M'_{01} = 0,$$

as $M_6 - (\text{all corrected bin masses}) \equiv 0$.

14. Calculate mass-on-screen distribution [g-to-mm], i.e., $M_{nm} = M_{n+1} - M_n$.

15. Determine the ratio between sieved mass and total mass-on-screen values of included laser-screening classes for all four sieve categories. The ratio is then used to determine whether it is necessary to add sieve value to laser-screening value for corresponding size class. Generally, the sieve value is added if the ratio is higher than 2, e.g., if

$$\text{Ratio} = \frac{M_{34}}{(\alpha_1 L_{1,34} + \dots + \alpha_4 L_{4,34})} = 4.57 \rightarrow M'_{34} = M_{34} + (\alpha_1 L_{1,34} + \dots + \alpha_4 L_{4,34}),$$

where all α -coefficients are assumed to be 1 for the sake of simplicity.

16. Finally, the calculated and corrected values are filled in the result table for plotting the mass-passing FSD of collated data from sieving and laser screening together.

Datasheets of (measuring) balance scales

[Appendix 11 - Datasheets of \(measuring\) balance scales](#)

Appendix 12 Statistical methods

Student's two-sample t-test

Student's two-sample t-test is used to determine if mean values of two random groups are equal (Snedecor & Cochran, 1989). This method assumes the following:

- the two test samples (groups) are independent,
- covered data are normally distributed, and
- the two samples have the same variance.

Here, the tested “null-hypothesis” states that the means (μ) of the two test groups are the same (i.e., with null difference):

$$H_0: \mu_1 - \mu_2 = 0 \quad \text{Equation 74}$$

Therefore, the “null-hypothesis” is tested against the following “alternative-hypothesis”:

$$H_a: \mu_1 - \mu_2 \neq 0 \quad \text{Equation 75}$$

The test statistic (t-test) is carried out with the following formula:

$$t = \frac{|\bar{X}_1 - \bar{X}_2|}{\sqrt{\left(\frac{(N_1 - 1) \cdot s_1^2 + (N_2 - 1) \cdot s_2^2}{N_1 + N_2 - 2}\right) \left(\frac{1}{N_1} + \frac{1}{N_2}\right)}} \quad \text{Equation 76}$$

where:

\bar{X} - sample mean,

N - quantity of test data (data count per group), and

s - sample variance.

The null-hypothesis is rejected only if:

$$t > t_{crit}$$

Equation 77

where t_{crit} is the two-tailed inverse of the Student's t-distribution (function 'TINV' in MS Excel) with the probability (confidence level) set to $\alpha = 0.05$ and the degrees of freedom calculated as:

$$df = N_1 + N_2 - 2$$

Equation 78

The same condition is obtained when:

$$p < \alpha$$

Equation 79

where p is the p-value, calculated in MS Excel as:

$$p = 2 \cdot [1 - T.DIST(|t|, df, TRUE)]$$

Equation 80

Here, the function 'T.DIST' returns the Student's left-tailed t-distribution and the enclosed argument 'TRUE' indicates that this t-distribution is cumulative.

Single-factor (One-way) ANOVA and the F-test

When two or more groups or treatments are being compared, the characteristic that distinguishes the groups or treatments from one another is called the factor under investigation. A one-way analysis of variance (ANOVA) uses a statistical model for assessing differences between mean values of sample groups (two or more sample groups) and related statistical parameters (e.g., "variation" within and between groups) (Strickland, 2014).

In general, this statistical analysis covers k samples (groups or treatments) presented as columns (represented with the index j) in the corresponding structural model. Each group consists of a sample of size n_j . The sample elements are rows (represented with the index i) in this model. Therefore, the j -th group can be written as:

$$\{x_{1j}, x_{2j}, \dots, x_{n_j j}\}$$

Equation 81

Here, the total sample is:

$$\{x_{ij}: 1 \leq i \leq n_j, 1 \leq j \leq k\}$$

Equation 82

The sums of squares are defined as:

$$\begin{aligned}
 SS_j &= \sum_i (x_{ij} - \bar{x}_j)^2 && \text{Equation 83} \\
 SS_T &= \sum_j \sum_i (x_{ij} - \bar{x})^2 \\
 SS_W &= \sum_j SS_j = \sum_j \sum_i (x_{ij} - \bar{x}_j)^2 \\
 SS_B &= \sum_j n_j (\bar{x}_j - \bar{x})^2 \\
 &\text{with } n = \sum_{j=1}^k n_j
 \end{aligned}$$

where:

\bar{x}_j – the mean value of the j-th group sample (i.e., the group mean),

\bar{x} – the mean value of the total sample (i.e., the total or grand mean),

SS_T – the sum of squares for the total sample (i.e., the sum of squared deviations from the total mean),

SS_W – the sum of squares within the groups (i.e., the sum of the squared means across all groups), and

SS_B – the sum of squares of the inter-group sample means (i.e., the weighted sum of the squared deviations of the group means from the total mean).

The corresponding degrees of freedom (see the indices) are defined as:

$$\begin{aligned}
 df_T &= n - 1, && \text{Equation 84} \\
 df_B &= k - 1 \\
 df_W &= \sum_{j=1}^k (n_j - 1) = n - k
 \end{aligned}$$

The mean square is defined as:

$$MS = SS/df \quad \text{Equation 85}$$

yielding:

$$\begin{aligned}
 MS_T &= SS_T/df_T && \text{Equation 86} \\
 MS_B &= SS_B/df_B \\
 MS_W &= SS_W/df_W
 \end{aligned}$$

This method assumes the following:

- tested sample groups have the same variance,
- data of the groups are normally distributed, and
- each value (for a test group) is sampled independently. In this way, each subject (group) provides only one value. If a subject provides two scores, the values are not independent.

These assumptions are equivalent to the t-test ones considering differences between test groups. Here, the “null-hypothesis” states that the means (μ) of k groups are the same under all conditions:

$$H_0: \mu_1 = \mu_2 = \dots = \mu_k \quad \text{Equation 87}$$

is tested against:

$$H_a: \text{At least two of the } \mu \text{ values are different} \quad \text{Equation 88}$$

Whether the null hypothesis of a One-way ANOVA should be rejected depends on how substantially the samples from the different groups or treatments differ from one another. The null-hypothesis is tested with the F-test. The assumptions of the method yield:

$$\frac{MS_B}{MS_W} \sim F(df_B, df_W) \quad \text{Equation 89}$$

$$F = \frac{MS_B}{MS_W} = \frac{\text{variance between groups}}{\text{variance within group}} \quad \text{Equation 90}$$

The null-hypothesis is rejected only if:

$$F > F_{crit} \quad \text{Equation 91}$$

where F_{crit} is the inverse of the (right-tailed) F-probability distribution (function ‘FINV’ in MS Excel) with the probability (confidence level) set to $\alpha = 0.05$, the numerator degrees of freedom calculated as the number of tested groups, and the denominator degrees of freedom calculated as the difference between the total data count and the number of tested groups. The method is implemented in MS Excel using the “data analysis” tool pack.

Two-factor (Two-way) ANOVA with replication and the F-test

Compared to One-way ANOVA, Two-way ANOVA covers an additional factor (independent variable). This analysis was used considering measurement replication (i.e., same measurements were conducted for each of the two factors).

The method assumes the following:

- all samples (data) are normally distributed,
- all populations (groups) have a common variance,
- all samples are drawn independently from each other, and
- within each sample, the observations are sampled randomly and independently of each other.

In general, there are two factors A and B, where factor A has r levels and factor B has c levels. The levels are organized for factor A as rows and the levels for factor B as columns. With the index i for the rows (factor A) and the index j for the columns (factor B), the corresponding structural model can be presented as a $r \times c$ table where the entries in the table are:

$$\begin{aligned} & \{x_{ij}: 1 \leq i \leq r, 1 \leq j \leq c\} & \text{Equation 92} \\ & \{X_{ij}: 1 \leq i \leq r, 1 \leq j \leq c\} \end{aligned}$$

where

$$X_{ij} = \{x_{ijk}: 1 \leq k \leq n_{ij}\} \quad \text{Equation 93}$$

The level means are estimated from the total mean by:

$$\begin{aligned} \text{Factor A: } \mu_i &= \mu + \alpha_i & \text{Equation 94} \\ \text{Factor B: } \mu_j &= \mu + \beta_j \end{aligned}$$

where α_i and β_j denote the effect of the i -th level (for factor A) and of the j -th level (for factor B), respectively. These effects represent the departure of the corresponding level mean from total mean (μ).

Similarly, the sample means are defined and estimated as:

$$\begin{aligned} \text{Factor A: } \bar{x}_i &- \text{mean over } \{x_{ijk}: 1 \leq j \leq c, 1 \leq k \leq m\} \\ \text{Factor B: } \bar{x}_j &- \text{mean over } \{x_{ijk}: 1 \leq i \leq r, 1 \leq k \leq m\} \end{aligned} \quad \text{Equation 95}$$

$$\begin{aligned} \text{Factor A: } \bar{x}_i &= \bar{x} + a_i \\ \text{Factor B: } \bar{x}_j &= \bar{x} + b_j \end{aligned}$$

$$\sum_i a_i = (\bar{x}_i - \bar{x}) = 0, \quad \sum_j b_j = (\bar{x}_j - \bar{x}) = 0$$

The effect (interaction) of level i of factor A with level j of factor B (δ_{ij}) is defined as:

$$\delta_{ij} = \mu_{ij} - \mu_i - \mu_j + \mu \quad \text{Equation 96}$$

This is similarly written for the sample means as:

$$\begin{aligned} d_{ij} &= \bar{x}_{ij} - \bar{x}_i - \bar{x}_j + \bar{x} \\ \sum_i d_{ij} &= \sum_j d_{ij} = 0 \end{aligned} \quad \text{Equation 97}$$

Such element can be represented in the sample as:

$$x_{ijk} = \mu + a_i + \beta_j + \delta_{ij} + \varepsilon_{ijk} \quad \text{Equation 98}$$

where ε_{ijk} denotes the error (of unexplained) quantity. For the sample, this can be written as:

$$x_{ijk} = \bar{x} + a_i + b_j + d_{ij} + e_{ijk} \quad \text{Equation 99}$$

where e_{ijk} is the counter part to ε_{ijk} in the sample.

From these relations, the following can be noted:

$$\begin{aligned} x_{ijk} &= \mu + a_i + \beta_j + \delta_{ij} + \varepsilon_{ijk} \\ &= \mu + (\mu_i - \mu) + (\mu_j - \mu) + (\mu_{ij} - \mu_i - \mu_j + \mu) + \varepsilon_{ijk} \end{aligned} \quad \text{Equation 100}$$

$$\varepsilon_{ijk} = x_{ijk} - \mu_{ij}, \quad e_{ijk} = x_{ijk} - \bar{x}_{ij}$$

$$\sum_j \sum_i e_{ijk} = \sum_j \sum_i (x_{ijk} - \bar{x}_{ijk}) = 0$$

The sums of squares are defined as:

Equation 101

$$\begin{aligned}
 SS_T &= \sum_k \sum_j \sum_i (x_{ijk} - \bar{x})^2 \\
 SS_A &= mc \sum_i (x_i - \bar{x})^2 \\
 SS_B &= mr \sum_j (x_j - \bar{x})^2 \\
 SS_{AB} &= m \sum_j \sum_i (\bar{x}_{ij} - \bar{x}_i - \bar{x}_j + \bar{x})^2 \\
 SS_E &= SS_W = \sum_k \sum_j \sum_i (x_{ijk} - \bar{x}_{ij})^2 \\
 SS_{Bet} &= SS_A + SS_B + SS_{AB}
 \end{aligned}$$

where:

SS_T – the sum of squares for the total sample (i.e., the sum of squared deviations from the total mean),

SS_A – the sum of squares within the group for factor A,

SS_B – the sum of squares within the group for factor B,

SS_{AB} – the sum of squares of the interaction between A and B,

SS_{Bet} – the sum of squares of the inter-group sample means (i.e., the weighted sum of the squared deviations of the group means from the total mean).

SS_W – the sum of squares within the groups (i.e., the sum of the squared means across all groups), and

SS_E – the error sum of squares.

The corresponding degrees of freedom (see the indices) are defined as:

Equation 102

$$\begin{aligned}
 df_T &= n - 1, \\
 df_A &= r - 1 \\
 df_B &= c - 1 \\
 df_{AB} &= (r - 1)(c - 1) \\
 df_E &= df_W = n - r \cdot c \\
 df_{Bet} &= df_A + df_B + df_{AB} \\
 &\text{with } n = \sum_{j+1}^k n_j
 \end{aligned}$$

The mean squares are defined as:

$$\begin{aligned}
 MS_T &= SS_T / df_T && \text{Equation 103} \\
 MS_A &= SS_A / df_A \\
 MS_B &= SS_B / df_B \\
 MS_{AB} &= SS_{AB} / df_{AB} \\
 MS_E = MS_W &= SS_W / df_W \\
 MS_{Bet} &= SS_{Bet} / df_{Bet}
 \end{aligned}$$

The “null-hypotheses” can be written as:

$$\begin{aligned}
 H_0: \mu_{1.} = \mu_{2.} = \dots = \mu_{r.} \text{ or } \alpha_i = 0 \forall i \text{ (Factor A)} &&& \text{Equation 104} \\
 H_0: \mu_{.2} = \mu_{.c} = \dots = \mu_{.c} \text{ or } \beta_j = 0 \forall j \text{ (Factor B)} \\
 H_0: \delta_{ij} = 0 \forall i, j \text{ (Interaction between A and B)}
 \end{aligned}$$

The null hypotheses are tested using the F-test. The assumptions of the method yield:

$$\begin{aligned}
 \text{Factor A: } & \frac{MS_A}{MS_W} \sim F(df_A, df_W) && \text{Equation 105} \\
 \text{Factor B: } & \frac{MS_B}{MS_W} \sim F(df_B, df_W) \\
 \text{Interaction between A and B: } & \frac{MS_{AB}}{MS_W} \sim F(df_{AB}, df_W)
 \end{aligned}$$

Each of these null-hypotheses are tested using the same criterion as for One-way ANOVA (Equation 91). The method is implemented in MS Excel using the “data analysis” tool pack.

Comparison of slopes of two linear-regression lines

The Student's t-test was also used to compare slopes of two regression lines from independent populations (groups) (Zaiontz, 2020a). Here, the following “null- and alternative-hypotheses” are tested:

$$H_0: \beta_1 - \beta_2 = 0 \quad \text{Equation 106}$$

$$H_a: \beta_1 - \beta_2 \neq 0 \quad \text{Equation 107}$$

The test statistic (t-test) is carried out with the following formula:

$$t = \frac{b_1 - b_2}{\sqrt{s_{b1}^2 + s_{b2}^2}} \sim T(N_1 + N_2 - 4) \quad \text{Equation 108}$$

where:

b – slope of regression line of a group,

N - quantity of test data (data count per group), and

s_b - sample variance.

The null-hypothesis is rejected only if:

$$t > t_{crit} \quad \text{Equation 109}$$
$$\sqrt{s_{b1}^2 + s_{b2}^2} \cdot t_{crit} > b_1 - b_2$$

where t_{crit} is the two-tailed inverse of the Student's t-distribution (function ‘TINV’ in MS Excel) with the probability (confidence level) set to $\alpha = 0.05$ and the degrees of freedom calculated as:

$$df = N_1 + N_2 - 4 \quad \text{Equation 110}$$

The same condition is obtained when:

$$p < \alpha \quad \text{Equation 111}$$

where p is the p-value, calculated in MS Excel as:

$$p = T.DIST(|t|, df, TRUE) \quad \text{Equation 112}$$

Here, the function 'T.DIST' returns the Student's left-tailed t-distribution and the enclosed argument 'TRUE' indicates that this t-distribution is cumulative.

If the “null-hypothesis” is true, then:

$$\beta_1 - \beta_2 \sim N(0, s_{b_1-b_2}) \quad \text{Equation 113}$$

$$s_{b_1-b_2} = \sqrt{s_{b_1}^2 + s_{b_2}^2}$$

If the two error variances are equal, then as for the test for the differences in the means, the estimates of the error variances can be pooled, weighing each of them by their degrees of freedom:

$$s_{Res}^2 = \frac{(N_1 - 2)s_{Res1}^2 + (N_2 - 2)s_{Res2}^2}{(N_1 - 2) + (N_2 - 2)} \quad \text{Equation 114}$$

This yields:

$$s_{b_1}^2 = \frac{s_{Res1}^2}{s_{x1}^2(N_1 - 1)} \quad s_{b_2}^2 = \frac{s_{Res2}^2}{s_{x2}^2(N_2 - 1)} \quad \text{Equation 115}$$

From here, the numerators can be replaced by the pooled value s_{Res}^2 , yielding:

$$s_{b_1-b_2} = s_{Res} \sqrt{\frac{1}{s_{x1}^2(N_1 - 1)} + \frac{1}{s_{x2}^2(N_2 - 1)}} \quad \text{Equation 116}$$

Comparison of multiple regression lines

Comparisons of multiple regression lines were carried out with multiple-regression analysis with “dummy variables” (Littell et al., 2002).

Here, for comparing n regression lines, $n-1$ dummy variables are used. The dummy variables, denoted as $d_1, d_2 \dots d_n$, are then assigned coded binary values (0 or 1) depending on the corresponding sample group. For example, when comparing three regression lines from separate sample groups (e.g., Group A, Group B, and Group C) with y - (dependent variable) and x -values (independent variable), the dummy variables are set to 1 for their corresponding group and 0 for the other groups:

$$d_n = 1 \text{ for Group } n, \quad \text{Equation 117}$$

$$d_n = 0 \text{ otherwise}$$

Group A: $d_1 = 1, d_2 = 0$
 Group B: $d_1 = 0, d_2 = 1$
 Group C: $d_1 = 0, d_2 = 0$

In this example, the structural model of the analysis includes the dummy variables as columns for Group A and Group B, leaving Group C as the reference group.

The equation to be fitted is:

$$y \sim x, d_1, d_2, x \cdot d_1, x \cdot d_2 \quad \text{Equation 118}$$

The following multiple regression returns coefficients $b_0, b_1, b_2 \dots b_5$ for the intercept (of the reference group), $x, d_1, d_2, d_1 \cdot x$, and $d_2 \cdot x$. The fitted regression equation is:

$$y = b_0 + b_1 \cdot x + b_2 \cdot d_1 + b_3 \cdot d_2 + b_4 \cdot x \cdot d_1 + b_5 \cdot x \cdot d_2 \quad \text{Equation 119}$$

$$\text{Group C: } d_1 = 0, d_2 = 0 \rightarrow y = b_0 + b_1 \cdot x$$

$$\text{Group A: } d_1 = 1, d_2 = 0 \rightarrow y = (b_0 + b_2) + (b_1 + b_4) \cdot x$$

$$\text{Group B: } d_1 = 1, d_2 = 1 \rightarrow y = (b_0 + b_3) + (b_1 + b_5) \cdot x$$

Further result interpretation is the same as for the comparison of two linear-regression lines. If the reference intersection or slope is evaluated as not significantly different from 0 (i.e., for $p < 0.05$ for coefficient b_1), the analysis is repeated with another group as the reference one. The regression lines were compared considering their intersections and their slopes. For example, the compared slopes ($b_1 + b_4$ for Group A and $b_1 + b_5$ for Group B) were evaluated significantly different from the reference one if the p-values of the corresponding coefficients (b_4 for Group B and $b_4 + b_5$ for Group C) were smaller than $\alpha = 0.05$.

The process can be extended to more groups by adding more dummy variables. The multiple-regression analysis was carried out in MS Excel using the “regression” tool in the “data analysis” tool pack.

This tool also returns results of a (One-way) ANOVA of the covered data (complete data set), indicating how well the data are fit to the regression model.

One-way analysis of covariance (ANCOVA)

One-way analysis of covariance (ANCOVA) is a statistical method, which is a combination of linear-regression analysis and One-way ANOVA. For the purpose of this study, One-way ANCOVA is used as an extension of multiple regression to compare multiple regression lines (McDonald, 2014; Zaiontz, 2020b), i.e., to evaluate the statistical differences within sample groups (for each regression line) and between the groups, considering effects of covariant(s) (e.g., blasted material and/or liner charge concentration). Like regression analysis, ANCOVA evaluates the effect(s) an independent variable on a dependent variable. However, it also “removes” any effect of covariates, which are of no interest.

In basic terms, the ANCOVA examines the influence of an independent variable on a dependent variable while removing the effect of the covariate factor. The analysis firstly conducts a regression of the independent variable (i.e., the covariate) on the dependent variable. The residuals (the unexplained variance in the regression model) are then subject to an ANOVA. Therefore, the ANCOVA tests whether the independent variable still influences the dependent variable after the influence of the covariate(s) has been removed. The method assumptions are the same as for One-way ANOVA.

This analysis was implemented using two methods. The first is the “simplified ANCOVA” and covers the following procedure:

1. Run a multiple regression between the independent and dependent variables (“regression” in the “data analysis” tool pack in MS Excel),
2. Identify the residual values (automatically generated table in the previous step), and
3. Run One-way ANOVA on the residuals.

The second is the “regression approach to ANCOVA,” described in detail by Zaiontz (2020b).

Appendix 13 Result data – Macro-mechanism event logs

Blast test 22.2 (mortar, 6 g/m)

Elapsed time [μ s]	Image	Propagation paths				Branching				Merging				Branching-merging			
		1.1	1.2	1.3	1.4	2.1	2.2	2.3	2.4	3.1	3.2	3.3	3.4	4.1	4.2	4.3	4.4
40.56	6	█	█														
81.12	7	█	█														
121.68	8	█	█	█	█	█		█					█				█
162.24	9	█	█			█		█				█	█				
202.80	10	█	█	█									█				
243.36	11	█	█	█				█					█				█
283.92	12	█	█					█					█				
324.48	13	█															
365.04	14	█															
405.60	15	█		█	█												

Blast test 23.2 (mortar, 6 g/m)

Elapsed time [μ s]	Image	Propagation paths				Branching				Merging				Branching-merging			
		1.1	1.2	1.3	1.4	2.1	2.2	2.3	2.4	3.1	3.2	3.3	3.4	4.1	4.2	4.3	4.4
40.56	6	█	█														
81.12	7	█	█														
121.68	8	█	█														
162.24	9	█	█		█								█				
202.80	10	█	█		█							█	█				
243.36	11	█			█	█						█	█	█			
283.92	12	█	█					█					█				
324.48	13	█	█		█			█				█	█	█	█		
365.04	14	█	█										█				
405.60	15	█	█	█	█	█		█					█				
446.16	16	█										█					

Blast test 20 (mortar, 12 g/m)

Elapsed time [μ s]	Image	Propagation paths				Branching				Merging				Branching-merging			
		1.1	1.2	1.3	1.4	2.1	2.2	2.3	2.4	3.1	3.2	3.3	3.4	4.1	4.2	4.3	4.4
40.56	6	■	■														
81.12	7	■											■				
121.68	8	■	■														
162.24	9	■	■				■										
202.80	10												■				■
243.36	11	■	■														
283.92	12	■	■										■				
324.48	13	■	■								■		■				
365.04	14	■	■					■									■
405.60	15	■	■					■									■
446.16	16	■	■														
486.72	17	■															

Blast test 21 (mortar, 12 g/m)

Elapsed time [μ s]	Image	Propagation paths				Branching				Merging				Branching-merging			
		1.1	1.2	1.3	1.4	2.1	2.2	2.3	2.4	3.1	3.2	3.3	3.4	4.1	4.2	4.3	4.4
40.56	2	■	■														
81.12	3	■	■		■			■		■	■		■				
121.68	4	■	■			■		■					■	■			■
162.24	5	■	■			■		■			■		■	■			■
202.80	6	■					■	■			■		■				■
243.36	7	■					■				■						■
283.92	8	■														■	
324.48	9	■						■	■		■						
365.04	10	■				■							■				
405.60	11	■		■				■									■
446.16	12	■	■	■	■						■		■				

Blast test 22.1 (mortar, 20 g/m)

Elapsed time [μ s]	Image	Propagation paths				Branching				Merging				Branching-merging			
		1.1	1.2	1.3	1.4	2.1	2.2	2.3	2.4	3.1	3.2	3.3	3.4	4.1	4.2	4.3	4.4
40.56	2	█	█														
81.12	3	█		█									█				
121.68	4	█	█	█				█					█	█			
162.24	5	█	█										█	█			█
202.80	6	█	█	█		█		█					█				
243.36	7	█	█	█	█			█					█				
283.92	8	█	█			█		█			█		█	█			
324.48	9	█	█	█		█							█				

Blast test 23.1 (mortar, 20 g/m)

Elapsed time [μ s]	Image	Propagation paths				Branching				Merging				Branching-merging			
		1.1	1.2	1.3	1.4	2.1	2.2	2.3	2.4	3.1	3.2	3.3	3.4	4.1	4.2	4.3	4.4
40.56	8	█	█														
81.12	9	█	█										█				
121.68	10	█	█										█				
162.24	11	█	█										█				
202.80	12	█	█										█				
243.36	13	█	█		█								█				
283.92	14	█	█		█	█		█					█				█
324.48	15	█	█	█	█			█		█			█				
365.04	16	█	█			█		█			█		█				
405.60	17	█	█	█	█	█		█		█	█		█				█
446.16	18	█						█	█		█		█	█			

Blast test 26.1 (granite, 6 g/m)

Elapsed time [μ s]	Image	Propagation paths				Branching				Merging				Branching-merging			
		1.1	1.2	1.3	1.4	2.1	2.2	2.3	2.4	3.1	3.2	3.3	3.4	4.1	4.2	4.3	4.4
40.56	2	■	■														
81.12	3	■	■			■							■				
121.68	4	■	■					■					■				
162.24	5	■	■		■								■				
202.80	6	■	■		■								■				
243.36	7	■	■		■								■				
283.92	8	■	■		■		■	■				■	■				
324.48	9	■	■		■			■			■	■	■				■
365.04	10	■	■		■	■		■		■	■	■	■			■	
405.60	11	■	■		■			■				■	■				
446.16	12	■	■	■	■						■	■	■			■	
486.72	13	■	■		■			■			■	■	■				
527.28	14	■	■		■	■		■			■	■	■	■		■	

Blast test 27 (granite, 6 g/m)

Elapsed time [μ s]	Image	Propagation paths				Branching				Merging				Branching-merging			
		1.1	1.2	1.3	1.4	2.1	2.2	2.3	2.4	3.1	3.2	3.3	3.4	4.1	4.2	4.3	4.4
40.56	4	■	■														
81.12	5	■	■		■												
121.68	6	■	■	■	■	■					■					■	
162.24	7	■	■	■	■		■	■	■		■		■	■		■	
202.80	8	■	■	■	■			■	■		■	■		■			■
243.36	9	■			■			■	■		■	■		■			■
283.92	10	■	■	■	■			■	■		■	■					■
324.48	11	■	■	■	■			■	■		■		■				■
365.04	12	■	■	■	■			■	■		■	■				■	■
405.60	13	■	■	■	■		■	■			■	■	■		■	■	■
446.16	14	■	■	■			■	■			■	■					■

Blast test 24 (granite, 12 g/m)

Elapsed time [μ s]	Image	Propagation paths				Branching				Merging				Branching-merging			
		1.1	1.2	1.3	1.4	2.1	2.2	2.3	2.4	3.1	3.2	3.3	3.4	4.1	4.2	4.3	4.4
40.56	4	■	■														
81.12	5	■	■	■	■												
121.68	6	■	■	■	■	■		■		■	■		■	■	■		■
162.24	7	■	■	■	■	■	■	■		■	■		■	■	■	■	
202.80	8	■	■		■			■		■	■			■	■	■	■
243.36	9	■	■		■	■		■		■	■		■		■	■	■
283.92	10	■		■	■			■		■	■		■		■	■	
324.48	11	■			■			■		■	■		■				■

Blast test 25 (granite, 12 g/m)

Elapsed time [μ s]	Image	Propagation paths				Branching				Merging				Branching-merging			
		1.1	1.2	1.3	1.4	2.1	2.2	2.3	2.4	3.1	3.2	3.3	3.4	4.1	4.2	4.3	4.4
40.56	3	■	■														
81.12	4	■	■														
121.68	5	■	■		■	■							■				
162.24	6	■	■		■	■		■		■	■		■			■	■
202.80	7	■	■	■	■	■		■		■	■		■	■	■	■	■
243.36	8	■	■	■	■	■		■		■	■		■		■	■	■
283.92	9	■	■	■	■	■		■		■	■		■	■	■	■	■
324.48	10	■	■		■	■		■		■	■		■		■	■	■
365.04	11	■	■	■	■	■		■		■	■		■				
405.60	12	■	■	■	■	■		■		■	■		■				

Blast test 26.2 (granite, 20 g/m)

Elapsed time [μ s]	Image	Propagation paths				Branching				Merging				Branching-merging			
		1.1	1.2	1.3	1.4	2.1	2.2	2.3	2.4	3.1	3.2	3.3	3.4	4.1	4.2	4.3	4.4
40.56	3	■	■														
81.12	4	■	■		■												
121.68	5	■	■		■	■		■		■	■		■				
162.24	6	■	■		■	■		■		■	■		■	■	■	■	
202.80	7	■	■	■	■	■		■		■	■		■	■	■	■	
243.36	8	■	■	■	■			■		■	■		■		■	■	

Appendix 14 Blast-hole expansion- raw measurement data of the normalized blast-hole radius

Table 172, Table 173, and Table 174 show raw measurement data of the average blast-hole radius.

Table 172: Raw measurements of average $r_{bh,a}$ from the CTt images (1 of 3).

Axial position [mm]		Blast configuration – material (g, m), l_c [g/m], and (blast test)				
other shots	for m12(21)	g6(26.1)	g12(28.1)	m6(23.2)	m12(21)	m20(23.1)
0	4.47	33.40	39.23	9.13	14.66	15.81
3	7.44	26.48	28.70	9.05	13.04	12.91
6	10.41	20.02	22.00	8.90	11.34	12.79
9	13.38	13.64	16.55	8.94	11.53	13.58
12	16.35	8.70	11.63	8.99	11.26	13.51
15	19.32	7.39	9.42	9.10	11.33	12.62
18	22.29	7.23	9.48	9.15	11.54	12.79
21	25.26	7.56	9.53	8.71	11.30	12.74
24	28.23	7.20	9.60	8.76	11.03	13.11
27	31.2	7.59	9.30	8.72	10.84	12.59
30	34.17	7.89	9.68	8.44	10.72	12.74
33	37.14	7.82	9.19	8.58	10.83	12.85
36	40.11	7.52	9.15	8.84	11.03	12.89
39	43.08	7.72	8.69	8.45	11.20	12.62
42	46.05	7.94	8.73	8.52	11.36	12.92
45	49.02	7.65	9.07	8.62	11.66	12.67
48	51.99	7.90	9.49	8.73	11.52	12.93
51	54.96	8.02	9.89	8.45	11.08	13.26
54	57.93	7.90	9.66	8.41	11.31	13.37
57	60.9	7.95	9.48	8.35	11.01	13.26
60	63.87	8.00	9.57	8.08	10.40	13.70
63	66.84	7.61	9.60	8.66	10.74	13.05
66	69.81	7.84	9.77	8.18	10.49	13.63
69	72.78	7.74	9.60	8.65	10.68	13.29
72	75.75	7.80	9.58	8.53	10.65	13.85
75	78.72	7.61	9.71	8.15	10.77	13.31
78	81.69	7.74	9.92	8.14	10.91	13.07
81	84.66	7.79	9.56	7.99	10.64	13.16
84	87.63	7.70	10.35	8.27	10.42	12.79
87	90.6	7.80	10.17	8.09	10.51	13.19
90	93.57	7.65	10.33	8.34	10.55	13.92
93	96.54	7.51	10.51	8.22	10.98	14.26

Table 173: Raw measurements of average $r_{bh,a}$ from the CTt images (2 of 3).

Axial position [mm]		Blast configuration – material (g, m), l_c [g/m], and (blast test)				
other shots	for m12(21)	g6(26.1)	g12(28.1)	m6(23.2)	m12(21)	m20(23.1)
96	99.51	7.58	10.74	8.29	11.02	13.67
99	102.48	7.58	10.68	8.12	10.88	14.02
102	105.45	7.75	11.22	8.39	10.79	13.47
105	108.42	7.56	11.83	8.74	10.48	13.90
108	111.39	7.89	10.80	8.32	10.24	13.41
111	114.36	8.02	10.75	8.43	10.34	13.76
114	117.33	7.95	11.22	8.57	10.27	13.82
117	120.3	7.53	10.90	8.76	10.19	13.60
120	123.27	7.80	12.43	8.41	10.11	13.41
123	126.24	7.79	11.73	8.44	10.06	13.27
126	129.21	7.99	11.36	8.28	9.97	13.19
129	132.18	7.77	11.78	8.26	10.12	13.64
132	135.15	7.72	11.43	8.26	10.36	13.43
135	138.12	7.72	11.69	8.06	10.35	13.08
138	141.09	7.94	11.64	8.42	10.34	14.00
141	144.06	7.86	11.28	8.21	10.22	13.71
144	147.03	7.82	10.79	8.12	9.92	13.66
147	150	7.74	11.81	8.19	10.04	13.53
150	152.97	7.98	10.98	8.12	9.94	13.84
153	155.94	7.59	11.22	8.06	9.94	13.40
156	158.91	8.03	11.59	8.00	10.11	13.60
159	161.88	7.75	11.75	8.05	9.63	13.54
162	164.85	7.67	11.53	8.11	9.48	13.54
165	167.82	7.60	11.56	8.00	9.55	12.35
168	170.79	7.81	12.70	7.97	9.40	12.55
171	173.76	7.82	10.91	8.03	9.31	12.61
174	176.73	7.81	11.76	8.01	9.21	12.49
177	179.7	7.72	11.93	7.82	9.14	12.64
180	182.67	7.91	11.94	7.98	9.09	12.87
183	185.64	7.82	11.69	8.01	9.30	12.99
186	188.61	7.89	10.98	7.98	9.19	13.12
189	191.58	7.80	12.22	7.87	9.18	13.49
192	194.55	7.71	12.44	7.73	9.20	13.57
195	197.52	7.60	11.27	7.83	9.19	13.51
198	200.49	7.45	10.88	7.96	9.17	13.17
201	203.46	7.52	12.38	7.87	9.46	13.31
204	206.43	7.49	11.82	7.91	9.27	13.24
207	209.4	7.66	11.73	7.94	9.25	13.35
210	212.37	7.50	11.61	7.95	9.09	13.05
213	215.34	7.52	13.23	7.94	8.99	12.80
216	218.31	7.64	13.22	7.84	9.03	12.86

Table 174: Raw measurements of average $r_{bh,a}$ from the CTt images (3 of 3).

Axial position [mm]		Blast configuration – material (g, m), l_c [g/m], and (blast test)				
other shots	for m12(21)	g6(26.1)	g12(28.1)	m6(23.2)	m12(21)	m20(23.1)
219	221.28	7.13	13.84	7.92	9.07	12.46
222	224.25	7.36	12.93	8.05	8.72	12.99
225	227.22	7.04	12.81	7.99	9.08	12.97
228	230.19	7.50	12.69	7.82	9.19	13.17
231	233.16	7.34	12.54	8.00	9.23	12.77
234	236.13	7.42	13.30	7.90	9.23	12.96
237	239.1	7.16	12.21	7.87	9.27	12.87
240	242.07	7.53	13.30	7.87	8.93	12.82
243	245.04	7.94	12.61	7.88	9.19	12.94
246	248.01	7.67	13.03	7.93	9.12	12.86
249	250.98	7.72	12.73	7.48	8.96	12.33
252	253.95	7.73	13.55	7.47	8.90	13.02
255	256.92	7.58	12.44	7.39	8.89	13.00
258	259.89	7.30	12.55	7.61	8.58	13.20
261	262.86	7.52	13.08	7.45	8.37	12.46
264	265.83	7.35	13.29	7.29	8.33	12.40
267	268.8	7.61	13.22	7.33	8.23	10.87
270	271.77	7.46	13.96	7.00	7.46	10.04
273		7.62	14.80	6.39		9.82
276		7.76	15.76	6.47		8.83
279		7.43	16.77	6.48		9.32
282		7.43	22.27	6.48		9.20
285		7.43	31.21	6.11		9.62
288		7.07	38.04	5.75		9.29
291		7.07	50.78	5.77		
294		23.00	56.91			

Table 175, Table 176, and Table 177 show raw measurement data of the average cylinder swelling.

Table 175: Raw measurements of average $r_{m,a}$ from the CTt images (1 of 3).

Axial position [mm]		Blast configuration – material (g, m), I_c [g/m], and (blast test)				
other shots	for m12(21)	g6(26.1)	g12(28.1)	m6(23.2)	m12(21)	m20(23.1)
0	76.05	77.63	76.39	77.85	76.60	76.05
3	76.05	77.61	76.52	78.10	76.63	76.05
6	76.05	77.60	76.47	78.13	76.63	76.05
9	76.04	77.56	76.53	78.11	76.65	76.04
12	76.03	77.57	76.53	78.11	76.64	76.03
15	76.04	77.57	76.53	78.03	76.64	76.04
18	76.04	77.50	76.53	78.08	76.64	76.04
21	76.01	77.48	76.53	78.10	76.68	76.01
24	76.01	77.48	76.53	78.03	76.68	76.01
27	76.01	77.45	76.53	78.07	76.68	76.01
30	76.01	77.57	76.53	78.12	76.68	76.01
33	76.01	77.57	76.53	78.05	76.69	76.01
36	76.01	77.62	76.53	77.93	76.71	76.01
39	76.03	77.62	76.53	77.93	76.71	76.03
42	76.03	77.69	76.53	77.99	76.71	76.03
45	76.03	77.70	76.53	77.96	76.71	76.03
48	76.03	77.78	76.53	77.91	76.71	76.03
51	76.00	77.81	76.53	77.76	76.71	76.00
54	76.00	77.92	76.50	77.66	76.71	76.00
57	76.00	77.93	76.50	77.74	76.71	76.00
60	76.00	77.98	76.50	77.62	76.71	76.00
63	76.00	78.04	76.50	77.55	76.71	76.00
66	76.00	78.07	76.50	77.66	76.71	76.00
69	76.00	78.07	76.50	77.63	76.71	76.00
72	76.00	78.07	76.50	77.61	76.71	76.00
75	76.00	78.13	76.50	77.58	76.72	76.00
78	76.01	78.13	76.50	77.53	76.72	76.01
81	76.01	78.13	76.50	77.49	76.72	76.01
84	76.01	78.13	76.50	77.45	76.74	76.01
87	76.01	78.33	76.50	77.50	76.74	76.01
90	76.01	78.34	76.50	77.41	76.74	76.01
93	76.01	78.34	76.50	77.42	76.74	76.01

Table 176: Raw measurements of average $r_{m,a}$ from the CTt images (2 of 3).

Axial position [mm]		Blast configuration – material (g, m), l_c [g/m], and (blast test)				
other shots	for m12(21)	g6(26.1)	g12(28.1)	m6(23.2)	m12(21)	m20(23.1)
96	99.51	76.01	78.34	76.50	77.38	76.74
99	102.48	76.01	78.34	76.50	77.47	76.74
102	105.45	76.01	78.34	76.55	77.42	76.74
105	108.42	76.01	78.34	76.55	77.40	76.74
108	111.39	76.01	78.51	76.55	77.36	76.74
111	114.36	76.03	78.51	76.55	77.34	76.74
114	117.33	76.03	78.51	76.55	77.42	76.74
117	120.3	76.03	78.69	76.55	77.43	76.74
120	123.27	76.03	78.69	76.55	77.43	76.74
123	126.24	76.03	78.65	76.55	77.50	76.74
126	129.21	76.03	78.65	76.48	77.47	76.74
129	132.18	76.03	78.65	76.51	77.36	76.74
132	135.15	76.03	78.65	76.54	77.32	76.74
135	138.12	76.03	78.65	76.54	77.32	76.74
138	141.09	76.03	78.57	76.54	77.34	76.74
141	144.06	76.03	78.57	76.54	77.22	76.74
144	147.03	76.03	78.57	76.54	77.37	76.74
147	150	76.03	78.57	76.54	77.20	76.74
150	152.97	76.03	78.94	76.54	77.26	76.74
153	155.94	76.03	78.94	76.54	77.29	76.74
156	158.91	76.03	78.94	76.54	77.37	76.74
159	161.88	76.03	78.94	76.54	77.41	76.74
162	164.85	76.03	78.94	76.54	77.36	76.74
165	167.82	76.03	78.94	76.54	77.37	76.74
168	170.79	76.03	78.94	76.54	77.35	76.74
171	173.76	76.03	79.18	76.54	77.30	76.74
174	176.73	76.03	79.18	76.54	77.11	76.74
177	179.7	76.03	79.18	76.54	77.19	76.74
180	182.67	76.03	79.18	76.54	77.09	76.74
183	185.64	76.03	79.18	76.54	77.13	76.74
186	188.61	76.04	79.14	76.49	77.26	76.74
189	191.58	76.04	79.14	76.49	77.18	76.74
192	194.55	76.04	79.14	76.49	77.20	76.74
195	197.52	76.04	79.14	76.49	77.19	76.74
198	200.49	76.04	79.14	76.49	77.17	76.74
201	203.46	76.01	79.14	76.49	77.30	76.74
204	206.43	76.01	79.62	76.49	77.13	76.74
207	209.4	76.01	79.49	76.45	77.14	76.74
210	212.37	76.01	79.38	76.45	77.17	76.74
213	215.34	76.01	79.38	76.45	77.12	76.74
216	218.31	76.01	79.38	76.45	77.08	76.74

Table 177: Raw measurements of average $r_{m,a}$ from the CTt images (3 of 3).

Axial position [mm]		Blast configuration – material (g, m), l_c [g/m], and (blast test)				
other shots	for m12(21)	g6(26.1)	g12(28.1)	m6(23.2)	m12(21)	m20(23.1)
219	221.28	76.01	79.38	76.45	77.15	76.74
222	224.25	76.01	79.38	76.45	77.13	76.74
225	227.22	76.01	79.38	76.45	77.12	76.74
228	230.19	76.01	79.38	76.45	77.07	76.74
231	233.16	76.01	79.38	76.45	77.04	76.74
234	236.13	76.01	79.36	76.45	77.09	76.74
237	239.1	75.99	79.36	76.45	77.12	76.75
240	242.07	75.99	79.36	76.38	77.19	76.75
243	245.04	75.99	79.36	76.38	77.38	76.75
246	248.01	75.99	79.36	76.38	77.32	76.75
249	250.98	75.99	79.36	76.38	77.25	76.75
252	253.95	75.99	79.81	76.38	77.16	76.75
255	256.92	76.02	79.81	76.38	77.08	76.75
258	259.89	76.02	79.53	76.38	77.12	76.74
261	262.86	75.93	79.53	76.38	77.18	76.74
264	265.83	75.93	79.53	76.38	77.22	76.74
267	268.8	75.93	79.53	76.38	77.23	76.74
270	271.77	75.93	79.53	76.38	77.38	76.74
273		75.90	79.53	76.38		76.74
276		75.88	79.53	76.50		76.74
279		75.84	80.30	76.50		76.74
282		75.84	80.30	76.50		76.74
285		75.88	80.30	76.50		76.74
288		75.90	80.30	76.50		76.74
291		75.90	80.30	76.50		
294		75.90	80.30			

Table 178 shows measured $r_{bh,norm}$ values for blast test 26.2 (granite, 20 g/m).

Table 178: Measured $r_{bh,norm}$ for blast test 26.2 (granite, 20 g/m).

uCT image	Axial position [mm]	$r_{bh,norm}$ [mm]
1220	-55.223	10.22
1240	-57.681	7.34
1245	-58.296	6.53
1270	-61.369	6.45
1295	-64.441	6.89
1320	-67.514	7.06
1345	-70.587	8.76
1370	-73.660	6.68
1395	-76.733	7.76
1420	-79.806	7.73
1445	-82.879	8.38
1470	-85.951	7.38
1495	-89.024	7.56
1520	-92.097	5.33
Ave:		7.43
Std:		1.17

The measured normalized blast-hole radius ($r_{bh,norm}$) was assumed constant for the cylinders of the same material blasted with the same linear charge concentration (l_c).

Appendix 15 **Selected sets of the uCT sections**

[Appendix 15 - Selected sets of the uCT sections](#)

Appendix 16 **Selected micrographs of thin sections and small fragments**

[Appendix 16 - Selected micrographs of thin sections and small fragments](#)

Appendix 17 **Blast-induced fracture surfaces (raw results)**

[Appendix 17 - Blast-induced fracture surfaces \(raw results\)](#)

Appendix 18 Screening data, FSDs, and curve-fitting results

This section covers the raw screening data for the blasted cylinders, fitted FSD curves, and fitted s-n(s) curves.

Sieving data

Blast test:		22.2 (mortar, 6 g/m)			Blast test:		23.2 (mortar, 6 g/m)		
Mesh size [mm]	Mass passing [g]	Mass passing [%]	s_n [-]	x_a [mm]	Mesh size [mm]	Mass passing [g]	Mass passing [%]	s_n [-]	x_a [mm]
150	8858.08	100	-	-	150	8712	100	-	-
125	5168.08	58.34312	-	-	125	4593	52.72039	-	-
100	5168.08	58.34312	1.33	123.87	100	1784	20.47750	4.24	113.53
80	3915.08	44.19784	1.24	89.72	80	113	1.29706	12.37	93.49
63	887.08	10.01436	6.21	72.89	63	113	1.29706	-	-
50	717.08	8.09521	0.92	56.23	50	113	1.29706	-	-
40	432.08	4.87781	2.27	45.05	40	113	1.29706	-	-
31.5	316.08	3.56827	1.31	35.63	31.5	113	1.29706	-	-
25	157.08	1.77330	3.03	28.38	25	93.97	1.07863	0.80	28.10
20	130.70	1.47549	0.82	22.39	20	93.97	1.07863	-	-
18	127.77	1.44241	0.22	18.97	18	77.76	0.89256	1.80	19.00
16	106.50	1.20229	1.55	16.99	16	70.63	0.81072	0.82	16.98
14	95.80	1.08150	0.79	14.97	14	53.79	0.61742	2.04	15.00
12.5	86.69	0.97865	0.88	13.23	12.5	49.19	0.56462	0.79	13.23
10	68.70	0.77556	1.04	11.21	10	38.91	0.44663	1.05	11.21
8	54.34	0.61345	1.05	8.96	8	33.42	0.38361	0.68	8.95
6.3	47.16	0.53240	0.59	7.10	6.3	29.46	0.33815	0.53	7.10
5	38.38	0.43328	0.89	5.62	5	25.58	0.29362	0.61	5.62
4	32.07	0.36204	0.80	4.48	4	21.91	0.25149	0.69	4.48
3.15	28.34	0.31993	0.52	3.55	3.15	19.92	0.22865	0.40	3.55
2	22.36	0.25242	0.52	2.51	2	16.82	0.19307	0.37	2.50
1	16.52	0.18650	0.44	1.41	1	13.52	0.15519	0.32	1.40
0.5	12.32	0.13908	0.42	0.70	0.5	10.37	0.11903	0.38	0.70
0.25	7.06	0.07970	0.80	0.36	0.25	6.54	0.07507	0.67	0.36
0.1	1.92	0.02168	1.42	0.17	0.1	2.01	0.02307	1.29	0.17
0.04	0.50	0.00564	1.47	0.07	0.04	0.49	0.00562	1.54	0.07

s_n – Local (GGS) slope (Equation 55)

x_a – Surface-equivalent fragment size (Equation 56)

Blast test:		20 (mortar, 12 g/m)			Blast test:		21 (mortar, 12 g/m)		
Mesh size [mm]	Mass passing [g]	Mass passing [%]	s_n [-]	x_a [mm]	Mesh size [mm]	Mass passing [g]	Mass passing [%]	s_n [-]	x_a [mm]
125	8706.79	100	-	-	-	-	-	-	-
100	6414.79	73.67572	1.37	112.21	-	-	-	-	-
80	6414.79	73.67572	-	-	80	8706.82	100	-	-
63	2439.79	28.02169	4.05	72.19	63	4860.15	55.82004	2.44	71.65
50	1112.79	12.78071	3.40	56.85	50	2002.66	23.00105	3.84	56.96
40	706.79	8.11769	2.03	45.01	40	1297.25	14.89924	1.95	44.99
31.5	510.79	5.86657	1.36	35.64	31.5	869.52	9.98665	1.67	35.70
25	413.79	4.75250	0.91	28.11	25	549.05	6.30598	1.99	28.25
20	278.53	3.19900	1.77	22.48	20	422.8	4.85596	1.17	22.42
18	264.13	3.03361	0.50	18.97	18	401.56	4.61202	0.49	18.97
16	214.36	2.46199	1.77	17.00	16	377.36	4.33407	0.53	16.97
14	186.12	2.13764	1.06	14.98	14	350.45	4.02501	0.55	14.97
12.5	169.44	1.94607	0.83	13.23	12.5	316.48	3.63485	0.90	13.23
10	148.02	1.70005	0.61	11.19	10	234.18	2.68962	1.35	11.22
8	128.01	1.47023	0.65	8.95	8	198.09	2.27511	0.75	8.95
6.3	114.67	1.31702	0.46	7.10	6.3	153.38	1.76161	1.07	7.12
5	99.37	1.14129	0.62	5.62	5	123.95	1.42360	0.92	5.62
4	89.49	1.02782	0.47	4.47	4	103.62	1.19010	0.80	4.48
3.15	81.49	0.93594	0.39	3.55	3.15	92.20	1.05894	0.49	3.55
2	70.02	0.80420	0.33	2.50	2	72.39	0.83142	0.53	2.51
1	57.13	0.65615	0.29	1.40	1	53.98	0.61997	0.42	1.41
0.5	29.25	0.33594	0.97	0.72	0.5	39.19	0.45011	0.46	0.71
0.25	17.08	0.19617	0.78	0.36	0.25	23.74	0.27266	0.72	0.36
0.1	5.08	0.05835	1.32	0.17	0.1	7.06	0.08109	1.32	0.17
0.04	1.56	0.01792	1.29	0.07	0.04	2.09	0.02400	1.33	0.07

s_n – Local (GGS) slope (Equation 55)

x_a – Surface-equivalent fragment size (Equation 56)

Blast test:		22.1 (mortar, 20 g/m)			Blast test:		23.1 (mortar, 20 g/m)		
Mesh size [mm]	Mass passing [g]	Mass passing [%]	s_n [-]	x_a [mm]	Mesh size [mm]	Mass passing [g]	Mass passing [%]	s_n [-]	x_a [mm]
-	-	-	-	-	-	-	-	-	-
100	9212.85	100	-	-	-	-	-	-	-
80	8615.27	93.51362	0.30	89.37	80	8783.77	100	-	-
63	5046.03	54.77165	2.24	71.58	63	7846.77	89.33260	0.47	70.98
50	2056.76	22.32490	3.88	56.97	50	3856.77	43.90791	3.07	56.77
40	1458.68	15.83310	1.54	44.91	40	2324.77	26.46665	2.27	45.05
31.5	799.05	8.67321	2.52	35.84	31.5	1474.86	16.79074	1.90	35.73
25	Not used for this cylinder				25	985.19	11.21603	1.71	22.47
20	426.83	4.63299	1.38	25.48	20	673.31	7.66539	1.71	22.47
18	379.78	4.12229	1.11	18.98	18	580.4	6.60764	1.41	18.99
16	322.45	3.50000	1.39	16.99	16	495.11	5.63665	1.35	16.99
14	305.74	3.31863	0.40	14.96	14	432.32	4.92180	1.02	14.98
12.5	271.7	2.94914	1.04	13.24	12.5	396.04	4.50877	0.77	13.23
10	216.09	2.34553	1.03	11.20	10	325.36	3.70410	0.88	11.20
8	185.59	2.01447	0.68	8.95	8	268.1	3.05222	0.87	8.96
6.3	160.31	1.74007	0.61	7.10	6.3	213.04	2.42538	0.96	7.11
5	134.58	1.46079	0.76	5.62	5	187.24	2.13166	0.56	5.61
4	115.35	1.25206	0.69	4.48	4	159.56	1.81653	0.72	4.48
3.15	103.32	1.12148	0.46	3.55	3.15	140.46	1.59909	0.53	3.55
2	84.24	0.91438	0.45	2.51	2	110.4	1.25686	0.53	2.51
1	63.88	0.69338	0.40	1.41	1	83.26	0.94788	0.41	1.41
0.5	48.15	0.52264	0.41	0.70	0.5	60.86	0.69287	0.45	0.71
0.25	29.08	0.31565	0.73	0.36	0.25	36.82	0.41918	0.73	0.36
0.1	8.43	0.09150	1.35	0.17	0.1	10.73	0.12216	1.35	0.17
0.04	2.3	0.02497	1.42	0.07	0.04	3.12	0.03552	1.35	0.07

s_n – Local (GGS) slope (Equation 55)

x_a – Surface-equivalent fragment size (Equation 56)

Blast test:		26.1 (granite, 6 g/m)			Blast test:		27 (granite, 6 g/m)		
Mesh size [mm]	Mass passing [g]	Mass passing [%]	s_n [-]	x_a [mm]	Mesh size [mm]	Mass passing [g]	Mass passing [%]	s_n [-]	x_a [mm]
125	13824.82	100	-	-	125	14384.81	100	-	-
100	10191.82	73.72118	1.37	112.21	100	10869.81	75.56450	1.26	112.15
80	1649.82	11.93375	8.16	92.20	80	2671.81	18.57383	6.29	91.56
63	584.82	4.23022	4.34	72.28	63	920.81	6.40127	4.46	72.32
50	408.08	2.95179	1.56	56.39	50	443.81	3.08527	3.16	56.79
40	248.75	1.79930	2.22	45.04	40	252.81	1.75748	2.52	45.10
31.5	210.68	1.52393	0.70	35.53	31.5	213.19	1.48205	0.71	35.53
25	163.44	1.18222	1.10	28.14	25	167.27	1.16282	1.05	28.13
20	123.73	0.89498	1.25	22.43	20	140.63	0.97763	0.78	22.39
18	116.60	0.84341	0.56	18.97	18	132.22	0.91916	0.59	18.98
16	110.98	0.80276	0.42	16.97	16	127.71	0.88781	0.29	16.97
14	100.09	0.72399	0.77	14.97	14	110.65	0.76921	1.07	14.98
12.5	92.10	0.66619	0.73	13.23	12.5	96.61	0.67161	1.20	13.24
10	72.83	0.52681	1.05	11.21	10	78.96	0.54891	0.90	11.20
8	56.23	0.40673	1.16	8.97	8	63.68	0.44269	0.96	8.96
6.3	47.91	0.34655	0.67	7.11	6.3	43.72	0.30393	1.57	7.14
5	38.22	0.27646	0.98	5.62	5	37.97	0.26396	0.61	5.62
4	33.55	0.24268	0.58	4.47	4	32.86	0.22844	0.65	4.47
3.15	29.46	0.21309	0.54	3.55	3.15	29.00	0.20160	0.52	3.55
2	23.72	0.17158	0.48	2.51	2	23.00	0.15989	0.51	2.51
1	17.10	0.12369	0.47	1.41	1	16.82	0.11693	0.45	1.41
0.5	11.54	0.08347	0.57	0.71	0.5	11.06	0.07689	0.60	0.71
0.25	6.57	0.04752	0.81	0.36	0.25	6.23	0.04331	0.83	0.36
0.1	2.78	0.02011	0.94	0.16	0.1	2.47	0.01717	1.01	0.16
0.04	0.76	0.00550	1.42	0.07	0.04	0.46	0.00320	1.83	0.07

s_n – Local (GGS) slope (Equation 55)

x_a – Surface-equivalent fragment size (Equation 56)

Blast test:		24 (granite, 12 g/m)			Blast test:		25 (granite, 12 g/m)		
Mesh size [mm]	Mass passing [g]	Mass passing [%]	s_n [-]	x_a [mm]	Mesh size [mm]	Mass passing [g]	Mass passing [%]	s_n [-]	x_a [mm]
125	13946.95	100	-	-	125	13743.78	100	-	-
100	13946.95	100	-	-	100	13743.78	100	-	-
80	11951.95	85.69580	0.69	89.51	80	13743.78	100	-	-
63	4694.95	33.66292	3.91	72.14	63	6764.78	49.22067	2.44	71.65
50	3201.95	22.95807	1.66	56.41	50	3267.78	23.77643	3.84	56.96
40	1788.93	12.82668	2.61	45.11	40	1433.78	10.43221	1.95	44.99
31.5	1478.95	10.60411	0.80	35.55	31.5	1148.78	8.35854	1.67	35.70
25	1110.61	7.96310	1.24	28.15	25	991.78	7.21621	1.99	28.25
20	903.65	6.47919	0.92	22.40	20	820.85	5.97252	1.17	22.42
18	807.27	5.78815	1.07	18.98	18	751.24	5.46604	0.49	18.97
16	700.82	5.02490	1.20	16.98	16	691.62	5.03224	0.53	16.97
14	594.61	4.26337	1.23	14.98	14	645.14	4.69405	0.55	14.97
12.5	528.54	3.78965	1.04	13.24	12.5	580.72	4.22533	0.90	13.23
10	441.88	3.16829	0.80	11.19	10	484.38	3.52436	1.35	11.22
8	375.59	2.69299	0.73	8.95	8	401.56	2.92176	0.75	8.95
6.3	313.55	2.24816	0.76	7.11	6.3	342.08	2.48898	1.07	7.12
5	265.26	1.90192	0.72	5.62	5	285.92	2.08036	0.92	5.62
4	225.11	1.61404	0.74	4.48	4	242.51	1.76451	0.80	4.48
3.15	199.94	1.43358	0.50	3.55	3.15	210.10	1.52869	0.49	3.55
2	151.90	1.08913	0.60	2.51	2	160.42	1.16722	0.53	2.51
1	106.77	0.76554	0.51	1.41	1	111.42	0.81069	0.42	1.41
0.5	66.08	0.47380	0.69	0.71	0.5	67.64	0.49215	0.46	0.71
0.25	35.16	0.25210	0.91	0.36	0.25	35.07	0.25517	0.72	0.36
0.1	11.97	0.08583	1.18	0.17	0.1	12.35	0.08986	1.32	0.17
0.04	2.50	0.01793	1.71	0.07	0.04	3.20	0.02328	1.33	0.07

s_n – Local (GGS) slope (Equation 55)

x_a – Surface-equivalent fragment size (Equation 56)

Blast test:		28.1 (granite, 12 g/m)			Blast test:		26.2 (granite, 20 g/m)		
Mesh size [mm]	Mass passing [g]	Mass passing [%]	s_n [-]	x_a [mm]	Mesh size [mm]	Mass passing [g]	Mass passing [%]	s_n [-]	x_a [mm]
-	-	-	-	-	-	-	-	-	-
100	13675.67	100	-	-	100	13736.16	100	-	-
80	10668.67	78.01205	1.11	89.67	80	8027.16	58.43817	2.41	90.15
63	6829.67	49.94030	1.87	71.46	63	5749.70	41.85813	1.40	71.30
50	2069.67	15.13396	5.17	57.28	50	4164.95	30.32106	1.40	56.35
40	1768.68	12.93304	0.70	44.76	40	3374.25	24.56473	0.94	44.80
31.5	1393.46	10.18934	1.00	35.58	31.5	2620.03	19.07396	1.06	35.59
25	1064.94	7.78711	1.16	28.15	25	2006.59	14.60809	1.15	28.14
20	922.86	6.74819	0.64	22.37	20	1563.84	11.38484	1.12	22.42
18	875.12	6.39910	0.50	18.97	18	1439.76	10.48153	0.78	18.98
16	816.71	5.97199	0.59	16.97	16	1342.30	9.77202	0.60	16.97
14	724.41	5.29707	0.90	14.98	14	1232.26	8.97092	0.64	14.97
12.5	667.74	4.88269	0.72	13.23	12.5	1122.44	8.17142	0.82	13.23
10	598.62	4.37726	0.49	11.18	10	946.65	6.89166	0.76	11.19
8	453.76	3.31801	1.24	8.97	8	803.79	5.85164	0.73	8.95
6.3	397.53	2.90684	0.55	7.10	6.3	712.30	5.18558	0.51	7.10
5	328.33	2.40083	0.83	5.62	5	608.55	4.43028	0.68	5.62
4	276.46	2.02155	0.77	4.48	4	522.58	3.80441	0.68	4.48
3.15	242.45	1.77286	0.55	3.55	3.15	459.08	3.34213	0.54	3.55
2	186.13	1.36103	0.58	2.51	2	352.68	2.56753	0.58	2.51
1	127.52	0.93246	0.55	1.42	1	239.57	1.74408	0.56	1.42
0.5	80.49	0.58856	0.66	0.71	0.5	145.59	1.05990	0.72	0.71
0.25	42.92	0.31384	0.91	0.36	0.25	77.71	0.56573	0.91	0.36
0.1	16.02	0.11714	1.08	0.16	0.1	28.48	0.20734	1.10	0.16
0.04	3.79	0.02771	1.57	0.07	0.04	9.16	0.06669	1.24	0.07

s_n – Local (GGS) slope (Equation 55)

x_a – Surface-equivalent fragment size (Equation 56)

Merged screening data (laser-diffraction granulometry and sieving)

Blast test: 22.2 (mortar, 6 g/m)					
Mesh size [mm]	Mass passing [g]	Mass passing [%]	Mesh size [mm]	Mass passing [g]	Mass passing [%]
150	8940.00	100	0.5	10.47	0.11814
125	5168.08	58.34312	0.25	7.24	0.08168
100	5168.08	58.34312	0.1	1.40	0.01582
80	3915.08	44.19784	0.04	0.32	0.00363
63	887.08	10.01436	0.032	2.31E-01	2.61E-03
50	717.08	8.09521	0.025	1.62E-01	1.83E-03
40	432.08	4.87781	0.02	1.18E-01	1.33E-03
31.5	316.08	3.56827	0.015	8.34E-02	9.41E-04
25	157.08	1.77330	0.0125	6.70E-02	7.56E-04
20	130.7	1.47549	0.01	5.11E-02	5.77E-04
18	127.77	1.44241	0.0071	3.47E-02	3.92E-04
16	106.5	1.20229	0.0063	3.10E-02	3.49E-04
14	95.8	1.08150	0.005	2.52E-02	2.84E-04
12.5	86.69	0.97865	0.004	2.05E-02	2.31E-04
10	68.7	0.77556	0.003	1.61E-02	1.81E-04
8	54.34	0.61345	0.002	1.18E-02	1.33E-04
6.3	47.16	0.53240	0.0016	9.65E-03	1.09E-04
5	38.38	0.43328	0.001	5.00E-03	5.64E-05
4	32.07	0.36204	0.00071	1.90E-03	2.14E-05
3.15	28.34	0.31993	0.00063	1.05E-03	1.19E-05
2	22.36	0.25242	0.0005	5.00E-05	5.64E-07
1	16.52	0.18645	0.0004	1.75E-12	1.97E-14

Blast test: 20 (mortar, 12 g/m)					
Mesh size [mm]	Mass passing [g]	Mass passing [%]	Mesh size [mm]	Mass passing [g]	Mass passing [%]
-	-	-	0.5	25.51	0.29299
125	8706.79	100	0.25	17.03	0.19558
100	6414.79	73.67572	0.1	3.83	0.04397
80	6414.79	73.67572	0.04	1.18	0.01351
63	2439.79	28.02169	0.032	9.47E-01	1.09E-02
50	1112.79	12.78071	0.025	7.46E-01	8.56E-03
40	706.79	8.11769	0.02	6.02E-01	6.92E-03
31.5	510.79	5.86657	0.015	4.67E-01	5.36E-03
25	413.79	4.75250	0.0125	3.97E-01	4.56E-03
20	278.53	3.19900	0.01	3.27E-01	3.76E-03
18	264.13	3.03361	0.0071	2.51E-01	2.88E-03
16	214.36	2.46199	0.0063	2.31E-01	2.65E-03
14	186.12	2.13764	0.005	1.99E-01	2.29E-03
12.5	169.44	1.94607	0.004	1.73E-01	1.99E-03
10	148.02	1.70005	0.003	1.42E-01	1.64E-03
8	128.01	1.47023	0.002	1.05E-01	1.21E-03
6.3	114.67	1.31702	0.0016	8.72E-02	1.00E-03
5	99.37	1.14129	0.001	5.33E-02	6.13E-04
4	89.49	1.02782	0.00071	3.21E-02	3.69E-04
3.15	81.49	0.93594	0.00063	2.60E-02	2.99E-04
2	70.02	0.80420	0.0005	2.03E-02	2.33E-04
1	57.13	0.65615	0.0004	2.00E-02	2.30E-04

Blast test: 22.1 (mortar, 20 g/m)					
Mesh size [mm]	Mass passing [g]	Mass passing [%]	Mesh size [mm]	Mass passing [g]	Mass passing [%]
-	-	-	0.5	40.98	0.44480
-	-	-	0.25	28.57	0.31016
100	9212.85	100	0.1	6.21	0.06740
80	8615.27	93.51362	0.04	1.74	0.01886
63	5046.03	54.77165	0.032	1.33E+00	1.45E-02
50	2056.76	22.32490	0.025	1.00E+00	1.09E-02
40	1458.68	15.83310	0.02	7.77E-01	8.44E-03
31.5	799.05	8.67321	0.015	5.75E-01	6.24E-03
25	-	-	0.0125	4.77E-01	5.18E-03
20	426.83	4.63299	0.01	3.83E-01	4.16E-03
18	379.78	4.12229	0.0071	2.89E-01	3.14E-03
16	322.45	3.50000	0.0063	2.65E-01	2.88E-03
14	305.74	3.31863	0.005	2.28E-01	2.47E-03
12.5	271.7	2.94914	0.004	1.98E-01	2.14E-03
10	216.09	2.34553	0.003	1.61E-01	1.75E-03
8	185.59	2.01447	0.002	1.16E-01	1.26E-03
6.3	160.31	1.74007	0.0016	9.49E-02	1.03E-03
5	134.58	1.46079	0.001	4.99E-02	5.42E-04
4	115.35	1.25206	0.00071	1.85E-02	2.01E-04
3.15	103.32	1.12148	0.00063	9.20E-03	9.98E-05
2	84.24	0.91438	0.0005	2.30E-04	2.50E-06
1	63.88	0.69333	0.0004	0	0

Blast test: 27 (granite, 6 g/m)					
Mesh size [mm]	Mass passing [g]	Mass passing [%]	Mesh size [mm]	Mass passing [g]	Mass passing [%]
-	-	-	0.5	8.43	0.05861
125	14384.81	100	0.25	5.79	0.04023
100	10869.81	75.56450	0.1	1.70	0.01184
80	2671.81	18.57383	0.04	0.44	0.00307
63	920.81	6.40127	0.032	3.15E-01	2.19E-03
50	443.81	3.08527	0.025	2.19E-01	1.53E-03
40	252.81	1.75748	0.02	1.63E-01	1.13E-03
31.5	213.19	1.48205	0.015	1.19E-01	8.29E-04
25	167.27	1.16282	0.0125	1.00E-01	6.99E-04
20	140.63	0.97763	0.01	8.34E-02	5.80E-04
18	132.22	0.91916	0.0071	6.59E-02	4.58E-04
16	127.71	0.88781	0.0063	6.12E-02	4.25E-04
14	110.65	0.76921	0.005	5.34E-02	3.71E-04
12.5	96.61	0.67161	0.004	4.63E-02	3.22E-04
10	78.96	0.54891	0.003	3.77E-02	2.62E-04
8	63.68	0.44269	0.002	2.61E-02	1.81E-04
6.3	43.72	0.30393	0.0016	2.00E-02	1.39E-04
5	37.97	0.26396	0.001	8.31E-03	5.78E-05
4	32.86	0.22844	0.00071	1.48E-03	1.03E-05
3.15	29.00	0.20160	0.00063	3.68E-04	2.56E-06
2	23.00	0.15989	0.0005	1.29E-12	8.95E-15
1	16.62	0.11555	0.0004	1.29E-12	8.95E-15

Blast test: 24 (granite, 12 g/m)					
Mesh size [mm]	Mass passing [g]	Mass passing [%]	Mesh size [mm]	Mass passing [g]	Mass passing [%]
-	-	-	0.5	52.04	0.37311
125	13946.95	100	0.25	33.98	0.24362
100	13946.95	100	0.1	9.05	0.06486
80	11951.95	85.69580	0.04	2.41	0.01730
63	4694.95	33.66292	0.032	1.83E+00	1.32E-02
50	3201.95	22.95807	0.025	1.36E+00	9.74E-03
40	1788.93	12.82668	0.02	1.05E+00	7.49E-03
31.5	1478.95	10.60411	0.015	7.85E-01	5.63E-03
25	1110.61	7.96310	0.0125	6.76E-01	4.85E-03
20	903.65	6.47919	0.01	5.77E-01	4.14E-03
18	807.27	5.78815	0.0071	4.43E-01	3.17E-03
16	700.82	5.02490	0.0063	3.99E-01	2.86E-03
14	594.61	4.26337	0.005	3.22E-01	2.31E-03
12.5	528.54	3.78965	0.004	2.52E-01	1.81E-03
10	441.88	3.16829	0.003	1.95E-01	1.40E-03
8	375.59	2.69299	0.002	1.34E-01	9.64E-04
6.3	313.55	2.24816	0.0016	1.04E-01	7.44E-04
5	265.26	1.90192	0.001	4.40E-02	3.15E-04
4	225.11	1.61404	0.00071	1.01E-02	7.24E-05
3.15	199.94	1.43358	0.00063	4.00E-03	2.87E-05
2	151.90	1.08913	0.0005	2.50E-04	1.79E-06
1	106.56	0.76404	0.0004	6.22E-13	4.46E-15

Blast test: 25 (granite, 12 g/m)					
Mesh size [mm]	Mass passing [g]	Mass passing [%]	Mesh size [mm]	Mass passing [g]	Mass passing [%]
-	-	-	0.5	50.12	0.35934
-	-	-	0.25	32.70	0.23449
-	-	-	0.1	9.01	0.06463
80	13743.78	100	0.04	2.54	0.01818
63	6764.78	49.22067	0.032	1.94E+00	1.39E-02
50	3267.78	23.77643	0.025	1.44E+00	1.04E-02
40	1433.78	10.43221	0.02	1.12E+00	8.00E-03
31.5	1148.78	8.35854	0.015	8.62E-01	6.18E-03
25	991.78	7.21621	0.0125	7.40E-01	5.30E-03
20	820.85	5.97252	0.01	6.18E-01	4.43E-03
18	751.24	5.46604	0.0071	4.82E-01	3.45E-03
16	691.62	5.03224	0.0063	4.46E-01	3.19E-03
14	645.14	4.69405	0.005	3.83E-01	2.75E-03
12.5	580.72	4.22533	0.004	3.28E-01	2.35E-03
10	484.38	3.52436	0.003	2.63E-01	1.88E-03
8	401.56	2.92176	0.002	1.77E-01	1.27E-03
6.3	342.08	2.48898	0.0016	1.35E-01	9.66E-04
5	285.92	2.08036	0.001	5.87E-02	4.21E-04
4	242.51	1.76451	0.00071	1.91E-02	1.37E-04
3.15	210.10	1.52869	0.00063	1.26E-02	9.01E-05
2	160.42	1.16722	0.0005	1.00E-02	7.17E-05
1	110.35	0.79118	0.0004	1.00E-02	7.17E-05

Blast test: 26.2 (granite, 20 g/m)					
Mesh size [mm]	Mass passing [g]	Mass passing [%]	Mesh size [mm]	Mass passing [g]	Mass passing [%]
-	-	-	0.5	137.73	1.00268
-	-	-	0.25	97.41	0.70912
100	13736.16	100	0.1	49.73	0.36206
80	8027.16	58.43817	0.04	10.68	0.07774
63	5749.70	41.85813	0.032	8.38E+00	6.10E-02
50	4164.95	30.32106	0.025	6.67E+00	4.86E-02
40	3374.25	24.56473	0.02	5.16E+00	3.75E-02
31.5	2620.03	19.07396	0.015	4.08E+00	2.97E-02
25	2006.59	14.60809	0.0125	3.11E+00	2.26E-02
20	1563.84	11.38484	0.01	2.68E+00	1.95E-02
18	1439.76	10.48153	0.0071	2.29E+00	1.66E-02
16	1342.30	9.77202	0.0063	1.80E+00	1.31E-02
14	1232.26	8.97092	0.005	1.65E+00	1.20E-02
12.5	1122.44	8.17142	0.004	1.39E+00	1.01E-02
10	946.65	6.89166	0.003	1.16E+00	8.45E-03
8	803.79	5.85164	0.002	9.04E-01	6.58E-03
6.3	712.30	5.18558	0.0016	6.05E-01	4.41E-03
5	608.55	4.43028	0.001	4.41E-01	3.21E-03
4	522.58	3.80441	0.00071	1.40E-01	1.02E-03
3.15	459.08	3.34213	0.00063	3.42E-02	2.49E-04
2	352.68	2.56753	0.0005	1.56E-02	1.13E-04
1	239.57	1.74408	0.0004	9.16E-04	6.67E-06

Data on specific surface areas and blast-energy register (BER)

Blast test: 22.2 (mortar, 6 g/m)			f_A : 15.04		m_{sieve} : 8858	
Mesh size [mm]	Mass passing [%]	s_n [-]	x_a [mm]	a_s [cm ² /cm ³]	a_m [cm ² /g]	ΔA_f [cm ²]
150	100.00	-	-	-	-	-
100	58.34	1.33	123.87	1.2	0.7	2698.2
80	44.20	1.24	89.72	1.7	1.0	1265.0
63	10.01	6.21	72.89	2.1	1.2	3762.7
50	8.10	0.92	56.23	2.7	1.6	273.8
40	4.88	2.27	45.05	3.3	2.0	573.0
31.5	3.57	1.31	35.63	4.2	2.5	294.9
25	1.77	3.03	28.38	5.3	3.2	507.5
20	1.48	0.82	22.39	6.7	4.0	106.7
18	1.44	0.22	18.97	7.9	4.8	14.0
16	1.20	1.55	16.99	8.8	5.3	113.4
14	1.08	0.79	14.97	10.0	6.0	64.7
12.5	0.98	0.88	13.23	11.4	6.8	62.3
10	0.78	1.04	11.21	13.4	8.1	145.4
8	0.61	1.05	8.96	16.8	10.1	145.1
6.3	0.53	0.59	7.10	21.2	12.8	91.6
5	0.43	0.89	5.62	26.7	16.1	141.4
4	0.36	0.80	4.48	33.6	20.2	127.6
3.15	0.32	0.52	3.55	42.4	25.5	95.2
2	0.25	0.52	2.51	59.9	36.1	215.7
1	0.19	0.44	1.41	106.6	64.2	375.0
0.5	0.14	0.42	0.70	213.3	128.5	539.6
0.25	0.080	0.80	0.36	420.2	253.1	1331.3
0.1	0.022	1.42	0.17	892.5	375.0	1927.4
0.04	0.006	1.47	0.07	2224.0	934.7	1327.3
0	0.000	-	-	14240.9	5966.2	2983.1
Notation: ΔA_f - Fragmented area of a fragment-size fraction A_f - Total fragmented area a_m - Mass-specific area (for a fragment-size fraction) a_{m_tot} - Total mass-specific area of a blasted cylinder a_s - Volume-specific area f_A - Particle-shape factor m_{sieve} - Total mass of sieved material s_n - Local slope (GGs exponent) x_a - The surface-equivalent fragment size					A_f :	19182.0
					a_{m_tot} :	2.166

Blast test: 23.2 (mortar, 6 g/m)			f_A : 15.11		m_{sieve} : 8712	
Mesh size [mm]	Mass passing [%]	s_n [-]	x_a [mm]	a_s [cm ² /cm ³]	a_m [cm ² /g]	ΔA_f [cm ²]
125	52.72	-	-	-	-	-
100	20.48	4.24	113.53	1.3	0.8	2251.9
80	1.30	12.37	93.49	1.6	1.0	1626.7
63	1.30	-	-	-	-	-
50	1.30	-	-	-	-	-
40	1.30	-	-	-	-	-
31.5	1.30	-	-	-	-	-
25	1.08	0.80	28.10	5.4	3.2	61.6
20	1.08	-	-	-	-	-
18	0.89	1.80	19.00	8.0	4.8	77.7
16	0.81	0.82	16.98	8.9	5.4	38.2
14	0.62	2.04	15.00	10.1	6.1	102.2
12.5	0.56	0.79	13.23	11.4	6.9	31.6
10	0.45	1.05	11.21	13.5	8.1	83.5
8	0.38	0.68	8.95	16.9	10.2	55.8
6.3	0.34	0.53	7.10	21.3	12.8	50.8
5	0.29	0.61	5.62	26.9	16.2	62.9
4	0.25	0.69	4.48	33.8	20.3	74.6
3.15	0.23	0.40	3.55	42.6	25.7	51.0
2	0.19	0.37	2.50	60.3	36.3	112.7
1	0.16	0.32	1.40	107.6	64.8	214.0
0.5	0.12	0.38	0.70	214.7	129.3	407.4
0.25	0.075	0.67	0.36	424.5	255.7	979.5
0.1	0.023	1.29	0.17	904.9	380.2	1722.4
0.04	0.006	1.54	0.07	2224.0	934.7	1420.8
0	0.000	-	-	14240.9	5966.2	2923.5
Notation: ΔA_f - Fragmented area of a fragment-size fraction A_f - Total fragmented area a_m - Mass-specific area (for a fragment-size fraction) a_{m_tot} - Total mass-specific area of a blasted cylinder a_s - Volume-specific area f_A - Particle-shape factor m_{sieve} - Total mass of sieved material s_n - Local slope (GGs exponent) x_a - The surface-equivalent fragment size					A_f :	12348.6
					a_{m_tot} :	1.417

Blast test: 26.1 (granite, 6 g/m)			f_A : 10.39		m_{sieve} : 13825	
Mesh size [mm]	Mass passing [%]	s_n [-]	x_a [mm]	a_s [cm ² /cm ³]	a_m [cm ² /g]	ΔA_f [cm ²]
125	100.00	-	-	-	-	-
100	73.72	1.37	112.21	0.9	0.3	1255.3
80	11.93	8.16	92.20	1.1	0.4	3591.9
63	4.23	4.34	72.28	1.4	0.5	571.2
50	2.95	1.56	56.39	1.8	0.7	121.5
40	1.80	2.22	45.04	2.3	0.9	137.1
31.5	1.52	0.70	35.53	2.9	1.1	41.5
25	1.18	1.10	28.14	3.7	1.4	65.1
20	0.89	1.25	22.43	4.6	1.7	68.6
18	0.84	0.56	18.97	5.5	2.0	14.6
16	0.80	0.42	16.97	6.1	2.3	12.8
14	0.72	0.77	14.97	6.9	2.6	28.2
12.5	0.67	0.73	13.23	7.9	2.9	23.4
10	0.53	1.05	11.21	9.3	3.5	66.7
8	0.41	1.16	8.97	11.6	4.3	71.8
6.3	0.35	0.67	7.11	14.6	5.5	45.4
5	0.28	0.98	5.62	18.5	6.9	66.8
4	0.24	0.58	4.47	23.2	8.7	40.5
3.15	0.21	0.54	3.55	29.3	10.9	44.7
2	0.17	0.48	2.51	41.4	15.5	88.7
1	0.12	0.47	1.41	73.5	27.4	181.7
0.5	0.08	0.57	0.71	146.5	54.7	304.0
0.25	0.048	0.81	0.36	290.2	108.3	538.2
0.1	0.020	0.94	0.16	637.4	237.8	901.4
0.04	0.005	1.42	0.07	1542.3	579.5	1170.7
0	0.000	-	-	7267.5	2684.9	2040.6
Notation:					A_f :	11492.3
ΔA_f - Fragmented area of a fragment-size fraction					a_{m_tot} :	0.831
A_f - Total fragmented area						
a_m - Mass-specific area (for a fragment-size fraction)						
a_{m_tot} - Total mass-specific area of a blasted cylinder						
a_s - Volume-specific area						
f_A - Particle-shape factor						
m_{sieve} - Total mass of sieved material						
s_n - Local slope (GGs exponent)						
x_a - The surface-equivalent fragment size						

Blast test: 27 (granite, 6 g/m)			f_A : 10.68		m_{sieve} : 14385	
Mesh size [mm]	Mass passing [%]	s_n [-]	x_a [mm]	a_s [cm ² /cm ³]	a_m [cm ² /g]	ΔA_f [cm ²]
125	100.00	-	-	-	-	-
100	75.56	1.26	112.15	1.0	0.4	1249.2
80	18.57	6.29	91.56	1.2	0.4	3568.9
63	6.40	4.46	72.32	1.5	0.6	965.0
50	3.09	3.16	56.79	1.9	0.7	334.8
40	1.76	2.52	45.10	2.4	0.9	168.8
31.5	1.48	0.71	35.53	3.0	1.1	44.4
25	1.16	1.05	28.13	3.8	1.4	65.1
20	0.98	0.78	22.39	4.8	1.8	47.4
18	0.92	0.59	18.98	5.6	2.1	17.7
16	0.89	0.29	16.97	6.3	2.3	10.6
14	0.77	1.07	14.98	7.1	2.7	45.4
12.5	0.67	1.20	13.24	8.1	3.0	42.3
10	0.55	0.90	11.20	9.5	3.6	62.8
8	0.44	0.96	8.96	11.9	4.4	68.0
6.3	0.30	1.57	7.14	15.0	5.6	111.5
5	0.26	0.61	5.62	19.0	7.1	40.8
4	0.23	0.65	4.47	23.9	8.9	45.5
3.15	0.20	0.52	3.55	30.1	11.2	43.3
2	0.16	0.51	2.51	42.6	15.9	95.3
1	0.12	0.45	1.41	75.7	28.2	174.5
0.5	0.08	0.60	0.71	150.4	56.1	323.3
0.25	0.043	0.83	0.36	298.2	111.3	537.4
0.1	0.017	1.01	0.16	652.1	243.3	914.9
0.04	0.003	1.83	0.07	1542.3	579.5	1164.9
0	0.000	-	-	7267.5	2684.9	1235.1
Notation: ΔA_f - Fragmented area of a fragment-size fraction A_f - Total fragmented area a_m - Mass-specific area (for a fragment-size fraction) $a_{m,tot}$ - Total mass-specific area of a blasted cylinder a_s - Volume-specific area f_A - Particle-shape factor m_{sieve} - Total mass of sieved material s_n - Local slope (GGS exponent) x_a - The surface-equivalent fragment size					A_f :	11376.9
					$a_{m,tot}$:	0.791

Blast test: 20 (mortar, 12 g/m)			f_A : 15.20		m_{sieve} : 8707	
Mesh size [mm]	Mass passing [%]	s_n [-]	x_a [mm]	a_s [cm ² /cm ³]	a_m [cm ² /g]	ΔA_f [cm ²]
125	100.00	-	-	-	-	-
100	73.68	1.37	112.21	1.4	0.8	1870.2
80	73.68	-	-	-	-	-
63	28.02	4.05	72.19	2.1	1.3	5041.6
50	12.78	3.40	56.85	2.7	1.6	2137.2
40	8.12	2.03	45.01	3.4	2.0	825.9
31.5	5.87	1.36	35.64	4.3	2.6	503.5
25	4.75	0.91	28.11	5.4	3.3	315.9
20	3.20	1.77	22.48	6.8	4.1	550.9
18	3.03	0.50	18.97	8.0	4.8	69.5
16	2.46	1.77	17.00	8.9	5.4	268.1
14	2.14	1.06	14.98	10.1	6.1	172.6
12.5	1.95	0.83	13.23	11.5	6.9	115.4
10	1.70	0.61	11.19	13.6	8.2	175.3
8	1.47	0.65	8.95	17.0	10.2	204.7
6.3	1.32	0.46	7.10	21.4	12.9	172.1
5	1.14	0.62	5.62	27.1	16.3	249.5
4	1.03	0.47	4.47	34.0	20.5	202.3
3.15	0.94	0.39	3.55	42.8	25.8	206.4
2	0.80	0.33	2.50	60.7	36.6	419.6
1	0.66	0.29	1.40	108.4	65.3	841.4
0.5	0.34	0.97	0.72	211.0	127.1	3543.4
0.25	0.196	0.78	0.36	425.1	256.1	3117.0
0.1	0.058	1.32	0.17	908.1	381.5	4578.5
0.04	0.018	1.29	0.07	2275.5	964.3	3394.3
0	0.000	-	-	14136.8	5900.1	9204.3
Notation: ΔA_f - Fragmented area of a fragment-size fraction A_f - Total fragmented area a_m - Mass-specific area (for a fragment-size fraction) a_{m_tot} - Total mass-specific area of a blasted cylinder a_s - Volume-specific area f_A - Particle-shape factor m_{sieve} - Total mass of sieved material s_n - Local slope (GGS exponent) x_a - The surface-equivalent fragment size					A_f :	38179.6
					a_{m_tot} :	4.385

Blast test: 21 (mortar, 12 g/m)			f_A : 15.24		m_{sieve} : 8707	
Mesh size [mm]	Mass passing [%]	s_n [-]	x_a [mm]	a_s [cm ² /cm ³]	a_m [cm ² /g]	ΔA_f [cm ²]
125	-	-	-	-	-	-
100	-	-	-	-	-	-
80	100.00	-	-	-	-	-
63	55.82	2.44	71.65	2.1	1.3	4928.8
50	23.00	3.84	56.96	2.7	1.6	4605.8
40	14.90	1.95	44.99	3.4	2.0	1439.4
31.5	9.99	1.67	35.70	4.3	2.6	1100.1
25	6.31	1.99	28.25	5.4	3.2	1041.5
20	4.86	1.17	22.42	6.8	4.1	516.9
18	4.61	0.49	18.97	8.0	4.8	102.8
16	4.33	0.53	16.97	9.0	5.4	130.9
14	4.03	0.55	14.97	10.2	6.1	165.1
12.5	3.63	0.90	13.23	11.5	6.9	235.6
10	2.69	1.35	11.22	13.6	8.2	673.4
8	2.28	0.75	8.95	17.0	10.3	370.0
6.3	1.76	1.07	7.12	21.4	12.9	576.6
5	1.42	0.92	5.62	27.1	16.3	480.5
4	1.19	0.80	4.48	34.0	20.5	416.8
3.15	1.06	0.49	3.55	42.9	25.9	295.4
2	0.83	0.53	2.51	60.7	36.6	724.2
1	0.62	0.42	1.41	108.1	65.1	1198.8
0.5	0.45	0.46	0.71	215.8	130.0	1923.1
0.25	0.273	0.72	0.36	427.2	257.4	3976.2
0.1	0.081	1.32	0.17	910.5	382.6	6381.4
0.04	0.024	1.33	0.07	2275.5	964.3	4792.5
0	0.000	-	-	14136.8	5900.1	12331.4
Notation: ΔA_f - Fragmented area of a fragment-size fraction A_f - Total fragmented area a_m - Mass-specific area (for a fragment-size fraction) $a_{m,tot}$ - Total mass-specific area of a blasted cylinder a_s - Volume-specific area f_A - Particle-shape factor m_{sieve} - Total mass of sieved material s_n - Local slope (GGS exponent) x_a - The surface-equivalent fragment size					A_f :	48407.1
					$a_{m,tot}$:	5.560

Blast test: 24 (granite, 12 g/m)			f_A : 9.42		m_{sieve} : 13947	
Mesh size [mm]	Mass passing [%]	s_n [-]	x_a [mm]	a_s [cm ² /cm ³]	a_m [cm ² /g]	ΔA_f [cm ²]
125	-	-	-	-	-	-
100	100.00	-	-	-	-	-
80	85.70	0.69	89.51	1.1	0.4	783.7
63	33.66	3.91	72.14	1.3	0.5	3537.2
50	22.96	1.66	56.41	1.7	0.6	930.6
40	12.83	2.61	45.11	2.1	0.8	1101.4
31.5	10.60	0.80	35.55	2.7	1.0	306.6
25	7.96	1.24	28.15	3.3	1.2	460.0
20	6.48	0.92	22.40	4.2	1.6	324.9
18	5.79	1.07	18.98	5.0	1.9	178.5
16	5.02	1.20	16.98	5.5	2.1	220.4
14	4.26	1.23	14.98	6.3	2.3	249.3
12.5	3.79	1.04	13.24	7.1	2.7	175.5
10	3.17	0.80	11.19	8.4	3.1	272.2
8	2.69	0.73	8.95	10.5	3.9	260.4
6.3	2.25	0.76	7.11	13.3	4.9	306.9
5	1.90	0.72	5.62	16.8	6.3	302.2
4	1.61	0.74	4.48	21.1	7.9	315.4
3.15	1.43	0.50	3.55	26.5	9.9	249.3
2	1.09	0.60	2.51	37.5	14.0	671.8
1	0.77	0.51	1.41	66.6	24.9	1121.7
0.5	0.47	0.69	0.71	132.3	49.3	2007.9
0.25	0.252	0.91	0.36	262.2	97.8	3025.2
0.1	0.086	1.18	0.17	568.7	212.2	4921.2
0.04	0.018	1.71	0.07	1371.8	515.4	4880.5
0	0.000	-	-	8039.1	2924.4	7311.0
Notation: ΔA_f - Fragmented area of a fragment-size fraction A_f - Total fragmented area a_m - Mass-specific area (for a fragment-size fraction) $a_{m,tot}$ - Total mass-specific area of a blasted cylinder a_s - Volume-specific area f_A - Particle-shape factor m_{sieve} - Total mass of sieved material s_n - Local slope (GGS exponent) x_a - The surface-equivalent fragment size					A_f :	33913.8
					$a_{m,tot}$:	2.432

Blast test: 25 (granite, 12 g/m)			f_A : 9.19		m_{sieve} : 13744	
Mesh size [mm]	Mass passing [%]	s_n [-]	x_a [mm]	a_s [cm ² /cm ³]	a_m [cm ² /g]	ΔA_f [cm ²]
125	-	-	-	-	-	-
100	-	-	-	-	-	-
80	100.00	-	-	-	-	-
63	55.82	2.44	71.65	1.3	0.5	2905.1
50	23.00	3.84	56.96	1.6	0.6	2714.8
40	14.90	1.95	44.99	2.0	0.8	848.4
31.5	9.99	1.67	35.70	2.6	1.0	648.4
25	6.31	1.99	28.25	3.3	1.2	613.9
20	4.86	1.17	22.42	4.1	1.5	304.7
18	4.61	0.49	18.97	4.8	1.8	60.6
16	4.33	0.53	16.97	5.4	2.0	77.2
14	4.03	0.55	14.97	6.1	2.3	97.3
12.5	3.63	0.90	13.23	6.9	2.6	138.9
10	2.69	1.35	11.22	8.2	3.1	396.9
8	2.28	0.75	8.95	10.3	3.8	218.1
6.3	1.76	1.07	7.12	12.9	4.8	339.9
5	1.42	0.92	5.62	16.3	6.1	283.2
4	1.19	0.80	4.48	20.5	7.7	245.7
3.15	1.06	0.49	3.55	25.9	9.7	174.1
2	0.83	0.53	2.51	36.6	13.6	426.8
1	0.62	0.42	1.41	65.2	24.3	706.6
0.5	0.45	0.46	0.71	130.1	48.6	1133.5
0.25	0.273	0.72	0.36	257.5	96.1	2343.7
0.1	0.081	1.32	0.17	548.9	204.8	5392.8
0.04	0.024	1.33	0.07	1371.8	515.4	4043.2
0	0.000	-	-	8039.1	2924.4	9647.9
Notation: ΔA_f - Fragmented area of a fragment-size fraction A_f - Total fragmented area a_m - Mass-specific area (for a fragment-size fraction) $a_{m,tot}$ - Total mass-specific area of a blasted cylinder a_s - Volume-specific area f_A - Particle-shape factor m_{sieve} - Total mass of sieved material s_n - Local slope (GGS exponent) x_a - The surface-equivalent fragment size					A_f :	33761.6
					$a_{m,tot}$:	2.456

Blast test: 28.1 (granite, 12 g/m)			f_A : 9.34		m_{sieve} : 13676	
Mesh size [mm]	Mass passing [%]	s_n [-]	x_a [mm]	a_s [cm ² /cm ³]	a_m [cm ² /g]	ΔA_f [cm ²]
125	-	-	-	-	-	-
100	100.00	-	-	-	-	-
80	78.01	1.11	89.67	1.0	0.4	1168.6
63	49.94	1.87	71.46	1.3	0.5	1872.3
50	15.13	5.17	57.28	1.6	0.6	2895.9
40	12.93	0.70	44.76	2.1	0.8	234.3
31.5	10.19	1.00	35.58	2.6	1.0	367.5
25	7.79	1.16	28.15	3.3	1.2	406.8
20	6.75	0.64	22.37	4.2	1.6	221.3
18	6.40	0.50	18.97	4.9	1.8	87.7
16	5.97	0.59	16.97	5.5	2.1	119.9
14	5.30	0.90	14.98	6.2	2.3	214.8
12.5	4.88	0.72	13.23	7.1	2.6	149.3
10	4.38	0.49	11.18	8.4	3.1	215.5
8	3.32	1.24	8.97	10.4	3.9	562.7
6.3	2.91	0.55	7.10	13.2	4.9	275.9
5	2.40	0.83	5.62	16.6	6.2	429.0
4	2.02	0.77	4.48	20.9	7.8	403.7
3.15	1.77	0.55	3.55	26.3	9.8	333.8
2	1.36	0.58	2.51	37.2	13.9	780.8
1	0.93	0.55	1.42	65.9	24.6	1441.6
0.5	0.59	0.66	0.71	131.2	49.0	2302.7
0.25	0.314	0.91	0.36	259.9	97.0	3643.5
0.1	0.117	1.08	0.16	567.5	211.8	5696.7
0.04	0.028	1.57	0.07	1371.8	515.4	6303.1
0	0.000	-	-	8039.1	2924.4	11083.7
Notation: ΔA_f - Fragmented area of a fragment-size fraction A_f - Total fragmented area a_m - Mass-specific area (for a fragment-size fraction) $a_{m,tot}$ - Total mass-specific area of a blasted cylinder a_s - Volume-specific area f_A - Particle-shape factor m_{sieve} - Total mass of sieved material s_n - Local slope (GGs exponent) x_a - The surface-equivalent fragment size					A_f :	41211.1
					$a_{m,tot}$:	3.013

Blast test: 22.1 (mortar, 20 g/m)			f_A : 14.64		m_{sieve} : 9213	
Mesh size [mm]	Mass passing [%]	s_n [-]	x_a [mm]	a_s [cm ² /cm ³]	a_m [cm ² /g]	ΔA_f [cm ²]
125	-	-	-	-	-	-
100	100.00	-	-	-	-	-
80	93.51	0.30	89.37	1.6	1.0	589.6
63	54.77	2.24	71.58	2.0	1.2	4396.9
50	22.32	3.88	56.97	2.6	1.5	4627.1
40	15.83	1.54	44.91	3.3	2.0	1174.2
31.5	8.67	2.52	35.84	4.1	2.5	1623.0
20	4.63	1.38	25.48	5.7	3.5	1288.1
18	4.12	1.11	18.98	7.7	4.6	218.5
16	3.50	1.39	16.99	8.6	5.2	297.6
14	3.32	0.40	14.96	9.8	5.9	98.5
12.5	2.95	1.04	13.24	11.1	6.7	226.8
10	2.35	1.03	11.20	13.1	7.9	437.6
8	2.01	0.68	8.95	16.4	9.9	300.5
6.3	1.74	0.61	7.10	20.6	12.4	313.8
5	1.46	0.76	5.62	26.1	15.7	403.8
4	1.25	0.69	4.48	32.7	19.7	378.9
3.15	1.12	0.46	3.55	41.2	24.8	298.9
2	0.91	0.45	2.51	58.4	35.2	670.9
1	0.69	0.40	1.41	103.9	62.6	1274.6
0.5	0.52	0.41	0.70	207.8	125.2	1968.8
0.25	0.316	0.73	0.36	410.3	247.1	4713.2
0.1	0.092	1.35	0.17	872.9	366.8	7574.0
0.04	0.025	1.42	0.07	2172.6	905.2	5549.1
0	0.000	-	-	14345.1	6032.4	13874.8
Notation: ΔA_f - Fragmented area of a fragment-size fraction A_f - Total fragmented area a_m - Mass-specific area (for a fragment-size fraction) $a_{m,tot}$ - Total mass-specific area of a blasted cylinder a_s - Volume-specific area f_A - Particle-shape factor m_{sieve} - Total mass of sieved material s_n - Local slope (GGs exponent) x_a - The surface-equivalent fragment size					A_f :	52299.2
					$a_{m,tot}$:	5.677

Blast test: 23.1 (mortar, 20 g/m)			f_A : 14.57		m_{sieve} : 8784	
Mesh size [mm]	Mass passing [%]	s_n [-]	x_a [mm]	a_s [cm ² /cm ³]	a_m [cm ² /g]	ΔA_f [cm ²]
125	-	-	-	-	-	-
100	-	-	-	-	-	-
80	100.00	-	-	-	-	-
63	89.33	0.47	70.98	2.1	1.2	1158.6
50	43.91	3.07	56.77	2.6	1.5	6168.9
40	26.47	2.27	45.05	3.2	1.9	2984.7
31.5	16.79	1.90	35.73	4.1	2.5	2087.5
25	11.22	1.75	28.22	5.2	3.1	1523.0
20	7.67	1.71	22.47	6.5	3.9	1218.1
18	6.61	1.41	18.99	7.7	4.6	429.4
16	5.64	1.35	16.99	8.6	5.2	440.7
14	4.92	1.02	14.98	9.7	5.9	367.9
12.5	4.51	0.77	13.23	11.0	6.6	240.6
10	3.70	0.88	11.20	13.0	7.8	554.0
8	3.05	0.87	8.96	16.3	9.8	561.0
6.3	2.43	0.96	7.11	20.5	12.3	679.2
5	2.13	0.56	5.61	26.0	15.6	403.4
4	1.82	0.72	4.48	32.5	19.6	542.7
3.15	1.60	0.53	3.55	41.0	24.7	472.2
2	1.26	0.53	2.51	58.0	34.9	1050.6
1	0.95	0.41	1.41	103.4	62.3	1690.6
0.5	0.69	0.45	0.71	206.4	124.4	2785.7
0.25	0.419	0.73	0.36	408.4	246.0	5914.4
0.1	0.122	1.35	0.17	869.2	365.2	9528.3
0.04	0.036	1.35	0.07	2172.6	905.2	6888.9
0	0.000	-	-	14345.1	6032.4	18821.6
Notation: ΔA_f - Fragmented area of a fragment-size fraction A_f - Total fragmented area a_m - Mass-specific area (for a fragment-size fraction) a_{m_tot} - Total mass-specific area of a blasted cylinder a_s - Volume-specific area f_A - Particle-shape factor m_{sieve} - Total mass of sieved material s_n - Local slope (GGs exponent) x_a - The surface-equivalent fragment size					A_f :	66511.9
					a_{m_tot} :	7.572

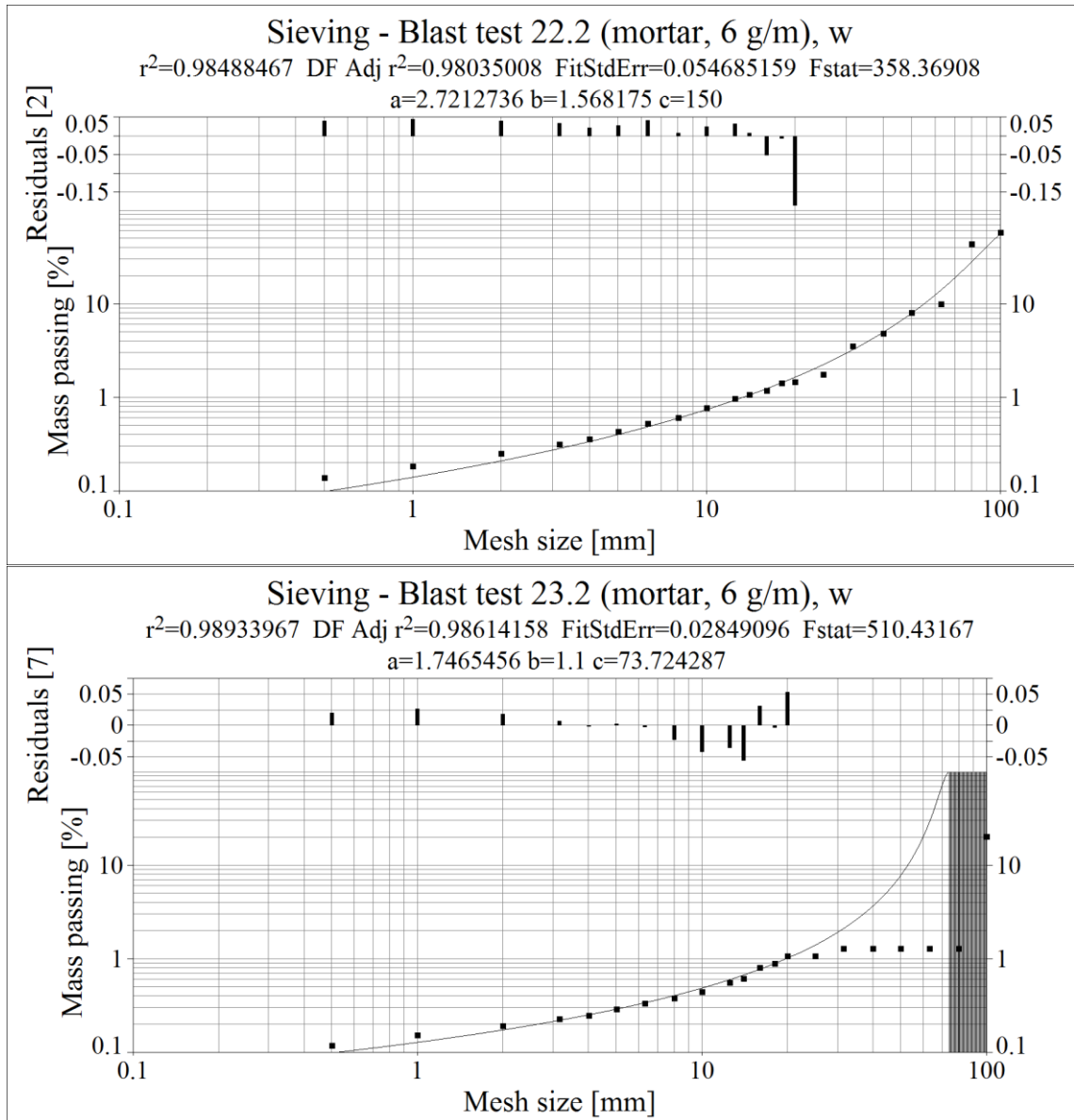
Blast test: 26.2 (granite, 20 g/m)			f_A : 11.40		m_{sieve} : 13736	
Mesh size [mm]	Mass passing [%]	s_n [-]	x_a [mm]	a_s [cm ² /cm ³]	a_m [cm ² /g]	ΔA_f [cm ²]
125	-	-	-	-	-	-
100	100.00	-	-	-	-	-
80	58.44	2.41	90.15	1.3	0.5	2693.9
63	41.86	1.40	71.30	1.6	0.6	1358.9
50	30.32	1.40	56.35	2.0	0.8	1196.4
40	24.56	0.94	44.80	2.5	0.9	750.7
31.5	19.07	1.06	35.59	3.2	1.2	901.5
25	14.61	1.15	28.14	4.1	1.5	927.2
20	11.38	1.12	22.42	5.1	1.9	840.2
18	10.48	0.78	18.98	6.0	2.2	278.1
16	9.77	0.60	16.97	6.7	2.5	244.3
14	8.97	0.64	14.97	7.6	2.8	312.7
12.5	8.17	0.82	13.23	8.6	3.2	353.0
10	6.89	0.76	11.19	10.2	3.8	668.1
8	5.85	0.73	8.95	12.7	4.8	678.8
6.3	5.19	0.51	7.10	16.1	6.0	548.2
5	4.43	0.68	5.62	20.3	7.6	785.7
4	3.80	0.68	4.48	25.5	9.5	817.1
3.15	3.34	0.54	3.55	32.1	12.0	760.8
2	2.57	0.58	2.51	45.4	16.9	1800.8
1	1.74	0.56	1.42	80.4	30.0	3394.5
0.5	1.06	0.72	0.71	159.8	59.6	5604.7
0.25	0.566	0.91	0.36	317.3	118.4	8036.2
0.1	0.207	1.10	0.16	691.9	258.2	12709.0
0.04	0.067	1.24	0.07	1712.9	643.7	12436.2
0	0.000	-	-	6495.8	2445.5	22400.7
Notation:					A_f :	80497.9
ΔA_f - Fragmented area of a fragment-size fraction					a_{m_tot} :	5.860
A_f - Total fragmented area						
a_m - Mass-specific area (for a fragment-size fraction)						
a_{m_tot} - Total mass-specific area of a blasted cylinder						
a_s - Volume-specific area						
f_A - Particle-shape factor						
m_{sieve} - Total mass of sieved material						
s_n - Local slope (GGs exponent)						
x_a - The surface-equivalent fragment size						

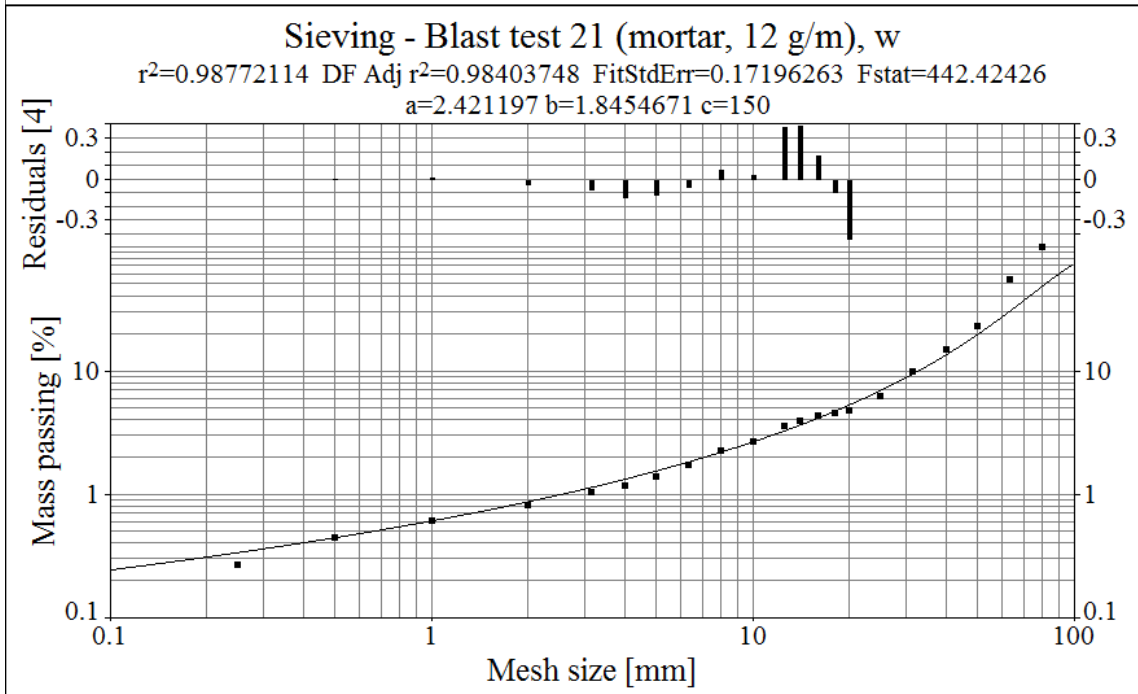
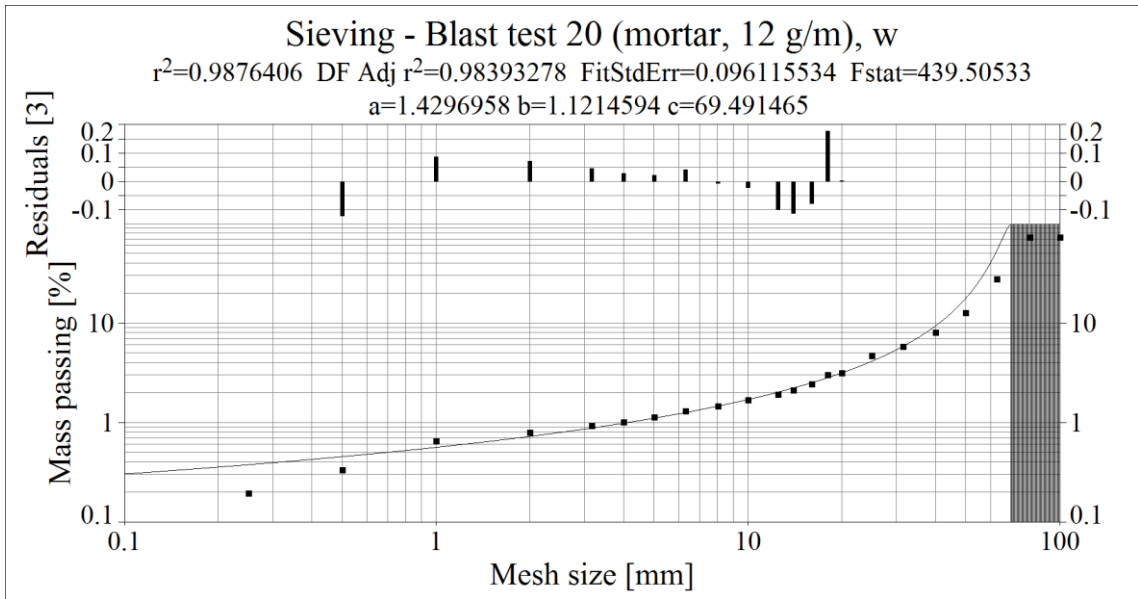
Fitting results – Swebrec 3p

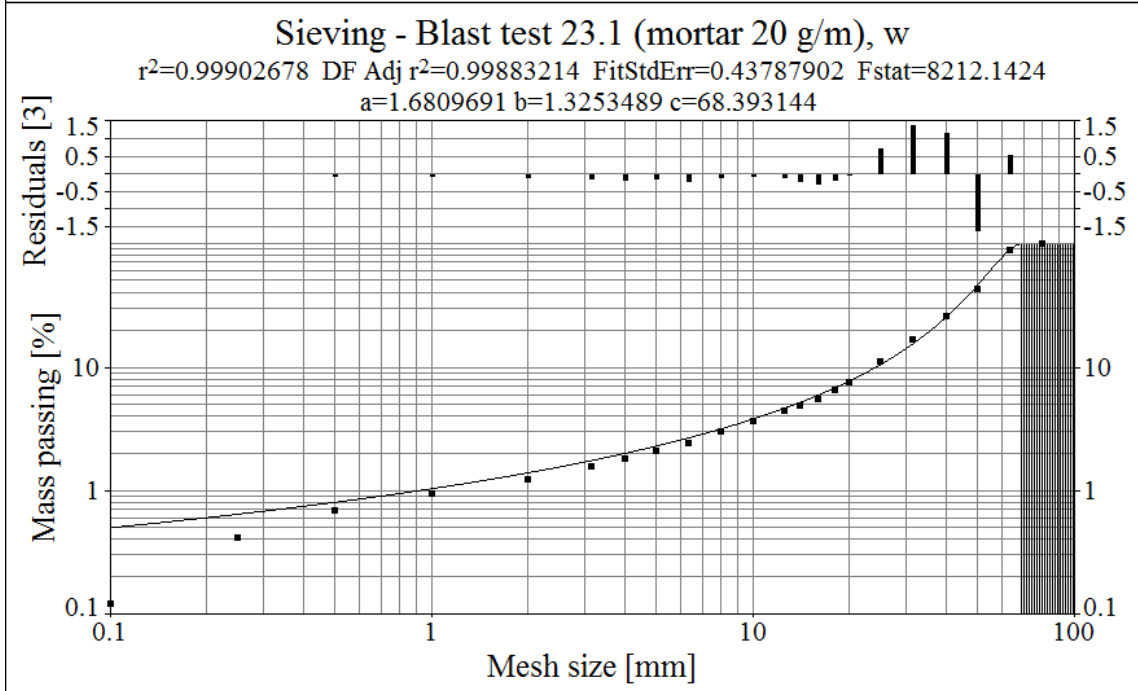
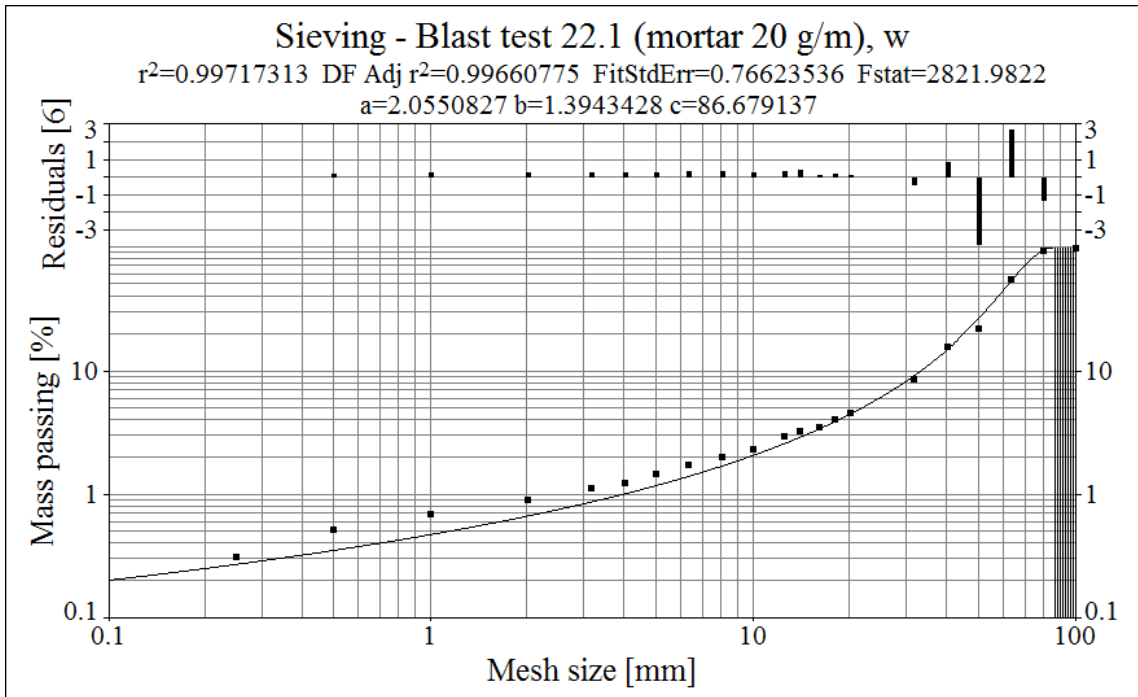
This section covers the curve-fitting results (see Section 5.10.1) for the Swebrec 3p function (Equation 46). The result parameters (a through c) in the following plots and result sets represent the parameters of this function written as:

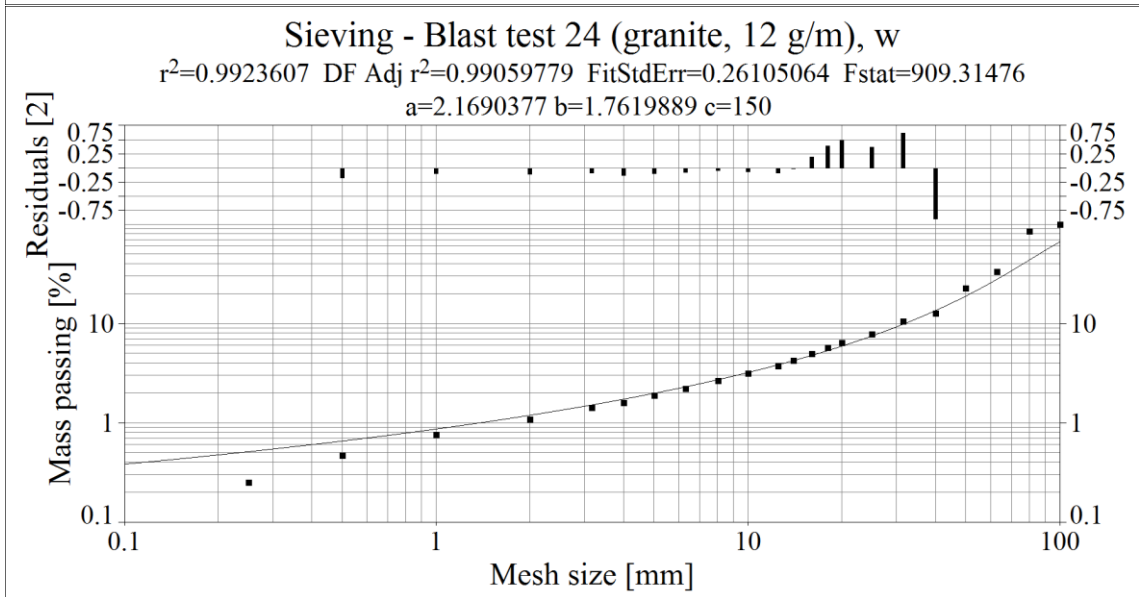
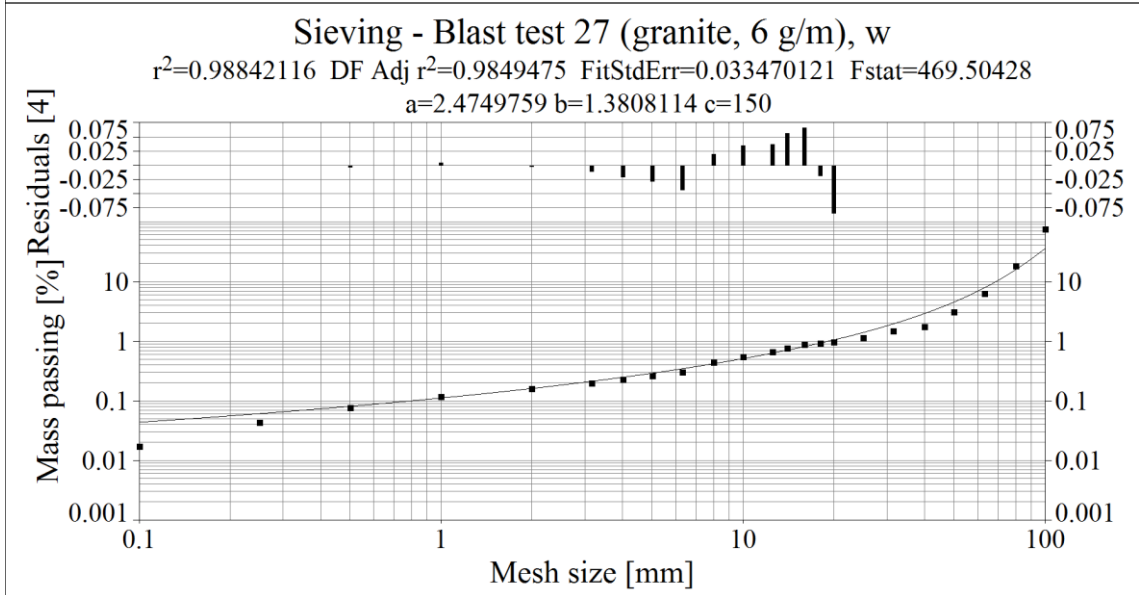
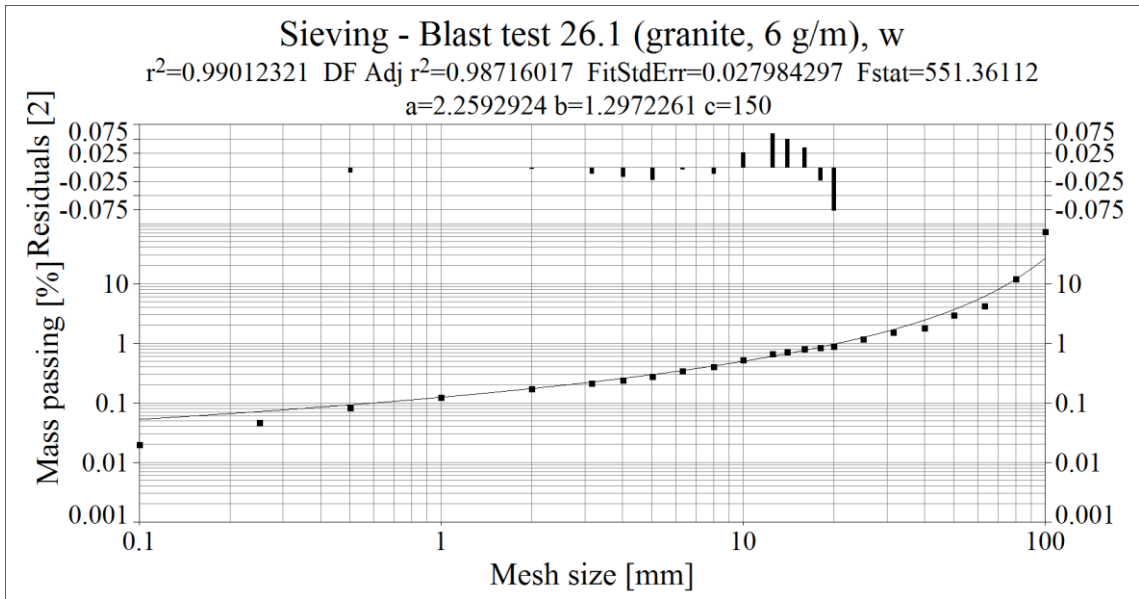
$$P(x) = 100 / (1 + (\text{LN}(c/x) / \text{LN}(b))^a)$$

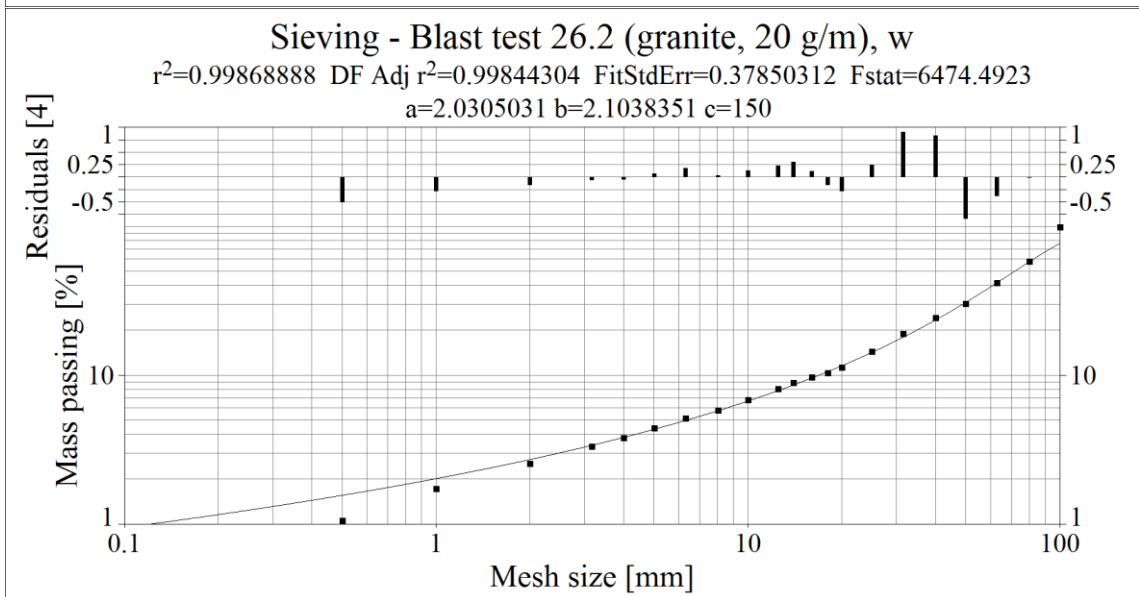
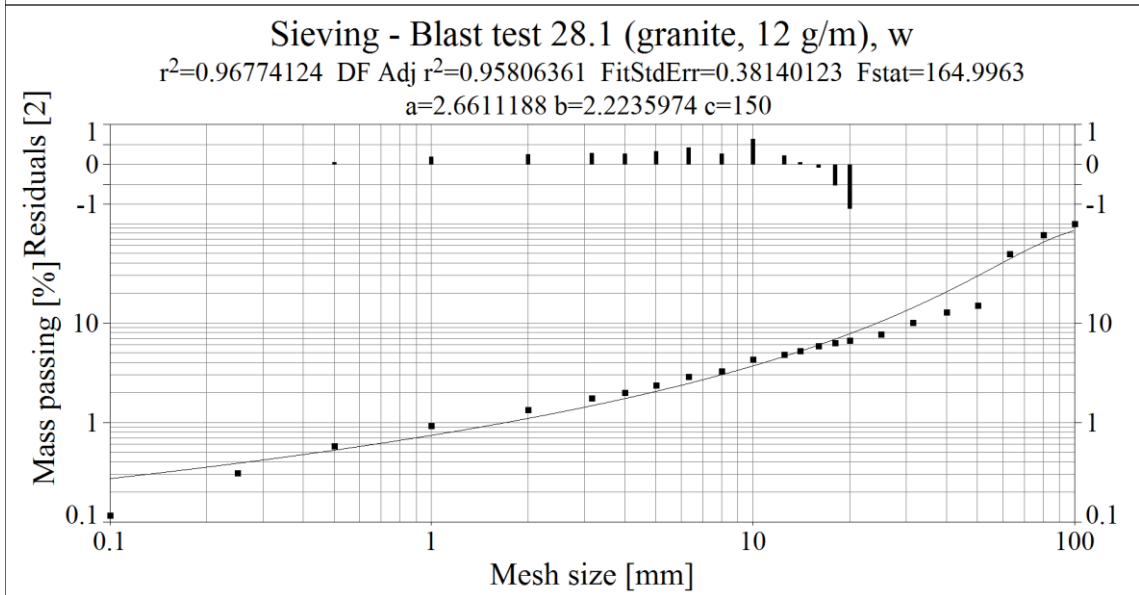
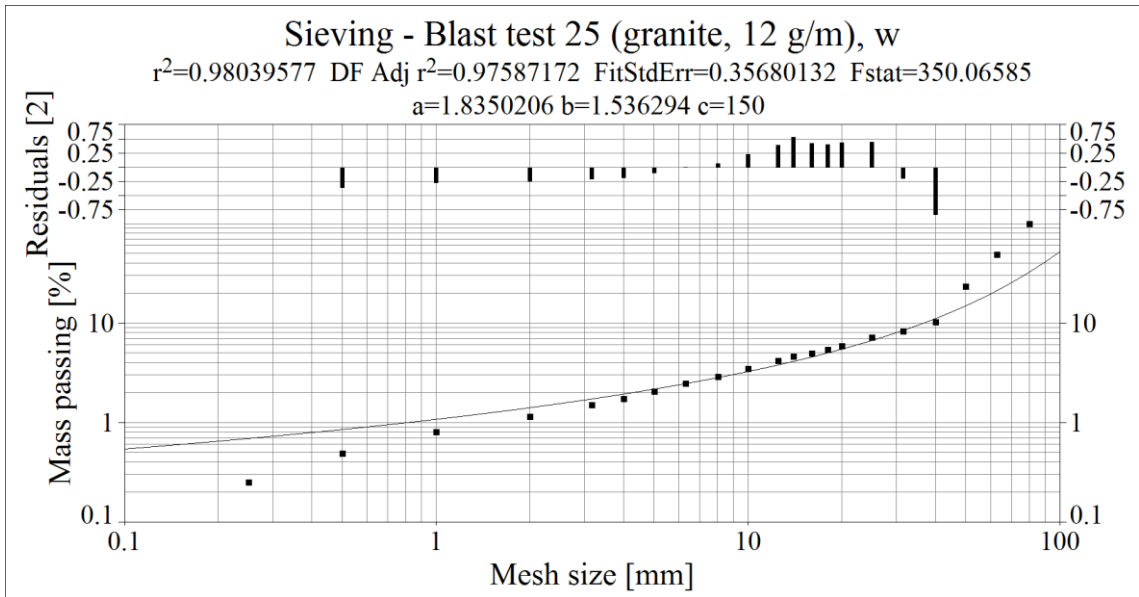
Equation 120







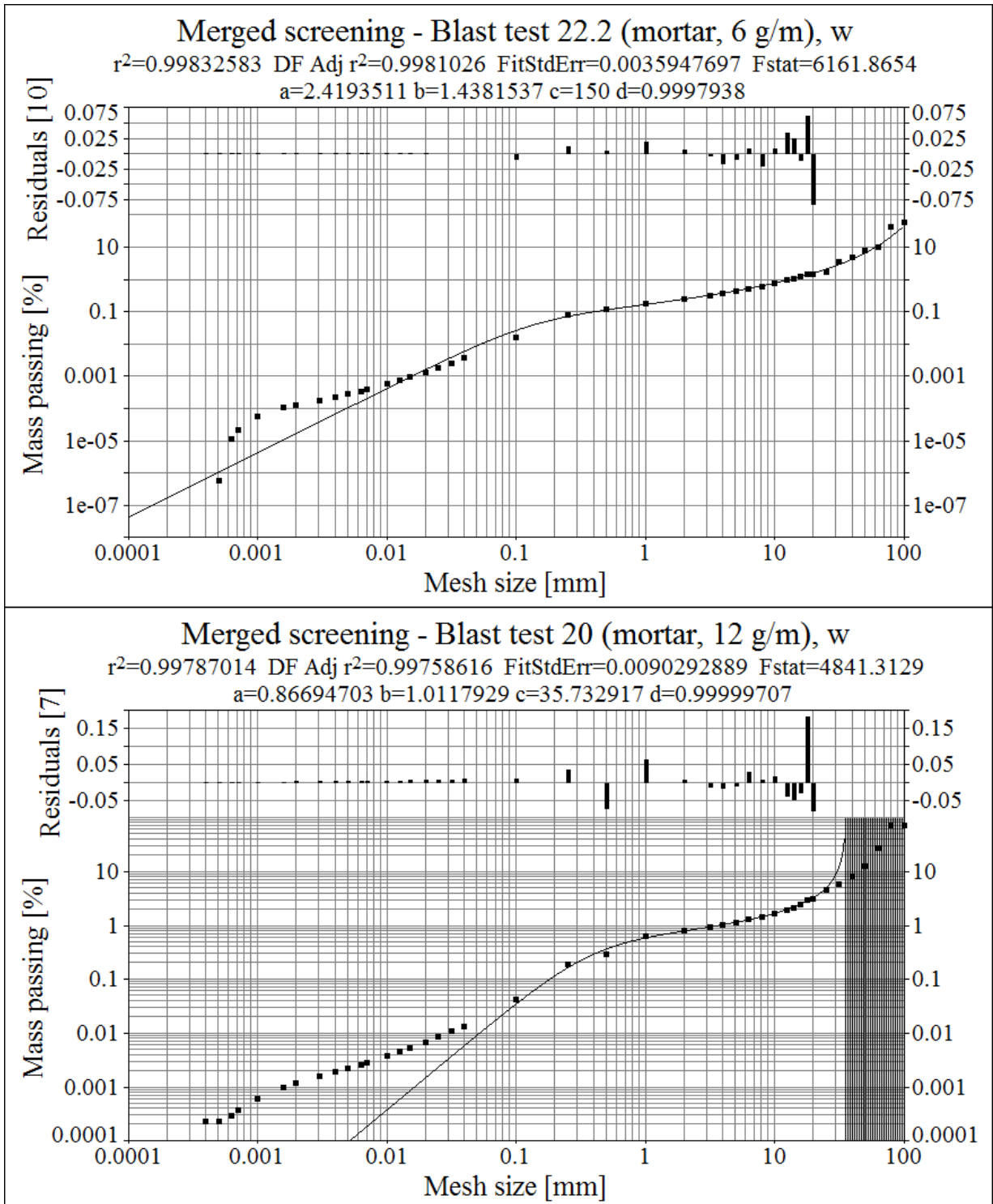


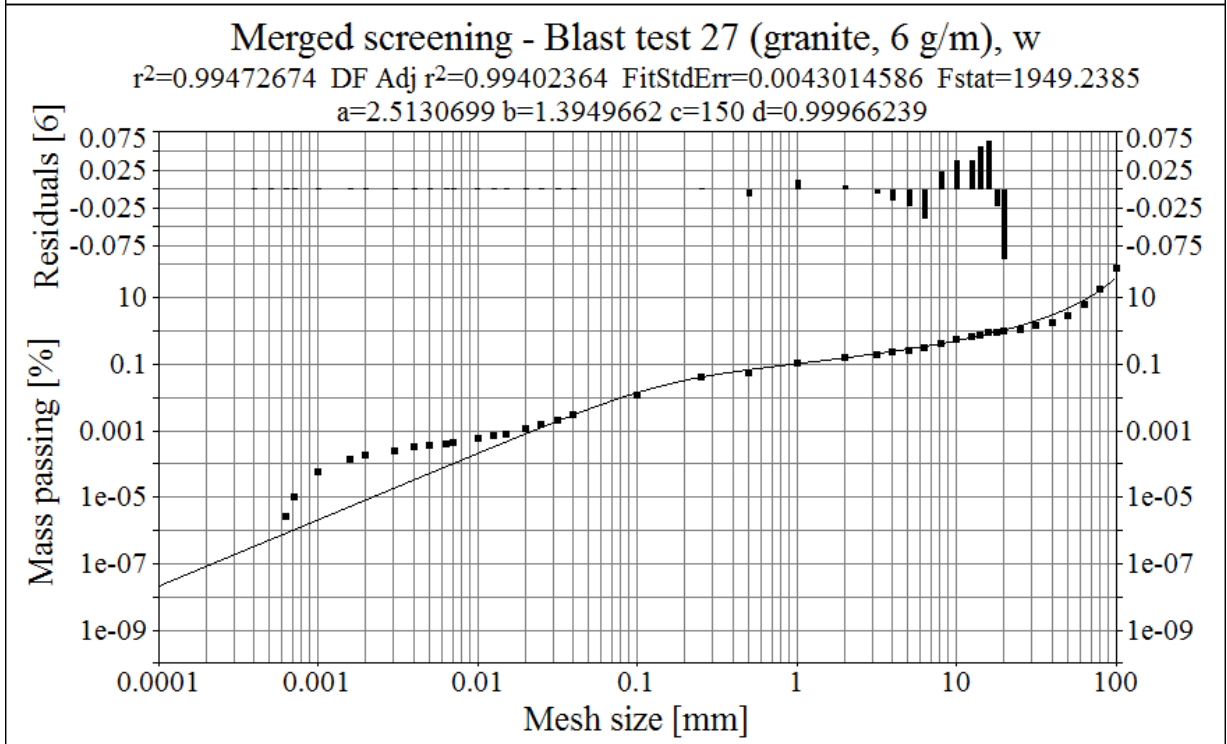
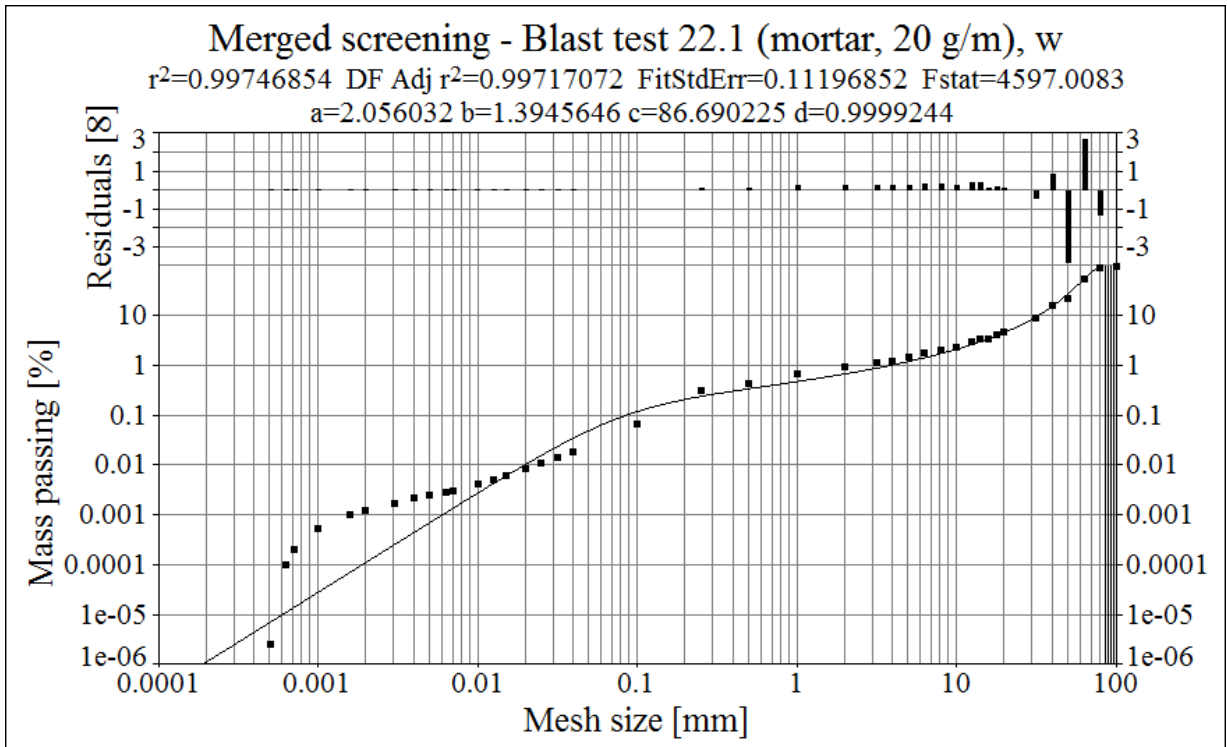


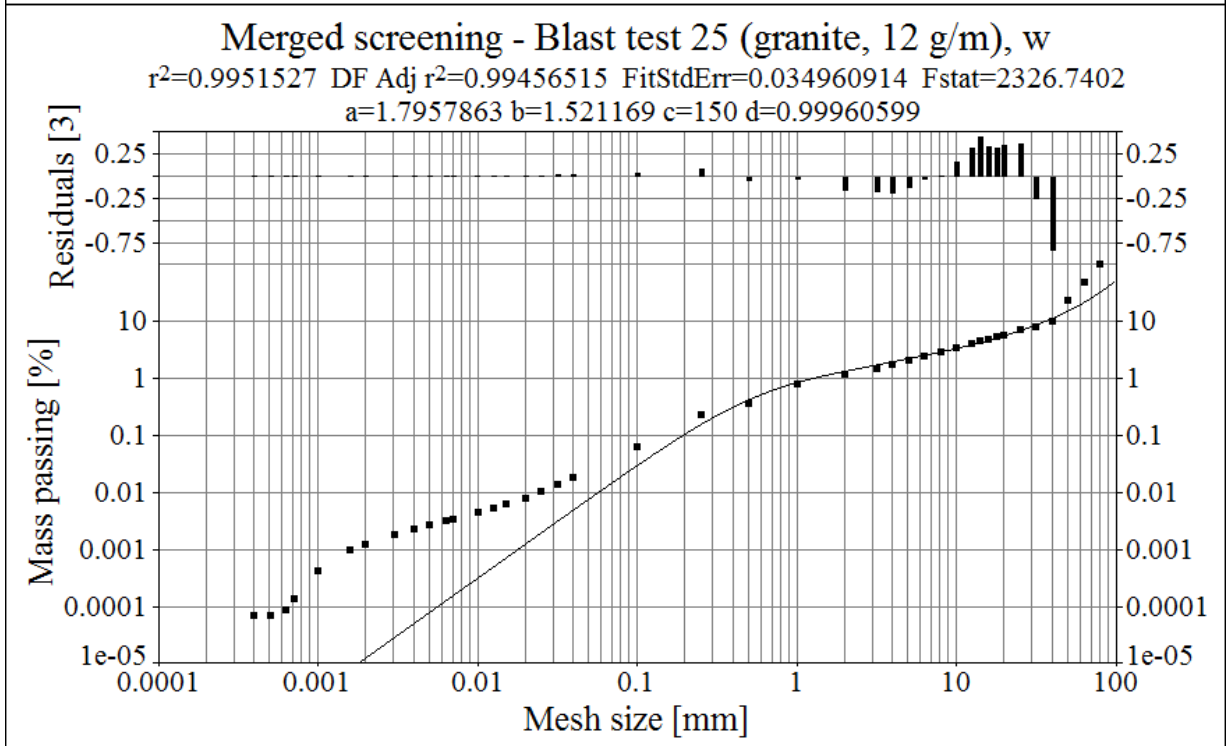
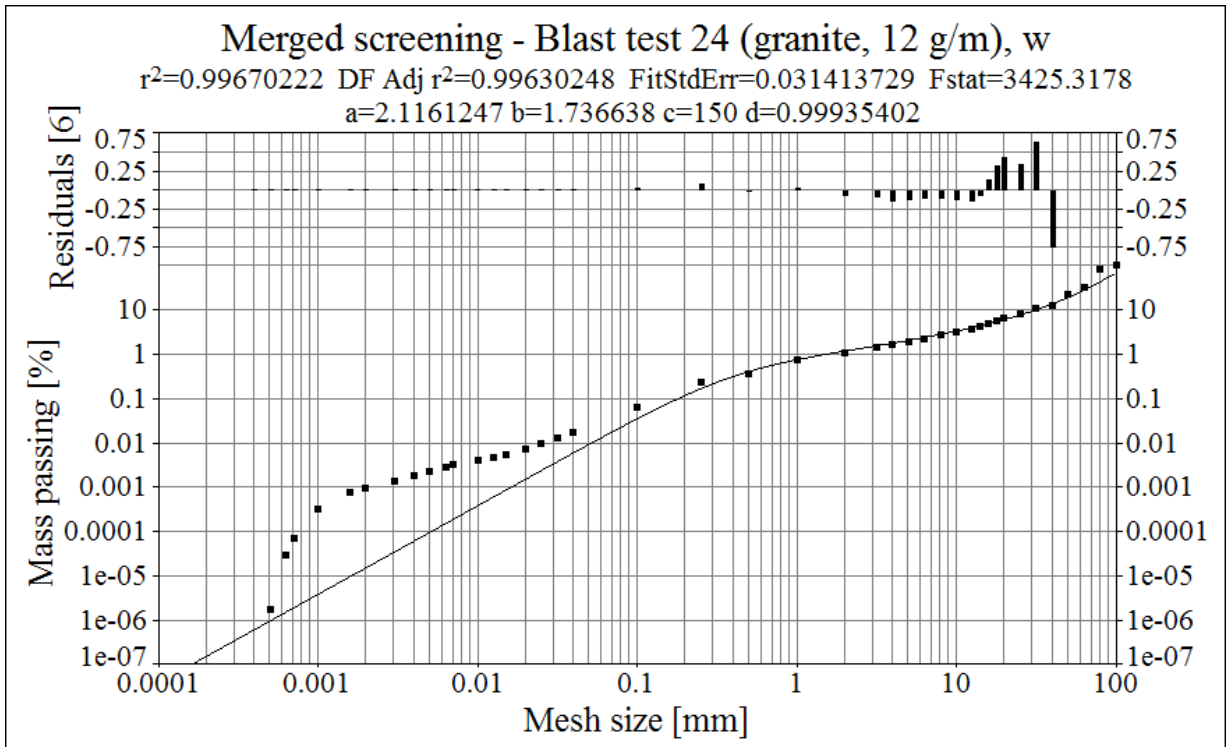
Fitting results – Swebrec 5p

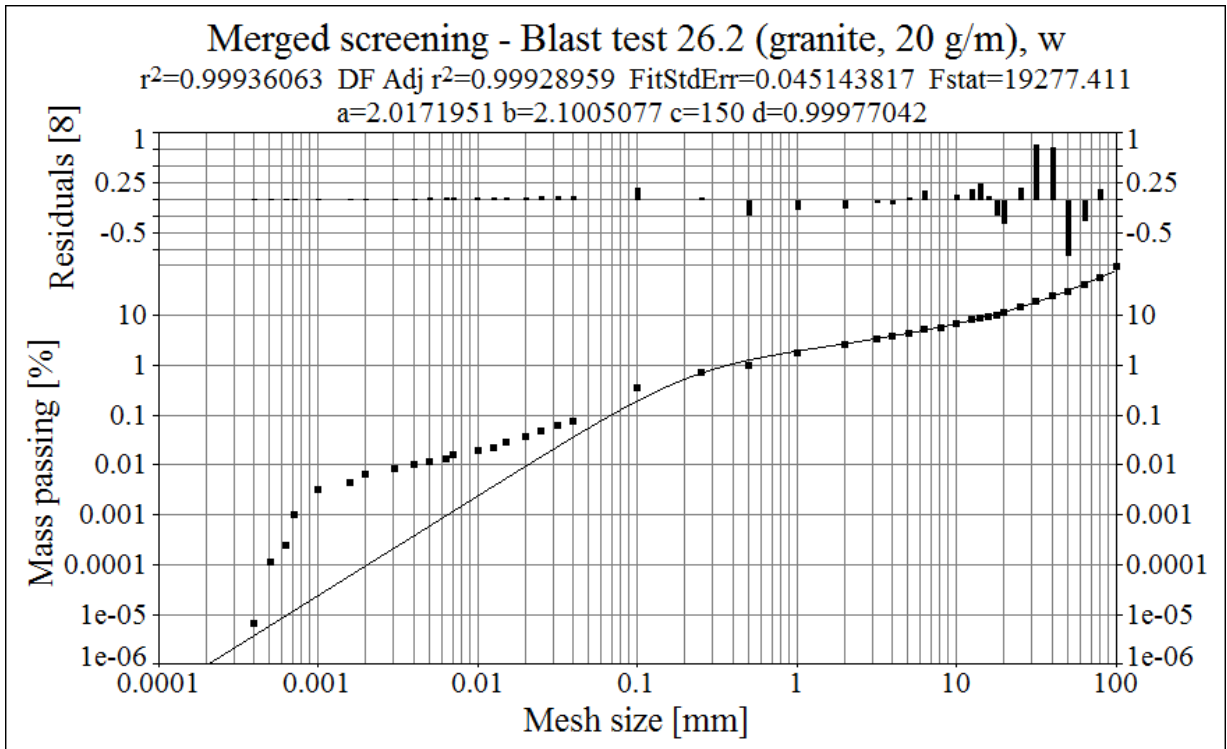
This section covers the curve-fitting results (see Section 5.10.1) for the Swebrec 5p function (Equation 47). The result parameters (a through d) in the following plots and result sets represent the parameters of this function written as:

$$P(x) = 100 / (1 + d * (\text{LN}(c/x) / \text{LN}(b))^a + (1 - d) * ((c/x - 1) / (b - 1))^2) \quad \text{Equation 121}$$

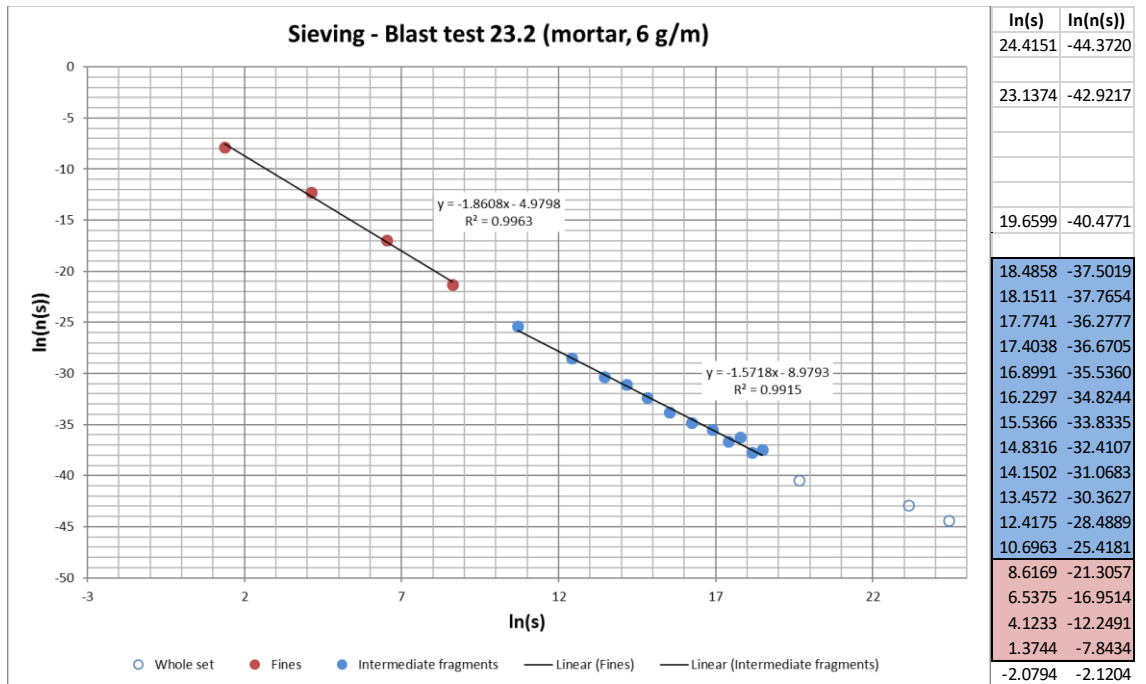
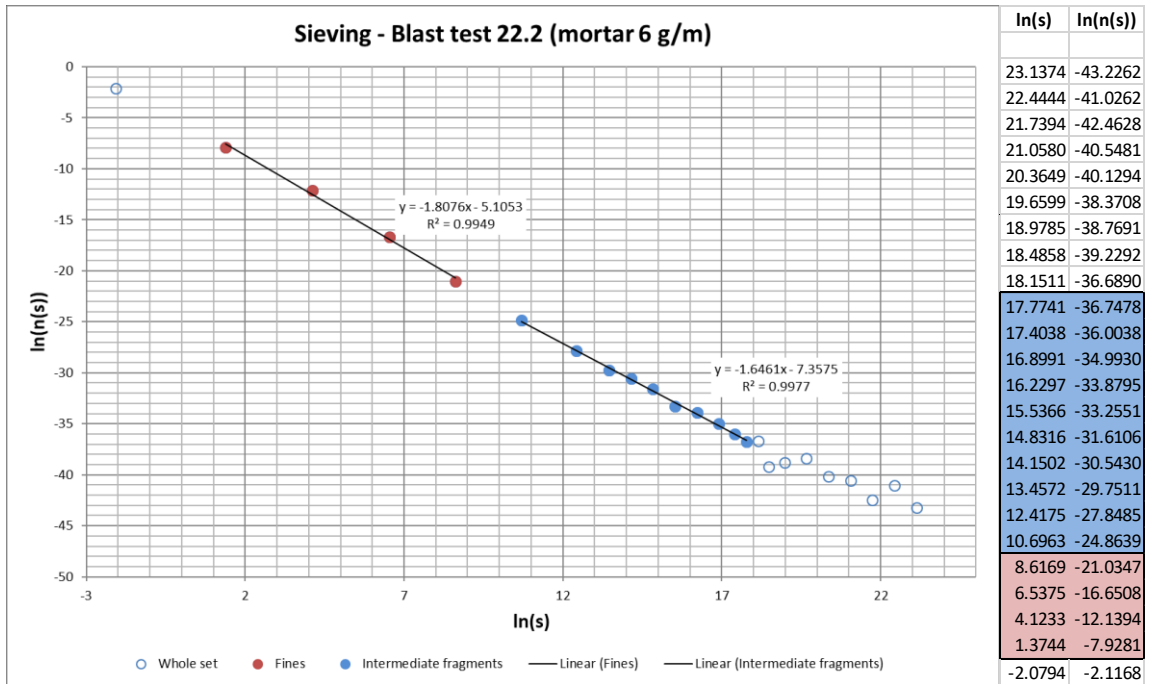


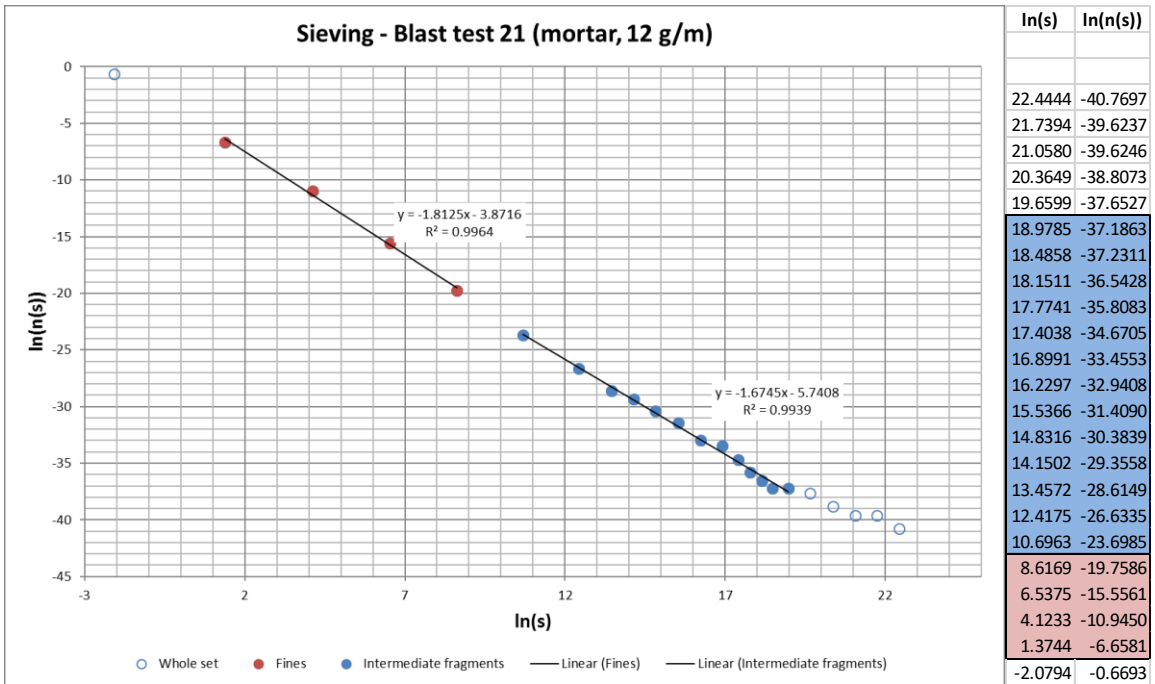
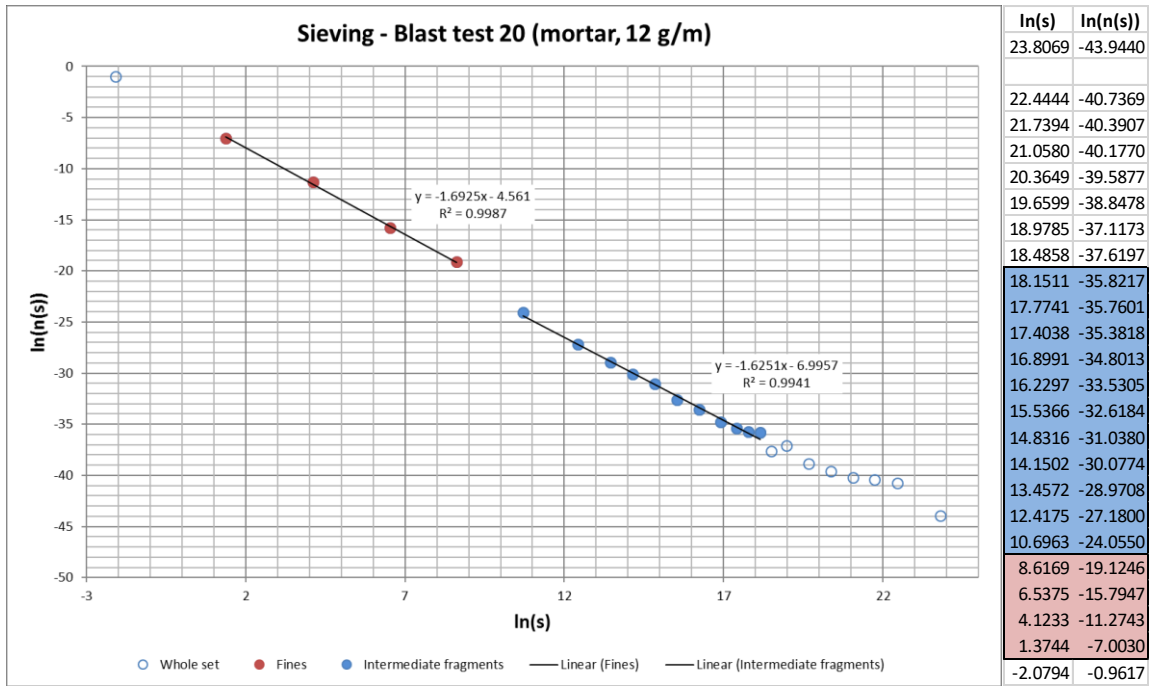


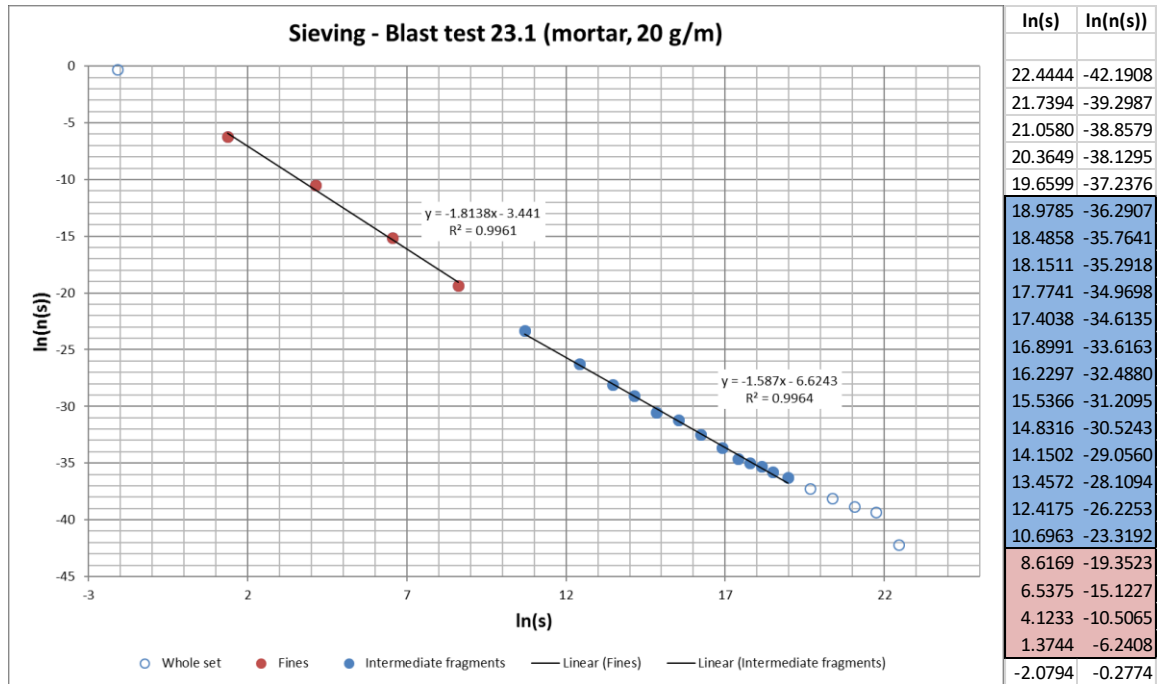
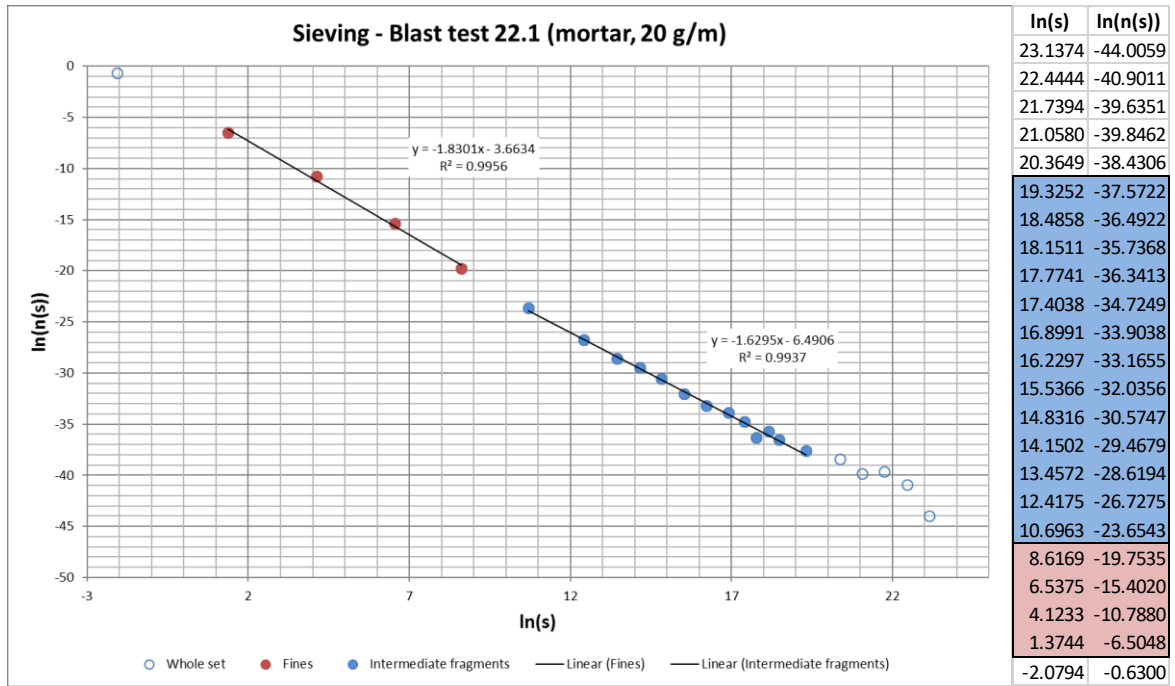


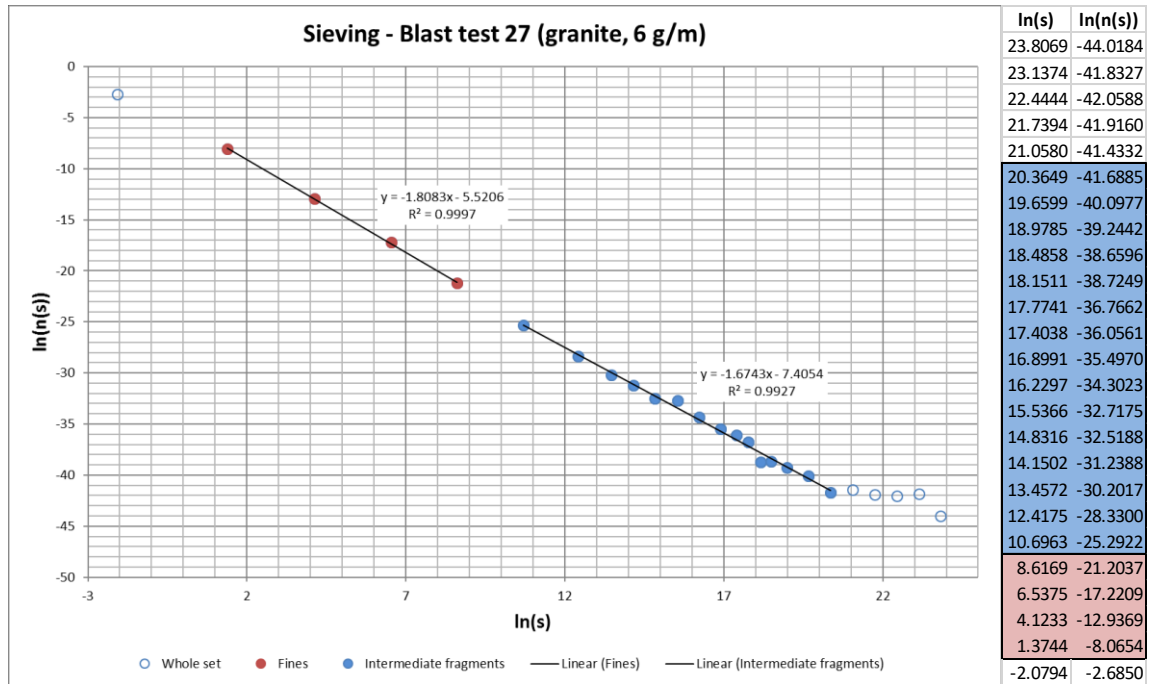
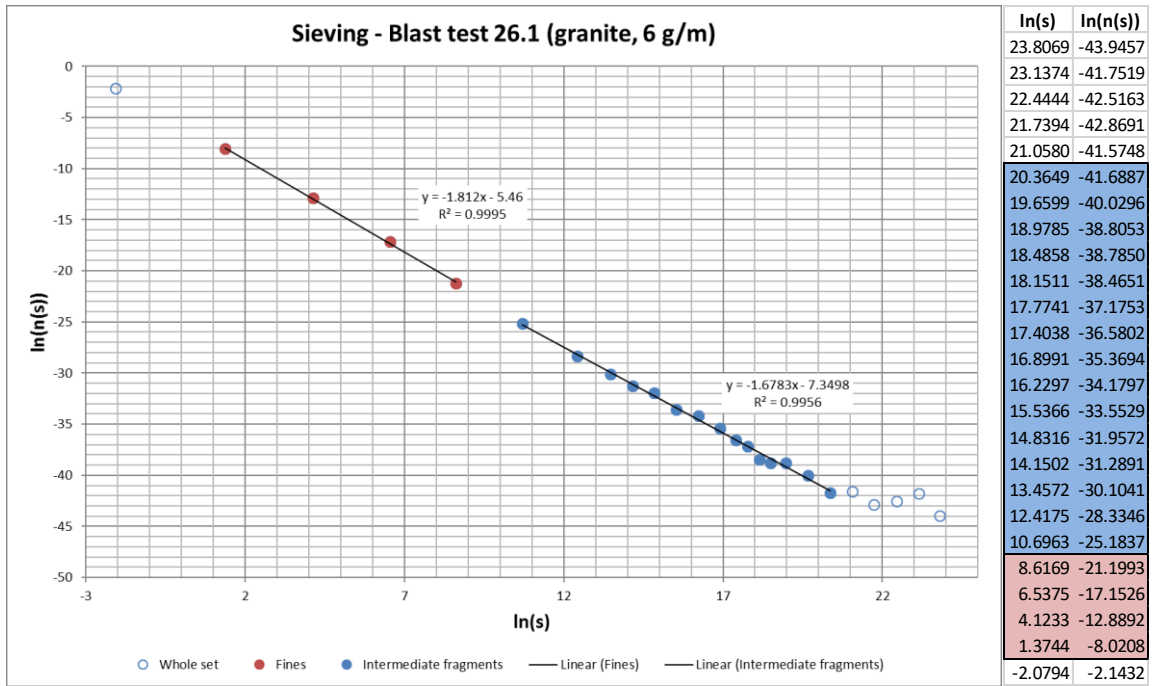


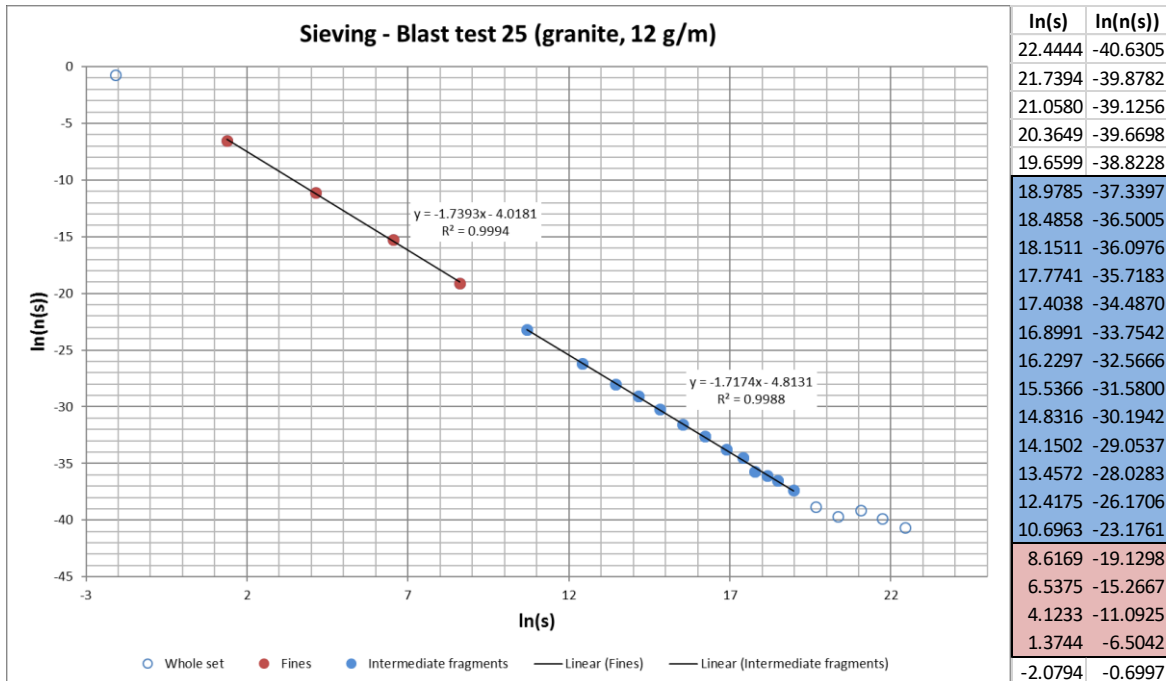
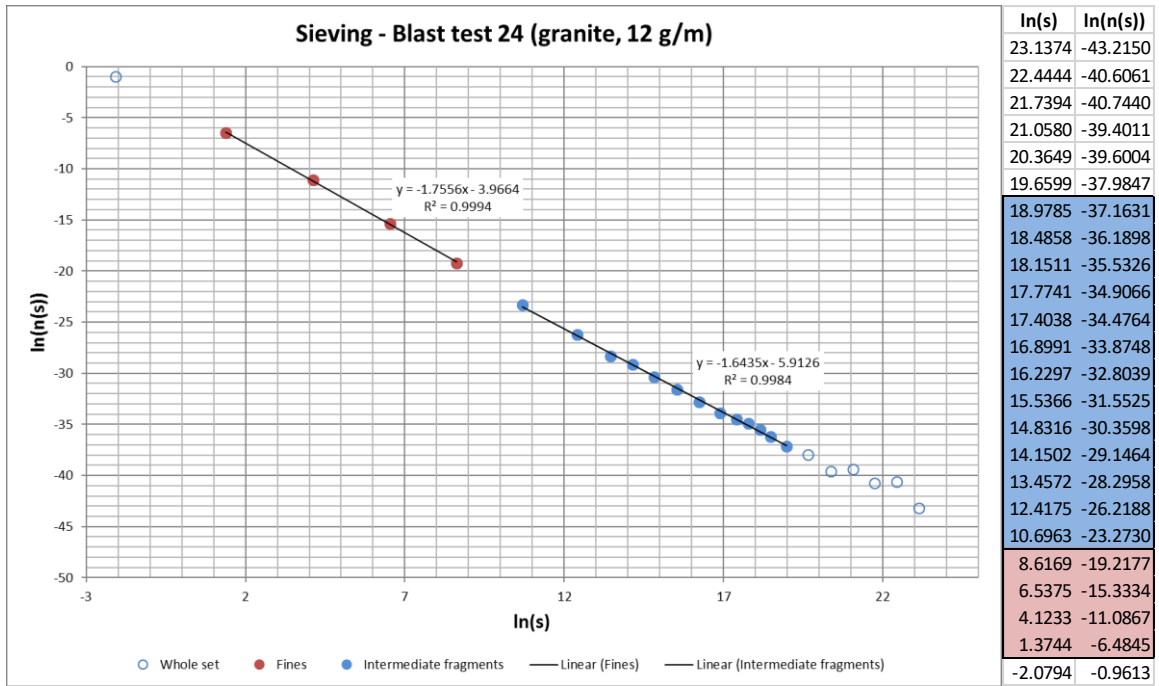
Resulting “s-n(s)” curves and raw fitting data

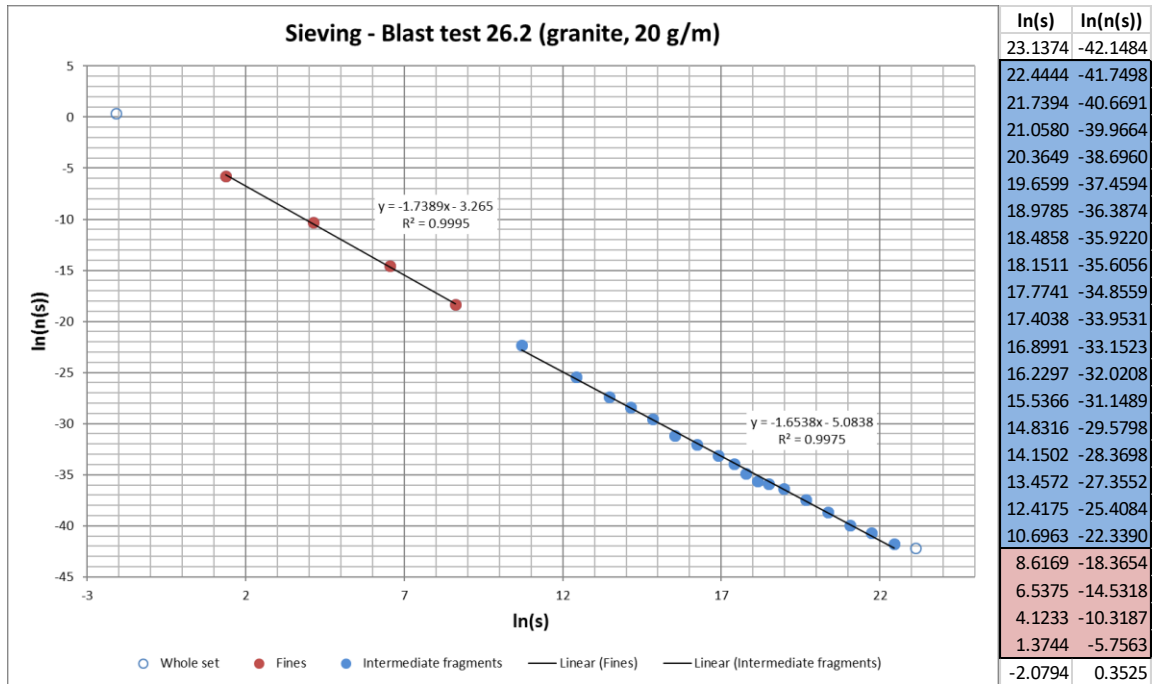
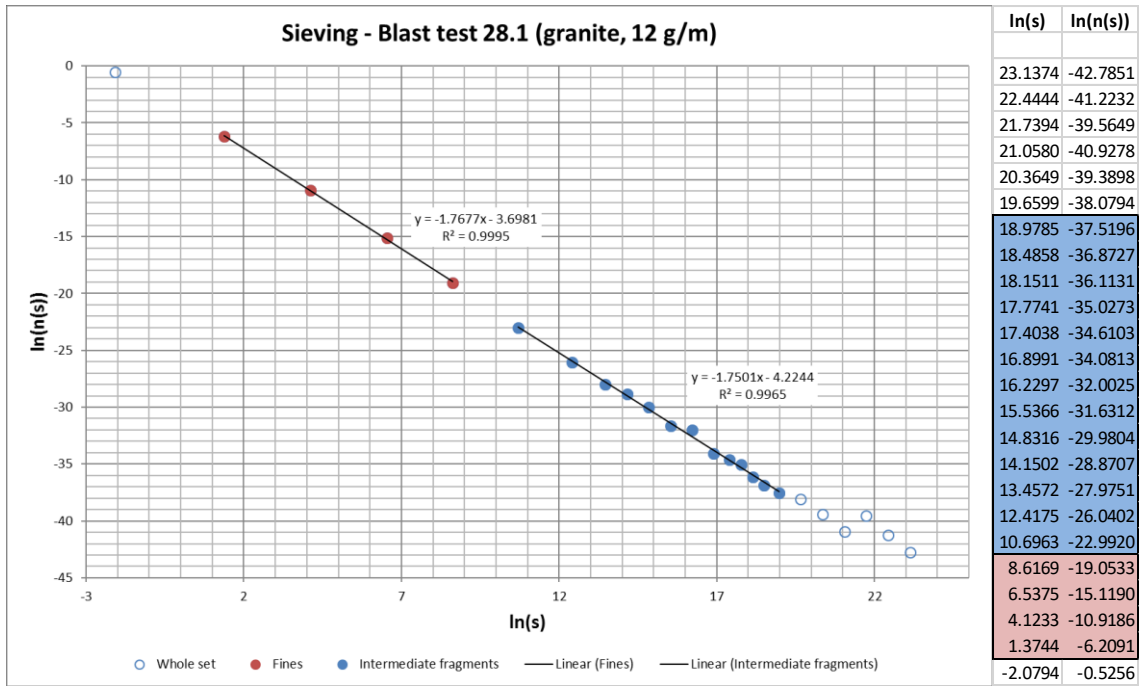


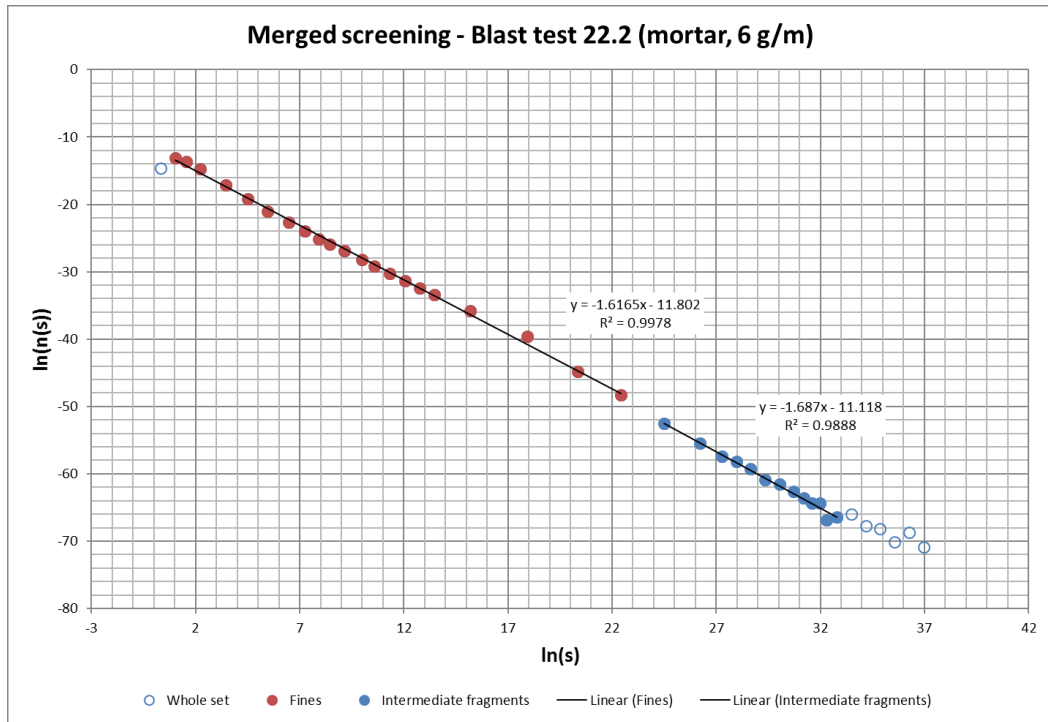




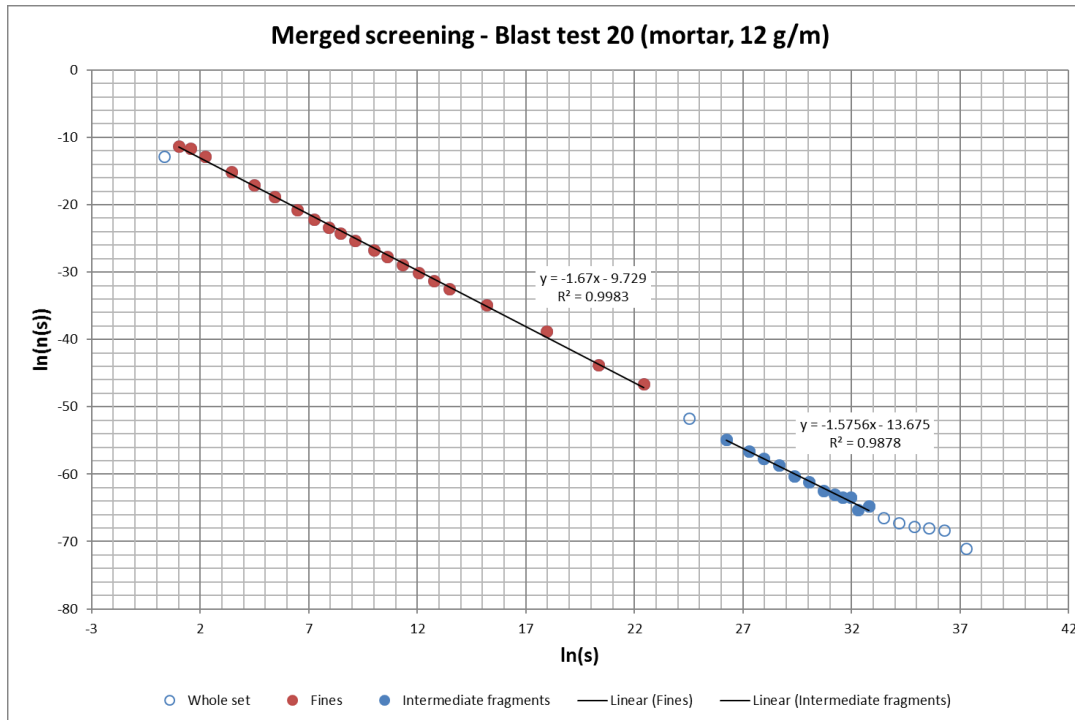




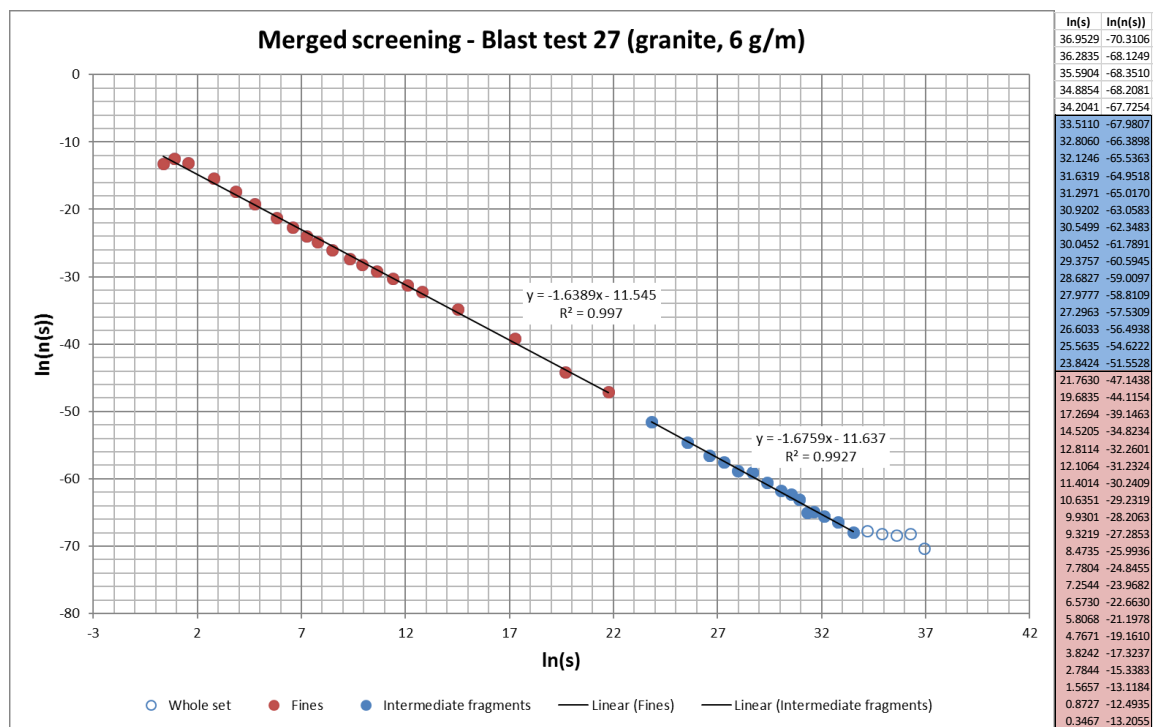
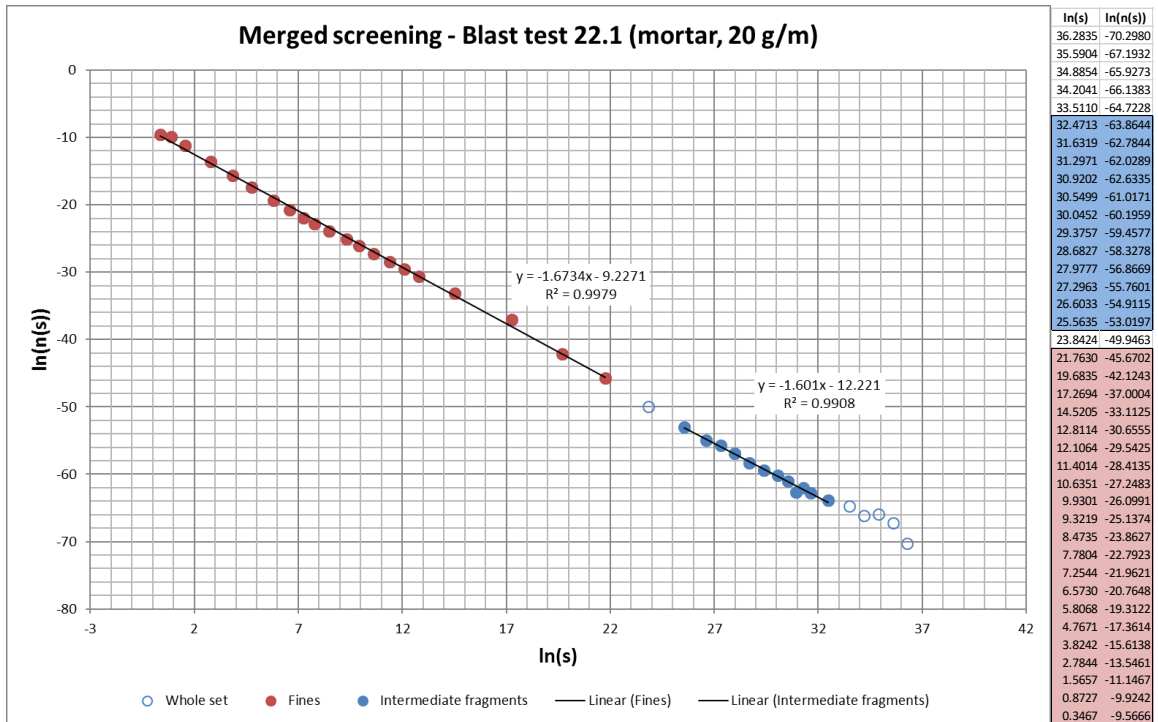


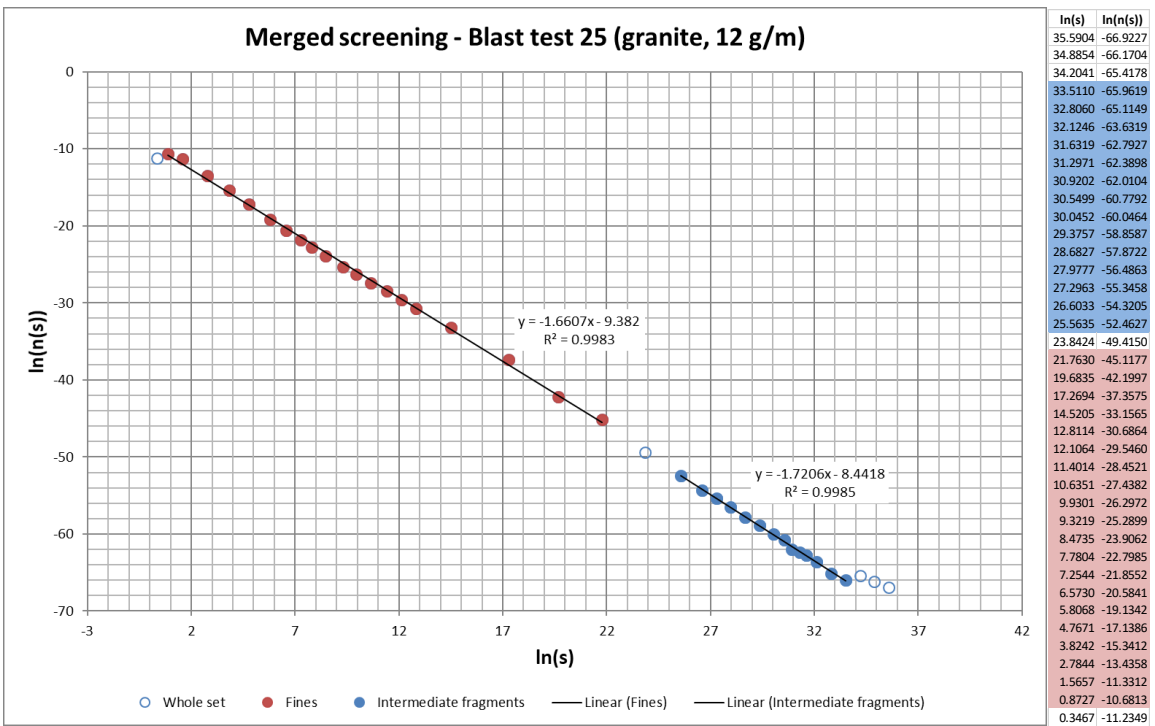
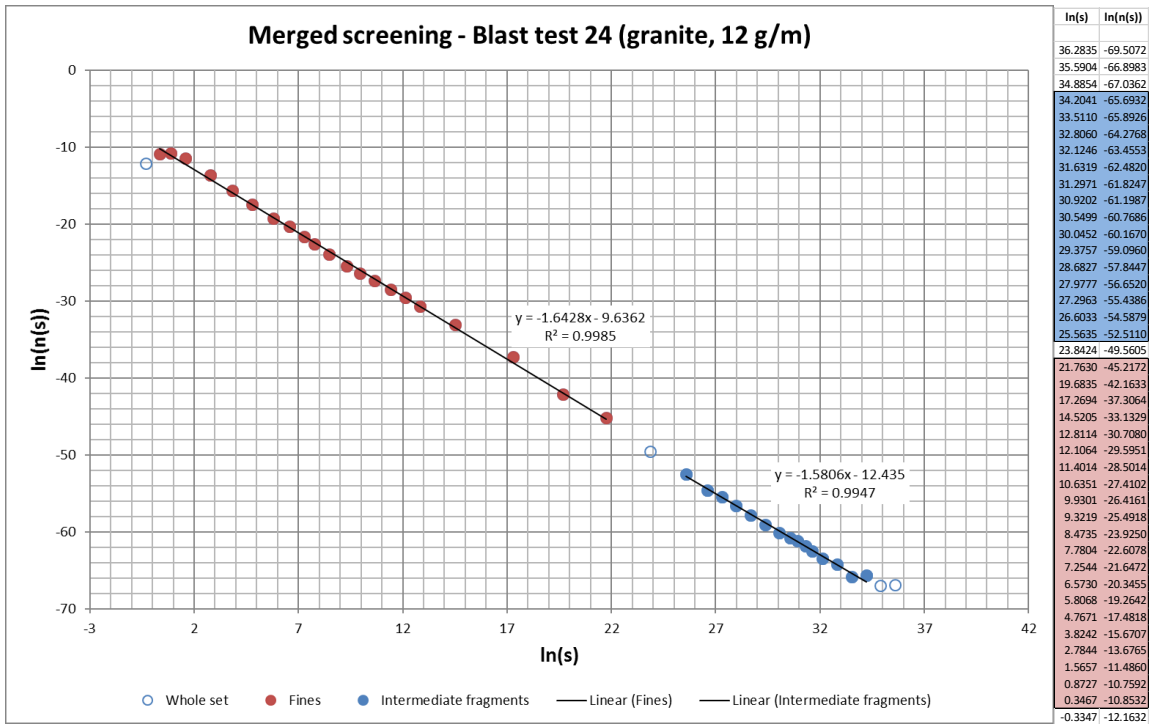


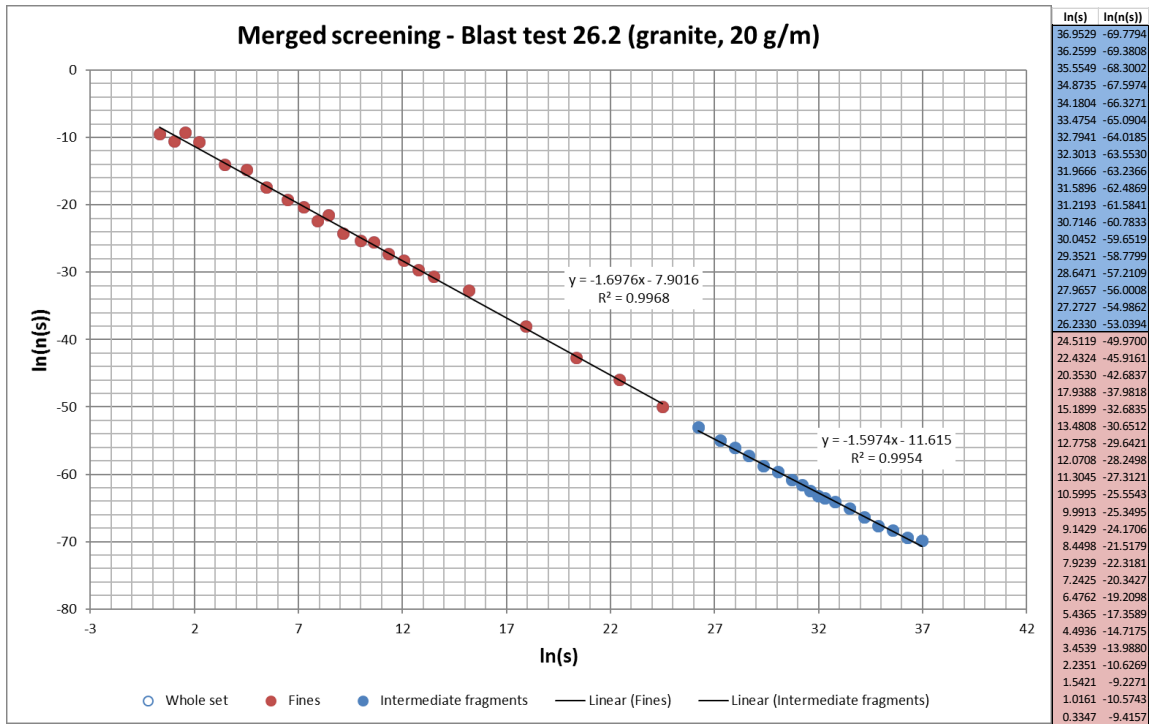
ln(s)	ln(n(s))
36.9529	-70.8572
36.2599	-68.6573
35.5549	-70.0938
34.8735	-68.1792
34.1804	-67.7604
33.4754	-66.0019
32.7941	-66.4002
32.3013	-66.8602
31.9666	-64.3201
31.5896	-64.3788
31.2193	-63.6349
30.7146	-62.6241
30.0452	-61.5106
29.3521	-60.8861
28.6471	-59.2417
27.9657	-58.1740
27.2727	-57.3821
26.2330	-55.4795
24.5119	-52.4942
22.4324	-48.3006
20.3530	-44.7694
17.9388	-39.6439
15.1899	-35.8329
13.4808	-33.4481
12.7758	-32.4070
12.0708	-31.3509
11.3045	-30.3102
10.5995	-29.1932
9.9913	-28.2082
9.1429	-26.9147
8.4498	-25.9400
7.9239	-25.1262
7.2425	-23.9298
6.4762	-22.7074
5.4365	-21.0088
4.4936	-19.2377
3.4539	-17.1153
2.2351	-14.7625
1.5421	-13.6135
1.0161	-13.0598
0.3347	-14.6576



ln(s)	ln(n(s))
37.2876	-71.0171
36.2599	-68.3679
35.5549	-68.0217
34.8735	-67.8081
34.1804	-67.2187
33.4754	-66.4788
32.7941	-64.7483
32.3013	-65.2508
31.9666	-63.4527
31.5896	-63.3911
31.2193	-63.0128
30.7146	-62.4323
30.0452	-61.1616
29.3521	-60.2494
28.6471	-58.6681
27.9657	-57.7084
27.2727	-56.6019
26.2330	-54.8110
24.5119	-51.6860
22.4324	-46.6298
20.3530	-43.7868
17.9388	-38.8100
15.1899	-34.9172
13.4808	-32.5008
12.7758	-31.3222
12.0708	-30.1503
11.3045	-28.9305
10.5995	-27.7252
9.9913	-26.7149
9.1429	-25.3567
8.4498	-24.2749
7.9239	-23.3930
7.2425	-22.2000
6.4762	-20.7616
5.4365	-18.8316
4.4936	-17.0732
3.4539	-15.1118
2.2351	-12.8201
1.5421	-11.6281
1.0161	-11.3032
0.3347	-12.8094







Appendix 19 **Blaine and Permeran tests (raw data)**

[Appendix 19 - Blaine and Permeran tests \(raw data\)](#)

Appendix 20 Correlation analysis (raw data tables)

This section contains raw results from the statistical correlation analysis of result parameters listed in Table 57 (see Section 5.11).

Table 179: Correlation of results from group A, covering all blast tests from the final test phase.

<i>Linear</i>	C_p [m/s]	q [kg/m ³]	$m_{-1\text{ mm}}$ [%]	x_{50} log [mm]	β (s-n(s)_F) sieving	α (s-n(s)_IF) sieving
C_p [m/s]	1.0000					
q [kg/m ³]	-0.0783	1.0000				
$m_{-1\text{ mm}}$ [%]	0.2286	0.8497	1.0000			
x_{50} log [mm]	-0.0121	-0.7513	-0.6462	1.0000		
β (s-n(s)_F) sieving	-0.2700	-0.1502	-0.3718	0.4403	1.0000	
α (s-n(s)_IF) sieving	0.6244	-0.1237	0.1232	-0.3288	-0.3693	1.0000
<i>LN</i>	C_p [m/s]	q [kg/m ³]	$m_{-1\text{ mm}}$ [%]	x_{50} log [mm]	β (s-n(s)_F) sieving	α (s-n(s)_IF) sieving
C_p [m/s]	1.0000					
q [kg/m ³]	-0.0459	1.0000				
$m_{-1\text{ mm}}$ [%]	0.0599	0.9264	1.0000			
x_{50} log [mm]	0.0466	-0.8469	-0.8214	1.0000		
β (s-n(s)_F) sieving	-0.2604	-0.2737	-0.4706	0.3704	1.0000	
α (s-n(s)_IF) sieving	0.6254	-0.0237	0.1450	-0.2659	-0.3632	1.0000

Table 180: Correlation of results from group B, covering blast test from group A without g12(28.1)

<i>Linear</i>	C_p [m/s]	q [kg/m ³]	p_c (HSI) slope	p_{20} (HSI) slope	p_{21} (HSI) slope	C_{ave} [m/s]	$m_{-1\text{ mm}}$ [%]	x_{50} log [mm]	β (s-n(s)_F) sieving	α (s-n(s)_IF) sieving	β (s-n(s)_UF) merged	α (s-n(s)_IF) merged
C_p [m/s]	1.0000											
q [kg/m ³]	0.0358	1.0000										
p_c (HSI) slope	0.6953	0.4193	1.0000									
p_{20} (HSI) slope	0.7664	0.2508	0.5627	1.0000								
p_{21} (HSI) slope	0.7786	0.5648	0.8940	0.8138	1.0000							
C_{ave} [m/s]	0.2152	0.6950	0.4548	-0.0330	0.3963	1.0000						
$m_{-1\text{ mm}}$ [%]	0.3475	0.8342	0.8027	0.4744	0.8423	0.5421	1.0000					
x_{50} log [mm]	0.0158	-0.7680	-0.0641	-0.4046	-0.4180	-0.1703	-0.5842	1.0000				
β (s-n(s)_F) sieving	-0.0458	0.0347	-0.0915	-0.2328	-0.1615	0.3545	-0.2222	0.2931	1.0000			
α (s-n(s)_IF) sieving	0.5648	-0.2553	0.1494	0.2626	0.2635	-0.2155	-0.0394	-0.0230	-0.1056	1.0000		
β (s-n(s)_UF) merged	0.1356	0.8605	0.5516	0.1219	0.5743	0.7376	0.8593	-0.5790	-0.2498	-0.0977	1.0000	
α (s-n(s)_IF) merged	0.1968	-0.5660	-0.1634	-0.1821	-0.2031	-0.3641	-0.4382	0.3709	0.2290	0.8235	-0.4620	1.0000
<i>LN</i>	C_p [m/s]	q [kg/m ³]	p_c (HSI) slope	p_{20} (HSI) slope	p_{21} (HSI) slope	C_{ave} [m/s]	$m_{-1\text{ mm}}$ [%]	x_{50} log [mm]	β (s-n(s)_F) sieving	α (s-n(s)_IF) sieving	β (s-n(s)_UF) merged	α (s-n(s)_IF) merged
C_p [m/s]	1.0000											
q [kg/m ³]	0.0628	1.0000										
p_c (HSI) slope	0.9352	0.6490	1.0000									
p_{20} (HSI) slope	0.8021	0.5389	0.9034	1.0000								
p_{21} (HSI) slope	0.7494	0.6407	0.9209	0.9802	1.0000							
C_{ave} [m/s]	0.2317	0.5952	0.7064	0.4127	0.5512	1.0000						
$m_{-1\text{ mm}}$ [%]	0.1749	0.9141	0.5377	0.5734	0.6469	0.3271	1.0000					
x_{50} log [mm]	0.0163	-0.8473	-0.4217	-0.4952	-0.5262	-0.1979	-0.8169	1.0000				
β (s-n(s)_F) sieving	-0.0356	-0.1226	0.1155	-0.2498	-0.2491	0.3121	-0.3912	0.2579	1.0000			
α (s-n(s)_IF) sieving	0.5677	-0.2178	0.2860	0.3016	0.2504	-0.2032	-0.0794	-0.0383	-0.0953	1.0000		
β (s-n(s)_UF) merged	0.1356	0.8542	0.5617	0.4719	0.6308	0.7375	0.7943	-0.5690	-0.2531	-0.0986	1.0000	
α (s-n(s)_IF) merged	0.1955	-0.5956	-0.1783	-0.2456	-0.3012	-0.3731	-0.5268	0.3451	0.2387	0.8222	-0.4630	1.0000

Table 181: Correlation of results from group C, covering blast tests m20(22.1), m12(20), m6(22.2), g20(26.2), g12(24), g12(25), and g6(27).

Linear	C_p [m/s]	q [kg/m ³]	p_c (HSI) slope	p_{20} (HSI) slope	p_{21} (HSI) slope	C_{ave} [m/s]	$m_{-1\text{mm}}$ [%]	x_{50} log [mm]	β (s-n(s)_F) sieving	α (s-n(s)_IF) sieving
C_p [m/s]	1.0000									
q [kg/m ³]	-0.0884	1.0000								
p_c (HSI) slope	0.3931	0.4681	1.0000							
p_{20} (HSI) slope	0.6909	0.2568	0.4472	1.0000						
p_{21} (HSI) slope	0.6203	0.5888	0.8317	0.8098	1.0000					
C_{ave} [m/s]	0.1271	0.6655	0.4320	-0.0448	0.3644	1.0000				
$m_{-1\text{mm}}$ [%]	0.1825	0.8622	0.7497	0.4900	0.8395	0.5344	1.0000			
x_{50} log [mm]	0.0542	-0.7640	-0.1683	-0.2953	-0.3975	-0.4684	-0.6315	1.0000		
β (s-n(s)_F) sieving	-0.2414	-0.1490	-0.0391	-0.4082	-0.3009	0.1522	-0.3550	0.4247	1.0000	
α (s-n(s)_IF) sieving	0.5809	-0.1687	-0.0816	0.2971	0.1818	0.0692	0.0111	-0.2610	-0.3599	1.0000
LN	C_p [m/s]	q [kg/m ³]	p_c (HSI) slope	p_{20} (HSI) slope	p_{21} (HSI) slope	C_{ave} [m/s]	$m_{-1\text{mm}}$ [%]	x_{50} log [mm]	β (s-n(s)_F) sieving	α (s-n(s)_IF) sieving
C_p [m/s]	1.0000									
q [kg/m ³]	-0.0754	1.0000								
p_c (HSI) slope	0.4234	0.5535	1.0000							
p_{20} (HSI) slope	0.7092	0.4879	0.7454	1.0000						
p_{21} (HSI) slope	0.5470	0.6005	0.8779	0.9419	1.0000					
C_{ave} [m/s]	0.1449	0.6024	0.6103	0.3844	0.5318	1.0000				
$m_{-1\text{mm}}$ [%]	-0.0118	0.9358	0.4479	0.5256	0.5917	0.3942	1.0000			
x_{50} log [mm]	0.1178	-0.8510	-0.2906	-0.3624	-0.4119	-0.4810	-0.8124	1.0000		
β (s-n(s)_F) sieving	-0.2325	-0.2655	0.2405	-0.3543	-0.2324	0.1257	-0.4557	0.3530	1.0000	
α (s-n(s)_IF) sieving	0.5807	-0.0911	-0.0705	0.3157	0.1161	0.0973	0.0097	-0.1808	-0.3535	1.0000

Table 182: Correlation of results from group D, covering blast tests m20(23.1), m12(21), m6(23.2), g12(28.1), and g6(26.1).

Linear	C_p [m/s]	q [kg/m ³]	N [-] (CT)	Std D_{cent} (CT)	Std D_{cent} (CTnp)	Ave p_c (CT)	p_{20} [mm ⁻²] (CT)	p_{21} [mm ⁻¹] (CT)	2D-frag. count (CT)	2D-frag. Std D_{cent} (CT)	C_{ave} [m/s]	Ave $r_{bh, norm}$ [mm]	Ave δr_m [mm]	$m_{-1 mm}$ [%]	$x_{50 log}$ [mm]	β (s-n(s)_F) sieving	α (s-n(s)_IF) sieving
C_p [m/s]	1.0000																
q [kg/m ³]	-0.3106	1.0000															
N [-] (CT)	-0.0083	0.7491	1.0000														
Std D_{cent} (CT)	0.0191	-0.9197	-0.9011	1.0000													
Std D_{cent} (CTnp)	-0.6030	0.0468	0.3648	-0.0290	1.0000												
Ave p_c (CT)	0.9604	-0.4964	-0.1422	0.2326	-0.4845	1.0000											
p_{20} [mm ⁻²] (CT)	-0.4248	0.8730	0.8430	-0.8832	0.3808	-0.6027	1.0000										
p_{21} [mm ⁻¹] (CT)	-0.3325	0.8879	0.8829	-0.9249	0.3268	-0.5201	0.9945	1.0000									
2D-frag. count (CT)	-0.1750	0.8047	0.8561	-0.9150	0.2117	-0.3951	0.9538	0.9690	1.0000								
2D-frag. Std D_{cent} (CT)	0.0963	-0.7778	-0.9531	0.9253	-0.3140	0.2814	-0.9310	-0.9574	-0.9699	1.0000							
C_{ave} [m/s]	0.0589	0.7073	0.9168	-0.8398	0.2861	-0.0035	0.6060	0.6707	0.6191	-0.7779	1.0000						
Ave $r_{bh, norm}$ [mm]	-0.5609	0.9204	0.4779	-0.6931	0.0633	-0.6909	0.7306	0.7152	0.5738	-0.5112	0.5427	1.0000					
Ave δr_m [mm]	0.6424	-0.0164	0.4397	-0.3652	-0.1379	0.4973	0.2097	0.2716	0.4761	-0.5072	0.2735	-0.3902	1.0000				
$m_{-1 mm}$ [%]	-0.0630	0.8926	0.8556	-0.9809	0.0187	-0.2998	0.9124	0.9447	0.9643	-0.9373	0.7279	0.6656	0.4245	1.0000			
$x_{50 log}$ [mm]	0.0049	-0.8565	-0.9714	0.9532	-0.2125	0.1560	-0.8359	-0.8815	-0.8335	0.9144	-0.9487	-0.6207	-0.3231	-0.8902	1.0000		
β (s-n(s)_F) sieving	-0.6288	-0.4312	-0.7610	0.7296	0.1823	-0.4688	-0.4202	-0.5099	-0.6049	0.7015	-0.9600	-0.0600	-0.7752	-0.6832	0.7534	1.0000	
α (s-n(s)_IF) sieving	0.7557	-0.0627	0.5158	-0.3239	-0.0317	0.6923	0.0840	0.1643	0.3060	-0.4406	0.5312	-0.4413	0.8910	0.2966	-0.4095	-0.8541	1.0000
LN	C_p [m/s]	q [kg/m ³]	N [-] (CT)	Std D_{cent} (CT)	Std D_{cent} (CTnp)	Ave p_c (CT)	p_{20} [mm ⁻²] (CT)	p_{21} [mm ⁻¹] (CT)	2D-frag. count (CT)	2D-frag. Std D_{cent} (CT)	C_{ave} [m/s]	Ave $r_{bh, norm}$ [mm]	Ave δr_m [mm]	$m_{-1 mm}$ [%]	$x_{50 log}$ [mm]	β (s-n(s)_F) sieving	α (s-n(s)_IF) sieving
C_p [m/s]	1.0000																
q [kg/m ³]	-0.2581	1.0000															
N [-] (CT)	0.0448	0.8429	1.0000														
Std D_{cent} (CT)	0.0401	-0.9714	-0.8625	1.0000													
Std D_{cent} (CTnp)	-0.7257	0.1140	0.2177	0.0669	1.0000												
Ave p_c (CT)	0.9612	-0.4499	-0.0853	0.2621	-0.6022	1.0000											
p_{20} [mm ⁻²] (CT)	-0.4674	0.8633	0.7260	-0.8149	0.3901	-0.6472	1.0000										
p_{21} [mm ⁻¹] (CT)	-0.3648	0.9126	0.8155	-0.8817	0.3306	-0.5517	0.9887	1.0000									
2D-frag. count (CT)	-0.2948	0.8604	0.7696	-0.8574	0.2600	-0.5005	0.9815	0.9862	1.0000								
2D-frag. Std D_{cent} (CT)	0.0814	-0.8690	-0.9319	0.8936	-0.2351	0.2631	-0.8960	-0.9456	-0.9416	1.0000							
C_{ave} [m/s]	0.1045	0.7320	0.9329	-0.7708	0.1768	0.0399	0.4233	0.5533	0.4682	-0.7480	1.0000						
Ave $r_{bh, norm}$ [mm]	-0.5974	0.8639	0.5019	-0.7469	0.1948	-0.7342	0.7287	0.7294	0.6450	-0.5429	0.5028	1.0000					
Ave δr_m [mm]	0.6521	-0.0111	0.4006	-0.1682	-0.1366	0.5783	0.1198	0.1774	0.2771	-0.4380	0.1957	-0.5023	1.0000				
$m_{-1 mm}$ [%]	-0.1557	0.9400	0.8759	-0.9552	0.1370	-0.3692	0.9321	0.9725	0.9667	-0.9723	0.6820	0.6870	0.2808	1.0000			
$x_{50 log}$ [mm]	0.0856	-0.9539	-0.9610	0.9489	-0.1517	0.2455	-0.7885	-0.8680	-0.8093	0.9143	-0.8941	-0.7095	-0.1818	-0.9219	1.0000		
β (s-n(s)_F) sieving	-0.6309	-0.5330	-0.7875	0.6928	0.3297	-0.4722	-0.3455	-0.4673	-0.4927	0.7094	-0.9719	-0.0614	-0.7231	-0.6419	0.6961	1.0000	
α (s-n(s)_IF) sieving	0.7540	0.0849	0.5408	-0.2603	-0.1937	0.6986	0.0450	0.1468	0.2020	-0.4544	0.5644	-0.4231	0.9343	0.2923	-0.3289	-0.8542	1.0000

Table 183: Correlation of results from group E, covering blast tests m20(23.1), m12(21), m6(23.2), and g6(26.1).

	C_p [m/s]	q [kg/m ³]	N [-] (CT)	Std D _{cent} (CT)	Std D _{cent} (CTnp)	p_c (HSI) slope	Ave p_c (CT)	p_{20} (HSI) slope	p_{21} (HSI) slope	p_{20} [mm ⁻²] (CT)	p_{21} [mm ⁻²] (CT)	2D-frag. count (CT)	2D-frag. Std D _{cent} (CT)	C_{ave} [m/s]	Ave $r_{bh, norm}$ [mm]	Ave δr_m [mm]	$m_{1 mm}$ [%]	x_{50} log [mm]	β (s-n(s)_F) sieving	α (s-n(s)_IF) sieving	
Linear	C_p [m/s]	q [kg/m ³]	N [-] (CT)	Std D _{cent} (CT)	Std D _{cent} (CTnp)	p_c (HSI) slope	Ave p_c (CT)	p_{20} (HSI) slope	p_{21} (HSI) slope	p_{20} [mm ⁻²] (CT)	p_{21} [mm ⁻²] (CT)	2D-frag. count (CT)	2D-frag. Std D _{cent} (CT)	C_{ave} [m/s]	Ave $r_{bh, norm}$ [mm]	Ave δr_m [mm]	$m_{1 mm}$ [%]	x_{50} log [mm]	β (s-n(s)_F) sieving	α (s-n(s)_IF) sieving	
	1.0000																				
	q [kg/m ³]	1.0000																			
	N [-] (CT)	-0.4861	1.0000																		
	Std D _{cent} (CT)	0.4052	-0.9735	-0.8866	1.0000																
	Std D _{cent} (CTnp)	-0.5027	0.1000	0.5845	-0.2394	1.0000															
	p_c (HSI) slope	-0.6445	0.9135	0.4650	-0.7991	-0.0746	1.0000														
	Ave p_c (CT)	0.9858	-0.5981	-0.3365	0.4990	-0.3892	-0.7620	1.0000													
	p_{20} (HSI) slope	0.3422	0.5152	0.7779	-0.6671	0.1438	0.1391	0.2830	1.0000												
	p_{21} (HSI) slope	-0.3387	0.9746	0.6506	-0.9259	-0.1203	0.9093	-0.4760	0.5221	1.0000											
	p_{20} [mm ⁻²] (CT)	-0.7559	0.8777	0.8333	-0.8888	0.5349	0.7887	-0.7952	0.3520	0.7492	1.0000										
	p_{21} [mm ⁻²] (CT)	-0.6965	0.9024	0.8694	-0.9231	0.5099	0.7866	-0.7433	0.4294	0.7831	0.9962	1.0000									
	2D-frag. count (CT)	-0.7448	0.8822	0.8413	-0.8956	0.5320	0.7876	-0.7854	0.3674	0.7551	0.9999	0.9975	1.0000								
	2D-frag. Std D _{cent} (CT)	0.5738	-0.8321	-0.9551	0.9068	-0.6248	-0.6300	0.6004	-0.5697	-0.6969	-0.9573	-0.9713	-0.9609	1.0000							
	C_{ave} [m/s]	0.0589	0.7073	0.9168	-0.8398	0.2861	0.3604	-0.0035	0.9579	0.6737	0.6060	0.6707	0.6191	-0.7779	1.0000						
	Ave $r_{bh, norm}$ [mm]	-0.5531	0.9760	0.6112	-0.9005	-0.0238	0.9788	-0.6748	0.3381	0.9695	0.8318	0.8451	0.8339	-0.7267	0.5427	1.0000					
	Ave δr_m [mm]	0.2478	-0.3673	0.3206	0.1520	0.7085	-0.6650	0.3743	0.3501	-0.4959	-0.0777	-0.0639	-0.0732	-0.1606	0.2735	-0.5492	1.0000				
	$m_{1 mm}$ [%]	-0.5695	0.9829	0.8397	-0.9812	0.2810	0.8712	-0.6564	0.5144	0.9173	0.9470	0.9654	0.9507	-0.9168	0.7279	0.9389	-0.2293	1.0000			
	x_{50} log [mm]	-0.2517	-0.8675	-0.9699	0.9581	-0.3741	-0.5941	0.3189	-0.8188	-0.8014	-0.8237	-0.8692	-0.8331	0.9221	-0.9487	-0.7385	-0.1210	-0.9015	1.0000		
	β (s-n(s)_F) sieving	-0.3333	-0.5137	-0.7858	0.6681	-0.1624	-0.1350	-0.2767	-0.9998	-0.5164	-0.3593	-0.4361	-0.3747	0.5785	-0.9600	-0.3345	-0.3640	-0.5164	0.8224	1.0000	
	α (s-n(s)_IF) sieving	0.5717	-0.2163	0.3979	-0.0069	0.3946	-0.5947	0.6347	0.6790	-0.2607	-0.1488	-0.0960	-0.1373	-0.1414	0.5312	-0.4211	0.8793	-0.1451	-0.2905	-0.6860	1.0000
LN	C_p [m/s]	1.0000																			
	q [kg/m ³]	-0.5114	1.0000																		
	N [-] (CT)	-0.2375	0.8387	1.0000																	
	Std D _{cent} (CT)	0.4235	-0.9946	-0.8403	1.0000																
	Std D _{cent} (CTnp)	-0.6223	0.2583	0.4771	-0.1755	1.0000															
	p_c (HSI) slope	-0.8036	0.8233	0.4163	-0.7860	0.1920	1.0000														
	Ave p_c (CT)	0.9845	-0.6089	-0.2738	0.5320	-0.5062	-0.8942	1.0000													
	p_{20} (HSI) slope	0.3396	0.5622	0.8274	-0.6190	0.0324	0.0010	0.2781	1.0000												
	p_{21} (HSI) slope	-0.3142	0.9576	0.7477	-0.9791	-0.0275	0.7690	-0.4485	0.6084	1.0000											
	p_{20} [mm ⁻²] (CT)	-0.8562	0.8563	0.6956	-0.7979	0.6335	0.8608	-0.8809	0.1934	0.6855	1.0000										
	p_{21} [mm ⁻²] (CT)	-0.7692	0.9128	0.7901	-0.8664	0.5980	0.8352	-0.8054	0.3370	0.7602	0.9887	1.0000									
	2D-frag. count (CT)	-0.8291	0.8773	0.7293	-0.8228	0.6236	0.8541	-0.8576	0.2423	0.7121	0.9987	0.9950	1.0000								
	2D-frag. Std D _{cent} (CT)	0.5736	-0.8996	-0.9319	0.8684	-0.6322	-0.6529	0.5990	-0.5713	-0.7500	-0.9066	-0.9539	-0.9249	1.0000							
	C_{ave} [m/s]	0.1045	0.7320	0.9329	-0.7708	0.1768	0.2166	0.0399	0.9707	0.7353	0.4233	0.5533	0.4682	-0.7480	1.0000						
	Ave $r_{bh, norm}$ [mm]	-0.6154	0.9494	0.6257	-0.9380	0.1167	0.9459	-0.7310	0.3162	0.9342	0.8389	0.8628	0.8488	-0.7595	0.5028	1.0000					
	Ave δr_m [mm]	0.3280	-0.3547	0.1974	0.3652	0.5278	-0.6917	0.4650	0.2828	-0.4915	-0.2279	-0.1934	-0.2164	-0.0409	0.1957	-0.6157	1.0000				
	$m_{1 mm}$ [%]	-0.6413	0.9725	0.8587	-0.9454	0.4730	0.8182	-0.7031	0.4874	0.8641	0.9423	0.9802	0.9574	-0.9644	0.6820	0.9040	-0.2247	1.0000			
	x_{50} log [mm]	0.3321	-0.9523	-0.9612	0.9571	-0.3352	-0.6170	0.4077	-0.7627	-0.8987	-0.7702	-0.8569	-0.8013	0.9354	-0.8941	-0.8090	0.0806	-0.9357	1.0000		
	β (s-n(s)_F) sieving	-0.3333	-0.5630	-0.8323	0.6187	-0.0454	-0.0006	-0.2738	-0.9999	-0.6055	-0.1994	-0.3424	-0.2481	0.5776	-0.9719	-0.3148	-0.2919	-0.4912	0.7651	1.0000	
	α (s-n(s)_IF) sieving	0.5713	-0.1099	0.4354	0.0752	0.2479	-0.6365	0.6360	0.6842	-0.1437	-0.2489	-0.1470	-0.2148	-0.1519	0.5644	-0.4133	0.8701	-0.0789	-0.1987	-0.6891	1.0000